

AD-A229 587

MATERIALS
RESEARCH
SOCIETY
SYMPOSIUM PROCEEDINGS



VOLUME 155

Processing Science of
Advanced Ceramics

EDITORS

I. A. Aksay

G. L. McVay

D. R. Ulrich

DTIC FILE COPY

DISTRIBUTION STATEMENT A

Approved for public release:
Distribution Unlimited

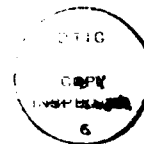
MRS

DTIC
ELECTE
NOV 15 1990
S E D

REPORT DOCUMENTATION PAGE			Form Approved OMB No. 0704-0188	
<small>Public reporting burden for this collection of information is estimated to average 1 hour per response, including the time for reviewing instructions, searching existing data sources, gathering and maintaining the data needed, and completing and reviewing the collection of information. Send comments regarding this Bureau estimate or any other aspect of this collection of information, including suggestions for reducing this burden, to Washington Headquarters Services, Directorate for Information Operations and Reports, 1215 Jefferson Davis Highway, Suite 1204, Arlington, VA 22202-4302, and to the Office of Management and Budget, Paperwork Reduction Project (0704-0188), Washington, DC 20503.</small>				
1. AGENCY USE ONLY (Leave blank)	2. REPORT DATE September 1990	3. REPORT TYPE AND DATES COVERED Final 15 Apr 89 - 14 Oct 89		
4. TITLE AND SUBTITLE The Processing Science of Advanced Ceramics		5. FUNDING NUMBERS 61102F 1203/A3		
6. AUTHOR(S) I. A. Aksay, G. L. McVay, and D. R. Ulrich				
7. PERFORMING ORGANIZATION NAME(S) AND ADDRESS(ES) Materials Research Society 9800 McKnight Road Pittsburgh, PA 15237		8. PERFORMING ORGANIZATION REPORT NUMBER		
9. SPONSORING/MONITORING AGENCY NAME(S) AND ADDRESS(ES) AFOSR/NC Building 410 Bolling AFB, DC 20332-6448		10. SPONSORING/MONITORING AGENCY REPORT NUMBER AFOSR-89-0360		
11. SUPPLEMENTARY NOTES				
12a. DISTRIBUTION/AVAILABILITY STATEMENT Approval for public release; distribution is unlimited		12b. DISTRIBUTION CODE		
13. ABSTRACT (Maximum 200 words) A symposium entitled "Processing Science of Advanced Ceramics" was organized as part of the Materials Research Society Fall Meeting held April 27-28, 1989 in San Diego, California. A total of 40 papers were presented during the symposium. The papers were arranged in the following five categories: (1) Powder Synthesis and Colloidal Processing; (2) Sol-Gel Processing and Ceramic-Polymer Composites; (3) Sol-Gel Processing of Thin Films and Electronic Ceramics; (4) Plasma-Assisted Processing and Novel Composites; (5) Fiber and Whisker-Reinforced Composites. All papers appear in their entirety in the Materials Research Society Symposium Proceedings, Volume 155, edited by Ilhan A. Aksay, Gary L. McVay, and Donald R. Ulrich, and published by the materials Research Society, Pittsburgh, PA.				
14. SUBJECT TERMS		15. NUMBER OF PAGES 387		
		16. PRICE CODE		
17. SECURITY CLASSIFICATION OF REPORT UNCLASSIFIED	18. SECURITY CLASSIFICATION OF THIS PAGE UNCLASSIFIED	19. SECURITY CLASSIFICATION OF ABSTRACT UNCLASSIFIED	20. LIMITATION OF ABSTRACT SAR	

Processing Science of Advanced Ceramics

Succession For	
RTIS GRA&I	<input checked="checked" type="checkbox"/>
ERIC TAB	<input type="checkbox"/>
Unannounced	<input type="checkbox"/>
Justification	
By	
Distribution/	
Availability Codes	
Dist	Avail and/or Special
A-1	



90 11 15 119

Processing Science of Advanced Ceramics

Symposium held April 27-28, 1989, San Diego, California, U.S.A.

EDITORS:

I. A. Aksay

University of Washington, Seattle, Washington, U.S.A.

G. L. McVay

Battelle Pacific Northwest Labs, Richland, Washington, U.S.A.

D. R. Ulrich

Air Force Office of Scientific Research, Washington, D.C., U.S.A.



MATERIALS RESEARCH SOCIETY
Pittsburgh, Pennsylvania

This work was supported by the Air Force Office of Scientific Research, Air Force Systems Command, USAF, under Grant Number AFOSR 89-0360.

This work was supported in part by the U.S. Army Research Office under Grant Number DAAL03-89-G-0024. The views, opinions, and/or findings contained in this report are those of the authors and should not be construed as an official Department of the Army position, policy, or decision unless so designated by other documentation.

CODEN: MRSPDH

Copyright 1989 by Materials Research Society.
All rights reserved.

This book has been registered with Copyright Clearance Center, Inc. For further information, please contact the Copyright Clearance Center, Salem, Massachusetts.

Published by:

Materials Research Society
9800 McKnight Road
Pittsburgh, Pennsylvania 15237
Telephone (412) 367-3003

Library of Congress Cataloging in Publication Data

Processing science of advanced ceramics : symposium held April 27-28, 1989, San Diego, California, U.S.A. / editors, I.A. Aksay, G.L. McVay, D.R. Ulrich.

p. cm. — (Materials Research Society symposium proceedings : ISSN 0272-9172 ; v. 155)

Includes bibliographical references.

ISBN 1-55899-028-3

1. Ceramics—Congresses. I. Aksay, İlhan A. II. McVay, G.L. III. Ulrich, Donald R. IV. Series.

TP786.P765 1989
666—dc20

89-13269
CIP

Manufactured in the United States of America

Contents

PREFACE	ix
ACKNOWLEDGMENTS	xi
MATERIALS RESEARCH SOCIETY SYMPOSIUM PROCEEDINGS	xii
PART I - Powder Synthesis and Colloidal Processing	
<p>* CHARACTERIZATION AND PROCESSING OF CVD POWDERS FOR FABRICATION OF COMPOSITE AND COMPOUND CERAMICS S. Hori, Y. Shigaki, Y. Hirata, M. Yoshimura, and S. Sōmiya</p>	3
<p>* PREPARATION OF SPHERICAL TITANIA PARTICLES FROM INORGANIC PRECURSOR BY HOMOGENEOUS PRECIPITATION A. Kato, Y. Takeshita, and Y. Katatae</p>	13
<p>THE EFFECTS OF ALUMINUM ALKOXIDES ON THE SYNTHESIS OF COMPOSITE POWDERS OF ALUMINA AND TITANIA M. T. Harris, C. H. Byers, and R. R. Brunson</p>	23
<p>PREPARATION AND CHARACTERIZATION OF COLLOIDAL ZnS PARTICLES A. Celikkaya and M. Akinc</p>	31
<p>THE MORPHOLOGY OF FREEZE-DRIED RUBIDIUM CHLORIDE POWDER J. K. G. Panitz, J. A. Voigt, F. A. Greulich, M. J. Carr, and M. O. Eatough</p>	37
<p>SOL-GEL PROCESSING OF ADVANCED DIELECTRIC CERAMICS FOR MICROWAVE APPLICATIONS M. Schnoeller and W. Wersing</p>	45
<p>STRUCTURAL TRANSITIONS INDUCED BY COLLOIDAL INTERACTIONS IN CERAMIC DISPERSIONS R. Rajagopalan</p>	53
<p>FLOW OF DISPERSIONS NEAR CLOSE PACKING L. Marshall and C. F. Zukoski IV</p>	65
<p>STABILITY OF A BINARY COLLOIDAL SUSPENSION AND ITS EFFECT ON COLLOIDAL PROCESSING W. Y. Shih, W.-H. Shih, J. Liu, and I. A. Aksay</p>	73
<p>MECHANICAL PROPERTIES OF COLLOIDAL GELS W.-H. Shih, J. Liu, W. Y. Shih, S. I. Kim, M. Sarikaya, and I. A. Aksay</p>	83

*Invited paper

PART II - Sol-Gel Processing and Ceramic-Polymer Composites

RHEOLOGICAL CHARACTERIZATION OF A SOL-GEL PROCESS FOR THE PREPARATION OF HIGH T_c SUPERCONDUCTORS S. A. Khan, B. G. Bagley, P. Barboux, and F. E. Torres	95
SiO_2 - TiO_2 - ZrO_2 GEL GLASSES: REACTION KINETICS AND PROPERTIES W. Beier and G. H. Frischat	103
THE FORMATION OF MOLECULAR COMPOSITES BY A MODIFIED SOL-GEL PROCESS R. B. Lessard, M. M. Wallace, W. A. Oertling, C. K. Chang, K. A. Berglund, and D. G. Nocera	109
HIGHLY EMISSIVE LANTHANIDE COMPOUNDS IN SOL-GEL DERIVED MATERIALS R. B. Lessard, K. A. Berglund, and D. G. Nocera	119
HAFNIUM METALLO-ORGANIC FILMS AND GELS PRODUCED BY SOL-GEL PROCESSING C. D. Gagliardi and K. A. Berglund	127
SOL-GEL NETWORKS: FUNDAMENTAL INVESTIGATIONS OF THE CHEMISTRY OF SOL-GEL SILICATE GLASSES AND POLY(SILOXANE) TOUGHENED SILICATES M. Spinu and J. E. McGrath	137
*CERAMIC FIBER-FLUOROPOLYMER COMPOSITES FOR ELECTRONIC PACKAGING MATERIALS J. D. Bolt	149
CERAMIC PROCESSING USING INORGANIC POLYMERS J. J. Lannutti, I. A. Aksay, and C. H. Schilling	155
CONVERSION OF ALKOXIDE SOLUTIONS TO OXIDES: EVAPORATION OF PRODUCTS R. A. Lipeles and D. J. Coleman	163
REMOVAL OF PROCESSING AIDS FROM CERAMIC/POLYMER COMPOSITES G. C. Stangle, D.-J. Rhee, and I. A. Aksay	171

PART III - Sol-Gel Processing of Thin Films and Electronic Ceramics

*PROCESSING OF CRYSTALLINE $\text{Li}(\text{Nb,Ta})\text{O}_3$ FILMS WITH PREFERRED ORIENTATION THROUGH METAL ALKOXIDES S.-I. Hirano and K. Kato	181
---	-----

*Invited paper

SINGLE CRYSTAL ZIRCONIA THIN FILMS FROM LIQUID PRECURSORS K. T. Miller and F. F. Lange	191
* TWO-DIMENSIONAL PROCESSING FOR NOVEL FUNCTIONS H. Yanagida	199
* PROCESSING AND THE MICROSTRUCTURE OF SrTiO ₃ -BASED BL CAPACITORS USING Pb(Fe,W)O ₃ FERROELECTRICS M. Kuwabara	205
 PART IV - Plasma-Assisted Processing and Novel Composites	
* PLASMA-ASSISTED CHEMICAL VAPOR DEPOSITION OF CERAMIC FILMS AND COATINGS R. F. Davis	213
BARRIERS TO THE NUCLEATION OF METHYL GROUPS ON THE DIAMOND (111) SURFACE S. M. Valone	227
PLASMA SPRAYING OF ZIRCONIA COATINGS D. J. Varacalle, Jr., G. R. Smolik, G. C. Wilson, G. Irons, and J. A. Walter	235
LASER-INDUCED MATERIALS SYNTHESIS OF ULTRAFINE CERAMIC PARTICLES FROM SPECIALLY DESIGNED MOLECULAR PRECURSORS T. D. Xiao, P. R. Strutt, and K. E. Gonsalves	247
* PROCESSING AND PROPERTIES OF NANOPHASE OXIDES J. A. Eastman, Y. X. Liao, A. Narayanasamy, and R. W. Siegel	255
TEMPERATURE MEASUREMENT FOR MICROWAVE PROCESSING OF ADVANCED CERAMICS T. T. Meek, S. S. Park, M. A. Nehls, and C. W. Kim	267
* THE EFFECT OF PROCESSING PARAMETERS ON THE GROWTH RATE AND MICROSTRUCTURE OF Al ₂ O ₃ /METAL MATRIX COMPOSITES A. S. Nagelberg	275
* RAPID OMNIDIRECTIONAL COMPACTION OF Y ₂ O ₃ -STABILIZED TETRAGONAL ZIRCONIA A. Pechenik, A. J. Pyzik, and D. R. Beaman	283
* PHOTOLITHOGRAPHY: A NEW TOOL FOR CERAMIC SCIENCE J. Rödel and A. M. Glaeser	293

*Invited paper

PART V - Fiber and Whisker-Reinforced Composites

*POWDER PROCESSING AND DENSIFICATION OF CERAMIC COMPOSITES F. F. Lange, D. C. C. Lam, and O. Sudre	309
*ZERO-SHRINKAGE WHISKER FRACTION IN CERAMIC MATRIX- CERAMIC WHISKER COMPOSITES E. A. Holm and M. J. Cima	319
PACKING AND MICROSTRUCTURE IN SYSTEMS CONTAINING ROD-LIKE PARTICLES L. A. Chick, C. Viney, and I. A. Aksay	331
*DISPERSION AND CONSOLIDATION OF THE COLLOIDAL SUSPENSION IN THE Al_2O_3 POWDER/ Si_3N_4 WHISKER SYSTEM Y. Hirata, S. Matsushita, S. Nakagama, I. Haraguchi, N. Hamada, Y. Ishihara, and S. Hori	343
*DENSIFICATION OF PARTICULATE CERAMIC COMPOSITES: THE ROLE OF HETEROGENEITIES L. C. De Jonghe and M. N. Rahaman	353
DENSIFICATION BEHAVIOR OF Al_2O_3 POWDERS CONTAINING ZrO_2 INCLUSIONS O. Sudre, D. C. C. Lam, and F. F. Lange	363
*PROCESSING OF SiC -WHISKER REINFORCED Si_3N_4 M. J. Hoffmann, A. Nagel, and G. Petzow	369
AUTHOR INDEX	381
SUBJECT INDEX	383

*Invited paper

Preface

Advanced ceramics and ceramic matrix composites play an increasingly important role in complex systems for structural, electronic, magnetic, and optical applications. This trend is expected to continue along with a specific goal to tailor composites that display spatial resolution in the micrometer and nanometer range. The fabrication techniques being used range from consolidation of submicron-sized powders to vapor phase deposition.

The papers included in this proceedings volume were presented at a symposium on "Processing Science of Advanced Ceramics" held at the Materials Research Society's Spring Meeting in San Diego, California, April 27-28, 1989. The objective of this symposium was to review the progress made in the field and to identify the remaining critical issues to be solved through innovative processing approaches to improve the properties and reliability of advanced ceramics. In addition, this symposium was intended to complement the series of MRS symposia on "Better Ceramics Through Chemistry" from a physics and engineering point of view.

Invited speakers from the United States, Japan, and Europe were asked to lead key areas with review presentations on:

- powder synthesis and colloidal processing
- sol-gel processing and ceramic/polymer composites
- sol-gel processing of thin films and electronic ceramics
- plasma-assisted processing and novel composites
- fiber and whisker-reinforced composites

Critical issues in two fundamental fabrication technologies were addressed: (1) fabrication through the consolidation of submicron-sized powders, and (2) fabrication through gas/solid processes. Both fabrication technologies emphasized structural design on a continuous scale from molecular dimensions to micrometer and macrometer levels.

Ilhan A. Aksay
Gary L. McVay
Donald R. Ulrich

Acknowledgments

We wish to thank all the symposium contributors, particularly the invited speakers, who provided excellent presentations and set the tone of the meeting. The invited speakers were:

James H. Adair	M. J. Hoffmann
John D. Bolt	Saburo Hori
Michael J. Cima	Akio Kato
Robert F. Davis	Makato Kuwabara
Lutgard C. De Jonghe	Fred F. Lange
Jeffrey A. Easman	Thomas T. Meek
Andreas M. Glaeser	Alan S. Nagelberg
Shin-Ichi Hirano	David A. Payne
Yoshihiro Hirata	Aleksander J. Pyzik
Hiroaki Yanagida	

We are indebted to our session chairmen who directed the sessions and guided the discussions. In addition to the symposium co-chairmen, these were:

James H. Adair
Robert F. Davis
Andreas M. Glaeser
Shin-Ichi Hirano
Akio Kato
Frederick F. Lange

We also wish to express special appreciation to the organizations who provided financial support:

Air Force Office of Scientific Research
Washington Technology Center
Pacific Northwest Laboratory

Special thanks are also due the peer reviewers for their conscientious review of all the manuscripts in this proceedings. We are grateful to Marie Jimenez, Pacific Northwest Laboratory, and Barbara Lalley, University of Washington, for their help in coordinating the publication of this proceedings.

MATERIALS RESEARCH SOCIETY SYMPOSIUM PROCEEDINGS

ISSN 0272 - 9172

- Volume 1—Laser and Electron-Beam Solid Interactions and Materials Processing, J. F. Gibbons, L. D. Hess, T. W. Sigmon, 1981, ISBN 0-444-00595-1
- Volume 2—Defects in Semiconductors, J. Narayan, T. Y. Tan, 1981, ISBN 0-444-07596-X
- Volume 3—Nuclear and Electron Resonance Spectroscopies Applied to Materials Science, E. N. Kaufmann, G. K. Shenoy, 1981, ISBN 0-444-00597-8
- Volume 4—Laser and Electron-Beam Interactions with Solids, B. R. Appleton, G. K. Celler, 1982, ISBN 0-444-00693-1
- Volume 5—Grain Boundaries in Semiconductors, H. J. Leamy, G. E. Pike, C. H. Seager, 1982, ISBN 0-444-00697-4
- Volume 6—Scientific Basis for Nuclear Waste Management IV, S. V. Topp, 1982, ISBN 0-444-00699-0
- Volume 7—Metastable Materials Formation by Ion Implantation, S. T. Picraux, W. J. Choyke, 1982, ISBN 0-444-00692-3
- Volume 8—Rapidly Solidified Amorphous and Crystalline Alloys, B. H. Kear, B. C. Giessen, M. Cohen, 1982, ISBN 0-444-00698-2
- Volume 9—Materials Processing in the Reduced Gravity Environment of Space, G. E. Rindone, 1982, ISBN 0-444-00691-5
- Volume 10—Thin Films and Interfaces, P. S. Ho, K.-N. Tu, 1982, ISBN 0-444-00774-1
- Volume 11—Scientific Basis for Nuclear Waste Management V, W. Lutze, 1982, ISBN 0-444-00725-3
- Volume 12—In Situ Composites IV, F. D. Lemkey, H. E. Cline, M. McLean, 1982, ISBN 0-444-00726-1
- Volume 13—Laser-Solid Interactions and Transient Thermal Processing of Materials, J. Narayan, W. L. Brown, R. A. Lemons, 1983, ISBN 0-444-00788-1
- Volume 14—Defects in Semiconductors II, S. Mahajan, J. W. Corbett, 1983, ISBN 0-444-00812-8
- Volume 15—Scientific Basis for Nuclear Waste Management VI, D. G. Brookins, 1983, ISBN 0-444-00780-6
- Volume 16—Nuclear Radiation Detector Materials, E. E. Haller, H. W. Kraner, W. A. Higginbotham, 1983, ISBN 0-444-00787-3
- Volume 17—Laser Diagnostics and Photochemical Processing for Semiconductor Devices, R. M. Osgood, S. R. J. Brueck, H. R. Schlossberg, 1983, ISBN 0-444-00782-2
- Volume 18—Interfaces and Contacts, R. Ludeke, K. Rose, 1983, ISBN 0-444-00820-9
- Volume 19—Alloy Phase Diagrams, L. H. Bennett, T. B. Massalski, B. C. Giessen, 1983, ISBN 0-444-00809-8
- Volume 20—Intercalated Graphite, M. S. Dresselhaus, G. Dresselhaus, J. E. Fischer, M. J. Moran, 1983, ISBN 0-444-00781-4
- Volume 21—Phase Transformations in Solids, T. Tsakalakos, 1984, ISBN 0-444-00901-9
- Volume 22—High Pressure in Science and Technology, C. Homan, R. K. MacCrone, E. Whalley, 1984, ISBN 0-444-00932-9 (3 part set)
- Volume 23—Energy Beam-Solid Interactions and Transient Thermal Processing, J. C. C. Fan, N. M. Johnson, 1984, ISBN 0-444-00903-5
- Volume 24—Defect Properties and Processing of High-Technology Nonmetallic Materials, J. H. Crawford, Jr., Y. Chen, W. A. Sibley, 1984, ISBN 0-444-00904-3
- Volume 25—Thin Films and Interfaces II, J. E. E. Baglin, D. R. Campbell, W. K. Chu, 1984, ISBN 0-444-00905-1

MATERIALS RESEARCH SOCIETY SYMPOSIUM PROCEEDINGS

- Volume 26—Scientific Basis for Nuclear Waste Management VII, G. L. McVay, 1984, ISBN 0-444-00906-X
- Volume 27—Ion Implantation and Ion Beam Processing of Materials, G. K. Hubler, O. W. Holland, C. R. Clayton, C. W. White, 1984, ISBN 0-444-00869-1
- Volume 28—Rapidly Solidified Metastable Materials, B. H. Kear, B. C. Giessen, 1984, ISBN 0-444-00935-3
- Volume 29—Laser-Controlled Chemical Processing of Surfaces, A. W. Johnson, D. J. Ehrlich, H. R. Schiessberg, 1984, ISBN 0-444-00894-2
- Volume 30—Plasma Processing and Synthesis of Materials, J. Szekeley, D. Apelian, 1984, ISBN 0-444-00895-0
- Volume 31—Electron Microscopy of Materials, W. Krakow, D. A. Smith, L. W. Hobbs, 1984, ISBN 0-444-00898-7
- Volume 32—Better Ceramics Through Chemistry, C. J. Brinker, D. E. Clark, D. R. Ulrich, 1984, ISBN 0-444-00898-5
- Volume 33—Comparison of Thin Film Transistor and SOI Technologies, H. W. Lam, M. J. Thompson, 1984, ISBN 0-444-00899-3
- Volume 34—Physical Metallurgy of Cast Iron, H. Fredriksson, M. Hillerts, 1985, ISBN 0-444-00938-8
- Volume 35—Energy Beam-Solid Interactions and Transient Thermal Processing/1984, D. K. Biegelsen, G. A. Rozgonyi, C. V. Shank, 1985, ISBN 0-931837-00-6
- Volume 36—Impurity Diffusion and Gettering in Silicon, R. B. Fair, C. W. Pearce, J. Washburn, 1985, ISBN 0-931837-01-4
- Volume 37—Layered Structures, Epitaxy, and Interfaces, J. M. Gibson, L. R. Dawson, 1985, ISBN 0-931837-02-2
- Volume 38—Plasma Synthesis and Etching of Electronic Materials, R. P. H. Chang, B. Abeles, 1985, ISBN 0-931837-03-0
- Volume 39—High-Temperature Ordered Intermetallic Alloys, C. C. Koch, C. T. Liu, N. S. Stoloff, 1985, ISBN 0-931837-04-9
- Volume 40—Electronic Packaging Materials Science, E. A. Giess, K.-N. Tu, D. R. Uhlmann, 1985, ISBN 0-931837-05-7
- Volume 41—Advanced Photon and Particle Techniques for the Characterization of Defects in Solids, J. B. Roberto, R. W. Carpenter, M. C. Wittels, 1985, ISBN 0-931837-06-5
- Volume 42—Very High Strength Cement-Based Materials, J. F. Young, 1985, ISBN 0-931837-07-3
- Volume 43—Fly Ash and Coal Conversion By-Products: Characterization, Utilization, and Disposal I, G. J. McCarthy, R. J. Lauf, 1985, ISBN 0-931837-08-1
- Volume 44—Scientific Basis for Nuclear Waste Management VIII, C. M. Jantzen, J. A. Stone, R. C. Ewing, 1985, ISBN 0-931837-09-X
- Volume 45—Ion Beam Processes in Advanced Electronic Materials and Device Technology, B. R. Appleton, F. H. Eisen, T. W. Sigmon, 1985, ISBN 0-931837-10-3
- Volume 46—Microscopic Identification of Electronic Defects in Semiconductors, N. M. Johnson, S. G. Bishop, G. D. Watkins, 1985, ISBN 0-931837-11-1
- Volume 47—Thin Films: The Relationship of Structure to Properties, C. R. Aita, K. S. SreeHarsha, 1985, ISBN 0-931837-12-X
- Volume 48—Applied Materials Characterization, W. Katz, P. Williams, 1985, ISBN 0-931837-13-8
- Volume 49—Materials Issues in Applications of Amorphous Silicon Technology, D. Adler, A. Madan, M. J. Thompson, 1985, ISBN 0-931837-14-6

MATERIALS RESEARCH SOCIETY SYMPOSIUM PROCEEDINGS

- Volume 50—Scientific Basis for Nuclear Waste Management IX, L. O. Werme, 1986, ISBN 0-931837-15-4
- Volume 51—Beam-Solid Interactions and Phase Transformations, H. Kurz, G. L. Olson, J. M. Poate, 1986, ISBN 0-931837-16-2
- Volume 52—Rapid Thermal Processing, T. O. Sedgwick, T. E. Seidel, B.-Y. Tsaur, 1986, ISBN 0-931837-17-0
- Volume 53—Semiconductor-on-Insulator and Thin Film Transistor Technology, A. Chiang, M. W. Geis, L. Pfeiffer, 1986, ISBN 0-931837-18-9
- Volume 54—Thin Films—Interfaces and Phenomena, R. J. Nemanich, P. S. Ho, S. S. Lau, 1986, ISBN 0-931837-19-7
- Volume 55—Biomedical Materials, J. M. Williams, M. F. Nichols, W. Zingg, 1986, ISBN 0-931837-20-0
- Volume 56—Layered Structures and Epitaxy, J. M. Gibson, G. C. Osbourn, R. M. Tromp, 1986, ISBN 0-931837-21-9
- Volume 57—Phase Transitions in Condensed Systems—Experiments and Theory, G. S. Cargill III, F. Spaepen, K.-N. Tu, 1987, ISBN 0-931837-22-7
- Volume 58—Rapidly Solidified Alloys and Their Mechanical and Magnetic Properties, B. C. Giessen, D. E. Polk, A. I. Taub, 1986, ISBN 0-931837-23-5
- Volume 59—Oxygen, Carbon, Hydrogen, and Nitrogen in Crystalline Silicon, J. C. Mikkelsen, Jr., S. J. Pearton, J. W. Corbett, S. J. Pennycook, 1986, ISBN 0-931837-24-3
- Volume 60—Defect Properties and Processing of High-Technology Nonmetallic Materials, Y. Chen, W. D. Kingery, R. J. Stokes, 1986, ISBN 0-931837-25-1
- Volume 61—Defects in Glasses, F. L. Galeener, D. L. Griscom, M. J. Weber, 1986, ISBN 0-931837-26-X
- Volume 62—Materials Problem Solving with the Transmission Electron Microscope, L. W. Hobbs, K. H. Westmacott, D. B. Williams, 1986, ISBN 0-931837-27-8
- Volume 63—Computer-Based Microscopic Description of the Structure and Properties of Materials, J. Broughton, W. Krakow, S. T. Pantelides, 1986, ISBN 0-931837-28-6
- Volume 64—Cement-Based Composites: Strain Rate Effects on Fracture, S. Mindess, S. P. Shah, 1986, ISBN 0-931837-29-4
- Volume 65—Fly Ash and Coal Conversion By-Products: Characterization, Utilization and Disposal II, G. J. McCarthy, F. P. Glasser, D. M. Roy, 1986, ISBN 0-931837-30-8
- Volume 66—Frontiers in Materials Education, L. W. Hobbs, G. L. Liedl, 1986, ISBN 0-931837-31-6
- Volume 67—Heteroepitaxy on Silicon, J. C. C. Fan, J. M. Poate, 1986, ISBN 0-931837-33-2
- Volume 68—Plasma Processing, J. W. Coburn, R. A. Gottscho, D. W. Hess, 1986, ISBN 0-931837-34-0
- Volume 69—Materials Characterization, N. W. Cheung, M.-A. Nicolet, 1986, ISBN 0-931837-35-9
- Volume 70—Materials Issues in Amorphous-Semiconductor Technology, D. Adler, Y. Hamakawa, A. Madan, 1986, ISBN 0-931837-36-7
- Volume 71—Materials Issues in Silicon Integrated Circuit Processing, M. Wittmer, J. Stimmell, M. Strathman, 1986, ISBN 0-931837-37-5
- Volume 72—Electronic Packaging Materials Science II, K. A. Jackson, R. C. Pohanka, D. R. Uhlmann, D. R. Ulrich, 1986, ISBN 0-931837-38-3
- Volume 73—Better Ceramics Through Chemistry II, C. J. Brinker, D. E. Clark, D. R. Ulrich, 1986, ISBN 0-931837-39-1
- Volume 74—Beam-Solid Interactions and Transient Processes, M. O. Thompson, S. T. Picraux, J. S. Williams, 1987, ISBN 0-931837-40-5

MATERIALS RESEARCH SOCIETY SYMPOSIUM PROCEEDINGS

- Volume 75—Photon, Beam and Plasma Stimulated Chemical Processes at Surfaces, V. M. Donnelly, I. P. Herman, M. Hirose, 1987, ISBN 0-931837-41-3
- Volume 76—Science and Technology of Microfabrication, R. E. Howard, E. L. Hu, S. Namba, S. Pang, 1987, ISBN 0-931837-42-1
- Volume 77—Interfaces, Superlattices, and Thin Films, J. D. Dow, I. K. Schuller, 1987, ISBN 0-931837-56-1
- Volume 78—Advances in Structural Ceramics, P. F. Becher, M. V. Swain, S. Sōmiya, 1987, ISBN 0-931837-43-X
- Volume 79—Scattering, Deformation and Fracture in Polymers, G. D. Wignall, B. Crist, T. P. Russell, E. L. Thomas, 1987, ISBN 0-931837-44-6
- Volume 80—Science and Technology of Rapidly Quenched Alloys, M. Tenhover, W. L. Johnson, L. E. Tanner, 1987, ISBN 0-931837-45-6
- Volume 81—High-Temperature Ordered Intermetallic Alloys, II, N. S. Stoloff, C. C. Koch, C. T. Liu, O. Izumi, 1987, ISBN 0-931837-46-4
- Volume 82—Characterization of Defects in Materials, R. W. Siegel, J. R. Weertman, R. Sinclair, 1987, ISBN 0-931837-47-2
- Volume 83—Physical and Chemical Properties of Thin Metal Overlayers and Alloy Surfaces, D. M. Zehner, D. W. Goodman, 1987, ISBN 0-931837-48-0
- Volume 84—Scientific Basis for Nuclear Waste Management X, J. K. Bates, W. B. Seefeldt, 1987, ISBN 0-931837-49-9
- Volume 85—Microstructural Development During the Hydration of Cement, L. Struble, P. Brown, 1987, ISBN 0-931837-50-2
- Volume 86—Fly Ash and Coal Conversion By-Products Characterization, Utilization and Disposal III, G. J. McCarthy, F. P. Glasser, D. M. Roy, S. Diamond, 1987, ISBN 0-931837-51-0
- Volume 87—Materials Processing in the Reduced Gravity Environment of Space, R. H. Doremus, P. C. Nordine, 1987, ISBN 0-931837-52-9
- Volume 88—Optical Fiber Materials and Properties, S. R. Nagel, J. W. Fleming, G. Sigel, D. A. Thompson, 1987, ISBN 0-931837-53-7
- Volume 89—Diluted Magnetic (Semimagnetic) Semiconductors, R. L. Aggarwal, J. K. Furdyna, S. von Molnar, 1987, ISBN 0-931837-54-5
- Volume 90—Materials for Infrared Detectors and Sources, R. F. C. Farrow, J. F. Schetzina, J. T. Cheung, 1987, ISBN 0-931837-55-3
- Volume 91—Heteroepitaxy on Silicon II, J. C. C. Fan, J. M. Phillips, B.-Y. Tsaur, 1987, ISBN 0-931837-58-8
- Volume 92—Rapid Thermal Processing of Electronic Materials, S. R. Wilson, R. A. Powell, D. E. Davies, 1987, ISBN 0-931837-59-6
- Volume 93—Materials Modification and Growth Using Ion Beams, U. Gibson, A. E. White, P. P. Pronko, 1987, ISBN 0-931837-60-X
- Volume 94—Initial Stages of Epitaxial Growth, R. Hull, J. M. Gibson, David A. Smith, 1987, ISBN 0-931837-61-8
- Volume 95—Amorphous Silicon Semiconductors—Pure and Hydrogenated, A. Madan, M. Thompson, D. Adler, Y. Hamakawa, 1987, ISBN 0-931837-62-6
- Volume 96—Permanent Magnet Materials, S. G. Sankar, J. F. Herbst, N. C. Koon, 1987, ISBN 0-931837-63-4
- Volume 97—Novel Refractory Semiconductors, D. Emin, T. Aselage, C. Wood, 1987, ISBN 0-931837-64-2
- Volume 98—Plasma Processing and Synthesis of Materials, D. Apelian, J. Szekely, 1987, ISBN 0-931837-65-0

MATERIALS RESEARCH SOCIETY SYMPOSIUM PROCEEDINGS

- Volume 99—High-Temperature Superconductors, M. B. Brodsky, R. C. Dynes, K. Kitazawa, H. L. Tuller, 1988, ISBN 0-931837-67-7
- Volume 100—Fundamentals of Beam-Solid Interactions and Transient Thermal Processing, M. J. Aziz, L. E. Rehn, B. Stritzker, 1988, ISBN 0-931837-68-5
- Volume 101—Laser and Particle-Beam Chemical Processing for Microelectronics, D.J. Ehrlich, G.S. Higashi, M.M. Oprysko, 1988, ISBN 0-931837-69-3
- Volume 102—Epitaxy of Semiconductor Layered Structures, R. T. Tung, L. R. Dawson, R. L. Gunshor, 1988, ISBN 0-931837-70-7
- Volume 103—Multilayers: Synthesis, Properties, and Nonelectronic Applications, T. W. Barbee Jr., F. Spaepen, L. Greer, 1988, ISBN 0-931837-71-5
- Volume 104—Defects in Electronic Materials, M. Stavola, S. J. Pearton, G. Davies, 1988, ISBN 0-931837-72-3
- Volume 105—SiO₂ and Its Interfaces, G. Lucovsky, S. T. Pantelides, 1988, ISBN 0-931837-73-1
- Volume 106—Polysilicon Films and Interfaces, C.Y. Wong, C.V. Thompson, K-N. Tu, 1988, ISBN 0-931837-74-X
- Volume 107—Silicon-on-Insulator and Buried Metals in Semiconductors, J. C. Sturm, C. K. Chen, L. Pfeiffer, P. L. F. Hemment, 1988, ISBN 0-931837-75-8
- Volume 108—Electronic Packaging Materials Science II, R. C. Sundahl, R. Jaccodine, K. A. Jackson, 1988, ISBN 0-931837-76-6
- Volume 109—Nonlinear Optical Properties of Polymers, A. J. Heeger, J. Orenstein, D. R. Ulrich, 1988, ISBN 0-931837-77-4
- Volume 110—Biomedical Materials and Devices, J. S. Hanker, B. L. Giammara, 1988, ISBN 0-931837-78-2
- Volume 111—Microstructure and Properties of Catalysts, M. M. J. Treacy, J. M. Thomas, J. M. White, 1988, ISBN 0-931837-79-0
- Volume 112—Scientific Basis for Nuclear Waste Management XI, M. J. Apted, R. E. Westerman, 1988, ISBN 0-931837-80-4
- Volume 113—Fly Ash and Coal Conversion By-Products: Characterization, Utilization, and Disposal IV, G. J. McCarthy, D. M. Roy, F. P. Glasser, R. T. Hemmings, 1988, ISBN 0-931837-81-2
- Volume 114—Bonding in Cementitious Composites, S. Mindess, S. P. Shah, 1988, ISBN 0-931837-82-0
- Volume 115—Specimen Preparation for Transmission Electron Microscopy of Materials, J. C. Bravman, R. Anderson, M. L. McDonald, 1988, ISBN 0-931837-83-9
- Volume 116—Heteroepitaxy on Silicon: Fundamentals, Structures, and Devices, H.K. Choi, H. Ishiware, R. Hull, R.J. Nemanich, 1988, ISBN: 0-931837-86-3
- Volume 117—Process Diagnostics: Materials, Combustion, Fusion, K. Hays, A.C. Eckbreth, G.A. Campbell, 1988, ISBN: 0-931837-87-1
- Volume 118—Amorphous Silicon Technology, A. Madan, M.J. Thompson, P.C. Taylor, P.G. LeComber, Y. Hamakawa, 1988, ISBN: 0-931837-88-X
- Volume 119—Adhesion in Solids, D.M. Mattox, C. Batich, J.E.E. Baglin, R.J. Gottschall, 1988, ISBN: 0-931837-89-8
- Volume 120—High-Temperature/High-Performance Composites, F.D. Lemkey, A.G. Evans, S.G. Fishman, J.R. Strife, 1988, ISBN: 0-931837-90-1
- Volume 121—Better Ceramics Through Chemistry III, C.J. Brinker, D.E. Clark, D.R. Ulrich, 1988, ISBN: 0-931837-91-X
- Volume 122—Interfacial Structure, Properties, and Design, M.H. Yoo, W.A.T. Clark, C.L. Briant, 1988, ISBN: 0-931837-92-8

MATERIALS RESEARCH SOCIETY SYMPOSIUM PROCEEDINGS

- Volume 123—Materials Issues in Art and Archaeology, E.V. Sayre, P. Vandiver, J. Druzik, C. Stevenson, 1988, ISBN: 0-931837-93-6
- Volume 124—Microwave-Processing of Materials, M.H. Brooks, I.J. Chabinsky, W.H. Sutton, 1988, ISBN: 0-931837-94-4
- Volume 125—Materials Stability and Environmental Degradation, A. Barkatt, L.R. Smith, E. Verink, 1988, ISBN: 0-931837-95-2
- Volume 126—Advanced Surface Processes for Optoelectronics, S. Bernasek, T. Venkatesan, H. Temkin, 1988, ISBN: 0-931837-96-0
- Volume 127—Scientific Basis for Nuclear Waste Management XII, W. Lutze, R.C. Ewing, 1989, ISBN: 0-931837-97-9
- Volume 128—Processing and Characterization of Materials Using Ion Beams, L.E. Rehn, J. Greene, F.A. Smidt, 1989, ISBN: 1-55899-001-1
- Volume 129—Laser and Particle-Beam Chemical Processes on Surfaces, G.L. Loper, A.W. Johnson, T.W. Sigmon, 1989, ISBN: 1-55899-002-X
- Volume 130—Thin Films: Stresses and Mechanical Properties, J.C. Bravman, W.D. Nix, D.M. Barnett, D.A. Smith, 1989, ISBN: 0-55899-003-8
- Volume 131—Chemical Perspectives of Microelectronic Materials, M.E. Gross, J. Jasinski, J.T. Yates, Jr., 1989, ISBN: 0-55899-004-6
- Volume 132—Multicomponent Ultrafine Microstructures, L.E. McCandlish, B.H. Kear, D.E. Polk, and R.W. Siegel, 1989, ISBN: 1-55899-005-4
- Volume 133—High Temperature Ordered Intermetallic Alloys III, C.T. Liu, A.I. Taub, N.S. Stoloff, C.C. Koch, 1989, ISBN: 1-55899-006-2
- Volume 134—The Materials Science and Engineering of Rigid-Rod Polymers, W.W. Adams, R.K. Eby, D.E. McLemore, 1989, ISBN: 1-55899-007-0
- Volume 135—Solid State Ionics, G. Nazri, R.A. Huggins, D.F. Shriver, 1989, ISBN: 1-55899-008-9
- Volume 136—Fly Ash and Coal Conversion By-Products: Characterization, Utilization, and Disposal V, R.T. Hemmings, E.E. Berry, G.J. McCarthy, F.P. Glasser, 1989, ISBN: 1-55899-009-7
- Volume 137—Pore Structure and Permeability of Cementitious Materials, L.R. Roberts, J.P. Skalny, 1989, ISBN: 1-55899-010-0
- Volume 138—Characterization of the Structure and Chemistry of Defects in Materials, B.C. Larson, M. Ruhle, D.N. Seidman, 1989, ISBN: 1-55899-011-9
- Volume 139—High Resolution Microscopy of Materials, W. Krakow, F.A. Ponce, D.J. Smith, 1989, ISBN: 1-55899-012-7
- Volume 140—New Materials Approaches to Tribology: Theory and Applications, L.E. Pope, L. Fehrenbacher, W.O. Winer, 1989, ISBN: 1-55899-013-5
- Volume 141—Atomic Scale Calculations in Materials Science, J. Tersoff, D. Vanderbilt, V. Vitek, 1989, ISBN: 1-55899-014-3
- Volume 142—Nondestructive Monitoring of Materials Properties, J. Holbrook, J. Bussiere, 1989, ISBN: 1-55899-015-1
- Volume 143—Synchrotron Radiation in Materials Research, R. Clarke, J.H. Weaver, J. Gland, 1989, ISBN: 1-55899-016-X
- Volume 144—Advances in Materials, Processing and Devices in III-V Compound Semiconductors, D.K. Sadana, L. Eastman, R. Dupuis, 1989, ISBN: 1-55899-017-8
- Volume 145—III-V Heterostructures for Electronic/Photonic Devices, C.W. Tu, A.C. Gossard, V.D. Mittera, 1989, ISBN: 1-55899-018-6

MATERIALS RESEARCH SOCIETY SYMPOSIUM PROCEEDINGS

- Volume 146—Rapid Thermal Annealing/Chemical Vapor Deposition and Integrated Processing, D. Hodul, T.E. Seidel, J. Gelpey, M.L. Green, 1989, ISBN: 1-55899-019-4
- Volume 147—Ion Beam Processing of Advanced Electronic Materials, N. Cheung, J. Roberto, A. Marwick, 1989, ISBN: 1-55899-020-8
- Volume 148—Chemistry and Defects in Semiconductor Heterostructures, M. Kawabe, E.R. Weber, T.D. Sands, R.S. Williams, 1989, ISBN: 1-55899-021-6
- Volume 149—Amorphous Silicon Technology-1989, A. Madan, M.J. Thompson, P.C. Taylor, Y. Hamakawa, P.G. LeComber, 1989, ISBN: 1-55899-022-4
- Volume 150—Materials for Magneto-Optic Data Storage, T. Suzuki, C. Falco, C. Robinson, 1989, ISBN: 1-55899-023-2
- Volume 151—Growth, Characterization and Properties of Ultrathin Magnetic Films and Multilayers, B.T. Jonker, J.P. Heremans, E.E. Marinero, 1989, ISBN: 1-55899-024-0
- Volume 152—Optical Materials: Processing and Science, D.B. Poker, C. Ortiz, 1989, ISBN: 1-55899-025-9
- Volume 153—Interfaces Between Polymers, Metals, and Ceramics, B.M. DeKoven, R. Rosenberg, A.J. Gellman, 1989, ISBN: 1-55899-026-7
- Volume 154—Electronic Packaging Materials Science IV, K.A. Jackson, R.C. Sundahl, R. Jaccodine, E.D. Lilley, 1989, ISBN: 1-55899-027-5
- Volume 155—Processing Science of Advanced Ceramics, I.A. Aksay, G.L. McVay, D.R. Ulrich, 1989, ISBN: 1-55899-028-3
- Volume 156—High Temperature Superconductors: Relationships Between Properties, Structure and Solid-State Chemistry, J.B. Torrance, K. Kitazawa, J.M. Tarascon, J.R. Jorgensen, M. Thompson, 1989, ISBN: 1-55899-029-1

MATERIALS RESEARCH SOCIETY CONFERENCE PROCEEDINGS

Tungsten and Other Refractory Metals for VLSI Applications, R. S. Blewer, 1986;
ISSN 0886-7860; ISBN 0-931837-32-4

Tungsten and Other Refractory Metals for VLSI Applications II, E.K. Broadbent, 1987;
ISSN 0886-7860; ISBN 0-931837-66-9

Ternary and Multinary Compounds, S. Deb, A. Zunger, 1987; ISBN 0-931837-57-x

Tungsten and Other Refractory Metals for VLSI Applications III, Victor A. Wells, 1988;
ISSN 0886-7860; ISBN 0-931837-84-7

Atomic and Molecular Processing of Electronic and Ceramic Materials: Preparation,
Characterization and Properties, Ilhan A. Aksay, Gary L. McVay, Thomas G. Stoebe,
1988; ISBN 0-931837-85-5

Materials Futures: Strategies and Opportunities, R. Byron Pipes, U.S. Organizing Com-
mittee, Rune Lagneborg, Swedish Organizing Committee, 1988; ISBN 0-55899-000-3

Tungsten and Other Refractory Metals for VLSI Applications IV, Robert S. Blewer,
Carol M. McConica, 1989; ISSN: 0886-7860; ISBN: 0-931837-98-7

PART I

**Powder Synthesis and
Colloidal Processing**

CHARACTERIZATION AND PROCESSING OF CVD POWDERS FOR FABRICATION OF COMPOSITE AND COMPOUND CERAMICS

SABURO HORI*, YOSHIKI SHIGAKI*, YOSHIHIRO HIRATA**, MASAHIRO YOSHIMURA***
AND SHIGEYUKI SŌMIYA***

* Kureha Chemical Industry Co., Ltd., 3-25-1 Hyakunincho, Shinjuku-Ku,
Tokyo 169, Japan

** Kagoshima University, 1-21-40 Korimoto, Kagoshima 890, Japan

*** Research Laboratory of Engineering Materials, Tokyo Institute of
Technology, 4259 Nagatsuta, Midori-Ku, Yokohama 227, Japan

ABSTRACT

Two-component oxide powders were prepared in the systems $\text{Al}_2\text{O}_3\text{-ZrO}_2$, $\text{Al}_2\text{O}_3\text{-TiO}_2$, and $\text{Al}_2\text{O}_3\text{-SiO}_2$ by a CVD (chemical vapor deposition) technique using a combustion flame for the purpose of fabricating respective composite or compound ceramics. The CVD powders were spherical and ultrafine (av. 30-70 nm) with log-normal size distribution, and exhibited either very homogeneous or nanoheterogeneous structure and crystallographic metastability in phases and solid solutions. By starting from these CVD powders, not only uniform and excellent microstructure was achieved in the sintered products, but also better sinterability and novel microstructure became possible owing to the metastability which reflected the formation mechanism of two-component powders at high temperatures. CVD powders, which were previously considered difficult to sinter, proved to be excellent starting materials for fabrication of composite and compound ceramics when improved processing techniques were applied.

INTRODUCTION

As the increasing demand for advanced ceramic materials cannot necessarily be satisfied by single-component ceramics, various kinds of composite and compound ceramics are being developed to meet the many different demands. In such multi-component composite or compound ceramics, uniformity (homogeneity or submicron-scale heterogeneity) is very important but usually difficult to achieve by starting from mechanically mixed powders. Therefore, various chemical mixing techniques are being applied to prepare powders for multi-component (mostly two-component) ceramics.

In the past, most chemically-mixed powders were prepared via liquid phase by sol-gel techniques. Even though it has long been known that chemical uniformity can be achieved in two-component powders more readily by chemical vapor deposition (CVD) techniques and that various two-component CVD powders were produced by several groups (including McPherson and co-workers [1] and Kato and co-workers [2]), CVD powders have not been considered appropriate as starting materials for two-component composite or compound ceramics because of the difficulty in achieving dense and uniform compaction.

With improved processing techniques, the present authors demonstrated that CVD powders could be processed without serious agglomeration and that they were excellent starting materials for two-component ceramics [3-10]. The CVD powders possessed not only chemical uniformity resulting in uniform microstructure, but also exhibited some metastability which often resulted in superior sinterability or in unique microstructural development.

This paper summarizes the authors' efforts with some additional data

in utilizing the two-component CVD powders in the systems $\text{Al}_2\text{O}_3\text{-ZrO}_2$, $\text{Al}_2\text{O}_3\text{-TiO}_2$, and $\text{Al}_2\text{O}_3\text{-SiO}_2$ as the starting materials for fabrication of composite and compound ceramics. Table I briefly indicates the compositions and phases of these powders and the ceramics sintered from them in this study. Detailed discussion in this paper will clarify the significance of microstructural control from powder level in nanometer scale.

Table I. Two-component ceramics in this study

System (range studied)	Detected Phases in Powder	Sintered Product
$\text{Al}_2\text{O}_3\text{-ZrO}_2$ (0-30 wt% ZrO_2)	$\delta\text{-Al}_2\text{O}_3$, tetragonal ZrO_2	ZrO_2 -Toughened Al_2O_3 (ZTA)
$\text{Al}_2\text{O}_3\text{-TiO}_2$ (47-73 wt% Al_2O_3)	$\gamma\text{-Al}_2\text{O}_3$, rutile TiO_2	Al_2TiO_5 + excess component (sintered at $\geq 1300^\circ\text{C}$) Corundum-Rutile Composite (sintered at $< 1280^\circ\text{C}$)
$\text{Al}_2\text{O}_3\text{-SiO}_2$ (65-80 wt% Al_2O_3)	amorphous + $\gamma\text{-Al}_2\text{O}_3$	Mullite + excess component

CVD POWDER PREPARATION

Fig. 1 shows the schematic flow diagram of the CVD method using combustion flame to produce $\text{Al}_2\text{O}_3\text{-ZrO}_2$ composite powders from chloride precursors [5,10]. The vapor mixture of the chlorides was fed into the flame and oxidized at the mixing zone temperature of $1600\text{-}1800^\circ\text{C}$ and quenched at the reactor outlet after 60-90 ms of residence time. For $\text{Al}_2\text{O}_3\text{-TiO}_2$ and $\text{Al}_2\text{O}_3\text{-SiO}_2$ powders, the apparatus was essentially the same with minor modifications [9-11].

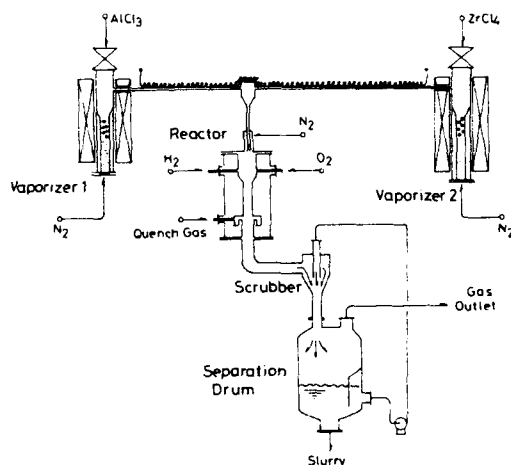


Fig. 1. Schematic flow diagram of CVD $\text{Al}_2\text{O}_3\text{-ZrO}_2$ powder preparation.

Fig. 2 shows a typical transmission electron micrograph (TEM) of $\text{Al}_2\text{O}_3\text{-ZrO}_2$ powder. The powder exhibited almost spherical but slightly faceted shape. The particle size distribution was log-normal, which is typical for powders produced by CVD techniques, and the average size was 30 nm. The $\text{Al}_2\text{O}_3\text{-TiO}_2$ and $\text{Al}_2\text{O}_3\text{-SiO}_2$ composite powders exhibited similar morphologies but were larger and barely faceted.

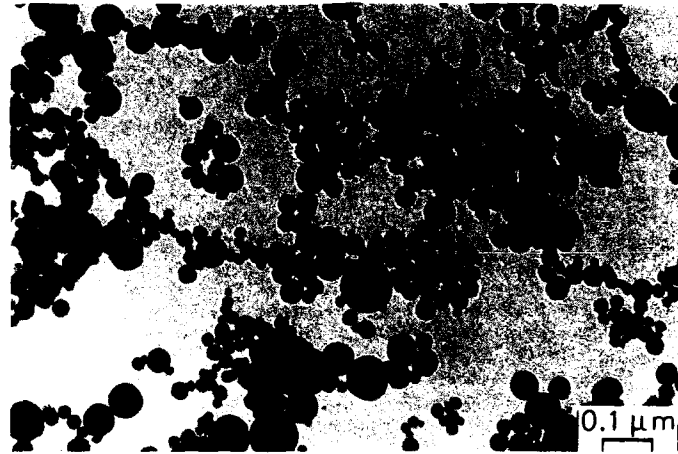


Fig. 2. Typical CVD $\text{Al}_2\text{O}_3\text{-ZrO}_2$ powder (15 wt% ZrO_2).

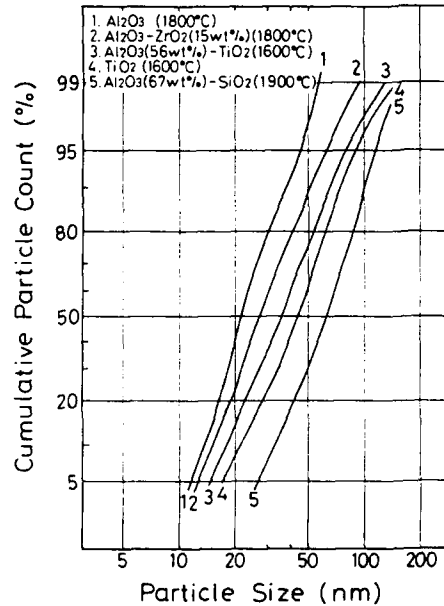


Fig. 3. Particle size distributions of various composite powders in this study. The temperature in parentheses is the peak temperature in the reactor for the experiment.

Fig. 3 indicates that the particle sizes varied with the composition. The Al_2O_3 and $\text{Al}_2\text{O}_3\text{-ZrO}_2$ powders were relatively small while the TiO_2 and $\text{Al}_2\text{O}_3\text{-TiO}_2$ were large. This difference can be explained by the theory that the particle growth was controlled mostly by the collision and was strongly influenced by the sticking coefficient [12].

CVD powders in previous studies were usually too small in size and/or poor in crystallinity to be processed properly. A few improvements were made to increase the particle size and to improve the crystallinity, such as the relatively long distance between the precursor injection nozzle and the hydrogen/oxygen nozzles to reduce the nucleation density at the first stage of reaction, and the refractory wall to keep the reactor temperature high for relatively long periods of time.

The phase composition of the composite powders reflected the particle formation scheme during the high-temperature vapor phase reaction, which often resulted in metastable phases and solid solutions. The formation of these metastable phases can be explained by Ostwald's step rule and the nucleation argument. Phases deposited from vapor often take metastable forms because the rearrangement of crystalline structure to the stable form is usually a slow process. In two-component systems, the phase composition is more complicated because the stability of a phase is influenced by the other phase. The phase boundary and the solid solution (which is often metastable) have strong influences in determining the phase and phase stability.

Detailed discussions concerning the formation of metastable phases in these two-component powders were given elsewhere [5,9-11,13]. Here the metastabilities and the nanostructures found in these composite powders are briefly described.

The $\text{Al}_2\text{O}_3\text{-ZrO}_2$ composite powder consisted of $\delta\text{-Al}_2\text{O}_3$ and tetragonal ZrO_2 , while the stable phases are $\alpha\text{-Al}_2\text{O}_3$ and monoclinic ZrO_2 , respectively. It was suggested that the small tetragonal ZrO_2 crystallites (8-15 nm) were dispersed in each of the Al_2O_3 particles [5, 10, 13].

The $\text{Al}_2\text{O}_3\text{-TiO}_2$ composite powder consisted mostly of $\gamma\text{-Al}_2\text{O}_3$ and rutile TiO_2 . The metastable solid solutions of Al_2O_3 into TiO_2 and TiO_2 into Al_2O_3 appeared to influence the preference and stability of phases [11].

The $\text{Al}_2\text{O}_3\text{-SiO}_2$ composite powder consisted of amorphous premullite as the major phase and $\gamma\text{-Al}_2\text{O}_3$ metastably containing SiO_2 as the minor phase. Both the amorphous phase and SiO_2 -containing $\gamma\text{-Al}_2\text{O}_3$ formed mullite between 900 and 1000°C. The phase composition probably reflects the metastable sub-liquidus region at ~1900°C between liquid and metastable $\gamma\text{-Al}_2\text{O}_3$ [9].

COMPOSITE AND COMPOUND CERAMICS PREPARED FROM CVD POWDERS

ZrO₂-Toughened Al₂O₃

By starting from CVD $\text{Al}_2\text{O}_3\text{-ZrO}_2$ composite powders, excellent ZrO_2 dispersion in Al_2O_3 was achieved. Fig. 4 compares the microstructure of ZrO_2 -toughened Al_2O_3 (ZTA) sintered from the CVD composite powder with that of a commercial ZTA. The ZrO_2 particles were dispersed much more uniformly, and the Al_2O_3 grains were smaller in the ZTA sintered from CVD powder than in the commercial ZTA from mechanically-mixed powders.

With this excellent ZrO_2 dispersion, high bending strength was expected because the uniform ZrO_2 dispersion reduces the Al_2O_3 grain sizes and also because more ZrO_2 can be added in tetragonal symmetry and toughen the matrix without making the flaw size much larger. But the strengths

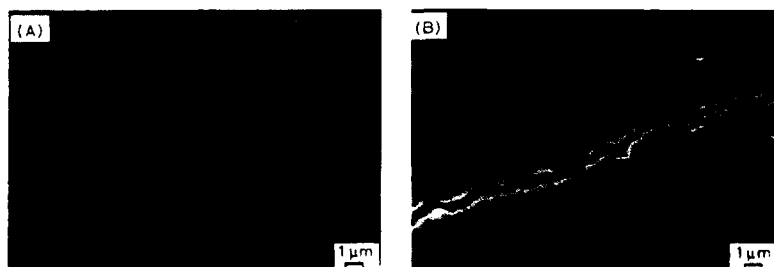


Fig. 4. Comparison of ZTA microstructures: (A) commercial ZTA, (B) ZTA from CVD Al_2O_3 - ZrO_2 powder, both containing $\sim 5\text{wt}\%$ ZrO_2 . The cracks were introduced by Vickers indentation.

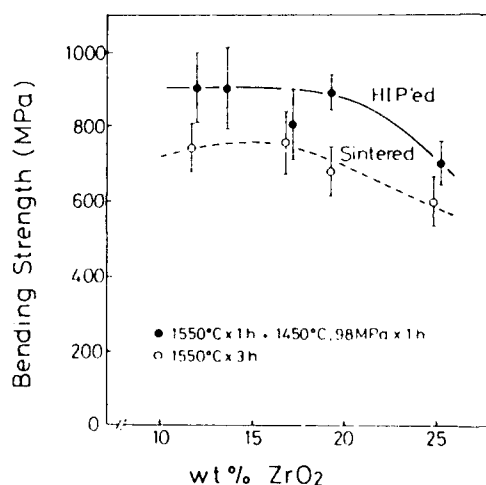


Fig. 5. Bending strength of ZTA prepared from CVD Al_2O_3 - ZrO_2 powders. These values have been obtained recently by improving the processing. Compare with ref. 13. Also note that the specimens were annealed to remove surface compressive stress before the bend tests.

actually achieved previously with the ZTA from CVD Al_2O_3 - ZrO_2 powders were not very impressive even though they are noticeably higher than those sintered from mechanically-mixed powders [4,14]. These ultrafine powders were prone to agglomerate and difficult to sinter uniformly, which often resulted in large flaws when they were sintered. By changing the powder processing, especially by revising the drying method for suppressing the agglomeration, the strength has been improved as shown in Fig. 5. High strength was achieved over a wide range of composition. The maximum bending strength of sintered ZTA reached 770 MPa at 17 wt% ZrO_2 . The value is probably the highest among the previously reported ZTA's prepared by pressureless sintering without addition of MgO nor Y_2O_3 . The strength of HIP'ed ZTA in Fig. 5 is still lower than those reported by Rühle et al. [15] probably because the combination of pre-sintering and HIP post-sintering was not optimized in this study.

Aluminum Titanate and Corundum-Rutile Composite

From CVD $\text{Al}_2\text{O}_3\text{-TiO}_2$ powders, two kinds of ceramics were prepared: one consisting mostly of aluminum titanate (Al_2TiO_5) and the other consisting of corundum and rutile. The former is known as a low thermal expansion material, and the latter is a novel material exhibiting crack deflection toughening due to the plate-shaped corundum grains.

The Al_2TiO_5 ceramics sintered from the CVD $\text{Al}_2\text{O}_3\text{-TiO}_2$ powders exhibited dense and large-grained structure with excess component (Al_2O_3 or TiO_2) uniformly dispersed on the grain boundaries. These dispersed particles strengthened the ceramics with little increase in thermal expansion [6, 7].

The $\text{Al}_2\text{O}_3\text{-TiO}_2$ powders can be sintered at low temperatures. Fig. 6 shows the densification behaviors of some of the $\text{Al}_2\text{O}_3\text{-TiO}_2$ powders. The powder compacts exhibited significant shrinkage between 1100° and 1300°C. With some sintering aids such as Na compounds, not only the densification was further accelerated but also a unique microstructure developed [8]. Fig. 7 shows the microstructural change of a corundum-rutile composite by extending the sintering time at 1250°C. Apparently a liquid was formed and the corundum grains grew by an Ostwald ripening in preferential directions such as to form anisotropic plate shapes. The plate-shaped grains could toughen the ceramics by crack deflection. In a typical case, as shown in Fig. 8, the toughness increased from 3 to 6 $\text{MPa}\cdot\sqrt{\text{m}}$, but the strength was unchanged at ~450 MPa with the development of plate-shaped grains. This unique microstructure was possible because the powder could be densified at very low temperatures below 1280°C without forming Al_2TiO_5 and also because the powder contained some metastability which led to the nucleation of the plate-shaped corundum grains [8].

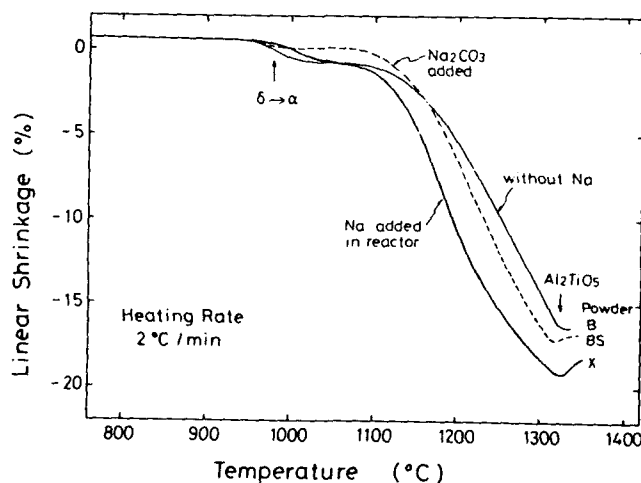


Fig. 6. Densification behaviors of CVD $\text{Al}_2\text{O}_3\text{-TiO}_2$ powder compacts with and without Na addition. Sample B: 56 wt% Al_2O_3 , balance TiO_2 ; Sample BS: Na_2CO_3 added to B (0.16 wt%); X: 53 wt% Al_2O_3 , Na added in the CVD reactor (0.12 wt%).

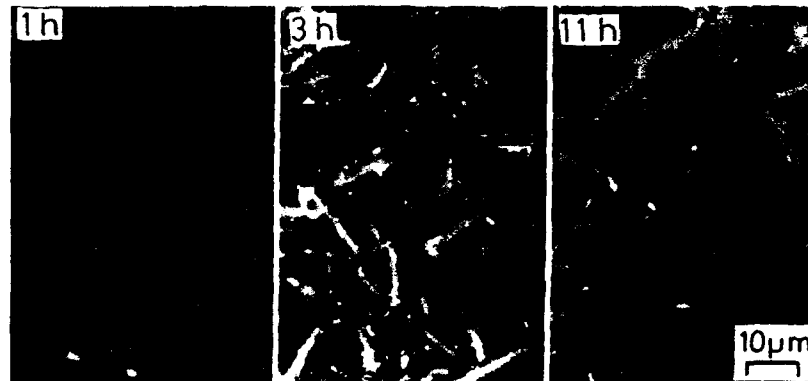


Fig. 7. Microstructural development of a corundum-rutile composite with extension of sintering time at 1250°C. Sample X; 53 wt% Al_2O_3 , balance TiO_2 and 0.12 wt% Na. The pictures were taken by SEM back-scattered electron image reverse mode. Those appearing white in the micrographs were corundum grains whose shapes were actually thin hexagonal plates.

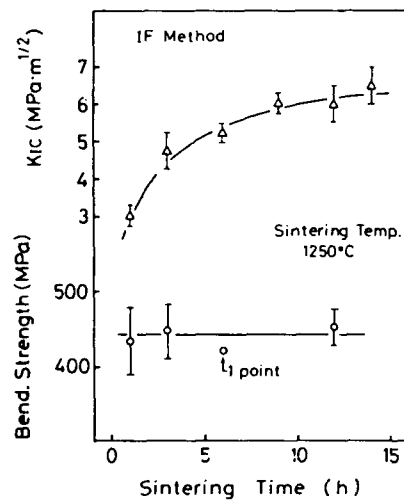


Fig. 8. Dependence of mechanical properties of a corundum-rutile composite (sample X) on sintering time at 1250°C.

Mullite

The techniques of fabricating high performance mullite ceramics can be categorized into two groups, depending on whether the powder is mullitized during sintering or before sintering by calcination. High-strength mullite ceramics have recently been fabricated from calcined and mullitized powders by several researchers [16-18]. The processings to use amorphous premullite powders or nanoheterogeneous Al_2O_3 - SiO_2 composite powders and to mullitize during sintering, though the densification could

be achieved at lower temperatures, could not achieve high strength because the microstructure was not uniform. It was thought that the problems in using premullite powders without calcination could be solved if the powders were chemically homogeneous.

The CVD Al_2O_3 - SiO_2 powders contained some heterogeneity in phase composition (amorphous premullite and SiO_2 -containing γ - Al_2O_3) but were probably much better in chemical homogeneity than the previously reported premullite powders as indicated by the DTA mullitization peaks at 900-1000°C. As the remaining glass phase was little after the mullitization, the densification behavior of the Al_2O_3 - SiO_2 powders was not very good but rather similar to the mullitized/milled powders. But as the particle sizes were smaller, the CVD powders could be sintered to nearly full density at 1600°C for 2 h from the compacts prepared by cold isostatic pressing and at 1550°C from the compacts by a colloidal technique [9, 19, 20]. The sintering temperatures are 50-100°C lower than those of the mullitized/milled powders.

Because of the lower sintering temperature and the chemical uniformity, a uniform fine-grained microstructure with little glass phase was achieved, especially in the compositional range where mullite and corundum are expected to coexist. Table II indicates semiquantitatively the amount of glass phase remaining in the sintered mullite and mullite-corundum ceramics. When the sintering temperature was low, very little glass formed even with the stoichiometrical mullite composition. With higher temperatures, the amount of glass increased.

One of the possible reasons for higher glass content at higher sintering temperatures is the kinetics of how the Al and Si atoms are mixed in the starting powders and rearranged during the sintering [21]. As the the CVD Al_2O_3 - SiO_2 powders crystallize to Al-rich mullite and gradually change to the stoichiometrical mullite [9], the sintering schedule has a significant effect on the phase composition. Another possible reason for the higher glass content at higher temperature is that the solid solution range of mullite at high temperatures shifts toward Al_2O_3 -rich region as Prochazka et al. suggested [22]. At present, it is not appropriate to draw any conclusion from very limited data.

The bending strengths of the mullite ceramics from CVD powders were excellent because of the uniform and fine-grained microstructure. With the stoichiometric mullite composition, the strength was almost the same as those reported by Kanzaki et al. [16, 17] and Ismail et al. [18]. But in the compositional range containing 76-80 wt% Al_2O_3 with the balance being SiO_2 , the bending strengths were 430-480 MPa [9]. This high strength

Table II. Semiquantitative analysis of remaining glass phase content in mullite obtained by dipping the samples into HF solution

composition wt% Al_2O_3	sintering conditions		
	1600°C x 2 h	1650°C x 2 h	1650°C x 4 h
67.2	0.13	0.20	-
71.2	0	0.16	0.13
76.5	0	0.07	0.08
79.0	0	0	-

Note 1) % weight loss after dipping in 2 wt% HF water solution at room temperature for 18 h.

2) Sample size: 3 x 3 x 10 mm³.

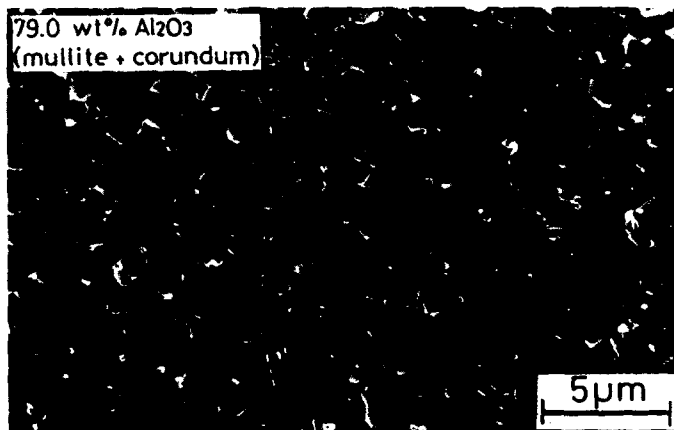


Fig. 9. Typical microstructure of mullite-corundum composite sintered at 1600°C for 2 h from CVD $\text{Al}_2\text{O}_3\text{-SiO}_2$ powder (composition, 79 wt% Al_2O_3).

can be attributed to the dense and fine-grained microstructure. Fig. 9 shows the microstructure of 79 wt% Al_2O_3 composition sintered at 1600°C for 2 h, which consisted of fine mullite (appearing dark) and corundum (appearing white) grains.

CONCLUSIONS

The possibility of utilizing two-component CVD powders for fabricating composite and compound ceramics was investigated in the systems $\text{Al}_2\text{O}_3\text{-ZrO}_2$, $\text{Al}_2\text{O}_3\text{-TiO}_2$, and $\text{Al}_2\text{O}_3\text{-SiO}_2$.

The powders were ultrafine and spherical, and exhibited either very homogeneous or nanoheterogeneous structure and metastable phases and solid solutions. These nanometer-scale structures and metastabilities reflected the powder formation mechanisms at high temperatures. It will be important to study further how these structures are formed and how they can be controlled to meet the requirements of sinterable powders.

The chemical uniformity of these CVD powders resulted in uniform microstructures and excellent mechanical properties of the sintered products. The $\text{Al}_2\text{O}_3\text{-TiO}_2$ powders exhibited some other advantages such as very good sinterability and a novel microstructure. These advantages, uniformity, sinterability and unique microstructures, are difficult to achieve by conventional techniques.

Since the CVD powders were not investigated extensively as the starting materials for advanced ceramics, it is believed that there is a wide unexplored area where multi-component CVD powders can be used to fabricate composite and compound ceramics with excellent properties or of novel microstructures and functions.

REFERENCES

1. R. McPherson, in Proceedings of the International Round Table on Study and Application of Transport Phenomena in Thermal Plasmas, edited by C. Bonet (IUPAC/CNRS, Odeillo, 1975).

2. A. Kato, Bull. Ceram. Soc. Japan 13, 625 (1978).
3. S. Hori, M. Yoshimura, S. Sōmiya and R. Takahashi, in Advances in Ceramics 12, edited by N. Claussen, M. Rühle and A.H. Heuer (The American Ceramic Society, Columbus, OH, 1984), pp. 794-805.
4. S. Hori, M. Yoshimura, S. Sōmiya, R. Kurita and H. Kaji, J. Mater. Sci. Letters 4, 413 (1985).
5. S. Hori, R. Kurita, H. Kaji, M. Yoshimura and S. Sōmiya, in Fundamental Structural Ceramics, edited by S. Sōmiya and R.C. Bradt (Terra Scientific Publishing Company, Tokyo, 1987), pp. 123-34.
6. S. Hori, R. Kurita, M. Yoshimura and S. Sōmiya, Int. J. High Tech. Ceram. 1, 59 (1985).
7. S. Hori, M. Yoshimura and S. Sōmiya, in MRS Symposia Proceedings 60, edited by Y. Chen, W.D. Kingery and R.J. Stokes (Materials Research Society, Pittsburgh, 1986), pp. 87-94.
8. S. Hori, H. Kaji, M. Yoshimura and S. Sōmiya, in MRS Symposia Proceedings 78, edited by P.F. Becher, M.V. Swain and S. Sōmiya (Materials Research Society, Pittsburgh, 1987), pp. 283-288.
9. S. Hori and R. Kurita, To appear in Proceedings of the 1st International Workshop on Mullite (as one volume of the Advances in Ceramics Series, The American Ceramic Society, Columbus, OH).
10. S. Hori, Dissertation, Tokyo Institute of Technology, 1987; the same content, Two-Component Oxide Ceramics from CVD Powders, published by Uchida Rokakuho, Tokyo, 1988.
11. S. Hori, Y. Ishii, M. Yoshimura and S. Sōmiya, Yogyo-Kyokai-Shi 94, 400 (1986).
12. G.D. Ulrich, Combust. Sci. Technol. 4, 47 (1971).
13. S. Hori, Nenshou-Kenkyu (Combustion Research), 80, 42 (1989).
14. S. Hori, M. Yoshimura and S. Sōmiya, J. Am. Ceram. Soc. 69, 169 (1986).
15. M. Rühle, N. Claussen and A.H. Heuer, J. Am. Ceram. Soc. 69, 195 (1986).
16. S. Kanzaki, H. Tabata, T. Kumazawa and S. Ohta, J. Am. Ceram. Soc. 68, C-6 (1985).
17. S. Kanzaki, T. Kumazawa, J. Asami, O. Abe and H. Tabata, Yogyo-Kyokai-Shi 93, 407 (1985).
18. M.G.M.U. Ismail, Z. Nakai and S. Sōmiya, J. Am. Ceram. Soc. 70, C-7 (1987).
19. Y. Hirata and I.A. Aksay, in Proceedings of the 22nd University Conference on Ceramics and the International Materials Symposium, edited by J.A. Pask and A.G. Evans (Plenum Press, 1987), pp. 611-22.
20. Y. Hirata, I.A. Aksay, R. Kurita, S. Hori and H. Kaji, To appear in Proceedings of the 1st International Workshop on Mullite (as one volume of the Advances in Ceramics Series, The American Ceramic Society, Columbus, OH).
21. J.A. Pask, X.W. Zhang, A.P. Tomsia and B.E. Yoldas, J. Am. Ceram. Soc. 70, 704 (1987).
22. S. Prochazka and F.J. Klug, J. Am. Ceram. Soc. 66, 874 (1983).

PREPARATION OF SPHERICAL TITANIA PARTICLES
FROM
INORGANIC PRECURSOR BY HOMOGENEOUS PRECIPITATION

A. KATO, Y. TAKESHITA AND Y. KATATAE
Kyushu University, Faculty of Engineering, Fukuoka, 812, Japan

ABSTRACT

Spherical titania particles can be prepared in a short time period from an aqueous solution of TiOSO_4 by homogeneous precipitation using urea at 70-90°C. Although the hydrolysis of TiOSO_4 continues to a considerable extent even in the absence of urea, the presence of urea is essential for the formation of spherical particles. The average particle size produced was 1-4 μm and changed mainly with the concentration of TiOSO_4 . As-synthesized powders are amorphous hydrates of titania containing sulfate group and crystallize by calcination into anatase (>500°C) and rutile (>900°C). In calcination, the particles shrink, but hold their original spherical shapes.

INTRODUCTION

In recent years, oxide powders consisting of fine spherical or equiaxed particles having a narrow size distribution which are in a nonagglomerated or unaggregated state are receiving increased attention as raw materials for ceramics. There are many studies on the preparation and sintering property of such oxide powders. Most of them have used metal alkoxides as the precursors.

On TiO_2 , Barringer and Bowen[1] synthesized the mono-dispersed TiO_2 particles by controlled hydrolysis of alcoholic solution of $\text{Ti}(\text{OC}_2\text{H}_5)_4$ or $\text{Ti}(\text{i-OC}_3\text{H}_7)_4$ and showed that this powder gave sintered body with a fine-grained microstructure and high density at a low sintering temperature. Following this work, the preparation of monodispersed TiO_2 particles from titanium alkoxides[2,3] and their thermal properties[4] were studied.

As the precursor of monodispersed oxide particles, however, inorganic compounds may be more economical than alkoxides. Matijevic et al.[5] have extensively studied the formation of monodispersed colloidal metal hydroxide by hydrolysis of metal salts in aqueous solutions. In 1976, Matijevic et al. produced monodispersed TiO_2 particles (1-4 μm in diameter) by aging highly acidic solutions of TiCl_4 at 98°C, which also contain Na_2SO_4 [6]. However, this method is very slow since aging continued for days.

In the present work, the homogeneous precipitation method using urea was used for the formation of titania particles by the hydrolysis of TiOSO_4 in the aqueous solution. This method can produce spherical TiO_2 particles with a relatively narrow size distribution in a short time period.

EXPERIMENTAL

Titanium oxysulfate from Mitsuwa's Pure Chemicals and urea from Wako Pure Chemical Industries were used as-recieved. For

each experiment, the reacting solution was prepared by dissolving urea and $\text{TiOSO}_4 \cdot n\text{H}_2\text{O}$ in distilled water below 10°C . It took 3-7 hr to dissolve TiOSO_4 completely. The solution was passed through filter paper twice immediately before use.

A flask containing the reacting solution (200ml) was set in the hot water bath kept at a given temperature. The flask was connected to a gas burette through a condenser. During the reaction, the solution was stirred by a magnetic stirrer. The pH and temperature of solution as well as the volume of CO_2 gas evolved by hydrolysis of urea, $(\text{NH}_2)_2\text{CO} + \text{H}_2\text{O} \rightarrow 2\text{NH}_3 + \text{CO}_2$, was measured during the reaction. After the reaction for a given time, the precipitate was centrifuged. To wash the precipitate, the centrifugation was repeated for several times by adding distilled water and applying ultrasonic agitation. The precipitate was dried at 80°C for 2-6 hr under reduced pressure and was ground lightly with agate mortar. The powders were characterized by XRD, TG and SEM. The specific surface area was measured by BET method at 77°K .

RESULTS AND DISCUSSION

The reaction products obtained under the present conditions were amorphous hydrated titania containing the sulfate group, $\text{TiO}_2 \cdot x\text{H}_2\text{O} \cdot y\text{SO}_3$, and consisted of either spherical particles 1-4 μm in size or agglomerated of fine particles. The present study was done mainly to find the reaction conditions which give spherical titania particles with narrow size distribution.

Reaction conditions and properties of powder product

The reaction conditions and results with a fixed holding time (30 min) are summarized in Table I. Heating reacting solution in a flask up to a given reaction temperature took 5-7 min for 70°C and 8-13 min for 90°C . In the course of the heating, the formation of the precipitate, milky turbidity, was observed at around 50°C . SEM photographs of powder products in all these runs are shown in Fig. 1. The mean particle size was obtained by measuring over 100-200 particles.

Urea gave a remarkable effect on the morphology of powder products. In the absence of urea (Run G), the product consists of agglomerated fine precipitates. This was also observed on the product at 70°C . In the presence of urea, on the other hand, the products consist of spherical or nearly spherical particles. The particle size increases with increase in the concentration of TiOSO_4 (Runs A, B and C). When $[\text{TiOSO}_4] = 0.5 \text{ mol/l}$, some coalescences of particles takes place. The concentration of urea in the range examined gave little effect on the morphology of products (Runs H, B and I). The effect of reaction temperature on particle-size distribution is shown in Fig. 2. The particle size shows a tendency to decrease with increasing reaction temperatures (Runs O, P and B). The narrowest particle-size distribution was obtained at 70°C .

Yield of titania

The yields of titania are plotted against reaction time in Fig. 3. Yield is based on the content of TiO_2 in the

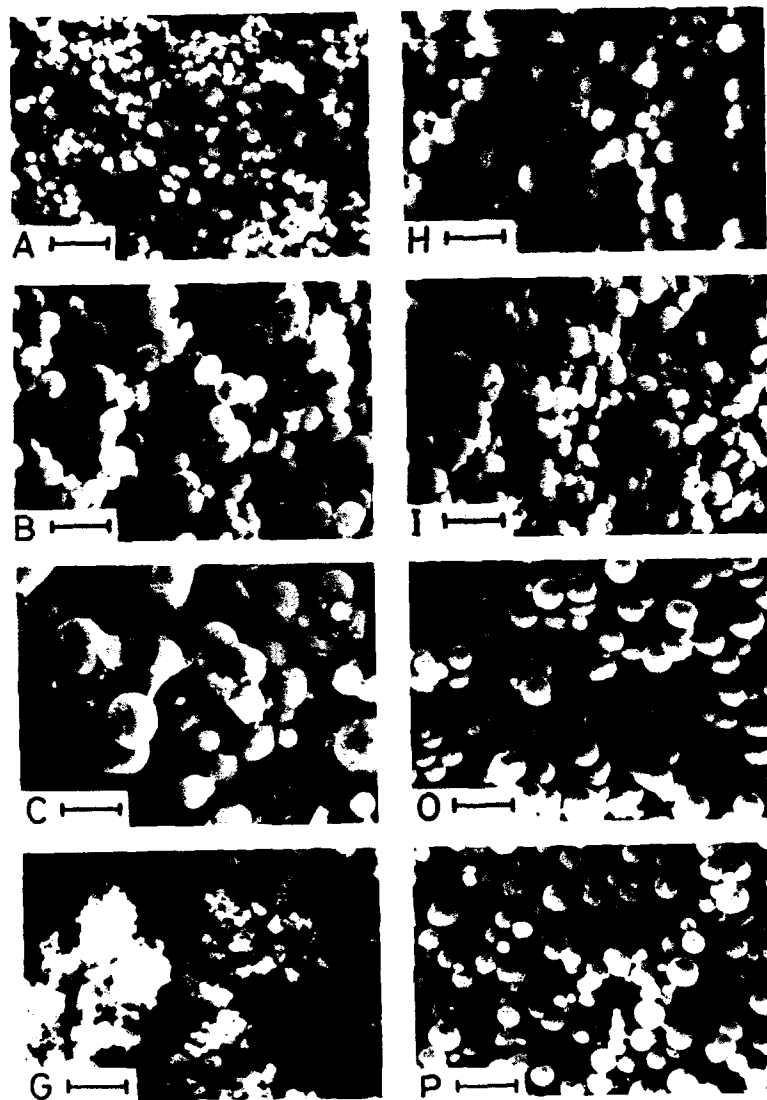


Fig. 1. As-synthesized particles. Reaction conditions are given in Table I. Marker = 5 μ m.

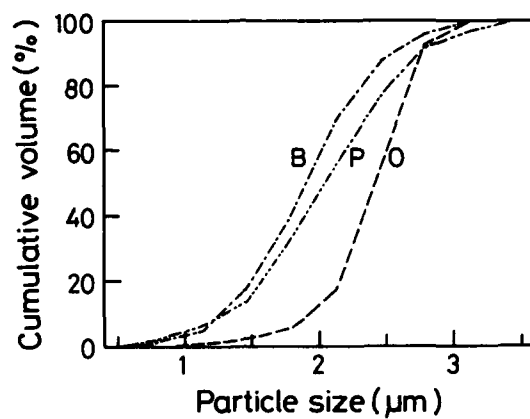


Fig. 2. Effect of reaction temperature on particle-size distribution. Reaction conditions are given in Table I.

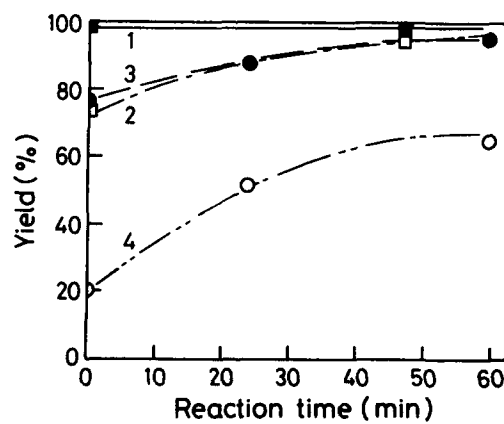


Fig. 3. Yield of titania as a function of reaction time.

No.	Reaction temp. (°C)	[TiOSO ₄] (mol/l)	[urea] (mol/l)
1	90	0.1	1.8
2	90	0.1	0
3	70	0.1	1.8
4	70	0.1	0

Table I. Reaction conditions and results.

Run	Reaction Conditions ^{a)}				Results	
	TiOSO ₄ (mol/l)	(NH ₂) ₂ CO (mol/l)	Reaction Temp. (°C)	Beginning of milky turbidity (°C)	CO ₂ evolved (ml) ^{b)}	Particle size (μm) D ₅₀ ^{c)}
A	0.05	1.8	90	53	700	0.9
B	0.1	1.8	90	50	650	2.0
C	0.5	1.8	90	50	650	4.1
G	0.1	0	90	87	0	-
H	0.1	0.9	90	58	310	1.9
I	0.1	4.0	90	64	1590	1.4
O	0.1	1.8	70	45	25	2.5
P	0.1	1.8	80	50	200	1.8

a) Holding time at reaction temperature was 30 min.

b) Values for 1 l of reacting solution. Equivalent amount of CO₂ for 0.1 mol TiOSO₄ is 2450 ml according to:
 $\text{TiOSO}_4 + (\text{NH}_2)_2\text{CO} + 2\text{H}_2\text{O} = \text{TiO}_2 + (\text{NH}_4)_2\text{SO}_4 + \text{CO}_2$

c) D₅₀ is the volume-mean diameter.

precipitate obtained. The reaction time is defined as the holding time after the reacting solution reached the reaction temperature. The pH of the solution (urea = 1.8 mol/l) was constant at 2.0 over 0-60 min at 70°C. At 90°C, on the other hand, pH (urea = 1.8 mol/l) changed as follows: 1.8(0 min), 1.5(10 min), 2.0(30 min), 3.0(50 min) and 6.0(60 min). At 70°C, the presence of urea increases the yield of the precipitate remarkably, although the hydrolysis of urea, $(\text{NH}_2)_2\text{CO} + \text{H}_2\text{O} \rightarrow 2\text{NH}_3 + \text{CO}_2$, was negligible at the early stage. In addition, the temperature at which the precipitates appear shifts to a higher temperature when urea is absent (Run G in Table I). These data indicate that urea accelerates the hydrolysis of TiOSO₄ for a reason other than the hydrolysis of urea itself.

Precipitation in heating process of reacting solution

As seen in Fig. 3, the precipitation proceeds to a large extent in the course of heating the reacting solution. In the presence of urea, the precipitation is brought to near completion during heating up to 90°C. Therefore, the yields of precipitate and morphology of particles were observed in the course of the heating process. The yields are shown in Fig. 4. In the course of heating, the first precipitation was observed at 50°C. The yields at 50°C in Fig. 4 are much higher than at 70°C in the absence of urea in Fig. 3, indicating the accelerating action of urea for the precipitation.

Photographs of particles produced in the course of "70°C" are shown in Fig. 5. Their particle-size distributions are shown in Fig. 6. The early precipitate 1 (15 sec after the appearance of precipitate) has a wide particle-size distribution. The distribution becomes narrower with the time elapsed or with the progress of precipitation. The yields of precipitate are 56 % at point 1 and 95 % at point 4. When no new nucleation occurs and remaining TiOSO₄ is consumed only for the

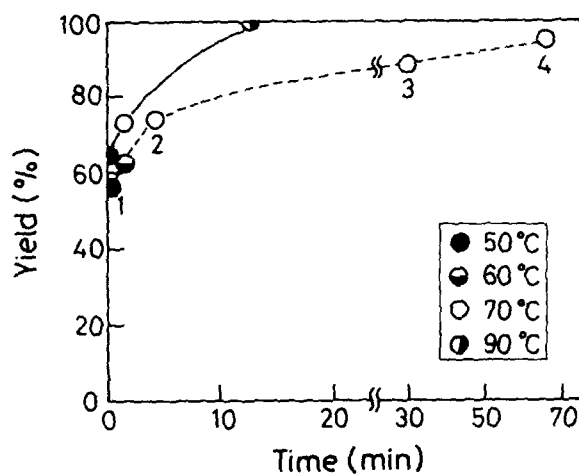


Fig. 4. Yield of titania at several temperatures in heating process. Time shows the time elapsed after the start of precipitation at $\sim 50^\circ\text{C}$.
 $[\text{TiOSO}_4] = 0.1 \text{ mol/l}$, $[\text{urea}] = 1.8 \text{ mol/l}$.

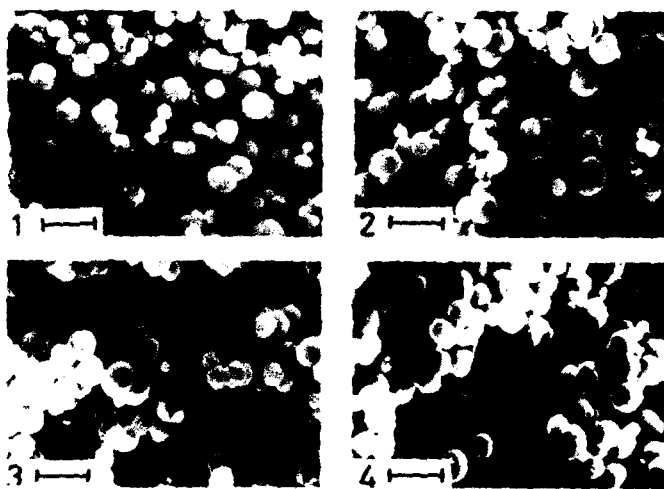


Fig. 5. Titania particles in the course of reaction. Number's are the same as in Fig. 4.

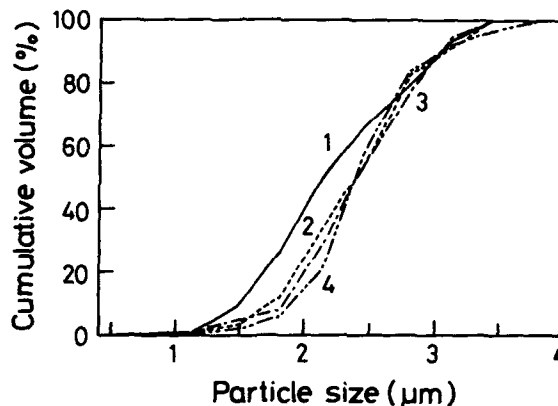


Fig. 6. Change of particle-size distribution in the course of reaction. Number's are the same as in Fig. 4.

growth of particles present after point 1, the particle size may increase by 1.2 times because the size is proportional to the cubic root of the yield, i.e., $(95/56)^{1/3} = 1.2$. This assumption appears to agree with the observation.

Thermal decomposition of as-synthesized titania

As mentioned above, the composition of as-synthesized titania can be represented as $\text{TiO}_2 \cdot x\text{H}_2\text{O} \cdot y\text{SO}_3$. The TG curve of as-synthesized powder is illustrated in Fig. 7. The weight

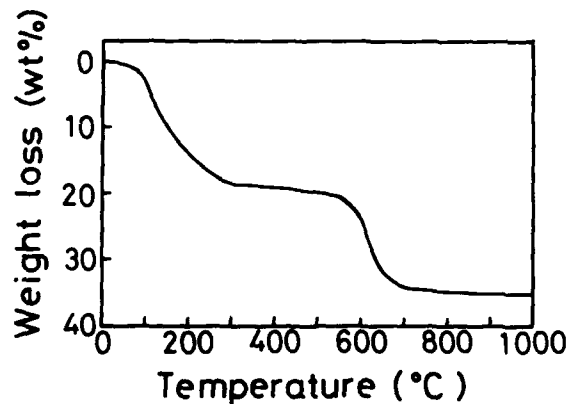


Fig. 7. TG of as-synthesized product in air. Heating rate = $10^\circ\text{C}/\text{min}$, sample = product of Run O given in Table I.

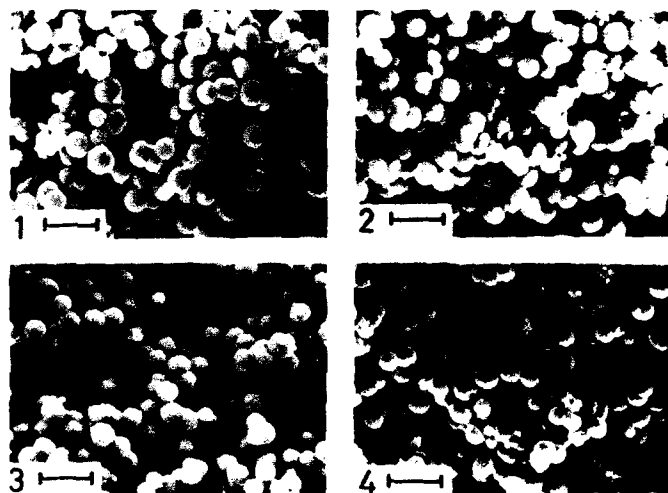


Fig. 8. Calcined particles. Original powders are the product of Run O in Table I. Calcination = 1 hr at 500°C(1), 600°C(2), 800°C(3) and 1000°C(4). Marker = 5 μ m.

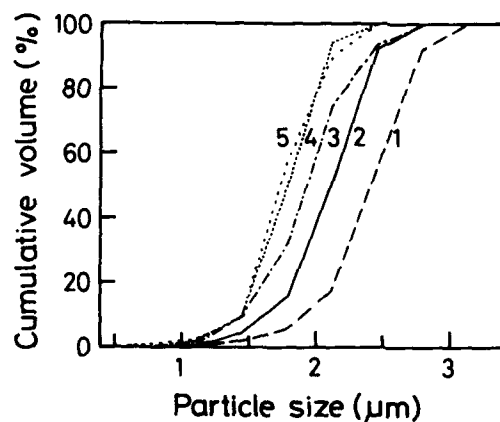
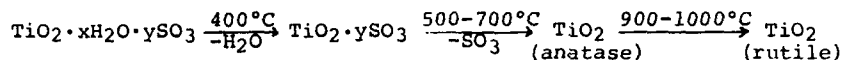


Fig. 9. Change of particle-size distribution with calcination temperature. Calcination = 1 hr at 500°C(2), 700°C(3), 900°C(4) and 1000°C(5). Curve 1 is as-synthesized powder of Run O.

decrease occurred in two steps; the first at 100-400°C and the second at 500-700°C. When the effluent gas in the TG analysis was passed through the BaCl₂ aqueous solution, a white precipitate of BaSO₄ appeared at around 570°C. From this fact, the first and second steps in the TG curve are considered to be the dehydration and dissociation of SO₃, respectively.



The amount of weight decreases in TG analysis are given in Table II. The weight decrease in the second step became smaller with increasing the final pH of the reacting solution.

Table II. Weight decreases in TG analysis.

Run a)	Reaction time (min)	Final pH	Weight decrease (wt%)	
			First step	Second step
A	30	5.6	22	<1
B	30	2.0	23	11
	60	6.0	29	<1
C	150	8.3	14	<1
	30	1.0	17	20
G	30	1.3	19	8
O	30	2.0	19	15
P	30	2.0	25	13

a) Composition of reacting solution is given in Table I.

The as-synthesized powder of Run O in Table I was calcined at 500-1000°C for 1 hr in air. The phases produced were anatase at 500-800°C, rutile + small amount of anatase at 900°C, and rutile at 1000°C. Calcined powders are shown in Fig. 8. The particle-size distributions are given in Fig. 9. The particles shrank with increasing calcination temperature up to 800°C while keeping the spherical shape. The surface area and crystallite size of calcined powders are plotted as a function of calcination temperature in Fig. 10. The surface area-equivalent particle diameters of powder calcined at 600 and 700°C are 280 and 670 Å, respectively. These sizes are close to the crystallite sizes in each powder.

CONCLUSION

The application of the homogeneous precipitation technique using urea for the hydrolysis of TiOSO₄ gives spherical titania particles with an average size of 1-4 μm in a short time period. Urea accelerates the hydrolysis of TiOSO₄ and gives a significant effect of the morphology of the product.

ACKNOWLEDGEMENT

The present work was supported by Nippon Sheet Glass Foundation.

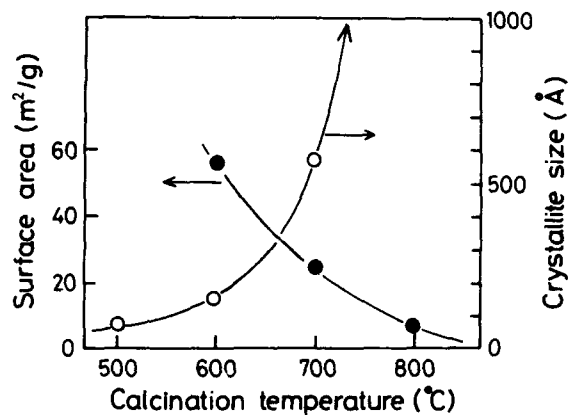


Fig. 10. Change of surface area and crystallite size with calcination temperature.
Calcination conditions: see Figs. 8 and 9.

References

1. E.A. Barringer and H.K. Bowen, *J. Am. Ceram. Soc.*, **65**, C-199 (1982).
2. T. Ikemoto, K. Uematsu, N. Mizutani and M. Kato, *Yogyo-Kyokai-Shi*, **93**, 261 (1985).
3. M.I. Diaz-Guemes, T. Gonzalez Carreno and C.J. Serna, *J. Mat. Sci. Lett.*, **7**, 671 (1988).
4. L.H. Edelson and A.M. Glaeser, *J. Am. Ceram. Soc.*, **71**, 225 (1988); **71**, C-198 (1988).
5. E. Matijevic, *Pure & Appl. Chem.*, **50**, 1193 (1978).
6. E. Matijevic, M. Budnik and L. Meites, *J. Colloid Interface Sci.*, **61**, 302 (1977).

THE EFFECTS OF ALUMINUM ALKOXIDES
ON THE SYNTHESIS OF COMPOSITE POWDERS
OF ALUMINA AND TITANIA

Michael T. Harris, Charles H. Byers, and Ronald R. Brunson
Chemical Technology Division, Oak Ridge National Laboratory, Oak Ridge, Tennessee

ABSTRACT

The synthesis of mixed oxide ceramic powders that consist of very fine (submicron)-monodisperse particles with uniform composition is desirable in the improvement of existing ceramics and the development of new ceramic materials. Metal alkoxide hydrolysis is a very attractive method for the synthesis of ultrapure composite powders at low temperatures by the sol-gel process.

The present study investigates the effects of the hydrolysis of aluminum alkoxides and the condensation products on the growth kinetics and morphology of composite particles containing alumina and titania. Alkoxides of titanium and aluminum are employed; therefore, powders of high purity are produced. Since various solvents are used as media for powder synthesis, the effect of the solvent on particle morphology will also be discussed.

INTRODUCTION

Mixed oxide particles of alumina and titania are important in the formation of aluminum titanate-based ceramics. The particle size distribution, morphology, and composition of these particles must be controlled if improved materials are to be fabricated.

Ordinarily, a stoichiometric mixture of TiO_2 and Al_2O_3 powders is prepared by ball-milling and isostatic pressing [1]. These techniques, however, do not result in homogeneity on the microscopic level and do not allow for the control of particle size and morphology. Several methods (aerosol reactor-alkoxide drops [2]; coating titania, by titanium alkoxide hydrolysis, on colloidal alumina substrates [3]) have recently been developed to produce a more ideal powder (i.e., monodisperse, spherical, and homogeneous particles). However, little information has been reported on the synthesis of alumina-titania particles by the low-temperature hydrolysis/homogeneous precipitation of mixed metal alkoxide solutions. The hydrolysis and subsequent homogeneous precipitation of metal alkoxides have been used to form monodisperse spherical particles of titania [1], silica [1,4], zirconia [1], and yttria-zirconia [5].

This present study investigates the formation of ideal powders by the hydrolysis of mixed alkoxides of titanium and aluminum in low-molecular-weight alcohols. The effects of the initial aluminum alkoxide concentration, condensation products, initial water concentration, and solvent on particle growth kinetics and particle morphology are evaluated. Ultimately, the goal of this research is to understand the mechanisms that govern the synthesis of monodisperse particles of aluminum titanate (Al_2TiO_5) by the homogeneous precipitation of mixed metal alkoxides.

MATERIALS AND METHODS

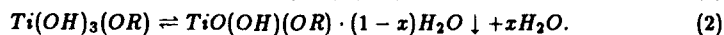
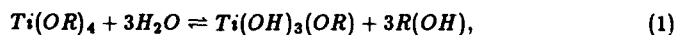
Stock solutions are prepared that contain a total metal alkoxide concentration of 3.0 mol/L and initial $\text{Al}^{3+}:\text{Ti}^{4+}$ (aluminum *sec*-butoxide (ASB): titanium ethoxide (TIE)) molar ratios of 0.00:1.00, 0.39:1.00, 0.81:1.00, 1.50:1.00, and 2.00:1.00 in 1-butanol. The alkoxides were purchased from ALFA Products. The reaction mixtures for the homogeneous precipitation studies are prepared by diluting the stock solutions to total metal concentrations of 0.02 to 0.225 mol/L in an appropriate solvent (i.e., anhydrous ethanol, 1-propanol, or 1-butanol). Separate solutions of alcohol-water and alcohol-alkoxide are prepared to minimize localized reaction zones. The two solutions are rapidly mixed for approximately 5 s. Immediately after mixing, a fraction of the sample is transferred to a clean quartz-spectrophotometer cell for particle size analysis by photon correlation spectroscopy [4]. A portion of the sample is also used to monitor the water concentration by Fourier transform infrared spectroscopic analysis. Using a solvent subtraction technique, a characteristic peak at approximately 1655 cm^{-1} is used to follow the water concentration. Transmission electron microscopy (TEM) and electron dispersive X-ray (EDX) analyses are performed on the precipitate.

RESULTS AND DISCUSSION

Figure 1 shows the effect of the initial molar ratio of ASB:TIE on the shape of "alumina" [probably $\text{AlO}(\text{OH})$] and "titania" [probably $\text{TiO}(\text{OH})(\text{OR})$] particles that are synthesized by the hydrolysis of aluminum-titanium alkoxides in ethanol containing an excessive amount of water. These data clearly show that as the initial ratio of ASB:TIE decreases [Fig. 1(a)-1(d)], the precipitate changes from an aggregation of nanometer-size particles that have an incoherent-open structure to an aggregation of more coherent and spherical 0.1 to 0.2- μm particles. The former structure is typical of gels while the latter, with the help of surfactants to minimize aggregation, can result in discrete submicron monodisperse particles.

The proposed mechanism that governs the growth of coherent-(spherical)-versus-incoherent particles of "alumina"- "titania" is coagulative nucleation (6). This mechanism, which is based on the electric double-layer theory, assumes that during nucleation, very small ($\sim 20\text{-}\text{\AA}$) primary nuclei, because of their colloidal instability, rapidly coagulate to form larger, more stable spherical particles. As nucleation proceeds, the primary nuclei preferentially attach to the larger particles rather than aggregate with other primary nuclei. Thus, monodisperse particles are formed. The formation of monodisperse spherical particles versus incoherent-open structures is affected by the relative rate of nucleation to the rate of aggregation (i.e., colloidal stability of the nuclei). If nucleation occurs faster than the primary nuclei are able to form larger particles by aggregation, the precipitate will exhibit an incoherent-open structure. However, spherical particles are formed when the primary nuclei aggregate faster than the formation of primary nuclei and under the condition where larger colloids are more stable than the smaller nuclei.

To elucidate how coagulative nucleation explains the effect of the initial ASB:TIE molar ratio, it is necessary to understand the hydrolysis and condensation reactions of aluminum and titanium alkoxides. The following reactions are proposed for the hydrolysis of titanium and aluminum alkoxides and the subsequent precipitation of the hydrolysis products:



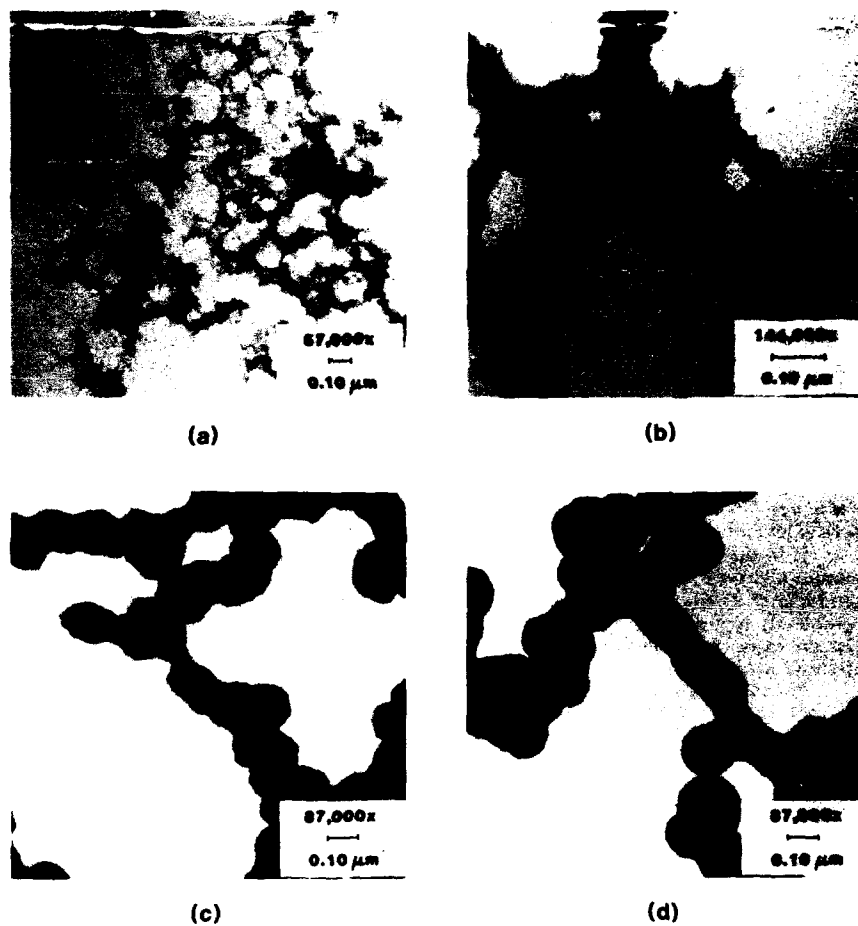
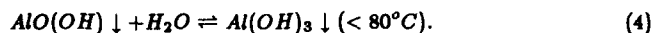
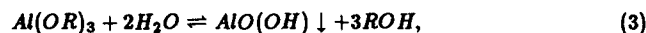


Figure 1. TEM of "alumina"-titania particles produced in ethanol (effect of the initial molar ratio of [ASB]:[TIE]; 0.8 M H₂O): (a) 0.015 M TIE, 0.023 M ASB; (b) 0.023 M TIE, 0.019 M ASB; (c) 0.031 M TIE, 0.012 M ASB; (d) 0.02 M TIE.



In addition to the above reactions, several other reactions may also occur (i.e., alcoholysis: $-M(\text{OR}) + \text{ROH} \rightleftharpoons -M(\text{OR}) + \text{ROH}$) and the formation of double metal alkoxides: $n\text{Al(OR)}_3 + \text{Ti(OR)}_4 \rightarrow \text{Al}_2\text{Ti(OR)}_{10}$ and/or AlTi(OR)_7 . Since it is beyond the scope of this investigation to study the chemistry of double alkoxides, it is proposed that Eqs. 1-4 describe the basic hydrolysis and precipitation reactions.

Fourier transform infrared spectroscopic analyses reveal that approximately 2.6 to 3 mol of water per initial mol of TIE are used in the hydrolysis/condensation of titanium alkoxides (Eqs. 1 and 2). For initial ASB:TIE molar ratios of 1:1 and 2:1, 6 and 9 mol of water per initial mol of TIE are used in the hydrolysis and condensation reactions (Eqs. 1-4). This indicates that the value of x in Eq. 2 is between 0 and 0.4.

It is seen from Eqs. 1-4 that titanium alkoxides are partially hydrolyzed, while aluminum alkoxides are completely hydrolyzed. It is assumed that the partially hydrolyzed products of titanium alkoxides should precipitate (nucleate) considerably slower than the completely hydrolyzed aluminum alkoxides. Furthermore, more compact-spherical particles are expected to be formed in the system where nucleation is the slowest and colloidal stability is lowest.

For comparable total metal concentrations and water concentrations, the experimental data show that titanium alkoxide hydrolysis products precipitate much slower than the hydrolyzed products from the aluminum-titanium mixed alkoxide system (i.e., longer induction times before precipitation occurs; minutes to hours compared with seconds). A portion of the samples is also filtered 10 min. after precipitation has begun. In the titanium alkoxide system, the filtrate turns turbid after 5 to 10 min. This indicates that either the hydrolysis of titanium alkoxide (Eq. 1) is occurring after 10 min, or the equilibrium precipitation reaction (Eq. 2) is affected by the removal of the precipitate. Fourier transform infrared spectroscopy suggests that the hydrolysis reaction is fast [7] and occurs within 1 to 2 min. Therefore, the precipitation in the filtrate is due to the shift in equilibrium condition that is caused by the removal of the precipitate.

The filtrate from the aluminum-titanium mixed alkoxide system remained clear and, therefore, suggests that both the aluminum and titanium hydrolysis products are probably precipitated together within 10 min of reaction. EDX analyses indicate that a homogeneous mixture of "alumina"- "titania" is achieved on the submicron level in the precipitate.

Zeta potentials have been determined for the precipitate from the hydrolysis of solutions with initial ASB:TIE molar ratios of 0:1, 1:0, 2:1, 1:1, and 1:2. These particles were suspended in the centrifuged reaction medium. At a pH of 6.9, the zeta potential increases from 10 mV for "titania" particles to 60 mV for "alumina" particles. This indicates that, based on the electric double-layer theory, the colloids become more stable as the "alumina" content of the particles is increased. However, this does not necessarily mean that a stable sol is formed. These particles can still aggregate; however, because of the higher rate of nucleation and the increase in colloidal stability, an increase in the "alumina" content of the particles is expected to form more incoherent-open structures [Fig. 1(a)-1(d)].

The theory of oriented flocculation also provides qualitative insight into the formation of spherical-versus-incoherent structures. This theory is based on the linear superposition of the Dryaguin-Verwey-Overbeek (D-V-O) theory of the electrical double layer for separate spherical particles [8]. Similar to the mechanism of coagulative nucleation, the theory assumes that spherical-charged nuclei are formed and these nuclei aggregate to form larger particles. However, this theory includes the postulate that, depending on

the relative magnitude between the electrostatic barrier V_T to aggregation and the average thermal kinetic energy kT of the particles, anisotropic-incoherent-open ($kT \leq V_T$) or coherent-spherical ($kT > V_T$) particles can be formed. Qualitatively, V_T increases with the surface potential or zeta potential; therefore, a more incoherent-open structure is expected to be produced as the "alumina" content increases (i.e., zeta potential increases).

Figure 2 shows growth kinetics of "alumina"- "titania" particles that are determined by dynamic-laser-light-scattering. Since larger particles are more intense scatterers, the effective diameters are more representative of the larger particles. This figure shows that as the "alumina": "titania" molar ratios increased from 0:1 (curves E and F), 1:1 (curve A), to 2:1 (curves B, C, and D), the first observable particle size decreases from 100-200 nm to 10-20 nm. Since dynamic-laser-light-scattering techniques are capable of obtaining particle sizes in 10 to 15 s, the first observable particle size represents 10 to 15 s of particle growth after the onset of nucleation. This growth can be due to either aggregation of smaller particles or to the addition of monomer to the surface of the nuclei. Electron microscopy (Fig. 1) indicates that the larger particles (>100 nm) of "alumina"- "titania" are agglomerates of smaller particles.

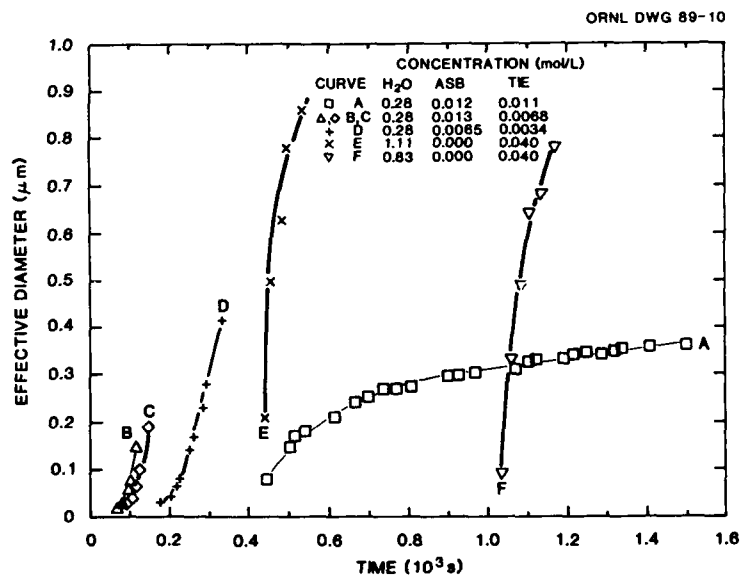


Figure 2. Particle growth kinetics in 1-butanol: Effect of the initial molar ratio of ASB:TiE.

Since "alumina"- "titania" particles (>100 nm) are formed by aggregation of smaller particles, the theory of coagulative nucleation is used to describe the observed particle growth kinetics. In the case of 2:1 "alumina": "titania" molar ratio, it is reported above that based on zeta potential measurements, these colloids are more stable than particles with a lower "alumina": "titania" molar ratio. Therefore, it is likely that the first observable

particle size after 10 to 15 s of nucleation should be smaller (because of greater colloidal stability) for particles with a higher "alumina" content than for particles with a lesser "alumina" content where, because of low colloidal stability, the very small nuclei (20-50 Å) rapidly aggregate to form 100- to 200-nm particles. The subsequent increase in the measured effective diameter from the first observable particle size (Fig. 2) is due to aggregation.

The ultimate goal of these studies is to synthesize monodisperse spherical particles of aluminum titanate (Al_2TiO_5) by the homogeneous precipitation of mixed aluminum-titanium alkoxides. During a matrix of experiments in which the water concentration and solvents are varied, it is observed that more compact-spherical particles are formed when the water concentration approaches the theoretical amount needed for hydrolysis and condensation reactions (see Eqs. 1-4). Figure 3 shows TEMs of particles that are synthesized by the hydrolysis of a 1:1.2 ASB:TIE solution in 1-butanol with water concentrations of 1.6 and 0.4 mol/L. It is clearly shown that a more incoherent-open precipitate is produced at the higher water concentration (i.e., higher rate of nucleation). At low water concentrations, aggregates of compact-near-spherical particles are obtained. The aggregation of the particles at lower water concentration can be minimized by the addition of surfactants during the reaction. To produce compact-spherical particles from the hydrolysis of a 2:1 ASB:TIE solution, it is necessary to initially add approximately 9 mol of water per mol of TIE. After this solution has reacted for 30 min, an additional 9 mol of water per mol of initial TIE are added. Figure 4 shows the "alumina"- "titania" particles that are produced in ethanol, 1-propanol, and 1-butanol. Fine powders (although aggregates of 100- to 300-nm particles) are produced in each solvent. The best powders are produced in 1-butanol.

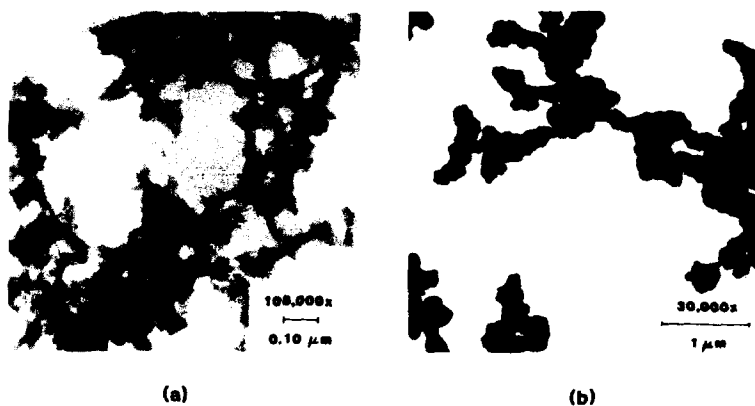


Figure 3. Transmission electron micrographs of "alumina"- "titania" particles produced in ethanol (effect of initial water concentration) (0.023 M TIE, 0.019 M ASB) : (a) 1.6 M H_2O ; (b) 0.4 M H_2O .

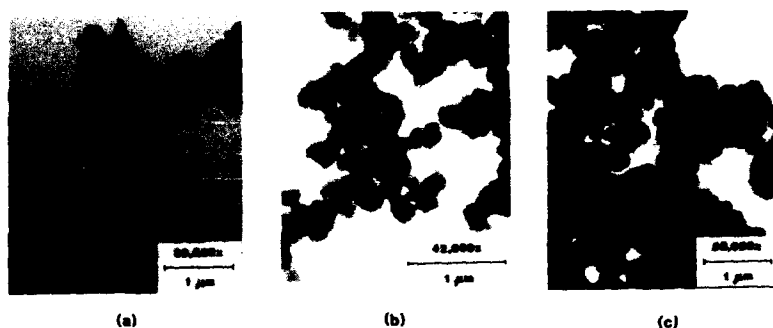


Figure 4. Transmission electron micrographs of "alumina"- "titania" particles (effect of solvent: 0.56 M H_2O , 0.025 M TIE, 0.05 M ASB): (a) ethanol; (b) 1-propanol; (c) 1-butanol.

Figure 5 shows the differential thermal analysis for 2:1 "alumina"- "titania" powder that is synthesized by the above method in 1-butanol. The plot shows an endotherm at 140°C (removal of hydroxides) and exotherms at 360°C (removal of alkoxide groups), 970°C (rutile and/or corundum formation), and 1400°C (formation of Al_2TIO_5). The formation of the various crystalline phases is confirmed by X-ray diffraction analysis.

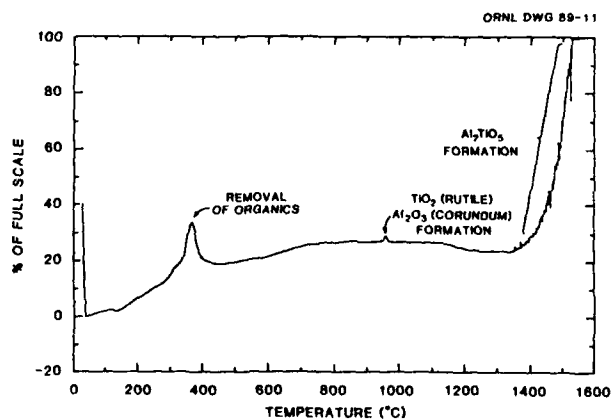


Figure 5. Differential thermal analysis for "alumina"- "titania" powder.

CONCLUSIONS

This investigation has shown that the "alumina" content affects the rate of precipitation and the colloidal stability which ultimately affects particle morphology. A procedure is proposed for the synthesis of 100- to 300-nm spherical particles of 2:1 "alumina"- "titania" by the controlled hydrolysis/condensation of a homogeneous mixture of aluminum and titanium alkoxides in low-molecular-weight alcohols. However, the aggregation of these spherical particles in solution lowers the green-body density of the final powder. To produce a more ideal powder for ceramic applications, future studies will investigate the use of surfactants to minimize aggregation of these spherical particles in solution.

ACKNOWLEDGMENTS

This research was sponsored by the Office of Basic Energy Sciences, U. S. Department of Energy under contract DE-AC05-84OR21400 with Martin Marietta Energy Systems, Inc.

REFERENCES

- [1] R. H. Heistand et al., *Science of Ceramic Chemical Processing*, eds. L. L. Hench and Donald R. Ulrich (John Wiley & Sons, New York 1985), p. 482.
- [2] B. J. Ingebrethsen, E. Matijevic, and R. E. Partch, *J. Colloid Interface Sci.* **95**, 228 (1981).
- [3] H. Okamura, E. A. Barringer, and H. K. Bowen, *J. Am. Ceram. Soc.* **69**, C-22 (1984).
- [4] C. H. Byers, M. T. Harris, and D. F. Williams, *Ind. Eng. Chem. Res.* **26**, 1916 (1987).
- [5] B. Fegley, Jr., P. White, and H. K. Bowen, *Ceram. Bull.* **64**, 1115 (1985).
- [6] E. Santecesaria et al., *J. Colloid Interface Sci.* **111**, 44 (1986). (1985).
- [7] M. T. Harris, and C. H. Byers, *J. NonCryst. Solids* **103**, 49 (1988).
- [8] I. L. Thomas and K. H. McCorkle, *J. Colloid Interface Sci.* **36**, 110 (1971).

PREPARATION AND CHARACTERIZATION OF COLLOIDAL ZnS PARTICLES

Ahmet Celikkaya and Mufit Akinc

Department of Materials Science and Engineering, Iowa State University, Ames, IA 50011

INTRODUCTION

The preparation of particles of uniform size, shape, and composition has been of interest to colloid chemists and has received serious attention in the ceramic processing community recently. Interest in making monodispersed sols is not based solely on esthetic appeal of such systems but has evolved from high tech applications which place stringent requirements on the properties of ceramic components and thus on starting powders. Uniform particle size and shape are also essential for the evaluation of validity of various sintering models as well as optical, magnetic and electrokinetic properties of colloidal systems developed assuming uniform particle size and shape.

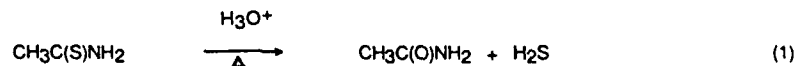
ZnS powders have long been prepared by various methods including gas phase, solid/vapor and aqueous solution reactions [1-5]. Chiu [3] was the first to prepare monodisperse ZnS sols by passing H_2S into Zn^{2+} solutions in the presence of EDTA. The particles were $0.2 \mu m$ in diameter but the solutions were too dilute to be of any practical value. Later, Wilhelmy and Matijevic [4] employed thermal decomposition of thioacetamide to prepare micron-sized spherical particles by aging the reaction mixture several hours. Williams et. al. [5] employed the same technique to prepare monosized, spherical particles of ZnS about $3 \mu m$ in diameter. However, a review of the latter two works indicates that subtle variations in experimental procedures change not only the particle size but also mechanism of particle growth, crystalline phases produced, and particle morphology.

In this article, the role of various anions in the kinetics of precipitation and the morphology of the particles will briefly be discussed.

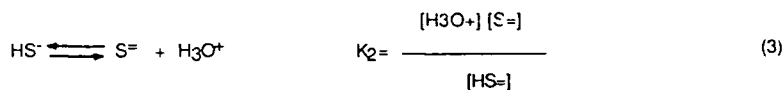
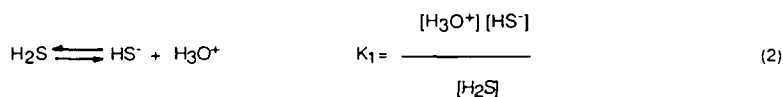
RESULTS AND DISCUSSION

ZnS powders were prepared by thermal decomposition of thioacetamide in acidic zinc solutions ($pH \leq 2$).

The process involves decomposition of thioacetamide according to the reaction



and dissociation of hydrogen sulfide in two steps producing sulfide ions



which cause precipitation of ZnS when the critical supersaturation is reached. The equilibrium precipitation reaction is given by



Slow introduction of sulfide ions into the system forms the basis for producing uniform particles. The rate of sulfide ion generation is determined by decomposition of thioacetamide and can be controlled by appropriate choice of experimental parameters such as temperature, pH, and the initial concentration of thioacetamide. It was found that the critical supersaturation, defined as

$$S' = \left[\frac{[\text{S}^{=}]_t [\text{Zn}^{2+}]}{K_{\text{sp}}} \right]^{1/2}$$

where $[\text{S}^{=}]_t$ is sulfide ion concentration at any time t , and K_{sp} is the solubility product for β -ZnS, remains constant at a value of about 10 for any combination of experimental variables [6]. Zinc ion concentration $[\text{Zn}^{2+}]$ was kept constant at 0.05 M so that the time elapsed to nucleation represents a relative measure of sulfide ion generation rate.

Figure 1 shows electron micrographs of particles precipitated under various conditions in the presence of nitrate ions (i.e. zinc nitrate stock solutions were used as the Zn^{2+} source and pH of the solutions was adjusted with HNO_3). Reaction mixtures were aged for 1 hour. Observed variation of the type of the particle size distribution is related to the difference between rates of sulfide ion generation and its consumption in the growth process. Monosized particles were obtained at low rates of sulfide ion generation (Figure 1a). At intermediate sulfide ion generation rates, a net buildup of excess sulfide ions leads to formation of a second burst of nuclei, resulting in a bimodal distribution (Figure 1b). If sulfide ions are not consumed at a high enough rate even after formation of a second generation of particles, a third, fourth etc., nucleation events are expected resulting in a continuous distribution of particle sizes (Figure 1c).

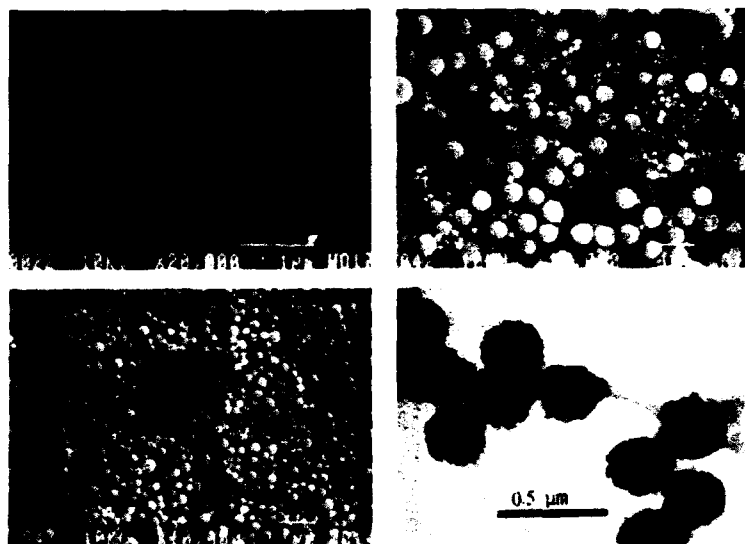


Figure 1 - Electron micrographs of particles from nitrate solutions at $[\text{Zn}^{2+}]_0 = 0.05\text{M}$, $\text{pH}=2$ and

- a) - $T=70^\circ\text{C}$ and $[\text{TAA}]_0 = 0.4\text{M}$ after aging for 1 hr.
- b) - $T=80^\circ\text{C}$ and $[\text{TAA}]_0 = 0.2\text{M}$ after aging for 1 hr.
- c) - $T=80^\circ\text{C}$ and $[\text{TAA}]_0 = 0.4\text{M}$ after aging for 1 hr.
- d) - $T=70^\circ\text{C}$ and $[\text{TAA}]_0 = 0.4\text{M}$ at an early stage of aging.

The polycrystalline nature of spherical particles is clearly seen in the transmission electron micrograph (Figure 1d) taken at an early stage of aging process. XRD patterns of the powders were identical to that of sphalerite and did not contain any indication of a second crystalline phase.

When the precipitation reaction was carried out in the presence of sulfate ions, nucleation was delayed as compared to the nitrate system under similar conditions. For example, at $\text{pH}=2$, $T=60^\circ\text{C}$ and $[\text{TAA}]=0.4\text{M}$, it took about 13 minutes for the sulfate solution to nucleate as opposed to 8 minutes for the nitrate solution. Equilibrium calculations indicated that 15% of the zinc ions were tied up in sulfate solutions due to complex formation (3% in nitrate solutions) and that the delay in nucleation is a result of lower free zinc ion concentration.

ZnS particles that were precipitated in sulfate solutions had a significantly different morphology than those formed in other systems. Under those conditions leading to a low rate of sulfide ion generation, monosized particles of $3\mu\text{m}$ diameter were obtained as shown in Figure 2a. In this case only, XRD patterns indicated the existence of some wurtzite phase in addition to sphalerite. However, no attempt was made to determine the relative amounts of these crystalline phases. This agrees well with the observations of

Williams et. al. [5] where they concluded that 20% of the mixture was wurtzite. At increased sulfide ion generation rates, a second generation of particles appeared (Figure 2b) at comparable times to those yielding monosize ($3\mu\text{m}$) particles. After an elongated aging time, very agglomerated powders were obtained (Figure 2c). Powders precipitated at high sulfide ion generation rates and in the presence of sulfate ions were composed only of sphalerite. The fibrous texture is believed to be nuclei that elongated before they attached onto the growing particles. However, it remains a mystery how a cubic structure may end up with a fibrous structure.

Formation constants [7] for complexes of various anions with zinc ion corrected for an ionic strength of 0.3 are given in Table I. Although, acetate ions are as good a complex former as sulfate ions, at a pH of 2,

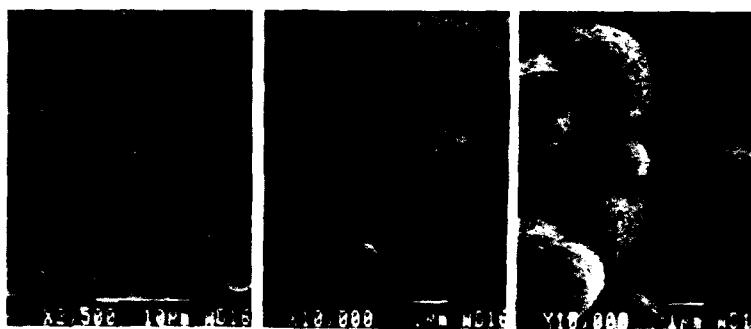


Figure 2 - Scanning electron micrograph of ZnS particles obtained from sulfate solutions with $[\text{Zn}^{2+}]_0 = 0.05\text{M}$, and

- a) - $T=70^\circ\text{C}$, $\text{pH} = 1$ and $[\text{TAA}]_0 = 0.2\text{M}$ after aging for 1 hr.
- b) - $T=70^\circ\text{C}$, $\text{pH} = 2$ and $[\text{TAA}]_0 = 0.4\text{M}$ after aging for 1 hr.
- c) - $T=70^\circ\text{C}$, $\text{pH} = 2$ and $[\text{TAA}]_0 = 0.4\text{M}$ after aging for 1.5 hr.

$T=60^\circ\text{C}$ and $[\text{TAA}]=0.4\text{M}$, precipitation in acetate solutions started earlier than it did in "inert" nitrate solutions. Obviously, the presence of acetate ions either catalyses the thioacetamide decomposition or forms intermediate species with zinc ions, which facilitates attachment of ions to subcritical nuclei. The concentration of undecomposed thioacetamide was followed with a UV-Vis spectrophotometer at 261 nm and compared with the expected concentration calculated from rate expression given by Swift [8]. It has been found that the experimentally-determined concentration strictly follows calculated values. FTIR spectra of ZnS powders prepared from acetate solutions did not contain any peaks, indicating involvement of an intermediate species in the solid phase. Thus, it is difficult to explain the observed unanimously early nucleation from acetate solutions.

Table I - Formation constants for acetate, nitrate, sulfate and chloro complexes of Zn^{2+} ion corrected for an ionic strength of 0.3.

Complex Specie	Ligand (L^-)			
	SO_4^{2-}	OAc^-	NO_3^-	Cl^-
$K_{f,1} [ZnL_1]^{-y+2}$	12.58	11.22	0.66	2.32
$K_{f,2} [ZnL_2]^{-2y+2}$	7.94	6.16	0.38	1.41
$K_{f,3} [ZnL_3]^{-3y+2}$	0.70	1.23	-	0.89
$K_{f,4} [ZnL_4]^{-4y+2}$	1.13	-	-	0.50

When prepared from acetate solutions, particle morphology did not vary considerably with experimental parameters. Spherical monosized particles of B-ZnS were obtained with all combinations of experimental variables investigated as shown in Figure 3.

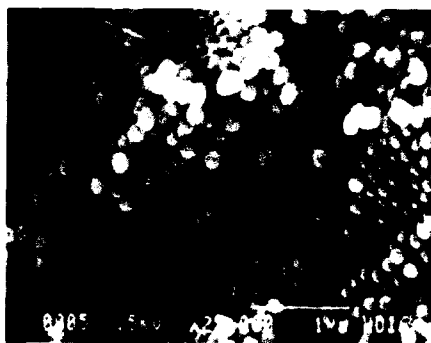


Figure 3 - Scanning electron micrograph of particles obtained by aging for 1 hr. in acetate solution with $[Zn^{2+}]_0 = 0.05M$, $pH=2$, $T=70^\circ C$ and $[TAA]_0 = 0.4M$.

Powders prepared from chloride solutions yielded monosized particles in a very narrow range of experimental parameters leading to intermediate sulfide ion generation rates. Particle characteristics were similar to those from nitrate solutions. In all other cases, highly agglomerated powders were obtained.

CONCLUSIONS

Mean ZnS particle size and type of particle size distribution were affected by the sulfide ion generation rate for all anion solutions except acetate. Depending on the sulfide ion generation rate, monosized, bimodal or continuous size distribution was observed. Nitrate, chloride, and acetate solution produced submicron particles while sulfate solutions produced particles up to 3 μm in diameter in the range of variables studied. Particles from sulfate solutions had a unique fibrous texture which was not apparent in other systems. Acetate ions appeared to hasten nucleation, yet growth was slow compared to other systems.

Powder morphology was more easily controlled in nitrate solutions and the powder characteristics obtained i.e. mean size and phase purity were superior to powders from other anion solutions.

REFERENCES

1. P.A. Miles, J. Opt. Soc. Am. 63, 1323 (1973).
2. H.W. Leverenz, Science 109, 183 (1929).
3. G. Chiu, J. Coll. and Int. Sci. 83 (1), 309 (1981).
4. D.M. Wilhelmy, E. Matijevic, J. Chem. Soc., Faraday Trans. I 80, 563 (1984).
5. R. Williams, P.N. Yocom, F.S. Sotofko, J. Coll. and Int. Sci. 106 (2), 388 (1985).
6. A. Celikkaya and M. Akinc, to appear in J. Am. Ceram. Soc. (1989).
7. S. Kotryl and L. Sucha, Handbook of Chemical Equilibria in Analytical Chemistry (Ellis Horwood Limited, West Sussex, England, 1985), pp. 143-208.
8. E. H. Swift and E. A. Butler, Anal. Chem. 28 (2), 146 (1956).

THE MORPHOLOGY OF FREEZE-DRIED RUBIDIUM CHLORIDE POWDER

J. K. G. Panitz, J. A. Voigt, F. A. Greulich, M. J. Carr, and M. O. Eatough
Sandia National Laboratories, Albuquerque, NM 87185

ABSTRACT

We have formed powders of a strongly ionic compound, RbCl by freeze-drying. Stock solutions, varying from very low concentrations with 4 gm RbCl reagent dissolved in 100 cc water to saturated solutions with 80 gm reagent in 100 cc water, were sprayed into isopentane at -160°C . The droplet size in the spray was varied from relatively large 4-mm diameter droplets to extremely small droplets in an aerosol spray. It was determined that both the concentration of the stock solution and the droplet size affect the average size and the size distribution of the primary particles formed and the way in which these primary particles are bonded together. Unlike the powders of many less ionic compounds that are produced by freeze-drying, the primary particles in these RbCl powders are crystalline rather than amorphous. Analysis with an x-ray diffractometer with a cold stage indicates that crystallization occurs during the freezing cycle rather than during the sublimation period of the freeze-drying process.

INTRODUCTION

Freeze-drying is a practical technique for preparing high purity, homogeneous, fine-grained powders. Fine-grained powders are of interest in the fields of ceramics, optics, catalysis, and lithography. Many groups have characterized the mechanisms associated with powder formation from freeze-dried solutions of nitrate, carbonate, sulfate, hydroxide, formate, oxalate and chlorate compounds, i.e., compounds which are not strongly ionic.¹⁻⁹ In general, it is believed that it is difficult to form homogeneous ultrafine powders of strongly ionic compounds by freeze-drying.¹ Rapid cooling of aqueous solutions of very ionic compounds can create very high levels of supersaturation. The supersaturated system generally will minimize its free energy by nucleation and growth of a solid phase, resulting in a powder with a relatively large distribution of particle sizes with some relatively large particles.

In the present study, we have formed powders of a strongly ionic compound, RbCl . We have varied the concentration of the RbCl solutions and the size of the droplets dispersed in the cryogen. Our results indicate that the characteristics of the powder that forms is dependent on both parameters.

EXPERIMENTAL

Solutions containing various concentrations of reagent grade RbCl , including a mixture of 4 gm RbCl in 20 cc water plus 80 cc ethanol, and aqueous solutions ranging in concentration from 4 gm RbCl plus 100 cc water to 80 gm RbCl plus 100 cc water (a saturated solution at room temperature) were dispersed via two techniques into isopentane at -160°C . Very large droplets, with a diameter of approximately 4 mm, were formed using a large bore (0.5-mm diameter) hypodermic needle and allowed to drop into the

cryogen. Alternatively, a very fine, aerosol mist with an estimated average droplet size of 0.05 mm was sprayed into the cryogen using a standard, double action artist's airbrush operated with 20 psi UHP nitrogen. The cryogen was stirred vigorously while a RbCl_2 solution was added. The volumetric ratio of solution to cryogen was approximately 1:5. After mixing, a flask containing the resultant slurry was connected to a vacuum manifold pumped by a Sargent Welch Model 1397 mechanical vacuum pump and a standard freeze-drying trap immersed in a large dewar of nitrogen. The flask with the product was placed in a small dewar of nitrogen and allowed to warm slowly to room temperature and dry in a vacuum of 2000 mT or less for approximately 20 hours.

Powder samples were evaluated using transmission electron microscopy (TEM), electron diffraction, scanning electron microscopy (SEM), and x-ray diffraction. The structure of the frozen droplets was investigated using low-temperature x-ray diffraction. X-ray samples were prepared by the freezing process previously described using a saturated RbCl_2 solution and the "hypodermic" method for droplet formation. The frozen droplets were sieved from the isopentane freezing medium (-160°C) and placed into a Paar TTK low-temperature x-ray attachment at -153°C . The x-ray diffraction data was taken using a Rigaku Geigerflex with an automated wide-angle theta/theta DmaxB goniometer. For comparison, low-temperature diffraction experiments were repeated for similarly frozen water droplets and crystalline RbCl_2 powder.

Representative powder samples were mixed with chlorodecane at a concentration of 1% by weight; these mixtures were ultrasonically agitated for varying amounts of time from 1 to 24 hours to determine the relative ease with which the agglomerates could be subdivided into primary particles.

RESULTS AND DISCUSSION

Crystalline rubidium chloride formed under all of the processing conditions investigated as determined by x-ray diffraction. This indicates that the crystallization processes of nucleation and growth took place at some point in the powder preparation process, i.e., during solution freezing, water sublimation, or dry powder warming to room temperature. To determine whether crystallization occurred during freezing, low-temperature x-ray diffraction was used. Figure 1 shows a typical low-temperature x-ray diffraction pattern of large droplets of a frozen rubidium chloride solution prepared using standard freezing conditions. The pattern clearly shows the presence of crystalline RbCl_2 and ice, indicating that RbCl_2 crystallization occurs during freezing.¹⁰ Since crystallization takes place during freezing, the process can be visualized as being driven by an effort to relieve the state of supersaturation created by lowering the temperature of the solution and the increase in RbCl_2 concentration caused by water removal as a result of ice formation during freezing.

Figures 2 and 3 show SEM micrographs of three samples of powder formed from a saturated aqueous RbCl_2 solution. The powder samples shown in views, 2a, 2b, and 2c were produced from an aerosol spray. Figure 2a shows a hemispherical fragment which is an artifact of one of the larger saturated droplets produced by the airbrush. Figure 2b shows with higher magnification the homogeneous mesh of densely interconnected RbCl_2 crystallites comprising this fragment. X-ray diffraction broadening indicates an average primary particle size of 100 nm. Figure 2c shows a portion of a dense aggregate with large crystallites from a powder that

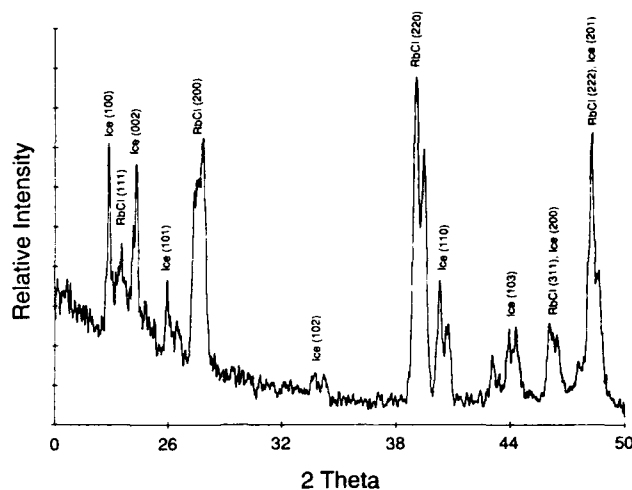


Fig. 1. Diffraction pattern taken at -153°C showing RbCl and ice. All but one minor peak are accounted for. Splitting and broadening of peaks are due to the uneven geometry of the sample.

was formed from a saturated RbCl solution when the pressure was allowed to rise above 2000 mT for some period during the freeze-drying process. It is probable that the ice and salt mixture partially melted and redissolved before the water had completely evaporated from the mixture, then refroze relatively slowly so that the crystal growth rate was high relative to the nucleation rate, which resulted in the formation of larger crystallites. Figure 3 shows the primary particles contained in a fragment of a powder aggregate that was produced from saturated droplets formed with a hypodermic needle. This powder contains very large aggregates, 4 mm in diameter with the shape of collapsed spheroids. These large aggregates fractured when transferred from the freeze-drying flask to a storage bottle. The aggregates are composed of homogeneously sized RbCl crystallites. No significant variation in the size or the shape of the primary particles was observed when the aggregates from the powder samples shown in Figs. 2 and 3 were scanned from the outside surface to the interior. The primary particles in the powder sample formed from fine saturated droplets are significantly smaller than the primary particles formed from the large saturated droplets. (Compare Fig. 2b with Fig. 3.) This is, perhaps, a manifestation of the longer amount of time required for the larger droplets to freeze.

Figure 4 shows SEM micrographs of three powder samples formed from an airbrush spray of (a) 16 gm RbCl per 100 cc water, (b) 8 gm RbCl per 100 cc water, and (c) 4 gm RbCl per 100 cc water. There is a relationship between the solution concentration and the number and dimensions of the interconnections between the primary particles. At higher concentrations, as a general rule, there are more interconnections; these junctures are larger with respect to the cross-sectional size of the primary particle.

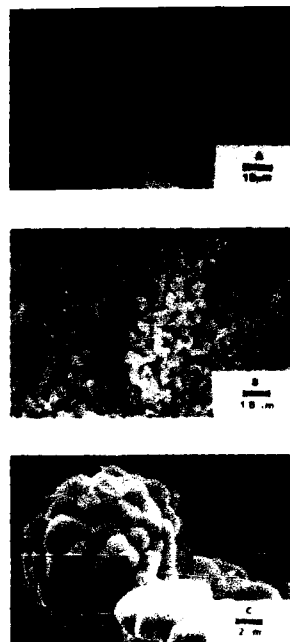


Fig. 2. Scanning electron microscope images of RbCl powder samples formed from an aerosol spray of a saturated, 80 gm RbCl:100 cc water solution. (a) Large field of view of a fragment formed from an aerosol spray. (b) High magnification image of the same fragment shown in (a). (c) Aggregate from a powder sample which was freeze-dried at too high a vacuum and/or at too warm a temperature during part of the freeze-drying process.



Fig. 3. Scanning electron micrograph showing fragments of large, 4-mm diameter aggregates formed from large, 4-mm diameter droplets from a hypodermic needle. All of the material formed from a saturated solution comprises a homogeneous distribution of primary particle sizes.

This observation is consistent with the hypothesis² that the voids between the primary particles in a freeze-dried powder are artifacts of the ice which was formed and sublimed during processing. At higher concentrations there is more salt and less ice.

It should be noted that the maximum size of the primary particles that form is not proportional to the concentration of the stock solution. Figure 2b, and Figs. 4a, 4b, and 4c show micrographs of particles that have formed from aerosol sprays of different concentrations of stock solution. From very dilute 4 gm/100 cc solutions, very small 0.1-0.5 μm sized primary particles form (Fig. 4c). From intermediate concentrations; 8 gm/100 cc and 16 gm/100 cc, larger 0.5-1.0 μm sized primary particles form (Figs. 4a and 4b). From saturated 80 gm/100 cc solutions, small 0.1 μm sized primary particles form (Fig. 2b). There is a progression from small to large to small sized primary particle formation as the concentration of the stock solution is increased. This is a result of a change in the nucleation rate relative to the growth rate. In general, both the nucleation rate and the crystal growth rate depend on 1) the free surface energy of the crystal vs. the free energy of the ions in solution, 2) the solution concentration and the compound's solubility, 3) temperature, 4) the diffusion coefficient, 5) the mean ionic diameter, and 6) the molecular volume of the solvent. The gross crystal growth rate depends also on the size and surface topography of existing crystals. In general, at high solution concentrations, nucleation predominates over growth.¹¹ Our observation that relatively small primary particles form from the saturated stock solution can be interpreted as evidence that nucleation is predominating here; the large

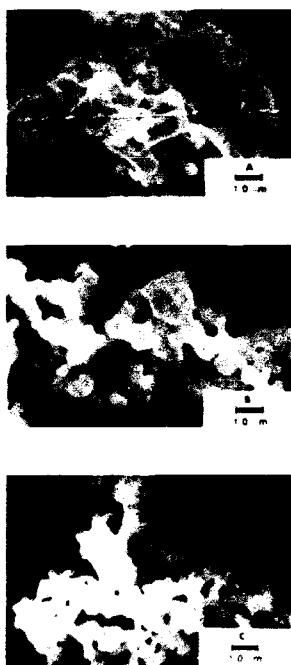
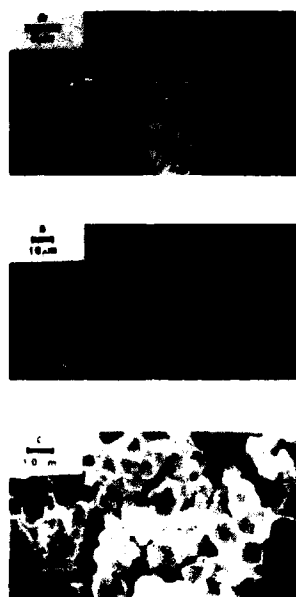


Fig. 4. Scanning electron microscope images of three powder samples all produced from an aerosol spray with different concentrations of RbCl in water. (a) 16 gm RbCl in 100 cc water stock. (b) 8 gm RbCl in 100 cc water stock. (c) 4 gm RbCl in 100 cc water stock.

number of nuclei and the speed at which they form leave relatively few Rb^+ and Cl^- ions to support particle growth. The larger crystallites which form from intermediate concentrations suggest that the nucleation rate is lower so that there is more material available for crystal growth to occur. The small crystallites which form from extremely dilute solutions suggest that although the nucleation rate is relatively slow, because of the reduced concentration, it is not probable that a particle will encounter a substantial amount of dissolved RbCl to feed continued growth.

The primary particles comprising the aggregates formed from dilute solutions vary more in size than the particles formed from a saturated solution (Figs. 5 and 6). Figure 5a shows a large field of view of a fragment of a very large aggregate formed from a dilute 4 gm/100 cc solution using the hypodermic needle. Larger primary particles form nearer the

Fig. 5. Scanning electron microscope images of different regions of a large, 4-mm diameter aggregate formed from a large, hypodermic needle droplet. (a) Large field of view of a portion from an intermediate region from the aggregate showing a distribution of particle sizes. Smaller particles form nearer the exterior surface of the aggregate. (b) Coral-like RbCl structure which forms at the exterior surface of the aggregate. (c) Large RbCl crystallites that formed near the center of the aggregate.

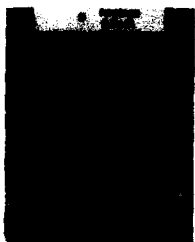


interior. Figure 5b shows the coral-like morphology that forms at the outer surface of the aggregate. Figure 5c shows in greater detail the structure of the large, ($1 \mu\text{m}$) particles near the center of the hypodermic needle aggregate.

A smaller distribution in particle size occurs for aggregates formed from smaller droplets of dilute solution. Figure 6 shows



Fig. 6. Transmission electron microscope images showing a distribution of crystallite sizes in a powder sample formed from an aerosol spray of a dilute 4 gm RbCl:100 cc water solution. The small, delicate aggregates in this powder sample have been broken into primary particles by sonication for seven hours.



a powder where the aggregates have been subdivided by sonication. Here there is a range of primary particle sizes from 0.1-0.5 μm formed from an aerosol of a 4 gm:100 cc water solution.

The range in particle size and morphology shown in Figs. 5 and 6 can be interpreted as evidence of a temperature gradient and freeze front moving through a droplet of dilute solution. The temperature of the outer surface of a droplet introduced into the cryogen, drops more rapidly than the insulated droplet interior. Some dissolved salt rapidly nucleates and forms small crystallites. Some of the solute is excluded from the forming ice lattice towards the center of the liquid droplet, effectively raising the concentration there. Because of the thermal insulation provided by the outer region of the droplet, and perhaps also because of the lower freezing point depression associated with the higher concentrations nearer the interior of the droplet, freezing occurs more slowly nearer the center; larger crystallites form. This effect is more pronounced for larger droplet sizes.

It is interesting to note that the coral-like structure (Fig. 5b) at the exterior of the large hypodermic needle droplet aggregates is similar to the morphology of freeze-dried $\text{Al}_2(\text{SO}_4)_3 \cdot 8\text{H}_2\text{O}$ aggregates observed by Lloyd and Kovel.² Lloyd and Kovel interpreted this structure as evidence of the formation of ovoids and spheroids of water as the water freezes and the salt precipitates. Some similar phenomenon may be occurring here at the exterior of the large, very dilute droplets where freezing occurs rapidly. At the interior of these droplets where freezing occurs more slowly, some different phase of ice may be forming. The variation in salt morphology across an aggregate illustrated in Fig. 5 may be a result of some variation in the ice phases which form.

There is a relationship between the characteristics of the aggregates which can be

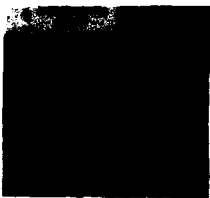


Fig. 7. Transmission electron microscope images of different powder samples sonicated for seven hours. (a) 16 gm RbCl:100 cc water aerosol spray powder, (b) 80 gm RbCl:100 cc water droplet powder, (c) 4 gm RbCl:100 cc water, large droplet powder.



Fig. 8. Fragment of an aggregate formed by freeze-drying an aerosol spray of RbCl, water, and ethanol.

formed and the ease with which these aggregates can be subdivided into primary particles. The small, filamentary aggregates that are formed by freeze-drying an aerosol of a dilute solution can be broken into primary particles most easily. Figure 6 shows transmission electron micrographs of powder formed from an aerosol spray of 4 gm RbCl: 100 cc water stock, after seven hours sonication. Figure 7 shows transmission electron micrographs of samples of (a) 16 gm RbCl:100 cc water, aerosol spray powder, (b) 80 gm RbCl:100 cc water, large droplet (hypodermic needle) powder, and (c) 4 gm RbCl:100 cc water, large droplet (hypodermic needle) powder after seven hours of sonication under identical temperature conditions and power levels. In general, we observed that the larger the size the aggregates are originally, and the more densely interconnected the primary particles within an aggregate are, the more difficult it is to break the aggregate into small primary particles.

Some researchers³ have proposed that freeze-drying can be accomplished more rapidly (and the yield improved) if a mixture comprising an aqueous solution of the reagent of interest is diluted with a high vapor pressure liquid such as ethanol. We have produced RbCl powder from an aerosol spray of a mixture of 2 gm RbCl in 12 cc water diluted with 45 cc ethanol. Aggregates of large (1- μ m cross section), densely interconnected primary particles form (Fig. 8). These primary particles are larger than the primary particles formed from a similar dilution of RbCl in water (Fig. 4). This is probably due to the lower freezing temperature and the lower thermal conductivity of ethanol compared to water; subsequently, more time would be required for the ethanol-plus-water droplets to freeze. The use of ethanol-plus-water mixtures may be a viable approach to forming freeze-dried powders for applications where more densely connected networks of large primary particles are desirable or acceptable.

SUMMARY

We have prepared powders of a strongly ionic salt, RbCl, by a freeze-drying process. Isopentane at -160°C was employed as a cryogen. The morphology of the powder that forms depends on the size of the freeze-dried droplets (aerosol spray vs. very large droplets produced using a hypodermic needle) and the concentration of the stock solution. A densely interconnected network comprising homogeneous RbCl crystallites 0.1 μ m in cross section forms from small droplets of saturated stock. A similar network comprising larger crystallites forms from larger droplets of saturated stock. Lower concentrations of stock solution produce powders comprising more delicate, less densely interconnected aggregates of RbCl crystallites which are more heterogeneous in size. The size of the primary particles which form is not proportional to the stock solution concentration, but rather varies in response to a shift in the relative importance of nucleation vs. growth. The size of the aggregates varies as

the size of the droplets. The very large aggregates formed from large droplets of dilute stock contain a broad distribution of primary particle sizes which can be interpreted as evidence of a freeze front traveling through the droplet. Larger crystallites are observed nearer the interior of the aggregate, where freezing would occur more slowly. Powders produced from mixtures of RbCl and water plus ethanol, which would freeze more slowly than RbCl and water solutions, contain larger primary particles. There is a relationship between the morphology of the particles in a powder and the ease with which the powder can be mechanically broken into smaller particles. The small, fragile aggregates formed from an aerosol spray of a dilute solution are the most easily broken.

ACKNOWLEDGEMENT

The authors would like to thank R. Tissot and R. J. Lujan for some of the x-ray diffraction data. This work was supported by the U.S. Department of Energy under contract number DE-AC04-76DP00789.

REFERENCES

1. D. W. Johnson, Jr. and P. K. Gallagher, Ch. 12, "Reactive Powders from Solution," Processing of Crystalline Ceramics (Materials Science Research, 11) eds. Hayne Palmour III, R. F. Davis, and T. M. Hare, Plenum Press, New York, NY (1978) 125.
2. I. K. Lloyd and R. J. Kovel, J. of Materials Science **23** (1988) 185.
3. M. D. Rigterink, Ceramic Bulletin **2** (1972) 158.
4. D. W. Johnson and F. J. Schnettler, J. American Ceramic Society **53**, 8 (1970) 440.
5. M. D. Rasmussen, M. Akins, and M. F. Berard, Ceramics Int'l. **10** 3 (1984) 99.
6. L. Rakotoson and M. Paulus, Advances in Ceramics **12** (1984) 727.
7. A. Roosen and H. Hausner, "The Influence of Processing Conditions on the Sintering Behavior of Co-precipitated Calcia-Stabilized Zirconia Powders," Ceramic Powders, ed. P. Vincenzini, Elsevier Scientific Publishing Co., Amsterdam, The Netherlands, (1983) 773.
8. C. Lacour and M. Paulus, Science of Sintering **11**, 3 (1979) 193.
9. M. Paulus, Ch. 3 "Freeze Drying: A Method for the Preparation of Fine Sinterable Powders and Low Temperature Solid State Reaction," Fine Particles Processing, ed. P. Somasundaran, American Institute of Mining, Metallurgical and Petroleum Engineers, Inc., New York, NY (1980) 27.
10. Powder Diffraction File, International Centre for Diffraction Data, 1601 Park Lane, Swarthmore, PA 19081-2389.
11. A. E. Nielsen, Kinetics of Precipitation, The MacMillan Company, New York, NY (1964).

SOL-GEL PROCESSING OF ADVANCED DIELECTRIC CERAMICS FOR MICROWAVE APPLICATIONS

M. SCHNOELLER AND W. WERSING
Siemens AG, Corporate Research and Development,
Otto-Bahn-Ring 6, D-8000 Munich 83, FRG

ABSTRACT

Highly dielectric ceramics make it possible to markedly miniaturize passive microwave components. We have successfully synthesized ceramic powders of the most important microwave ceramic systems $(\text{ZrTiSn})\text{O}_2$, $\text{Ba}(\text{TiNiZnTa})\text{O}_3$ and $\text{Ba}(\text{MgTa})\text{O}_3$ by using the sol-gel process. Nonaqueous solutions of metal organics together with different inorganic metal salts were used as precursors. The gels derived from these solutions are homogeneous and transparent. Different drying procedures were investigated in order to optimize powder morphology. Thermoanalytic methods and high-temperature x-ray diffraction were used to study the decomposition of xerogels and the formation of crystal phases, respectively. The calcination process was found to be complete at temperatures well below 750°C .

For the production of barium-containing powders, wet milling must be avoided because this washes out barium and thus causes undesired phases to appear. A dry milling step of the xerogel solves this problem. The prepared $(\text{ZrTiSn})\text{O}_2$ and $\text{Ba}(\text{TiNiZnTa})\text{O}_3$ already equal or surpass the quality of conventionally prepared ceramics.

1. INTRODUCTION

Highly dielectric ceramics make it possible to markedly miniaturize passive microwave components. These ceramics have to fulfill the requirements of high permittivity, extremely low dielectric losses, and low-temperature coefficient of the permittivity to yield temperature-stable resonators. Low dielectric losses result in high quality factors for dielectric resonators made from these ceramics. This makes it possible to produce frequency-stable and low noise oscillators as well as microwave filters with narrow band width and very low insertion losses in a simple way [1].

The dielectric losses of microwave ceramics are caused on the one hand by phonon scattering at impurities and by anharmonic phonon coupling, on the other hand by relaxations of space charge polarization present at interfaces (Maxwell-Wagner effect) [2]. To obtain the highest resonator quality factors, one therefore tries to produce as perfect as possible single-phase material without dopants in the crystallites. The quality factor is then solely limited by the intrinsic anharmonic damping. Measurement of the frequency dependence of quality factors [2] and the determination of quality factors by infrared reflection spectrometry using a Kramer Kronig analysis [3] show that even in the best materials available to date with very high quality factor, relaxation effects still contribute to losses. It seems possible therefore, to pronouncedly increase the quality factors by preparing extremely pure and homogeneous materials. This is the reason why sol-gel techniques were employed for the preparation of microwave ceramics in this paper. The sol-gel

technique was developed for the following three materials:

- $Zr_{0.8}Ti_{0.9}Sn_{0.3}O_4$ which is today's most often employed microwave ceramic [4],
- $Ba\{Ti_{0.05}[(Ni_{0.1}Zn_{0.9})_{1/3}Ta_{2/3}]_{0.95}\}O_3$ which is a temperature-stable ceramic with a quality factor of 5000 at 20 GHz [2],
- $Ba(Mg_{1/3}Ta_{2/3})O_3$ which is the ceramic with the highest known quality factors between 10000 and 15000 at 20 GHz [5].

2. SYNTHESIS OF THE CERAMIC POWDERS

The synthesis of the sol-gel components was carried out according to the alkoxide method by formation of inorganic polymers. The elements titanium, zirconium and tantalum were used in the form of alkoxides; the elements barium, magnesium, nickel and zinc were used as acetates. The application of barium as acetate in the alkoxide technique has been described by P.P. Phule and S.H. Risbud [6]. Tin has been used as an acetate as well as in its chloride form.

The single compounds were dissolved in organic solvents (starting solutions) and transferred into gel by hydrolysis under mild conditions using a mixture of water and organic solvents. The gels were carefully dried to xerogel by extraction of the solvents and transferred to ceramic powder by a calcination step. Figures 1...2 show a detailed review of the synthesis

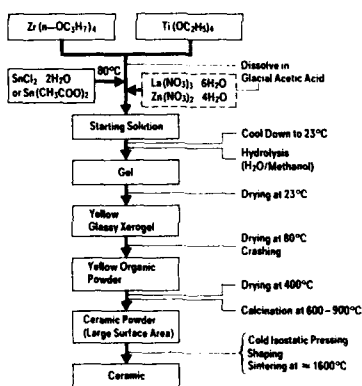


Fig. 1. Sol-gel process for $Zr_{0.8}Ti_{0.9}Sn_{0.3}O_4$.

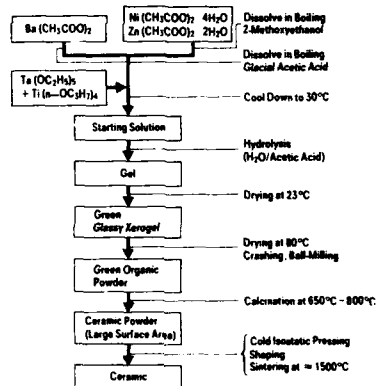


Fig. 2. Sol-gel process for $Ba\{Ti_{0.05}[(Ni_{0.1}Zn_{0.9})_{1/3}Ta_{2/3}]_{0.95}\}O_3$.

paths to the different ceramic powders. In the following, the critical steps in the synthesis will be described in more detail:

- formation of the gel by hydrolysis of the starting solutions (sols)
- drying of the gels to xerogels, and
- calcination of the xerogels.

2.1. Gel formation

Hydrolysis of the starting solutions is a very sensitive step especially for the tantalum compounds. In order to initiate the formation of gel homogeneously, the water used for hydroly-

sis always has to be diluted with organic solvents. The type of organic solvent to be used depends on the composition of the starting solution. It must be adapted to every starting solution. If, for example, methanol is applied as a diluting medium in the hydrolysis of barium magnesium tantalum compounds, the gel forms rapidly within a couple of minutes. The formed gel, however, tends to decompose during drying to xerogel and contains crystalline components even at room temperature. If, however, 2-methoxyethanol is used as the diluting agent, the gel forms after a longer period of standing. This gel can then be dried without separating. Fig. 3 shows the influence of the two solvents on the formation of the perovskite lattice in two high temperature x-ray diffraction measurements.

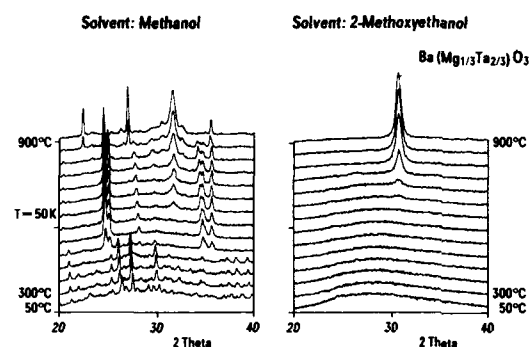


Fig. 3. Influence of organic solvent on hydrolysis and formation of perovskite lattice.

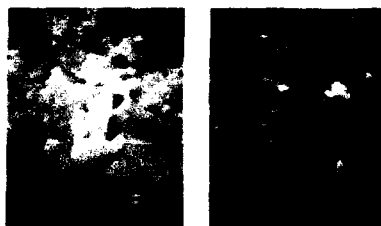
Acetic acid has proven itself as a suitable dilution medium for the hydrolysis of barium titanium nickel zinc tantalum starting solutions. Methanol can be used to hydrolyze zirconium titanium tin starting solutions. In addition to the type of organic solvent, the molar ratio of water and alkoxide is also important for the hydrolysis step. If the amount of water is too high, the gel will decompose during drying by separation of the bariumacetate. For the

hydrolysis of tantalum-containing compounds, a ratio of 3.5:1 of water to alkoxide is suitable. For the hydrolysis of zirconium titanium tin sol, a ratio of 1.1:1 is sufficient.

2.2. Drying of gels

While the drying of zirconium titanium tin gels does not cause any problems, drying of tantalum-containing gels must be controlled carefully. Drying has to be accomplished in a way so that the process yields a glasslike xerogel without pores or ca-

Fast Drying



Slow Drying

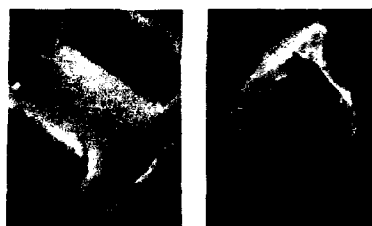


Fig. 4. Influence of drying process on the microstructure of ceramic powders.

vities. If the volatile components are extracted too fast, the ceramic powder will develop cracks, pores and cavities after the calcination process (fig. 4). This may result in poor densification during firing. Extraction of the solvent in vacuum at 80 °C leads to rapid formation of a glasslike gel. High-temperature x-ray diffraction shows, however, that between 350 °C and 850 °C, intermediate crystalline BaCO_3 , and above 800 °C, stable $\text{Ba}_{0.5}\text{TaO}_3$ form as undesired impurity phases in addition to other impurities (fig. 5). If the gel is dried in too thick a layer, crystalline components will form in addition to the gel. These will show up again as impurity phases in high temperature x-ray diffraction.

Tantalum-containing gels are best dried in layers approximately 3 mm thick at room temperature in petri dishes until the hard and glasslike xerogel forms after a couple of days. The powder is further dried in a drying closet in flowing air at 50 °C and later at 80 °C until a coarse powder is created by the formation of drying cracks.

Zirconium-containing gel is first dried to a coarse yellow powder under a hood in a thick layer or on filter paper. The powder is further dried slowly in flowing air in a drying closet up to 400 °C. The powder becomes black during this process caused by the formation of crack products. However, if the temperature is increased very slowly (0.1 K/min), a coarse white powder will result at 400 °C.

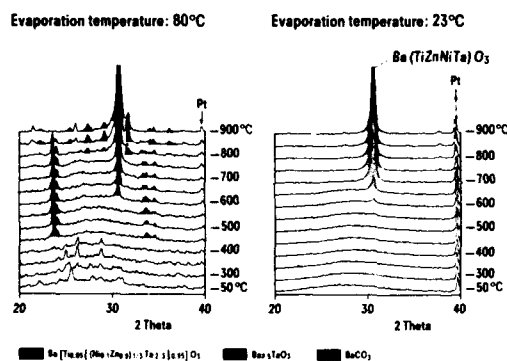


Fig. 5. Influence of evaporation temperature on development of perovskite structure.

2.4. Calcination and firing

All calcinations of xerogel powders were performed in flowing oxygen

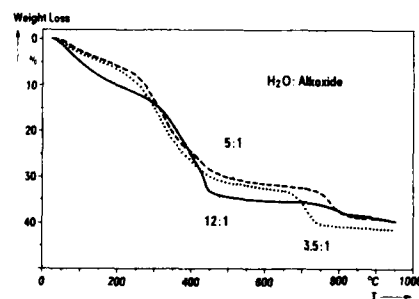


Fig. 6. Weight loss of $\text{Ba}(\text{MgTa})\text{O}_3$ xerogels temperature for different amounts of water used for hydrolysis.

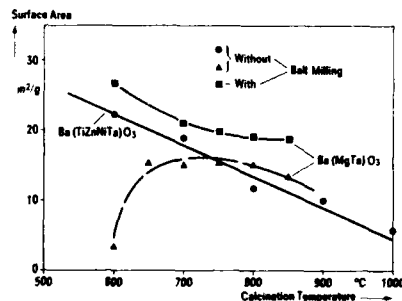


Fig. 7. Influence of calcination temperature on surface area of $\text{Ba}(\text{TiZnMgTa})\text{O}_3$ and $\text{Ba}(\text{MgTa})\text{O}_3$ powders.

at temperatures between 600 °C and 900 °C. The xerogels were ground in an agate mortar, calcined, ball-milled (agate balls) for 18 hours in a watery suspension, drained and dried. Since barium was lost during this procedure (up to 2 % depending on the calcination temperature) the xerogel powder was ball milled dryly before calcination in later experiments. In this way, very fine ceramic powders with large surface areas could be produced after relatively short milling times.

The ceramic powders produced by the calcination step were isostatically pressed without binder, shaped cylindrically on the turning lathe, and fired at temperatures between 1500 °C and 1600 °C for 4 hours in flowing oxygen.

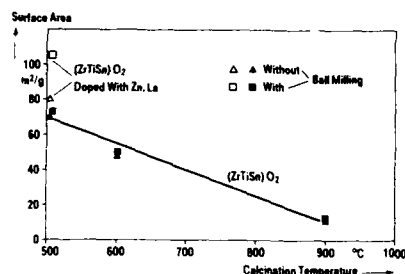


Fig. 8. Influence of calcination temperature and ball-milling on surface area of $(\text{ZrTiSn})\text{O}_2$ powders.

$\text{Ba}(\text{MgTa})\text{O}_3$ xerogel powder as a function of temperature for various water to alkoxide ratios used during hydrolysis. For low water contents, the high temperature weight loss starts much earlier and with a higher percentage.

Figures 7 and 8 show the dependence of the surface area on the calcination conditions with and without ball-milling of the calcined powders. For $\text{Ba}(\text{TiNiZnTa})\text{O}_3$ and $(\text{ZrTiSn})\text{O}_2$ powders, the surface area decreases with increasing calcination temperature. The undoped $(\text{ZrTiSn})\text{O}_2$ powders are only slightly dependent on milling in contrast to samples doped with lanthanum and zinc. For $\text{Ba}(\text{MgTa})\text{O}_3$ the surface area of the powders seems to be almost independent of the calcination temperature. The anomalously low values at 600 °C and 650 °C are, however, obviously caused by residual organic material (cf. fig. 6) which agglomerates the x-ray amorphous powder material (fig. 3). For calcination temperatures higher than 800 °C, the milling effect on the surface area increases.

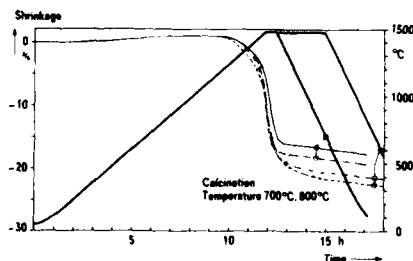


Fig. 9. Shrinkage behaviour of $\text{Ba}(\text{TiNiZnTa})\text{O}_3$ powders.

3. PHYSICAL CHARACTERIZATION OF THE SYNTHESIS STEPS

The single synthesis steps were characterized by physical analysis methods. The methods employed were high temperature x-ray diffraction scanning electron microscopy with secondary electrons and back scatter electrons, laser granulometry, determination of the surface area according to the BET method, thermogravimetry and dilatometry. Fig. 6

shows the weight loss of $\text{Ba}(\text{TiNiZnTa})\text{O}_3$ powders as a function of temperature for various water to alkoxide ratios used during hydrolysis. For low water contents, the high temperature weight loss starts much earlier and with a higher percentage.

The shrinking behaviour of $\text{Ba}(\text{TiNiZnTa})\text{O}_3$ powders is shown as a function of calcination temperature and firing time in fig. 9. The sample calcined at 700 °C shrinks less during short firing than the sample calcined at 800 °C. But longer firing times (4 h) with smaller grain sizes clearly show that the powders calcined at 700 °C lead to ceramics with higher density.

4. CHARACTERIZATION OF THE CERAMICS

4.1. Microstructure

Table I shows (in a similar manner as fig. 7) the influence of calcination temperature on density and porosity of $\text{Ba}(\text{MgTa})\text{O}_3$ ceramics. As can also be seen in fig. 7, the wet-milling step levels out the differences in specific surface area of the calcined powders and thus yields, in all cases, equally high densi-

Calcination- temperature [$^{\circ}\text{C}$]	Sintering- temperature [$^{\circ}\text{C}$]	Ceramic density [g/cm^3]	Porosity [%]
650	1500	7.49	2.0
	1525	7.52	1.6
700	1500	7.48	2.1
	1525	7.49	2.0
800	1500	7.51	1.7
	1525	7.52	1.6

Table I. Density of $\text{Ba}(\text{MgTa})\text{O}_3$ ceramics fired for 4 hours. Powders had been wet milled for 18 hours.

ty of about 98% of the theoretically possible value ($7.64 \text{ g}/\text{cm}^3$). Since wet milling causes barium loss and thus initiates the formation of unwanted phases, we tried to replace this step by dry milling the xerogel before calcination. The results for



Fig. 10. Microstructure of sol-gel prepared $\text{Ba}(\text{TiZnNiTa})\text{O}_3$ ceramics. Micrograph with secondary electrons (left), and backscatter electrons (right).

$\text{Ba}(\text{MgTa})\text{O}_3$. However, at the highest possible firing temperature available to us (1580°C), the density is only 65 % of the theoretical value. We will therefore present results on these ceramics at a later time. In $\text{Ba}(\text{MgTa})\text{O}_3$ ceramics, which had been prepared from wet-milled powders, two phases form in addition to $\text{Ba}(\text{MgTa})\text{O}_3$ due to barium loss. The first of these contains less Ba and less Mg, the second contains only Mg and Ta. Barium deficiency in these ceramics obviously promotes shrinking because dense ceramics can be produced at 1525°C .

$\text{Ba}(\text{TiZnNiTa})\text{O}_3$ ceramics are shown in Table II. One finds that dry milling for 2 hours also yields ceramics with high density better than 98 % of the theoretical value ($7.8 \text{ g}/\text{cm}^3$). Fig. 10 shows the microstructure of such a ceramic in a SEM micrograph, giving proof not only of the high density but also of phase purity. The results obtained from dry milled $(\text{ZrTiSn})\text{O}_2$ powders are shown in table III. One also gets extremely fine powders after calcination by dry milling of

Ball-milling time [h]	Sintering-temperature [°C]	Ceramic-density [g/cm ³]	Porosity [%]
1	1500	7.28	6.7
	1525	7.30	6.4
2	1500	7.65	1.9
	1525	7.67	1.7

Table II. Density of Ba(TiNiZnTa)O₃ ceramic fired for 4 hours. Powders had been dry milled and calcined at 700 °C.

Ball-milling time [h]	Calcination-temperature [°C]	Ceramic-density [g/cm ³]	Porosity [%]
2	550	4.95	7.6
	650	4.90	8.6
	750	4.90	8.6
4	550	4.91	8.4
	650	4.96	7.5
	750	4.98	7.1
8	550	4.96	7.5
	650	5.02	6.3
	750	5.04	6.0

Table III. Density of (ZrTiSn)O₂ ceramics fired for 4 hours at 1550 °C. Powders had been dry milled.

Ceramic	Sol-Gel					Mixed oxide	
	Milling time [h]	Calc. temp. [°C]	Sint. temp. [°C]	ε _r	Q at (f[GHz])	ε _r	Q at (f[GHz])
(ZrTiSn)O ₂	18 (wet)	900	1500	31.0	8500 (5)	38	6000 (7)
	8 (dry)	550	1550	33.7	6200 (7)		
	2 (dry)	650	1550	33.1	5800 (7)		
	4 (dry)	650	1550	33.7	6600 (7)		
	8 (dry)	650	1550	34.4	6800 (7)		
	8 (dry)	750	1550	34.6	6600 (7)		
Ba(TiNiZnTa)O ₃	18 (wet)	750	1500	29.5	5300(10)	30	9000(10)
	18 (wet)	750	1525	---	6300 (8)		
	2 (dry)	750	1525	35.5	11000 (8)		
Ba(MgTa)O ₃	18 (wet)	650	1525	26.2	~1300 (8)	25	30000(10)
	18 (wet)	700	1525	25.7			
	18 (wet)	800	1525	26.4			

Table IV. Permittivities ε_r and quality factors Q at microwave frequencies.

4.2. Dielectric properties

The dielectric properties at microwave frequencies of the prepared ceramics are shown in Table IV. For comparison, table IV also shows the typical values of $(\text{ZrTiSn})\text{O}_2$ and $\text{Ba}(\text{TiNiZnTa})\text{O}_3$ ceramics prepared according to the mixed oxide method, and of the $\text{Ba}(\text{MgTa})\text{O}_3$ ceramic from ref. 5. As can be seen from Table III and from the ϵ_r values of Table IV, the sol-gel powder prepared from $(\text{ZrTiSn})\text{O}_2$ ceramics (which do not contain any sintering help) do not complete densification at the applied firing temperatures. The quality factors are, however, already 10 % higher than those of conventionally prepared ceramics. Further improvement by completing the firing step can be expected. The $\text{Ba}(\text{TiNiZnTa})\text{O}_3$ ceramics show that quality factors are greatly reduced by secondary phases. Although SEM micrographs of ceramics prepared from wet-milled powders show only very few grains of secondary phases, the quality factor of these ceramics is only half as great as in phase-pure ceramics. One can also conclude from these high quality factors of dry milled ceramics that the sol-gel technique can successfully be applied to materials with such complex composition. Since, as can be seen in fig. 3 and fig. 5, the perovskite phase in $\text{Ba}(\text{MgTa})\text{O}_3$ forms at a 100 K higher temperature than in $\text{Ba}(\text{TiNiZnTa})\text{O}_3$, wet milling causes higher barium losses. This can also be proven by a chemical analysis of the liquids separated after the milling step. This means that the amount of impurity phases in $\text{Ba}(\text{MgTa})\text{O}_3$ is much higher as can also be seen in the SEM micrographs. This explains the unexpectedly low quality factors in these ceramics. Since the porosity of these ceramics is very low, one finds high permittivities compared to conventionally prepared ceramics. Our further work will concentrate on this ceramic system starting with the firing process of dry milled powders since theory predicts the highest quality factors in this system [2].

ACKNOWLEDGEMENT

We wish to express our gratitude to Ms. M. Huber for the preparation of samples and for the microwave measurements, to Dr. Zorn for the high-temperature x-ray diffraction measurements, and to Dr. R. Weyl for the SEM measurements.

REFERENCES

1. K. Pöbl and G. Wolfram, *Siemens-Components* 17, 14 (1982)
2. W. Wersing, to be published in *Proc. of the 1989 European Conf. on Electronic Ceramics*, London.
3. K. Wakino, M. Murata and H. Tamura, *J. Am. Ceram. Soc.* 69, 34 (1986)
4. G. Wolfram and H.E. Göbel, *Mat. Res. Bull.* 16, 1455 (1981)
5. K. Matsumoto, T. Hiuga, K. Tanaka and H. Ichimura, *Proc. of the Sixth IEEE Int. Symp. on Applications of Ferroelectrics* (1986) pp. 118-121.
6. P.P. Phule and S.H. Risbud, *Adv. Cer. Mat.* 3, 183 (1988)

STRUCTURAL TRANSITIONS INDUCED BY COLLOIDAL INTERACTIONS IN CERAMIC DISPERSIONS

Raj Rajagopalan

Department of Chemical Engineering, University of Houston, Houston, Texas
77204-4792

ABSTRACT

A discussion of the formation of periodic colloid structures, liquid-like ordering, and compact and fractal aggregates caused by colloidal forces in ceramic dispersions is presented. Construction of phase diagrams based on simple forms of repulsive potentials is often not adequate, and it is important to include appropriate attractive interactions in the theoretical analyses. Examples of radial distribution functions, osmotic pressures, and phase diagrams are given for dispersions interacting through Derjaguin-Landau-Verwey-Overbeek potentials. Densification of colloidal aggregates due to positional relaxation and the effects of such densification on the structure of the aggregates are discussed.

I. INTRODUCTION

It has been known for some time that the packing characteristics and the resulting microstructure of colloidal dispersions used in ceramic processing depend on the physics and chemistry of colloidal interactions [1]. Experimental studies demonstrate that highly dense and uniform packing is possible in the case of particles in the submicron-size range, but above nanometer sizes. Particles in the lower size range produce low-density gels, which typically exhibit large shrinkage during drying and sintering and subsequent cracking and incomplete sintering [2, 3].

The role of colloidal interactions on the structure of aggregates is also beginning to receive more attention lately [4]. Neutron scattering studies on colloidal aggregates indicate that the aggregate structure has a sensitive dependence on solution chemistry, the surface properties of particles, and the nature of any adsorbed polymers (e.g., steric stabilizers). For instance, dispersions dominated by weak electrosteric interactions or 'stabilized' by uncharged polymers of high molecular weight (e.g., by polyethylene oxide) lead to aggregates characterized by liquid-like ordering (invariant under translation) over a length scale of a few particle diameters and by fractal (scale-invariant) structures at larger length scales (prior to the gelation cross-over region). In contrast, dispersions rich in multivalent counterions appear to display conventional fractal structures even at moderate volume fractions of the dispersed particles. In addition to determining the core structure, the near-field interactions dictate the strength (and number) of inter-particle bonds. Since the short-range structure, coordination numbers, bond lengths and bond energies control the mechanical (and subsequently the transport) properties of the resulting gels and bulk specimens, the steric, electrosteric and other colloidal interactions in dense dispersions and their effects on aggregation and gelation require systematic investigation.

In order to place the renewed interest in colloid physics in proper context, it is important to cite the relevance of this area in certain fundamental studies as well. The structure and dynamics of colloidal (or, supramolecular) dispersions

and assemblies have received considerable attention in recent years for a number of reasons [5-9]. One major motivation for this interest, particularly from the point of view of condensed-matter physics, is the observation that colloidal dispersions offer excellent *model many-body systems* for studying a variety of fundamental (or, applied) problems which are much more difficult to study by other means. Some notable examples include shear-induced phase transitions and lattice dynamics in crystalline materials [10], symmetry-lowering in two-dimensional systems (using two-dimensional colloidal crystals and monolayers [11]), cooperative phenomena in supercooled Yukawa fluids [12, 13], nucleation, growth and order/disorder phenomena in solutions of macroions [14-16], and fractal growth and aggregation phenomena [17-22]. The last example is especially relevant in the case of ceramic processing and in certain classes of phenomena in materials physics concerned with pattern formation (e.g., in film-deposition techniques [23] and nucleation, aggregation, and gelation phenomena in sol-gel processes [24]). Excellent reviews of the structures of aggregates which one might expect in the case of diffusion-limited aggregation (DLA), reaction-limited aggregation (RLA) and cluster-cluster aggregation (CCA) have been presented by Meakin [19-21], and the recent monograph by Jullien and Botet [18] offers a brief overview of these topics; related discussions on gelation, percolation and other applications may be found in Pietronero and Tosatti [25] and Family and Landau [26]. As noted by Abraham [27], the above-described interest in the growth and form of statistical structures, particularly in the case of fractal growth, is motivated by the following questions -- 'How can one best characterize the form of an object?' and 'What growth processes determine a given form?'.

In this paper, we examine briefly two extreme limits of the effects of colloidal forces on the microstructure of dispersions. Specifically, in Section II, the formation of periodic colloid structures and liquid-like ordering is reviewed. This is then followed, in Section III, by some observations on the structure of colloidal aggregates when the interaction forces allow a restructuring of particles after aggregation. A few closing remarks follow in Section IV. Because of space limitations, equations and theoretical and computational details are not presented here; however, these may be obtained from the numerous references listed at the end of the paper.

II. MICROSTRUCTURES IN STABLE DISPERSIONS

Phase transitions in colloidal dispersions have been studied by a number of investigators [7, 28-31]. In the case of the formation of periodic structures, the simplest possible analysis of such crystallization is to treat the dispersion as a suspension of hard, mutually-impenetrable spheres. This is of course equivalent to assuming the simplest possible pair interaction force between the particles, namely, one corresponding to a hard-sphere interaction potential. The adequacy of this approximation, some of the needed (empirical and theoretical) modifications of this approximation, and the implication of this approach to the classical theories of phase transitions have been discussed extensively in the literature [7].

Attempts to explain ordering and its implications to the nature of interaction forces have also been made from the point of view of known systems such as electron crystals and solutions of strong electrolytes. Although such analogies are only approximate, they have been helpful in providing some additional insight into the nature of many-body interactions relevant in both

molecular and supramolecular systems. The following observations are relevant in this context:

- If the hard core of the potential is fairly steep and the influence of attraction is not strong enough to cause flocculation, an *ad hoc* procedure of the above type is adequate for *estimating* the volume fractions at which freezing (ordering) and melting (disordering) occur.
- However, the other properties (such as osmotic pressures or isothermal compressibilities) derived from hard-sphere fluids using the above effective diameters may not necessarily match the actual values; that is, there is no uniquely defined value for the effective hard-sphere diameter that can represent the dispersion in its totality.
- Consequently, these *ad hoc* procedures must be seen as highly-simplified exploratory attempts to represent the many-body effects in terms of convenient reference potentials. In fact, as has been discussed elsewhere [28], hard-sphere fluids are frequently used as *reference fluids* in perturbation theories; therefore, the above procedures may be thought of as zeroth-order perturbation approaches, although selecting the effective diameter on the basis of the magnitude of the pair potential at that distance does not rigorously account for the statistical nature of many-body interactions.

Simple analyses based on hard-sphere approaches are not always sufficient for constructing phase diagrams which can accurately indicate structural transitions (such as body-centered cubic structure to face-centered cubic structure and reentrant transitions) in addition to simple 'melting' and 'freezing'. Conflicting results have appeared in the literature (see [29-30]), partly because of severely restrictive assumptions concerning the interaction potentials or due to finite-size effects in computation. Some of these will be discussed in detail elsewhere [32]; here we merely present some results based on computer experiments and statistical mechanical perturbation theories for the disordered (liquid-like) dispersions and some results based on a 'cell' model for the ordered dispersions near 'melting'; see Figures 1 - 7. These figures present sample radial distribution functions, phase diagrams, and results for osmotic pressures and pressure gradients.

A few general observations based on these figures are appropriate. While Figure 1 shows the development of structure as the volume fraction is increased, it can be seen from Figure 2 that for otherwise identical conditions the dispersion becomes more stable (and the average relative interparticle spacing increases) for smaller particles. Notice that this is consistent with the earlier observation (see Section I, 'Introduction') concerning the looser gels formed by smaller particles. Figure 3 shows the first-order phase change that occurs in dispersions as the volume fraction is increased. Similar diagrams can be used to construct phase diagrams such as the one shown in Figure 4. Figure 4, corresponding to interaction forces that are dominated by steep repulsions and moderately small attraction, also demonstrates, as mentioned earlier, that simple hard-sphere approximations are sufficient for constructing the phase diagrams for such interaction potentials.

As mentioned previously, the 'melting' of the ordered phase has been approximated in these computations by a cell model known as the Lennard-

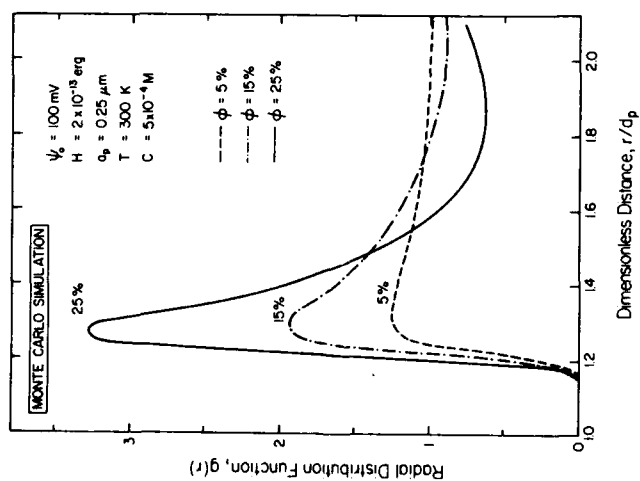


Figure 1. Radial distribution functions (based on computer experiments) for various volume fractions. See reference [28] for details of the interaction potential parameters shown in the legend. The particle radius and diameter are denoted by a_p and d_p , respectively.

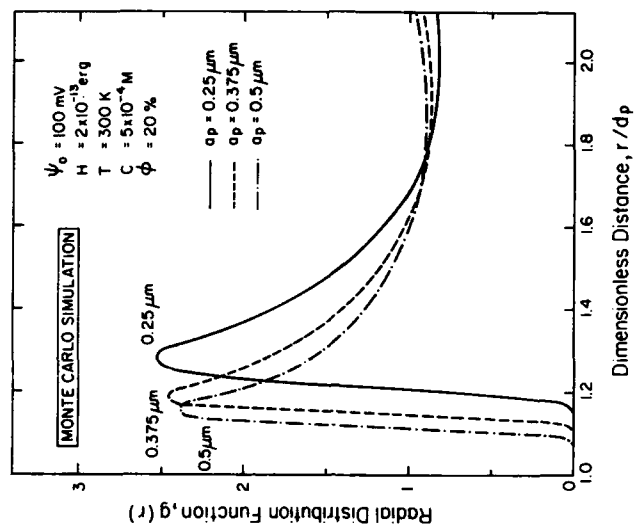


Figure 2. Radial distribution functions showing the effect of particle size for otherwise identical parameters.

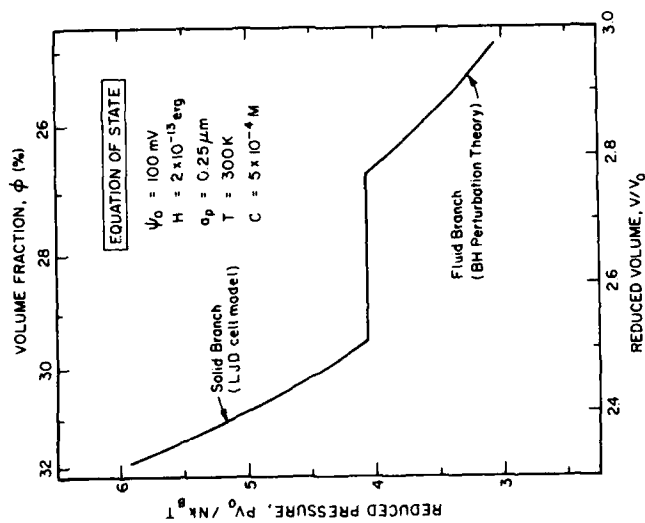


Figure 3. Osmotic pressure of as a function of volume fraction. The figure illustrates a first-order phase transition. (See reference [28] for details.) The *total* volume needed for the particles when they are stacked in ordered close packing (with a face-centered cubic structure) is denoted by V_0 .

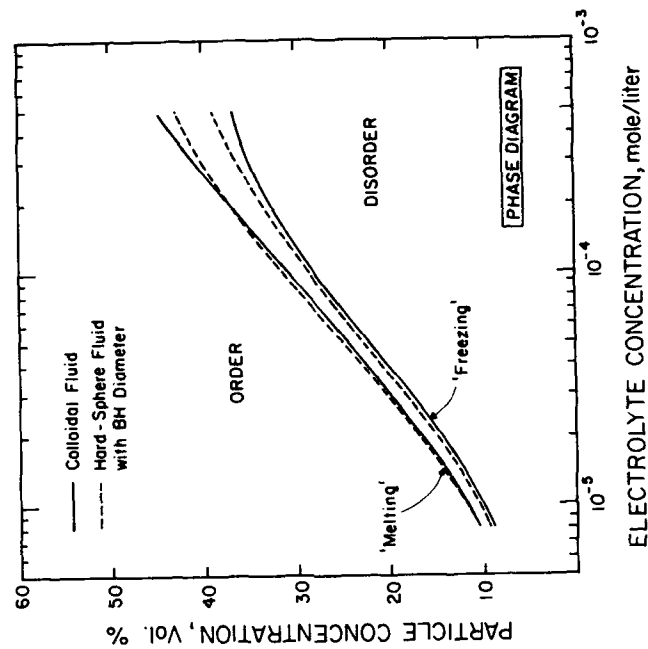


Figure 4. Phase diagram for a dispersion in terms of the electrolyte concentration [28, 33].

Jones/Devonshire model (see [28]). Figure 5 demonstrates, through osmotic pressure calculations, that this model is sufficiently accurate for representing the ordered phase near melting. Osmotic pressure calculations and pressure gradients [with respect to density of the dispersion (i.e., volume fraction)] for the 'liquid-like' phase are presented in Figures 6 and 7, respectively. The calculations are based on computer simulations and perturbation theories as indicated in the legends. Additional computational details and information on interaction forces are available in references cited earlier [28, 32, 33] and in a forthcoming publication [34].

III. STRUCTURE OF AGGREGATES

We now turn our attention to the structure of colloidal aggregates when the aggregates are allowed to undergo positional relaxation.

Diffusion-limited aggregation and corresponding nucleation and growth processes address the dynamic and the nonequilibrium structures of aggregates. On the other hand, experimental observations on colloidal flocs seem to suggest that, depending on the chemical constituents present in the dispersions, near-field structural rearrangements may be possible as a result of relaxation of the particles during or after aggregation. In addition, the resulting near-field density function can be sensitive to the colloidal forces and to the shape of local attractive or repulsive interactions. Changes in the distribution on longer length scales are also likely as a consequence of densification with time. For example, experimental evidence shows that addition of surfactants to gold flocs formed through cluster-cluster aggregation (with an initial fractal dimension of 1.7) causes the flocs to restructure and densify (thereby increasing the fractal dimension [1]).

Off-lattice versions of well-known cluster-growth models can be used, in combination with Metropolis Monte Carlo simulations, to examine the relaxation of particles in an aggregate after the aggregate is formed [35]. The results of such an examination suggest that radiation scattering experiments on such aggregates can be expected to lead to at least four separately identifiable regions, in the following order of decreasing scattering vector: (i) the Porod regime at large scattering vectors, corresponding to scattering from the surface of the primary particles, (ii) a compact region, of size about a few particle diameters, with a statistical, translationally-invariant structure arising purely from packing considerations, (iii) a fractal region, the dimension of which will depend on the initial fractal dimension and the extent of relaxation of the particles after deposition, and, finally, (iv) a non-fractal outer surface, with a very rapidly decreasing density.

This observation is consistent with some experimental results available in the literature on colloidal flocs. In addition to the determination of the fractal dimensionality of aggregates grown by various mechanisms, the core structure of colloidal aggregates and its dependence on the chemical additives in the dispersion have become the focus of experimental investigations recently. For instance, Wong, Cabane and Duplessix [4] have recently reported small-angle neutron-scattering data on aggregates of silica spheres in water. Their results indicate that the flocculation of silica particles by weakly charged or uncharged polymers of very high molecular weight leads to flocs with short-range, translationally invariant structures which extend over a few (roughly four) particle diameters. Beyond this range, the structure becomes loose and self-

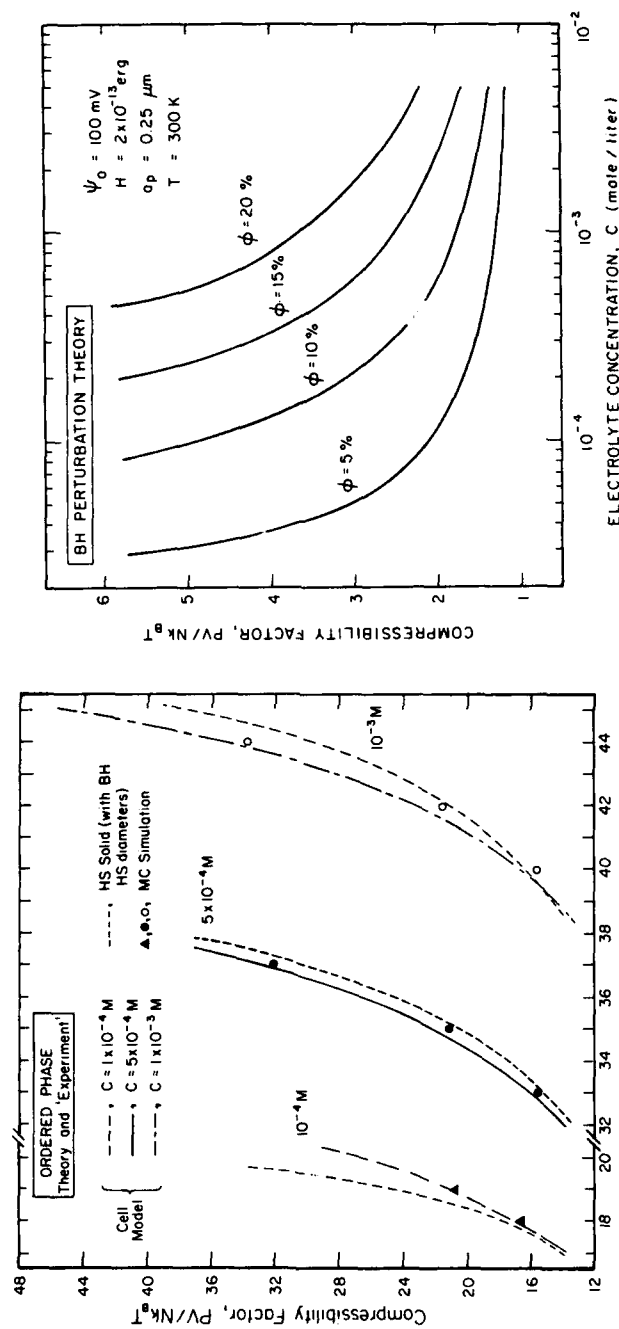


Figure 5. Pressure in an ordered dispersion based on computer experiments compared with cell model results and a theory for hard-sphere solids [28, 33].

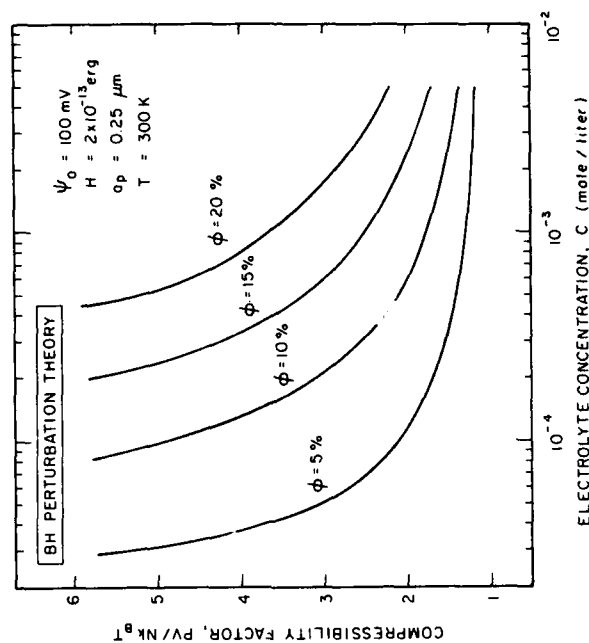


Figure 6. Pressure in a disordered dispersion as a function of volume fraction and electrolyte concentration (based on a perturbation theory; [33])

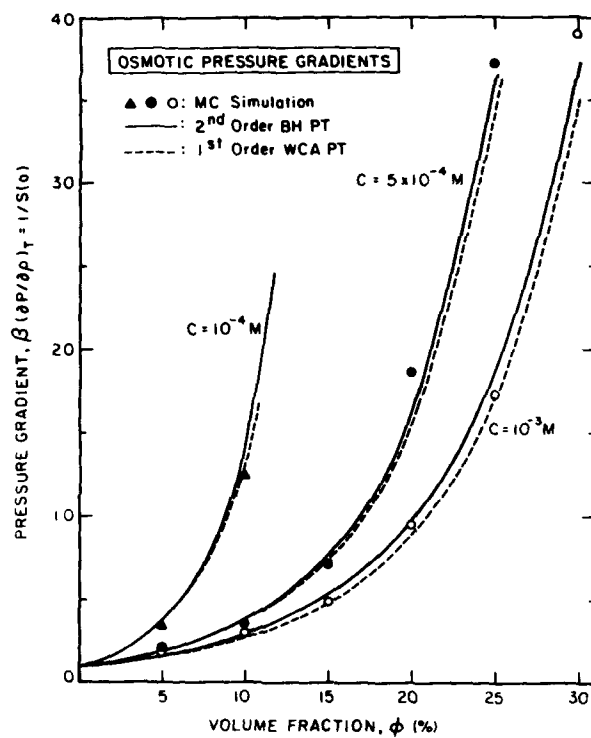


Figure 7. Pressure gradient in a disordered dispersion based on computer experiments and two perturbation theories [28, 33].

similar (fractal). (In this case, the steric barrier imposed by the polymer effectively eliminates the London-van der Waals attraction between the particles. Further, since the polymer is uncharged, the net interaction is effectively equivalent to a hard-sphere interaction.) For aggregates with a large number of particles and sufficient bond relaxation, the compact core may extend beyond four or five diameters. Wong *et al.* also report that the silica aggregates formed through neutralization or screening of the negative charges on the spheres are fractals down to radial distances of the order of the diameter of the spheres. This observation implies that these latter fractals are kinetically-limited in their growth, as one would expect. The strong van der Waals bond in this case is also unlikely to allow the particles to rearrange themselves after contact, thus eliminating the formation of fully compact cores.

IV. CONCLUDING REMARKS

The discussion above illustrates the critical role colloidal interactions play in determining the equilibrium structures of dense dispersions used in colloidal processing of ceramics. However, it is important to note that the equilibrium structure is only a part of the broader picture that needs to be studied in developing one's understanding of the role of colloidal phenomena in ceramic processing. In particular, the dynamic aspects of structural evolution and their impact on the final microstructure obtained during processing cannot be underestimated. Nevertheless, equilibrium studies are essential for determining what is thermodynamically possible, so that the controllable physical and chemical parameters can be chosen appropriately. While not discussed here, it is important to note that the control of polydispersity and the corresponding changes in colloidal interactions offer *additional* control over the microstructure of the final green body. Physical and computer experiments demonstrate that the microstructure of the green body has a strong influence on the densification of the specimen during sintering and on the corresponding changes in the defect and void structures in the final specimen [36, 37].

ACKNOWLEDGMENTS

The author thanks the Texas Advanced Technology Program and the National Science Foundation for partial support of the work reported here.

REFERENCES

1. B. J. Tarasevich, J. Liu, M. Sarikaya, and I. A. Aksay, in **Better Ceramics Through Chemistry III**, MRS Proc., Vol. 121, edited by C. J. Brinker, D. E. Clark, and D. R. Ulrich (Materials Research Society, Pittsburgh, PA, 1988) p. 225.
2. E. M. Rabinovitch, D. W. Johnson, J. B. MacChesney, and E. M. Vogel, *J. Amer. Cer. Soc.* **66**, 683 (1983).
3. C. J. Brinker, W. D. Drotning, and G. W. Scherer, in **Better Ceramics Through Chemistry**, MRS Proc., Vol. 32, edited by C. J. Brinker, D. E. Clark, and D. R. Ulrich (Elsevier Sci. Publ., New York, NY, 1984) p. 25.
4. K. Wong, B. Cabane and R. Duplessix, *J. Colloid Interface Sci.* **123**, 446 (1988).

5. N. Ise and I. Sogami, Eds., **Ordering and Organisation in Ionic Solutions** (World Scientific, Singapore, 1988).
6. S. A. Safran and N. A. Clark, Eds., **Physics of Complex and Supermolecular Fluids** (Wiley, New York, 1987).
7. C. S. Hirtzel and Raj Rajagopalan, **Colloidal Phenomena: Advanced Topics** (Noyes Publ., Park Ridge, NJ, 1985).
8. D. W. Schaefer and K. D. Keefer, in **Fractals in Physics**, edited by L. Pietronero and E. Tosatti (North-Holland, Amsterdam, 1986) p. 39.
9. R. H. Ottewill, in **Ordering and Organisation in Ionic Solutions**, edited by N. Ise and I. Sogami (World Scientific, Singapore, 1988) p. 421.
10. A. J. Hurd, N. A. Clark, R. C. Mockler, and W. J. O'Sullivan, *Phys. Rev. A* **26**, 2869 (1982).
11. Y. Tang, R. M. Malzbender, R. C. Mockler, W. J. O'Sullivan, and J. A. Beall, *J. Phys. A: Math. Gen.* **20**, L189 (1987).
12. K. Kremer, M. O. Robbins, and G. S. Grest, *Phys. Rev. Lett.* **57**, 2694 (1986).
13. K. Kremer, G. S. Grest, and M. O. Robbins, *J. Phys. A: Math. Gen.* **20**, L181 (1987).
14. N. Ise, T. Okubo, M. Sugimura, K. Ito, and M. J. Nolte, *J. Chem. Phys.* **78**, 323 (1983).
15. N. Ise, T. Okubo, M. Sugimura, K. Ito, and M. J. Nolte, *J. Chem. Phys.* **78**, 536 (1983).
16. N. Ise, T. Okubo, K. Yamamoto, M. Matsuoka, H. Kawai, T. Hashimoto, and M. Fujimura, *J. Chem. Phys.* **78**, 541 (1983).
17. J. Feder, **Fractals** (Plenum Press, New York, 1988).
18. R. Jullien and R. Botet, **Aggregation and Fractal Aggregates** (World Scientific, Singapore, 1987).
19. P. Meakin, in **Time-Dependent Effects in Disordered Materials**, edited by R. Pynn and T. Riste (Plenum Press, New York, 1987) p. 45.
20. P. Meakin, *Phys. Rev. A* **35**, 2234 (1987).
21. P. Meakin, in **Phase Transitions and Critical Phenomena**, edited by C. Domb and J. L. Lebowitz (Academic Press, New York, 1987).
22. D. W. Schaefer, J. E. Martin and A. J. Hurd, in **On Growth and Form**, edited by H. E. Stanley and N. Ostrowsky (Martinus Nijhoff Publ., Boston, MA, 1986) p. 198.

23. P. Meakin, *CRC Critical Reviews in Solid State and Materials Sciences* **13**, 143 (1987).
24. K. D. Keefer, *MPS Bulletin*, p. 29, Oct. 1/Nov. 15, 1987.
25. L. Pietronero and E. Tosatti, Eds., **Fractals in Physics** (North-Holland, Amsterdam, 1986).
26. F. Family and D. P. Landau, Eds., **Kinetics of Aggregation and Gelation** (North-Holland, Amsterdam, 1984).
27. F. F. Abraham, *Adv. in Phys.* **35**, 1 (1986).
28. C. A. Castillo, R. Rajagopalan and C. S. Hirtzel, *Rev. in Chem. Eng.* **2**, 248 (1984).
29. R. O. Rosenberg and D. Thirumalai, *Phys. Rev. A* **35**, 5390 (1987).
30. M. O. Robbins, K. Kremer, and G. S. Grest, *J. Chem. Phys.* **88**, 3286 (1988).
31. W. Y. Shih, I. A. Aksay, and R. Kikuchi, *J. Chem. Phys.* **86**, 5127 (1987).
32. R. Rajagopalan and C. S. Hirtzel, *Physics Reports*, to appear.
33. C. A. Castillo, **Equilibrium Structure of Interacting Colloidal Dispersions**, Ph. D. Dissertation (Rensselaer Polytechnic Institute, Troy, NY, 1984).
34. C. S. Hirtzel and R. Rajagopalan, in **Micellar Solutions: Structure, Dynamics, and Statistical Thermodynamics**, edited by S-H. Chen and R. Rajagopalan (Springer-Verlag, New York, NY, 1990).
35. H. Kim and R. Rajagopalan, unpublished (1989).
36. H. E. Exner in **Reviews on Powder Metallurgy and Physical Ceramics, Vol. 1**, edited by F. Lenel (Freund Publishing House, Tel Aviv, Israel, 1979), p.7.
37. L. Madhavrao and R. Rajagopalan, *J. Mater. Res.*, in press (1989).

Flow of Dispersions Near Close Packing

L. Marshall and C. F. Zukoski IV, Department of Chemical Engineering, University of Illinois, Urbana, Illinois 61801

Abstract

The flow of hard sphere-like suspensions near close packing is explored. The change in viscosity with stress and volume fraction shows that at volume fractions above 0.5 shear thickening occurs and that the characteristic shear rates for shear thinning and shear thickening decrease rapidly above this volume fraction. The creep compliance is well characterized by a stretched exponential relaxation time spectrum above volume fractions of 0.52. These results suggest that the limiting volume fraction where the zero shear rate viscosity diverges is determined by a liquid/glass phase transition very similar to that predicted for hard sphere liquids.

Introduction

The quality of a fired ceramic is greatly aided by controlling the state of agglomeration and the packing characteristics of ceramic precursor powders during green body formation (1-5). Flaws produced by packing defects and agglomerates are found to limit green density, raise the temperature required to reach full density upon sintering, and to result in ceramic fabrication processes that produce unreliable products. These results have motivated efforts to develop techniques to increase the packing densities in green bodies through the control of particle interaction potentials and particle size distribution. In this paper we address questions about the useful limits of particle loadings in suspensions used in ceramic fabrication.

Agglomerate free suspensions have a maximum packing fraction above which they will not flow and thus are not formable. For suspensions of uniform spheres, this maximum volume fraction appears to be near 0.60-0.63, i.e., the density of random close packing (6,16). Thus, when using uniform precursor particles, ceramic fabrication is necessarily carried out at substantially lower volume fractions. Such low loadings result in typical volume shrinkages of 50% upon sintering to full density, and the large void volume allows defects to develop. Lower shrinkage and fewer defects can be achieved working with suspensions of higher solids loading. However, as higher loadings are achieved, the suspensions become very viscous and difficult to process.

While suspensions of uniform particles showing no long-range order have

viscosities that diverge at a volume fraction less than 0.64, through judicious choice of particle size distribution, dramatic increases in the limiting volume fraction can be achieved. The reasons for this are not well understood but are linked to factors controlling the volume fraction of random close packing (7).

In this paper, we report on initial studies of suspensions near close packing. We have investigated the flow properties of homogeneous suspensions of uniform spheres with interaction potentials very close to those of theoretical hard spheres, at volume fractions approaching 0.6. One goal of this work is to elucidate the changes in suspension properties as random close packing is approached. Results from these investigations will aid in development of strategies to avoid the high viscosities found for suspensions at these elevated volume fractions.

Experimental

Hydrophobic silica particles were prepared by the method pioneered by Van Helden et al. (8) where silica particles are synthesized by ammonia catalyzed hydrolysis of tetraethylortho silicate. The resulting particles are esterified with octadecanol and then washed into decalin where numerous studies have shown that the particles interact with a short range repulsive potential providing suspensions with properties very similar to the properties expected for suspensions of hard spheres (6,9).

The particles studied here have an average size of 205 ± 7 nm as determined with a transmission electron microscope and 210 ± 10 nm as determined by dynamic light scattering. Particle densities of 1.926 gcm^{-3} were determined from the mass and volume of a suspension containing a known mass of particles. Suspensions were made from dry particles suspended in decalin and then concentrated under vacuum. Volume fractions were determined from particle density, the density of decalin, and the solid's weight fraction in the suspension. Repeated drying, resuspension, and concentration did not affect particle physical properties or alter suspension flow behavior. Suspensions showed no signs of ordering unless diluted and allowed to stand undisturbed for a long period of time. On settling an iridescent sediment was formed. The iridescence is due to Bragg scattering off ordered planes of spheres. From this we conclude that the suspensions can undergo an order/disorder phase transition if the conditions are correct but can be prepared in a metastable amorphous state at elevated volume fractions by rapid concentration. All suspensions used in the rheological studies reported here were in the disordered state.

Rheological measurements were made with a Bohlin constant stress rheometer using a concentric cylinder geometry. A solvent trap, which consisted of a knife-edge vane, clipped to the shaft of the bob, dipping into a cylindrical trough

filled with decalin, was used to eliminate evaporation. Extensive calibration of the instrument showed that the solvent trap had no measurable effect on the rotation rate of the bob at a given torque even for the least viscous solvents used in this study. Creep compliance and recovery studies were carried out over a 0.025 - 235 Pa stress range. Creep and recovery times of 250 to 10000 seconds were used to allow the samples to reach steady state viscosities. All rheological measurements were made at 18°C.

Results and Discussion

As found in studies on similar systems (6), the suspension viscosity is independent of shear stress at low volume fractions. Shear thinning occurs as volume fractions are raised above 0.2 (Fig. 1). Limiting high, η_{∞} , and low, η_0 , shear stress Newtonian viscosities and the shear rate where the viscosity drops to halfway between these two limiting values, $\dot{\gamma}_{1/2}$, can be defined from these measurements. As the volume fraction is raised above 0.5, the samples become shear thickening. This shear thickening shows up as an increase in viscosity as stress is raised and can be characterized by the shear rate at the onset of shear thickening, $\dot{\gamma}_m$, where the viscosity reaches a (relative) minimum. Samples showing shear thickening fractured when stirred rapidly with a spatula.

The zero shear rate viscosity is found to increase many orders of magnitude in the volume fraction range of 0.55-0.60 (Fig. 2). Despite the large increase, a zero stress Newtonian plateau viscosity was found for all volume fractions showing that even at the highest volume fraction studied, these samples behave like liquids and will conform to the shape of the container into which they are placed if allowed enough time to deform. Characteristic shear rates, $\dot{\gamma}_{1/2}$ and $\dot{\gamma}_m$, are found to decrease rapidly as the volume fraction is raised above 0.52 (Fig. 3), implying relaxation times for structural rearrangement, defined by the inverse of the shear rates, lengthen rapidly. In addition, the degree of shear thinning as characterized by $(\eta_0 - \eta_{\infty})/\eta_0$ is found to increase rapidly at volume fractions near 0.5.

At stresses where suspensions display a low shear stress Newtonian viscosity, the temporal behavior of the creep compliance (strain /applied stress), J , was found to be well modeled by an expression of the form

$$J = J_0 + J_1 (1 - \exp(-(t/\tau)^\beta)) + t/\eta_0 \quad (1)$$

where J_0 and J_1 are constants, τ is a characteristic relaxation time (dependent on volume fraction), β is a constant dependent on volume fraction, and t is the time after the stress has been applied to the suspension. When β equals unity, eqn.(1) has the form of a generalized Kelvin or Voigt model with one characteristic

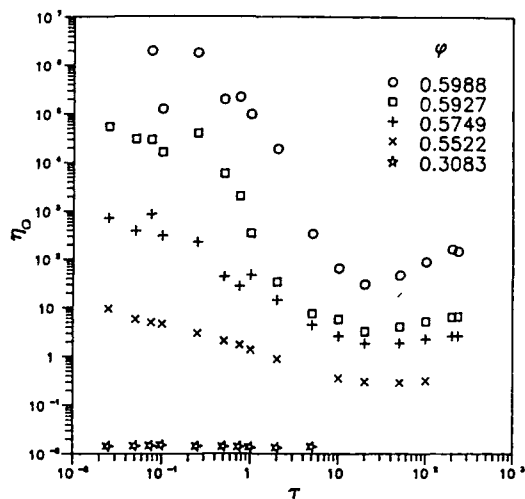


Fig. 1. Viscosity (Pa.s) as a function of applied stress (Pa) for several volume fractions.

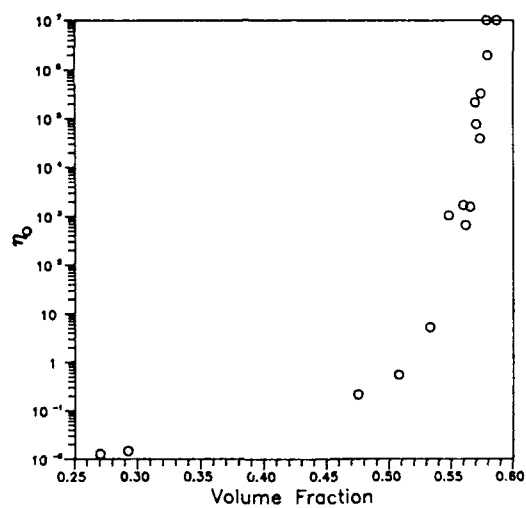


Fig. 2. Zero stress viscosity as a function of volume fraction.

relaxation time. The creep compliance of the suspensions studied here were well modeled with $\beta = 1$ for volume fractions below 0.5. For volume fractions above 0.54, eqn. (1) would only provide a good fit to the data if β dropped to a value less than unity, typically around 0.5 (Fig. (4)).

Relaxation behavior described by eqn. (1) with $\beta < 1$ has been used to characterize the behavior of molecular glasses. The form of the relaxation time spectrum ($\exp(-(t/\tau)^\beta)$) is referred to as the Kolrausch law (12). Typically molecular liquids are found to have relaxation behavior characterized by the stretched exponential form of eqn. (1) with β dropping in value from 1 to 0.3-0.5 near the glass transition (18). The observation that the suspensions investigated here have relaxation behavior similar to that seen in molecular glasses suggests that a more detailed comparison of molecular and colloidal glasses may provide insight to the factors controlling concentrated suspension rheology.

Molecular glasses are characterized by their mechanical properties which are similar to those of a solid while their microstructural properties are like those of a liquid. The transition from a supercooled liquid to a glass is accompanied by dramatic increases in viscosity and decreases in relaxation times. Many theoretical studies (10-13) have suggested that hard spheres undergo a phase transition from a meta-stable liquid to a glass at a volume fraction in the 0.52-0.62 range. The range of values stems from the different techniques used to describe the thermodynamic properties of glasses. Indeed there is continued controversy over the nature of the liquid/glass transition and the nature of the glassy state (18).

Recently, Pusey and van Megen (15) studied the particle self diffusion in suspensions containing hard sphere-like particles of a different chemistry than those investigated here and found that relaxation times longer than could be characterized by their instrument developed at volume fractions near 0.56. The existence of very long (i.e., much longer than the experimental time scale) relaxation times is a hallmark of molecular glasses. As mentioned above, the relaxation time spectrum of molecular glasses is characterized by a stretched exponential form (as in eqn. (1)).

Molecular dynamic and experimental studies suggest that shear thinning in molecular systems (14) and colloidal suspensions (17) is associated with the formation of layers of particles that slip past one another. The characteristic shear rate $\dot{\gamma}_{1/2}$ is the inverse of the characteristic time scale required for the initial amorphous suspension structure to rearrange under the action of shear stresses. Woodcock (14) suggests that $\dot{\gamma}_{1/2}$ goes to zero at the volume fraction where close packed hexagonal layers are unable to slide over one another in random registry. This occurs at a volume fraction of 0.605 which corresponds to the glass transition volume fraction as determined from simulation results where the particle self-diffusivity vanishes (14).

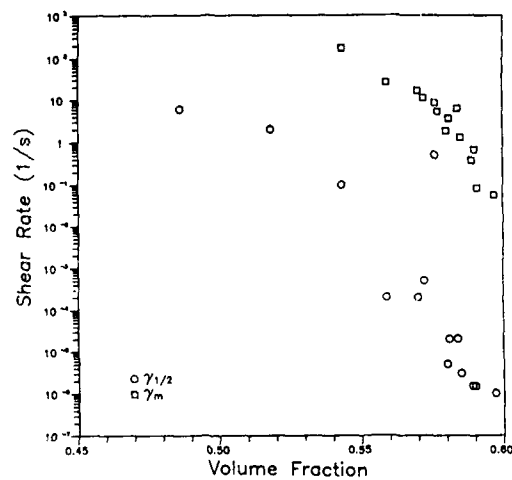


Fig. 3. Shear rate where the viscosity drops to $1/2(\eta_o + \eta_\infty)$, $\gamma_{1/2}$, and the shear rate at the onset of the shear thickening region, γ_m as a function of volume fraction.

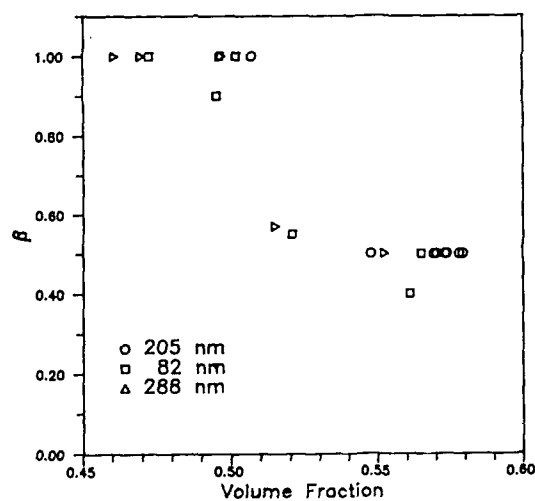


Fig. 4. Exponent in stretched exponential relaxation time spectrum (eqn. 1) determined for the best fit to creep compliance in the zero stress viscosity plateau region. Data for three different particle diameters are summarized here to emphasize observed trends.

Shear thickening is attributed to the inability of the layers of particles (molecules or colloids in suspension) to relax on a time scale of the deformation. As the structural relaxation time grows near the glass transition, γ_m decreases. The divergence of the zero shear rate Newtonian viscosity at the glass transition is the result of the inability of the system to undergo large scale cooperative rearrangement required for deformation. Woodcock (14) argues that above volume fractions of 0.605, as the shear stress is raised, suspensions should display a yield stress and shear thin to a point where shear thickening is observed before reaching a stable high shear rate Newtonian viscosity. This model suggests that γ_m vanishes at a volume fractions of 0.64 corresponding to random close packing. Suspensions at this volume fraction will respond to stress in a purely elastic fashion and, if forced to strain at a fixed rate, will fracture.

In combination, the results given in Figs. 1-4, the theoretical work carried out on the transport behavior of hard spheres near the glass transition, and the experimentally determined behavior of molecular glasses, suggest that hard sphere-like suspensions studied here undergo a liquid/glass phase transition that closely mimics molecular glass behavior. The abrupt drop in β at a volume fraction of 0.52 corresponds to the dynamic light scattering studies of Pusey and van Meegen in suggesting that there is a qualitative change in the relaxation behavior of the suspension near this volume fraction. The large increase in shear thinning in the same volume fraction range suggests that the particle structures giving rise to the long relaxation times act to increase the zero shear rate Newtonian viscosity but are degraded by shear. It is interesting to note that if the increased zero shear stress viscosity corresponds to the "freezing in" of glassy structures, these structures do not percolate (and thus provide a yield stress) until volume fractions 0.6 or greater. Further analysis of the data presented in Figs. 1-4, and extension of the measurements to suspensions containing particles of a different size is currently being undertaken to further relate concentrated suspension transport behavior to the glass transition.

Conclusions

We conclude from these studies that in ceramic fabrication, the limit on loadings of uniform particles occurs at volume fractions below 0.64. This upper limit is set by the divergence of the zero shear rate viscosity and the occurrence of shear thickening at shear rates easily approached during fabrication. The flow of suspensions at volume fractions approaching 0.6 follows the behavior predicted for hard sphere liquids undergoing a glass transition. Preparation of suspensions with higher loadings will require postponing the glass transition to higher volume fractions. This may be accomplished through the use of bi- or multi-modal particle size distributions - a possibility currently under investigation.

Acknowledgements.

This work was supported by the U.S. Department of Energy through the Materials Research Laboratory at the University of Illinois under contract number DOE-AC 02-76ER 01198.

References

1. Lange, F. F., J. Am. Ceramic Soc. 66, 396 (1983)
2. Lange, F. F., J. Mat. Energy Systems 6, 107 (1984)
3. Lange, F. F., B. I. Davis and I. A. Aksay, J. Am. Ceramic Soc. 66, 407 (1983)
4. Barringer, E., N. Jubb, B. Fegley, R. L. Pober and H. K. Bowen in Ultrastructural Processing of Ceramics, Glasses and Composites, L. L. Hench and D. R. Ulrich Eds., John Wiley and Sons, NY (1984)
5. Sacks, M. D., and T-Y Tseng, J. Am. Ceramic. Soc. 67 526 and 532 (1984)
6. de Kruif, C. G., E. M. F. van Iersel, A. Vrij and W. B. Russel, J. Chem. Phys 83, 4717 (1986)
7. Farris, R. J., Trans. Soc. Rheol. 12, 281 (1968)
8. van Helden, A., J. W. Jensen and A. Vrij, J. Colloid Interface Sci. 81, 354 (1981)
9. de Kruif, C. G., J. W. Jensen and A. Vrij in "Physics at Complex and Supra-Molecular Fluids", edited by S. A. Safran and V. A. Clark, Wiley, NY 1987
10. Woodcock, L. V., and C. A. Angell, Phys. Rev. Lett 47, 1129 (1981)
11. Angell, C. A., J. H. R. Clarke and L. V. Woodcock, Adv. Chem. Phys 48, 397 (1981)
12. Woodcock, L. V., Ann. N.Y. Acad. Sci. 37, 274 (1981)
13. Stossel, J. P., and P. G. Wolynes, J. Chem. Phys. 80, 4502 (1984)
14. Woodcock, L. V., and Chem. Phys. Lett. 111, 455 (1984)
15. Pusey, P. N., and W. van Megen, Phys. Rev. Lett. 59, 2083 (1987)
16. Krieger, I. M., Adv. Colloid Interface Sci. 3, 137 (1972)
17. Clark, N. A., and B. J. Ackerson, Phys. Rev. Lett. 44, 1005 (1980)
18. Fredrickson, G. H., Ann. Rev. Phys. Chem. 39, 149 (1988)

STABILITY OF A BINARY COLLOIDAL SUSPENSION AND ITS EFFECT ON COLLOIDAL PROCESSING

WAN Y. SHIH, WEI-HENG SHIH, JUN LIU, and ILHAN A. AKSAY

Department of Materials Science and Engineering, and
Advanced Materials Technology Program, Washington Technology Center
University of Washington, Seattle, WA 98195

INTRODUCTION

The stability of a colloidal suspension plays an important role in colloidal processing of materials. The stability of the colloidal fluid phase is especially vital in achieving high green densities. By colloidal fluid phase, we refer to a phase in which colloidal particles are well separated and free to move about by Brownian motion. By controlling parameters such as pH, salt concentration, and surfactants, one can achieve high packing (green) densities in the repulsive regime where the suspension is well dispersed as a colloidal fluid, and low green densities in the attractive regime where the suspensions are flocculated [1,2]. While there is increasing interest in using bimodal suspensions to improve green densities, neither the stability of a binary suspension as a colloidal fluid nor the stability effects on the green densities have been studied in depth as yet. Traditionally, the effect of using bimodal-particle-size distribution has only been considered in terms of geometrical packing developed by Furnas and others [3,4]. This model is a simple packing concept and is used and useful for hard sphere-like repulsive interparticle interactions. With the advances in powder technology, smaller and smaller particles are available for ceramic processing. Thus, the traditional consideration of geometrical packing for the green densities of bimodal suspensions may not be enough. The interaction between particles must be taken into account.

The purpose of this paper is to take into account the interparticle interactions explicitly and to examine the stability of a binary suspension as a colloidal fluid using analytic calculations as well as numerical simulations. From suspension stability, we will then discuss how the use of a bimodal (binary) suspension affects the green density. We will divide our studies into two regimes, i.e., the repulsive regime and the weakly attractive regime.

In the repulsive regime, when gravity can be neglected, the behavior of the suspension is mainly governed by equilibrium conditions. We examine the stability of the suspensions by constructing the solid-fluid phase diagrams. On the contrary, in the weakly attractive regime, at least one of the species has attractive interparticle interaction. The suspension may undergo flocculation and is more dominated by the kinetic conditions. To take into account the kinetic effect more accurately, we use Monte Carlo simulations to study the clustering behavior of the suspensions.

REPULSIVE REGIME

Model

We consider an electrostatically stabilized binary aqueous suspension of N_1 particles of radius a_1 , charge Z_1 , and N_2 particles of radius a_2 , charge Z_2 with volume Ω . In the absence of added electrolytes, there are $N_1 Z_1 + N_2 Z_2$ counter ions (H_3O^+ or OH^- depending on the system) in solutions to neutralize the charges on the colloidal particles. If the number density of the colloidal particles is not too high or the temperature is not too low, the effective interactions between the colloidal particles can be adequately treated within the Debye-Hückel approximation. In MKSA units, the interaction takes the form

$$U(r_{ij}) = \frac{Z_i Z_j e^2}{4\pi\epsilon_0 \epsilon_r r_{ij}} \left[\frac{e^{qa_i}}{1 + qa_i} \right] \left[\frac{e^{qa_j}}{1 + qa_j} \right] e^{-qr_{ij}}. \quad (1)$$

Here r_{ij} is the separation between the centers of particle i and particle j , ϵ is the static dielectric constant of water, ϵ_0 is the permittivity of free space, e is the electronic charge, and q is the inverse screening length which satisfies

$$q^2 = \frac{e^2}{\epsilon_0 \epsilon_r k_B T} \sum_i n_i (z_i^2), \quad (2)$$

where k_B is the Boltzmann constant, T is the absolute temperature, z_i and n_i are the charge and the number density of the i^{th} species of ions, respectively. The terms in the brackets of Eq. (1) is the size correction which takes into account the fact that part of the volume of the suspension is not available for screening due to the finite sizes of the colloidal particles.

When the colloidal suspension is at equilibrium, its thermodynamic properties are determined by the Helmholtz free energy $F = E - TS$, where E is the total energy and S is the entropy. For a system of particles interacting via the potential of Eq. (1), the free energy per particle takes the following form:

$$F = \frac{1}{2N} \sum_{i,j} \frac{Z_i Z_j e^2}{4\pi\epsilon_0 \epsilon_r} \left(\frac{e^{qa_i}}{1 + qa_i} \right) \left(\frac{e^{qa_j}}{1 + qa_j} \right) \left\langle \frac{1}{|\vec{r}_i - \vec{r}_j|} \right\rangle e^{-q|\vec{r}_i - \vec{r}_j|} + E_{kin} - TS, \quad (3)$$

where E_{kin} and S are the kinetic energy and the entropy per particle, $N = N_1 + N_2$ is the total number of particles in the system, $\langle \rangle$ denotes the thermal average over the canonical ensemble, and \vec{r}_i is the position of particle i . Equation (3) includes only the part of the free energy that depends on the arrangement of the particles. These are the terms that are relevant in determining the structure of the colloidal suspension.

The free energy can be obtained from Eq. (3) by the use of a variational principle based on the Gibbs-Bogolyubov inequality which states as follows:

$$F \leq F_0 + \langle U - U_0 \rangle_0 \equiv F', \quad (4)$$

where F_0 is the free energy of the reference system and $\langle U - U_0 \rangle$ is the potential energy difference of the system of interest and the reference system. Since F is upper bounded by F' , we can then approximate F to be the minimum of F' with respect to the appropriate variables, that is, $F \approx F'(x_0, y_0)$ and

$$\left. \frac{\partial F'(x, y)}{\partial x} \right|_{x=x_0} = 0 \quad \text{and} \quad \left. \frac{\partial F'(x, y)}{\partial y} \right|_{y=y_0} = 0 \quad (5)$$

where x and y are the appropriate variables.

For the solid phases, it is convenient to choose an ensemble of Einstein oscillators to define the reference system: each particle of type 1 or 2 oscillates about a lattice point independently in a potential well with a frequency ω_1 and ω_2 . The free energy may then be written in terms of ω_1 and ω_2 , and the free energy of the equilibrium state is determined by minimizing the free energy with respect to ω_1 and ω_2 .

For the reference system of the liquid phase, we consider a binary hard-sphere fluid where particles are interacting via the hard-sphere potential,

$$U_o(r_{ij}) = \begin{cases} \infty & r_{ij} < \sigma_{ij} \\ 0 & r_{ij} \geq \sigma_{ij} \end{cases} \quad (6)$$

in which $\sigma_{ij} = (\sigma_i + \sigma_j)/2$, where σ_i , the effective hard-sphere diameter of particle i , is not, in general, equal to a_i , the actual diameter of a type- i particle. Again, the free energy of the fluid state can be expressed in terms of σ_1 and σ_2 , and the free energy of the equilibrium fluid state is determined by minimizing the free energy with respect to σ_1 and σ_2 .

The phase diagrams are then constructed by directly comparing the free energies of the solid phases to that of the fluid phase (we consider face-centered-cubic (fcc) and body-centered-cubic (bcc) substitutional alloys in this paper) to that of the fluid phase. The details of the approach are described in Ref. 5.

Results

We plot the freezing densities of mixtures with actual particle diameter ratios ranging from 0.9 to 0.7 in Figure 1(a)-(d). For all the cases shown, the large particles have a radius $a_1 = 545 \text{ \AA}$ and a surface charge $Z_1 = 300$. For the small particles, we use the linear-diameter-charge relationship proposed by Pincus [6] to determine the charge for particles of a given size: $a_2 = 491 \text{ \AA}$, $Z_2 = 270$ in Figure 1(a); $a_2 = 445 \text{ \AA}$, $Z_2 = 245$ in Figure 1(b); $a_2 = 409 \text{ \AA}$, $Z_2 = 225$ in Figure 1(c); and $a_2 = 382 \text{ \AA}$, $Z_2 = 210$ in Figure 1(d). The actual particle diameter ratio is 0.9 in Figure 1(a), 0.817 in Figure 1(b), 0.75 in Figure 1(c) and 0.7 in Figure 1(d), while the diameter ratio of the effective hard spheres is 0.96 in Figure 1(a), 0.92 in Figure 1(b), 0.89 in Figure 1(c), and 0.86 in Figure 1(d). One can see that as the particle diameter ratio decreased more from unity, the freezing curve in the $D - x$ phase diagram begins to show a maximum with respect to x . Note that there is indeed a weak maximum which occurs near $x = 0$ in curve (a) which may be better seen from the minimum in the $\bar{T} - x$ plane when we plot the effective

freezing temperature in Figure 2. We define the effective temperature $\tilde{T} = k_B T / (Z^2 e^2 / 4\pi\epsilon_0 \epsilon a_s)$ where $Z = x_1 Z_1 + x_2 Z_2$ is the average charge and $a_s = D^{-1/3}$ is the average nearest distance between particles. The maximum becomes more pronounced as the diameter ratio is progressively decreased, which has been observed experimentally [7]. As a result, the disordered crystalline alloy phase shrinks to small regions near $x=0$ and $x=1$ for the small particle diameter ratio as is shown in Figure 1 (c)-(d), in agreement with experiments [7,8]. Note that the solubility of small spheres in the crystals of large spheres is always larger than the solubility of large spheres in the crystals of small spheres. This feature is also seen in the recent density-functional calculations of binary hard spheres [9]. Also note that the solid-liquid phase boundaries in Figure 1(d) almost open up vertically at the high densities, and the effective hard-sphere diameter ratio is 0.86 in this case. When the effective hard-sphere diameter ratio decreases further, the solid-liquid phase boundaries rise even more sharply from $x=0$ and $x=1$ (not shown). We also plot the effective freezing densities for all four cases in Figure 2. As the particle diameter ratio becomes smaller, the minimum freezing temperature becomes deeper. We have shown elsewhere that the minimum in the freezing temperature or the maximum in the freezing density is actually related to a eutectic, and the depth of the extrema does reflect the difficulty of mixing the particles [5]. This suggests that the Hume-Rothery rule [10] for metallic alloys (which states that no substitutional alloys can be formed when the diameter of the two species differs more than 15%) may be used in binary colloids, except that the effective hard-sphere diameters must be used for the miscibility criterion instead of the bare particle diameters.

ATTRACTIVE REGIME

For convenience, we perform calculations only on a two-dimensional square lattice. Consider a mixture of N_1 particles 1 and N_2 particles 2 placed in a square lattice of area A . The number density of particles 1 is $c_1 = N_1/A$ and that of particles 2 is $c_2 = N_2/A$. The total particle number density is $c = c_1 + c_2$. We will take the area of a unit cell to be unity. Thus, $c = 1$ represents the case where the lattice is fully occupied. An unoccupied site represents the solvent. For the interactions, we assume that only nearest neighbors have non-zero interactions.

Simulations

Initially, we randomly distribute the N_1 particles 1 and the N_2 particles 2 in a $M \times M$ lattice with periodic boundary conditions. The random distribution is to mimic the initial mixing in the experiments. The particles then perform Brownian motion (random walk). A particle of the i^{th} species moves one lattice constant after every $\tau_{D,i}$. However, the Brownian motion of a particle may be modified when the particle is in the vicinity of other particles. Such modification is incorporated in the simulations by the use of a Boltzmann factor. When a particle is attempting motion, the motion is achieved according to the probability $e^{-\Delta E/T}$, where ΔE is the energy change due to the motion. When two particles are adjacent to each other, they can form a cluster and diffuse as a whole. The mobility of a cluster is roughly assumed to be inversely proportional to its mass. Except for this difference, a cluster is treated in the same way as a particle: the clusters are also performing Brownian motion and the motion is also modified by the Boltzmann factor. When two clusters collide, they form a larger

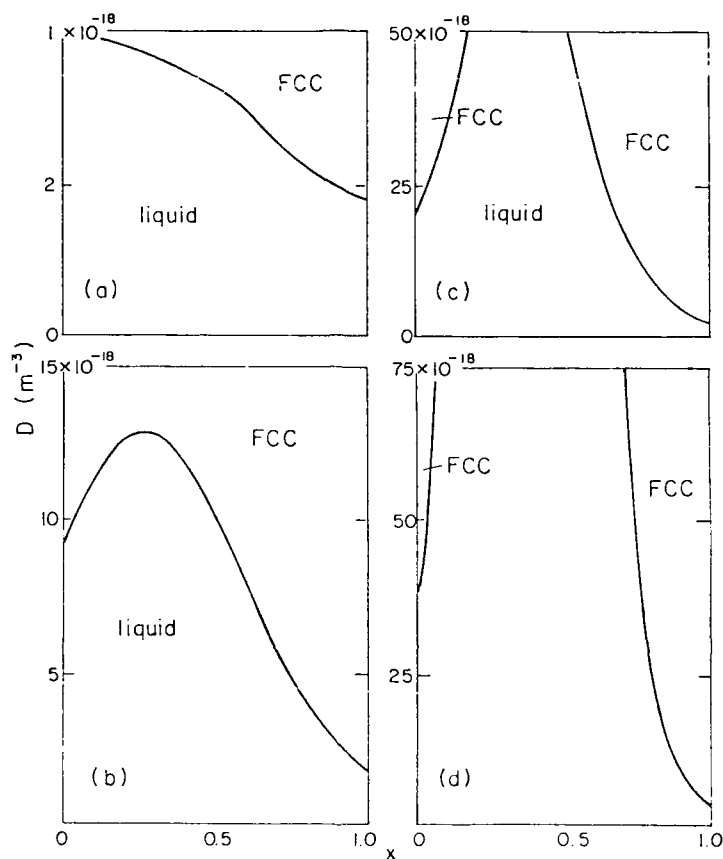


Figure 1. D - x phase diagrams of binary colloidal particles with diameter ratio ranging 0.9 - 0.7. $a_1 = 545$ Å, $Z_1 = 300$ for all cases, while $a_2 = 491$ Å, $Z_2 = 270$ in (a); $a_2 = 445$ Å, $Z_2 = 245$ in (b); $a_2 = 409$ Å, $Z_2 = 225$ in (c); and $a_2 = 382$ Å, $Z_2 = 210$ in (d).

cluster. A particle within a cluster can also unbind from its neighbors by thermal motion due to the finite attraction energy, leading to the fragmentation of the cluster. The unbinding of an i^{th} -species particle takes place according to the rate $(1/\tau_{R,i})e^{-(\Delta E/T)}$, where ΔE again is the energy change associated with the process and $\tau_{R,i}$ is the time constant associated with the unbinding of the i^{th} -species particles. For the modification of the Brownian motion and the unbinding process, we use the Monte Carlo method (the Metropolis algorithm). A more detailed description of the aggregation model is given in Refs. 2 and 11.

There are seven parameters in general in a binary aggregation model such as this; namely, the interactions E_{11} , E_{12} , and E_{22} , and the time constants $\tau_{D,1}$, $\tau_{D,2}$, $\tau_{R,1}$, and $\tau_{R,2}$. The param-

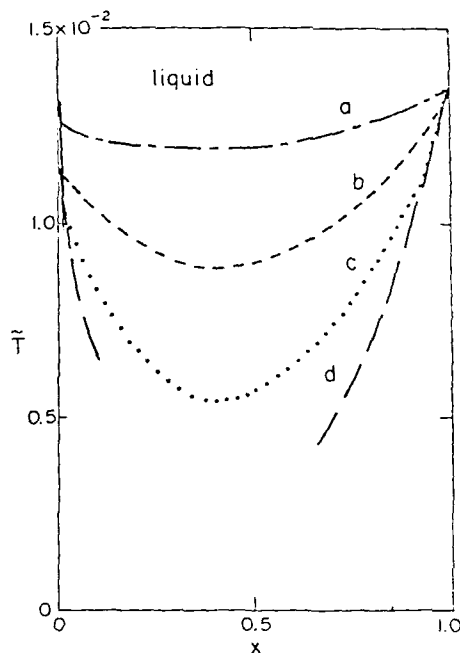


Figure 2. $\tilde{T} - x$ phase diagrams of binary colloidal particles. Curves (a)-(d) correspond to the freezing temperatures of Figures 1(a)-(d).

eter $\tau_{D,i}$, where $i = 1$ or 2 , is related to the mobility of the particles, while the parameter $\tau_{R,i}$ is the inverse of the unbinding attempt frequencies and is more related to the surface properties of the particles. In general, $\tau_{D,i}$ is different from $\tau_{R,i}$. The mobility of the particles 1 can also be different from that of the particles 2. Unless mentioned, in most simulations we use $\tau_{R,i} = \tau_{D,i} = \tau$. The choice of a different set of $\tau_{R,i}$ and $\tau_{D,i}$ will mainly affect the aggregation rate but not the qualitative behavior [2], and our choice for $\tau_{D,i}$ and $\tau_{R,i}$ in this paper is arbitrary. However, it is worth noting that a smaller value of $\tau_{D,i}$ may be interpreted as a larger particle mobility and a smaller $\tau_{R,i}$ as a larger relaxation rate. In the simulations, we monitor the cluster size of particles 1 as well as the effective mobility of all particles. The reported results are the average over 10 different runs for each case.

Results

In the experiments, the first species always flocculates before the second species, indicating that the interaction between particles 1 is more attractive than that between particles 2 or that between particles 1 and particles 2. Since we are only interested in the qualitative behaviors,

for convenience we choose E_{11} to be attractive and $E_{12} = E_{22}$ to be repulsive. In the following, the energies will be expressed in units of the room temperature T .

As an example of how the aggregation of the first-species particles changes with the density of the second-species particles, in Figure 3 we show the pictures of the systems taken at $t = 100\tau$ for three different particle-2 densities $c_2 = 0, 0.122$, and 0.245 with $c_1 = 0.245$ fixed. With the periodic boundary conditions, it is clearly shown that the largest cluster (the darkened circles) in the system is larger in the mid particle-2 density than in the other two cases.

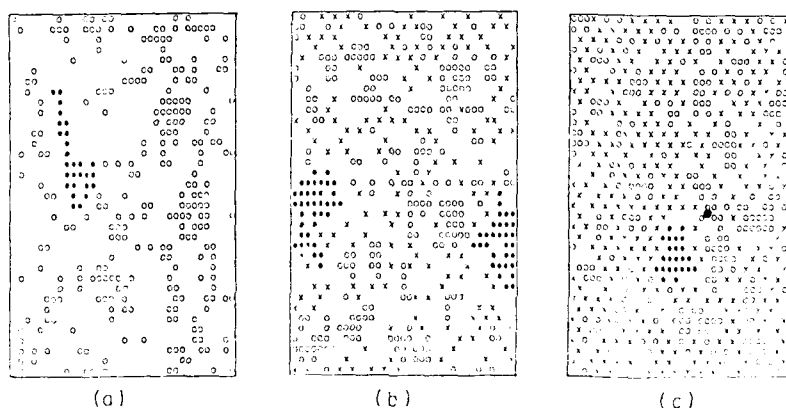


Figure 3. Monte Carlo simulations at different densities of particle 2 (with periodic boundary conditions). "o" denotes a particle 1 and "x" denotes a particle 2. The darkened circles denote the largest cluster in the system. (a) $c_2 = 0$, (b) $c_2 = 0.122$, and (c) $c_2 = 0.245$. In all three cases, $c_1 = 0.245$, $t = 100\tau$, $E_{11} = -1$, $E_{12} = E_{22} = 3$. Note that particles 2 remain dispersed while particles 1 are undergoing clustering and that the largest cluster size in (b) is larger than in (a) and (c).

To show the time dependence of the N -versus- c_2 curve, we plot in Figure 4a for $c_1 = 0.25$, $E_{11} = -1$, $E_{12} = E_{22} = 3$ at different times $t = 100\tau$, 400τ , and 1000τ . The calculations were done on a 20×20 lattice. For all cases, the curve shows a peak, consistent with the experimental observation [12]. Note that the peak of the curve shifts to a higher value of c_2 at a later time; and at higher values of $c_2 > 0.2$, the initially small clusters grow with time. This kind of aging behavior has also been observed experimentally [12]. Also shown in Figure 4b is the effective particle mobility μ_{eff} versus c_2 for the same system as in Figure 4a at $t = 100\tau$, where μ_{eff} is defined as the average number of movements made per particle within a time interval $\Delta t = 2\tau$. One can see that as c_2 increases, the movement of a particle becomes more and more hindered. As a result, the effective mobility decreases. Thus, Figures 4a and 4b together indicate that the decrease in cluster size and the restabilization at high c_2 is a kinetic effect and hence *cannot* be predicted by equilibrium calculations. For instance, if one waits long enough, one should

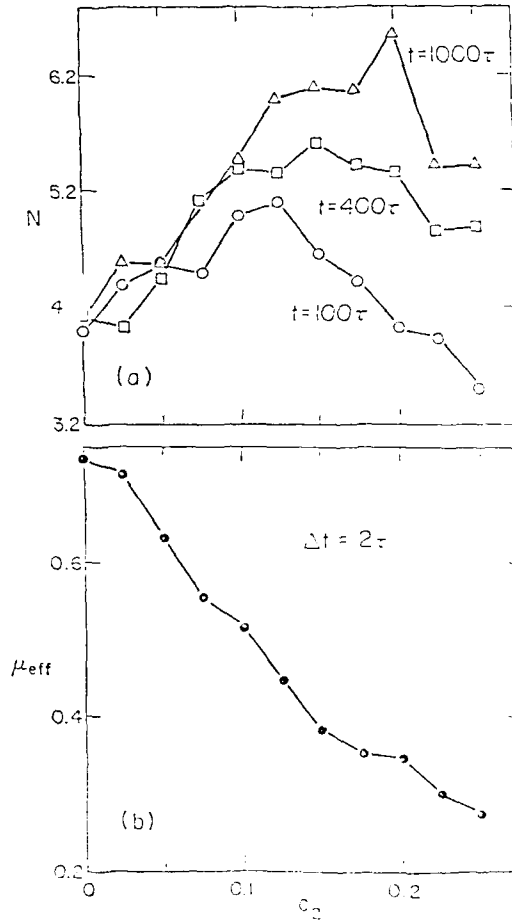


Figure 4. (a) The average cluster size N versus the particle-2 density c_2 at different times whose $c_1 = 0.25$, $E_{11} = -1$, and $E_{12} = E_{22} = 3$. Note that the cluster size increases with time and that the peak shifts to a higher value of c_2 at a later time. (b) The effective particle mobility μ_{eff} at $t = 100\tau$ is plotted versus c_2 . Note that μ_{eff} decreases with increasing c_2 . The smaller μ_{eff} at high c_2 is responsible for the decrease in flocculation rate.

always see that the curve N versus c_2 goes upward and should not bend over as it does at an earlier time, as shown in Ref. 11. The maximum flocculation rate in the mixtures in the attractive regime implies a minimum green density in the colloidal processing.

SUMMARY

We studied the stability of a binary colloidal suspension by explicitly taking into account the interparticle interactions. For the repulsive regime, we determined the boundaries between the liquid phase and the disordered substitutional crystalline alloys for binary colloids by comparing the free energies of both the liquid and the solid phases. We have shown the following: (1) for binary-charged colloids, the freezing density as a function of the number fraction has a maximum. The maximum freezing density occurs in small particle-rich mixtures and the maximum freezing density increases sharply with decreasing particle diameter ratio. It should be noted that our result is in terms of number fraction and does not contradict the Furnas prediction, which is in terms of volume fraction. If the number fraction is used instead of the volume fraction, the Furnas concept would also give maximal packing density in the small-particle-rich regime. (2) When the effective hard-sphere diameter ratio is about 0.86 ~ 0.85, the solid-liquid boundaries rise almost vertically; the liquid phase is stable in most of the phase space except for small regions near the pure cases.

The fact that the fluid phase can be stable up to an especially high density in a binary colloidal suspension can be helpful in colloidal processing where a high green-compact density is desired. Indeed, this has been observed experimentally: a suspension of bimodal particle distribution does have a lower viscosity [13] and does give a higher green density [14] than a monodisperse suspension.

For the weakly attractive regime, we have used Monte Carlo simulations to study the flocculation behavior of a binary suspension. (1) We have shown that upon the addition of particles 2, the flocculation rate of particles 1 has a peak with respect to the particle-2 concentration. (2) We have clearly shown the aging phenomenon occurring at high particle-2 concentrations; namely, the cluster size grows with time. Both (1) and (2) have been observed experimentally [12]. (3) Therefore, the restabilization at high particle-2 concentrations is due to slow kinetics, i.e., slow particle movements but not thermodynamic reasons. The maximum flocculation rate occurring in the mixtures in the attractive regime implies a minimum green density in the mixtures in colloidal processing. Thus, the use of a binary suspension in the attractive regime may not always be advantageous.

ACKNOWLEDGMENT

This work was supported by the Air Force Office of Scientific Research (AFOSR) and the Defense Advanced Research Projects Agency (DARPA) under Grant No. AFOSR-87-0114.

REFERENCES

1. I. A. Aksay and R. Kikuchi, in *Science of Ceramic Chemical Processing*, edited by I. L. Hench and D. R. Ulrich (Wiley, New York, 1986), pp. 513-21.
2. W. Y. Shih, I. A. Aksay, and R. Kikuchi, *Phys. Rev. A* **36**, 5015 (1987).
3. C. C. Furnas, *U. S. Bur. of Mines Res. Invest.* No. 2894 (1928).
4. A. E. R. Westman and H. R. Hugill, *J. Am. Ceram. Soc.*, **13**, 767 (1930).

5. W. Y. Shih, W.-H. Shih, and I. A. Aksay, *J. Chem. Phys.*, **90**, 4506 (1989) and the references therein.
6. P. A. Pincus, Invited Paper at March Meeting of the American Physical Society, Los Angeles, California, 1983 (unpublished).
7. P. M. Chaikin and P. A. Pincus, unpublished.
8. E. Liniger and R. Raj, *J. Am. Ceram. Soc.* **70**, 843 (1987).
9. J. L. Barrat, M. Baus, and J. P. Hansen, *Phys. Rev. Lett.* **56**, 1063 (1986).
10. W. Hume-Rothery, R. F. Smallman, and C. W. Haworth, The Structure of Metals and Alloys (The Metals and Metallurgy Trust, London, 1969).
11. J. Liu, W. Y. Shih, R. Kikuchi, and I. A. Aksay, *J. Coll. and Interf. Sci.*, in press.
12. M. Yasrebi, W. Y. Shih, and I. A. Aksay, submitted to *J. Coll. and Interf. Sci.*
13. K. P. Darcovich and I. A. Aksay, unpublished.
14. C. Han, I. A. Aksay, and O. J. Whittemore, in Advances in Materials Characterization II, edited by R. L. Snyder, R. A. Condrate, P. F. Johnson (Plenum, New York, 1985), p. 339.

MECHANICAL PROPERTIES OF COLLOIDAL GELS

W.-H. SHIH, J. LIU, W. Y. SHIH, S. I. KIM, M. SARIKAYA, and I. A. AKSAY

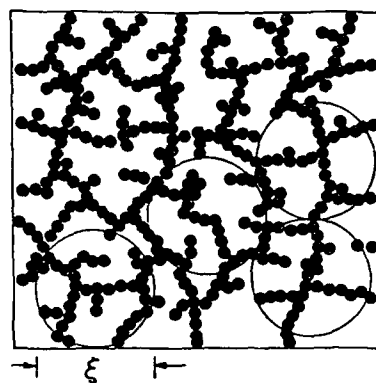
Department of Materials Science and Engineering, and
Advanced Materials Technology Program, Washington Technology Center
University of Washington, Seattle, WA 98195

INTRODUCTION

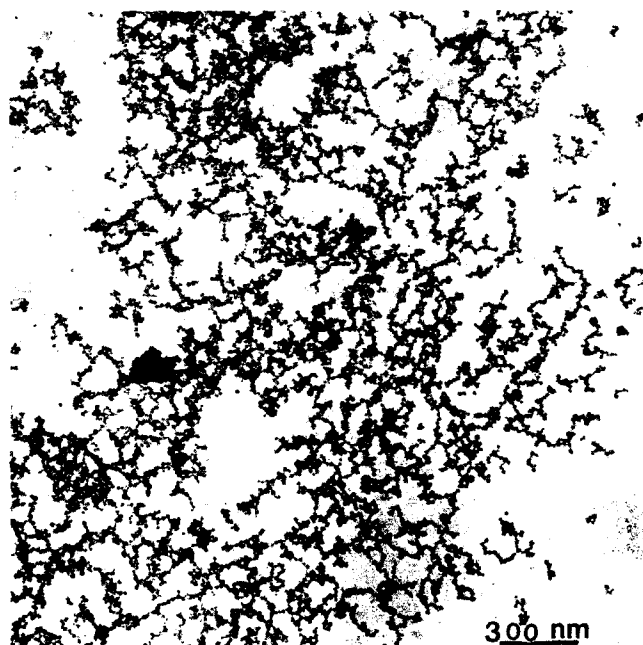
A colloidal suspension can be either dispersed or flocculated depending on the interaction between the colloidal particles. If the interaction is repulsive, particles can relax to the minimum of the potential due to their neighboring particles, and the system can reach an equilibrium dispersed state. In the case of attractive interaction, particles form aggregates that settle to the bottom of the container. As the concentration of particles is increased, the overcrowding of the aggregates produces a continuous network throughout the suspension before they settle and a colloidal gel is formed. A major difference between a colloidal gel and a colloidal suspension is that the gel can sustain finite stress and is therefore viscoelastic. Previously we studied the storage modulus and the yield strain of boehmite gels and found that they are related to the particle concentration in a power-law fashion [1]. Similar scaling behavior of the shear modulus was found for other colloidal particulate networks by Buscall et al. [2]. We developed a scaling theory [1] which successfully explains the experimental results on boehmite gels. The theory further predicts that there can be two types of power-law behavior depending on the relative elastic strength of the clusters to that of the links between clusters within the gel network. Furthermore, there can be a crossover from one type of behavior to the other as the particle concentration is varied.

In this paper, with a dynamical rheology study on colloidal silica gels we clearly demonstrate the crossover. In addition, we find that depending on whether surfactant is added or not, we may have two types of mechanical behavior of colloidal gels: hard gels and soft gels. (1) In hard gels, the storage modulus G' increases with particle volume fraction in a power-law fashion as described by the scaling theory. (2) In soft gels, G' increases with concentration in an exponential fashion. Monte Carlo simulations on restructuring of clusters show an exponential relationship between the largest cluster size and the concentration, indicating that the exponential behavior in G' may be a result of the restructuring of clusters. Moreover, the exponential behavior of G' with respect to particle concentration is similar to the behavior of the applied pressure as a function of resultant cake density in pressure filtration, suggesting that the pressure filtration behavior may also be understood in terms of the restructuring of the particle network.

In the following, we briefly summarize our theory on the elastic constant and yield strain of colloidal gels, followed by the experimental results on silica gels. Finally, we end with discussions and conclusions.



(a)



(b)

Figure 1. The schematic structure of a gel network is shown in 1a in which some clusters with average size ξ are circled. 1b shows TEM micrograph of a typical colloidal silical gel.

$$K \sim \phi^{(d+x)/(d-D)} \quad (4)$$

In the weak-link regime, $K_s \gg K_l$, we replace K_s in Eq. (3) with K_l and obtain

$$K \sim \phi^{(d-2)/(d-D)} \quad (5)$$

The yield strain γ_y of a colloidal gel can also be obtained by studying the breaking of the weakest springs in the network. In the strong-link regime,

$$\gamma_y \sim \phi^{-(1+x)/(d-D)} \quad (6)$$

while in the weak-link regime,

$$\gamma_y \sim \phi^{1/(d-D)} \quad (7)$$

As is clear from Eqs. (4)–(7), the scaling behavior of the elastic constant and that of the yield strain are different in the two regimes. Although the elastic constant increases with concentration in a power-law fashion in both regimes, the exponent in the strong-link regime is larger than that in the weak-link regime. Moreover, the yield strain decreases with increasing concentration in the strong-link regime whereas the yield strain increases with concentration in the weak-link regime. The scaling theory further predicts that there can be a crossover from the strong-link behavior to the weak-link behavior as concentration is increased since increasing concentration reduces the average cluster size and thus increases K_s as is clear from Eq. (2).

EXPERIMENTS

Silica gels were prepared from Ludox Colloidal Silica H30. The particle size was 12 nm and the as-received suspensions were electrostatically stabilized. Two types of samples were prepared. In the first type which we call hard gels, the pH of the suspensions was adjusted to 9.5 and the suspensions were mixed with KCl. The particle concentration was adjusted to a predetermined value (0.65 to 11.25%) and the KCl concentration was set at 0.25M. In the second type of samples which we call soft gels, the suspensions were adjusted to pH = 2 first, followed by the addition of the nonionic surfactant, octylphenol, such that the surfactant-to-particle weight ratio was 15.64%. The gels were grown in situ within the test fixtures to prevent disturbance, and the growth of gels took about 10 minutes to 1 hour, depending on the particle concentration.

Two types of test fixtures were applied in the dynamic-rheological study using Rheometrics Fluids Spectrometer (RFS-8400). In the couette fixture, the gels were grown between two cylinders with a gap of 1 mm. We exert torsional stress on the outside cylinder and measure the response of a torsion wire attached to the inner cylinder. In the parallel plate fixture, the gels were grown between two parallel disks 25 mm in diameter and the gap between the disks was between 1 to 2 mm. When the bottom disk was stressed, the dynamic response of the sample was obtained by looking at the torsion wire attached to the upper disk. An oscillatory strain is imposed on the system by either rotating the bottom disk or outer cylinder with a

SCALING THEORY

A scaling theory has been developed to correlate the elastic constant and the yield strain of colloidal gels to their structures [1]. Here we briefly summarize the main results of the theory and refer readers to Ref. 1 for a more detailed description of the theory. The theory is based on the fact that in the dilute regime of flocculated systems there are isolated clusters which are fractal objects with a fractal dimension D . As the concentration of particles increases, individual clusters begin to overlap and eventually form a continuous network before they settle to the bottom of the container. In a simple approximation, we may view the continuous gel network as a system of uniformly-sized clusters closely packed together. A schematic representation of a gel structure is shown in Figure 1a and a transmission electron micrograph (TEM) of a silica gel is shown in Figure 1b for comparison. The model structure is similar to the TEM picture and contains the essential features of a gel network. The average cluster size ξ can be related to the particle volume fraction ϕ as

$$\xi \sim \phi^{1/(D-d)} \quad (1)$$

by assuming the average mass density within a cluster to be the same as the total particle density. d is the Euclidean dimension of the system. Equation (1) has been confirmed for silica gels by Dietler et al. [3].

The next step in constructing the theory is to calculate the elastic constant of a cluster K_ξ , and then relate K_ξ to the macroscopic elastic constant K of the system. To calculate the elastic properties, we replace the particulate network with a network of springs which represent the elastic bonds between two particles. Furthermore, we replace the fractal spring network with a backbone network, which is also a fractal, since many dangling springs do not contribute to the elastic properties of the system. There are two elastic constants involved. One is the spring constant of each spring. The other is the bending constant between two springs connected to the same particle. It has been shown by Kantor and Webman [4] that for a very long, tortuous spring network, the elastic constant is dominated by the bending constant and can be related to its radius of gyration, in this case ξ , as

$$K_\xi \sim K_0 / \xi^{2+x}, \quad (2)$$

where K_0 is the local bending constant between two adjacent springs and the exponent x is the fractal dimension of the elastic backbone, which may be different from that of the clusters, D . The macroscopic elastic constant K is related to K_ξ as

$$K \sim (L/\xi)^{(d-2)} K_\xi, \quad (3)$$

where L is the sample size.

We now need to divide our discussion into two situations since the elastic constant of the link between the clusters K_l can be quite different from K_ξ . In the strong-link regime in which $K_l > K_\xi$, by combining Eqs. (1), (2), and (3), we get

certain frequency and amplitude. The frequency of the oscillation was fixed at 1 rad/sec and the amplitude was varied over a range from 0.1 to 50%. The viscoelastic properties of the gels are characterized by the storage and the loss moduli, G' and G'' , respectively. In the present study, we focus our attention on the storage modulus G' .

The storage and the loss moduli, G' and G'' , as a function of particle volume fraction for silica gels without surfactant are shown in Figure 2. Note that there is a clear change in the slope of G' at around 9% volume fraction. We interpret the change in the slope of G' as the crossover from the strong-link behavior to the weak-link behavior as predicted by the theory. The slope in the weak-link regime at higher concentrations is indeed much smaller than in the strong-link regime at smaller concentrations. Furthermore, the crossover from the strong-link regime at low concentrations to the weak-link regime at higher concentrations is also evidenced in the behavior of the yield strain as shown in Figure 3. In Figure 3, the storage modulus as a function of the strain amplitude for several volume fractions of silica gels is presented. As can be seen from Figure 3, the constant G' region decreases in the strong-link regime when the particle volume fraction is small and it begins to increase in the weak-link regime at higher concentrations. The crossover of the yield strain also takes place at around 9% volume fraction and is consistent with the crossover of G' as shown in Figure 2.

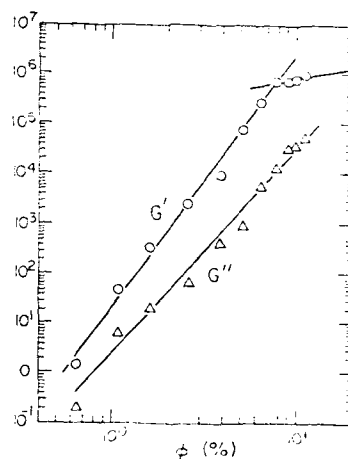
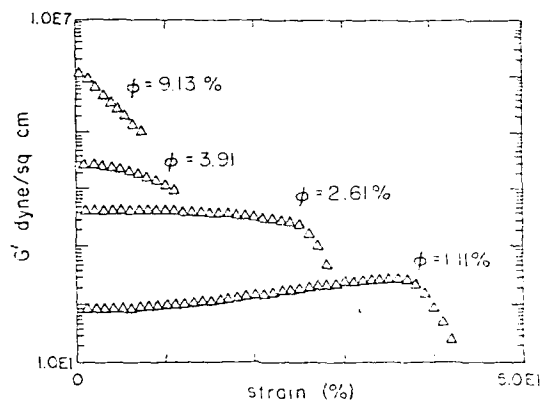
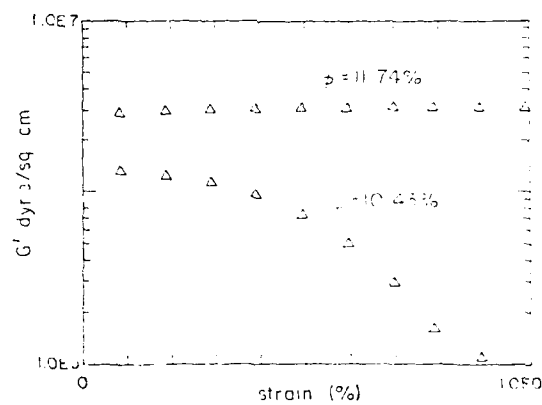


Figure 2. G' and G'' of silica gels at pH = 9.5 as a function of particle volume fraction ϕ . A clear crossover occurs at around $\phi = 9\%$.



(a)



(b)

Figure 3. The storage modulus G' of silica gels as a function of the strain amplitude γ for various concentrations. Figure 3a shows results in the strong-link regime in which γ_v is shrinking with increasing concentration. Figure 3b shows results in the weak-link regime in which γ_v increases with concentration. The crossover occurs at around 9% volume fraction, which is consistent with the crossover of G' in Figure 2.

In the strong-link regime, the behavior of the G' can be fitted to

$$G' \sim \phi^5 \quad (8)$$

while in the weak-link regime,

$$G' \sim \phi^{1.2} \quad (9)$$

with an error bar of 0.2 in the exponent since we have only four data points. Using the result of the scaling theory, we estimated $D = 2.17$ and $\alpha = 1.17$. The value of D obtained from the rheological study is consistent with that obtained from our preliminary light scattering studies on diluted samples where we found D to be between 2.0 and 2.2.

Adding surfactant to the silica suspensions greatly changes the behavior of G' . The G' of silica gels with surfactant as a function of particle volume fraction is shown in Figure 4. The data can not be fitted to a straight line in a log-log plot, indicating that it is not a power-law behavior. Rather the behavior of G' can be described better by

$$G' \sim \exp(a\phi) \quad (10)$$

with $a = 13.48$ with unit $\ln \text{dyne cm}^2$.

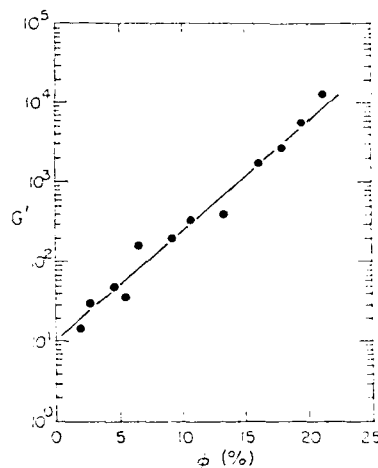


Figure 4. G' of silica gels with surfactant as a function of particle volume fraction ϕ .

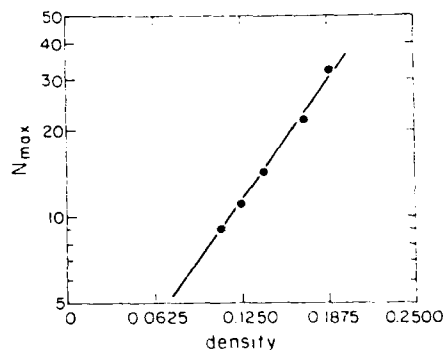


Figure 5. The number of particles in the largest cluster N_{\max} as a function of particle concentration in the dilute regime from Monte Carlo simulations.

DISCUSSIONS AND CONCLUSIONS

While the scaling behavior of the hard gels results from the fractal nature of the clusters, which is a result of the aggregation process, the exponential behavior of G' as a function of

particle volume fraction is probably due to the restructuring of the clusters before they form the network. The attraction between surfactant-coated particles is weakened by the adsorbed surfactant layers which prevent particles from strong attraction at contact, resulting in more frequent and, hence, observable restructuring of the gel network. With restructuring, there will be a distribution of cluster sizes within the gel network. The mechanical behavior of the network will be dominated by the weakest cluster which is also the largest cluster in the network (see Eq. (2)). A possible explanation of Eq. (10) is that Eq. (1) no longer holds for the largest cluster ξ_{\max} and is replaced by an exponential relation

$$\xi_{\max} \sim \exp(-a\phi). \quad (11)$$

To see whether this is true, we did Monte Carlo simulations on the aggregation of particles and clusters with restructuring [5]. Both particles and clusters are allowed to move according to the relation between the diffusivity and the cluster size. In the present calculation, the diffusivity is assumed to be independent of the cluster size. Figure 5 shows the number of particles in the largest cluster N_{\max} as a function of concentration in the dilute regime. N_{\max} is found to be related to the concentration exponentially,

$$N_{\max} \sim \exp(b\phi). \quad (12)$$

Since $N_{\max} = \xi_{\max}^D$, we expect ξ_{\max} to be an exponential function of concentration as well. This suggests that at higher concentrations when overlapping among clusters occurs, Eq. (11) may be expected, leading to Eq. (10).

The exponential behavior of G' as a function of concentration provides a basis for understanding pressure filtration. In pressure filtration of colloidal suspensions, a typical particle volume-vs.-pressure curve is shown in Figure 6 for alumina. For dispersed suspensions, the final density is high and is insensitive to the applied pressure, while for flocculated suspensions, the final density is usually a logarithmic function of the applied pressure

$$\phi = A \ln(P) + \phi_0, \quad (13)$$

where A is the slope and ϕ_0 is some constant. This equation can be inverted to be

$$P = \exp((\phi - \phi_0)/A), \quad (14)$$

which is essentially an exponential relation between the applied pressure and the resultant concentration, similar to the behavior of G' . This suggests that the pressure filtration behavior is also governed by the restructuring of the network under pressure.

In conclusion, two types of elastic behavior of colloidal gels are found: hard gels and soft gels. In the case of hard gels, there are two regimes that need to be specified depending on the relative elastic strength of the clusters to that of the link between clusters [1]. The storage modulus G' increases with concentration in a power-law fashion in both regimes, but the exponent is larger in the strong-link regime than in the weak-link regime [2]. The yield strain decreases with concentration in the strong-link regime, whereas it increases in the weak-link

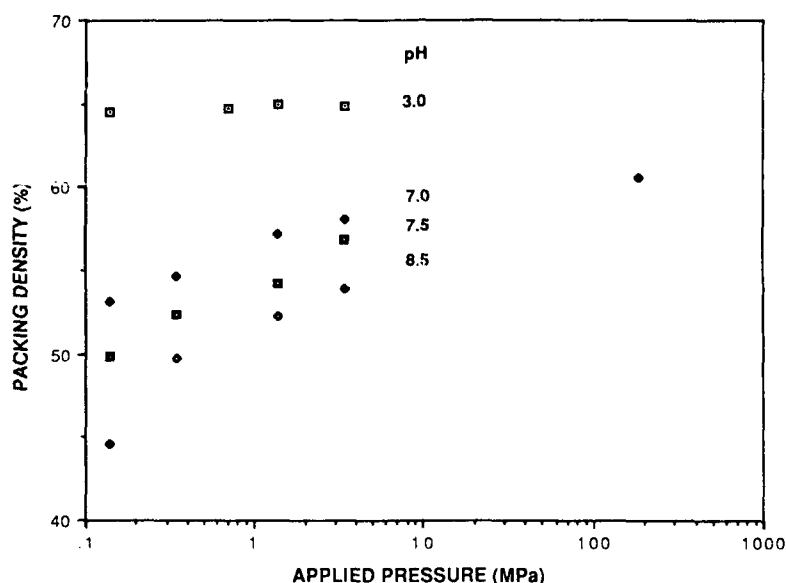


Figure 6. The cake density as a function of the applied pressure in pressure filtration for alumina at pH = 3.0, 7.0, 7.5, and 8.5.

regime [3]. There is a crossover from the strong-link behavior to the weak-link behavior as the concentration is increased. The predictions of the scaling theory are shown to be in good agreement with the results from the rheological study of silica gels.

In the case of soft gels, which were achieved by surfactant addition in the present studies, the power-law behavior of G' with concentration changes to exponential. Monte Carlo simulations on the restructuring of clusters showed that the largest cluster size increases exponentially with concentration, indicating that the exponential behavior of G' may be a result of the restructuring of clusters. Finally, we have shown that in the pressure filtration of flocculated colloidal suspensions, the applied pressure also increases exponentially with the resultant density. The exponential behavior of the applied pressure can also be understood in terms of the restructuring of the particulate networks.

ACKNOWLEDGMENT

This work is supported by the Air Force Office of Scientific Research (AFOSR) and the Defense Advanced Research Projects Agency (DARPA) under Grant No. AFOSR-87-0114.

REFERENCES

1. W.-H. Shih, W. Y. Shih, S. I. Kim, and I. A. Aksay, preprint.
2. R. Buscall, P. D. A. Mills, J. W. Goodwin, and D. W. Lawson, *J. Chem. Soc. Faraday Trans. I.*, **84**, 4249 (1988).
3. G. Dietler, C. Aubert, D. S. Cannel, and P. Wiltzius, *Phys. Rev. Lett.*, **57**, 3117 (1986).
4. Y. Kantor and I. Webman, *Phys. Rev. Lett.*, **52**, 1891 (1984).
5. W. Y. Shih, I. A. Aksay, and R. Kikuchi, *Phys. Rev. A*, **36**, 5015 (1987).

PART II

Sol-Gel Processing and
Ceramic-Polymer Composites

RHEOLOGICAL CHARACTERIZATION OF A SOL-GEL PROCESS FOR THE PREPARATION OF HIGH T_c SUPERCONDUCTORS

S.A. Khan^{*}, B.G. Bagley^{*}, P.Barboux[†], F.E. Torres^{*}

^{*} Bellcore, 331 Newman Springs Road, Red Bank, NJ 07701

[†] Universite P. et. M. Curie, 4 Place Jussieu, 75005 Paris

^{*} Princeton University, Chemical Engineering Dept., Princeton, NJ 08540

ABSTRACT

Superconducting thick films of yttrium-based cuprates can be prepared using a sol-gel technique. Rheological measurements on the precursors are used to identify processing parameters that can lead to better film properties. Steady and dynamic experiments reveal a direct correlation between the properties of the precursor, the final product, and the "age" of the yttrium component used in the precursor. Measurements support a proposed mechanism relating the "age" of the yttrium to the other properties and help to establish a processing methodology to obtain effective superconducting properties.

INTRODUCTION

High temperature superconductivity [1] in the cuprate oxide phase $YBa_2Cu_3O_{7-x}$ with a transition temperature, T_c , of 93 °K [2, 3] has generated considerable interest towards developing processes that could yield this material in bulk or film forms. Most of the bulk material can be obtained by conventional ceramic techniques that involve mixing oxides with appropriate nitrates or carbonates and firing the mixture. Thick and thin films, which have potential application in microelectronics, however, are not amenable to such a process [4]. While thin films have been successfully obtained using evaporation techniques, thick films (1-5 μ m) can be conveniently prepared (e.g. by spin coating) using solution techniques [5]. In the application of a solution technique, the solution viscosity and stability, as well as the processing procedure are very important in determining the superconducting properties of the fired film. Rheology has been shown [6] to be a sensitive technique for the characterization of these parameters and in this paper we discuss such a characterization as applied to the preparation of $YBa_2Cu_3O_{7-x}$ via a sol-gel technique.

EXPERIMENTAL

The superconducting material is prepared by firing a dried xerogel of a multicomponent precursor composed of copper acetate, barium acetate and yttrium hydroxide. The preparation of this precursor involves a two step process; first, an ion exchange is used to obtain the colloidal suspension of yttrium hydroxide from yttrium nitrate [7], and second, a sequential mixing of appropriate amounts of solutions of copper acetate and barium acetate to the yttrium hydroxide. The details of the process are described elsewhere [7].

Rheological tests were done on both the yttrium hydroxide suspension and the three component precursor. Steady shear and dynamic oscillatory measurements [8] were used along with other complementary techniques such as dynamic

light scattering [9]. The steady state viscosity data provide information pertaining to flows under process conditions (e.g. spin coating), and the dynamic elastic (G') and loss (G'') moduli help characterize the structure of the system. All tests were done at room temperature using a Rheometrics Mechanical Spectrometer (RMS 800).

RESULTS & DISCUSSION

Our experiments [6] indicate that (i) the properties of the yttrium hydroxide solution are time-dependent and change as the material "ages", and, (ii) there is a direct correlation between the properties of the yttrium hydroxide, the multicomponent precursor, and the properties of the fired film. These results are summarized in Fig. 1. Fig. 1a illustrates the differences between the viscosity shear-rate behavior for two-day and two-month old yttrium hydroxide suspensions. The viscosity of the fresh sample is lower, especially at low shear rates, and exhibits a Newtonian zero shear plateau. The aged yttrium shows a power-law viscosity, with a slope close to -1, that spans the entire shear-rate regime and indicates the presence of structure in the material. Dynamic light scattering experiments on the samples also reveal that the average size of the colloidal particles (Table I; also labelled next to the viscosity curves) doubled in two months and increased eightfold in a year. The growth in particle size can be attributed to Ostwald ripening.

TABLE I

Average Hydrodynamic diameter of Y(OH)₃ Particles

Sample Age:	2 days	2 months	12 months
Diameter (μm):	0.16	0.3	1.3

Multicomponent precursors were made using yttrium hydroxide 2 weeks and 10 weeks old. The time-dependent elastic modulus, $G'(t)$, reveals that the sol-gel kinetics (Fig. 1b) are significantly influenced by the properties/age of the yttrium component. The G' of the precursor containing fresh yttrium (2 weeks old) essentially remains unchanged with time. The G' of the precursor containing aged yttrium (10 weeks old) is time dependent and exhibits three distinct behavior patterns: initially there is an increase for 50 minutes, then a plateau for the next 50 hours, followed by a decline in value. Finally, fired (920 °C for 20 mins.) films containing "fresh" and "aged" yttrium hydroxide show differences in their resistance versus temperature behavior (Fig. 1c). The former sample never achieves zero resistance whereas, that containing the "aged" yttrium shows superconductivity with zero resistance at -70 °K. However, *bulk samples* containing "fresh" yttrium can be made superconducting upon prolonged heating (6 hrs. at 850 °C) which indicates that the use of fresh yttrium inhibits the rate of reaction.

The rheological data shown in Fig. 1 has direct implications for processing and fabrication because we can identify factors that can lead to better products. One of the early problems with the sol-gel method had been the inconsistent transport and superconducting properties as illustrated by resistance versus temperature curves (e.g. Fig. 1c). Our data indicate that fired films made with "aged" yttrium hydroxide should have more reproducible

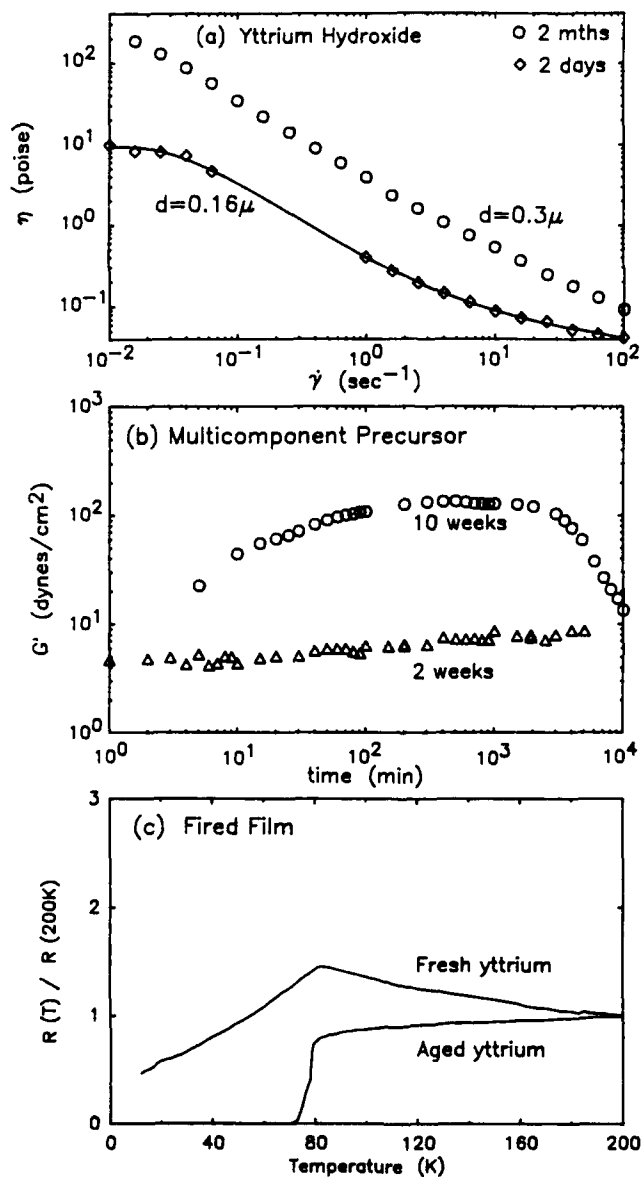


Figure 1. Effect of the "age" of the yttrium hydroxide on the: a) viscosity shear-rate response of the yttrium hydroxide suspension, b) time-dependent elastic modulus G' of the multicomponent precursor, where the numbers correspond to the age of the yttrium component, and c) temperature dependence of resistance (normalized to 200 °K) of a thick film on an MgO substrate.

properties. Samples containing fresh yttrium hydroxide are not useful for the preparation of thick films because the extended firing time required to make them superconducting can lead to undesirable substrate interactions.

Fig. 1b also specifies the time-window for obtaining useful results. The properties of the multicomponent precursor (containing aged yttrium) changes from a sol to a gel-like consistency in the first 50 minutes as G' increases by an order of magnitude. The optimal time-window for utilizing this precursor is when this material has a high modulus and a fully developed structure, i.e. between 50 and 3000 minutes. After this, the G' starts to decline because the gel structure destabilizes with the formation of precipitates of copper oxide. This precursor then becomes ineffective for making superconductors. The precursor containing fresh yttrium has a longer shelf-life and shows no destabilization (although the G' values of the two samples seem to approach each other), rendering it useful at least for preparing bulk superconductors.

The aforesaid conclusions are applicable to such processes (bulk sample, dip coating) where the precursor is exposed to minimum shear. In order to evaluate the relevancy of the results for high shear application (e.g. spin coating), we have studied the effects of shear history on both the precursor and the yttrium hydroxide. Fig. 2a illustrates the effect of shear on the sol-gel behavior of a multicomponent precursor containing 19-day old yttrium hydroxide [10]. We observe the growth in structure in "Run 1" as G' increases with time. After about 3 hours, the sample was subjected to a shear rate of 250 s^{-1} for 2 minutes. The subsequent $G'(t)$ is shown as "Run 2". In both cases we observe an increase in $G'(t)$, indicating the development of a structure, prior to levelling off. However, the modulus of the sheared sample reaches a much lower value suggesting that the initial gel structure has been irreversibly altered or disrupted. This structural breakdown is also evident from sequential measurements of the steady shear viscosity (Fig. 2b) in which we find the viscosity to be lower in the second run. We believe that shearing destroys any long-range order of the system, some of which is recoverable in a time period of 25-30 minutes (Fig. 2a; Run 2) but a large fraction of which is not. However, there remains sufficient elasticity and short-range order, even after shearing. This is evident from the flat shape of the moduli versus frequency plot of the precursor (Fig. 2c), done immediately after it has been sheared.

In order to determine the role of the yttrium hydroxide in the shear history behavior of the precursor, we made successive viscosity versus shear rate measurements of a two-month old yttrium hydroxide suspension (Fig. 3). Unlike the multicomponent precursor, we find very good overlap between the two runs. The absence of thixotropy suggests that the yttrium suspension does not form strong aggregates but has weak particle-particle interactions. This supports our previous notion [6] that its behavior does not play a role in the gelation (structure formation) of the multicomponent precursor.

Despite a breakdown of the structure, a sheared multicomponent precursor containing "aged" yttrium hydroxide still yields a good superconductor. This behavior is consistent with, and can be explained by, our proposed mechanism [6] relating the age of the yttrium hydroxide to the sol-gel behavior of the precursor and the fired-film characteristics. When copper acetate is added to yttrium hydroxide, the pH is lowered from ~ 10 to ~ 6 . The smaller particles (presence confirmed by light scattering) of the fresh yttrium hydroxide dissolve completely, whereas the larger particles of the aged yttrium hydroxide reduce in size. When barium acetate is added, the increase in pH causes a re-precipitation. In the aged yttrium case (Fig. 4b), copper-rich precipitates are formed either individually or on existing yttrium particles. In the fresh

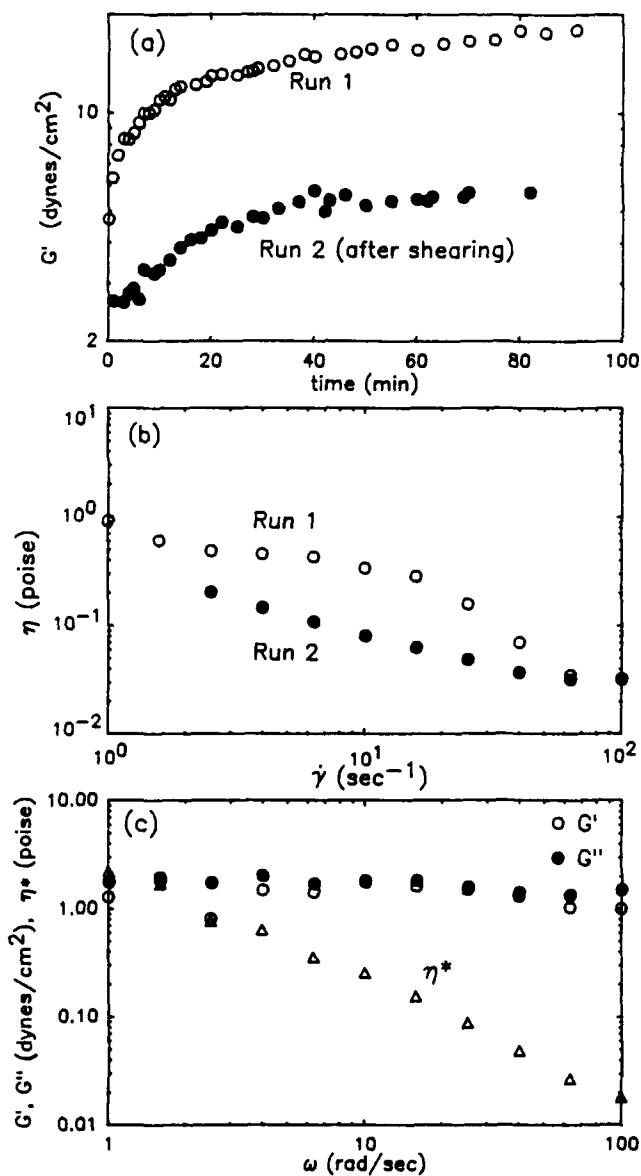


Figure 2. Effect of shear history on a precursor solution. a) Elastic modulus G' vs time before and after a sample has been sheared. b) Viscosity vs shear rate showing thixotropic behavior. c) Dynamic moduli and complex viscosity as a function of frequency immediately after the sample has been sheared.

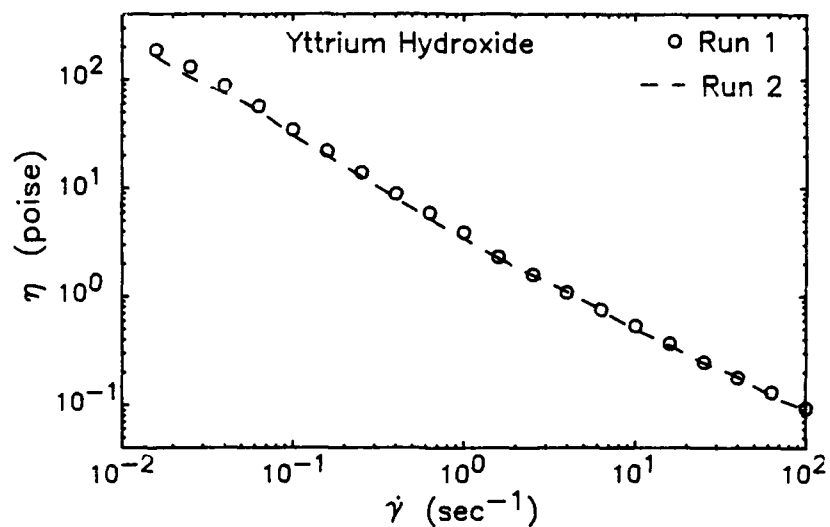


Figure 3. Two successive viscosity vs shear rate runs of a two-month old yttrium hydroxide suspension showing good overlap.

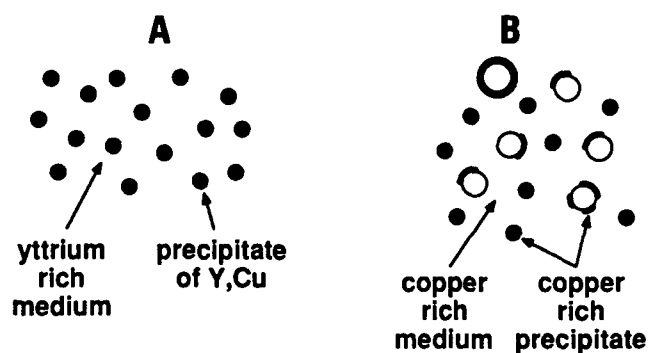


Figure 4. Schematic representation of the microstructures in precursor solutions containing (a) "fresh" and (b) "aged" yttrium hydroxide components. The fresh sample contains precipitates composed of yttrium and copper. The aged sample has a copper rich liquid phase together with new copper rich precipitates formed individually or on existing yttrium hydroxide particles.

yttrium case, precipitates composed of yttrium and copper form (Fig. 4a). On a relative scale, the aged sample has a copper rich liquid phase together with the copper rich new precipitate because a lot of the yttrium never dissolved. This copper helps to form ligands which give rise to the gel-like structure. Although shearing can alter the linkages, the composition of the liquid matrix and the particles remain unchanged. The final product is insensitive to the shear history because it is this composition that controls the reaction when a sample is being fired. Consequently, our suggested guidelines for making better products is applicable for both high and low shear processes.

ACKNOWLEDGEMENTS

The authors gratefully acknowledge J.M. Tarascon and R.K. Prud'homme for useful discussions.

References

1. J.G. Bednorz and K.A. Muller, *Z. Phys.*, **B64**, 189 (1986).
2. M.K. Wu, J.R. Ashburn, C.J. Torng, P.H. Hor, R.L. Meng, L. Gao, Z.J. Huang, Y.Q. Wang, and C.W. Chu, *Phys. Rev. Lett.*, **58**, 908 (1987).
3. R.J. Cava, B. Batlogg, R.B. van Dover, D.W. Murphy, S. Sunshine, T. Siegrist, J.P. Remieka, E.A. Rietman, S. Zahurak, G. Espinosa, *Phys. Rev. Lett.*, **58**, 1676 (1987).
4. B.G. Bagley, L.H. Greene, P. Barboux, J.M. Tarascon, T. Venkatesan, E.W. Chase, S.W. Chan, W.L. Feldman, B.J. Wilkins, S.A. Khan and M. Giroud, in Advances in Superconductivity: Proc. 1st International Symp. Superconductivity (ISS'88), 1988, Nagoya, edited by K. Kitazawa and T. Ishiguro (Springer Verlag, Tokyo, 1989), p.477.
5. P. Barboux, I. Valente, J.M. Tarascon, S. Khan, F. Shokoohi, M. Henry, R. Morineau and B.G. Bagley, in Superconductors: Relationships Between Properties, Structure, and Solid State Chemistry, edited by J.B. Torrance, K. Kitazawa, J.M. Tarascon, J.R. Jorgensen and M. Thompson (Mater. Res. Soc. Pittsburgh, PA), submitted.
6. S.A. Khan, P. Barboux, B.G. Bagley, F.E. Torres, *J. Non-Crystalline Solids* (in press).
7. P. Barboux, J.M. Tarascon, L.H. Greene, G.W. Hull and B.G. Bagley, *J. Appl. Phys.*, **63**, 2725 (1988).
8. R.B. Bird, R.C. Armstrong and O. Hassager, Dynamics of Polymeric Liquids, Vol. 1: Fluid Mechanics, 2nd ed. (Wiley, New York, 1987), pp. 112.
9. B.J. Berne and R. Pecora, Dynamic Light Scattering, (Wiley, New York, 1976).
10. S.A. Khan, P. Barboux, B.G. Bagley and J.M. Tarascon, *Appl. Phys. Lett.*, **53** (8), 700 (1988).

SiO₂-TiO₂-ZrO₂ GEL GLASSES - REACTION KINETICS AND PROPERTIES

W. BEIER AND G. H. FRISCHAT

Technical University Clausthal, Institut für Nichtmetallische
Werkstoffe, Professur für Glas, 3392 Clausthal-Zellerfeld,
Federal Republic of Germany

ABSTRACT

Solutions have been prepared containing silicon ethoxide, titanium butoxide, and zirconium propoxide as metal organic compounds. Additions of water (for hydrolysis), solvents (ethanol, formamide), and hydrochloric acid (as a catalyst) have been varied systematically. The reaction kinetics of the hydrolysis and condensation steps in these mixtures have been studied by measuring viscosity and ²⁹Si NMR data as a function of time. After gelling, the products have been dried and then converted to glassy materials by firing. Temperatures well below 1000 °C have been used for that. Glasses from the title system have been obtained both in bulk and in thin film form. Properties like density, specific surface, and hardness have been investigated and are reported as well.

INTRODUCTION

The glass system SiO₂-TiO₂ is an important one. By varying the TiO₂ content, the index of refraction can be shifted in a wide range [1] and the thermal expansion can be adjusted at values around zero [2]. But it is difficult to incorporate more than 10 wt.-% TiO₂ into the glass conventionally. Thus, if higher TiO₂ contents are desired, the sol-gel route is the method of choice.

By this technique, it is also possible to incorporate further components. We added ZrO₂ in order to enhance the chemical durability of the products. The target composition of all glasses in this study is 65 SiO₂.20 TiO₂.15 ZrO₂ (by moles) and only alkoxides were used to prepare them. Information on monolithic samples can be found in [3] while preparation and characterization of thin films are treated in [4, 5].

In this paper results are presented which concern the reaction kinetics of the precursor solutions as well as properties of the final glasses. The first kinetic data were published in [6] and more will be reported in [7]. Some older papers on SiO₂-TiO₂-ZrO₂ sol-gel products are [8] to [10].

EXPERIMENTAL, RESULTS

The viscosities of several ternary alkoxide solutions are plotted versus time in Fig. 1. All mixtures contained 50 ml TEOS, the appropriate amounts of Zr-propoxide and Ti-butoxide, and the additional components listed in the legend. The falling sphere method was used. The overall behavior of all solutions is similar so far as η remains nearly constant at low values for a time and then rises sharply. The increase occurs after some days of ageing and its onset depends strongly on the contents of the other components.

For example, the amount of water is essential. Addition of 7.5 ml H₂O instead of 5 ml leads to much shorter low η periods. The replacement of H₂O by diluted HCl, on the other hand, doesn't affect very much, see curves 7 and 8. The rise of η can be delayed by dilution with ethanol, see curve 3.

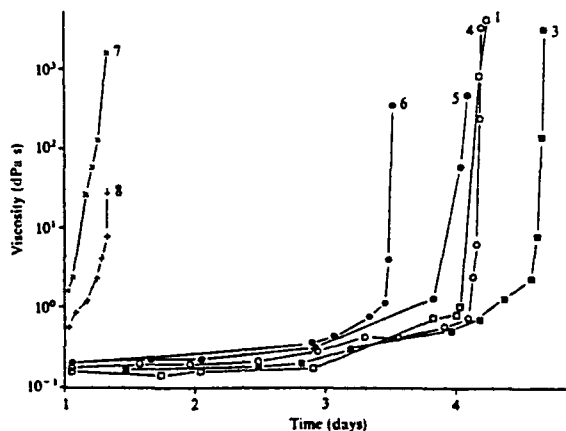


Fig. 1: Viscosity of ternary alkoxide solutions as a function of time. All mixtures with 55 ml ethanol E and 4ml 0.01 N HCl but without formamide F in the first step. Last step:

7	40	ml E + 50 ml F + 7.5 ml H ₂ O
8	40	ml E + 50 ml F + 7.5 ml 0.01 N HCl
6	80	ml E + 5 ml H ₂ O
5	40	ml E + 50 ml F + 5 ml H ₂ O
1	40	ml E + 50 ml F + 5 ml 0.01 N HCl
4	120	ml E + 5 ml 0.01 N HCl
3	120	ml E + 5 ml H ₂ O

The influence of the drying control chemical additive formamide is of special interest. This shall be demonstrated for the gelling times which were determined simply by tilting the samples by 90° and recording when they didn't change their forms. When F was added in the last step (for the exact procedure, we refer to [6] or [7]), the gelling time was much reduced when only H₂O was used in the first step. See 1b and 2b in Fig. 2 for that.

If, on the other hand, HCl is added already in the first step (3b, 4b), F effects a slight delay. Thus, NH₂CHO and HCl seem to exhibit contrary effects on the gelling behavior of Si-Ti-Zr alkoxide solutions. If F is added in the first step but not in the last, the gelling times become very short (one hour or less). By adding NH₂CHO also in the last step they can be raised again.

In order to investigate the reactions in the solutions on a molecular level, ²⁹Si NMR was applied. For technical details see [6] and [7], but some typical results are presented here. In Fig. 3 the spectrum of an ethanolic TEOS/0.01 N HCl mixture is shown which was recorded after 90 min of reaction.

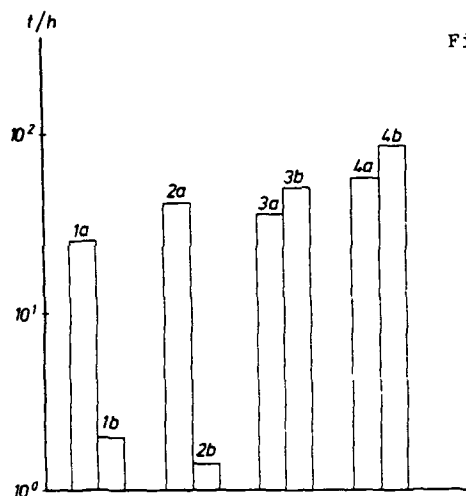


Fig. 2: Gelling time of solutions without (a) and with (b) formamide in the last step. All mixtures had 55 ml E, 50 ml TEOS and 3 ml H_2O or HCl in the first and 5 ml H_2O/HCl in the last step.

First step:

- 1: H_2O
- 2: H_2O
- 3: 0.01 N HCl
- 4: 0.1 N HCl

Last step:

- 1: 0.01 N HCl
- 2: H_2O
- 3: 0.01 N HCl
- 4: 0.1 N HCl

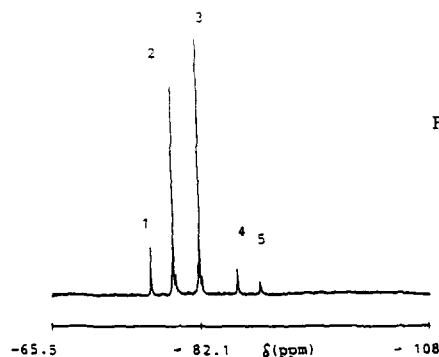


Fig. 3: ^{29}Si NMR spectrum of a TEOS solution after 90 min

Five peaks at different chemical shifts (relative to tetramethylsilane) can be differentiated. They can be associated to the following molecular groups: 1) - 76.7 ppm: $Si(OH)_2(OEt)_2$; 2) - 79.2 ppm: $Si(OH)(OEt)_3$; 3) - 82.1 ppm: $Si(OEt)_4 = TEOS$; 4) - 86.4 ppm: $Si-O-Si(OH)(OEt)_2$; 5) - 88.9 ppm: $Si-O-Si(OEt)_3$. The signals 1 and 2 result from hydrolyzed species, and the peaks 4 and 5 from condensed ones.

After adding the other alkoxides, the situation has completely changed, see Fig. 4. All peaks resulting from OH-carrying species have vanished or are heavily reduced. Similar spectra are obtained if formamide is added instead of the Ti- and Zr-alkoxides.

Several properties of bulk samples have also been measured. Gels and glasses of $65 SiO_2 \cdot 20 TiO_2 \cdot 15 ZrO_2$ composition could be obtained as monoliths only if formamide was added in the last (but not in the first) step of the preparation procedure.

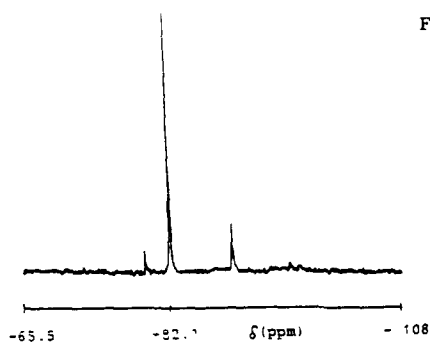


Fig. 4: ^{29}Si NMR spectrum of an alkoxide mixture, 3 h 25 min after the addition of $\text{Ti}(\text{OC}_4\text{H}_9)_4$ and $\text{Zr}(\text{OC}_3\text{H}_7)_4$

Densities of such products were measured and some results are plotted in Fig. 5. To determine the bulk density, the Hg-buoyancy method was applied, while the apparent densities were measured pycnometrically.

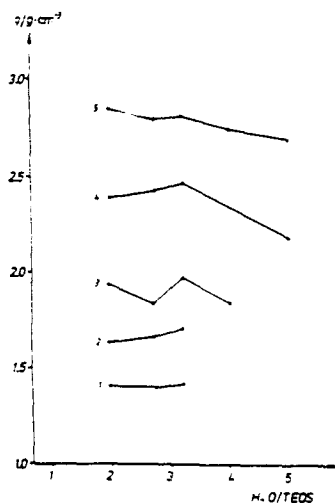


Fig. 5: Bulk density and apparent density of ternary gels and glasses as functions of heat treatment and of the $\text{H}_2\text{O}/\text{TEOS}$ ratio.
 1) at room temperature (bulk density)
 2) after baking at 350°C , bulk density
 3) after baking at 650°C , bulk density
 4) after baking at 350°C , apparent density
 5) after baking at 650°C , apparent density

The densities evidently are not much influenced by the $\text{H}_2\text{O}/\text{TEOS}$ ratios of the precursor solutions, but they depend strongly on the firing temperature. The glassy samples which were heat treated at 650°C exhibit matrix densities up to 3 g cm^{-3} . This skeletal density is always higher than the bulk value of the same piece because even at 650°C , there remains some porosity. It is important to know the different densities of all sol-gel products e. g. for thin film applications.

The specific surface of the samples was determined by the BET method. Gels dried at room temperature showed values from 390 to $560 \text{ m}^2\text{g}^{-1}$ when the $\text{H}_2\text{O}/\text{TEOS}$ ratio was varied from 1 to 5.

The corresponding ranges for 350 °C samples and for 650 °C pieces are 300 to 480 and 220 to 280 m²g⁻¹, respectively [11].

The solid material was further characterized by DSC, x-ray diffraction, SEM, chemical analysis, and the determination of the microhardness. Only a few of these details can be presented here. The target composition was obtained quite well for all samples, i. e. selective evaporations could be avoided during all preparation steps. The gels exhibited rather high carbon contents (some %), but these decreased during the heat treatment drastically. After baking at 650 °C, e. g. values of 0.09, 0.07 and 0.04 were measured for initial H₂O/TEOS ratios of 1, 2 and 4.75.

The Knoop microhardness was determined by a load-independent method [12]. After heat treatments at 350 and 650 °C, quite low L₂KH values of 490 and 640 MPa were obtained. But, after baking at 900 °C, a hardness of 3190 MPa was observed which equals that of conventional silica glass. Probably, the formation of dispersed crystals is responsible for this distinct increase, similar to the ZrO₂ toughened SiO₂-ZrO₂ gel glasses in [13].

DISCUSSION AND CONCLUSIONS

The η -t behavior and the gelling times of Si-Ti-Zr alkoxide solutions can be strongly influenced by additions of formamide and/or HCl at different steps of their preparation. NH₂CHO acts physically by reducing the vapour pressure and by increasing the viscosity. Chemically, it binds much water so that a shortage for the TEOS hydrolysis may result. Thus, F should be added considerably later after mixing TEOS and water when enough complex Si-containing species have been formed. If F is added only in the first step, a network seems to form mainly from Zr- and Ti-containing species.

Using IR techniques, several authors found some evidence for Si-O-Ti linkages in fired SiO₂-TiO₂ sol-gel glasses, [8] and [14] to [17]. Considering our ²⁹Si NMR results, it seems unlikely that such bonds will form already in the solutions. So, from the absence of new peaks, we deduce that reactions like

$\text{Si(OH)(OEt)}_3 + \text{Ti(OH)(OBu)}_3 \longrightarrow (\text{OEt})_3\text{Si-O-Ti(OBu)}_3 + \text{H}_2\text{O}$
do not take place. Consequently, the mixed linkages have to be formed during later steps of the preparation. According to [18], Si-O-Ti bonds should form in SiO₂-TiO₂-ZrO₂ gel glasses if more Ti than Zr atoms are present. This condition is valid in the present investigation.

Concerning solid samples, it is possible to obtain SiO₂-TiO₂-ZrO₂ gels and gel glasses as monoliths only if formamide is added in the last step. Properties like density, porosity and microhardness can be adjusted as desired by varying the composition and the preparation scheme of the liquid precursors and the heat treatment of the gels.

ACKNOWLEDGEMENTS

The authors thank Prof. W. Müller-Warmuth, Dr. K. Meise-Gresch and Dr. C. Wies, all University Münster, and Dr. A. A. Göktas

for valuable discussions and experimental help. Financial support by the DFG Bonn Bad-Godesberg is gratefully acknowledged.

REFERENCES

- [1] B.E. Yoldas and T.W. O'Keeffe, Appl. Opt. 18, 3133 (1979).
- [2] G.A. Pavlova and A.N. Amatuni, Inorg. Mat. 11, 1443 (1975).
- [3] W. Beier, A.A. Göktas and G.H. Frischat, J. Amer. Ceram. Soc. 69, C 148 (1986).
- [4] W. Beier, A.A. Göktas and G.H. Frischat, J. Non-Cryst. Sol. 100, 531 (1988).
- [5] W. Beier and G. H. Frischat, Mat. Res. Soc. Symp. Proc. 121, 817 (1988).
- [6] C. Wies, K. Meise-Gresch, W. Müller-Warmuth, W. Beier, A. A. Göktas and G.H. Frischat, Ber. Bunsenges. Phys. Chem. 92, 689 (1988).
- [7] W. Beier, A.A. Göktas, G.H. Frischat, C. Wies, K. Meise-Gresch and W. Müller-Warmuth, Phys. Chem. Glasses 30, 69 (1989).
- [8] M. Nogami and Y. Moriya, Yogyo-Kyokai-Shi 85, 448 (1977).
- [9] L. Hou, C. Zhu and J. Xie, J. Chinese Silicate Soc. 11, 422 (1983).
- [10] C. Zhu, L. Hou, F. Gan and Z. Jiang, J. Non-Cryst. Sol. 63, 105 (1984).
- [11] A.A. Göktas, PhD thesis, Techn. Univ. Clausthal (1988).
- [12] G.H. Frischat in Strength of Inorganic Glass, edited by C.R. Kurkjian, Plenum Press, New York, London, pp 135 - 145 (1985).
- [13] M. Nogami and M. Tomozawa, J. Amer. Ceram. Soc. 69, 99 (1986).
- [14] R. Jabra, J. Phalippou, M. Prassas and J. Zarzycki, J. Chim. Phys. 78, 777 (1981).
- [15] M.F. Best and R.A. Condrate, J. Mat. Sci. Lett. 4, 994 (1985).
- [16] J. Rhee, U.U. Chi, T.S. Kang, D.S. Jo and S.K. Ko, Yoop Hakhoechi 23, 27 (1986).
- [17] B. Karmakar and D. Ganguli, Indian J. Technol. 25, 282 (1987).
- [18] F. Jiang, L. Hou, C. Zhu and Z. Jiang, J. Non-Cryst. Sol. 80, 571 (1986).

THE FORMATION OF MOLECULAR COMPOSITES BY A MODIFIED SOL-GEL PROCESS

Ronald B. Lessard*, Mary M. Wallace†, W. Anthony Oertling*, Chi K. Chang*, Kris A. Berglund†‡ and Daniel G. Nocera*

Departments of *Chemistry, †Chemical Engineering, ‡Agricultural Engineering, and the Center for Fundamental Materials Research at Michigan State University, East Lansing, MI 48824

ABSTRACT

Standard sol-gel procedures have been modified to permit sol-gel synthesis to be performed at varying hydrogen ion concentrations and in a variety of organic solvents. These modifications greatly expand the variety of guest molecules that can be incorporated into nondense glassy environments. Processing conditions can be controlled such that the guest compounds generally retain their solution properties thereby allowing new molecular composites to be formed. Reported herein is the incorporation of both porphyrins and metalloporphyrins into silica matrices. Electronic absorption, vibrational, and excited state luminescence properties of the resulting composites clearly demonstrate that the molecular and electronic structure of the porphyrins and metalloporphyrins are preserved during sol-gel processing and in the ceramic matrices. This retention of properties has been shown for guest molecules doped into monoliths as well as films.

INTRODUCTION

The advent of optically transparent, sol-gel derived, ceramic materials has heralded the beginning of a new generation of molecular composites that can be used in the design of chemical and optical devices. The ability to process ceramics at or near room temperature permits a variety of molecules, with specially tailored optical and chemical properties, to be incorporated as guests within ceramic matrices [1-7]. This accomplishment is especially noteworthy because the high temperatures that characterize ceramic processing, exclusive of sol-gel chemistry, often preclude the synthesis of molecular composites owing to the relatively low thermal stability of most inorganic and organic guest molecules. From a chemical standpoint, high porosities of sol-gel derived ceramics [8,9], which has often been considered a drawback of ceramic processing, permit guest molecules to undergo ion-exchange and/or diffusion in the ceramic matrix thereby enabling the diffusing compound to come into intimate contact with the guest molecule. Furthermore, optically good quality ceramic films can be prepared by sol-gel methods because the glass is formed from pure and homogeneous sols and unlike organic polymeric-based host materials the polymeric inorganic ceramic matrix exhibits excellent photolytic and thermal stabilities. These properties are prerequisites to the development of these molecular composites as chemical and optical sensors and uniquely qualifies these materials for the development of optodes [10].

Despite these significant advances over conventional high temperature processing, the design of molecular composites by sol-gel methods until now has been restricted to complexes that are soluble in water or alcohols [1-7]. Consequently, the study of water or alcohol insoluble compounds in sol-gel derived glassy matrices has generally relied on the derivatization of guest compounds by the incorporation of functional groups that render them water soluble. An alternative approach that heretofore has been relatively unexplored is to modify existing sol-gel procedures to directly accommodate alcohol or water insoluble materials.

We report the preparation of optically transparent ceramic materials containing both water soluble and insoluble porphyrins and metalloporphyrins prepared by derivatization of the guest molecule and modification of conventional sol-gel processes such that stable nondense glasses are formed. The porphyrins studied included octaethylporphyrin (H₂OEP) and *meso*-tetra-*N*-methylpyridiniumporphyrin (H₂T(PyMe)P), whose structures are shown in Figure 1. The optically transparent nature of the molecular composites derived from these procedures has allowed the study of absorption and emission properties as well as the resonance Raman spectra of these porphyrin-based materials. The large flexibility in the preparative conditions of the glasses has allowed us to also study the fully protonated (diacid) and free-base forms of the porphyrins. The spectroscopic properties of the porphyrin-based materials derived from glasses formed from aqueous and nonaqueous solutions are compared.

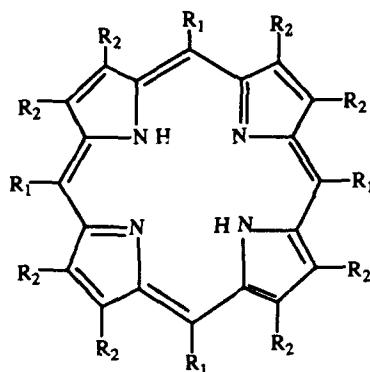


Figure 1. Free base porphyrin structures. For octaethylporphyrin (H_2OEP) $R_1 = H$; $R_2 = CH_2CH_3$ and for *meso*-tetra-*N*-methylpyridiniumporphyrin ($H_2T(PyMe)P$) $R_1 = C_5H_4N^+-CH_3$; $R_2 = H$. Further protonation at the imine nitrogens yields the diacid $H_4(porphyrin)$.

EXPERIMENTAL

A. Chemicals and characterization

All compounds used in the preparation of the sol-gel materials as well as the guest molecules added to these materials were of reagent grade or purer. Purchased guest molecules, or those obtained from literature procedures, were characterized by IR, Raman, and UV-visible spectroscopies. $Cu(T(PyMe)P)^{4+}$ (where $T(PyMe)P$ is the completely deprotonated amine *meso*-tetra-*N*-methylpyridiniumporphyrin) and H_2OEP were prepared according to standard methods [11,12].

B. Variable solvent systems

The sol-gel method of Hench [8,9] was modified in the following manner: the formamide was replaced by an equal volume of 2,2-dimethoxypropane (dmp), the HNO_3 was replaced by an equal volume of HCl, and one half of the volume of methanol was replaced by another organic solvent (method 1). Alternatively, nondense glasses were prepared by replacing the formamide and HNO_3 with equal volumes of dmp and HCl respectively (method 2). Chloroform, cyclohexane, dichloromethane, hexane, *n*-pentane and tetrahydrofuran were solvents used in place of methanol. Colorless optically transparent monoliths were prepared by casting the above solutions in polyethylene or polypropylene containers. These glasses were prepared under the same heating conditions as described by Hench or they were allowed to age and dry at room temperature. For the latter condition, gels shrink and harden in approximately five days to form monoliths. These glassy materials were approximately one-third more dense than the glasses formed by Hench's procedure (under the same set of drying conditions). Molecular composites of these glasses were formed by adding guest molecules to solution during the mixing process.

C. Basic glasses

Monoliths and films have also been prepared by base hydrolysis. Method 2, from Part B, was followed except that the concentrated HCl was replaced by the desired amount of 0.1 M NaOH. Optically transparent glasses were prepared with hydroxide ion concentrations as great as 6.6×10^{-3} M (based on the initial number of moles of 0.1 M NaOH added). These samples

generally formed gels in just a few minutes at room temperature and after several days, shrunk and hardened.

D. Use of buffers

Buffers over a pH range from 1 to 12 were incorporated in sol-gel procedures. The exact amount of buffer used depends on the solvent composition of the glass itself. Typically 25-50% of the water (no acid added) was replaced by the desired buffer. Buffer concentrations higher than this tended to lead to phase separation. Glasses prepared in this manner are not "buffered," but they do expand the range of possible hydrogen ion concentrations in the glasses.

E. Preparation of films

Films supported on glass microscope slides as well as quartz plates were prepared by spinning the slides or plates at several hundred rpm and pipetting the solution of choice onto the slide, one drop at a time, until the desired area was coated with a thin layer of solvent. These films, with their large surface area, dried in just a few minutes. A variety of guest molecules were placed into these films by first dissolving the desired compound in the solution and then applying it to the spinning slide. In turn, it is also possible to coat these guest containing films with another layer of glassy material thereby allowing ceramic sandwich structures to be prepared.

F. Instrumentation

UV-visible spectra were measured on a Perkin-Elmer Lambda 3A UV/vis Spectrophotometer and recorded on a Perkin-Elmer R100A Recorder. IR spectra were measured on a Perkin-Elmer 1750 Infrared Fourier Transform Spectrometer equipped with a Perkin-Elmer 7700 Professional Computer and spectra were plotted on a Perkin-Elmer Model PP-Plotter Printer. Raman spectra and emission spectra were measured on instruments described elsewhere [13,14].

RESULTS AND DISCUSSION

The glasses prepared by the methods described in Part B are more dense than those prepared by Hench [8,9]. In the latter procedure the solvent remains in the pores of the gel long after the gel ages and hardens, owing to the high boiling point of formamide (111°C). Indeed, the formamide is extremely difficult to remove from hardened glasses and is known to remain in monoliths for periods of over one year [15]. Figure 2 shows the Raman spectra of neat formamide as well as a silica based sol-gel which was prepared with formamide. These spectra illustrate that the formamide is truly incorporated into the glassy matrix. The intense C-H bending vibration at 1392 cm^{-1} observed in the spectrum of neat formamide is clearly apparent in the Raman spectrum of the glass, indicating that the formamide is trapped in cavities of the glassy matrix. Although formamide occluded in pores supports the silicon oxide polymeric matrix thereby reducing the strain which can lead to cracking [8,9], it directly hinders diffusion of reagents within the glassy matrix. The problem of solvent clogging of the pores is circumvented by the removal of formamide from the sol-gel procedure and by incorporating other organic solvents into the process. In this case, solvent can be driven out of the pores under milder conditions. Figure 3 reproduces the Raman spectrum of a sol-gel derived monolith prepared by using chloroform and methanol. The Raman spectrum of this glass exhibits the characteristic peaks arising from silicon oxide vibrations of the ceramic matrix at 978 cm^{-1} and 488 cm^{-1} , which have been assigned to the Si-O stretching [16,17] and silica ring vibrations [16,18] respectively, and no bands attributable to the organic solvents are observed. Surprisingly, nondense glasses of this type are of excellent optical quality; although there can be no structural support resulting from solvents occluded in the matrix, cracking of these glasses is not observed.

With the formation of stable, optically transparent glassy materials, it is possible to study the spectroscopic properties of these molecular composites. The use of CHCl_3 in the sol-gel process has enabled us to incorporate water insoluble octaethylporphyrin into silica matrices. Porphyrins are spectroscopically characterized by their intense luminescence. The spectrum of octaethylporphyrin in HCl acidified CHCl_3 solution appears in Figure 4. Also shown is the steady-state emission spectrum of the porphyrin in a monolith. Intense luminescence from the

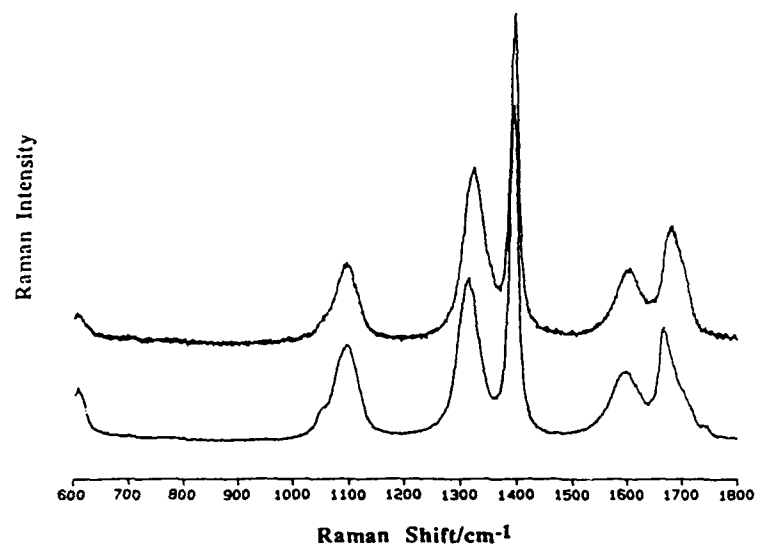


Figure 2. Raman spectra of neat formamide (bottom) and of a sol-gel monolith (top) processed by using formamide as a drying chemical control agent. Excitation was with the 406.7-nm line of a krypton ion laser.

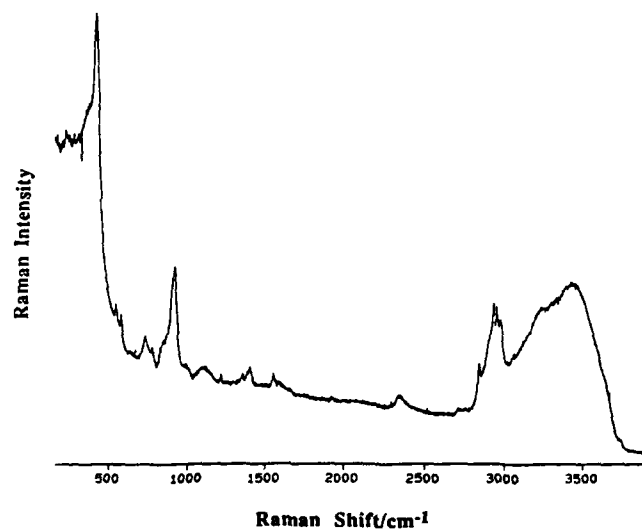


Figure 3. Raman spectrum of a sol-gel derived monolith prepared with methanol and chloroform (method 1 in Part B). Excitation was with the 488.0-nm line of an argon ion laser at 500 mW, 2 scans at 1 $\text{cm}^{-1}/\text{sec}$ [22].

porphyrin in the ceramic is observed. Moreover, that the emission profile is similar to the emission spectrum of the octaethylporphyrin, which is known to be in its diacid (H_4OEP) form, in HCl acidified chloroform, indicates that the diacid is present in the glass. Thus, these results imply that the porphyrin's molecular and electronic structure are preserved in the sol-gel environment.

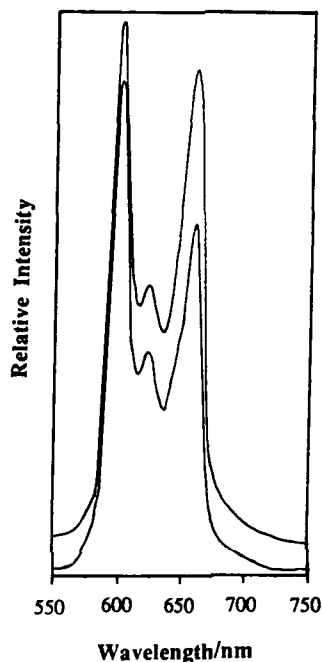


Figure 4. Steady-state emission spectra of octaethylporphyrin in a sol-gel derived monolith prepared by method 1 in Part B (bottom) and in HCl acidified $CHCl_3$ (top). Excitation was at 435 nm.

In order to further investigate the properties of porphyrins in a variety of glassy matrices, the electronic absorption and emission properties of the water-soluble *meso*-tetra-*N*-methylpyridiniumporphyrin were also determined. Figure 5 reproduces the emission spectra of the porphyrin in aqueous solution and compares it to similar spectra of this porphyrin in sol-gel derived silica matrices of different hydrogen ion concentrations. Analysis of these spectra reveals that the porphyrin is introduced into the monolith as a mixture of free base, $H_2T(PyMe)P$, and diacid, $H_4T(PyMe)P$, forms. The steady-state emission of this porphyrin in the silica matrix (prepared according to method 2 in Part B) is blue-shifted from that in aqueous solution ($\lambda_{em,max} = 668$ nm in glass; $\lambda_{em,max} = 686$ nm in water of pH = 5.6). Additionally, the emission profile of the porphyrin in the glass exhibits a low energy shoulder. The porphyrin in solution and glassy environments is distinguished further by its absorption spectra. The porphyrin Soret band, located at 422 nm in aqueous solution, is positioned at 442 nm in the glass. The 442-nm Soret band is a signature of the diacid form of the porphyrin ($H_4T(PyMe)P$) [19]. In agreement with these observations, replacement of HCl with NaOH by the procedures described in Part C, leads to emission spectra displaying two bands located at 661 nm and 719 nm. The former corresponds to the diacid form of $H_2T(PyMe)P$ and the appearance of the low energy band is attributed to the presence of the free base, $H_2T(PyMe)P$. This

conclusion is further supported by spectra of glasses that are prepared at varying concentrations of NaOH. The intensity of the low energy band increases, whereas the high energy emission intensity decreases with increasing hydrogen ion concentration (Figure 5). Conditions that were basic enough to prevent the formation of the diacid and contain only free base do not result in optically transparent glasses.

These differences in the emission spectra between the free base and diacid forms establish the potential use of these glassy matrices for sensors. Films containing $H_2T(PyMe)P$ in its free base form were prepared. Upon contacting the film with 0.1 M HCl the free base form was

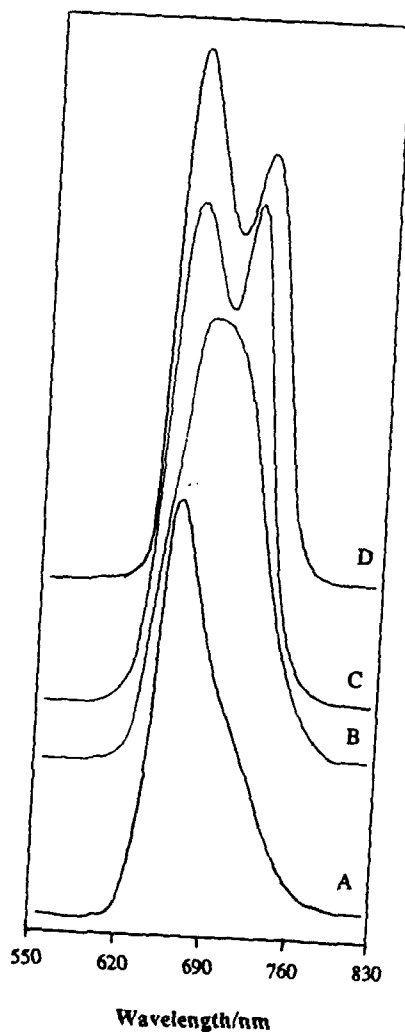


Figure 5. Steady-state emission spectra of *meso*-tetra-*N*-methylpyridiniumporphyrin in acidic (A), basic (C), and neutral (D) sol-gel derived monoliths, and in aqueous solution (B). Excitation was at 435.0 nm.

protonated resulting in the appearance of the diacid form *in the film*. This process was shown to be reversible by contacting the diacid containing film with base to attain the original free base form. Therefore, the porphyrin must be contained in cavities that are connected and accessible from the film surface.

In order to selectively measure the vibrations of the free base porphyrin in the sol-gel environment, resonance Raman studies were undertaken. By using the 413.1-nm excitation line of a krypton ion laser, the Raman scattering of the free base is selectively enhanced over that of the diacid. Figure 6 shows the resonance Raman spectra of the porphyrin in a film, monolith, and solution. The spectrum of $H_2T(PyMe)P$ in solution is similar to those of the porphyrins in glass environments. The differences in relative intensities of some of the features indicate that some spectral contributions from the diacid forms are present in the ceramic materials. These results provide conclusive evidence for the presence and stability of $H_2T(PyMe)P$ in sol-gel derived glasses, and support our assignment of the 716-nm emission band to the free-base porphyrin.

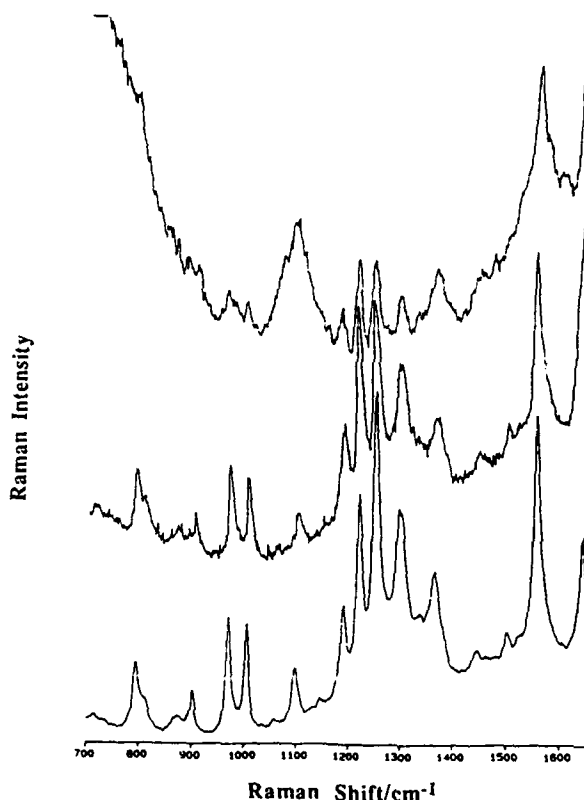


Figure 6. Resonance Raman spectra of $H_2T(PyMe)P$ in aqueous solution (bottom), sol-gel derived film (middle) and sol-gel derived monolith (top). Excitation was with the 413.1-nm line of a krypton ion laser.

Metalloporphyrins are also stable in the sol-gel environment. The resonance Raman spectra of $Cu(T(PyMe)P)^{4+}$ in a sol-gel prepared by the method described by Hench [8,9] is shown in

Figure 7 along with that of the Cu(II) porphyrin in aqueous solution. The vibrations of the metalloporphyrin are unaffected by the sol-gel environment. The additional features present in the bottom spectrum are due to formamide. Thus, the metal remains coordinated during sol-gel processing and the metalloporphyrin, similar to the unmetallated porphyrins, are robust in the sol-gel matrix.

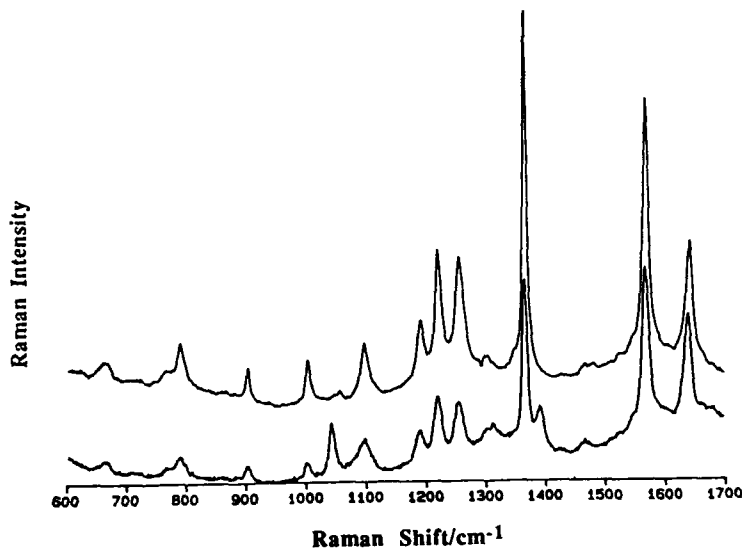


Figure 7. Resonance Raman spectra of $\text{Cu}(\text{T}(\text{PyMe})\text{P})_4^{4+}$ in a sol-gel derived monolith (bottom) and in aqueous solution (top). Excitation was with the 413.1-nm line of a krypton ion laser.

SUMMARY AND CONCLUSION

We have shown that it is possible to prepare silica-based sol-gel materials under a variety of conditions that allow for the incorporation of either water soluble, or water insoluble porphyrins and metalloporphyrins. More generally the ability to modify the processing method to include nonaqueous solvents, in conjunction with approaches to derivatize guest molecules in order to enhance their compatibility with aqueous/methanol-based glasses, considerably broadens the scope of the types of materials that can be included in ceramic oxide matrices.

Our observation that the resonance Raman spectra of these porphyrin-based materials is the same in solution as in the glassy matrix was unexpected. That bands assigned to the porphyrin N-H or N-C vibrations at 1222 cm^{-1} and 1253 cm^{-1} , respectively, [20] are not affected by the glassy environment suggests little hydrogen bonding between the amine functional groups and the sol-gel matrix. It appears that the porphyrin and metalloporphyrin compounds are located in cavities of the silicon oxide framework in such a manner that they cannot be leached out. The insensitivity between the porphyrin and the glass, as evidenced by electronic and vibrational properties, precludes their use as molecular probes of the sol-gel environment. These results parallel those observed for molecular composites incorporating organic dyes [6] or lanthanide [21] complexes, which also yield little information on silicon oxide environments. In contrast, the porphyrin-based nondense glasses are extremely sensitive to external reagents of vital importance, the high porosity of these nondense glasses, which is often thought of as a drawback, is a property that allows reagents to come in contact with the guest compound. For

instance, the large shift in absorption of the very sharp Soret band of porphyrins and ring vibrations with pH presages the usefulness of porphyrin-based compounds as a means to monitor dynamic chemical processes, by resonance Raman, absorption, and emission spectroscopies. Thus, these molecular composites are ideal candidates for chemical sensing applications.

ACKNOWLEDGEMENT

Financial support from the Center for Fundamental Materials Research at Michigan State University and the Ford Motor Company are gratefully acknowledged. Raman spectroscopic studies were performed in the LASER Laboratory in the Department of Chemistry at Michigan State University.

REFERENCES

1. D. Avnir, D. Levy and R. Reisfeld, *J. Phys. Chem.*, **88**, 5956 (1984).
2. S. Dave and R. K. MacCrone, in *Better Ceramics Through Chemistry II*, edited by C. J. Brinker, D. E. Clark and D. R. Ulrich (Mater. Res. Soc. Proc., vol. 73, Palo Alto, California, 1984) p. 605.
3. V. Kaufman and D. Avnir, *Langmuir*, **2**, 717 (1986).
4. M. D. Newsham, M. K. Cerreta, K. A. Berglund and D. G. Nocera, in *Better Ceramics Through Chemistry III*, edited by C. J. Brinker, D. E. Clark and D. R. Ulrich (Mater. Res. Soc. Proc., vol. 121, Reno, Nevada, 1988) p. 627.
5. B. Dunn, E. Knobbe, J. M. McKiesman, J. C. Pouxviel and J. I. Zink, in *Better Ceramics Through Chemistry III*, edited by C. J. Brinker, D. E. Clark and D. R. Ulrich (Mater. Res. Soc. Proc., vol. 121, Reno, Nevada, 1988) p. 331.
6. J. C. Pouxviel, B. Dunn and J. I. Zink, *J. Phys. Chem.*, **93**, 2134 (1989).
7. E. J. A. Pope and J. D. Mackenzie, in *Better Ceramics Through Chemistry II*, edited by C. J. Brinker, D. E. Clark and D. R. Ulrich (Mater. Res. Soc. Proc., vol. 73, Palo Alto, California, 1984) p. 809.
8. S. Wallace and L. L. Hench, in *Better Ceramics Through Chemistry*, edited by C. J. Brinker, D. E. Clark and D. R. Ulrich (Mater. Res. Soc. Proc., vol. 32, Albuquerque, New Mexico, 1984) p. 47.
9. L. L. Hench, in *Science of Ceramic Chemical Processing*, (Wiley-Interscience, New York, 1986) p. 52.
10. S. M. Angel, D. G. Garvis, S. K. Sharma and A. Seki, *Appl. Spect.*, **43**, 430 (1989).
11. J. W. Buchler, *Porphyrins and Metalloporphyrins*, edited by K. M. Smith (Elsevier, The Netherlands, 1975), p. 179.
12. C-B. Wang and C. K. Chang, *Synthesis*, **7**, 548 (1979).
13. M. K. Cerreta and K. A. Berglund, submitted to the *J. of Crystal Growth*.
14. R. D. Mussell and D. G. Nocera, *J. Am. Chem. Soc.* **110**, 2764 (1988).
15. G. W. Scherer, *J. Non-Cryst. Solids*, **100**, 77 (1988).
16. C. J. Brinker, E. P. Roth, D. R. Tallant and G. W. Scherer, in *Science of Ceramic Chemical Processing*, (Wiley-Interscience, New York, 1986) p. 37.
17. D. M. Krol and J. G. vanLierop, *J. Non-Cryst. Solids*, **3**, 131 (1984).
18. F. L. Galeener, *J. Non-Cryst. Solids*, **49**, 53 (1982).
19. P. Hambright and E. B. Fleischer, *Inorg. Chem.*, **9**, 1757 (1970).
20. R. B. Lessard and W. A. Oertling, K. A. Berglund and D. G. Nocera, work in progress.
21. R. B. Lessard, K. A. Berglund and D. G. Nocera, these proceedings.
22. W. A. Oertling, A. Salehi, Y. C. Chung, G. E. Leroi, C. K. Chang and G. T. Babcock, *J. Phys. Chem.*, **91**, 5887 (1987).

HIGHLY EMISSIVE LANTHANIDE COMPOUNDS IN SOL-GEL DERIVED MATERIALS

Ronald B. Lessard*, Kris A. Berglund†, and Daniel G. Nocera*

Departments of *Chemistry, †Chemical Engineering and Agricultural Engineering, and the Center for Fundamental Materials Research at Michigan State University, East Lansing, MI 48824

ABSTRACT

Molecular composites that possess unique emission properties have been prepared by introducing luminescent molecules into sol-gel based silica glasses. The lumophores chosen for study are terbium(III) and europium(III) ions whose emissions are quenched in aqueous and sol-gel environments owing to coordination of water molecules to the lanthanide ion. To overcome the quenching process the ions have been encapsulated within cryptands. The resulting terbium(III) and europium(III) cryptates possess long-lived excited states in both aqueous solution and sol-gel glassy matrices. Measurements of the excited state dynamics of these molecularly engineered composites demonstrate the feasibility of tailoring molecules to retain their excited state properties in sol-gel derived glasses.

INTRODUCTION

The function of a wide variety of cathodoluminescent (CL), photoluminescent (PL), and electroluminescent (EL) devices is predicated on intense luminescence from lanthanide ions residing in solid matrix supports [1]. Major advances in the development of optical and electrochemical displays, avionics, and detectors have been preceded by discoveries of new lanthanide-based phosphors [2-6]. Host lanthanide ions Eu(III), Tb(III), Ce(III), Dy(III), Ho(III), and Er(III) have been used to obtain CL, PL, and EL phosphors spanning the entire visible spectrum with excited state lifetimes ranging from milliseconds to nanoseconds [6]. In these materials, the nature of the solid support is manifest to the color and lifetime of the emission [1] and hence the synthesis and investigation of novel supports for the lanthanide ions bear directly on the design of new lanthanide-based materials. To date, the inorganic host structures that have found the most utilization are simple oxides, sulfides, and halides. Because lanthanide ion luminescence is efficiently quenched by water (*vide infra*), the use of supports derived from protic environments has been precluded. Practically, protic host structures can greatly expand the scope of lanthanide-based materials for several reasons. These include the ability to process 'phosphor-type' materials at low temperatures, and to control and modify the host's infrastructure (e.g. porosity) as well as its optical and electronic properties. Accordingly, the preservation of the excited state properties of lanthanide ions in protic host structures may open avenues toward the design of novel 'phosphor' materials.

We have concentrated our efforts on synthesizing lanthanide glasses derived from sol-gel methods. Silicon-oxide based sol-gels are attractive host materials for highly lumiphoric lanthanide ions because of their relative ease of preparation, their high degree of homogeneity, and importantly, their optically transparent nature. A major obstacle to the preparation of such materials is the suppression of channels that lead to excited state deactivation of the lanthanide. We now report the preparation of highly emissive glasses by the encapsulation of the lanthanide ion in a cryptand, which shields it from the sol-gel environment.

EXPERIMENTAL

A. Chemicals and characterization

All compounds used in the preparation of the sol-gel materials were of reagent grade or purer. The cryptands, TbCl₃·6H₂O, and EuCl₃·6H₂O were purchased from Aldrich Chemical Company and used without further purification. Compounds were characterized by IR, UV-visible, and emission spectroscopies.

B. Preparation of complexes, monoliths, and films

Synthesis of $[Tb\subset 2.2.1]Cl_3$, $[Tb\subset 2.2.2]Cl_3$, and $[Eu\subset 2.2.1]Cl_3$. $[Tb\subset 2.2.1]Cl_3$, $[Tb\subset 2.2.2]Cl_3$, and $[Eu\subset 2.2.1]Cl_3$ (where $\subset 2.2.1$ is 4,7,13,16,21-pentaoxa-1,10-diazabicyclo-[8.8.5]tricosane and $\subset 2.2.2$ is 4,7,13,16,21,24-hexaoza-1,10-diazabicyclo-[8.8.5]-hexacosane; cryptand structures are illustrated in Figure 1) were prepared according to the procedure described by Gansow [7] and Pruet [8], except that the procedure was scaled up to one gram of cryptand. The yields of the cryptates are as follows: 1.6 g or 86% for $[Tb\subset 2.2.1]Cl_3$; 1.2 g or 72% for $[Tb\subset 2.2.2]Cl_3$; and 1.9 g or 100% for $[Eu\subset 2.2.1]Cl_3$.

Synthesis of $[Tb\subset 2.2.2Bz]Cl_3$. The compound $[Tb\subset 2.2.2Bz]Cl_3$ (where $\subset 2.2.2Bz$ is 5,6-benzo-4,7,13,16,21,24-hexaoza-1,10-diazabicyclo[8.8.5]-hexacosane) was prepared according to the procedure described for that of $[Tb\subset 2.2.1]Cl_3$ [7,8] where the $\subset 2.2.1$ was replaced by $\subset 2.2.2Bz$. The procedure was scaled up such that 0.44 g of $TbCl_3 \cdot 6H_2O$ and 0.5 g of $\subset 2.2.2Bz$ (dissolved in 0.5 g of toluene, as purchased from Aldrich) were used. The yield was 0.72 g or 87%.

Preparation of monoliths and films. Sol-gel derived nondense glasses were prepared by previously described methods [9].

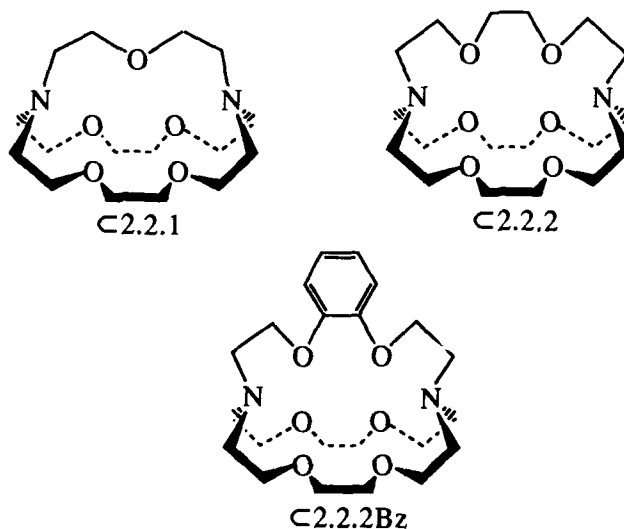


Figure 1. Structure of cryptands

C. Instrumentation

UV/visible spectra were measured on a Perkin-Elmer Lambda 3A UV/vis Spectrophotometer and recorded on a Perkin-Elmer R100A Recorder. IR spectra were measured on a Perkin-Elmer 1750 Infrared Fourier Transform Spectrometer controlled by a Perkin-Elmer 7700 Professional Computer and spectra were plotted on a Perkin-Elmer Model PP-Plotter Printer. Lifetime determinations and emission spectra were measured on instruments described elsewhere [10,11]. Lifetimes were determined by using the third or fourth harmonics of a Nd:YAG laser (fwhm = 8 ns) as excitation lines. The 313-nm excitation wavelength used for steady-state emission experiments was selected by excitation and emission monochromators with

slit widths of 5 mm and 3 mm, respectively. The entrance slit of the emission spectrometer was equipped with a Schott KV-399 cut-off filter. The instrument response function of the emission spectrometer is relatively flat over the spectral region of lanthanide luminescence and therefore it was unnecessary to correct emission spectra.

RESULTS AND DISCUSSION

The luminescence intensity of the lanthanide ions, and more generally of any emissive molecule, is directly proportional to the excited state lifetime [12]. The observed lifetime, τ_{obsd} , can be expressed as follows:

$$\tau_{\text{obsd}} = 1/k_{\text{obsd}} = [k_r + ak_{\text{nr}}(\text{hf}) + bk_{\text{nr}}(\text{lf})]^{-1} \quad (1)$$

where k_{obsd} is the inverse of the observed excited state lifetime, k_r is the radiative rate constant, $k_{\text{nr}}(\text{hf})$ is the nonradiative rate constant due to high frequency oscillators, and $k_{\text{nr}}(\text{lf})$ is the nonradiative rate constant due to low frequency oscillators. In the above expression, nonradiative decay resulting from all other possible processes (*e.g.* photochemistry) has been considered to be small. The constants a and b are based on the number of normal modes for high and low frequency oscillators, respectively. The excited state lifetime is typically dominated by $k_{\text{nr}}(\text{hf})$ [13-20] and k_r , whereas the low frequency oscillators (metal-ligand) are known to have much smaller effect upon excited state deactivation pathways. Therefore eq 1 can be reduced to

$$\tau_{\text{obsd}} = 1/k_{\text{obsd}} \approx [k_r + ak_{\text{nr}}(\text{hf})]^{-1} \quad (2)$$

Because k_r is an intrinsic molecular parameter and relatively constant for a given series of complexes of similar electronic structure, it is the nonradiative rate constant that determines the observed lifetime, and hence intensity of luminescence. For the case of the lanthanide ions, the high frequency O-H vibrations of coordinated water molecules result in large values of $k_{\text{nr}}(\text{hf})$. From eq 2, as $k_{\text{nr}}(\text{hf})$ increases, τ_{obsd} decreases and thus the overall luminescence will be attenuated. The lifetimes reproduced in Table I, for the aqua Tb(III) complexes, illustrate the significant affect of high frequency oscillators on their excited state lifetimes. The well-documented increase in lifetime of the lanthanide ion upon substitution of D₂O for H₂O [21-24], which results from the reduced oscillator frequency of the O-D vibration as compared to an O-H vibration, is also included. These data clearly establish that the previous assumption of $k_{\text{nr}}(\text{hf}) \gg k_{\text{nr}}(\text{lf})$ used in the derivation of eq 2 is valid, and suggest that luminescence from Tb(III) and Eu(III) ions in the sol-gel environment, with its many O-H oscillators, should be short-lived. This prediction is verified by the lifetime data shown in Table I for the Tb(III) and Eu(III) sol-gel derived glasses. The high concentrations of water and alcohol in the sol-gel matrix is manifested in observed lifetimes that are comparable or shorter than those for the ions in aqueous solution, and luminescence from these glasses is weak.

The deleterious effect of O-H oscillators on the excited state properties of the lanthanide ions can be minimized by encapsulating the ions in molecular cages [25-27]. The nitrogens and oxygens comprising the three straps of the cryptand (see Figure 1) coordinate the lanthanide ion to expel water from the first coordination sphere. Shielding by the $\text{C}2.2.1$ cryptand is better than that for the $\text{C}2.2.2$ owing to tighter cavity dimensions of the former. This is reflected by comparison of the lifetime data in Tables I and II. Whereas the lifetimes of the $\text{C}2.2.2$ cryptates are comparable to those of aqueous solution, the lifetimes of the $\text{C}2.2.1$ complexes are much longer. Moreover, an important observation in regard to the work described here is that the lifetimes of either of the cryptate complexes do not coincide with those of the free Tb(III) and Eu(III) ions in a glass, but rather are similar to the lifetimes of the respective cryptates in aqueous solution. This result clearly establishes that the lanthanide cryptate complexes can withstand sol-gel processing and most importantly, that the lanthanide ion is not extracted from the cryptand cage.

The results of the time-resolved lifetime measurements are entirely consistent with steady-state emission experiments. The lanthanide cryptates in aqueous solution and in the sol-gel matrix are intensely luminescent. Steady-state emission spectra of aqueous solutions and sol-gel derived silica glasses of $[\text{TbC}2.2.1]\text{Cl}_3$ are dominated, as shown in Figure 2, by four

Table I. Excited state lifetimes of Tb(III) and Eu(III) aqua complexes at 298 K.

Complex	Environment	$\tau/\mu s^a$
TbCl ₃ ·6H ₂ O	H ₂ O	427
	H ₂ O ^b	400
	Sol-Gel Monolith	431
	D ₂ O ^c	3880
EuCl ₃ ·6H ₂ O	H ₂ O	112
	H ₂ O ^d	110
	Sol-Gel Monolith	25
	D ₂ O ^d	3200

^a λ_{ex} = 266 nm or 355 nm and λ_{em} = 546 nm for Tb(III) and 619 nm for Eu(III). ^bMeasured at 300 K [25]. ^cMeasured at 300 K [26]. ^dMeasured at 293 K [27].

Table II. Excited state lifetimes of lanthanide cryptates at 298 K.

Complex	Environment	$\tau/\mu s^a$
[TbC2.2.1]Cl ₃	H ₂ O	1520
	H ₂ O ^b	1300
	Sol-Gel Monolith	1280
	Sol-Gel Film	1270
	D ₂ O ^b	3100
[TbC2.2.2]Cl ₃	H ₂ O	469
	Sol-Gel Monolith	424
[TbC2.2.2Bz]Cl ₃	H ₂ O	504
	Sol-Gel Monolith	356
	Sol-Gel Film	514
[EuC2.2.1]Cl ₃	H ₂ O	230
	H ₂ O ^c	215
	Sol-Gel Monolith	127
	D ₂ O ^c	640

^a λ_{ex} = 266 nm or 355 nm and λ_{em} = 546 nm for Tb(III) and 619 nm for Eu(III). ^bMeasured at 300 K [27]. ^cMeasured at 293 K [28].

characteristic peaks that are the signature of Tb(III) species. These bands originate from radiative relaxation of electronically excited Tb(III) ion from its ⁵D₄ excited state to ground state ⁷F₃ manifold [29]. The energy and intensity similarities of the luminescence of [TbC2.2.1]Cl₃ complex in these very different environments attest to the high stability of this complex in the sol-gel matrix. The emission spectral behavior of [EuC2.2.1]Cl₃ in sol-gel derived glasses and in solution parallels that of its Tb(III) counterpart. Figure 3 illustrates the emission spectra of [EuC2.2.1]Cl₃ in a sol-gel derived monolith and in aqueous environments. The multi-line

emission profiles of $[\text{Eu}(\text{2.2.1})\text{Cl}_3]$, originating from the radiative transition between the $^5\text{D}_0$ excited state and $^7\text{F}_j$ states [29], are virtually identical. As originally inferred from lifetime data, the luminescence from glasses containing the cryptate is much more efficient than glasses containing the free ions. Relative quantum yields of the Tb(III) and Eu(III) cryptates are ten times greater than that observed for the free ions in the sol-gel derived glassy environment.

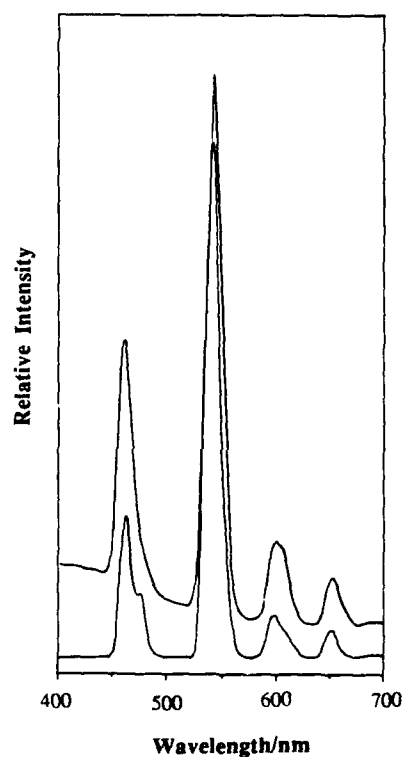


Figure 2. Steady-state emission of $[\text{Tb}(\text{2.2.1})\text{Cl}_3]$ in aqueous solution (bottom) and in a sol-gel derived monolith (top). Excitation was at 313 nm.

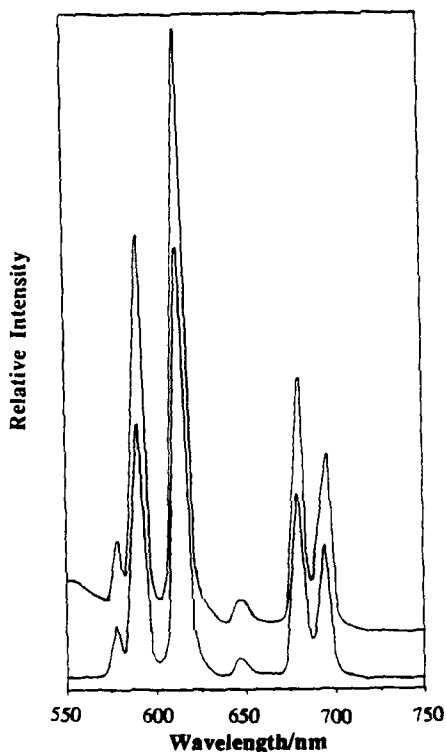


Figure 3. Steady-state emission of $[\text{Eu}\subset 2.2.1]\text{Cl}_3$ in aqueous solution (bottom) and in a sol-gel derived monolith (top). Excitation was at 313 nm.

SUMMARY AND CONCLUSIONS

Thus the immediate environment of lanthanide ions can be engineered to engender extremely long-lived excited states in sol-gel derived glassy environments. The lanthanide ion can effectively be protected from sol-gel processing conditions by encapsulation in cryptands. Because the lanthanide ions exhibit excited state properties that are congruent with the properties exhibited by these complexes in solution, the glassy materials are true molecular composites. Comparison of steady-state and time-resolved luminescence of these cryptands in glasses indicates that the lanthanide complexes are intact in the glass and most probably situated in cavities of the silicon-oxide framework. Interactions of the complexes with the solid matrix appear to be negligible.

ACKNOWLEDGEMENT

Financial support from the Center for Fundamental Materials Research at Michigan State University, and the Ford Motor Company are gratefully acknowledged. Raman and time resolved electronic spectroscopic studies were performed in the LASER Laboratory in the Department of Chemistry at Michigan State University.

REFERENCES

1. H. G. Brittain, in *Molecular Luminescence Spectroscopy Methods and Applications: Part 2, Chemical Analysis Series*, vol. 77, edited by S. G. Schulman (John Wiley & Sons, New York, 1988) p.401.
2. G. Urbain, *Ann. Chim. Phys. (Paris)*, **18**, 222, 289 (1909).
3. A. K. Levine and F. C. Palilla, *Appl. Phys. Lett.*, **5**, 118 (1964).
4. P. Avouris, I. F. Chang, P. H. Duvigneaud, E. A. Giess and T. N. Morgan, *J. Lumin.*, **26**, 213 (1982).
5. A. Bril, G. Blasse, A. H. Gomes de Mesquita and J. A. dePoorter, *Philips Tech. Rev.*, **32**, 125 (1971).
6. F. C. Palilla, A. K. Levine and M. Rinkevics, *J. Electrochem. Soc.*, **112**, 776 (1965).
7. D. J. Pruett, Ph.D. Dissertation, Michigan State University, 1978.
8. O. A. Gansow, and K. B. Triplett, US Patent 4 257 955 (24 March 1981).
9. Sol-gel materials have been prepared by the procedure described in the Experimental Part B in R. B. Lessard, M. M. Wallace, W. A. Oertling, C. K. Chang, K. A. Berglund and D. G. Nocera, these proceedings.
10. R. D. Mussell and D. G. Nocera, *J. Am. Chem. Soc.* **110**, 2764 (1988).
11. M. D. Newsham, E. P. Giannelis, T. J. Pinnavaia and D. G. Nocera, *J. Am. Chem. Soc.*, **110**, 3885 (1988).
12. N. J. Turro, in *Modern Molecular Photochemistry* (Benjamin/Cummings, Menlo Park, CA, 1978).
13. R. B. Lessard, Ph.D. Dissertation, Wayne State University, Detroit, Michigan, 1988.
14. A. F. Fucaloro, L. S. Forster, J. V. Rund and S. H. Lin, *J. Phys. Chem.* **87**, 1796 (1983).
15. L. S. Forster and O. Mønsted, *J. Phys. Chem.* **90**, 5131 (1986).
16. A. M. Ghaith, L. S. Forster and J. V. Rund, *Inorg. Chem.* **26**, 2493 (1987).
17. M. Mvele and F. Wasgestian, *Inorg. Chim. Acta*, **119**, 25 (1986).
18. A. Ditze and F. Wasgestian, *Ber. Bunsen-Ges. Phys. Chem.* **90**, 111 (1986).
19. C. K. Ryu, R. B. Lessard, D. Lynch and J. F. Endicott, *J. Phys. Chem.*, **93**, 1752 (1989).
20. J. F. Endicott, T. Ramasami, R. Tamilarasan, R. B. Lessard, C. K. Ryu and G. R. Brubaker, *Coord. Chem. Rev.*, **77**, 1 (1987).
21. W. DeW. Horrocks, Jr. and D. R. Sudnick, *Acc. Chem. Res.*, **14**, 384 (1981).
22. W. DeW. Horrocks, Jr., in *Progress in Inorganic Chemistry*, vol. 31, edited by S. J. Lippard (John Wiley & Sons, New York, 1984) p. 1.
23. Y. Haas and G. Stein, *J. Phys. Chem.*, **75**, 3677 (1971).
24. S. P. Sinha, in *Systematics and the Properties of the Lanthanides*, NATO ASI Series No. 109, Edited by S. P. Sinha (D. Reidel, Dordrecht, 1983) p. 451.
25. B. Alpha, V. Balzani, J-M. Lehn, S. Perathoner and N. Sabbatini, *Angew. Chem., Int. Ed. Engl.* **26**, 1266 (1987).
26. G. Stein and E. Wurzburg, *J. Chem. Phys.* **62**, 208 (1975).
27. N. Sabbatini, S. Dellonte, M. Ciano, A. Bonazzi and V. Balzani, *Chem. Phys. Lett.*, **107**, 212 (1984).
28. N. Sabbatini, S. Dellonte and G. Blasse, *Chem. Phys. Lett.*, **129**, 541 (1986).
29. S. P. Sinha, in *Complexes of the Rare Earths* (Pergamon Press, Oxford, 1966) pp. 145,148.

HAFNIUM METALLO-ORGANIC FILMS AND GELS PRODUCED BY SOL-GEL PROCESSING

CHARLES D. GAGLIARDI AND KRIS A. BERGLUND

Michigan State University, Department of Chemical Engineering and
Center for Fundamental Materials Research, East Lansing, MI 48824

ABSTRACT

Metallo-organic materials are often used as precursors for highly refractory oxides and high-temperature composites. The feasibility of producing hafnium metallo-organic films and gels by sol-gel techniques is demonstrated in the present study. Since hafnium alkoxides are not commercially available, their preparation is an obstacle in the development of their sol-gel processing applications. A common synthesis technique was used to produce hafnium isopropoxide, which was subsequently hydrolyzed under acid catalyzed conditions to produce films and gels. The films were prepared by spin casting and remained optically transparent. Initially, the gels were also optically transparent, but became translucent upon drying. Raman, IR, and light scattering spectroscopies were used to characterize this sol-gel process, and it is compared with the analogous processing of titanium and zirconium alkoxides.

INTRODUCTION

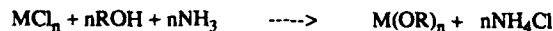
Alkoxides of titanium and zirconium have received increasing interest as precursors for powdered ceramics, sols, gels, and film coatings. Substantially fewer studies have been undertaken with hafnium alkoxides, partly due to the lack of any commercial source. Hafnium oxide films have been made from a hafnium alkoxide using low-pressure chemical vapor deposition (CVD) [1], and ion-sputtering [2]. Our current work is aimed at producing metallo-organic films which can be prepared by sol-gel processing at room pressures and temperatures, and characterizing the process.

Livage has shown that optically clear titanium monoliths can be made from $\text{Ti}(\text{O}-\text{Bu}^n)_4$ when hydrolyzed with butanol and acetic acid [3]. Clear solutions have been made from the hydrolysis of a zirconium alkoxide with acetic acid [4], and transparent, colorless gels have been made from mixtures of titanium and zirconium alkoxides with acetic acid, water, and metal acetates [5]. In addition, acetic acid has also been used for making films with mixtures of lead, zirconium, and titanium alkoxides [6]. Since acetic acid has been used successfully in these similar alkoxide systems, we investigated the effect of acetic acid on the hydrolysis of hafnium isopropoxide. The isopropoxide was chosen for direct comparison to titanium isopropoxide [3] and for its established synthesis [7-10].

The hafnium isopropoxide synthesis is presented, along with a description of the sol-gel processing for the formation of the sols, gel monoliths, and films. The acetic acid and metal alkoxide systems were compared for hafnium, zirconium, and titanium alkoxides. Light scattering was used to characterize sol stability and gelation rates. Infrared and Raman spectroscopies were used to probe the structure of sols and gels.

MATERIALS AND METHODS

Hafnium isopropoxide was prepared by the direct action of ammonia on hafnium tetrachloride in the presence of isopropanol, as described by Mehrotra [11]:



The reaction was carried out in excess benzene to keep the product in solution, as in previous syntheses [8,9]. Twenty-five grams of HfCl_4 were dissolved in 350 ml benzene and 35 ml isopropanol. The benzene and the isopropanol were dried as described below, and the benzene was added to the HfCl_4 prior to the addition of isopropanol. An excess of NH_3 was bubbled through a gas dispersion tube while rapidly stirring the solution. The white NH_4Cl was removed by filtration through a fine glass frit, rinsing the solid with two ~30 ml portions of benzene. The excess NH_3 and solvents were driven off under vacuum with the gradual application of heat. The product was refluxed at $\sim 170^\circ\text{C}/0.35\text{mm Hg}$, but was not purified by distillation. The mixture was then cooled and returned to atmospheric pressure. About 60 ml of dry isopropanol was then added and the flask was slowly reheated until the solid melted. As the product was slowly cooled, it formed a wet slurry which could be easily removed from the flask. Although this slurry/paste was used directly in some initial experiments, for subsequent preparations it was transferred to other containers and dried under vacuum to give a white solid. The entire synthesis was performed under vacuum or argon atmosphere to avoid moisture, and the product was stored under argon. The hafnium isopropoxide produced in the manner described still contains isopropanol. Complete removal of the isopropanol requires drying at $120\text{--}130^\circ\text{C}$ under vacuum of 0.5mm Hg [8]. Since the material used in the current study was not dried under these conditions, it should more correctly be referred to as hafnium isopropoxide isopropanolate to reflect the residual isopropanol content.

Titanium isopropoxide, NH_3 , and HfCl_4 were used as purchased from Aldrich Chemical Company with no further purification. The NH_3 was anhydrous, 99.99% pure, and packaged in a lecture bottle. Zirconium *n*-propoxide was purchased from Alpha Products of Morton Thiokol, with no further purification. However, the zirconium compound had an amber color which was possibly due to an impurity, as further evidenced by the observation of a fluorescent baseline in its Raman spectrum. Isopropanol was refluxed over freshly prepared CaO , distilled, refluxed with magnesium filings, and redistilled just prior to its use. Benzene was refluxed over Na metal until the benzoquinone indicator appeared grayish blue, then distilled as needed. Glacial acetic acid was purchased from Fisher Scientific and used without further purification. Kimax brand microscope slides and commercial grade fused silica windows ($1/8''\text{T} \times 3/4''\text{D}$) were used as substrates for films and were pretreated by rinsing with acetone. De-ionized water with a resistance of 18 Mohm was used throughout.

INSTRUMENTATION

The light scattering experiments were performed on a Coulter sub-micron particle size analyzer, model N4MD. Polystyrene and acrylic cuvetts were used to hold the samples. Raman spectra were collected on a Spex 1877 triple spectrometer using an OMA detector. The Raman spectra were recorded using the 514.5 nm line from an argon laser. The IR transmission spectra were taken on a Perkin-Elmer model 1750 FTIR. The samples were held in a short-path liquid cell holder with NaCl windows.

PROCESSING

(a) Sols and Gels

Gels made from titanium isopropoxide, acetic acid, and water were compared with the zirconium *n*-propoxide and hafnium isopropoxide analogues. In each case, the alkoxide was first mixed with the acetic acid, producing a strongly exothermic reaction which resulted in a colorless, transparent liquid. These mixtures were usually used immediately in the next step of the sol preparation; however, if allowed to age, they all solidified. The hafnium mixture solidified most quickly (< 20 minutes), the zirconium complexes solidified next (~ 1 hour), and the titanium complexes were slowest to solidify (a few days). The solids formed emit a characteristic ester odor; the generation of an ester during the sol-gel processing of $\text{Ti}(\text{O}-\text{Bu})_4$ with acetic acid was also noted by Livage [3].

The next step of the process involves combining these complexes with water. If the complex is still in a liquid phase at the time of this addition, it may rapidly solidify, become a white paste, form translucent clumps, or remain a clear liquid -- depending on the type of complex and the molar ratios. As additional water is added, the solid can usually be redissolved. The liquid was passed through a 0.44 micron filter and stored in vials or in capped cuvetts. The basic steps in the sol-gel process are summarized in Fig. 1.

(b) Films

The films were made by spin-casting the solutions described in the previous section. The coating liquid was applied to the surface of the substrate, which was then spun to remove the excess, resulting in a relatively even film. Films were also made by dropwise addition of the liquid onto a spinning substrate, or by angling the surface of the substrate and allowing the excess-coating material to drip off.

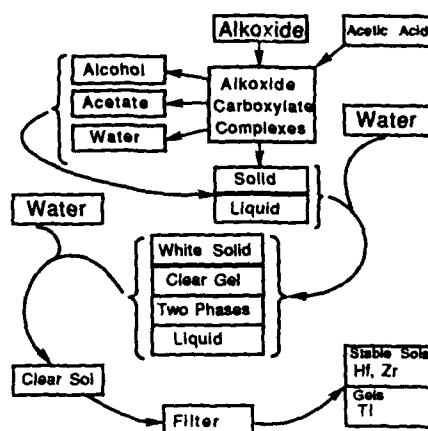


Figure 1. Schematic of Sol-Gel Process

RESULTS AND DISCUSSION

When sufficient acetic acid was mixed with titanium or hafnium isopropoxide, or zirconium *n*-propoxide, a water soluble product resulted. For titanium alkoxides, Livage has described this general complex as $Ti(OR)_x(Ac)_y$ [3]. In the case of zirconium, several carboxylate complexes have been made by reacting alkoxides with carboxylic acids [11]: $((RCO_2)_3Zr)_2O$, $Zr(O_2CR)(OPr^i)_3$, and $Zr(O_2CR)_2(OPr^i)_2$. These compounds are metal carboxylates, and the last two compounds listed are also metal alkoxide carboxylate complexes [11]. For simplicity, the complexes which result from mixing acetic acid with an alkoxide will be regarded as metal alkoxide acetates. TiPA, ZnPA, and HiPA will be used as acronyms for titanium isopropoxide acetates, zirconium *n*-propoxide acetates, and hafnium isopropoxide acetates, respectively.

The titanium-containing sols, produced from TiPA and water, gelled in times ranging from two days to more than a week. The sols derived from hafnium and zirconium never formed solid monoliths if a solid phase was created and then redissolved, providing the sols were made from only alkoxides, acetic acid, and water. Sols from these latter two alkoxides have remained stable for months showing little or no change in particle size as detected by light-scattering. Examples of sols of this type are given in Tables I-III. The acid/alkoxide and the water/alkoxide ratios will be designated r_a and r_w , respectively, throughout the discussion.

Titanium-containing sols with the r_a values of 5.20 and 10.4 evolved into transparent gels for r_w values of 46.3 and 66.1. The compositions of these four sols are summarized in Table I. The solutions with the smaller r_a values gelled several days sooner, and for a given r_a , the solution with the smaller r_w gelled more quickly. The particle growth was apparent from light scattering experiments.

Table II shows the samples studied for the zirconium-type sols. For the sample with an r_a of 1.00, the complex gelled immediately when exposed to a little water and never fully redissolved for a r_w of 51.9. The gel apparently softened and reset at the bottom of the vial. For sols with r_a values of 1.50 and 1.75, the solid complex eventually redissolved, except for some small translucent particles which were only apparent when the vials were gently shaken. The remaining samples, with r_a values ranging from 1.79 to 5.20, all formed entirely clear sols with no visible particles; except for the sol with an r_a of 1.79, none of these samples formed a

TABLE I. Dependence of Gelation Rates on Composition for Sols from TiPA^a

R _a ^b	R _w ^c	Gelation Time	Average Particle Size
5.2	46.3	~2 Days	~50 nm after the first hour.
5.2	66.1	~5 Days	~22 nm after the first hour.
10.4	46.3	more than 1 week	~12 nm after first hour ~38 nm after 68 hours.
10.4	66.1	longest	~12 nm after 68 hours ^d .

^aFormed solid phase with initial addition of water. ^bAcetic acid/alkoxide molar ratio. ^cWater/alkoxide molar ratio. ^dCounts/sec were initially too low to permit the particle size measurement.

TABLE II. Dependence of Sol Stability on Composition for ZnPA Derived Sols^a

R _a ^b	R _w ^c	Comments
1.00	51.9	No measurement ^{d,e}
1.50	51.9	No measurement ^{d,e}
1.75	51.9	No measurement ^{d,e}
1.79	20.8	Counts/sec: 1.3e4
1.82	13.9	Counts/sec: 2.8e4
1.88	13.9	Counts/sec: 2.2e4
2.00	17.3	Counts/sec: 1.75e4
3.00	13.9	Counts/sec: 1.00e4
5.20	16.5	Counts/sec: 5.5e3
5.20	46.3	No measurement ^f

^aWe have never observed gelation in Zr alkoxide/acetic acid sols of this type, except when it occurs immediately. ^bAcetic acid/alkoxide molar ratio. ^cWater/alkoxide molar ratio. ^dFormed solid phase upon exposure to water. ^eNever entirely redissolved. ^fCounts/sec. were too low to allow measurement.

TABLE III. Dependence of Sol Stability on Composition for HiPA Derived Sols^a

R _a ^b	R _w ^c	Comments
11.8	106	particle size: ~60 nm, stable with aging.
5.30	46.5	no size measurement: counts/sec were too low
3.76	108	particle size: ~300 nm, showed slight decrease with aging (~20nm/month)

^aFormed solid phase with initial addition of water. ^bAcetic acid/alkoxide molar ratio. ^cWater/alkoxide molar ratio.

significant solid phase which then entirely dissolved.

The hafnium sol-gel solutions behaved similarly to those from the zirconium system with the exception that a solid phase always formed during the initial moment of hydration. Significantly higher values of r_a and/or r_w were used for hafnium sols except for the sol with r_a and r_w values of 5.30 and 46.5, respectively. The behavior of both the hafnium and zirconium based sols contrasted sharply with that of the titanium-type sols, which gel over a wide range of compositions.

Hafnium-containing gel monoliths were prepared from hafnium isopropoxide, acetic acid, hydrochloric acid, and isopropanol. Initially, a solid phase was formed which subsequently redissolved. The resulting sols became clear gels within one to two weeks. These gels took on a bluish tint as they aged, presumably due to the greater scattering efficiency of blue light off the small particles.

The titanium-derived gels also took on a bluish tint as they aged and became cloudier than the hafnium gels. Aging of these gels at 70° C in sealed vials, over the period of several days, caused a further whitening of the gels and the formation of a colorless liquid phase surrounding the gels. When shaken, the solid structure was easily destroyed, forming a white emulsion. This emulsion thickened over time, but never set so firmly that vigorous shaking could not produce dramatic shear-thinning behavior.

The sols created were also used in making films on glass and fused silica substrates. The two hafnium-containing solutions with the largest r_a values (11.8 and 5.30, shown in Table III) worked well as a coating material immediately after their preparation, and the

characteristics of these solutions did not change appreciably over time. Many of the zirconium-containing mixtures were too viscous to produce an even coating, but the films showed good adhesion. The zirconium sol with r_a and r_w values of 5.20 and 46.3, respectively, provided good films when diluted to slightly lower the viscosity. The titanium-type sols produced very thin films when freshly prepared. However, these sols were in the initial stages of gelation, and the quality of the film was dependent on the age of the sample. The best titanium films from this system were aged for several hours and then diluted slightly with water before being applied. Samples aged for significantly longer periods produced flaky films with poor adhesion. These systems have not been carefully optimized for film coating; however, the hafnium and zirconium films appear to be easier to make, just as the titanium system appears to be better suited for the formation of gel monoliths over a wide range of compositions.

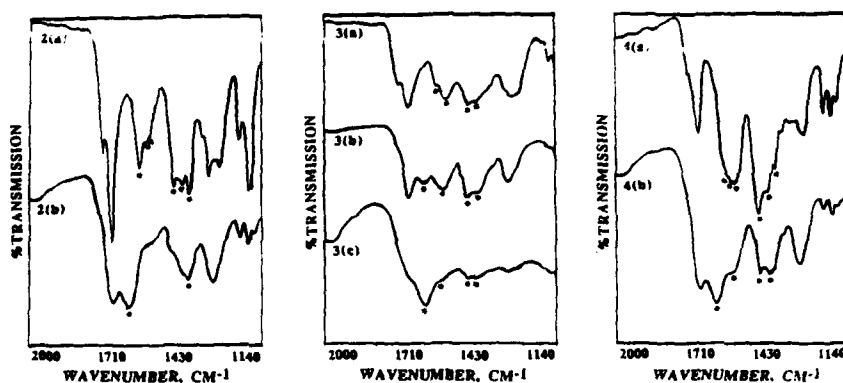
The ester formation which was observed may play an important role in the sol-gel process. If the solidification of the complexes formed from the alkoxide and the acetic acid requires water, it should be noted that water is generated at the same rate as the ester. Alcohols and carboxylic acids are known to react in the presence of mineral acids when heated. The reactivity of primary alcohols is greater than that of secondary alcohols, and the less bulky carboxylic acids are more reactive [12]:



A plausible mechanism for this acid catalyzed reaction has been proposed [12]; however, in the presence of the alkoxide, and in the absence of a mineral acid, this reaction does not necessarily have the same mechanism. If the water is consumed by reaction with the metal, it would drive the reaction forward by removing one of the products and generating one of the two reactants through displacement of either an acetate ion or an ester group from the metal. Water may be a necessary reactant in this solidification since a small amount of water causes immediate formation of a solid phase in many mixtures of titanium or hafnium isopropoxide and acetic acid. Although water may be necessary for solidification, the presence of too much water may actually prevent the formation of a solid phase. This can be seen with initially liquid ZnPT samples that solidify in less than an hour, but do not solidify, or even cloud, when water is added.

The acetic acid and alkoxide derived complexes for titanium, zirconium, and hafnium have been analyzed with infrared spectroscopy before and after the addition of water (Fig. 2-4). The acetate anion may form ionic associations with a metal, or it may bind as a monodentate, chelating or bridging ligand [11,13]. The difference between symmetric and asymmetric CO_2^- stretching vibrations, $[\nu_s(\text{CO}_2^-) - \nu_a(\text{CO}_2^-)] = \Delta$, occurs within a characteristic range for each type of acetate ligand [13]. This characteristic has been used by Livage to conclude that the complexes formed by mixing acetic acid and $\text{Ti}(\text{O-Bu}^n)_4$ are probably characterized by chelating and bridging acetate ligands [3]. After hydrolysis, the samples in Livage's study showed a decrease in Δ , indicating a decrease in the number of bridging acetate ligands [3]. In our study, the titanium complexes, prior to hydration, showed a strong asymmetric stretch at 1599 cm^{-1} , with weak shoulders at 1566 cm^{-1} and 1552 cm^{-1} as shown in Fig. 2a. The symmetric stretch gave a broad band with three peaks at 1447 , 1413 , and 1379 cm^{-1} . The Δ 's thus occurred at 220 , 153 , and 105 cm^{-1} , indicating that all three types of acetate ligand bonding were probably present, and that the number of monodentate ligands was probably greater than for the conditions studied by Livage [3]. After hydration, strong bands in Fig. 2b appeared at 1646 and 1388 cm^{-1} indicating that Δ has increased to 258 cm^{-1} . This showed that the addition of water further increased the relative number of monodentate ligands, probably by breaking some bridging acetate bonds.

The non-hydrated complexes, of zirconium and hafnium, both demonstrated predominantly bidentate character in their IR spectra shown in the lower sections of Figures 3a and 4a. The peak assignments are given in Table IV. For the hafnium complex, Δ 's were found at 100 , 150 , and 207 cm^{-1} , and for the zirconium, Δ 's were found at 96 and 178 cm^{-1} . In the case of zirconium, two different hydrated samples have been examined which yield very different results. A sample with an r_a of 4 was mixed with water in a 1:1 volumetric ratio, yielding Δ 's of 109 and 227 cm^{-1} , where the first Δ has been calculated from the more dominant peaks (Fig. 3b). This indicates that both monodentate and bidentate ligands are probably present, with the bidentate ligands predominating. The IR spectrum of the second sample ($r_a = 2.00$ and $r_w = 17.3$) shows the monodentate ligand predominating with $\Delta = 225 \text{ cm}^{-1}$; the weaker peaks gave a



Figures 2-4. IR spectra of TiPA, ZnPA, and HiPA, before and after the addition of water. TiPA: 2(a) $r_a = 5.2$, $r_w = 0$; 2(b) $r_a = 5.2$, $r_w = 46.3$. ZnPA: 3(a) $r_a = 5.2$, $r_w = 0$; 3(b) $r_a = 5.2$, $r_w = 46.3$; 3(c) $r_a = 1.75$, $r_w = 51.94$. HiPA: 4(a) $r_a = 5.3$, $r_w = 0$; 4(b) $r_a = 5.3$, $r_w = 46.5$. The "*" indicates bands that are given in Table IV and used in Δ calculations.

Δ value calculated at 110 cm^{-1} (Fig. 3c). The symmetric stretch is very weak in this spectrum. The water-treated hafnium sample ($r_a = 5.30$ and a $r_w = 46.5$) showed a dominant $\Delta = 233\text{ cm}^{-1}$, with weaker bands giving $\Delta = 129\text{ cm}^{-1}$ (Fig. 4b). In comparing these systems we see that acetate ligands of all possible types are probably present, in various relative amounts, in most of these samples. One should bear in mind that if this analysis is being applied to sols under highly acidic conditions, or with a high ion concentration, the non-bonded acetate ion would probably have a Δ similar to that of the bridging acetate [13]. Even in a system as complex as this, with three ligand types and free acetic acid present in a single sample, it is relatively easy to study the effect of the composition on the relative predominance of a given acetate ligand. From the zirconium study, it appears that increasing the amount of water, or decreasing the amount of acid, lowers the concentration of bidentate ligands. Neither r_a nor r_w are the same between the two samples which correspond to the spectra in Figures 3b and 3c. However, the relative difference between the r_a values is much greater than that for the r_w ; therefore, one could argue that the observed differences between the

TABLE IV. Absorbance Peaks for Calculation of Characteristic Frequency Separation for the Acetate Ligand

	ν_a asymmetric stretch ^a	ν_s symmetric stretch ^a	$\Delta = \nu_a(\text{CO}_2^-) - \nu_s(\text{CO}_2^-)$ characteristic frequency separation ^b
(TiPA)			
2(a)	1599 (s)	1379 (s)	220 (1)
	1566 (sh)	1413 (s)	153 (2)
	1552 (sh)	1447 (s)	105 (3)
2(b)	1646 (s)	1388 (s)	258 (1)
(ZnPA)			
3(a)	1594 (sh)	1358 (sh)	178 (2)
	1548 (m)	1452 (m)	96 (1)
3(b)	1643 (w)	1416 (sh)	227 (2)
	1561 (m)	1452 (m)	109 (1)
3(c)	1644 (s)	1419 (w)	225 (1)
	1562 (sh)	1452 (w)	110 (2)
(HiPA)			
4(a)	1587 (sh)	1380 (sh)	207 (3)
	1569 (sh)	1419 (sh)	150 (2)
	1556 (s)	1456 (s)	100 (1)
4(b)	1645 (s)	1412 (w)	233 (1)
	1584 (sh)	1455 (w)	129 (2)

^aThe intensity of the peak is indicated by the symbol in parentheses: s=strong, m=medium, w=weak, sh=shoulder. ^bThe relative dominance of the ligand-type corresponding to the Δ is shown by the number in parentheses: 1=most dominant, 3=least dominant.

spectra shown in Figures 3b and 3c are predominantly due to the difference in r_a , while the differences between 3a and 3b are predominantly due to the difference in r_w . Increasing r_w had the same effect on the hafnium and zirconium systems.

The Raman spectra for the titanium complex, before and after the addition of water, are compared with the various solvent bands in Fig. 5. The reaction with acetic acid liberates isopropanol and generates isopropyl acetate. Both of these organics have a strong band near 820 cm^{-1} and this band appears in the spectra of the non-hydrated mixture and the sols. The broad peak in the spectrum near 630 cm^{-1} , in Fig. 5c for the non-hydrated sample, probably receives contributions from the acetate $\delta(\text{O}-\text{C}=\text{O})$ and the $\nu(\text{M}-\text{O})$ of the alkoxide. When water is added, the intensity of this peak is severely reduced as is clearly shown by Fig. 5d, presumably because additional ester groups have been displaced from the titanium by water.

A comparison of the Raman spectra of sols prepared from hafnium and titanium (before it has gelled), neat isopropanol, and acetic acid are presented in Fig. 6. The similarity of the spectra for the two sols is striking (Fig. 6a and 6b), and emphasizes the chemical similarity between the two systems. The slight differences in relative band height for the three peaks between $800\text{--}1000\text{ cm}^{-1}$ may be due to the additional isopropanol in the hafnium system.

The Raman spectrum of the zirconium complex, before and after the addition of water, was compared with the spectrum of neat acetic acid (Fig. 7); the presence of water did not noticeably change the appearance of the spectrum for the zirconium complex, which is especially interesting because this sample did not form a solid when water was added. The generation of water which accompanies the ester generation may offer some explanation for this strange result: the generated water may have already reacted with the system to the extent that additional water caused no further observable changes. It would be interesting to examine the hafnium and acetic acid

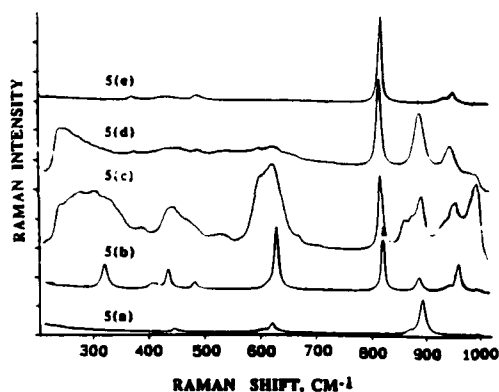


Figure 5. Raman spectra of TiPA, before and after the addition of water, are compared with spectra of some processing reagents and side products: (a) acetic acid; (b) isopropyl acetate; (c) TiPA, $r_a = 5.2$, $r_w = 0$; (d) TiPA, $r_a = 5.2$, $r_w = 46.3$; (e) isopropanol.

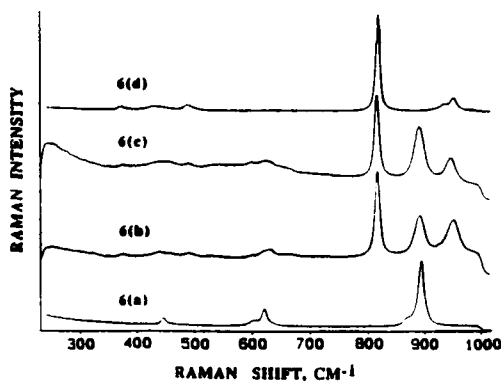


Figure 6. Raman spectra of TiPA and HiPA are compared with one another and with isopropyl alcohol and acetic acid: (a) acetic acid; (b) HiPA + water, ($r_a = 5.3$, $r_w = 46.5$); (c) TiPA + water, ($r_a = 5.2$, $r_w = 46.3$); (d) isopropanol.

complex, but the solidification occurred too rapidly. In the case of zirconium, the complex had begun to whiten and solidify soon after the spectrum was finished.

The Raman spectra of the gel monoliths of hafnium and titanium are shown in Fig. 8. These spectra are quite similar, just as the Raman spectra of the sols were similar. The peaks near 820 cm^{-1} indicate that isopropanol and probably isopropyl acetate are trapped in these gels. The metal alkoxide $\nu(\text{M}(\text{O}-\text{C}))$ band near 1029 cm^{-1} is weak in the titanium gel and not apparent in the hafnium gel, indicating that few metal ester groups remain.

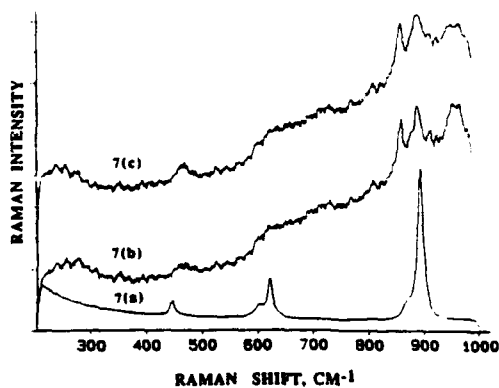
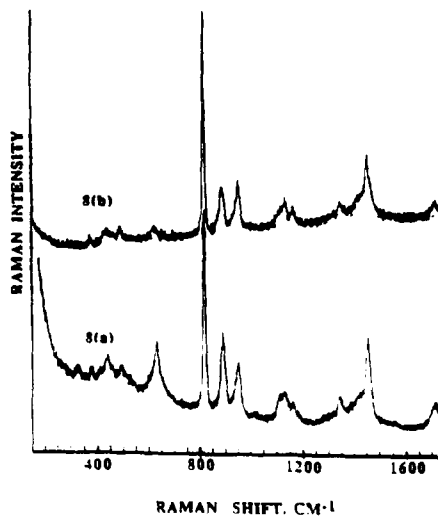


Figure 7. Raman spectra of ZnPA, before and after the addition of water, are compared with the spectrum of acetic acid: (a) acetic acid; (b) ZnPA, $r_a = 5.2$, $r_w = 0$; (c) ZnPA, $r_a = 5.2$, $r_w = 46.3$.

Figure 8. Comparison of Raman spectra for the titanium and hafnium gels derived from TiPA and HiPA, respectively: (a) titanium gel; (b) hafnium gel.



CONCLUSIONS

The sol-gel processing of hafnium isopropoxide can lead to translucent, monolithic gels (when dried) and transparent films. However, this hafnium alkoxide appears to be better suited for the making of films, which are quite sensitive to the exact composition of the sol. Sols made from ZnPA and HiPA by the resolution of an initially formed solid are quite stable over time, showing no tendency for significant particle growth.

Increasing r_w or reducing r_s appears to reduce the relative number of bidentate ligands. Increasing r_w decreases the gelation time for the titanium system which is contrary to the behavior observed for other similar systems [3].

The spectroscopic evidence for all three systems indicates that acetic acid is active in the coordination chemistry of the metal. Furthermore, the differences in the gel-forming versus film-forming characteristics are probably directly related to the role played by acetic acid. The extension of the current work to organic acids of longer chain and different ligand behavior should allow engineering of systems with widely varying attributes.

ACKNOWLEDGMENTS

The support for this work by the Composite Materials and Structures Center (CMSC) and the Center for Fundamental Materials Research (CFMR) at Michigan State University is gratefully acknowledged. All Raman spectra were taken at the Michigan State University LASER Laboratory. Thanks is likewise extended to Dr. R. B. Lessard and Dr. W. A. Oertling for their helpful discussions.

REFERENCES

1. M. Yoshiie, Jpn. Patent 53 236 335 (3 October 1988).
2. A. F. Stewart, D. R. Tallant, K. L. Higgins in Laser Induced Damage in Optical Materials: 1985, edited by H. E. Bennet, A. H. Guenther, D. Milam, B. E. Newnam (NBS U.S. Spec. Publ. 746.; 1985) pp. 362-365
3. J. Livage in Better Ceramics Through Chemistry II, edited by C. J. Brinker, D. E. Clark, D. R. Ulrich (Mater. Res. Soc. Proc. 73, Pittsburgh, PA 1986) pp. 717-724
4. B. E. Yoldas, J. Mat. Sci., 21 1080 (1986).
5. G. Tomandl, H. Rosch, A. Stiegelschmitt in Better Ceramics Through Chemistry III, edited by C. J. Brinker, D. E. Clark, D. R. Ulrich (Mater. Res. Soc. Proc. 121, Pittsburgh, PA 1988) pp. 665-670
6. R. A. Lipeles, D. J. Coleman, M. S. Leung in Better Ceramics Through Chemistry II, edited by C. J. Brinker, D. E. Clark, D. R. Ulrich (Mater. Res. Soc. Proc. 73, Pittsburgh, PA 1986) pp. 665-670
7. D. C. Bradley, R. C. Mehrotra, D. P. Gaur, Metal Alkoxides (Acad. Press, New York, 1978) pp. 19-20
8. D. C. Bradley, R. C. Mehrotra, W. Wardlaw, J. Chem. Soc., 1634 (1953)
9. S. K. Anad, J. J. Singh, R. K. Multani, and B. D. Jain, Israel J. Chem. 7 171 (1969).
10. R. C. Mehrotra, Inorg. Chim. Acta Rev. 1 99 (1967).
11. R. C. Mehrotra, and R. Bohra, Metal Carboxylates (Acad. Press, New York, 1983) pp. 233-240.
12. R. T. Morrison, and R. N. Boyd, Organic Chemistry 3rd ed. (Allyn and Bacon, Boston, 1981), pp. 602-603, pp. 680-682.
13. K. Nakamoto, Infrared and Raman Spectra of Inorganic and Coordination Compounds (John Wiley and Sons, New York, 1986) pp. 231-233.

SOL-GEL NETWORKS: FUNDAMENTAL INVESTIGATIONS OF THE CHEMISTRY OF
SOL-GEL SILICATE GLASSES AND POLY(SILOXANE) TOUGHENED SILICATES

M. SPINU AND J. E. McGRATH*

Chemistry Department, Science and Technology Center: High Performance
Polymeric Adhesives and Composites; Virginia Polytechnic Institute
and State University; Blacksburg, VA 24061

*To whom correspondence should be addressed.

ABSTRACT

The low-temperature sol-gel process opens a number of new materials possibilities for generation of glasses with predetermined properties by the incorporation of organic modifiers into the network. Polysiloxanes are potentially interesting organic modifiers for toughening and possibly surface-modifying the silicate networks. Some fundamental studies of the hydrolysis and condensation processes in a tetramethylorthosilicate (TMOS) system, in the absence of added catalyst, have been conducted using ^1H and ^{29}Si NMR. The effects of some of the reaction parameters and processing conditions for the subsequent conversion of the gel to monolithic dried gels by heat treatment have been investigated by techniques such as thermal analysis and mass spectroscopy. Procedures which employ mild pressures have been established that permit the generation of monolithic products which show greatly reduced cracking tendencies. Finally, methoxy functionalized poly(dimethylsiloxane) oligomers that can react into the sol-gel network have been prepared. The intermediates are commercially accessible and the process is scaleable. Utilization of a catalyst-free system eliminates the tendency of the siloxane modifier to undergo undesired rearrangements that are known to occur in the presence of strong acids or bases.

INTRODUCTION

"Sol-gel" technology refers to a relatively low-temperature technique for the preparation of single-component or multicomponent oxide glasses. During this process, hydrolyses and subsequent condensation of organic or inorganic alkoxides leads to the formation of a three-dimensional glass network. Hydrolytic polycondensation reactions of tetraalkoxysilanes generate an oxide network similar to that of quartz, thus suggesting a possible way to form glass and ceramic materials by chemical polymerization [1]. Chemical reactions open new possibilities for the incorporation of organic modifiers into the network and therefore generation of glasses with predetermined properties [14-17]. Polysiloxanes are potentially interesting modifiers which are capable of microphase separation and which could provide some toughening of the otherwise brittle glasses.

The most commonly used silicon alkoxide that has been studied is tetraethylorthosilicate (TEOS). Some aspects of the hydrolysis and condensation polymerization reactions of TEOS have been investigated in our own laboratories [2]. However, the strong acids typically utilized to hydrolyze TEOS would probably also cause undesirable degradation of the polysiloxane chains used as network modifiers. Thus, a relatively neutral reaction environment is required for the polysiloxanes to fully exhibit their potential bulk and surface modifying capability. Literature data suggest that tetramethylorthosilicate (TMOS) could hydrolyze in the absence of added catalyst [3,4]. For example, it has been shown that the rate of hydrolysis in the alkoxysilane series decreases [3] and the gelation time increases [4] with increasing size of the alkoxyl group. It is also known that TMOS is environmentally more difficult to work with and, hence, well-ventilated hoods and good safety practices are required.

While hydrolysis and condensation reactions of silicon alkoxides in the presence of both acid and base catalysts have been extensively investigated [17-20], there is only limited information on the reaction of a catalyst-

free system [8,21]. The present paper describes the effects of the reaction conditions on the hydrolysis and condensation rate in a TMOS system, in the absence of added catalyst, using both ^1H and ^{29}Si NMR. The effect of the processing parameters on the subsequent conversion of the gel to monolithic dried gels by heat treatment was also investigated. Among other variations in processing, the utilization of mild pressures during drying of the gels seems to play a critical role in producing crack-free specimens. Finally, the synthesis of a functionalized polysiloxane oligomer modifier, capable of reacting into the sol-gel network, is described and demonstrated.

EXPERIMENTAL

Materials

Chemical grade (99%) tetramethylorthosilicate (TMOS) from Petrarch, and HPLC grade water and solvents (methanol and tetrahydrofuran) from Aldrich, were used without further purification. Octamethylcyclotetrasiloxane (D_4) was purchased from Union Carbide and distilled from calcium hydride before use. Methyltrimethoxysilane and 1,3-divinyltetramethyldisiloxane from Petrarch were used as received. Hydrogen hexachloroplatinate (IV) hydrate catalyst was obtained from Aldrich and stored under inert atmosphere.

Sol-gel reactions

The general scheme for the preparation of silicate networks via sol-gel processes is outlined in Figure 1. The sol-gel reactions (up to the gelation) were carried out at room temperature (RT), under stirring. A one-necked flask was charged with the reactants in the order TMOS, CH_3OH , and H_2O at the desired molar ratios (deuterated methanol was used for the NMR studies). The flask was then closed using a fitted stopper and allowed

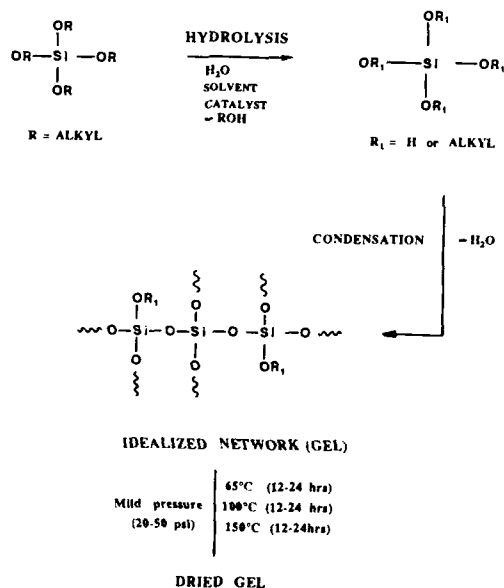


Figure 1. Generalized Reaction Scheme for the Preparation of Silicate Networks via Sol-Gel Processes

to stir at room temperature. At desired time intervals, NMR samples were removed as a function of reaction time. Most of the compositions investigated generated homogeneous reaction mixtures. For a few compositions, however, the initial reaction mixtures were heterogeneous, but they became homogeneous as the water coreactant was consumed and more methanol was generated in hydrolysis reactions. Prior to gelation, the reaction mixture was poured into glass vials, which were equipped with tightly fitting caps, and was allowed to gel at room temperature ($\sim 20^\circ\text{C}$). Further drying of the gels was carried out under controlled conditions to generate (for most cases) monolithic dried gels. In the present study, the drying of the gels was carried out in sealed glass vials or in a pressure reactor using a maximum pressure of 50 psig. A stepwise temperature profile (of 65°C , 100°C and 150°C) was used (see Figure 1), the heating rate between the steps being ca 0.5°deg./min . In some cases, higher reaction temperatures (up to 500°C) were investigated, as discussed later.

Polysiloxane synthesis

Synthesis of methoxy functionalized polydimethylsiloxane oligomers was achieved in a two-step reaction. In the first reaction step, a vinyl terminated poly(dimethylsiloxane) oligomer was synthesized by a base-catalyzed redistribution reaction of the cyclic siloxane tetramer (D_4) and 1,3-divinyltetramethyldisiloxane as the chain transfer agent or end capper, as shown in Figure 2. The number average molecular weights (M_n) were controlled by the appropriate ratio of the end-blocker to the cyclic tetramer (D_4). A transient silanolate catalyst was used and the reaction was carried out in bulk, at 80°C . The silanolate catalyst synthesis and the typical conditions for siloxane equilibration reactions have been extensively studied in our laboratory and are described elsewhere [5-7]. In the second step, Figure 3, the terminal vinyl groups were converted to methoxy end groups using methyldimethoxysilane as the hydrosilylation agent. The reaction was carried out in bulk, at 40 - 50°C , using H_2PtCl_6 as the hydrosilylation catalyst (ca. 5×10^{-5} moles catalyst/mole vinyl group). The resulting product is then capable of co-reacting efficiently with TMOS in the hydrolysis/condensation sol-gel process.

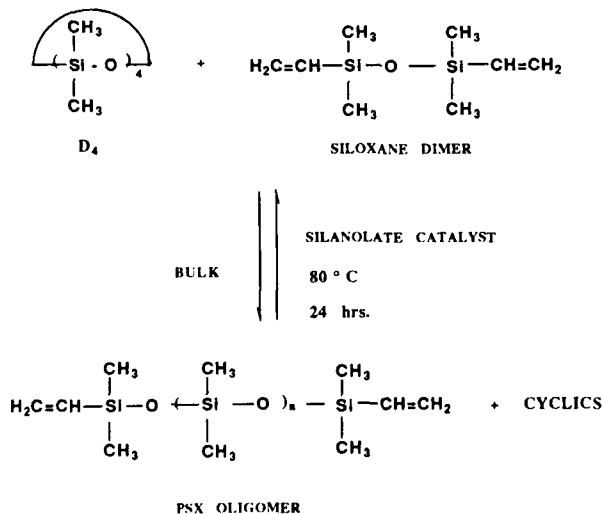


Figure 2. General Scheme for the Synthesis of Poly(Dimethylsiloxane) Oligomers with Vinyl Functional Groups

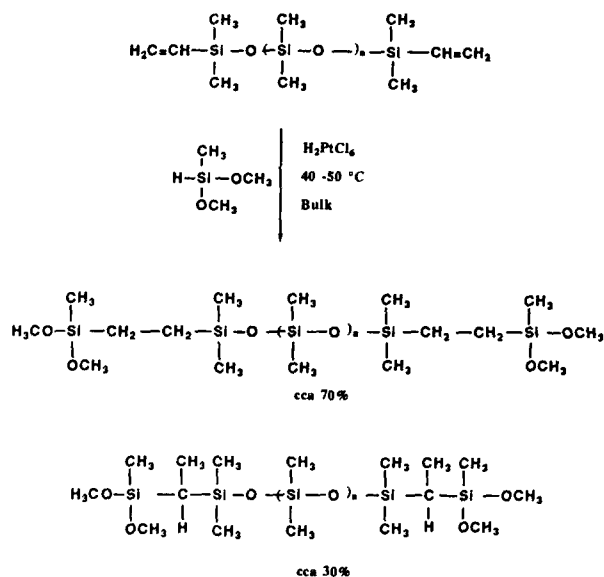


Figure 3. General Scheme for the Synthesis of Poly(Dimethylsiloxane) Oligomers with Methoxy Functional Groups

Analytical techniques

Spectral analysis: ^1H NMR data were acquired at RT on a Bruker WP 270 spectrometer operating at 270 MHz. CD_3OD , used as the reaction solvent, provided the deuterium lock signal and all resonances were referred to

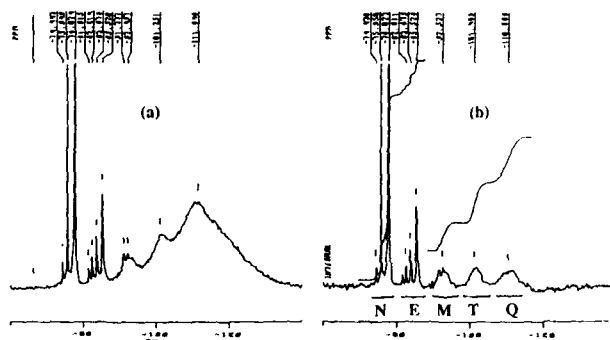


Fig. 4. ^{29}Si NMR spectrum of a TMOS reaction, before (a) and after (b) subtraction of the glass peak. Assignments are shown according to ref. [8].

N = Monomer starting material and hydrolyzed silicate
 E = Monosubstituted (end group)
 M = Disubstituted (middle group)
 T = Trisubstituted (branched)
 Q = Tetrasubstituted (network point)

Figure 4. ^{29}Si NMR Spectrum of a TMOS Reaction, before (a) and after (b) subtraction of the glass peak. Assignments are shown according to ref. 8.

tetramethylsilane (TMS). ^{29}Si NMR spectra were acquired at RT on a Bruker WP 200 spectrometer operating at 39.759 MHz. The spectra were obtained with inverse-gated decoupling; the decoupler was on during acquisition and off during the delay, to suppress any negative nuclear Overhauser effect (NOE). Chromium acetylacetonate $[\text{Cr}(\text{acac})_3]$ was added at $\sim 0.4\text{M}$ concentration to reduce the ^{29}Si spin lattice relaxation times. A pulse repetition rate of 6s was used and line broadening of 2.0 Hz was applied. Again, the deuterium lock of the instrument was provided by CD_3OD , the reaction solvent. For each ^{29}Si NMR sample, 600 scans were accumulated in order to obtain a high signal/noise ratio. The reported times of the spectra are the midpoints of data acquisition. In order to eliminate the interference of the ceramic and quartz components (from the probe and NMR tube), a subtraction technique was used. An example of a ^{29}Si NMR spectra before and after subtraction is shown in Figure 4 along with the assignments of each resonance frequency according to previous literature data [8]. ^{13}C CP/MAS NMR spectra were acquired at room temperature on a Bruker spectrometer operating at 22.53 MHz, with a ChemMagetics double-bearing CP/MAS probe. Samples were spun at the magic angle at $\sim 2.2\text{ kHz}$.

Thermal analysis: Thermogravimetric analyses of the dried gels were obtained using a Perkin-Elmer thermogravimetric analyzer (model TGS-2). The volatile products were conveyed to a mass selective detector (Hewlett-Packard 5970 series MSD) via a two meter long, 10 μm ID, deactivated capillary column. This capillary also serves to restrict the flow between the TGA experiment performed at ambient pressure (in a self-generated atmosphere, with no sample purge) and the MS experiment performed in vacuum ($\sim 2 \times 10^{-5}$ torr). The sample was heated from 30°C to 800°C at a heating rate of 20 deg./min. To determine whether any component of interest was actually released, selected ion chromatograms were obtained at the mass-to-charge ratio for the base peak of each component (ex: $m/e=18$, water; $m/e=31$, methanol).

RESULTS AND DISCUSSION

Effect of reaction parameters on the sol-gel reaction rate

Effects of silicon alkoxide content: Four different TMOS concentrations were investigated, corresponding to the $\text{CH}_3\text{OH}/\text{TMOS}$ molar ratios of 1.4, 1.8, 3.0, and 5.0. The rate of hydrolysis reactions was followed by ^1H NMR. An increase in the alcohol content (decrease in the concentration of silicon alkoxide) resulted in a reduction of the overall reaction rate and longer gelation times. Figure 5 summarizes the results for such an experimental series.

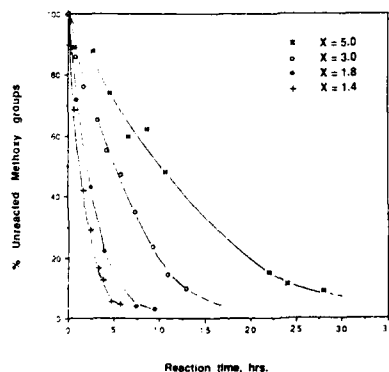


Figure 5. Concentration Effect on the Reaction Rate in a TMOS System
(TMOS : H_2O : CH_3OH = 1.0 : 4.0 : X)

Effects of $H_2O/Si(OCH_3)_4$ ratio: The present work describes the investigation on the hydrolysis/condensation reactions for TMOS solutions having water content of 2.5 and 4.0 $[(H_2O)/(TMOS)]$. The rate of hydrolysis was followed by 1H NMR and the results are summarized in Figures 6a and 6b. In the absence of any added catalyst, it was observed that the rate of hydrolysis was increased with increasing water content from 2.5 to 4.0 and the gelation time was reduced accordingly.

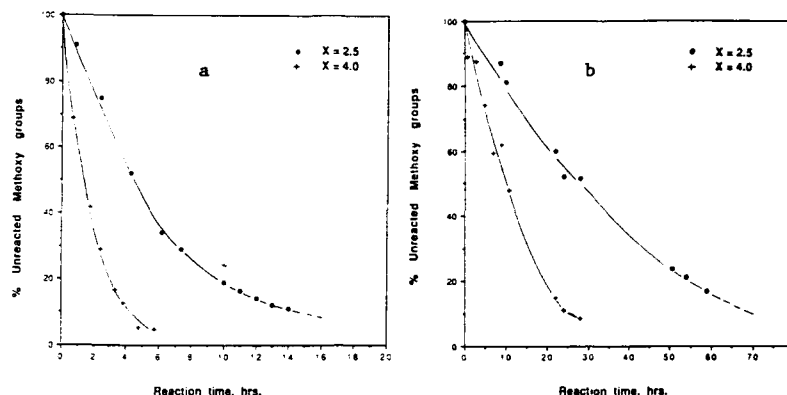


Figure 6. Effect of the Water Level on the Reaction Rate in a TMOS System
a. (TMOS:CH₃OH:H₂O=1.0:1.4:X) b. (TMOS:CH₃OH:H₂O=1.0:5.0:X)

Preliminary results on the drying of the gels indicated that monolithic dried gels were produced with much higher frequency from the reaction compositions containing 4.0 moles of water than from the corresponding reactions in which only 2.5 moles of water were used. It was therefore of interest to determine whether higher water contents resulted in a change in

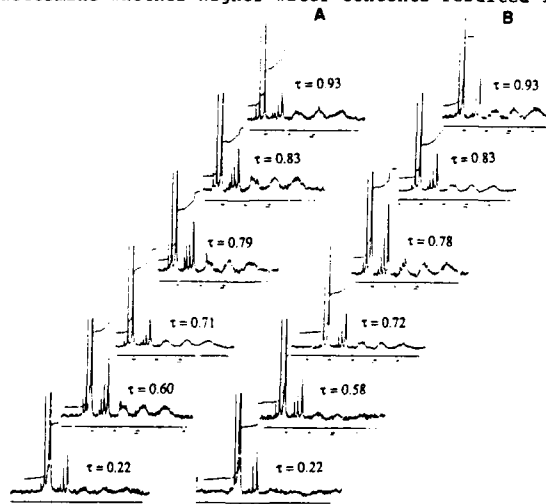


Fig. 7. ^{29}Si NMR Spectra as a Function of Reaction Time for Sol-Gel Reactions: (A) TMOS : H₂O : CH₃OH = 1.0 : 4.0 : 1.4; t_g = 7.5 hrs
(B) TMOS : H₂O : CH₃OH = 1.0 : 2.5 : 1.4; t_g = 19 hrs

the polymerization mechanism. The evolution of the reaction species as a function of reaction time was followed by ^{29}Si NMR, and the results for the two compositions investigated are shown in Figure 7. A reduced time scale was used for the normalization of the data for the two reactions [8]. Here τ represents the ratio between the time of scanning (t) and the gelation time (t_g). The sample was considered to have gelled when the solution would no longer flow.

The first observation is that the time evolution of the reaction species is similar under the two reaction conditions investigated, suggesting no mechanistic difference. However, even though this is not obvious from the figure, the integration indicated that the reaction containing 4.0 moles of water (7A) reached higher conversions when the gelation was approached ($\tau = 0.93$) than the reaction containing 2.5 moles of water (7B). Higher conversions resulted in higher contents of polymeric species and correspondingly lower levels of starting materials. This is also in agreement with higher hydrolysis rate of the reaction containing 4.0 moles of water, according to the ^1H NMR data.

A second observation was that hydrolysis and condensation are concurrent reactions, occurring simultaneously in both systems investigated. The presence of condensation species at low reaction conversions ($\tau = 0.22$) indicated that condensation reactions began long before hydrolysis was completed. On the other hand, the presence of unreacted starting materials at long reaction time ($\tau = 0.93$) indicated that the hydrolysis was not completed when the gelation occurred.

Effect of processing parameters on the dried gels

The most promising route to obtain glasses from gels through the sol-gel method is to first prepare monolithic dried gels. However, due to the expected very high compression forces inside the pores during the drying of the gels (when a liquid-gas curved interface is formed within the pores), the material most often loses its integrity [10].

According to the theory of drying gels introduced by Scherer [11], the stress developed in a plate during drying is dependent upon the evaporation rate of the solvent and the mechanical properties of the gel. When drying is slow, the stress is independent of the mechanical properties of the gel [11]. This is probably the reason for some success in generating monolithic gels by very slow drying at room temperature [12]. However, when the relaxation time of the materials becomes much greater than the drying time, the stress developed will also depend on the mechanical properties of the gel; therefore, the stronger the network becomes, one expects it will better withstand the stresses developed during drying.

With this understanding of the factors involved during drying of the gels, we believed that the use of relatively high temperatures and mild pressures during the drying process would allow us to approach the following conditions: (a) low evaporation rates due to low vapor pressure of the solvent at high external pressures; (b) decreased compressive forces in the capillaries of the gels, as a result of decreased solvent surface tension at higher temperatures; (c) increased overall conversion of the reaction with increasing temperature, resulting in a stronger network, which is capable of withstanding the stresses during drying. Following these procedures, monolithic dried gels could be obtained in most of the experiments that were conducted.

Thermogravimetric analysis was used for the characterization of the dried gels. As previously documented in the literature [13], the weight loss below 150–200°C is due to desorption of physically adsorbed water and alcohol. The weight loss that occurs above 200°C can be attributed, at least partially, to the removal of by-products of the step-growth or polycondensation reactions that can take place in the incompletely reacted network. If, as seems reasonable, the weight loss above 200°C is related to the extent of conversion, it follows that both the reaction composition

and the drying parameters will affect the extent of conversion of the network system as shown in Figure 8 and Figure 9, respectively.

Using TGA-MS, ion chromatograms for methanol and water (possible by-products of condensation reactions) have been constructed and typical chromatograms are shown in Figure 10 and Figure 11. Both ion chromatograms show two peaks, one below 200°C and corresponding to the adsorbed water and methanol, and the other above 200°C which can be attributed to further condensation reactions of the type:

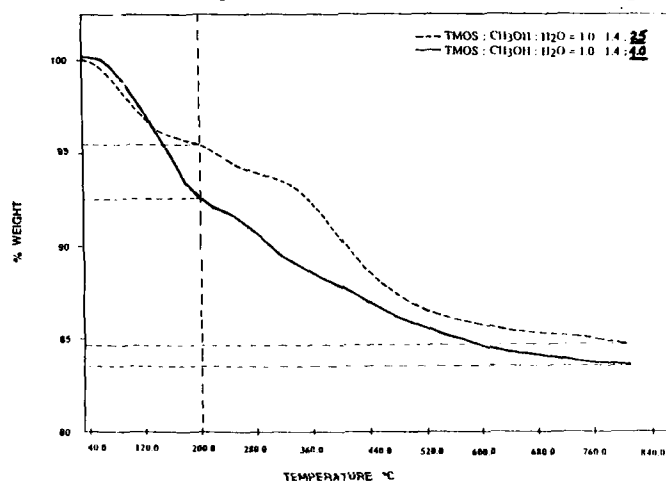
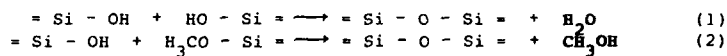


Figure 8. TGA - Effect of the Initial Reaction Composition on the Weight Loss in a SiO₂ System

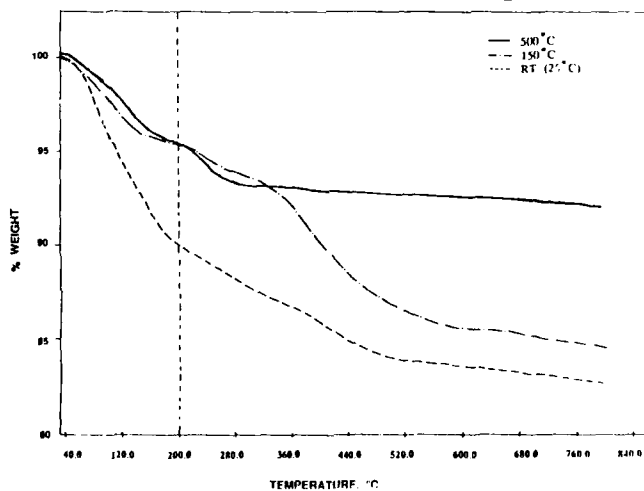


Figure 9. TGA - Effect of the Post-Gelation Treatment on the Weight Loss in a SiO₂ System

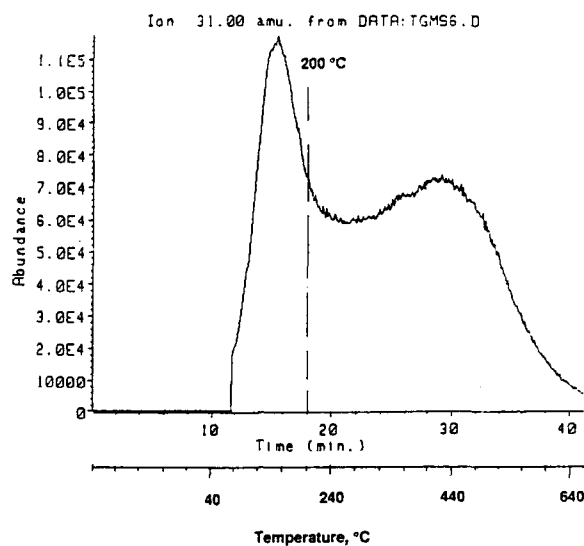


Figure 10. TGA - MS for a Dried SiO_2 Gel (max. drying temp: 150°C). Ion Chromatogram for CH_3OH Evolution During Heating (Heating Rate: $20.00^\circ\text{C}/\text{min}$)

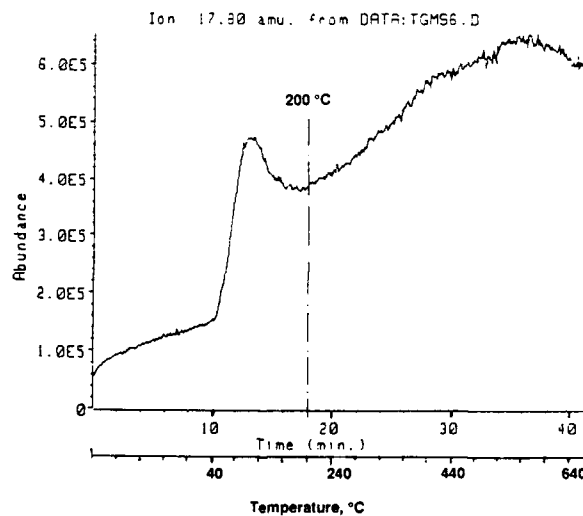


Figure 11. TGA - MS for a Dried SiO_2 Gel (max. drying temp: 150°C). Ion Chromatogram for H_2O Evolution During Heating (Heating Rate: $20.00^\circ\text{C}/\text{min}$)

Polysiloxane modifiers

Three different molecular weight methoxy functionalized poly(dimethylsiloxane) oligomers were synthesized, as indicated below:

Table I
Theoretical vs Experimental Molecular Weights for Polysiloxane Oligomers

No.	Number Average Molecular Weight $\langle M_n \rangle$, [g/mole]	
	Theoretical	From GPC*
1	1,000	1,400
2	2,000	3,700
3	5,000	8,000

* According to poly(dimethylsiloxane) standards prepared in our laboratory

The functionalized polysiloxanes can react into the sol-gel network, and some preliminary experiments did indicate that it is possible to incorporate up to 10-20 weight percent of the siloxane oligomer without significant loss of transparency. Our present investigations involve the study of the effect of the molecular weight and molecular design of the polysiloxane modifiers on the properties of the gels and the development of the reaction conditions for their incorporation into the silica glass.

CONCLUSIONS

The current study has shown that TMOS can be efficiently hydrolyzed and subsequently condensed in the absence of added catalyst to produce monolithic dried gels, under controlled reaction and processing conditions. Using ^{29}Si NMR and subtraction techniques to eliminate the quartz interference with the ceramic resonances, the evolution of species during the sol-gel process could be closely monitored up to the gelation point. New information on the type of condensation reactions that occur at higher processing temperatures was obtained using TGA-MS techniques and solid state NMR. Controlled molecular-weight methoxy-functionalized poly(dimethylsiloxane) oligomers that can be reacted into the sol-gel network were synthesized. Further studies of the incorporation of poly(siloxane) modifiers into the sol-gel glasses and their effect on solid state bulk and surface behavior is currently being investigated.

ACKNOWLEDGEMENTS:

The authors would like to thank the Air Force Office of Scientific Research for support of this research under AFOSR-86-0133.

REFERENCES

1. B. E. Yoldas, J. Mat. Sci., **12**, 1203, (1977); **14**, 1843 (1979).
2. J. E. McGrath, J. P. Pullockaren, J. S. Riffle, S. Kilic, and C. S. Elsbernd, Ultrastructure Processing of Advanced Ceramics, edited by J. D. Mackenzie and D. R. Ulrich (John Wiley & Sons, New York, 1988) p 55.
3. R. Aelion, A. Loebel, and E. Erich, J. Am. Chem. Soc., **72**, 5705 (1950).
4. K. C. Chen, T. Tsuchiya, and J. D. Mackenzie, J. Non-Cryst. Solids, **81**, 227, (1986).
5. J. E. McGrath, P. M. Sormani, C. S. Elsbernd, and S. Kilic, Makromol. Chem., Makrom. Symp., **6**, 67, (1986).
6. C. S. Elsbernd, P. M. Sormani, S. Kilic, and J. E. McGrath, Polymer Preprints, **27(2)**, 152 (1986); I. Yilgor and J. E. McGrath, Adv. in Polymer Sci., **86**, 1 (1988).
7. C. S. Elsbernd, M. Spinu, S. Kilic, and J. E. McGrath, Polymer Preprints, **29(1)**, 355, (1986).
8. L. W. Kelts, N. J. Effinger, and S. M. Melpolder, J. Non-Cryst. Solids, **83**, 353, (1986).
9. I. Artaki, S. Sinha, A. D. Irwin, and J. Jonas, J. Non-Cryst. Solids, **72**, 391, (1985).

10. M. Prassas, J. Phalippou, J. Zarzycki, J. Mater. Sci., 19, 1656, (1984).
11. G. W. Scherer, J. Non-Cryst. Solids, 89, 217, (1987).
12. M. Yamane, S. Aso, and T. Sakaino, J. Mater. Sci., 13, 865, (1978).
13. J. Zarzycki, J. Non-Cryst. Solids, 48, 105, (1982).
14. H. Huang, B. Orlor, and G. L. Wilkes, Polym. Bull. 14, 557 (1985).
15. H. Huang and G. L. Wilkes, Polym. Bull., 18, 45, (1987).
16. H. Huang, B. Orlor, and G. L. Wilkes, Macromolecules, 20, 1322 (1987).
17. C. J. Brinker, K. D. Keefer, D. W. Schaefer, and C. S. Ashley, J. Non-Cryst. Solids, 48, 47 (1982).
18. C. J. Brinker, K. D. Keefer, D. W. Schaefer, R. A. Assink, B. D. Kay, and C. S. Ashley, J. Non-Cryst. Solids, 63, 45 (1984).
19. R. A. Assink and B. D. Kay, Mat. Res. Soc. Symp. Proc. 32, 301 (1984).
20. A. H. Boonstra and C. A. M. Mulder, J. Non-Cryst. Solids 105, 201 (1988).
21. T. W. Zerda and G. Hoang, J. Non-Cryst. Solids, 109, 9 (1989).

CERAMIC FIBER - FLUOROPOLYMER COMPOSITES FOR ELECTRONIC PACKAGING MATERIALS

JOHN D. BOLT

E. I. du Pont de Nemours & Co., Experimental Station,
Wilmington, DE 19880-0262

ABSTRACT

Aluminum nitride (AlN), alumina and aramid fibers have been incorporated into epoxy and fluoropolymer matrices. The fluoropolymer composites have dielectric constants less than 3.4 and losses below 0.3%, measured out-of-plane. In-plane and out-of-plane thermal conductivities of the AlN-fluoropolymer composites averaged 5.2 and 1.3 W/mK, respectively, at fiber volume fractions of 0.26 to 0.29. In-plane thermal conductivities of woven fabric composites were accurately predicted by mixing rules; for non-woven and short fiber composites, thermal conductivities were less than predicted. These composites had higher out-of-plane thermal conductivities due to out-of-plane components of the fiber orientations.

INTRODUCTION

Basic requirements for improved electronic packaging dielectric materials are lower dielectric constant and loss, higher thermal conductivities and lower thermal expansion mismatches. Existing materials generally fall into two classes: ceramics with high thermal conductivities and low thermal expansions but moderate or high dielectric constants; and, polymers with low dielectric constants but poor thermal conductivities. We reasoned that composites containing ceramic fibers in polymer matrices could be designed to combine the favorable properties of each phase. In a planar composite, ceramic fibers oriented in-plane will impart dimensional stability and high thermal conductivity in-plane. Thus, thermal stresses of components mounted on the composite surface will be minimized and thermal dissipation by convective cooling will be favorable. A low dielectric constant will be maintained in the out-of-plane direction where the polymer is the only continuous phase.

In previous work these concepts were confirmed by the properties of unidirectional and quasi-isotropic composites of alumina fibers in polyimide matrices [1]. Thermal modeling confirmed the role of in-plane thermal conductivity in convective cooling [2]. For further improvements, we anticipated use of AlN fibers in fluoropolymer matrices. Here we present our initial results from these composites. For comparative purposes, composites of woven, non-woven and short fibers in fluoropolymer and epoxy matrices were prepared.

EXPERIMENTAL

Fluoropolymer composites were prepared by alternating 4 to 6 layers of fiber fabrics between sheets of polymer film. These were consolidated by laminating under vacuum at 295°C and 250 psi. Alumina fibers were polycrystalline alpha phase, DuPont Fiber FP; AlN fibers were prepared as described previously [3].

E-glass reinforced epoxy was a commercial FR4 circuit board with copper cladding removed by persulfate etching. Composites of short fibers in epoxy were prepared by infiltrating alumina and AlN fiber mats (papers) with epoxy (Buehler® Epoxide), and compressing and curing in a mold.

Dielectric properties and thermal expansions were measured as previously described [1]. In-plane thermal diffusivity measurements were made using Angstrom's bar method [4] at the Applied Thermal Physics Laboratory (ATPL), Department of Physics, University of Delaware. Out-of-plane thermal diffusivity was determined by the electronic pulse method [5] at DuPont and ATPL. Thermal conductivity is the product of diffusivity, density and heat capacity. Heat capacities were calculated based on literature values of the fibers and polymers and were in good agreement with values measured at ATPL. All measurements are at room temperature unless specified.

RESULTS AND DISCUSSION

Table I summarizes the composite types prepared for this study. Composites containing woven fabrics of aramid (aramid-PFA), alumina (alumina-FEP) and glass fibers (glass-epoxy) were available for direct comparison. Because AlN fibers were not available as woven fabrics, two alternatives were used. Short AlN fiber mats were incorporated in epoxy (AlN-epoxy). For comparison, similar alumina fiber mats were incorporated into epoxy (alumina-epoxy). In addition, non-woven fabrics of AlN fibers were incorporated into the fluoropolymer matrix (AlN-FEP).

TABLE I

TEFLON®* FLUOROCARBON and EPOXY RESIN MATRIX COMPOSITES

<u>FIBER</u>	<u>FABRIC</u>	<u>MATRIX</u>	<u>DESIGNATION</u>
-	-	Teflon® FEP	FEP
Kevlar® 49 aramid	woven	Teflon® PFA	Aramid-PFA
Fiber FP, alumina	woven	Teflon® FEP	Alumina-FEP
E-Glass	woven	Epoxy	Glass-Epoxy (FR4)
Fiber FP, alumina	short fiber mat	Epoxy	Alumina-Epoxy
Aluminum Nitride	short fiber mat	Epoxy	AlN-Epoxy
Aluminum Nitride	non-woven mat	Teflon® FEP	AlN-FEP

* DuPont registered trademark

Table II compiles the composite in-plane and out-of-plane thermal conductivities. With fibers oriented in-plane the composite thermal conductivity, K_{xy} , can be predicted by:

$$K_{xy} \sim \frac{1}{2} \cdot K_f \cdot V_f \quad \text{for } K_f \gg K_m \quad (1)$$

where K_f and K_m are the fiber and matrix thermal conductivities and V_f is the fiber volume fraction. For woven fabric composites of aramid and alumina fibers, this prediction was found to be accurate. However, for the short fiber and non-woven composites, the measured in-plane thermal conductivities were less than the calculated values (Table II). In the alumina-epoxy composite, two factors may contribute to the lower-than-predicted thermal conductivity -- low fiber aspect ratios and out-of-plane orientations. It is evident that orientation plays a role because the out-of-plane thermal conductivity of this composite is greater than the woven fabric alumina-FEP composites despite a lower V_f .

TABLE II
Thermal and Dielectric Properties of Ceramic and Aramid Fiber Composites

Thermal Conductivity (W/mK)					Dielectric Properties ^b , 1MHz		TCE ^a 30-150°C (10 ⁻⁶ /°C)
Composite	Vf	Kxy ^a		Kz ^b	k'	loss	
		meas'd	calc'd	meas'd			
<u>woven</u>							
Alumina-FEP	.30	4.4	4.1	.54	3.35	.0014	8.1
Alumina-FEP	.31	3.5,4.3	4.2	.53	3.38	.0013	10.7
Aramid-PFA	.19	.66	.53 ^c	.23	2.40	.0017	13.2
Aramid-PFA	.24	.72	.62 ^c	.25	2.49	.0025	7.7
Glass-Epoxy	-	-	-	.30	4.63	.0217	14.0
<u>short fiber</u>							
Alumina-Epoxy	.26	2.4	3.5	.70	4.61	.0281	21.8
AlN-Epoxy	.19	3.4	7.6	.59	4.26	.0256	11.8
<u>non-woven</u>							
AlN-FEP	.26	4.9	10.4	1.4	3.21	.0029	20.8
AlN-FEP	.29	5.9	11.6	1.2	3.21	.0215	18.6
AlN-FEP	.26	4.8	10.4	1.2	2.98	.0334	20.0
<u>matrix</u>							
FEP film	0	-	-	.21	2.06	.0028	154.

a - in-plane; b - out-of-plane; c - calculation includes matrix contribution

In the AIN fiber composites, the in-plane thermal conductivities are only half that predicted by eqn. (1). For the non-woven AIN-FEP composites, long fiber lengths are preserved, Fig. 1a. Therefore, it seems likely that fiber thermal conductivities lower than expected were present in these samples. (For the calculations, K_f values were: alumina, 27; AIN, 80; and aramid 3.8 W/m K.) In addition, significant out-of-plane components to fiber orientation were observed, Fig. 1b. Again, this is evident in the out-of-plane thermal conductivities of these composites, 1.2 to 1.4 W/mK, which are 2.5X the values of the alumina-FEP woven fabric composites of comparable V_f .

Composite in-plane thermal expansion coefficients (TCEs) are given in Table II. Fiber reinforcement of the fluoropolymer reduces TCE from 150 to between 8 and 20 ppm/°C. Many factors influence TCE values: moduli, Poisson's ratios, and TCEs of the fiber and matrix; volume fraction, orientation and aspect ratios of the fibers; and fiber-matrix adhesion. The non-woven and short fiber composites have somewhat greater TCEs than the woven alumina fiber composites, attributed to both lower V_f and out-of-plane fiber orientations. However, the expansion curves were smoother, indicative of less thermal stress anisotropy inherent in woven fabric composites.

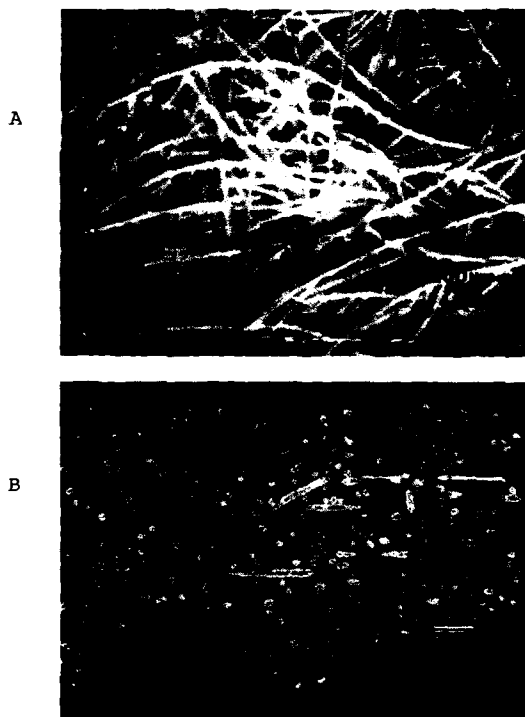


Fig. 1. Composite of non-woven AIN fibers in Teflon® FEP fluorocarbon matrix (AIN-FEP). a) Surface view shows random in-plane fiber orientation. b) Cross-section view reveals some out-of-plane fiber orientations.

Out-of-plane dielectric properties are given in Table II. All of the fluoropolymer matrix composites had dielectric constants below 3.4, decreasing with decreasing dielectric constant of the fibers and frequency independent from 10 KHz to 5 MHz. Loss factors for the fluoropolymer composites were quite low, below 0.3 % for the aramid fiber, alumina fiber, and one of three AlN fiber composites. However, the other AlN-FEP composites had loss factors as large as the epoxy composites. The frequency dependence (increasing loss at lower frequency) and void contents (6-10 % vs typical 2 %) suggest current leakage in these two AlN-FEP composites. The AlN- and alumina-epoxy composites have dielectric constants and losses comparable to glass-epoxy (FR4).

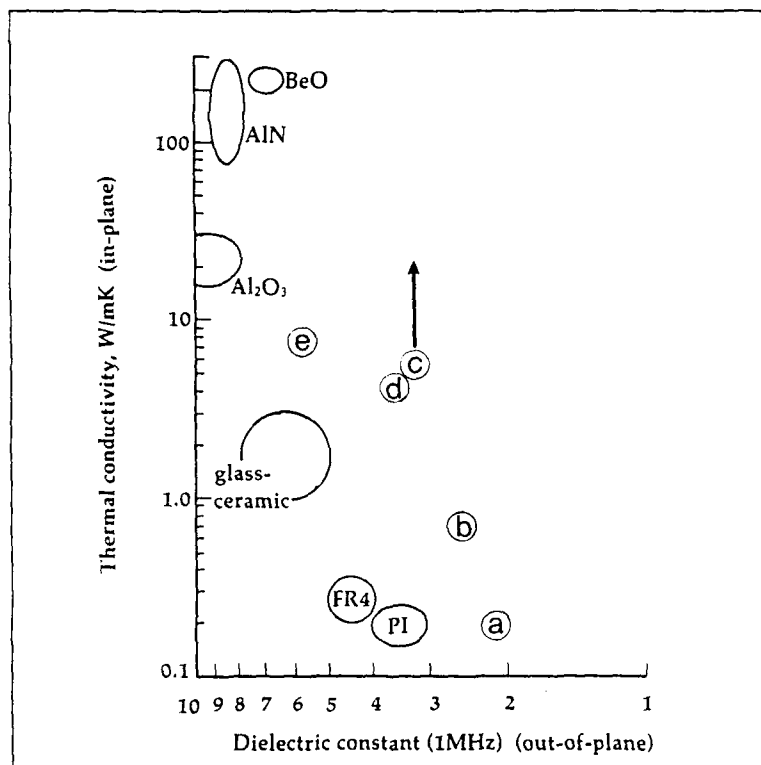


Fig. 2. Thermal conductivity vs. dielectric constant for electronic packaging materials, including conventional ceramics, polymer based materials, and new ceramic fiber composites: a) Fluoropolymer (FEP); b) Aramid-FEP, $V_f=22$; c) AlN-FEP, $V_f=27$, arrow shows increased composite thermal conductivity anticipated with improved fiber conductivity; d) Alumina-FEP, $V_f=30$; e) alumina-polyimide, $V_f=50$, ref. [1].

SUMMARY

Alumina and AlN fibers significantly enhance the thermal conductivity of polymer matrix composites. Figure 2 illustrates that these composites have a unique combination of properties relative to conventional electronic packaging materials. In particular, fluoropolymer-ceramic fiber composites combine low dielectric constant and low loss, high in-plane thermal conductivity and moderate in-plane thermal expansion. Fiber orientations in non-woven and short fiber mats impart increased out-of-plane thermal conductivity.

ACKNOWLEDGMENTS

Composites fabrication by M. F. Lemon and thermal conductivity measurements by H.-M. Zhang and D. G. Onn are gratefully acknowledged. M. Zussman provided the aramid composites.

REFERENCES

1. D. P. Button, B. A. Yost, R. H. French, W. Y. Hsu, J. D. Bolt, M. A. Subramanian, H.-M. Zhang, R. E. Giedd, A. J. Whittaker, D. G. Onn, in Advances in Ceramics Vol. 26 Ceramic Substrates and Packages, edited by H. M. O'Bryan, K. Niwa, W. Young, M. F. Yan, (American Ceramics Society, Columbus, OH 1989) in press.
2. R. H. Jensen, B. A. Bydal, D. P. Button, in Advances in Ceramics Vol. 26 Ceramic Substrates and Packages, edited by H. M. O'Bryan, K. Niwa, W. Young, M. F. Yan, (American Ceramics Society, Columbus, OH 1989) in press.
3. J. D. Bolt, F. N. Tebbe, in Electronic Packaging Materials Science III, edited by R. Jaccodine, K. A. Jackson, R. C. Sundahl (Mater. Res. Soc. Proc. 108, Pittsburgh, PA 1988), pp. 337-44.
4. M. A. J. Angstrom, Philosophy Magazine, 25, 130 (1863).
5. R. E. Giedd, D. G. Onn, in Thermal Conductivity 20 (Plenum Press, New York, 1989) edited by D. P.H. Hasselman, p. 339.

CERAMIC PROCESSING USING INORGANIC POLYMERS

JOHN J. LANNUTTI,* CHRISTOPHER H. SCHILLING**, AND ILHAN A. AKSAY*

*Department of Materials Science and Engineering, and
Advanced Materials Technology Program, Washington Technology Center
University of Washington, Seattle, WA 98195

**Pacific Northwest Laboratory, Richland, WA 99352

ABSTRACT

Inorganic polymers are used in the formation of green compacts via sedimentation of colloidal alumina suspended in chloroform. Polymers containing highly polar components tend to produce constant density profiles of greater than 55% density, while those containing nonpolar, reactive components produce profiles with a large gradient in packing density. Density profiles describing the sedimentation behavior versus time and the final dried density of the compacts are generated via the use of gamma-ray densitometry. These polymers have the potential not only to increase green compact density but also to reduce weight losses due to "burnout" and subsequent sintering requirements by pyrolyzing to a ceramic phase.

INTRODUCTION

Polymer additives are important in nearly all types of ceramic processing [1]. However, they can create problems during burnout such as void formation from gaseous decomposition products, unwanted carbon-based residues, and the generally slow heating rates required to pyrolyze the polymer.

The present study addresses the use of inorganic polymer additives which may transform to useful ceramic upon pyrolysis. Our goal is to develop inorganic additives that give high green density compacts with high ceramic yield. Ideally, introduced oxide should act to increase the effective density of the green compact by occupying the interparticle pore spaces. If the polymer "backbone" remains in the body, less weight loss will be experienced during burnout, decreasing the possibility of void formation.

The effects of four different polymers on sedimentation were analyzed in this study. Three have oxide-forming capabilities, and one can form direct chemical bonds to the powder surface. A fully organic polymer is included for comparison. Experiments were performed in order to evaluate the effect of varying alumina water and/or hydroxyl concentrations on compaction behavior during sedimentation. Further studies seek to gauge the effect of polymer molecular

* Pacific Northwest Laboratory is operated for the U.S. Department of Energy by Battelle Memorial Institute under Contract DE-AC06-76RI0 1830.

weight and the presence of highly polar groups in the polymer on the time evolution of density profiles.

EXPERIMENTAL

The polymers used in this study were: (1) Hydrosiloxanes (Figure 1): This polymer^a consists of an inorganic -Si-O-Si- backbone and protons along the polymer chain. Figure 1a shows the mechanism of direct chemical attachment to the particle surface which this particular polymer can undergo [2]. A variety of molecular weights were used in this investigation; (2) Polyacryloxypropylsiloxane (PAS) (Figure 2): This polymer^a is similar to the hydrosiloxanes in that it also consists of an -Si-O-Si- backbone, but it possesses acryloxypropyl groups containing highly polar carbonyls along its length; (3) "Mullite-former" (MF) (Figure 3): A polymeric material shown to be capable of forming 100% mullite [3] after pyrolysis. This was synthesized from the reaction of aluminum triisopropoxide acetoacetic chelate and diphenyl silane diol.^b The compound has not yet been fully characterized; and (4) Fluorinated Polyester (FPE) (Figure 4): A fluorinated polyester^c is used that has the inexact structure [4] shown (note the presence of highly polar -C=O and -F groups).

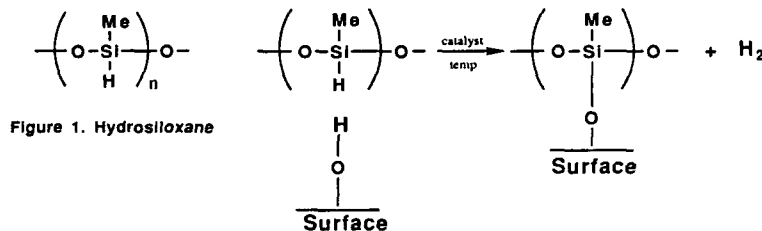


Figure 1. Hydrosiloxane

Figure 1a. Chemical attachment of hydrosiloxanes to a surface.

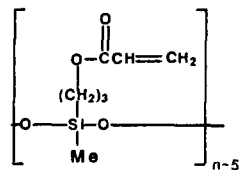


Figure 2. Polyacryloxypropylsiloxane (PAS).

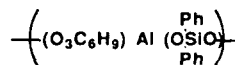


Figure 3. "Mullite-former" (MF).

^a Huls America, Bristol, PA.

^b Alfa Chemicals, Danvers, MA.

^c 3M Corporation, Minneapolis, MN.

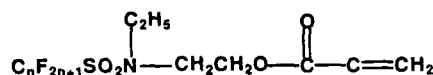


Figure 4. Fluorinated polyester (FEP).

The following techniques were used to characterize the effects of the various inorganic polymers on net particle/particle motion:

1. Gamma-ray Densitometry (GRD) was used for non-destructive analysis of density [5-7] as a function of time and position during the consolidation of green compacts. This technique uses the Beer-Lambert Law to describe the absorption of gamma rays by ceramic compacts as a function of particle packing density. GRD allows the monitoring of time- and position-dependent sedimentation behavior in much more detail than by visual estimation of sediment heights alone.
2. Near IR (NIR) uses shorter wavelength IR (0.7 to 3 μm) to create third and fourth overtones for molecular detection and identification [8-10].
3. Nuclear Magnetic Resonance (NMR) was used in the detection and quantification of -OH [11] and other groups [12] on the surface of oxide powders.

Processing

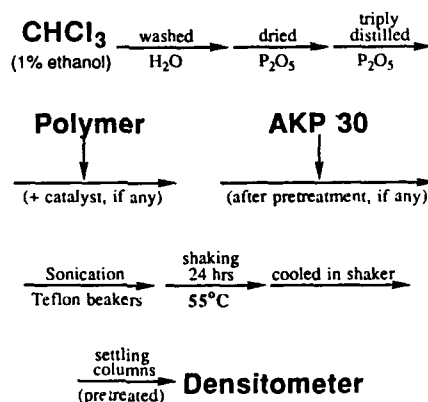


Figure 5. Processing route used in the treatment of alumina particles.

The processing route used to treat the alumina powders is pictured in Figure 5. The polymers, dispensed under Ar in a glove box, were added to the dried CHCl_3 [13] (at a concentration of 4×10^{18} chains/ μm) with any needed catalyst. Four volume % alumina^f (with an average particle size of 0.41 μm) was then added to the solution followed by 10 min of sonication over a heat source. The parent solution level was adjusted before addition to fluorinated polyester (FEP) centrifuge tubes. These tubes were then placed in a shaker arm, heated to 55°C and agitated for 24 h before pouring the solution into Pyrex sedimentation tubes that were pretreated with $(\text{CH}_3)_3\text{SiCl}$ to decrease wall effects [14].

RESULTS AND DISCUSSION

Suspensions were first prepared from as-received powder, powder treated in a vacuum, and powders heated to 100° and 300°C, respectively, in argon. The GRD results obtained from stable sediments are shown in Figure 6. The as-received and vacuum-treated powders formed spherical agglomerates of 2-3 mm in size, while the 100°C treated powder suspension agglomerates exhibited a flake-type morphology. The 300°C treated powder suspension had no discernible characteristics. These results seem to show that at least part of the barrier to forming high density green compacts in chloroform could possibly be due to adhesive surface-induced phase-separation of water (which is immiscible in chloroform); this type of phase-separation has been shown to occur between two surfaces when they are still well separated [15].

Figure 7 shows that there was no significant effect from attaching different molecular weight hydrosiloxanes (given here as the approximate number of monomeric units/chain) on the sedimentation profiles of as-received powder. Preliminary adsorption studies suggest that this behavior is not a function of the molecular weight of the additive but more a function of the amount adsorbed. The polymer chains compete with each other for adsorption sites on the powder surface, and each unit in any size polymer chain that reacts with the powder surface will occupy an identical amount of space. If these chemisorbed polymers adsorb strongly to the surface and nearly all the bonding sites of any size chain are involved in surface interactions, then only the area of powder surface/polymer chain will increase with molecular weight, not the overall thickness of the polymer layer. The higher molecular weight polymers will occupy more surface area and limit the apparent adsorption; this is responsible for the apparent poor adsorption of the higher molecular weights in comparison to the lower molecular weights. Thus it may be that a similar layer of adsorbed polymer is produced on the surface of each particle regardless of molecular weight, giving rise to similar sedimentation behavior.

The corresponding density profiles (versus time) for the PAS system are seen in Figure 8. A more dense region less than 2 cm high has built up after 72 h; this region has a relatively dispersed (less than 5% dense) region above it which extends to 15 cm. This figure indicates that, after a certain time, compaction seems to occur mostly at the interface between the compact and the more dispersed region.

^f AKP-30, Sumitomo Corp., San Francisco, CA.

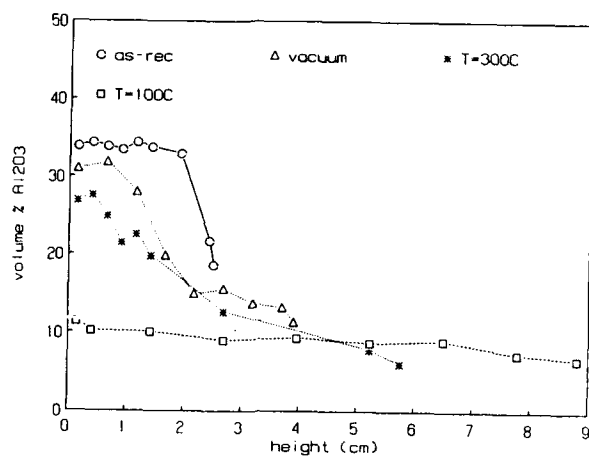


Figure 6. Density profiles as a function of powder surface pretreatment. Agglomerate morphology in this solvent varied markedly with powder pretreatment.

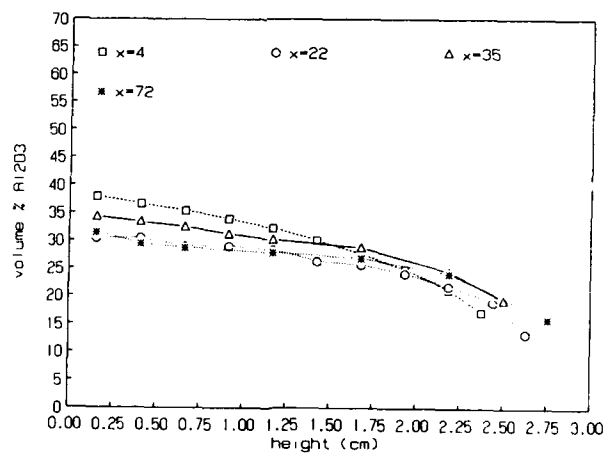


Figure 7. Density profiles as a function of hydrosiloxane molecular weight. All these polymers were chemically attached to the surface. Observed variances are negligible.

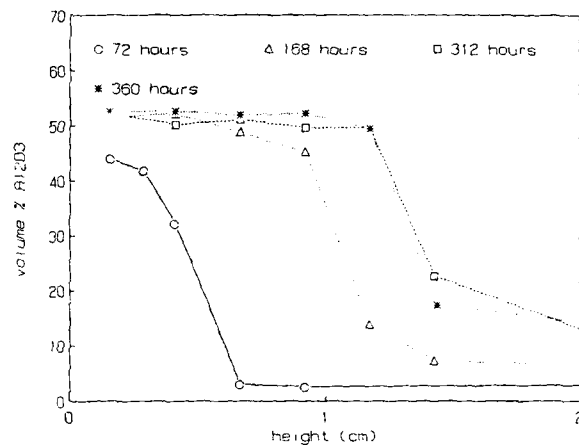


Figure 8. PAS density profiles versus time. Only a portion of the data is shown here; at 72 h the observed sediment extended to over 15 cm in height.

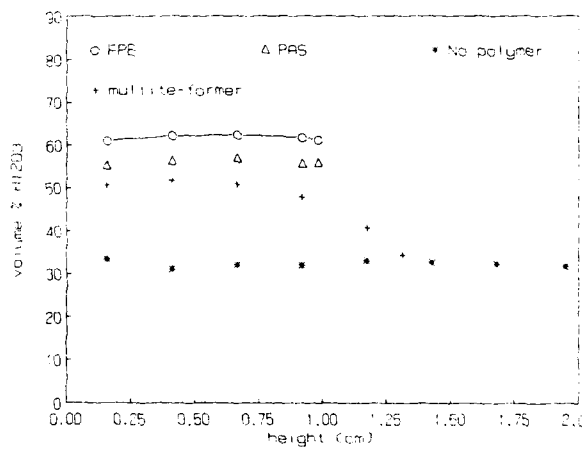


Figure 9. Comparison of net dried density profiles for the non-attached systems investigated.

The dried compact profile for PAS is shown in Figure 9. By comparing this profile to that of the final "wet" profile (Figure 8, 360 h), we see that the bulk of the compact experiences only a few percent compaction upon drying, while the upper less dense region has collapsed into a small fraction of its former height.

Figure 9 compares the PAS dried density to that produced by FPE, the mullite-former, and a compact prepared from as-received powder. Note that the additives containing highly polar groups give rise to fairly constant density profiles, while the mullite-former exhibits a "tail" of decreasing density. This behavior was also observed in the presence of hydrosiloxanes and a clear explanation for this behavior is not provided presently.

Strictly qualitative observations of these suspensions indicated differences in their relative sedimentation behavior. Some suspensions required several weeks before a stable sediment was formed, had a poorly defined sediment/supernatant interface, and tended to have a visible concentration of fines in the supernatant. Other suspensions formed a stable sediment in less than 48 h, had a sharply defined sediment/supernatant interface, and had no fines visible in the supernatant. If we characterize the first group as being more dispersed than the second, we can rank this "dispersity" as PAS > FPE > mullite-former > no additive. This observation, when combined with the dry density data, is at odds with studies involving aqueous-forming techniques, which suggests that the more dispersed system will form higher density compacts [16]. Although the FPE system did not display as much dispersed behavior as the PAS system, it produced a denser compact.

Finally, although it was found that NIR is not sensitive enough to monitor -OH concentration on the powder surface, it can be used to accurately monitor dilute concentrations of polymer remaining in solution after adsorption by the powder surface. Further studies with this technique will be used to gauge the amount of polymer adsorbed onto the surface of the powder.

The NMR spectra of these powders consist of two components, a broad chemisorbed (strongly bonded) -OH component and a narrow physisorbed (mobile) component. After adsorption of hydrosiloxanes to the surface, the chemisorbed -OH's appear to be unaffected while the concentration of the physisorbed -OH's is decreased. This behavior supports the idea that polymer-surface bonding is taking place under these conditions. Also detectable are the methyl protons of the polymer lying on the surface of the powder. This data may be quantifiable and could provide numerical information on the spatial distribution of -OH and -CH₃ on the powder surface [11]. Coupling this data with NIR data is expected to provide an accurate picture of polymer/surface interactions in these systems.

CONCLUSIONS

Inorganic polymer additives can modify particle/particle interactions and thus the overall powder compaction behavior in these nonaqueous systems. We have found evidence suggesting the identity of the desired components of inorganic polymers which can produce both high green densities and ceramic yield.

The addition of almost any polymeric material to a particle surface in chloroform changes these interactions, at least partially, via "screening" of adhesive forces between water molecules adsorbed on different particles. The changes these additives induce on the density profiles produced by gross particle motion can be efficiently monitored by GRD. Polymers containing highly polar components tend to produce constant density profiles of greater than 55% density, while those with nonpolar, reactive components produce profiles with a large gradient in packing density.

ACKNOWLEDGMENTS

This work was supported by the Office of Basic Energy Sciences, U.S. Department of Energy, through a subcontract by Pacific Northwest Laboratory under Contract No. 063961-A-F1.

REFERENCES

1. J. S. Reed, in Ceramic Transactions, Vol. I, Ceramic Powder Science II, edited by G. L. Messing, E. R. Fuller, and H. Hausner, (American Ceramic Society, Westerville, OH, 1988), p. 601.
2. Silicon Compounds, Petrarch Systems (1987), p. 275.
3. J. J. Lannutti and I. A. Aksay, to be submitted to the *J. Am. Ceram. Soc.*
4. D. G. Gallagher, Ph.D. Thesis, University of Washington, Seattle (1988).
5. C. H. Schilling, G. L. Graff, W. D. Samuels, and I. A. Aksay, in Atomic and Molecular Processing of Electronic and Ceramic Materials: Preparation, Characterization, and Properties, edited by I. A. Aksay, G. L. McVay, T. G. Stoebe, and J. F. Wager (Mater. Res. Soc. Symp. Proc., Pittsburgh, PA 1987), pp. 239-51.
6. L. Stroosnijder and J. G. De Swart, *Soil Science* **118**, 61 (1974).
7. D. L. Nofziger and D. Swartzendruber, *J. Appl. Phys.* **45**, 5443 (1974).
8. D. M. Mayes and J. B. Callis, *Appl. Spect.* **43**, 27 (1989).
9. L. G. Weyer, *Appl. Spect. Rev.* **21**, 1 (1985).
10. O. H. Wheeler, *Chem. Rev.* **59**, 629 (1959).
11. L. B. Schreiber and R. W. Vaughan, *J. Catal.* **40**, 226 (1975).
12. G. J. Exarhos, K. F. Ferris, D. M. Friedrich, and W. D. Samuels, *J. Am. Ceram. Soc.* **71**, C-406 (1988).
13. D. D. Perrin and W. L. F. Armarego, Purification of Laboratory Chemicals, 3rd ed., (Pergamon Press, New York, 1988), p. 121.
14. J. V. Dawkins and G. Taylor, *Polymer* **20**, 599 (1979).
15. H. K. Christenson, R. G. Horn, and J. N. Israelachvili, *J. Colloid Interface Sci.* **88**, 79 (1982); H. K. Christenson, *ibid.* **104**, 234 (1985).
16. T. Yeh and M. D. Sacks, *J. Am. Ceram. Soc.* **71**, 841 (1988).

CONVERSION OF ALKOXIDE SOLUTIONS TO OXIDES: EVAPORATION OF PRODUCTS

R. A. LIPELES and D. J. COLEMAN

Chemistry and Physics Laboratory, The Aerospace Corporation, El Segundo,
CA 90245

ABSTRACT

The evaporation of organic by-products released during drying of 1-mm thick silicon tetramethoxide gels was analyzed using gas chromatography. The evaporation kinetics of methanol depended on the drying rate achieved by flowing dry air over the gel. For drying at flow rates less than 50 cm³/min, exponential kinetics were observed initially with a long time constant (about 100- to 400-min). For drying rates greater than 70 cm³/min, diffusional ($t^{-1/2}$) kinetics were observed initially. Cracking of the gel during drying was used to indicate the degree of stress. At low drying rates, minor cracking was observed near the edges of the gel. At high flow rates, extensive cracking was observed in samples that exhibited early $t^{-1/2}$ kinetics. Monitoring the kinetics of drying is essential to optimizing the drying conditions to minimize stress and cracking in gels.

INTRODUCTION

The rate of solvent and organic by-product removal from wet gels prepared by metallo-organic solution deposition (MOSD or sol-gel) affects the structure and quality of the dry gels and films.¹⁻³ At slow drying rates, evaporation of solvent from the gel depends on the vapor pressure of the solvent, its surface concentration, and its surface area.⁴ When the surface dries faster than the solvent can diffuse to the surface, transport of the solvent molecules to the surface becomes rate limiting. Drying conditions are usually optimized by the traditional method of examining dried gels or films and adjusting the drying conditions to avoid cracking. An understanding of evaporation kinetics would result in easier optimization of drying conditions. Thermogravimetry (TG) could be used to monitor the evaporation kinetics. However, in multicomponent solvent systems measurement of the evaporation of the individual components is desirable, which is possible by gas chromatography. In this paper we show that gas chromatography can be used to characterize drying kinetics of gels. Tetramethylorthosilicate (TMOS) was studied as a model system to demonstrate the application of this technique. The rate of dry air flow was used to vary the drying rate over a wide range, and the observed evaporation kinetics were correlated to cracking in the dried gel.

EXPERIMENTAL PROCEDURE

Gels were cast from solutions with mole ratios of TMOS:water:methanol:ammonium hydroxide of 1:4:4:0.13. Distilled TMOS, reagent grade methanol, and aqueous ammonium hydroxide were used. Gelation occurred after 2 hours at 24°C. The gel was aged for an additional hour prior to drying measurements.

The drying experiments were carried out in a 2-ml volume sample tube containing a 1-mm thick wet gel cast into a 1-cm x 2-cm area. The drying rate was controlled by flowing dry air into the sample tube at rates between 11 and 105 cm³/min. The gas exiting the tube through a 3-mm diameter capillary was sampled at 1- to 20-minute time intervals by an automatic 6-port gas sampling valve. The concentration of methanol vapor in 2 ml gas samples was determined with an HP 5480A gas chromatograph equipped with an Alltech AT-1000/Graphpac column. The column was run at 160°C, the nitrogen carrier flow was set at 25 cm³/min, and a flame ionization detector was used. The peak intensity was related to the vapor pressure of methanol by running methanol in the cell under the same conditions as the gels.

RESULTS AND DISCUSSION

The primary species observed by gas chromatography during drying in air at 24°C were methanol and TMOS monomer. (Water cannot be detected using a flame ionization detector.) Figure 1 presents a sequence of gas chromatograms obtained by sampling the gas exiting the flow cell at 20-minute intervals. The evaporation rates of methanol and TMOS are compiled in Table 1.

Table 1. Gas Chromatography of Gases Removed from Base-Catalyzed TMOS Gel by Dry Air Flowing at 35 cm³/min

Sampling time (min)	Observed time (min)	Compound	Evaporation rate (μ moles/min cm ²)
1.5	2.0	methanol	35.
	6.4	TMOS	1.3
21.	21.5	methanol	23.
	25.9	TMOS	0.8
41.	41.5	methanol	20.
	45.8	TMOS	0.9
61.	61.5	methanol	8.
	65.8	TMOS	0.9
81.	81.5	methanol	11.
	85.8	TMOS	0.7

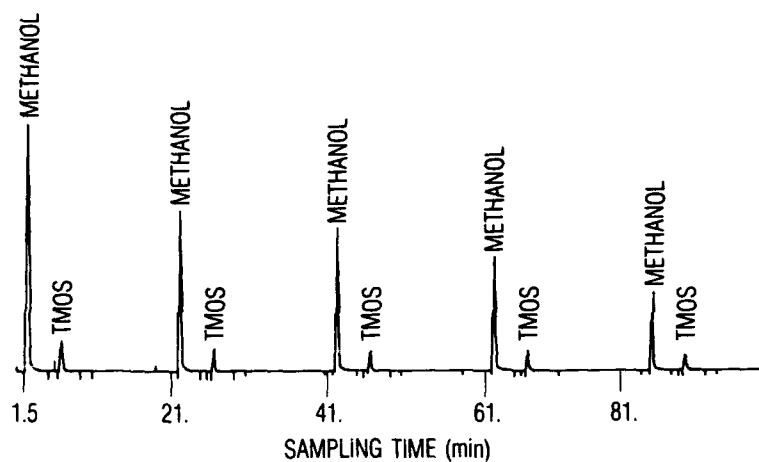


Figure 1. Gas chromatograph of TMOS sample. Carrier flow = 35 cm³/min

The high degree of polymerization and lower monomer volatility accounts for the very low TMOS evaporation rate. Most of the volume change of the gel is due to the evaporation of methanol. The evaporation kinetics, which were investigated in detail, were related to cracking of the gel.

The flow rate through the cell was varied between 11 to 105 cm³/min to measure its effect on the drying rate of the gel. The evaporation kinetics of methanol from the TMOS gels with three different air flow rates are compared in Figures 2 and 3. The data in Figure 2 for moderate flow rates (11 and 35 cm³/min) indicate two distinct regions: an initial region (until about 80% of the methanol is lost) where the evaporation rate is fairly constant, and a region where the rates abruptly decrease. These regions are referred to, respectively, as the "constant rate period" and the "transition period" in the ceramics literature.⁵ The evaporation kinetics in the constant rate period shown in Figure 3 can be fitted by

$$dN/dt = E_0 \exp(-t/t_0) \quad (1)$$

where E_0 is the initial evaporation rate and t_0 is the time constant. These parameters are tabulated for several flow rates in Table 2.

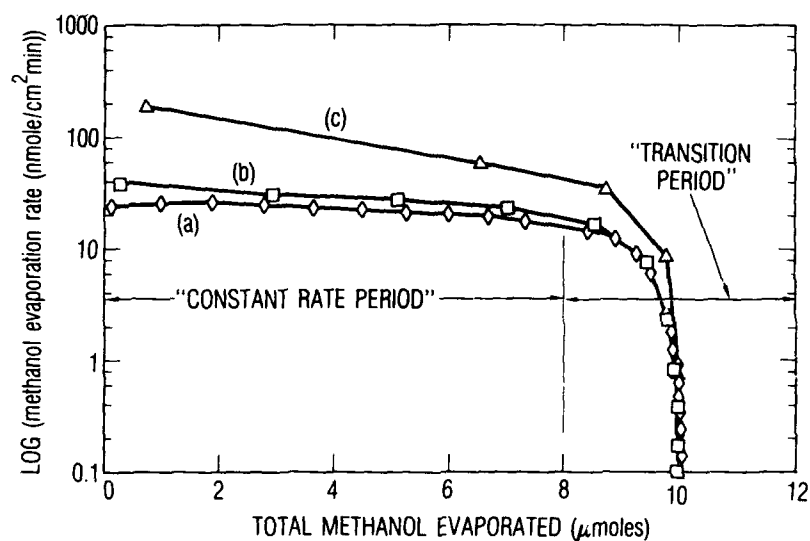


Figure 2. Evaporation rate of methanol from TMOS gels at 24°C for flow rates of (a) 11 cm³/min, (b) 19 cm³/min, and (c) 105 cm³/min

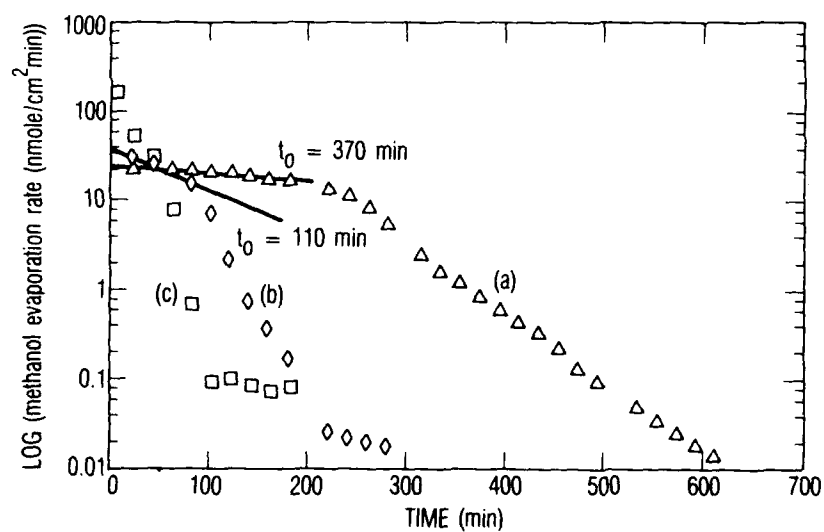


Figure 3. Evaporation rate of methanol from TMOS gels at 24°C for flow rates of (a) 11 cm³/min, (b) 19 cm³/min showing exponential fit to initial data, and (c) 105 cm³/min.

Table 2. Effect of Air Flow Rate on Drying

Air Flow, f (cm^3/min)	E_o ($\text{nmole}/\text{min cm}^2$)	t_o (min)	VE_o/f ($\text{nmole}/\text{min cm}^2$)	ft_o/V
11	8	370	1.5	2000
19	12	210	1.2	2000
35	17	110	1.0	1900
72	$t^{-0.42}$		-	-
105	$t^{-0.51}$		-	-

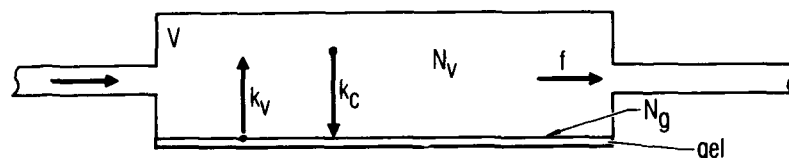


Figure 4. Kinetic model for drying of gels in flowing air

A simple model of drying in Figure 4 was proposed to understand the observed kinetics. At low rates of air flow, the surface of the gel remains wet as the gel collapses.⁶ Assuming ideal solution behavior for methanol in the gel, the surface concentration of methanol available for evaporation is nearly proportional to the concentration of methanol remaining in the gel. Under this assumption, the equations for the rate of change of methanol in the vapor phase, dN_v/dt , and in the gel phase, dN_g/dt , are the same as those for outgassing:⁷

$$dN_v/dt = k_v N_g - k_c N_v - f N_v / V \quad (2)$$

$$dN_g/dt = -k_v N_g + k_c N_v \quad (3)$$

where k_v is the vaporization rate of methanol from the surface, k_c is the condensation rate, f is the gas flow rate, N_g is the number of moles of methanol in the gel, V is the volume of gas sampled by the gas chromatograph, and N_v is number of moles of methanol in the vapor phase in the cell. The quantity measured by sampling the gas at the exit of the sample cell is dN_v/dt . At a constant air flow rate, a steady state is established in the vapor phase and dN_v/dt in Eq. (2) can be set equal to zero. Under these conditions the solutions of Eqs. (2) and (3) are

$$N_g(t) = (k_c/k_v)N_{eq}\exp[-k_vft/(Vk_c+f)] \quad (4)$$

$$N_v(t) = [k_c/(k_c+f/V)]N_{eq}\exp[-k_vft/(Vk_c+f)] \quad (5)$$

where N_{eq}/V is the equilibrium concentration of methanol with no air flow. The evaporation rate measured by the gas chromatograph was calculated from Eq. (5) and is:

$$dN_v(t)/dt = [k_c/(k_c+f/V)][k_vf/(Vk_c+f)]N_{eq}\exp[-k_vft/(Vk_c+f)] \quad (6)$$

Assuming low to moderate flow rates ($f/V < k_c$), E_o and t_o can be related to the kinetic parameters of the model by comparing Eq. (6) to Eq. (1). The initial evaporation rate is given by

$$E_o = (k_vf/Vk_c)N_{eq} \quad (7)$$

and the time constant is given by

$$t_o = Vk_c/k_vf. \quad (8)$$

As predicted from the model, VE_o/f and ft_o/V calculated from the data in Table 2 are constant within the experimental uncertainty. Thus, for flow rates less than 35 cm³/min, the observed exponential drying kinetics are consistent with evaporation of methanol of an ideal solution consisting of methanol and nonvolatile gel. The stress on the gel is low under these conditions.⁶

At high air flow rates, the initial kinetics change to a $t^{-1/2}$ law. This is shown for the data in Figure 5 obtained with a flow rate of 105 cm³/min. The $t^{-1/2}$ law is expected for plane diffusion from an infinitely thick plate [7]. These conditions exist for a limited time in a rapidly drying gel when solvent is removed more rapidly than a gel can contract or the liquid can flow. Based on our observations, drying under these conditions seriously increases the cracking in the gel.

Cracking of the 1-mm thick gels did not significantly change the surface area of the gels or change the measured drying rates. At flow rates less than 35 cm³/min, minor cracking developed along the edges of the gel after about 20% of the methanol was removed (Figure 6). Further drying caused the gel to shrink, but no additional cracks developed. At flow rates greater than 70 cm³/min, extensive cracking occurred before 10% of the methanol was removed. The type of cracking typical of rapid drying and diffusion-limited kinetics is shown in Figure 6b. Further cracking occurred as the gel shrank during additional drying.

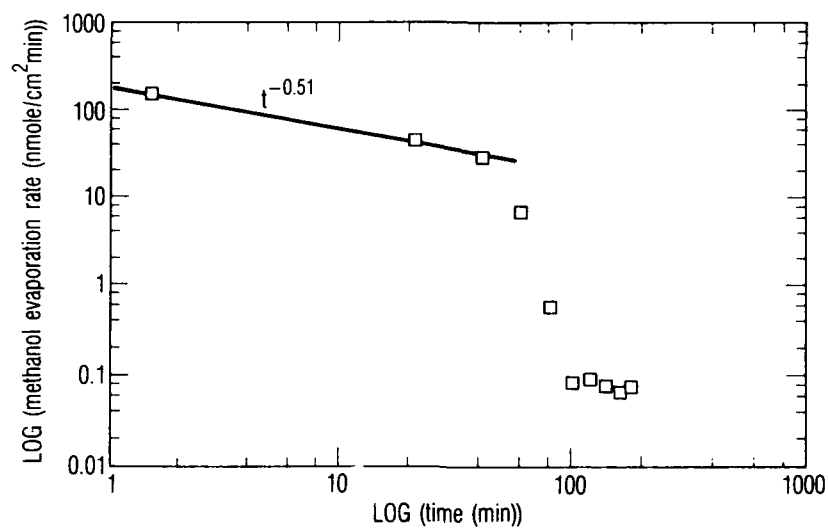


Figure 5. Evaporation of the methanol at a high ($105 \text{ cm}^3/\text{min}$) flow rate.

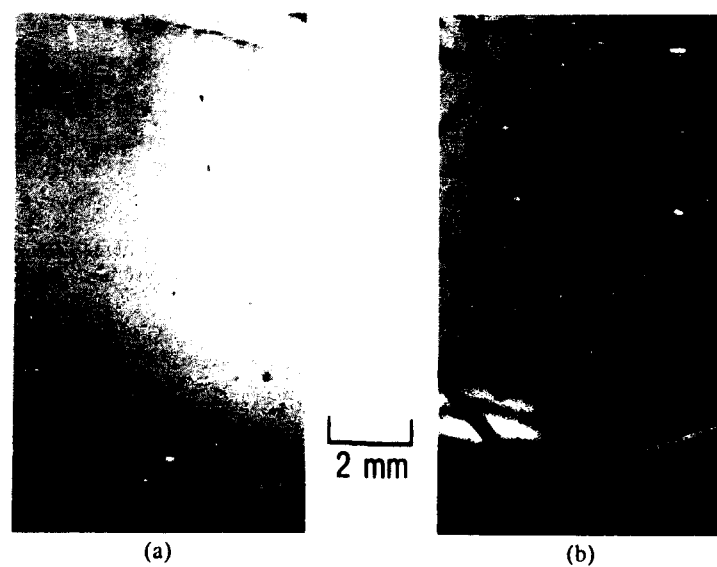


Figure 6. Cracking in gels dried at (a) $19 \text{ cm}^3/\text{min}$ to remove 20% of the methanol and (b) $105 \text{ cm}^3/\text{min}$ to remove 25% of the methanol.

CONCLUSIONS

Evaporation kinetics over a wide range of air flow rates (11 to 105 cm³/min) were measured using gas chromatography and were correlated to the cracking of the gels. Cracking in TMOS gels was minimized when the rate of methanol evaporation followed exponential kinetics and the gel dried uniformly. Extensive cracking was observed when the methanol evaporation followed diffusion-limited kinetics. Using this correlation between kinetics and cracking, gas chromatography can be used to measure the kinetics and optimize the drying rate of wet gels. This technique will be particularly useful in understanding the effects of evaporation in mixed solvent systems.

ACKNOWLEDGMENTS

We thank Drs. M. S. Leung, G. S. Arnold, and G. Eng for useful discussions. The work was supported by Aerospace Sponsored Research.

REFERENCES

1. T. M. Shaw, in Better Ceramics Through Chemistry II, edited by C. J. Brinker, Clark, and D. R. Ulrich, (Mater. Res. Soc. Symp. Proc. **73**, Pittsburgh, PA 1986) pp. 215-223.
2. J. Zarzycki, in Ultrastructure Processing of Ceramics, Glasses, and Composites, edited by L. L. Hench and D. R. Ulrich, (John Wiley & Sons, Inc., New York, NY 1984) pp. 27-42.
3. L. C. Klein and G. J. Garvey, in Ultrastructure Processing of Ceramics, Glasses, and Composites, edited by L. L. Hench and D. R. Ulrich, Eds. John Wiley & Sons, Inc., New York, NY, 1984) pp. 88-99.
4. G. W. Scherer, in Better Ceramics Through Chemistry II, edited by C. J. Brinker, D. E. Clark, and D. R. Ulrich, (Mater. Res. Symp. Proc. **73**, Pittsburgh, PA 1986) pp. 225-236.
5. R. W. Ford, Drying, Inst. of Ceramics Textbook Series, Vol 3, (Maclaren, London, 1964).
6. G. W. Scherer, J. Non-Crystal. Solids, **100**, 77-92 (1988).
7. R. Glang, R. A. Holmwood, and J. A. Kurtz, in Handbook of Thin Film Technology, edited by L. I. Maissel and R. Glang, (McGraw-Hill, New York, NY 1970) pp. 2-39 to 2-59

REMOVAL OF PROCESSING AIDS FROM CERAMIC/POLYMER COMPOSITES

GREGORY C. STANGLE, DONG-JOO RHEE, AND ILHAN A. AKSAY

Department of Materials Science and Engineering, and
Advanced Materials Technology Program, Washington Technology Center
University of Washington, Seattle, WA 98195

ABSTRACT

Fundamental issues in the removal of processing aids from ceramic compacts prior to sintering have been investigated, both experimentally and theoretically. A general theoretical model has been developed that couples simultaneous momentum, heat, and mass transfer phenomena in disordered porous materials with the mechanical response predicted by an appropriate poroelasticity theory for partially saturated porous granular materials. The kinetics of pyrolytic degradation of organic processing aids were studied using a thermogravimetric analysis-mass spectrometry (TGA-MS) system.

INTRODUCTION

Net shape or near-net shape forming of flaw-free and homogeneous bodies must be possible for commercial applications to be realized. For this purpose, fabrication of ceramics by injection molding techniques is a favored approach since this technique offers the advantages of production of complex shapes and high rates of automated production [1,2]. This approach consists of dispersing the powder and processing aids in a molten polymer, injection molding, debinding, and densifying.

Following consolidation and prior to sintering, it is necessary to remove various processing aids from the consolidated green body. This might include the organic vehicle used in dispersion, polymeric dispersant, and various binders, plasticizers, and lubricants. Approaches to the removal of processing aids include thermal degradation [3,4], chemical degradation [5], evaporation or sublimation at ambient or reduced pressures [6], solvent extraction [7], and capillary action [8]. Thermal (or thermal plus chemical) methods are often preferred [3]. The underlying goal of any scheme to remove processing aids is to reproducibly fabricate a debinded ceramic compact without any defect creation.

This paper summarizes the results of our theoretical studies of the removal process, which include the movement of energy and material into and out of the green body, as well as the material response to internal stresses generated during the removal process. Experimental polymer degradation studies complete the picture by supplying necessary reaction rate data.

MOMENTUM, HEAT, AND MASS TRANSFER

Theoretical studies of the debinding process were undertaken in order to develop predictive capabilities in the design of an improved debinding process. Further, the design of experimental debinding studies can be improved since a theoretical model, once developed and verified, can test a much larger array of variables in less time than an analogous experimental approach. The theoretical model developed describes the simultaneous momentum, heat, and mass transfer with chemical reaction in a disordered porous medium [8]. Table I summarizes the various processes responsible for the redistribution of material and energy into, out of, and within the body during the removal process. Where appropriate, the driving force for the process and the transport coefficient are listed.

Table I. Processes Responsible for Redistribution of Material and Energy.

PHASE	PROCESS	IMPORTANT QUANTITIES	
		MATERIAL	ENERGY
Gas	Diffusion	Concentration gradient Effective diffusivity	-----
	Convection	Pressure gradient Effective permeability	Temperature, pressure gradients Effective permeability
	Evaporation	Vapor pressure	Heat of vaporization
	Chemical reaction(s)	Reaction rate(s) Concentration of reactant(s)	Heat(s) of reaction
Liquid	Convection	Pressure gradient Effective permeability	Temperature, pressure gradients Effective permeability
	Evaporation	Vapor pressure	Heat of vaporization
	Chemical reaction(s)	Reaction rate(s) Concentration of reactant(s)	Heat(s) of reaction
Solid	Conduction	-----	Temperature gradient Effective conductivity

Heat transfer between the hot and cold regions of a composite depends on the amount of each phase (gas, liquid, and solid), the thermal conductivity of each phase, and the *specific spatial arrangement* of the phases. Similarly, fluid flow through such a "composite" is restricted to *available pathways*. Gas may flow (or diffuse) only through a connected network of liquid-free pores that "communicate" with the surface of the sample. Volumes occupied by solid and liquid are obviously eliminated from the allowable pathway, but so are bubble-like regions of gas that are completely enclosed by liquid and solid and thus unable to communicate with the surface of the sample. Allowable pathways for liquid flow are restricted to continuous, con-

nected networks of liquid-phase material, such that islands of liquid are incapable of capillary flow. A suitable approach is to estimate effective transport coefficients based on percolation concepts as applied to disordered media [10-13].

The more generalized form of transport equations [13,14] has been reduced to the appropriate form by Stangle and Aksay [9] for the present problem. Energy, momentum, and mass balance equations form a set of highly non-linear partial differential equations, to which the usual initial and boundary conditions apply [9]. External heat and mass transfer coefficients take into account the change in conditions external to the ceramic green body during the removal process. Profiles of temperature, gas- and liquid-phase holdup, gas-phase composition, and fluid velocities can then be predicted. Figure 1 shows a comparison of the simulated and experimental removal processes (i.e., the removal of paraffin wax from an α - Al_2O_3 /paraffin compact) wherein parameters for simulation were determined *a priori*. Good agreement is seen between the predicted and experimental results and serves to validate the accuracy of the model and provides confidence that the model can be used to estimate internal stresses that are difficult to measure experimentally.

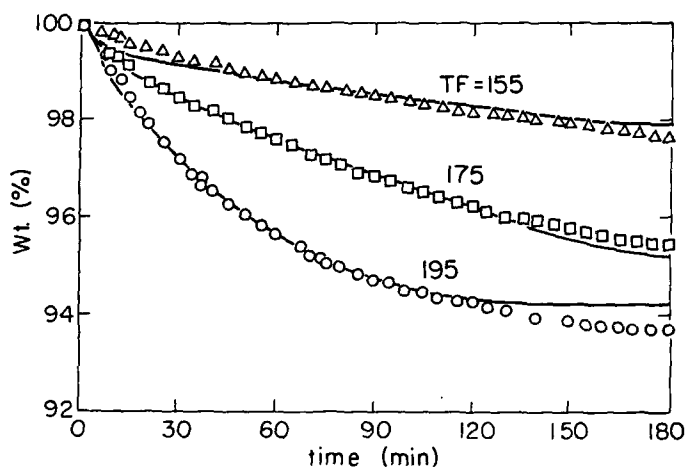


Figure 1. Comparison of model predictions with experimental thermogravimetric data. From Ref. 9.

POLYMER DEGRADATION KINETICS

Degradation of polymers by thermal and oxidative mechanisms is well documented in the literature [5,15-17]. Thermal degradation may take place by one or both of the following mechanisms: (a) depolymerization, whereby the backbone of the polymer is broken, effectively "unzipping" the polymer, or (b) removal of polymer side groups by substitution or rearrangement

processes. The former mechanism results in a decrease in molecular weight of the polymer and may leave a wide or narrow molecular weight distribution of fragments, depending upon whether the depolymerization takes place at random sites or at regularly spaced sites possessing high reactivity. The latter mechanism has little effect upon the molecular weight of the polymer. Many oxidative degradation mechanisms exhibit results similar to those of thermal degradation by depolymerization, usually differing only in the "point to attack" on the polymer chain and the oxygen-content of the resulting species. Oxidative degradation is usually more highly exothermic than thermal degradation. Two factors that are most important to the debinding of consolidated ceramic compacts are the rate at which the polymer is broken into fragments and the size of the resulting fragments. The first factor may cause the process to fall into the kinetic-limited regime, while the second influences volatility and diffusivity and hence may cause the process to fall into the diffusion-limited regime.

In our studies, we used the thermogravimetric analysis-mass spectroscopy (TGA-MS) system [18,19]. TGA-MS provides simultaneous monitoring of sample weight and complete gas-phase composition (functional group analysis and molecular weight distribution) in a real-time sampling/analysis mode. Figure 2 shows the TGA data for identical samples of paraffin wax heated in different atmospheres (air and N_2), while Figure 3 shows the mass spectra of gaseous material evolved from the samples at 80% weight loss, as detected by a triple-quadrupole mass spectrometer using an atmospheric pressure chemical ionization detector. Pyrolysis atmosphere is seen to have a profound effect on the mean fragment size and on the width of the fragment distribution. It is important to note that the generation of many low molecular weight degradation products may result in increased gas pressure and thus burnout-related cracking. Conversely, the formation of high molecular weight species may make the complete removal of binder material difficult.

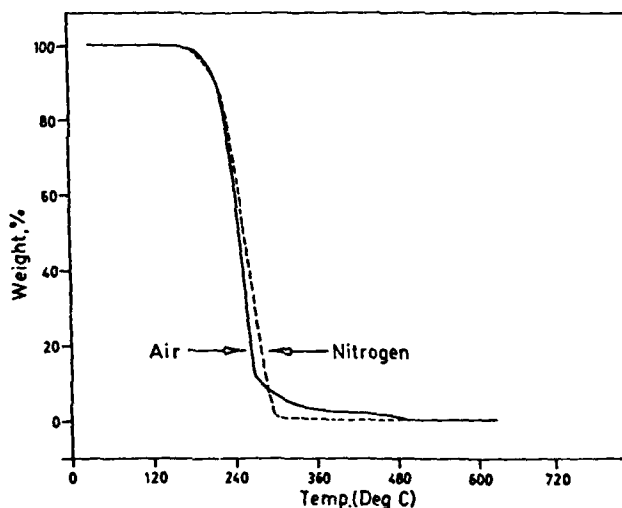


Figure 2. TGA weight loss data for paraffin wax in different furnace atmospheres.

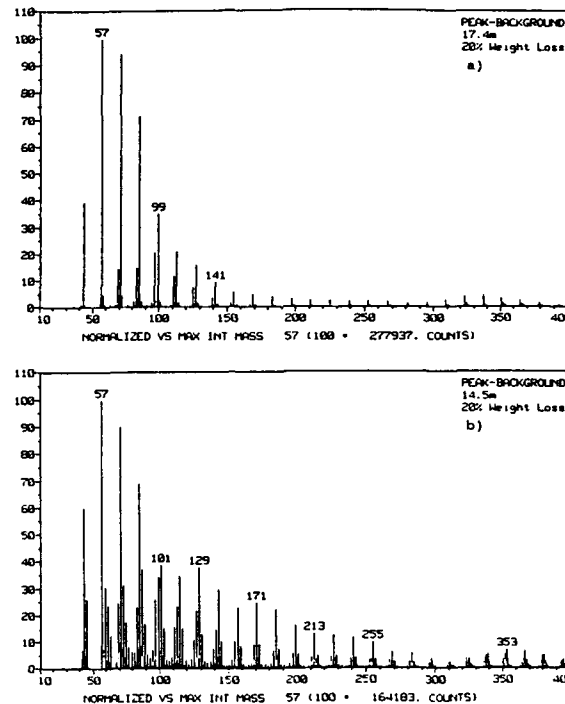


Figure 3. Mass spectra at 80% weight loss in (a) N_2 and (b) air.

MECHANICAL RESPONSE

The mechanical response of the compact throughout most of the removal process (constitutive relationship and failure criterion) is quantified by applying appropriate poroelasticity theory to a partially saturated porous granular material [9]. The geophysics and geomechanics literature is literally littered with treatment of important geological materials that are highly anisotropic and very heterogeneous, and may contain a number of solid-phase and fluid-phase materials [20-23]. A usual approach to the problem is to separate the contribution of each phase's stress to the total stress at a point. Such total stresses are related to the degree of deformation by constitutive relationships that include solid particle, drained skeleton, and liquid- and gas-phase compressibilities. Redistribution of gas, liquid, and solid may be retarded by drag forces between phases, thereby modifying mechanical response of the material. In addition, such variations in temperature as occur during the removal of processing aids require an inclusion of temperature-dependence in the relationship. Finally, a failure (or material strength) criterion is available from either micromechanical or empirical points of view [20-22]; the former can be more cumbersome than the latter but eliminates many of the simplifying assumptions required by the latter.

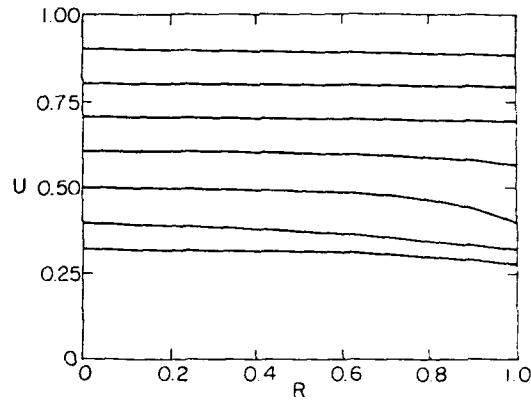


FIGURE 4a

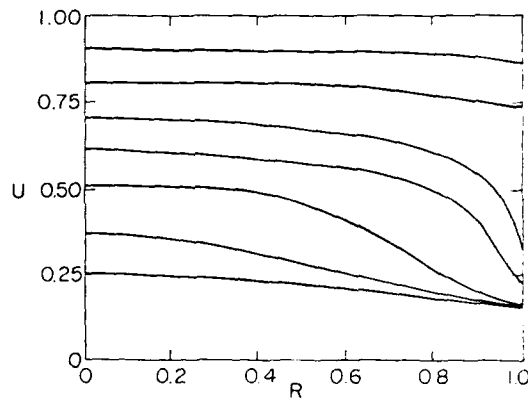


FIGURE 4b

Figure 4. Liquid saturation profiles at (a) $T_f = 155^\circ\text{C}$ and (b) 230°C . By definition: $R = r/r_p$ = dimensionless radial coordinate; U = dimensionless saturation parameter ($U = 1$ when pores are full, and $U = 0$ when empty); and $\tau = \alpha_s t / r_p^2$ = dimensionless time. The quantities r_p and α_s are sample radius and thermal diffusivity, respectively.

Figures 4 and 5 illustrate the relationship between the temperature (T_f) at which the removal process takes place, the liquid saturation (U) profiles, and internal stress distribution [9]. For $T_f = 155^\circ\text{C}$ (Figure 4a), the liquid saturation decreases steadily as a function of time and evenly as a function of position. For $T_f = 230^\circ\text{C}$, on the other hand, Figure 4b shows predictions of nonuniform saturation and thus relatively steep liquid gradients, particularly between $U(0) = 0.70$ and $U(0) = 0.40$, where $U(0)$ is the value of U at the center of the sample. Calculation of the stress profiles for both cases was undertaken and showed the largest tensile stresses occur at the surface of the sample. This is significant, since it is known that (i) partially saturated granular materials are much weaker in tension than in compression and (ii) failure

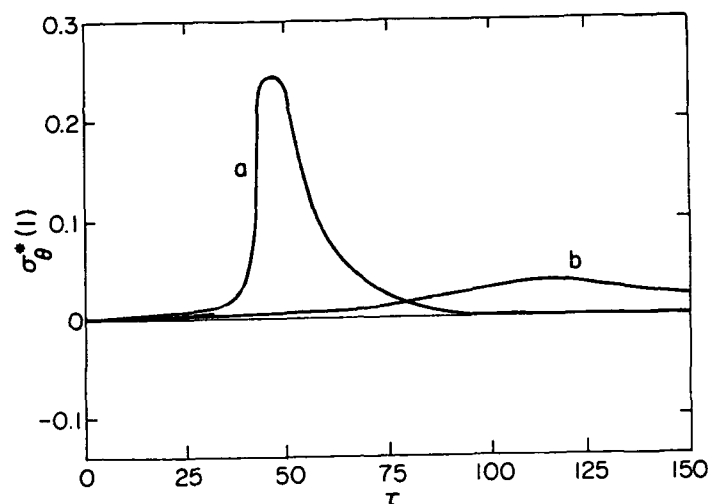


Figure 5. Internal stress profiles corresponding to saturation profiles in Figure 5. (a) $T_f = 230^\circ\text{C}$; (b) $T_f = 155^\circ\text{C}$.

(that is, cracking and other permanent microstructural deformation) can occur if any component of stresses locally exceeds the tensile strength of the material [24]. Curves (a) and (b) in Figure 5 illustrate the significant differences in tensile stress buildup and decay for $T_f = 230^\circ\text{C}$ and 155°C , respectively. The magnitude of the surface tensile stress thus results from the steepness of the liquid saturation profile, which in turn derives from the relative rates of (i) convective mass transfer from the surface and (ii) that of capillary liquid flow that replenished the "drier" surface region. In addition, another possible source of sample failures is gas pressure build-up by organic vaporization. However, the results presented in Figures 4 and 5 indicate that at the indicated temperatures, stresses due to capillary forces are more significant.

CONCLUSIONS

The kinetics of pyrolytic degradation of the nonceramic processing aids was investigated with the TGA-MS technique and showed marked differences in the time-temperature-composition behavior of both solid and gas phases during decomposition. Poroelasticity theory provided a basis for quantifying the stress-strain-failure relationship. Predictions were verified by comparison with experimental removal processes. The verified theoretical model can thus be employed to improve (and possibly optimize) processing conditions in the removal of processing aids from a consolidated ceramic green body.

ACKNOWLEDGMENTS

This work was supported by the IBM Corporation as part of a block grant on the microdesigning of ceramics and ceramic/polymer composites, and the Air Force Office of

Scientific Research (AFOSR) and the Defense Advanced Research Projects Agency (DARPA) under Grant No. AFOSR-87-0114. We gratefully acknowledge R. Bruce Prime at IBM, San Jose, for conducting TGA-MS experiments.

REFERENCES

1. M. J. Edirisinghe and J. R. G. Evans, *Int. J. High Tech. Ceram.*, **1**, 1 (1986).
2. M. J. Edirisinghe and J. R. G. Evans, *Int. J. High Tech. Ceram.*, **2**, 249 (1986).
3. B. C. Mutsuddy, *Proc. Brit. Ceram. Soc.*, **33**, 117 (1983).
4. A. Johnsson, E. Carlstrom, L. Hermansson, and R. Carlsson, *Proc. Brit. Ceram. Soc.*, **33**, 137 (1983).
5. L. Reich and S. S. Stivala, *Elements of Polymer Degradation* (McGraw-Hill, New York, 1971).
6. R. E. Weich, U.S. Patent 4,305,756 (15 Dec. 1981).
7. M. A. Strivens, U.K. Patent 808,583 (4 Feb. 1959).
8. I. Peltzman and M. Peltzman, *Interceram.*, **4**, 56 (1984).
9. G. C. Stangle and I. A. Aksay, *Chem. Eng. Sci.*, submitted (1989).
10. S. Reyes and K. F. Jensen, *Chem. Eng. Sci.*, **37**, 905 (1982).
11. G. K. Batchelor and R. W. O'Brien, *Proc. Roy. Soc. Lond. A*, **7**, 179 (1974).
12. R. B. Stinchcombe, *Phys. C: Solid State Phys.*, **355**, 313 (1977).
13. R. B. Bird, W. E. Stewart, and E. N. Lightfoot, *Transport Phenomena* (Wiley, New York, 1960).
14. S. Whitaker, *Adv. Heat Transfer*, **13**, 119 (1977).
15. R. T. Couley, editor, *Thermal Stability of Polymers* (Marcel Dekker, New York, 1970). See also *J. Anal. Appl. Pyrolysis*, **11** (1987).
16. A. D. Jenkins, ed., *Polymer Science* (North Holland, Amsterdam, 1972).
17. Y. Tschuiga and K. Sami, *J. Polym. Sci.*, **40**, 1723 (1985).
18. G. C. Stangle, R. B. Prime, D.-J. Rhee, J. C. Seferis, and I. A. Aksay, *SPE Conf. Proc.: ANTEC 89* (1989).
19. G. C. Stangle, D.-J. Rhee, and I. A. Aksay, *J. Am. Ceram. Soc.*, submitted (1989).
20. J. G. Berryman and L. Thigpen, in *Physics and Chemistry of Porous Media II*, edited by J. R. Banavar, J. Koplik, and K. W. Winkler (American Institute of Physics, New York, 1987), p. 209.
21. I. Vardoulakis and D. E. Beskos, *Mech. Mat.*, **5**, 87 (1986).
22. D. F. McTigue, R. K. Wilson, and J. W. Nunziato, in *Mechanics of Granular Materials: New Model and Constitutive Relations*, edited by J. T. Jenkins and M. Satake (Elsevier, Amsterdam, 1983), p. 195.
23. M. A. Biot, *J. Acoust. Soc. Am.*, **28**, 168 (1956).
24. P. J. Sherrington and R. Oliver, *Granulation* (Heyden, Philadelphia, 1981), p. 19.

PART III

Sol-Gel Processing of Thin Films
and Electronic Ceramics

PROCESSING OF CRYSTALLINE $\text{Li}(\text{Nb}, \text{Ta})\text{O}_3$ FILMS WITH PREFERRED ORIENTATION THROUGH METAL ALKOXIDES

SHIN-ICHI HIRANO AND KAZUMI KATO

Department of Applied Chemistry, Faculty of Engineering,
Nagoya University, Furo-cho, Chikusa-ku, Nagoya 464 Japan

ABSTRACT

LiNbO_3 and LiTaO_3 are very attractive and useful materials, which have been applied to piezoelectric and electro-optic devices. The authors have synthesized the stoichiometric crystalline fine powders and films of LiNbO_3 at temperatures as low as 250°C by the controlled hydrolysis of double alkoxide solutions; and this method was used to prepare $\text{Li}(\text{Nb}, \text{Ta})\text{O}_3$ solid solution films with and without the preferred orientation. Water used during the processing played an important role in the low-temperature crystallization and the elimination of free carbon in the films. The water for the partial hydrolysis affected the properties of alkoxide solutions for dip-coating, and the morphologies of crystalline films. Water in a mixed gas flow with oxygen during calcination accelerated the crystallization of the alkoxy-derived films at low temperatures.

INTRODUCTION

Recently, the sol-gel method using organometallic compounds was studied to synthesize electronic materials. This method has many advantages : high purity, low-temperature processing, composition control and shape control.

LiNbO_3 and LiTaO_3 are very useful materials for surface acoustic wave and electro-optic devices. In both the $\text{Li}_2\text{O}-\text{Nb}_2\text{O}_5$ system and the $\text{Li}_2\text{O}-\text{Ta}_2\text{O}_5$ system, there are solid solution ranges around the stoichiometric compositions. The congruent melt compositions of these systems are located at the lower Li_2O content. Thus, single crystals have been grown not from the stoichiometric but from the non-stoichiometric congruent melts by the Czochralski method. The control of compositions of LiNbO_3 and LiTaO_3 ceramics synthesized by solid reactions is difficult due to the vaporization of Li_2O at higher

temperatures. The properties of these crystals have been known to be very sensitive to the composition. The processing of the films with stoichiometry was required to develop for the better control of the electro-optic properties and the diffusivity of Ti for the wave guides. The sol-gel processing of LiNbO_3 and LiTaO_3 has been studied [1-9]. The authors have reported the low temperature processing of crystalline films as follows [1-4] :

1. The synthesis of a double alkoxide was necessary for preparations of stoichiometric LiNbO_3 .
2. LiNbO_3 films with preferred orientation were prepared on sapphire substrates, which have the same crystal system as LiNbO_3 .
3. $\text{LiNb}_x\text{Ta}_{1-x}\text{O}_3$ ($0 \leq x \leq 1$) films with preferred orientation could be prepared by controlling the ratio of Nb to Ta of alkoxides in solutions.

This paper describes the role of water in the sol-gel processing of $\text{Li}(\text{Nb,Ta})\text{O}_3$ films to achieve crystallization at low temperatures. The effects of added water on the partial hydrolysis of double alkoxides and the crystallization of films from precursor solutions, and the morphologies of crystallized films are investigated.

EXPERIMENTAL PROCEDURE

Figure 1 illustrates the flow diagram for the preparation of $\text{Li}(\text{Nb,Ta})\text{O}_3$ films. The formation of the complex alkoxide and the detailed experimentation have been mentioned elsewhere [1-4]. For a partial hydrolysis of the double alkoxide solutions, an adequate amount of CO_2 -

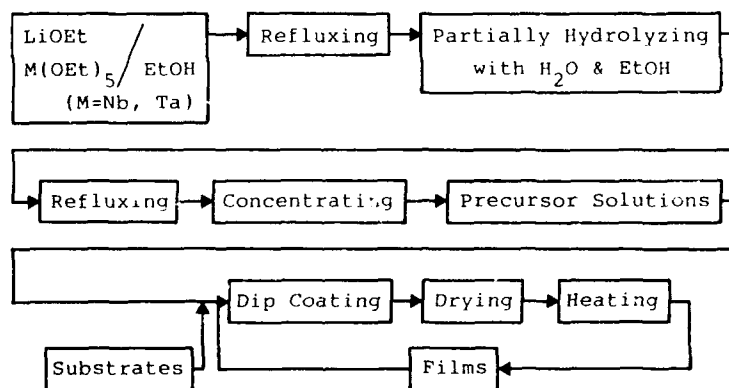


Fig. 1. Flow diagram for synthesis of $\text{Li}(\text{Nb, Ta})\text{O}_3$ films

free, distilled water with ethanol was dropped in slowly. Alkoxy-derived films, which were prepared from precursor solutions, were heat-treated in a mixed gas flow of water vapor and oxygen or in flowing dry oxygen.

The viscosity and the density of the precursor alkoxide solutions were measured with a rotational viscometer and a picnometer. The crystallization process of alkoxy-derived films was analyzed by XRD and FT-IR. The morphologies of films were observed by SEM.

RESULTS AND DISCUSSION

Properties of Solutions

Table I shows the viscosity and the density of solutions with and without the partial hydrolysis for LiNbO_3 films. The viscosity of the

Table I. Viscosity and density of solution with and without partial hydrolysis for preparation of LiNbO_3 films

Conc. of Soln. (mol/L)	Partial Hydrolysis ($\text{H}_2\text{O}/\text{LiNb}(\text{OEt})_6$)	Viscosity (cP)	Density (g/cm^3)
0.6	0	5	0.86
0.6	1.0	7	0.86

(20°C)

solution, being partially hydrolyzed with water ($\text{Rw} : \text{H}_2\text{O}/\text{LiNb}(\text{OEt})_6 = 1.0$), was higher than the alkoxide solution without the partial hydrolysis. The densities of both solutions were the same.

Table II shows the viscosity and the density of the partially hydrolyzed alkoxide solutions as a function of concentration. Both the viscosity and the density changed with the concentration. This suggests that a part of the OR groups of the double

Table II. Viscosity and density of solution with the partial hydrolysis ($\text{H}_2\text{O}/\text{LiNb}(\text{OEt})_6 = 1.0$) for preparation of LiNbO_3 films

Conc. of Soln. (mol/L)	Viscosity (cP)	Density (g/cm^3)
0.2	6	0.82
0.6	7	0.86
0.8	8	0.89
1.0	8	0.92
1.3	8	0.95

(20°C)

alkoxide were changed to OH groups by partial hydrolysis, leading to condensation of molecules with several original alkoxides. Molecular weight of the molecules did not change with the concentration of the solution. Homogeneous gel films could be formed from solutions with concentrations up to 1.0 mol dm^{-3} but not from the saturated solution 1.3 mol dm^{-3} .

Table III. Viscosity and density of solution for preparation of LiTaO_3 films.

Conc. of Soln. (mol/L)	Viscosity (cP)	Density (g/cm ³)
0.2	6	0.83
0.6	7	0.91

(20°C)

A double alkoxide of $\text{LiTa}(\text{OEt})_6$ was more sensitive to water than $\text{LiNb}(\text{OEt})_6$ and was readily hydrolyzed with water ($R_w \cdot \text{H}_2\text{O}/\text{LiTa}(\text{OEt})_6 = 1/8$) to form a precipitate. The viscosity and the density of solutions without the partial hydrolysis for LiTaO_3 films are shown in Table III. The viscosity of the solutions was also appropriate for the preparation of homogeneous films.

Crystallization of Gel Films

Figures 2 (a) and (b) illustrate FT-IR spectra of LiNbO_3 films formed from solutions with and without the partial hydrolysis on Si substrates and heated in a mixed gas flow of water vapor and oxygen. The as-prepared film showed an absorption band at 540 cm^{-1} attributable to a Nb-O bond. The band at 540 cm^{-1} shifted to the higher frequency side because of the strengthening of the Nb-O bond on crystallizing, and film crystallized at 400°C showed a strong absorption band at 590 cm^{-1} , which corresponds to the band in single crystals. The partial hydrolysis of the alkoxide solution does influence the crystallization of LiNbO_3 films through pre-formed intermediate condensed oligomers in solution.

Figures 3 (a) and (b) illustrate FT-IR spectra of LiNbO_3 films formed from solutions with and without the partial hydrolysis on Si

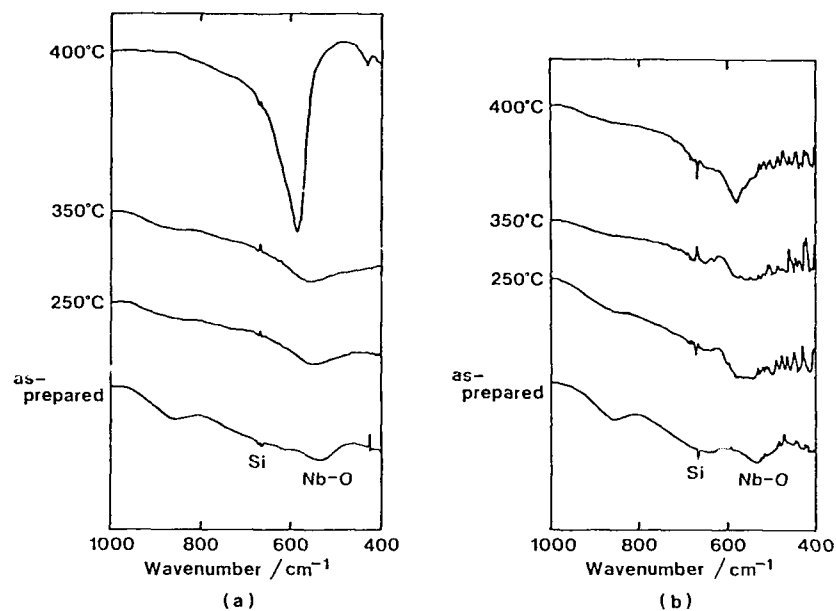


Fig. 2. FT-IR spectra of films prepared from solutions (a) with and (b) without the partial hydrolysis and heated in a mixed flow of water vapor and oxygen.

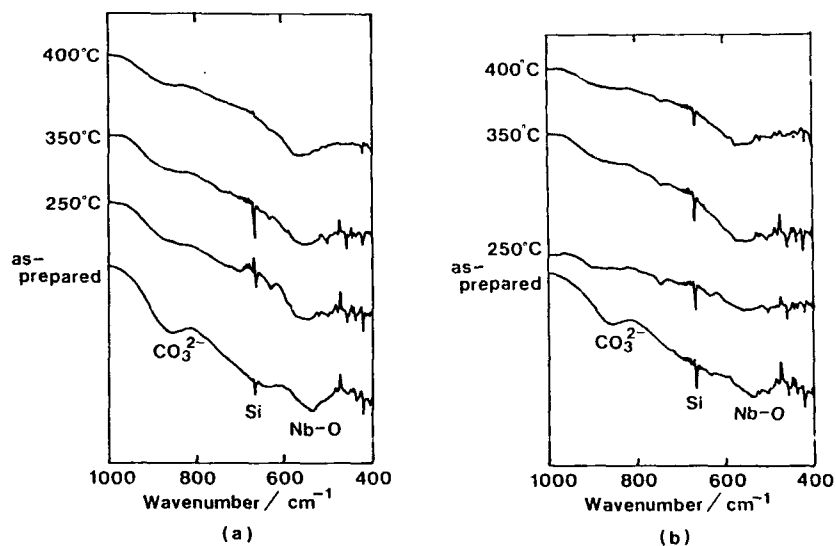


Fig. 3. FT-IR spectra of films prepared from solutions (a) with and (b) without the partial hydrolysis and heated in flowing dry oxygen.

substrates and heated in dry oxygen without any water vapor. These spectra were different from the spectra in Fig. 2. The strong absorption band at 590 cm^{-1} could not be observed even after heat treatment at 400°C and a weak absorption band at around 860 cm^{-1} is attributable to residual CO_3^{2-} groups in the films. Heating with water vapor present clearly exhibits a clean-off effect and acceleration effect on crystallizing gel films made via the organometallic route. The results of FT-IR mentioned above agreed with the results of XRD. Figure 4 shows XRD profiles of films heat-treated at 400°C on Si substrates. The alkoxy-derived films, prepared from solutions with and without partial hydrolysis crystallized to LiNbO_3 by heating in the presence of water vapor at 400°C . These facts indicate that water vapor affects the conversion and the elimination of organic groups, which are left in the alkoxy-derived films, and promotes the crystallization of the films at low temperatures.

Sapphire has the same packing structure of atoms as in LiNbO_3 and LiTaO_3 . The mismatches along the a-axis and c-axis between sapphire and these materials were not larger than 9 % and 7 %, respectively. LiNbO_3 and LiTaO_3 films crystallized with preferred orientations such as (012), (110) and (001) on sapphire substrates as shown in Fig. 5 for a (012) $\text{Li}(\text{Nb}_{0.5}\text{Ta}_{0.5})\text{O}_3$ film.

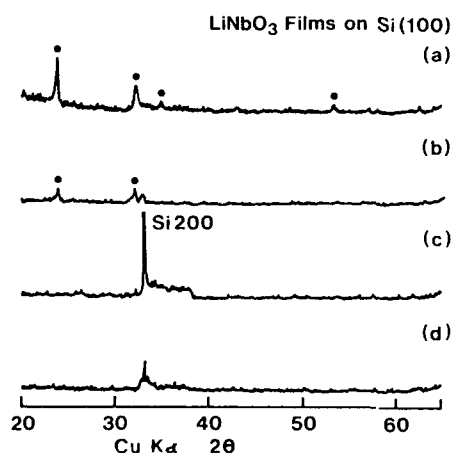


Fig. 4. XRD profiles of films heated at 400°C .

(a), (b); films heated in a mixed flow of water vapor and oxygen.

(c), (d); films heated in flowing of dry oxygen.

(a), (c); films prepared from solutions with partial hydrolysis.

(b), (d); films prepared from solutions without partial hydrolysis.

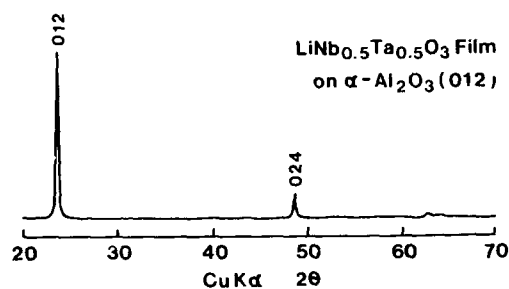


Fig. 5. XRD profile of $\text{LiNb}_{0.5}\text{Ta}_{0.5}\text{O}_3$ film crystallized on $\alpha\text{-Al}_2\text{O}_3$ (012) at 500°C.

Morphologies of Films

LiNbO_3 films, which were prepared from the solution with partial hydrolysis and then crystallized at 400°C in a mixed gas flow of water vapor and oxygen on Si and sapphire substrates, were very homogeneous, flat and crack-free.

Figures 6 and 7 show SEM photographs of edge profiles of fracture surfaces of LiTaO_3 films, which were prepared from the solution without partial hydrolysis, and crystallized at 500°C in a mixed gas flow of water vapor and oxygen on Si and sapphire, respectively. The films crystallized on Si substrates were homogeneous and flat. In contrast, the films crystallized on sapphire substrates showed a granular structure.

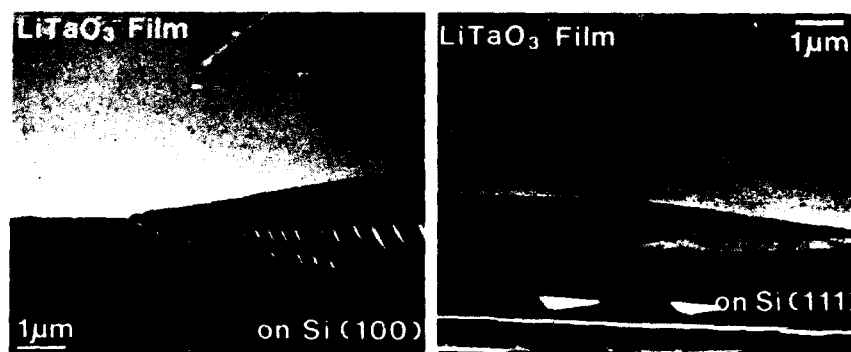


Fig. 6. SEM photographs of edge-on profiles of the fracture surfaces of LiTaO_3 films crystallized at 500°C

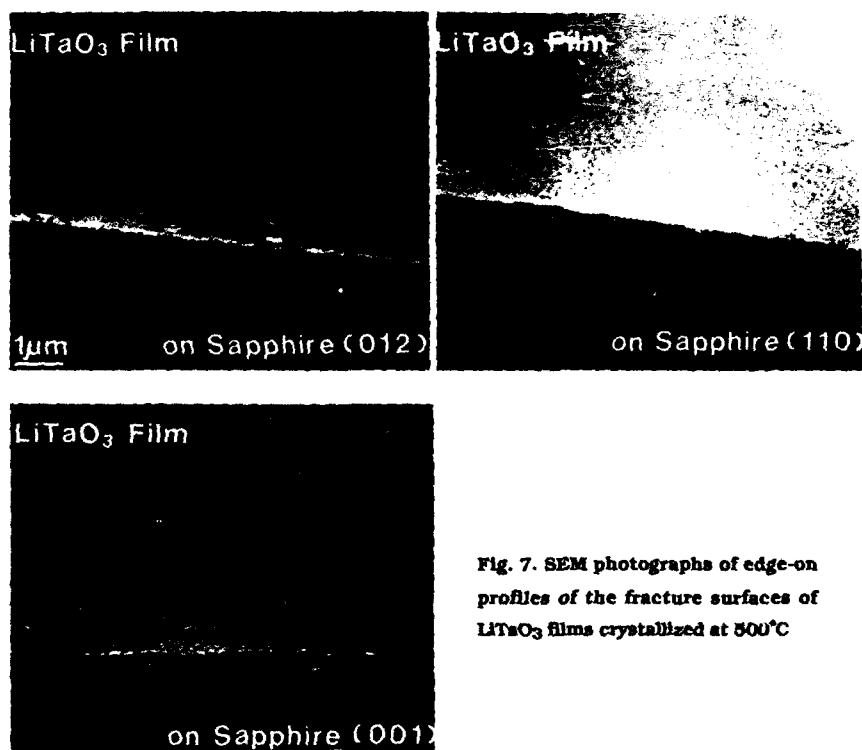


Fig. 7. SEM photographs of edge-on profiles of the fracture surfaces of LiTaO_3 films crystallized at 500°C

It was found that the following two factors affected the morphologies of these crystalline films. The first concerns the rapid hydrolysis reaction during heating; alkoxy-derived Li-Ta-O films on substrates must be hydrolyzed quickly by water vapor in the mixed gas flow and precipitates must grow during heating. The second factor concerns anisotropic thermal expansions of LiTaO_3 . The a-axis of LiTaO_3 elongates and the c-axis contracts with temperature. The film on sapphire (012) substrates does suffer anisotropic stress, resulting in granular structure for the stress release.

The thickness of these crystallized films was uniform and can be controlled by the concentration of the solutions, the speed of withdrawing substrates, and repeating the dip-coating procedure. The composition of the film was very homogeneous in the directions perpendicular to and along the surface of the film, and also can be controlled by adjusting the ratio of metal alkoxide of Nb and Ta in the starting alkoxide solutions.

CONCLUSIONS

Crystalline and composition-controlled, homogeneous $\text{Li}(\text{Nb}, \text{Ta})\text{O}_3$ films can be prepared from double alkoxide solutions. Water for the partial hydrolysis of the solution affected the properties of the precursor solutions and the morphologies of the films. Water vapor during heat treatment exhibits a remarkable effect on lowering the crystallization temperatures below 500°C by promoting the conversion and elimination of the residual organic groups in the alkoxy-derived films. $\text{Li}(\text{Nb}, \text{Ta})\text{O}_3$ films which crystallized on sapphire substrates showed preferred orientation according to each orientation such as (012), (110) and (001), of the sapphire substrates, while the preferred orientation could not be observed on Si substrates.

Figure 8 illustrates a proposed chemical process for LiNbO_3 -based optical waveguide fabrication with a comparison to the conventional process. Chemical process offers a simpler and lower temperature fabrication technique. Chemical processing of $\text{Li}(\text{Nb}, \text{Ta})\text{O}_3$ films will be applied to the hybrid device systems of SAW and electro-optics.

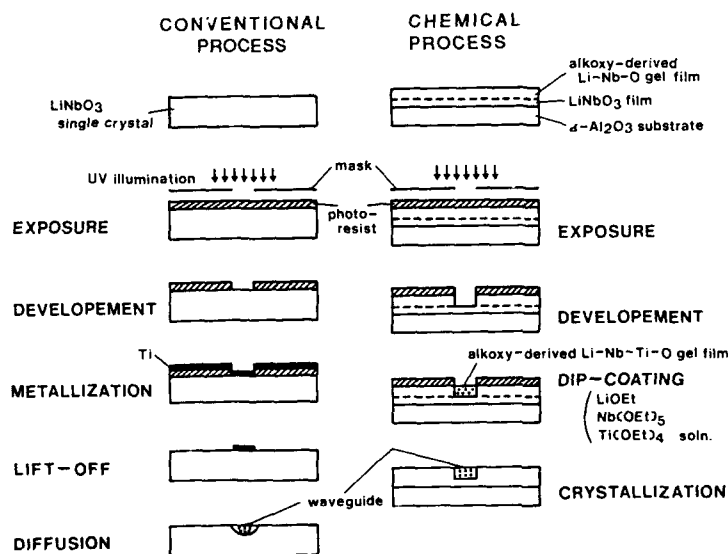


Fig. 8. Optical waveguide fabrication

REFERENCES

1. S. Hirano and K. Kato, Adv. Ceram. Mat. 2, 142 (1987)
2. S. Hirano and K. Kato, J. Non-Cryst. Solids 100, 538 (1988)
3. S. Hirano and K. Kato, Adv. Ceram. Mat. 3, 503 (1988)
4. S. Hirano and K. Kato, Bull. Chem. Soc. Jpn. 62, 429 (1989)
5. M.I. Yanovskaya, et al., J. Mater. Sci. 23, 395 (1988)
6. D.J. Eichorst and D.A. Payne, to be published in Better Ceramics Through Chemistry III, (1988)
7. Y. Suwa, et al., J. Japn. Soc. Powd. Metall. 28, 28 (1981)
8. N.P. Castaings, et al., Mat. Res. Bull. 22, 261 (1987)
9. T. Furusaki, et al., J. Ceram. Soc. Jpn. 95, 209 (1987)

SINGLE CRYSTAL ZIRCONIA THIN FILMS FROM LIQUID PRECURSORS

K. T. MILLER AND F. F. LANGE

Department of Materials, University of California, Santa Barbara, CA 93106

ABSTRACT

Epitaxial, single-crystal films of ZrO_2 (Y_2O_3) were formed on (100) oriented single crystal substrates of ZrO_2 (9.5 mol% Y_2O_3) using water-based solutions of zirconium acetate and yttrium nitrate as a precursor. Film compositions of ZrO_2 (0 - 40 mol% Y_2O_3) were examined; since the lattice parameter of ZrO_2 (Y_2O_3) increases with yttria content, the lattice mismatch was systematically varied to a maximum of 1.5%. Precursor films were deposited by spin coating, pyrolyzed, and held for 1 hour at 900°C, 1000°C, and 1100°C. X-ray diffraction showed that a strongly oriented film had developed after pyrolysis of the precursor. In addition, all samples, except those treated at 1100°C containing 6 - 15 mol% Y_2O_3 , gave (111) peaks, indicating film polycrystallinity. Electron back-scattering patterns showed that epitaxial single crystals were formed at 1100°C for films containing 3 - 20 mol% Y_2O_3 . Scanning electron microscopy showed that the epitaxial films had a porous structure. These results indicate that the epitaxy is a two-stage process: oriented nucleation upon pyrolysis, followed, for low mismatches, by subsequent consolidation into a single-crystal film above 1000°C.

1. INTRODUCTION

Liquid precursors (for example, solutions of alkoxides, acetates, nitrates, or citrates) offer several advantages in the synthesis of ceramics. Liquid precursors permit easy and precise control over composition, intimate mixing of the constituent elements, and relatively low processing temperatures.

Liquid precursor methods are especially suited to the formation of thin films. Recent work has examined the formation of thin films in the ZrO_2 - Y_2O_3 binary system using zirconium acetate / yttrium nitrate precursor solutions.^{1,2} Uniform thin films were formed by spin-coating the precursor on sapphire substrates; the precursor films were then pyrolyzed to form the oxide. The polycrystalline films, initially porous and very fine grained, were completely densified with further heat treatment.

Partlow and Gregg³ have produced homoepitaxial films of LiNbO_3 using metal alkoxide precursors. Preliminary observations indicated that homoepitaxial films of ZrO_2 (9.5 mol% Y_2O_3) could likewise be formed from zirconium acetate / yttrium nitrate precursor solutions. In this study, we systematically investigate the formation of these epitaxial yttria-zirconia layers as a function of film composition and processing conditions to better understand the mechanisms of this epitaxial process.

2. EXPERIMENTAL PROCEDURE

ZrO_2 films, containing between 0 and 40 mol% Y_2O_3 , were deposited on single crystal, (100) oriented, cubic ZrO_2 (9.5 mol% Y_2O_3) substrates (Ceres Corporation, North Bellerica, MA), by spin coating water-based solutions of zirconium acetate (Magnesium Elektron, Inc., Flemington, NJ) and yttrium nitrate (Aesar, Johnson Matthey Inc., Seabrook, NH). The precursor solutions were mixed from stock solutions of yttrium nitrate (50 w% in water) and as-received zirconium acetate (40 w% in water). Samples were spun at 5000 rpm for 30 s, producing final oxide films with thicknesses of 100 - 150 nm. The samples were pyrolyzed and heat treated at 900°C, 1000°C, and 1100°C for 1 h. Selected experiments were also performed using a heat treatment temperature of 500°C. The thin films were analyzed using x-ray diffraction, electron back-scattering patterns,⁴ and scanning electron microscopy.

Since the Y^{+3} ion is larger than the Zr^{+4} ion, the lattice parameter of cubic ZrO_2 increases with the content of Y_2O_3 . The expected lattice parameter of cubic ZrO_2 as a function of $\text{YO}_{1.5}$ content, based upon the measurements of Scott,⁵ is shown in Figure 1. The percentage lattice mismatch with a ZrO_2 (9.5 mol% Y_2O_3) substrate is also shown. By varying the film composition, lattice mismatches of over 1.5% can be obtained.

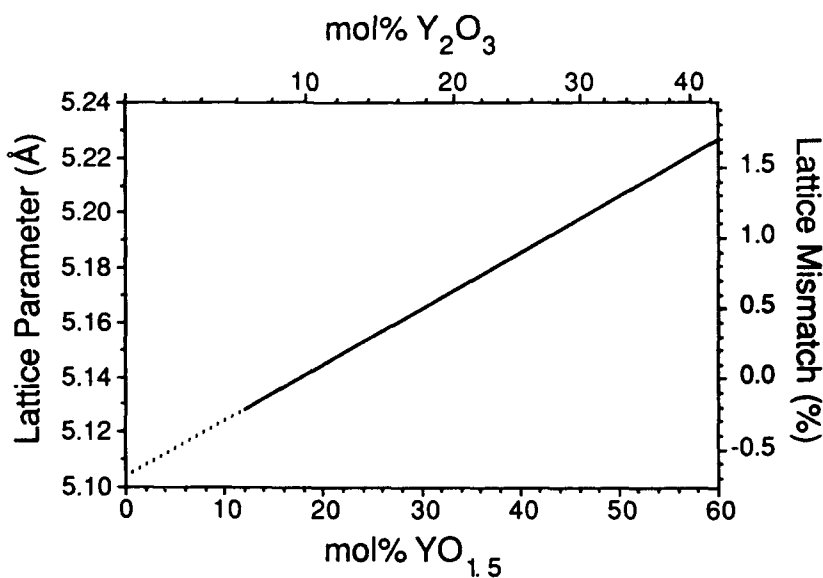


Figure 1. Lattice parameter of cubic ZrO_2 (Y_2O_3) as a function of yttria content, based upon the data of Scott.⁵ The dotted region is an extrapolation of the data. The lattice mismatch is calculated assuming a ZrO_2 (9.5 mol% Y_2O_3) substrate.

3. RESULTS

X-ray Diffraction

X-ray diffraction cannot directly determine when thin films are epitaxial single crystals; it can, however, detect polycrystallinity and preferred orientation. In powder diffraction patterns of cubic ZrO_2 , the (111) peak is most intense, while the (200) peak is normally 15% of the maximum intensity. If the films are polycrystalline, the (111) peak should be detected. If the films have preferred orientations matching the (100) substrate, only diffraction peaks of type ($h00$), h even, should be observable. The (200) peak would therefore be the most intense peak in oriented samples. Detection of the (200) film peak is complicated by overlap of the (200) substrate peak. Recalling Bragg's Law, $n\lambda = 2d \sin \theta$, the (200) film peaks should nevertheless be detectable in lattice mismatched samples.

The samples that exhibited polycrystallinity, as determined by the detection of (111) diffraction peaks, are summarized in the chart of Figure 2. All samples heat treated below 1100°C exhibit some polycrystallinity. Of those treated at 1100°C , only the closely lattice-matched samples show no polycrystallinity. All of the films are, nevertheless, strongly oriented. As an example, Figure 3 shows the x-ray diffraction pattern of a ZrO_2 (25 mol% Y_2O_3) film in the region of the (200) peaks. This film was pyrolyzed and held for 1 h at 500°C , a temperature just above the completion of the pyrolysis.⁶ The (200) film peak, which is clearly distinguished from the substrate peak, gives an intensity 100 times greater than the (111) peak, indicating very strong orientation in the film. All of the lattice mismatched samples display this orientation, strongly suggesting that film orientation develops during pyrolysis.

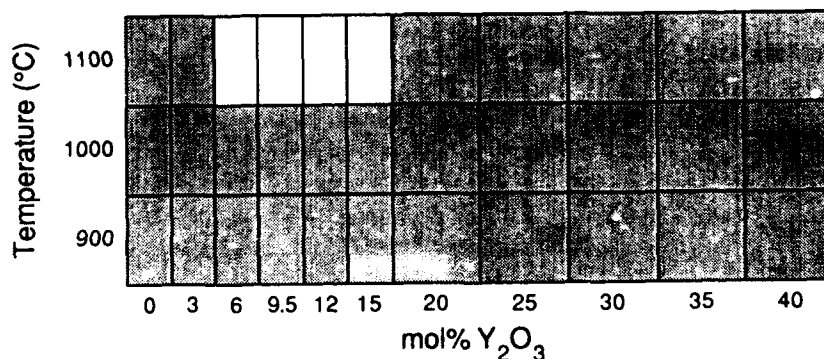


Figure 2. Summary of x-ray diffraction data. Shaded area signifies detection of (111) film peaks, indicating polycrystallinity.

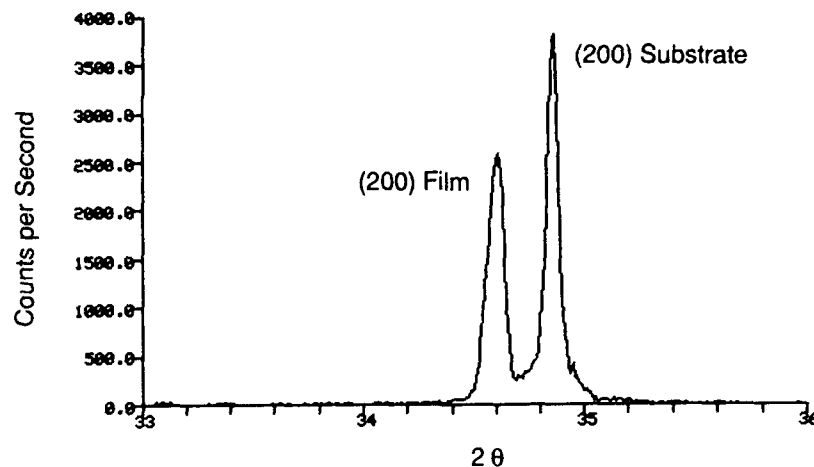


Figure 3. X-ray diffraction pattern of a ZrO_2 (25 mol% Y_2O_3) film, heat treated at 500°C for 1 hour, showing that the strong orientation of the film is present immediately after pyrolysis. While normally the strongest in ZrO_2 , the (111) peak of the film (not shown) is only approximately 1% of the intensity of the (200) film peak.

Electron Back-Scattering Patterns

Electron back-scattering patterns (EBSP)⁴ can be used to obtain crystallographic information in the scanning electron microscope. EBSP is a relatively surface sensitive technique, yielding information from the top 20 nm of the sample. The lateral resolution is limited by the beam interaction volume, giving a maximum resolution of approximately $0.2 \times 1.0 \mu\text{m}$.

EBSP can directly verify when thin films are epitaxial single crystals. If the films are single crystals, the same pattern should be observed over wide areas of the film. If the films are epitaxial, the film pattern should show the same orientation as the substrate. Results for the ZrO_2 (9.5 mol% Y_2O_3) film are shown in Figure 4. At 900°C , no pattern is detected from the film; although the film is highly oriented (as shown by the x-ray diffraction data), the top surface of the film has not developed into a single crystal. At 1100°C , a good EBSP pattern was observed, showing that the film has developed into an epitaxial single crystal.

The samples which have developed epitaxial single-crystal films are shown in the chart of Figure 5. The results agree well with the x-ray diffraction data. No films were single crystal below 1100°C . At 1100°C , only the films with the lowest mismatches developed into epitaxial single crystals. (The samples containing 0 and 25 mol% Y_2O_3 showed some regions which yielded patterns and some which did not.)

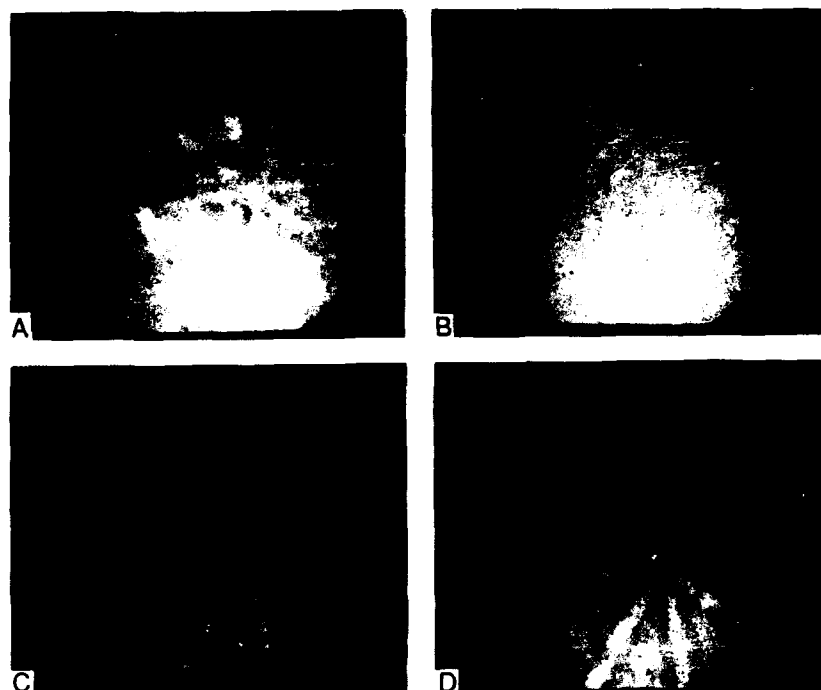


Figure 4. EBSD patterns of substrate and films, for 900°C and 1100°C. a) 900°C substrate. b) 900°C film. No pattern detectable. c) 1100°C substrate. d) 1100°C film. The pattern matches the substrate over large film areas, indicating an epitaxial single crystal has formed.

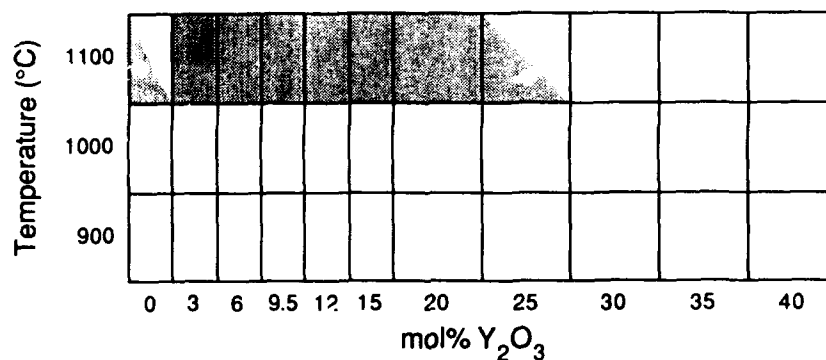


Figure 5. Summary of EBSD data. Shaded area signifies the detection of a film pattern that matches the substrate pattern, indicating epitaxial single crystals have formed. Half-shaded boxes signify that some areas of the film produced patterns, while others did not.

Scanning Electron Microscopy

Figure 6 shows an SEM micrograph of a ZrO_2 (9.5 mol% Y_2O_3) film, heat treated at 1200°C for 1 h. The film displays a porous microstructure, presumably developed during the initial pyrolysis of the precursor film.

4. DISCUSSION

The data suggest a two stage process for the formation of epitaxial single crystals, shown schematically in Figure 7. During the pyrolysis, the region of the film in contact with the substrate becomes strongly oriented, as indicated by x-ray diffraction. The top of the film, however, develops very fine polycrystallinity, as indicated by the EBSD results. At high temperature and low lattice mismatch, the polycrystalline regions are consumed by the oriented regions of the film, presumably by a grain growth process, producing epitaxial single crystal films with a porous microstructure.

5. CONCLUSION

Porous epitaxial thin films of ZrO_2 (Y_2O_3) were formed using zirconium acetate / yttrium nitrate precursor solutions. The formation of the single crystal films is a two stage process. There is an oriented nucleation of the film during pyrolysis of the precursor, followed by a coalesce into single crystal films at higher temperatures for low lattice mismatches.

ACKNOWLEDGEMENT

This work was supported by the Air Force Office of Scientific Research, under Contract Number AFOSR-87-0291.

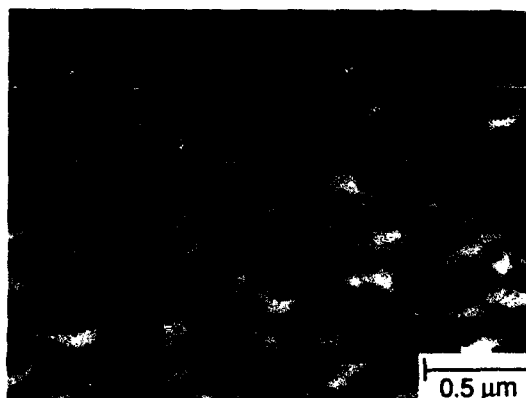


Figure 6. Porous microstructure of a single crystal film of ZrO_2 (9.5 mol% Y_2O_3), heat treated for 1 hour at 1200°C .

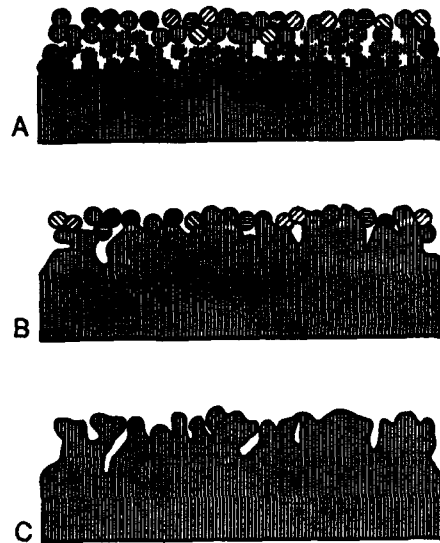


Figure 7. Schematic illustration of the two-stage epitaxial process. a) Oriented nucleation of the film region contacting the substrate, together with homogeneous nucleation of the top of the film. b,c) Substrate grows through polycrystalline region, producing porous single crystal film.

REFERENCES

1. K. T. Miller, F. F. Lange, and D. B. Marshall, p. 823-830 in *Better Ceramics Through Chemistry III*, edited by C. J. Brinker, D. E. Clark, and D. R. Ulrich, Materials Research Society (1988).
2. K. T. Miller, F. F. Lange, and D. B. Marshall, submitted to *J. Mater. Res.*
3. D. P. Partlow and J. Gregg, *J. Mater. Res.* **2** (5) 595-605 (1987).
4. D. J. Dingley, *Scanning Electron Microscopy/1984/III* 569-575 (1984).
5. H. G. Scott, *J. Mater. Sci.* **10** 1527-35 (1975).
6. M. E. Khavari, F. F. Lange, P. Smith, and D. B. Marshall, p. 617-621 in *Better Ceramics Through Chemistry III*, edited by C. J. Brinker, D. E. Clark, and D. R. Ulrich, Materials Research Society (1988).

TWO-DIMENSIONAL PROCESSING FOR NOVEL FUNCTIONS

HIROAKI YANAGIDA

Research Center for Advanced Science and Technology
University of Tokyo
Tokyo, Japan

INTRODUCTION

Since many interesting and novel phenomena arise from non-linear interactions between two or more different materials with opposite properties, e.g., acid vs. base, p-type vs. n-type semiconduction, reducing vs. oxidizing, host vs. guest, conducting vs. insulating, etc., it is very important to design or set the fields where the non-linear interactions take place. This is a very important aspect of materials design. The most interesting and probably most understandable study field for non-linear interactions is interfaces. Since design of interfaces is called "two-dimensional" design [1], and processing is necessary after design, processing may therefore be called "two-dimensional processing" for novel functions.

Interfaces at two-dimensional structures are classified into groups based on categories such as same or different materials, open or closed, perpendicular or parallel action in the phenomenon, etc. These categories are summarized in Table I. Closed interfaces are familiar to us.

Table I. Classification of Various Two-Dimensional Structures

CATEGORY		
INTERFACE OR SURFACE		
CLOSED OR OPEN		
BETWEEN SAME OR DIFFERENT MATERIALS		
and		
PHENOMENA OCCURRING PERPENDICULARLY OR ALONGSIDE		
TYPE OF TWO-DIMENSIONAL STRUCTURE AND NOTATION		
GRAIN BOUNDARY	INTERFACE, CLOSED, SAME	GBp, GBa
HETERO-JUNCTION	INTERFACE, CLOSED, DIFFERENT	HJp, HJa
NECK	INTERFACE, OPEN, SAME	NKp, NKa
HETERO-CONTACT	INTERFACE, OPEN, DIFFERENT	HCp, HCa
SURFACE	SURFACE, OPEN, DIFFERENT	SFp, SFa
p = perpendicular		
a = alongside		

A closed interface between the same material is a grain boundary. A closed interface between different materials is a junction if its phenomenon takes place across the interface. A phenomenon taking place along the closed interface between different materials may not necessarily be well known. Enhanced ionic migration is observed when insulating powders are introduced into the matrix of an ionic conductor. The mechanism is analyzed as rapid ionic migration along the interface [2]. Open interfaces are the interfaces where there are some contact points and channels for chemical species along the interface. When a phenomenon across the interface is measured, the phenomenon may be modified with a migration of chemical species around the contact points. Open interfaces are, therefore, excellent candidate structures for chemical sensors. There is, however, a big difference between interfaces with the same materials and interfaces with different materials. As will be discussed later, open interfaces between different materials are promising for setting intelligence to inorganic materials [3].

Some typical structures and phenomena related to the respective structure are discussed below.

Closed interface between same materials

Phenomena taking place across the interface, GBp, are observed on the high thermal conductivity in SiC with a small amount of BeO additive; non-linear voltage vs. current characteristics in ZnO varistor; PTC effect in semiconducting barium titanate ceramics, etc.

The most typical phenomenon occurring along the interface, GBa, is grain boundary diffusion, which is very important during sintering or processing.

Open interface between the same materials

In a zinc oxide gas sensor, the conductivity change (with a trace of flammable gaseous species) is due to the change in barrier height across the interface, which changes with atmosphere. This structure is also used for a humidity sensor in porous ceramics. The structure is designated as NKp.

Open interface between different materials

There are two typical cases when open interface phenomena occur in the structure as shown in Figure 1. They are very important for chemical sensors [3-10]. Phenomena taking place across the open interface, IICp, are important in chemical sensors with intelligence [3-9]. The voltage vs. current characteristics with humidity across the open interface between CuO and ZnO are shown in Figure 2. Selective detection of carbon monoxide gas using the same combination is shown in Figure 3. These phenomena are considered to take place with an electric charge transfer from a p-type semiconductor to chemisorbed species on the p-type semiconductor surface and the chemisorbed species on an n-type semiconductor around the contact points. Finally, the charge of chemisorbed species on the n-type semiconductors is compensated by combining a negative charge from the n-type semiconductor electrode. If the chemisorbed species are water molecules, an electrolysis takes place; and in the case of selective

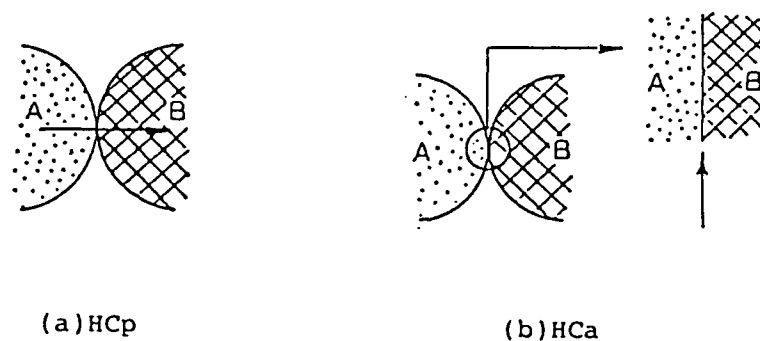


Figure 1. Open interface between different materials; phenomenon taking place across (a) and along (b).

detection of carbon monoxide, evolution of carbon dioxide takes place through the chemical reaction accompanied with electron transfer. The reaction and sensitivity to respective gaseous species are controlled by applied bias as shown in Figure 3b.

The electric current change along the open interface between different materials occurs for humidity sensors with the combination of base and acid [10].

INTRODUCTION OF INTELLIGENT MECHANISMS BY THE OPEN INTERFACE BETWEEN DIFFERENT MATERIALS

If the materials can have intelligent mechanisms such as self-recovery, stand-by, self-adjustment, and tunability from outside, we are able to obtain materials performances. We can then avoid the so-called spaghetti syndrome. The benefits of these intelligent mechanisms are discussed in Refs. 3 and 11.

If we look at the CuO/ZnO open interface or hetero contact from the viewpoint of the humidity sensor mechanism compared with the humidity sensor made of porous ceramic semiconductors, we see intelligence in the former. This is summarized in Table II. The working mechanism of humidity sensors with hetero contact types is accompanied by electrolysis of water. The contact points are always kept fresh for adsorption of water, while the humidity sensor with porous ceramic semiconductor only measures conductivity change with humidity. Humidity change is not necessarily consistent with the amount of adsorbed water, since it needs some time to achieve equilibrium for the porous type. Sometimes we need the so-called cleaning treatment. For details concerning other points of intelligence, Ref. 3 should be consulted. Using a combination of p-type silicon and n-type silicon, one can distinguish the type of solvents [6].

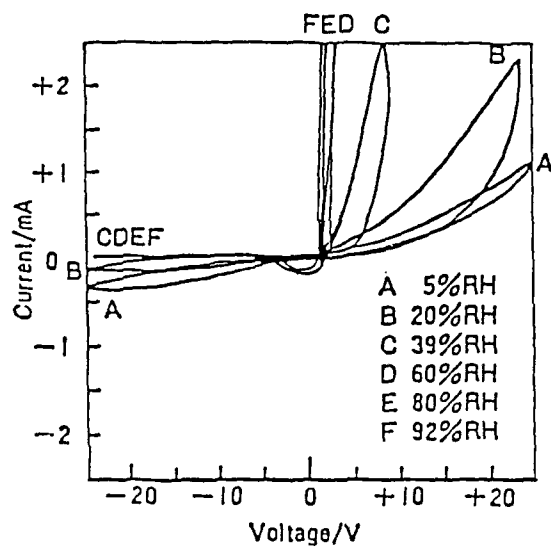


Figure 2. Change in voltage vs. current characteristic with humidity on CuO/ZnO hetero-contact [6].

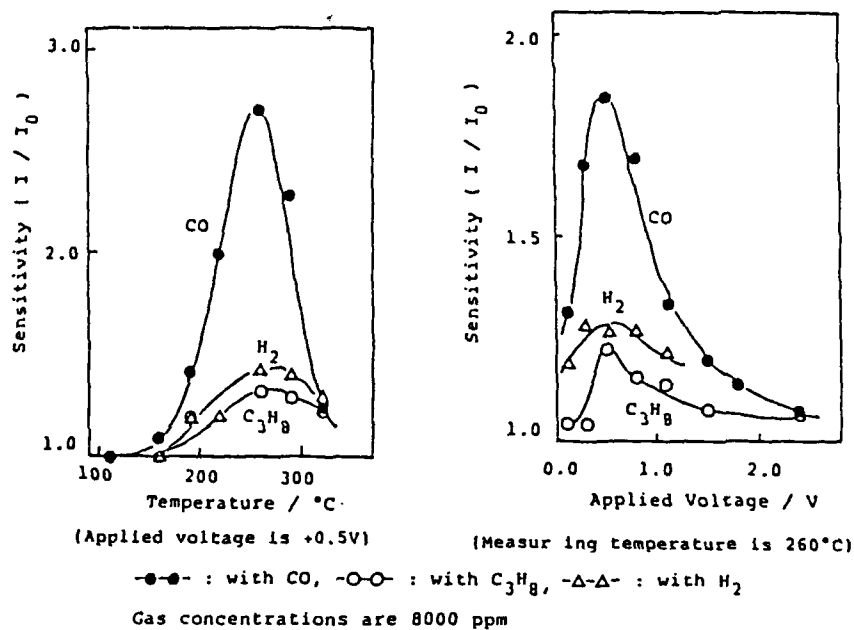


Figure 3. Selective monitoring to carbon monoxide with CuO/ZnO hetero-contact [7]; (a) the temperature dependence of the gas sensitivity of CuO/ZnO hetero-contact; (b) the relation between the gas sensitivity and the forward bias voltage in CuO/ZnO hetero-contact.

Table II. Comparison of Two Types of Humidity Sensor from the Viewpoint of Intelligent Material

	POROUS ZINC OXIDE	CuO/ZnO CONTACT
STRUCTURE	OPEN INTERFACE BETWEEN IDENTICAL MATERIALS, NKp	OPEN INTERFACE BETWEEN DIFFERENT MATERIALS, HCp
MEASUREMENT	CONDUCTIVITY CHANGE	VOLTAGE/CURRENT CHARACTERISTIC
MECHANISM	PROTON MIGRATION THROUGH ADSORBED WATER NEAR NECKS	ELECTROLYSIS OF ADSORBED WATER NEAR CONTACTS
HYSTERESIS	CAUSES PROBLEMS	NONE; NO PROBLEMS
CLEANING	NECESSARY	NOT NEEDED; WORKING MECHANISM ITSELF GIVES CLEANING
SELF-RECOVERY	INEFFECTIVE; FREQUENT CLEANING TREATMENT NECESSARY	EFFECTIVE

REFERENCES

1. H. Yanagida, *Kagaku to Kogyo*, **39** (11) 831 (1986).
2. S. Fujitu, K. Koumoto, and H. Yanagida, *Solid State Ionics*, **18/19** 1147 (1986).
3. H. Yanagida, *Angewandte Chemie*, **100** (10) 1443 (1988).
4. H. Yanagida, *Seramikkusu (Bull. Ceram. Soc. Jpn.)*, **19** (5) 417 (1984).
5. K. Kawakami and H. Yanagida, *Yogyo Kyokai Shi (J. Ceram. Soc. Jpn.)*
6. H. Yanagida and Y. Nakamura, presented at the 87th Annual Meeting of the American Ceramic Society, 4E85, Cincinnati, May 6, 1985; Y. Toyoshima, M. Miyayama, H. Yanagida, and K. Koumoto, *Jpn. J. Appl. Phys.*, **22** 1933 (1983); Y. Nakamura, M. Ikejiri, M. Miyayama, K. Koumoto, and H. Yanagida, *J. Chem. Soc. Jpn.*, **1985** (6) 1154 (1985).
7. Y. Nakamura, T. Tsurutani, M. Miyayama, O. Okada, K. Koumoto, and H. Yanagida, *J. Chem. Soc. Jpn.*, **1987** (3) 477 (1987).

8. H. Yanagida, *Bull. Chem. Soc. Jpn.*, 39 (11) 257 (1986).
9. Y. Nakamura, M. Miyayama, H. Yoshioka, H. Yanagida, T. Tsurutani, and Y. Nakamura, submitted to *J. Electrochem. Soc.*, February 1989.
10. K. Kubota, Y. Nakamura, M. Miyayama, and H. Yanagida, *J. Ceram. Soc. Jpn.*, 96 (9) 958 (1988).
11. H. Yanagida, Overview lecture, U. S., India, and Japan Joint Symposium on Electronic Ceramics, January 16, 1989, Pune, India.

PROCESSING AND THE MICROSTRUCTURE OF SrTiO_3 -BASED BL CAPACITORS USING $\text{Pb}(\text{Fe,W})\text{O}_3$ FERROELECTRICS

MAKOTO KUWABARA

Department of Applied Chemistry, Faculty of Engineering,
Kyushu Institute of Technology, Tobata, Kitakyushu, 804 Japan

ABSTRACT

A preliminary experiment was conducted to prepare semiconducting strontium titanate-based internal barrier layer capacitors with ferroelectric $\text{Pb}(\text{Fe,W})\text{O}_3$ forming insulating layers along the grain boundaries. Processing, microstructure and the dielectric properties of this new type of BL capacitors are described. The idea to obtain this type of BL capacitors with a very high dielectric constant may be realized when the ferroelectric materials can uniformly be diffused along the grain boundaries by using a more sophisticated processing of the second firing.

INTRODUCTION

There have been many studies on semiconducting strontium titanate, SrTiO_3 (STO)-based internal barrier layer (BL) capacitors to obtain materials with high-performance dielectric properties, i.e., high apparent dielectric constant, low dissipation factor, and small temperature coefficient of dielectric constant. The microstructure of STO-based BL capacitors with high apparent dielectric constants may substantially be described as semiconducting large STO grains separated by thin insulating layers, which are responsible for providing the materials with high apparent dielectric constants, consisting mainly of $\text{PbO-Bi}_2\text{O}_3\text{-B}_2\text{O}_3$ glasses. The procedure for preparing STO-based BL capacitors with such appropriate microstructures has entirely been established so that it is now quite easy to produce BL capacitors with an apparent dielectric constant of more than 40,000 and $\tan\delta < 1\%$. Thus, new types of BL capacitors made by novel processings under new concepts of materials design are needed today.

To that end, a preliminary experiment was conducted in an attempt to produce a new type of STO-based BL capacitor with ferroelectric $\text{Pb}(\text{Fe}_{2/3}\text{W}_{1/3})\text{O}_3$ (PFW) along the grain boundaries to form thin insulating layers having a much higher dielectric constant than that of $\text{PbO-Bi}_2\text{O}_3\text{-B}_2\text{O}_3$ glasses normally used as forming the second-phases in the conventional STO-based BL capacitors. This paper is concerned with the processing, microstructures, and the electrical and dielectric properties of the present STO-based (STO-PFW) BL capacitors prepared in this study.

EXPERIMENTAL

STO-PFW BL capacitors were prepared using basically the same procedure as described in the literature [1-3] except that PFW was used as the second-phase material to form grain boundary insulating layers. Semiconducting STO ceramics were made by sintering powder compacts mixed with commercially obtained STO powders*, Nb_2O_5 and TiO_2 at 1450°C for 3h in a 5% H_2 - N_2 ambient gas. The obtained STO ceramics had relative sintered densities of 83 to 90%. PFW ferroelectric materials to be diffused into STO ceramics were, on the other hand, prepared by firing a mixture of PbO , Fe_2O_3 , and WO_3 (3:1:1 in mol ratio) at 870°C for 2h in air; then the obtained PFW powders were mixed with ethyl cellulose to make a PFW paste. A second firing of STO ceramics coated with the PFW paste was carried out at 1160°C 1h in air to let PFW diffuse into the STO samples along the grain boundaries.

Electrical measurements were conducted on the obtained STO-PFW BL capacitors with In-Ga alloy electrodes rubbed on both of their surfaces at room temperature down to about 120K, where the resistivity, dielectric constant, and dissipation factor of the capacitors were measured.

Examination of the microstructures of the obtained BL capacitors and analysis of the second-phases present at the grain boundaries of the materials were made using X-ray microanalysis (XMA).

RESULTS AND DISCUSSION

Electrical Resistivity

Figure 1 shows the electrical resistivities of both semiconducting STO and insulating PFW ceramics obtained at room temperature down to 150K. The resistivity of the PFW ceramic below 230K was too high to be measured with the instruments used in the experiment. From this figure it may be concluded that the resistivity of the PFW ceramics is more than 10^{10} times as high as that of semiconducting STO grains, so that the resistivity of STO-PFW BL capacitors should be reflected by that of the PFW second-phase forming grain boundary layers (if this is true) even if the thickness of the grain boundary layers is 1/1000 to 1/10,000 times smaller than the diameter of the STO grains.

The resistivity-temperature characteristic obtained for a STO-PFW BL capacitor, however, as shown in Fig. 2, is found to be considerably different from that expected from the data in Fig. 1. A decrease in resistivity below about 170K seen in the figure seems quite curious, considering the NTCR (negative temperature coefficient of resistivity) characteristics in the temperature dependence of resistivity usually observed in insulators or semiconductors. Although the mechanism of the phenomenon cannot be explained as yet, it may be connected with the ferroelectric phase transition of PFW. Another point is that the resistivity of the PFW ceramic showed a change of more than two decades in the temperature range of only 270 to 230K, while that of the STO-PFW BL capacitor prepared here showed only a small variation within one decade in a wider temperature range of 270 to 150K. This resistivity-temperature characteristic may be interestingly compared with the dielectric constant-temperature characteristic obtained for the same sample, which will be shown later. The resistivity of the STO-PFW BL capacitor shown in Fig. 2 does not seem high enough for practical use, but one may expect that this would be improved by the use of certain additives effective to increase the resistivity of the materials.

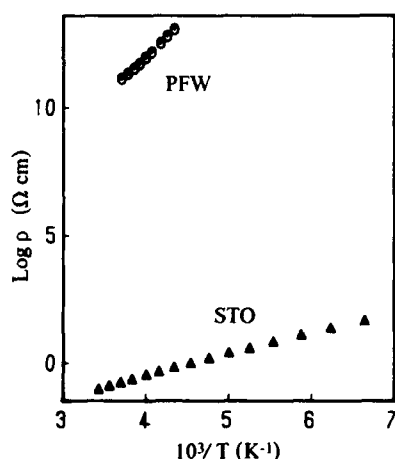


Fig. 1. Arrhenius plots of the resistivities obtained for STO and PFW ceramics.

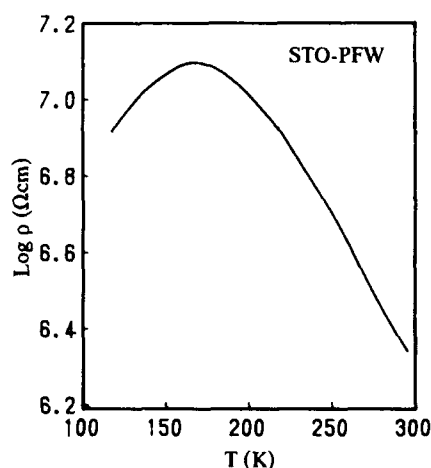


Fig. 2. The resistivity-temperature characteristic obtained for a STO-PFW BL capacitor prepared in this study.

Dielectric Properties

Figures 3 and 4 show the temperature dependences of apparent dielectric constant and $\tan \delta$, respectively, obtained at various frequencies for the same STO-PFW BL capacitor as used for the resistivity measurement. From these figures one may confirm that the BL capacitor prepared using the new processing certainly has a large apparent dielectric constant up to 100,000 at 1 kHz, which is accompanied by a significant large $\tan \delta$ as well. Distinct anomalous peaks in the dielectric constant-temperature characteristics, shown in Fig. 3, which are considered to be connected with the ferroelectric phase transition of PFW, can be seen in the temperature range of 160 to 190K. These anomalies show a decrease in magnitude with a shift of their peak temperature to higher temperatures with increasing frequency. One may also recognize that the dielectric constant of this material shows a significant decrease with increasing frequency over the whole temperature range of the measurement. These features of the dielectric constant of this material may indicate the existence of significant dispersions of dielectric constant. This is evidently demonstrated by the data given in Fig. 4, in which $\tan \delta$ of the sample was plotted as a function of temperature but not frequency, for one may find dispersions by replotting the $\tan \delta$'s of Fig. 4 as a function of frequency at any constant temperatures in the figure. It may also be interesting to note that peaks of $\tan \delta$ seen in Fig. 4 shift to higher temperatures with an increase in frequency, just coincident with the feature of the peak of dielectric constant seen in Fig. 3.

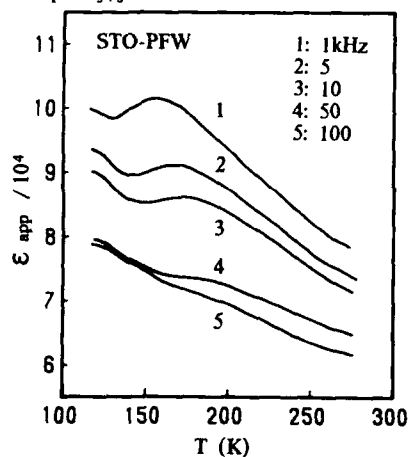


Fig. 3. Temperature dependences of dielectric constant obtained for the STO-PFW BL capacitor at various frequencies.

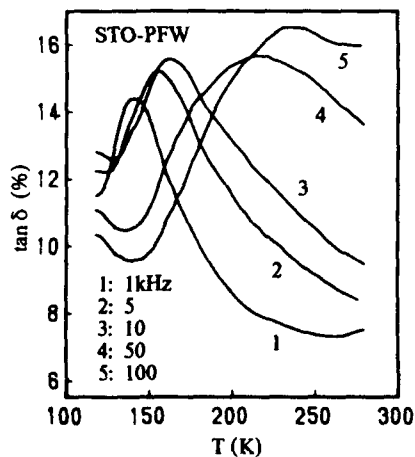


Fig. 4. Temperature dependences of $\tan \delta$ obtained for the STO-PFW BL capacitor at various frequencies.

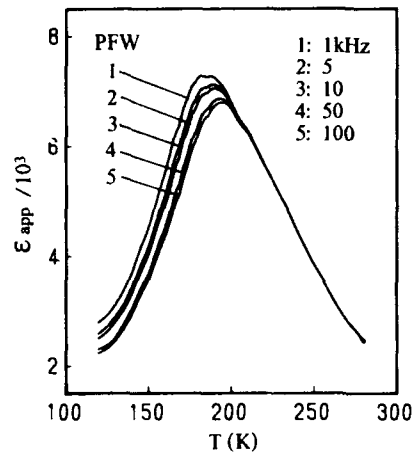


Fig. 5. Temperature dependences of dielectric constant obtained for a PFW ceramic at various frequencies.

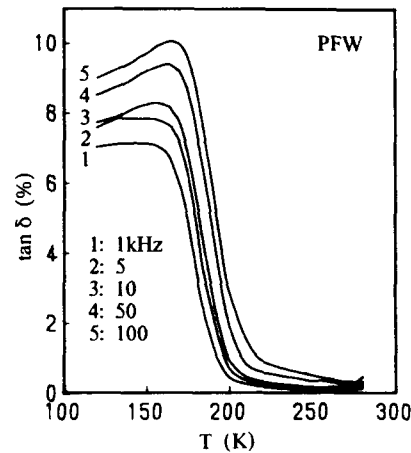


Fig. 6. Temperature dependences of $\tan \delta$ obtained for the PFW ceramic at various frequencies.

These dielectric properties of the STO-PFW BL capacitor, given in Figs. 3 and 4, may be evaluated by comparing them with those of a PFW ceramic, which are shown in Figs. 5 and 6. Temperature dependences of dielectric constant and $\tan \delta$ obtained for the PFW ceramic show typical ones of ferroelectrics with a dielectric constant peak around 180 K, which is the Curie point of PFW, and an abrupt change of $\tan \delta$ in the same temperature range due to the ferroelectric phase transition. Consideration based on these dielectric properties of the PFW ceramic may suggest that the dielectric properties of the present STO-PFW BL capacitor are characterized by a space charge-caused dispersion. Large space charge polarization is expected to exist at the interfaces between semiconducting STO grains and insulating PFW grain boundary layers; it is also expected to enhance both the dielectric constant and $\tan \delta$ of the material with their characteristic temperature dependences. Since space charge polarization is considered to be strongly microstructural dependent, analytical consideration on the microstructure of the BL capacitors is necessary to improve the dielectric properties of the materials.

Microstructure

Figure 7 shows compositional and XMA images of constituent elements of a STO-PFW BL capacitor prepared in this study. From XMA images of the elements of Pb, Fe and W, one may recognize that the second phase present at the grain boundaries does not consist of PFW only but is multiphase with various compositions inclusive of the PFW composition in the Pb-Fe-W system. The microstructure of this kind in the BL capacitors is considered to be a major factor causing large dispersions of dielectric constant and $\tan \delta$. To obtain STO-PFW BL capacitors with high-performance dielectric properties, therefore, a more sophisticated processing of the second firing is needed to diffuse PFW into STO ceramics along the grain boundaries without the formation of any phases different from PFW during the process of diffusion.

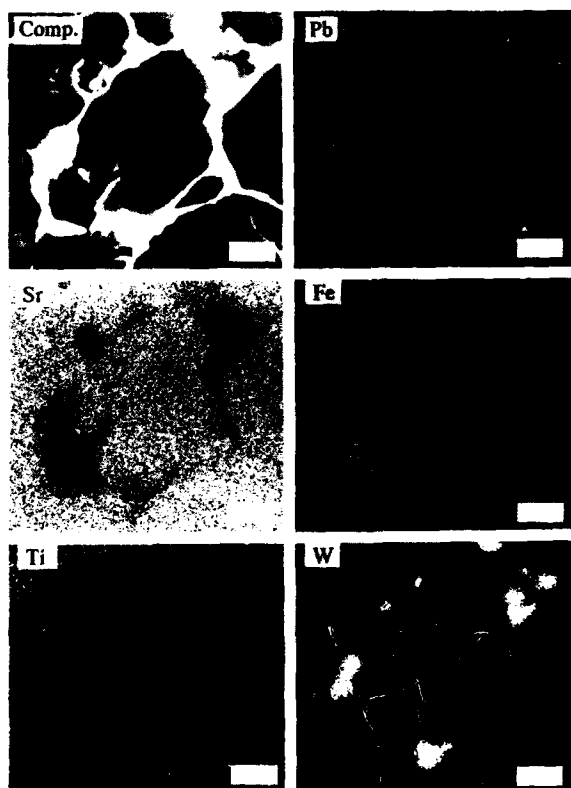


Fig. 7. Compositional and XMA images of the STO-PFW BL capacitor prepared in this study. (Bars=10 μm).

CONCLUSION

Results obtained in the present study may be summarized as follows:

1. A preliminary experiment to prepare a new type of BL capacitor based on semiconducting STO ceramics with insulating PFW grain boundary layers was conducted.
2. The obtained STO-PFW BL capacitors showed large apparent dielectric constant and $\tan\delta$ with significant dispersion, which may be due to space charge polarization.
3. A more sophisticated processing of the second firing is needed to produce BL capacitors with such microstructures as described by semiconducting STO grains surrounded only by the PFW second phase.

References

1. R. Wernicke, in *Advances in Ceramics I, Grain Boundary Phenomena in Electronic Ceramics*, Ed. by L.M. Levinson (Am. Ceram. Soc., 1981) pp. 261-271.
2. M. Fujimoto and W.D. Kingery, *J. Am. Ceram. Soc.*, **68**, 169 (1985).
3. N. Yamaoka, *Ceram. Bull.*, **65**, 1149 (1986).

* Kyoritsu Ceramic Materials Co. Ltd., Nagoya, Japan: ST.HP1.

PART IV

**Plasma-Assisted Processing
and Novel Composites**

Plasma-Assisted Chemical Vapor Deposition of Ceramic Films and Coatings

Robert F. Davis

North Carolina State University, Department of Materials Science and Engineering,
Raleigh, NC 27695-7907

Abstract

Plasma-assisted chemical vapor deposition uses energetic electrons to decompose reactant gas molecules into more simple and more highly reactant species to achieve deposition of amorphous and crystalline films and coatings at reduced temperatures. The basis of this technique, as well as the deposition conditions and properties of several ceramic films including Al_2O_3 , TiO_2 , ZnO , AN , BN , TiN , SiC , Si , GaAs , SiC , C (diamond) and GaN , are briefly described. Modifications of the classical immersed method, including remote plasmas, the use of microwave frequencies and electron cyclotron resonance techniques, are also described with material examples.

Introduction

The term "plasma-assisted (or plasma-enhanced) chemical vapor deposition" (PA(E)CVD) indicates its relationship to thermally driven chemical vapor deposition in that both processes use gaseous starting materials. In these processes, the gases are decomposed either by impact of electrons derived from an electrical discharge and accelerated in an electrical field or by thermal energy to yield condensible radicals which may undergo additional decomposition on a heated substrate. PACVD may be divided into two techniques: thermal plasmas such as arc discharges at atmospheric pressure where the neutral molecules, ions and electrons are in local thermodynamic equilibrium with each other and cold-plasmas such as low pressure glow discharges where the electrons and the ions are much more energetic than the background gas molecules and definitely not in equilibrium. The latter technique is the subject of this chapter.

High frequency power can be indirectly coupled into the gas via the capacitance of a dielectric wall of the vacuum chamber by the use of external electrodes or a coil. A more common and direct method involves two opposing parallel electrodes located inside the vacuum chamber. The latter configuration allows a greater degree of flexibility in reactor design and process control than can be obtained with external electrodes or coils.

The earliest and still common parallel plate production reactor was designed by Reinberg [1,2] and shown in Figure 1 [3]. In this configuration, the gas flows from the periphery of a circular, grounded substrate plate, across the substrates and out the center of the reactor. The discharge begins to decompose the gas as it enters the parallel plate assembly. However, the direction of flow is such that the deposition occurs on a continually decreasing area of the substrate plate. Thus, the flow velocity increases toward the center of the reactor, since the effective channel area of the flow is continually decreased. The higher flow velocity compensates for the reduced reactant concentration to give a uniform coverage. A detailed discussion regarding uniformity control in a radial flow reactor has been presented by Egitto [4].

Another important commercial reactor design is shown in Fig. 2. In this configuration, gas flows inside the quartz tube between sets of parallel plates which are alternately driven positive and negative by the RF voltage. Operation at low power results in a deposition rate that is limited by the power density instead of the gas concentration. These two reactors and other designs have been compared by Burggraaf [5]. Additional designs will be discussed below in conjunction with the deposition of a particular material.

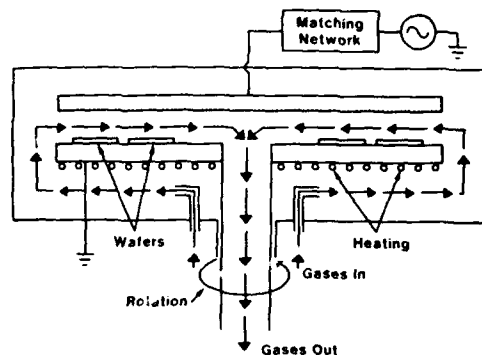


Figure 1. Parallel plate reactor used to generate plasma between the electrodes. Note that the reactant gases flow radially inward to counter the effect of progressive depletion as a result of decomposition. (From Ref. 3).

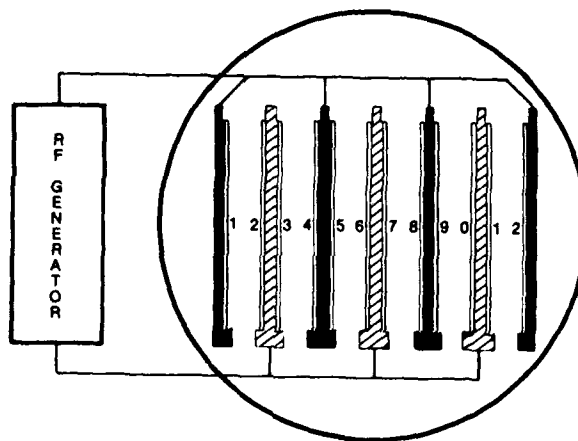


Figure 2. Cross-section of longitudinal flow, parallel plate PACVD reactor containing multiple anode/cathode sets made of graphite. The wafers (not shown) reside on each electrode and thus face one another. (From Ref. 3).

The plasma excitation process is inherently complicated. However, it may be qualitatively understood with a few simplifying statements. Power (d.c. or r.f. (usually 13.56 MHz or 2.45 GHz)) is applied to the cathode, and energy from the electric field is coupled into the gas almost entirely via the kinetic energy of the free electrons. At the outset there are only a few free electrons produced by the interaction of the gas molecules with cosmic rays or other background radiation. However, these electrons acquire energy rapidly from the field and lose it slowly in elastic collisions. Ionization and thus secondary electrons are produced, process avalanche occurs, and the discharge begins. This and associated phenomena dictate roughly the pressure range for PACVD. In parallel plate

reactors at $P < 0.1$ Torr (< 13.3 Pa) the mean free path is too great and collisions too infrequent to sustain the plasma; at $P \sim 5$ Torr ($\sim 6.5 \times 10^{-2}$ Pa), filamentary discharges and other plasma instabilities may appear, and the conditions are likely to promote homogeneous nucleation (particulate formation) in the gas phase. Newer methods such as electron cyclotron resonance (see below) have allowed this pressure range to be extended, especially on the low end.

In PACVD, the actual reactants are the dissociation fragments produced by the discharge. The spatial distribution of the free radicals in the discharge is the dominant factor affecting the film growth kinetics. Thus, PACVD is CVD by free radicals created in the discharge. Film formation proceeds by the adsorption of these radical species on the substrate or growing film surface, migration and desorption of by-products of the surface reaction. Glow discharge plasmas are weakly ionized; the ratio of the electron concentration/neutral species is $< 10^{-3}$. Thus, neutral species rather than ions are the primary contributor to film deposition.

By far, the most common ceramic films deposited by PACVD are SiO_2 and Si_3N_4 . So numerous are the publications of these studies that only selected reviews will be cited [6-9]. The purpose of this paper is to review the studies regarding the PACVD of some of the less commonly deposited ceramic films. These particular materials have been selected to illustrate a diversity in composition, deposition process technique and application. The PACVD configuration and the films should be considered to be parallel plate and amorphous, respectively, unless otherwise noted.

Materials

Aluminum Oxide

The deposition of Al_2O_3 at low temperatures by PACVD has been investigated as a replacement of SiO_2 in Si integrated circuit technology to provide a more robust isolation and gate oxide vis-à-vis the generation of interface states as a result of exposure to UV light as well as X- and e⁻-beam radiation during lithography. The diffusion rate of alkali ions (e.g., Na) is much lower in Al_2O_3 than in SiO_2 , thus the concentration of mobile ion charge can be reduced to a minimum under carefully controlled processing conditions. Finally, the plasma deposition of Al_2O_3 has been studied as an alternative to sputtered or ion exchanged glass or sputtered metal oxide films for use as waveguides in integrated optics.

Pande *et al* [10] have deposited Al_2O_3 gate dielectric films using (1) a type of remote PACVD (the substrate was not directly exposed to the plasma, thus minimizing radiation damage to it and the growing film), (2) the separately introduced precursor species of NO_2 (directly into the plasma) and trimethylaluminum (TMA) (outside the plasma but onto the heated substrate), (3) n-type Si and p-type InP substrates and (4) temperatures and pressures of $T \leq 523\text{K}$ and $P = 133$ Pa, respectively. The uniform (within 3% over a 3-inch diameter) films had a nominal resistivity of $10^{14} \Omega\text{-cm}$, a dielectric constant of 7.9 ± 0.2 and a breakdown field $> 10^6 \text{ Vcm}^{-1}$. Metal-oxide-semiconductor device structures were fabricated on both substrates. The device/substrate interfaces were chemically sharp (Auger analysis) with a minimum density of states in the range of $8 \times 10^{10} - 4 \times 10^{11} \text{ cm}^{-2} \text{ eV}^{-1}$. The only process parameter reported altered during the study was the flow rate of TMA. An increase in this parameter caused a linear increase in growth rate as would be expected.

A much lower temperature (523–573K) deposition of Al_2O_3 has recently been achieved by Catherine and Talebian [11] using plasma-assisted MOCVD. The plasma contained a mixture of TMA with He (or Ar) as the carrier gas and CO_2 as the oxidizing agent and was ignited using either a 450 kHz or a 13.56 MHz discharge. Glass slides or Si(100) wafers served as substrates. In contrast to the previous study, these substrates were immersed within the plasma, which is the more common, though not necessarily the best, method for highest quality films. The mass deposition rate was found to be independent of the TMA flow rate (or partial pressure) for the 13.56 MHz discharge but a linear function of the second power of this flow rate for the low frequency discharge. This difference was postulated by the authors to be related to the enhanced adsorption rate by

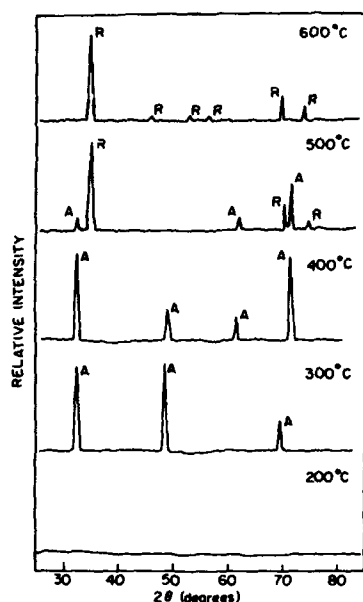


Figure 3. X-ray diffraction spectra of titanium oxide films deposited on glass substrates at the indicated temperatures. Fe K α was used to produce the spectra. A = anatase; R = rutile. (From Ref. 14).

ion bombardment. Raising the temperature of the substrate to 573K resulted in films of high density (to 3.3 grams/cm³) and low dielectric constant (8.1) with a considerably decreased C content from the TMA. However, even at this temperature the films were nonstoichiometric (oxygen deficient).

Two very different precursors of Al[OCH(CH₃)C₂H₅]₃ or AlCl₃ with O₂ have been used by Bailey *et al* [12]. The total pressure was 33 Pa. In the case of the alkoxide, the deposition rate passed through a maximum as a separate function of electrode separation or chamber pressure. In any event, the rate of deposition using this precursor was low, at best 35 Å min⁻¹. Moreover, the direct use of the alkoxide resulted in poor stoichiometry accompanied by considerable optical losses. These problems were ameliorated with the simultaneous injection of O₂ into the chamber. Alumina produced from AlCl₃ and O₂ showed no apparent stoichiometry problems, although Cl⁻ ions were incorporated into and etched the growing films. As such, an optimized alkoxide/O₂ process was preferred, but not obtained. No informative microstructural studies were conducted in either study. Thus, the effectiveness of remote and immersed plasmas and the various reactants, substrates and deposition temperatures on the microstructure of the Al₂O₃ materials is unknown.

Titanium Dioxide

Titanium dioxide films normally possess an exceptionally high dielectric constant, excellent optical transmittance and a high refractive index. As such, these films have been considered for capacitor materials in microelectronic devices, as optical coatings and as photoelectrochemical anodes for conversion of solar energy.

The reactants of either titanium tetrachloride [13,14] or titanium isopropylate [15] have been used in concert with PACVD to deposit TiO₂. The former has been employed with O₂ in an extensive study by Williams and Hess [3] in a parallel plate reactor at 13.56 MHz and 0.15 Torr. The atomic structure and the microstructure were strongly dependent on substrate temperature (298–973K), rf power (0.06–2 W/cm²) and substrate material (Si, sapphire, glass, NaCl and Ti). Figure 3 reveals that below 573K, films deposited on glass were always amorphous; at 573K ≤ T ≤ 673K the films were usually

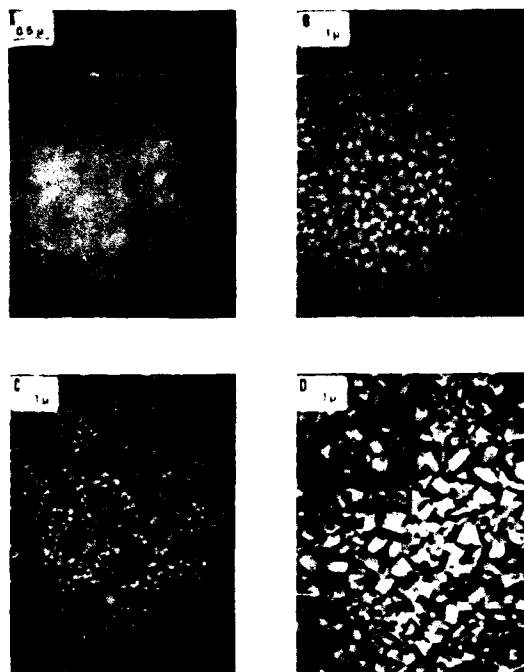


Figure 4. Scanning electron micrographs of titanium dioxide films deposited on Si substrates at temperatures (and phases) of (a) 473K (amorphous), (b) 673K (anatase and rutile (very small amount)), (c) 873K (anatase (larger crystals)) and rutile and (d) 973K (essentially all rutile). (From Ref. 14).

anatase (denoted A) and at $T > 673\text{K}$, either pure rutile (denoted R) or a mixture of rutile and anatase occurred. Films deposited on other substrates showed similar behavior, but the temperatures for the occurrence of specific crystalline forms differed for each substrate material at a given temperature. A comparative study for TiO_2 deposited on Si substrates held at various temperatures is presented in Figure 4.

Williams and Hess [16] also showed that the electrical properties of PACVD TiO_2 films depend on deposition conditions. The resistivity increased as the substrate temperature increased which is consistent with an increased oxygen vacancy concentration, larger grain size and decreased Cl concentrations (from the TiCl_4) at elevated temperatures. In one of the few comparative studies with films made by standard CVD techniques, it was found by these authors that the structural stability of the PACVD films is improved and the grain size 3–4 times larger for the same substrate and deposition temperature. The cause of the latter phenomenon may be due to (1) desorption of weakly bound species and cleaning as a result of atomic particle bombardment, (2) nucleation site generation and/or (3) enhanced surface mobility of the adsorbed species.

Zinc Oxide

Highly c-axis oriented crystalline films of ZnO have been deposited on Si, SiO_2/Si and polyimide substrates by PACVD using diethylzinc carried in Ar and CO_2 or N_2O as the oxygen source [17]. The substrate temperatures and RF power input were in the ranges of 473–623K and 150–260 W, respectively. Epitaxial films were obtained on sapphire (0001) at substrate temperatures higher than 523K and rf power > 100 Watts. In all cases, the films could be grown at lower substrate temperatures and lower rf input power levels in N_2O than CO_2 . The films had low resistivities of 10^{-3} – $10\Omega\cdot\text{cm}$, Hall mobilities of 0.5 – $50\text{ cm}^2\text{V}^{-1}\text{s}^{-1}$ and carrier concentrations of 10^{18} – 10^{19} cm^{-3} . However, these characteristics were strongly dependent on substrate temperature, the rf input power and the mole ratio of CO_2 (or N_2O) to the diethylzinc.

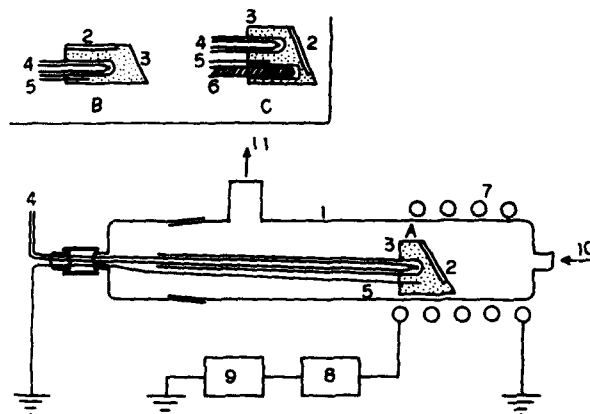


Figure 5. Schematic drawing of the horizontal, rf coil PACVD reactor used to heat a graphite susceptor for the deposition of AlN. The labeled parts are (1) quartz reactor tube; (2) substrate; (3) susceptor; (4) thermocouple; (5) molybdenum wire; (6) cooling tube; (7) RF coil; (8) matching network; (9) RF generator; (10) reactant gas inlet; and (11) vacuum pump. (From Ref. 19).

Aluminum Nitride

As AlN is covered with a strongly passivating Al_2O_3 film in an oxidizing atmosphere, it has been investigated as a protective coating for graphite. Bauer *et al* [18] conducted one of the initial studies of its deposition by PACVD using AlCl_3 and NH_3 at substrate temperatures between 1073 and 1473K. The films were polycrystalline with resistivities between 10^{14} and $10^{16} \Omega\cdot\text{cm}$, a dielectric constant equal to 8.4, fixed charge densities in the range $(3\text{--}10) \times 10^{11} \text{ cm}^{-2}$ and an optical gap of 6.0 eV.

In an attempt to lower the substrate temperature to $T \leq 1073\text{K}$, Itoh *et al* [19] have recently used a mixture of the reactants of AlBr_3 , N_2 , H_2 and Ar. An induction coil was used to heat a graphite substrate in the temperature range of 473–1073K. The details of their horizontal reactor are shown in Fig. 5. It was necessary to heat the substrate above 773K in order to obtain single phase AlN free of NH_4Br . The growth rate passed through a maximum with increasing pressure at the high pressure of $\approx 2.0 \times 10^3 \text{ Pa}$. The mass of the deposit also increased with an increase in substrate temperature. A translucent hexagonal film with highly preferred c-axis orientation was obtained at 15 Torr, as shown in Figure 6. This film was composed of a densely packed columnar structure. It is the recommended structural orientation for an oxidation-resistant film on graphite.

Boron Nitride

Boron nitride films are of interest as passivating coatings, insulating films, gate dielectrics on compound semiconductors and membranes for X-ray lithography masks. In the PACVD of this material, investigators have used the reactant combinations of B_2H_6 and NH_3 [20–23], BCl_3 and NH_3 [24], or borane-triethylamine $[\text{BH}_3\text{N}(\text{C}_2\text{H}_5)_3]$ and NH_3 [25,26]. In general, BN crystallizes either in the graphite-like hexagonal form or in the diamond-like cubic form. Films deposited by conventional CVD or PACVD have been either amorphous or polycrystalline hexagonal form. The structure depends primarily on the deposition temperature. Below 873K, the films are essentially amorphous, while above this temperature, polycrystalline material occurs. The resistivity of the latter material is $2 \times 10^7 \Omega\cdot\text{cm}$. PACVD-derived BN has a dielectric constant between 3 and 8 [20,21,25]. The breakdown strength is between 3 and 6 [21,25].

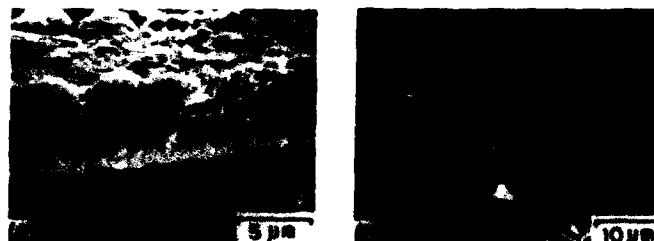


Figure 6. SEM micrograph of the surface and the fractured cross section of AlN films grown at 15 Torr total pressure and 973K substrate temperature. (From Ref. 19).

Early high-temperature studies (823–1273K) using $B_2H_6 + NH_3$ at 13.56 MHz in the pressure range of 40–66 Pa resulted in growth rates of polycrystalline hexagonal BN that increased with temperature and with the B_2H_6/NH_3 ratio [20]. The grain size was a function of the substrate material; with graphite substrates, grains exceeding 10 μm were obtained. Using a NH_3/B_2H_6 ratio of 7 at 1273K, stoichiometric BN was obtained having a resistivity of $2 \times 10^9 \Omega \cdot cm$.

The discovery of low-pressure chemical routes to achieve the synthesis of diamond particles and films (see discussion below) has also catalyzed an interest in producing cubic BN, which is the second hardest material. Films and coatings of this form may be used for wear-resistant, corrosion-resistant and electrically insulating films. As with diamond, cBN is metastable to the graphite-like hexagonal phase noted above. The tribological advantage of cBN is in the machining of mild steels. The heat load causes a transformation of diamond to graphite, the resultant loss of cutting ability and often the incorporation of C into the metal workpiece.

All plasma-containing, non-sputtering deposition techniques used to date to produce cBN have been a variation on the PACVD method described in the Introduction. The electron beam evaporation of B in a nitrogen plasma by Weissmantel *et al* [27] resulted in the formation of BN crystallites (5–20 nm) embedded in an amorphous film matrix. From the electron energy loss spectra of the matrix, these investigators concluded that cBN was present [28]. Shanfield and Wolfson [29] extracted ions from a borazine plasma in a Kaufman source and accelerated them to 100 eV onto the substrate. X-ray spectra of the samples showed peaks of cBN. Auger analysis yielded a B/N ratio of 1:1.

Research by Chopra *et al* [30] and more recently by Lin *et al* [31] have used a modified activated reactive evaporation (ARE) process to prepare coatings containing cBN via evaporation of H_3BO_3 in an NH_3 plasma. ARE involves the e^- beam or resistance heated evaporation of a metal or compound in the presence of a reactive gas. In this case, the B_2O_3 formed by the decomposition of H_3BO_3 is reduced by atomic H to B which reacts with atomic N produced in the plasma to form BN. Various substrates, including steel and quartz, Si and NaCl single crystals, have been used. Microstructural (TEM diffraction), optical (UV-IR transmission spectra and optical band gap measurements) and hardness studies indicate the existence of the zincblende [30] or a simple cubic (a most unusual form) [31] structure of cBN in the polycrystalline films. No hexagonal phase was detected.

Similar research has been conducted by Inagawa and coworkers [32] using the evaporation of metallic B via beams of electrons derived from a standard 270° deflection-type gun or a hollow cathode discharge gun, plasma activated atomic N and a substrate bias in the range of 0 to –600 V. The simultaneous addition of Ar into the N plasma considerably assisted the formation of cBN. At an Ar/ N_2 ratio of 4:1, the films contained virtually 100% of the cubic phase. It is obvious that additional growth and analysis research must be conducted to ascertain the parameters under which the various forms of cBN occur as a single phase.

Titanium Nitride

Tools having hard, wear resistant layers of TiN, deposited by CVD or P(physical)VD techniques are widely used in machining and metal forming operations. However, heat treatment after coating (especially after CVD) is frequently required to meet the strength requirements for tool steel substrates. This latter process can introduce distortion problems, especially in high precision tools. This material, as well as other refractory nitrides, exhibit low electrical resistivity and the ability to reflect infrared radiation. Thus, these films are potentially useful in microelectronic applications and as heat mirrors. In all cases, it is desirable to reduce the substrate temperature. To this end, studies using PACVD have been conducted by Mayr and Stock [33] and Gleason and Hess [34] using TiCl_4 (or $\text{Ti}(\text{OC}_3\text{H}_7)_4$) and N_2 (mixed with H_2 and Ar) and TiCl_4 and NH_3 , respectively, and conventional glow discharge methods.

The research of Mayr and Stock [33] showed that unlike PVD processes, stoichiometric TiN could be deposited over a wide range of partial pressures of TiCl_4 and N_2 . Moreover, the composition of the layers was nearly independent of substrate temperature between 773 and 973K. Similar results were found with the use of $\text{Ti}(\text{OC}_3\text{H}_7)_4$. However, C and O were detected in these films.

Gleason and Hess [34] found that at a substrate temperature of 873K, the polycrystalline films had resistivities of 100–200 $\mu\Omega\cdot\text{cm}$ and contained $\geq 15\text{at}\%$ Cl and showed poor electrical resistivities. Increasing the temperature and rf power resulted in progressively higher deposition rates. Increasing only the temperature caused a decrease in the film resistivity. Extensive microbeam characterization of the samples deposited at 873K showed a Ti/N ratio of 1, even in the presence of excess NH_3 . The films were preferentially oriented along the [100] direction in a columnar structure.

Silicon Carbide

The formation via PACVD of amorphous silicon carbide (a-SiC) having a wide range of Si/C ratios has been intensively studied for optoelectronic applications. The optical quantum efficiency is $\approx 10^3$ greater in a-SiC than in the crystalline polytypes. Moreover, the optical response within the visible spectrum varies as a function of the Si/C ratio. The reactant gases most commonly employed include SiH_4 with C_2H_4 [35,36] or CH_4 [36–39] or $\text{Si}(\text{CH}_3)_4$ [40]. Substrate temperatures have varied from 300 to 873K.

The Si/C ratio has been intentionally varied within the range from 0.1 to 4 [35,38–40]. These ratios depend strongly on the ratio of reactants (where applicable) but are nearly independent of substrate temperature. The films usually contain 20–40at% H_2 . Infrared spectra show that the Si and C form a random tetrahedral network with one H bonded to the Si and three H bonded to the C.

The resistivities of these films are $\approx 10^{12}\Omega\cdot\text{cm}$ [35,40], refractive indices between 1.96 and 2.6 [39], compressive stresses in the range $(0.2\text{--}5) \times 10^9 \text{ dynes/cm}^2$ [32] and a microhardness in the range of 1200–1600 kg/mm^2 [38].

Recent Innovations in PACVD

Deposition of the Monocrystalline Materials of Si and GaAs

Films produced by PACVD are rarely single crystal. However, if monocrystalline substrates and careful control of the deposition parameters are used and homoepitaxial deposition is desired, single crystal films can be achieved. This is particularly true if the material is an element. The premier example of this is the deposition of Si. Epitaxial layers of Si have been deposited by PACVD in horizontal and vertical [42,43] reactors at temperatures as low as 1023K which is 200–400K below that used in conventional CVD.

In the above studies, the Si wafers were immersed in the plasma which raises the potential for surface damage. The reactant gases are also subject to direct plasma

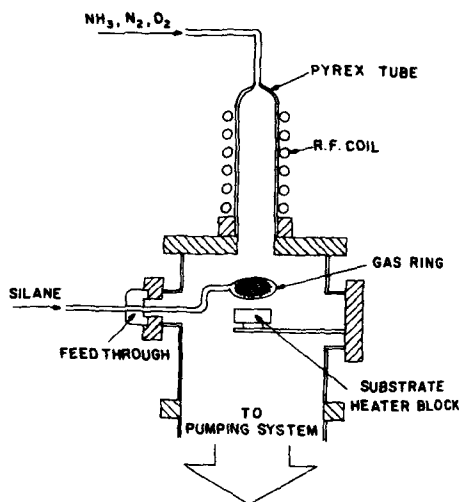


Figure 7. Schematic of a remote plasma deposition unit (From Ref. 45).

excitation which makes the control of the reaction pathways difficult. Tasch and coworkers [44] have very recently used a remote plasma CVD process developed by Lucovsky, Markunas and coworkers [45] for the deposition of amorphous SiO_2 and Si_3N_4 (see Fig. 7) and similar to that used by Pande *et al* [10] for the deposition of Al_2O_3 (see above), except that only the nonreactive gases of Ar and/or He were exposed to the plasma contained in the region of the rf coils. The plasma produced long lived excited noble species which subsequently flowed through a ring external to the plasma (see Fig. 7) and from which issued SiH_4 . The interaction of the excited noble gas with the SiH_4 carried it to the substrate and assisted its decomposition such that monocrystalline films could be homoepitaxially deposited as low as 673K.

Huelsman *et al* [46] have used another modification of the classical PACVD to deposit monocrystalline films of GaAs. As shown in Fig. 8, the plasma is generated between two perforated Ta disk electrodes. The triethylgallium (TMG) flows through the grounded electrode and thus does not come in contact with the plasma. By contrast, the AsH_3 is decomposed in the plasma to produce the As monomer above the substrate which is heated in the range of 843–923K. A similar deposition was conducted in the same chamber without the use of the plasma. Table I shows that as the substrate temperature decreased, the mobilities dropped for both materials. However, the plasma-deposited films have higher mobilities than those deposited without the plasma. This is believed to be due to a C scavenging effect created in the plasma which is not present in the nonplasma process. Finally, the band-edge photoluminescence at 77K was always stronger for the plasma-derived material. These results indicated less electron compensation in the plasma deposited layers.

Microwave Plasmas and Electron Cyclotron Resonance

The efficiency of plasmo-chemical synthesis of films and therefore their growth rate increase with an increase in the electron density of the plasma. All of the studies described above were conducted using rf frequencies, primarily of 13.56 MHz or lower, in which the electron densities are in the range of 10^9 – 10^{10}cm^{-3} . However, if microwave frequencies (2.45 GHz is the FCC assigned frequency for processes such as deposition and etching) are used, the electron density increases to $\sim 10^{13}\text{cm}^{-3}$. The microwave plasma is also a rich source of intense emission of photons in the vacuum and near-UV region. This emission can stimulate various photo-chemical processes which significantly influence film growth.

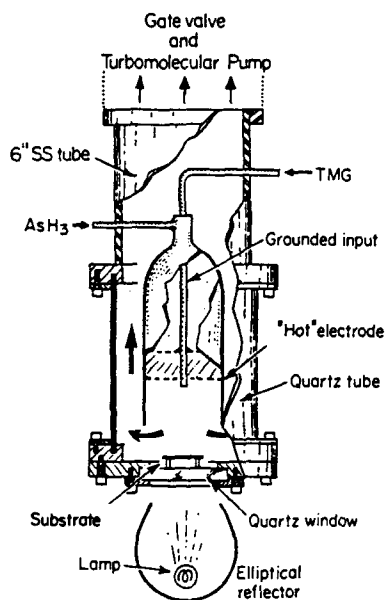


Figure 8. Schematic of a PACVD system used to deposit monocrystalline GaAs. Note that the trimethylgallium (TMG) is never exposed to the plasma. (From Ref. 46).

TABLE I. Electron mobilities and concentrations for GaAs epilayers grown with and without plasma from 843 to 923K. (From Ref. 46).

Growth Temp. (°K)	With plasma		Without plasma	
	$\mu(\text{cm}^2/\text{V}\cdot\text{s})$	$n(\times 10^{16}\text{cm}^{-3})$	$\mu(\text{cm}^2/\text{V}\cdot\text{s})$	$n(\times 10^{16}\text{cm}^{-3})$
843	2840	7.5	300	9.3
883	3540	6.1	2300	3.1
923	3840	2.3	3910	7.4

The most notable current use of microwave PACVD for thin film deposition is that of the low (or lowered) pressure ($13\text{--}10^4$ Pa), low temperature (823–1273K) growth of diamond using a hydrocarbon (e.g. 0.2–5.0vol% CH_4) and H_2 as the active gases [47–49]. Both species are normally passed directly through the plasma where they are decomposed. The exact mechanism of growth is not known; however, atomic hydrogen appears critical to the process. Tsuda *et al* [50] and Frenklach and Spear [51] have postulated different mechanisms of diamond growth on diamond surfaces.

For standard rf or microwave plasmas to be ignited, gas pressures must be in the range of 1–150 Pa. The ionization ratios are very small—in the range of 10^{-6} to 10^{-4} . In these plasmas, neutral molecules and radicals are the primary species in the plasma. A microwave plasma coupled with electron cyclotron resonance (ECR) can easily be generated at much lower gas pressures—in the range of 0.001–0.1 Pa with ionization ratios of 10^{-3} – 10^{-1} . Stable plasma generation is possible with reactive gases, as in the case of the rf discharge, since no electrode configuration is needed.

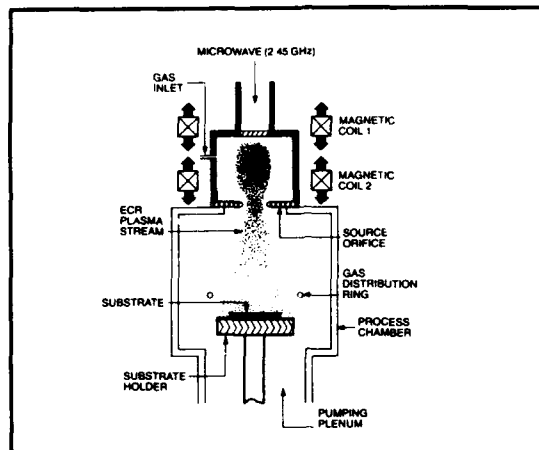


Figure 9. Schematic showing the principles of operation of an ECR unit. (From Ref. 52).

The principle of operation of an ECR source may be understood with the aid of Fig. 9 [52]. Energy from the electric field of the microwave radiation is transferred to the electrons in the plasma chamber. These electrons describe circular orbits along the magnetic field lines (the cyclotron effect) and produce collisions with the gas molecules. These collisions produce more ions and electrons to create a breakdown process and a plasma. When the orbital frequency of these electrons equal the microwave frequency, resonance occurs and the process becomes very efficient, producing a high electron and ion density, as noted above.

ECR sources have been used almost exclusively to produce amorphous films of Si, SiO₂ and Si₃N₄ for passivating layers for various semiconductor materials. A brief review of the principles of ECR and the character of the films produced by this method, is presented in Ref. 53. However, recently these sources are beginning to find increasing use for the deposition of crystalline films at much lower temperatures than standard CVD. One example is the growth of monocrystalline films of the III-V nitrides, especially GaN and AlN, using thermal evaporation from a Knudsen cell of the metals and an ECR plasma to produce reactive atomic and ionic N [54]. Silicon and β -SiC substrates have been used as low as 773K. Cubic GaN has been observed to grow on the cubic β -SiC surface, as verified by TEM [54].

This process method, as well as that of remote plasma CVD, offer considerable advantages relative to the classical immersed PACVD in terms of lowered deposition temperature and increased quality of the films and coatings.

Summary

Plasma CVD involves the decomposition of gaseous species, primarily by the impact of electrons derived from an electrical discharge and the deposition and possible reaction of the product species, to produce thin films and coatings. The majority of the deposits produced to date have been amorphous. However, the use of this technique or modifications of this method are being increasingly used to deposit poly- and single-crystalline materials. Recent innovations including the removal of the substrate from the plasma and the use of microwave sources have expanded the potential of PACVD.

Acknowledgements

The writer was partially supported by SDIO/IST through ONR under contract N00014-86-K-0686.

References

1. A. R. Reinberg, U. S. Patent No. 3,757,733, Sept. 1, 1973.
2. A. R. Reinberg, J. Electron. Mater. **8**, 345 (1979).
3. B. Gorowitz, T. B. Gorpzyca and R. J. Saia, Solid State Technol., **6**, 197 (1985).
4. F. D. Egitto, J. Electrochem. Soc. **126**, 1354 (1980).
5. P. S. Burggraaf, Semicond. Int. **3**, 23 (1980).
6. J. R. Hollahan and R. S. Rosler in *Thin Film Processes*, edited by J. L. Vossen and W. Kern, (Academic Press, New York, 1978) pp. 335-360.
7. Thomas D. Bonifield, in *Deposition Technologies for Films and Coatings*, edited by R. F. Bunshah (Noyes Publications, Park Ridge, New Jersey, 1982) pp. 365-384.
8. T. B. Gorpzyca and B. Gorowitz in *VLSI Electronics: Microstructure Science*, Vol. 8, edited by N. G. Einspruch and D. M. Brown, (Academic Press, New York, 1984) pp. 69-87.
9. A. C. Adams in *Plasma Deposited Thin Films*, edited by J. Mort and F. Jansen, (CRC Press, Boca Raton, FL, 1986) pp. 129-160.
10. K. P. Pande, V. K. R. Nair and D. Gutierrez, J. Appl. Phys. **54**, 5436 (1983).
11. Y. Catherine and A. Talebian, Jour. Electron. Mater. **17**, 127 (1988).
12. A. H. Bailey, D. A. Darbyshire, A. P. Overbury, C. W. Pitt and J. Newton, Vacuum **36**, 139 (1986).
13. J. H. Alexander, R. J. Joyce and H. F. Sterling in *Thin Film Dielectrics*, edited by F. Vratny, (Electrochemical Society, New York, 1980) pp. 186-197.
14. L. M. Williams and D. W. Hess, J. Vac. Sci. Technol. A **1**, 1810 (1983).
15. D. R. Secrist and J. D. MacKenzie, Ceram. Bull. **45**, 784 (1966).
16. D. W. Hess, J. Vac. Sci. Technol. A **2**, 244 (1984).
17. M. Shimizu, Y. Matsueda, T. Shiosaki and A. Kauabata, J. Cryst. Growth **71**, 209 (1985).
18. J. Bauer, L. Bischoff and D. Bolze, Phys. Status Solidi **32**, 173 (1977).
19. H. Itoh, M. Kato and K. Sugiyama, Thin Solid Films **146**, 255 (1987).
20. S. B. Hyder and T. O. Yep, J. Electrochem. Soc. **123**, 1721 (1976).
21. H. Miyamota, M. Hirose and Y. Osaka, Jpn. Jour. Appl. Phys. Pt. 2 Lett. **22**, L216 (1983).
22. D. C. Liu, G. J. Valco, G. G. Skebe and V. J. Kapoor in *Silicon Nitride Thin Insulating Films*, edited by V. J. Kapoor, H. J. Stein (Electrochemical Society, Pennington, NJ, 1983) pp. 141-151.
23. T. H. Yuzuriha and D. W. Hess, Thin Solid Films **140**, 199 (1986).
24. O. Gafri, A. Grill, D. Itzhak, A. Inspektor and R. Avni, Thin Solid Films **72**, 523 (1980).
25. W. Schmolla and H. L. Hartnagel, J. Electrochem. Soc. **129**, 2636 (1982).
26. S. M. Ojha, Phys. Thin Films **12**, 237 (1982).
27. C. Weissmantel, J. Vac. Sci. Technol. **18**, 179 (1981).
28. C. Weissmantel, K. Bewilgova, K. Breuer, D. Dietrich, U. Ebersbach, H. J. Erler, B. Rau and G. Reisse, Thin Solid Films **96**, 31 (1982).
29. S. Shanfield and R. Wolfson, J. Vac. Sci. Technol. A **1**, 323 (1983).
30. K. L. Chopra, V. Agarwal, V. D. Vankar, C. V. Deshpandey and R. F. Bunshah, Thin Solid Films **126**, 307 (1985).
31. P. Lin, C. Deshpandey, H. J. Doerr, R. F. Bunshah, K. L. Chopra and V. D. Vankar, Thin Solid Films **154**, 487 (1987).
32. K. Inagawa, K. Watanabe, H. Ohsone, K. Saitoh and A. Itoh, J. Vac. Sci. Technol. A **5**, 2696 (1987).
33. P. Mayr and H. R. Stock, J. Vac. Sci. Technol. A **4**, 2726 (1986).
34. E. F. Gleason and D. W. Hess, in *Plasma Processing*, edited by J. W. Coburn, R. A. Gottscho and D. W. Hess (Mater. Res. Soc. Proc. **68**, Pittsburgh, PA 1986) pp. 343-349.
35. D. A. Anderson and W. E. Spear, Philos. Mag. **35**, 1 (1977).

36. H. Weider, M. Cardona and C. R. Guarnieri, *Phys. Status Solidi* **22**, 99 (1979).
37. Y. Catherine, G. Turban and B. Grolleau, *Thin Solid Films* **76**, 23 (1981).
38. H. Yoshihara, H. Mori and M. Kiuchi, *Thin Solid Films* **76**, 1 (1981).
39. Y. Catherine and G. Turban, *Thin Solid Films* **60**, 193 (1979).
40. H. Munkata, S. Murasato and H. Kukimoto, *Appl. Phys. Lett.* **37**, 538 (1980).
41. W. G. Townsend and M. E. Uddin, *Solid State Electron.* **16**, 39 (1973).
42. S. Suzuki and T. Itoh, *J. Appl. Phys.* **54**, 1466 (1983).
43. T. J. Donahue, W. R. Burger and R. Reif, *Appl. Phys. Lett.* **44**, 346 (1984).
44. A. Tasch, private communication.
45. G. Lucovsky, P. D. Richard, D. V. Tsu, S. Y. Lin and R. J. Markunas, *J. Vac. Sci. Technol A* **4**, 681 (1986).
46. A. D. Huelsman, R. Reif and C. G. Fonstad, *Appl. Phys. Lett.* **50**, 206 (1987).
47. P. K. Bachmann and R. Messier, *Chemical and Engineering News*, May 15, 24 (1989).
48. J. T. Glass, B. E. Williams and R. F. Davis, *SPIE* **877**, 56 (1988).
49. K. Kobashi, K. Nishimura, Y. Kawate and T. Horiuchi, *Phys. Rev. B* **38**, 4067 (1988).
50. M. Tsuda, M. Nakajima and S. Oikawa, *J. Am. Chem. Soc.* **108**, 5780 (1986).
51. M. Frenklach and K. E. Spear, *J. Mater. Res.* **3**, 133 (1988).
52. Courtesy Microscience, Inc. Norwell, MA 02061.
53. S. Matsuo in *Handbook of Thin Film Deposition Processes and Techniques*, edited by K. K. Schuegraf (Noyes Publications, Park Ridge, NJ, 1988) pp. 147-169.
54. M. J. Paisley, Z. Sitar, J. B. Posthill and R. F. Davis, to be published in the *Jour. Vac. Sci. and Technol.*

BARRIERS TO THE NUCLEATION OF METHYL GROUPS ON THE DIAMOND (111) SURFACE

Steven M. Valone
Materials Science and Technology Division,
Los Alamos National Laboratory, Los Alamos, NM 87545

ABSTRACT

Questions about the mechanism of diamond film growth by low-pressure, plasma-assisted chemical vapor deposition methods have persisted for some time now. As an attempt to explore one aspect of the problem, we examine the energetics of several adsorbed diamond (111) surfaces. The adsorbates are mixtures of methyl groups and hydrogen atoms. The model for these systems is the molecular orbital hamiltonian of Dewar and coworkers.

From these calculations we find that H adsorption is preferred due both to bond energy and steric effects. Thus, nucleation of a cluster of three or more methyl groups, as assumed in earlier work, is energetically very demanding.

INTRODUCTION

Recent interest in the growth of diamond thin films has stimulated the study of single crystal diamond surfaces in ever greater detail [1]. The hope is that such studies will eventually contribute to a synthetic pathway for the epitaxial growth of high quality, crystal films on a variety of substrates. One synthetic approach, diamond growth by plasma-assisted chemical vapor deposition, possesses a bewildering number of variables. Understanding the detailed morphology and behavior of diamond surfaces may shed light on the roles played by some of these variables. In general, we want to know the chemistry of the deposition in the near-surface region (Fig. 1) so that we will know what we want the plasma to do. It must be added, however, that the degree

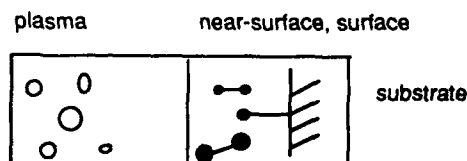


Figure 1. Schematic of CVD reactor. The areas of concern here are the near-surface and surface regions.

to which the state of the diamond surface is controlling the growth process is still a topic of intense debate.

The premise of this work is that the surface is of substantial importance and we proceed on that basis. One of the major theories of diamond film growth is that the termination of the surface changes the carbon-carbon particle spacings which, in turn, promote or inhibit the growth of diamond over graphite due to lattice matching constraints. In particular, both experimental and theoretical work shows that the atomic level behavior of diamond surfaces is sensitive to both temperature and chemical environment. Below 1200 K, the (111) surface, for instance, is in a 1X1 configuration as observed by LEED. Above that temperature, the surface reconstructs to a 2X2 or a 2X1 pattern. There are several theories about the detailed nature of the reconstruction. The one which seems most favorable in terms of its ability to account for the most experimental data is the 2X1 pi-bonded reconstruction of Pandey [2,3]. These are motivated by analogy to Si surfaces. On the other hand, addition of any of several adsorbates restores the diamond (111) surface nearly to its bulk configuration.

Here we report numerical results on various surfaces and modified surfaces of diamond (111), based on a molecular orbital model of the surfaces [4]. These are the relative energies of various mixtures of H and methyl group termination of the surface, clean surface reconstruction as described within the model, and estimates of the energy required to remove a methyl group or a hydrogen atom from the surface as a function of coverage. We have chosen H and methyl group coverage in order to compare with earlier work [5]. There it is assumed that some sort of methyl group coverage arises spontaneously. Then it is argued that it is possible to promote some sort of epitaxy by gas-phase attack of a cation.

However, the present calculations give a picture of the difficulty incurred by trying to initiate nucleation of a cluster of methyl groups on the (111) surface. The reason for this is that the H-terminated surface is so much more favorable energetically. The difference arises from both bond energy and steric interferences. A compounding factor is the frequency with which clusters of methyl groups form so that some initiation of growth can take place. The question of the frequency and barriers associated with nucleation naturally lead to concerns about the details of the deposition mechanism. These might fall into two categories, one being Eley-Rideal (ER)-like and the other being Langmuir-Hinshelwood (LH)-like [6]. At some future date, it may be profitable to identify which mechanism dominates under which plasmatic conditions.

The conclusion of the present study is that the presence of H is a two-edged sword. On the one hand, it does stabilize the (111) surface to maintain the diamond lattice in the presence of the plasma. On the other, it imposes a serious barrier to the attachment of methyl groups to the surface, thereby inhibiting growth. So, while diamond does manage to grow in a hydrogen-rich environment, the likelihood that this happens by methyl groups displacing a hydrogen overlayer, as conceived in Reference 5, seems very remote. Naturally, as the experimental evidence for what the dominant reactive species in various plasmas becomes more apparent, it will be desirable to study the relative adsorption of those species as well.

The remainder of the paper is as follows. The next section describes the numerical and strategic methodology used. The section after that presents the results of the computations. The final section summarizes the salient points of the research and points out a few of the possible directions of future work.

METHOD

Numerical

Our numerical method is based on a semiempirical molecular orbital theory of organic molecules and polymers due to Dewar, Thiel, Stewart, and others [4]. An orbital matrix equation, whose matrix elements are approximated using experimental data, is produced from the theory. The particular approximations used here are referred to as the AM1 hamiltonian. The form of the individual matrix elements is based on the Hartree-Fock equations for the system. The approximations serve two purposes : 1) The calculation of matrix elements is greatly reduced and 2) The use of experimental data allows inclusion of some important correlation effects neglected in the formal theory.

Solving the matrix equation allows estimates of an optimum geometry, heat of formation, dipole moments, charge distributions, and a variety of other properties for any given combination of atoms. The AM1 approach has been found to give reasonable properties for many molecules and polymers, predicts a reasonable value for the lattice constant of bulk diamond, and can be confidently operated with periodic boundary conditions in one dimension.

Here we focus primarily on the geometry and heat of formation of several related systems to be described below. A comparison of the relative stability of various adsorbates on the (111) surface of diamond gives some sense of which species will reside on the surface, as well as an understanding of what is driving the stability. To achieve some description of the surface, it is necessary to adopt a representation of the real physical system. In the MOPAC routine, this is done by taking the bulk cell and terminating the supposedly unexposed surfaces with hydrogen atoms and by keeping some of the carbon atoms fixed in space. Because the routines can only reliably handle periodicity in one dimension, all surfaces are therefore represented as strips or "polymers". In instances where two-dimensional periodicity is reliable, the two representations give comparable results.

Systems

Eight different systems are considered here; namely, bulk diamond, the clean (111) surface, an H terminated surface, a surface terminated by 50% H and 50% methyl groups, a surface terminated by 25% H and 75% methyl groups, a methyl group terminated surface, a surface in which an H atom has been abstracted, and, finally, a surface in which a methyl group has been abstracted.

These choices are motivated by the following two questions. One, what is the nature of the surface reconstruction relative to bulk diamond? Two, how stable are these surfaces relative to each other? By allowing each system to find an optimum geometry, both of these questions may be answered by simple comparison. There is also a third question; namely, what is the surface coverage of H and methyl groups as

a function of temperature? This method, as it stands, can only address the last question at 0 K, but this is still of some utility. The method can be readily adapted to nonzero temperatures using suitable Monte Carlo averaging techniques.

Due to problems in calculating correlation effects, it is difficult to obtain a reliable potential energy surface at all points in configuration space. Consequently, we focus chiefly on certain key metastable configurations corresponding to relaxed or reconstructed surfaces or an abstracted system in which a hydrogen atom or methyl group has been moved to infinity. In the latter instances, the calculation assumes a biradical configuration. Otherwise, a closed-shell, restricted electronic configuration is assumed.

RESULTS

Geometries

The clean surface reconstructs in a manner similar to the π -bonded reconstruction model of Pandey [2], but not precisely the same. The top layer of carbon atoms (Fig. 2) contracts, while the second layer dilates perpendicular to the surface. However, little dimerization is seen.

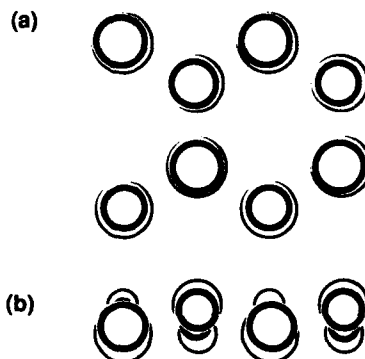


Figure 2. Clean diamond (111) surface : (a) Top view of first two carbon layers. The heavy circles represent the relaxed surface, while the light circles represent the equivalent bulk atoms. (b) Side view analogous to (a). The layer spacing has decreased from 0.56 to 0.28 Å.

For all the fully terminated surfaces, near-bulk-like configurations are seen for the first layer of carbon atoms which are not considered adsorbates (Fig. 3). The C-H

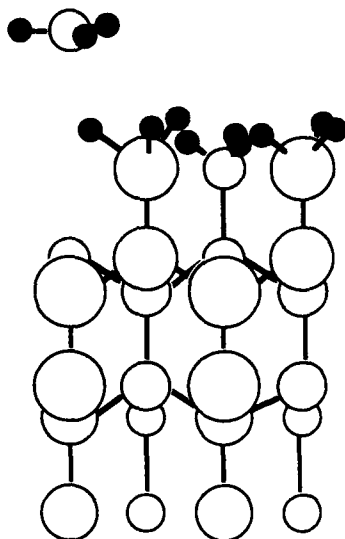


Figure 3. Methyl radical abstracted from diamond (111) surface which is covered with other methyl groups. Because of the periodicity of the calculation, the abstraction reduces the coverage to 75%. The hollow circles represent carbons, while the solid circles represent hydrogens. This figure typifies the configurations of the other seven systems reported in the text.

bond distances for the H-terminated sites are 1% longer than those in methane, while the C-H distances on adsorbed methyl groups are 1% shorter. More importantly, the H-H distances for H atoms on adjacent methyl groups can be closer than 2.4 Å, twice the van der Waals radius of an H atom. Consequently, to help alleviate some of the steric interference, the CCH bond angle for the methyl groups changes as a function of coverage from nearly normal, 109°, to very oblique, 123°. One might think that the C(surface)-C(methyl) distances show some alternating pattern, but none has been found. They are all about 1.51 Å.

Binding energies

The binding energy of H atoms to the diamond (111) surface at high coverages, above 75%, is calculated to be 120 kcal/mole, compared to 102 kcal/mole found experimentally. This is considered to be an indication of the quality of the AM1 hamiltonian in describing diamond-related systems.

The binding energy of methyl groups when abstracted as methyl radicals at high coverages, above 75%, is about 105 kcal/mole. The author is unaware of any experimental data of this type at this time.

Relative surface energies

The binding energy of methyl groups, when substituted for an H atom on the same surface, varies from about 25 kcal/mole at low coverages, below 25% methyl-75% H, up to 130 kcal/mole at high coverages, above 75% methyl-25% H. Thus it is apparent that the H covered surface is much preferable energetically than any amount of methyl coverage. Any appearance of methyl groups on the diamond (111) surface ought to be purely transitory. Furthermore, the energy required to cluster three methyl groups into nearest-neighbor proximity is 210 kcal/mole. This energy difference is almost an order of magnitude larger than the one found in an earlier study of the epitaxy mechanism [5]. Note also that these are energy differences rather than actual barriers, which are generally considered to be unreliable in this method and may be substantially more than this. Also, the shape of the barrier will depend on the mechanism of deposition, i.e. ER vs. LH. In all, this seems to cast some doubt about any possible role that surface methyl groups would play in diamond epitaxy.

SUMMARY

As found experimentally, the present molecular orbital calculations on the behavior of H covered diamond (111) surfaces show that the adsorbate restores the clean surface to a nearly bulk configuration. Coverage by methyl groups shows similar restorative powers. However, the relative energy of the H terminated diamond (111) surface is always found to be less than that of mixtures of methyl groups and H atoms. Consequently, displacement of H atoms by methyl groups seems to represent a transient phenomenon. The energy required to bring three methyl groups to nearest-neighbor proximity is about 210 kcal/mole. A substantial amount of this is due to steric interactions among the methyl groups. This presents an additional barrier to nucleation of methyl groups on the surface, which is thought by some to be a precursor to the advent of diamond epitaxial growth. Specifically, it would seem, from this study, very unlikely that nucleation takes place by methyl groups displacing a hydrogen overlayer, as envisioned by Tsuda and coworkers [5].

For future work, the present research suggests the study of different adsorbed species once the relevant ones are identified through diagnostic studies, the transitory surface damage done by the plasma, the calculation and measurement of surface diffusion barriers for various surface species, and the investigation of nonhydrogenic systems.

REFERENCES

1. S. P. Chauhan, J. C. Angus and N. Gardner, *J. Appl. Phys.* **47**, 4764 (1976); M. Kamo, Y. Sato, S. Matsumo and N. Setaka, *J. Cryst. Growth* **62**, 642 (1983); D. V.

Fedoseev, V. P. Varnin and B. V. Derygin, *Russian Chem. Rev.* **53**(5), 435 (1984); Y. Saito, S. Matsuda and S. Nigita, *J. Mater. Sci. Lett.* **5**, 565 (1986); S. Matsumoto, M. Hino, and T. Kobayshi, *Appl. Phys. Lett.* **51**, 737 (1987); R. Messier, K. E. Spear, A. R. Badzian and R. Roy, *J. Metals September*, 8 (1987); *First International Conference on the New Diamond Science and Technology*, Keidanren Kaikan, Japan, Oct. 24-26, 1988 and *Extended Abstracts for the Technology Update on Diamond Films*, Spring MRS Meeting, San Diego, CA, 1989.

2. K. C. Pandey, *Phys. Rev. B* **25**, 4338 (1982).

3. D. Vanderbilt and S. G. Louie, *Phys. Rev. B* **29**, 7099 (1984); R. Dovesi, C. Pisani, C. Roetti and J. M. Ricarti, *Surf. Sci.* **185**, 120 (1984); V. Barone, F. Leij, N. Russo, G. Abbate, *Solid State Comm.* **49**, 925 (1984).

4. M. J. S. Dewar, E. G. Zoebisch, E. F. Healy and J. J. P. Stewart, *J. Amer. Chem. Soc.* **107**, 3902 (1985); M. J. S. Dewar and D. M. Storch, *ibid.*, 3898 (1985); M. J. S. Dewar and W. Thiel, *ibid.* **99**, 4899 (1977); R. C. Bingham, M. J. S. Dewar and D. H. Lo, *ibid.* **97**, 1285 (1975).

5. M. Tsuda, M. Nakajima and S. Oikawa, *ibid.* **108**, 5780 (1986).

6. D. L. Freeman and J. D. Doll, *J. Chem. Phys.* **78**, 6002 (1983); **79**, 2343 (1983).

PLASMA SPRAYING OF ZIRCONIA COATINGS

D. J. VARACALLE, Jr., G. R. SMOLIK, G. C. WILSON* and G. IRONS,
J. A. WALTER**

*Idaho National Engineering Laboratory, EG&G Idaho, Inc., P.O. Box 1625,
Idaho Falls, ID 83415-2210

**Miller Thermal Inc., 555 Communications Drive, P.O. Box 1081, Appleton, WI
54912

ABSTRACT

As part of an investigation of the dynamics that occur in the plume of a thermal spray torch, an experimental and analytical study of the deposition of yttria-stabilized zirconia has been accomplished. Experiments were conducted using a Taguchi fractional factorial design. Nominal spray parameters were: 900 A, 36 kW, 100 scfh argon primary gas flow, 47 scfh helium secondary gas flow, 11.5 scfh argon powder carrier gas flow, 3.5 lb/h powder feed rate, 3 in. spray distance, and an automated traverse rate of 20 in./s. The coatings were characterized for thickness, hardness, and microstructural features with optical microscopy, scanning electron microscopy, and x-ray diffraction. Attempts are made to correlate the features of the coatings with the changes in operating parameters. Numerical models of the physical processes in the torch column and plume were used to determine the temperature and flow fields. Computer simulations of particle injection (10 to 75 μm zirconia particles) are presented.

INTRODUCTION

Plasma spraying is one of the most versatile and rapid methods of applying coatings, and the number of applications of this technology is increasing [1]. With a multitude of operational parameters affecting the quality of the coating, it is often difficult to find the optimum process conditions [2,3].

As specific demands for coating quality increase, a better knowledge of the basic phenomena occurring in the process is necessary. This work attempts to further the scientific understanding of the physical mechanisms involved in the formation of yttria-stabilized zirconia coatings by determining which processing parameters affect the structure and properties of the coatings and using computer models to analyze the dynamics of the plasma spraying process.

Plasma sprayed zirconia coatings have been used for some time for thermal barrier applications in the automotive, transportation, aerospace, and aircraft industries because of their refractory nature and low thermal conductivity. Porosity and cracking are two microstructural features which influence thermal cyclic lifetime behavior and environmental resistance [4-7] and are therefore important parameters to control. Coatings consisting primarily of either the cubic and/or tetragonal phases as demonstrated in References 6-8 are desired to reduce the tendency for spalling and destruction of the bond.

EXPERIMENTAL PROCEDURE

A Taguchi style [9], fractional factorial experimental design was employed to evaluate the effect of seven plasma processing variables on three coating characteristics. The parameters varied were amperage, primary gas flow, secondary gas flow, powder feed rate, standoff distance, traverse rate, and injection angle. The coating characteristics measured were zirconia

thickness using optical microscopy, hardness using a Rockwell 15T test, and porosity using a scanning electron microscope. Phase structure was also determined using x-ray diffraction.

Two levels of each variable were selected to bracket the nominal settings of Experiment ZY01. Experiments ZY02-ZY09 in Table I represent the eight runs evaluated with the Taguchi approach. The quantitative Taguchi evaluation of the plasma spray process is ideal because it statistically delineates the impact of each factor on the measured coating characteristics across all combinations of other factors. This information is extremely useful in examining the physical science involved in plasma spray coatings, establishing realistic coating specifications, and developing new equipment. The Taguchi analysis was accomplished with PC-based software [10].

A Miller Thermal Plasmadyne SG-100 plasma spray system was used for this study. The primary gas was argon and the secondary gas was helium. A four hole gas ring was utilized to induce vortex flow. The powder carrier gas was argon, typically at a flow rate of 11.5 scfh. The powder was injected inside the torch, either perpendicular to the flow or at a 20 degree angle rearward into the flow. An x-y manipulator was used to ensure the standoff distance and repeatability in the experiments. Traverse rates were varied from 17 to 23 in./s with a y step of 0.125 inches. Forty passes were used to fabricate each of the coatings.

A commercially available zirconia ceramic powder was used (Alloys International AI-1075 Powder). The powder was blended in proportion in a slurry, spray dried, sintered, and then granulated down to size with light crushing. The powder chemistry and sieve analysis are shown in Table II. The powder was plasma sprayed onto 304 stainless steel plates (51 x 63 x 3 mm) cooled by air jets on the back side. The coupons were grit blasted with #30 alumina grit and sprayed with a nickel-aluminum bond coat (~100 μ m thick, plasma sprayed at a power of 31 kW) before spraying with zirconia.

MATERIALS CHARACTERIZATION

Coating thicknesses, as revealed by optical metallographic observations at 100X magnification, are listed in Table III. Average thicknesses from 12 measurements of the Ni-Al bond coats and zirconia layers are given. While the bond coatings were fairly uniform (157 to 204 μ m), the zirconia

Table I. Zirconia Thermal Spray Experiments

	Amperage/ Power, A / kW	Gas flow rate, scfh		Particle Feed Rate, lb/h	Standoff Distance, in.	Traverse Rate, in./s	Particle ^a Injection Angle
		Primary	Secondary				
ZY01	900/36.0	100	47	3.5	3.0	20	r
ZY02	800/28.2	75	30	2	2.5	17	p
ZY03	1000/42.8	125	60	5	2.5	17	p
ZY04	800/31.1	75	60	5	3.5	23	p
ZY05	1000/39.2	125	30	2	3.5	23	p
ZY06	800/31.8	125	30	5	2.5	23	r
ZY07	1000/39.8	75	60	2	2.5	23	r
ZY08	800/33.9	125	60	2	3.5	17	r
ZY09	1000/35.1	75	30	5	3.5	17	r

^a r = 20 degrees rearward to flow, p = perpendicular to flow

Table II. Zirconia Powder Chemistry and Sieve Analysis

Chemistry						
Y ₂ O ₃	SiO ₂	TiO ₂	Al ₂ O ₃	Fe ₂ O ₃	HfO ₂	ZrO ₂
7.71	0.41	0.063	0.28	0.022	1.73	90.4
Particle size fraction						
μm :	>106	75-106	45-75	10-45	<10	
%:	0.0	3.7	57.1	39.2	0.1	

Table III. Materials Characterization Results

	Ni-Al Thickness, μm	ZrO ₂ Thickness, μm	Hardness ^a	Porosity, %
ZY01	178	322	92	11.7
ZY02	182	272	88	12.6
ZY03	204	515	90	7.3
ZY04	164	423	93	16.4
ZY05	163	154	84 ^b	19.3
ZY06	157	429	92	8.7
ZY07	162	212	87 ^b	7.9
ZY08	192	267	90	8.1
ZY09	169	587	92	11.5

^a Rockwell 15T hardness measurement.

^b Deposit was thin for the hardness measurement.

deposits, reflecting influences of spraying parameters, ranged from 154 to 587 μm . This corresponds to 3.8 to 14.7 μm per pass.

Variances in the extent of porosity and macroscopic cracking were also evident. Figure 1 presents optical micrographs of coating cross sections for Experiments ZY01 (base condition) and ZY03. The latter coating had the lowest porosity but most apparent macroscopic cracking (segmented cracking appearing both parallel and normal to the substrate) of all the coatings within the test matrix. The porosity of the zirconia coatings ranged between 7.9 and 19.3%.

Scanning electron microscopy revealed finer microstructural features. Porosity as small as 1 μm and fine microcracking were revealed at a magnification of 2000X (see Figure 2). Image analyses were performed on 10 randomly selected views of each coating at the magnification and conditions given in Figure 2. Average values of porosity, including micro- and macrocracking, are listed in Table III. The ZY03 coating, shown in Figure 2, was unique among the coatings examined. Segments of nearly fully dense material are separated by major cracks, suggesting a molten or vapor-phase deposition. A more extensive distribution of finer cracks existed throughout the structure of the other coatings. The curved, parallel geometry of the cracks in coating ZY03 suggests formation by shattering upon impact. Surface examinations with SEM revealed splat-like formations and rounding on protrusions and particles, indicating the predominance of molten conditions upon deposition (see Figure 3). Surface appearances varied at different locations on a given coupon and distinctive features are not readily correlated with experimental parameters.

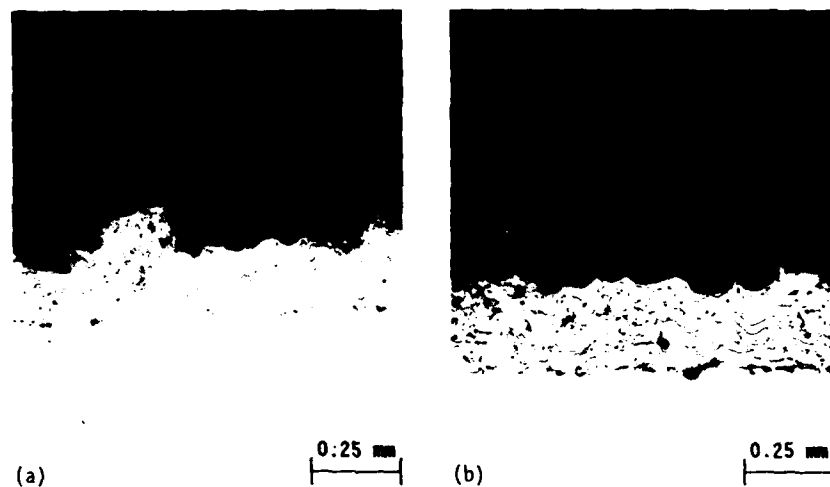
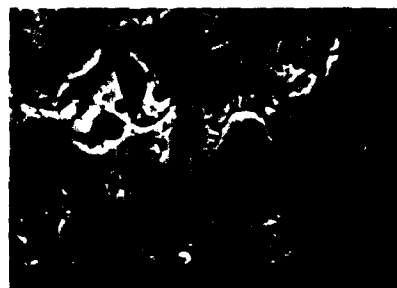
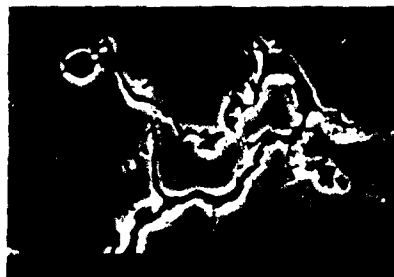


Figure 1. Microstructure of coating cross sections revealed by optical metallography. (a) ZY01, (b) ZY03.



(a)



(b)



(c)

Figure 2. SEM micrographs revealing porosity and cracking in (a) ZY01, (b) ZY03 and (c) ZY05 deposited at standoffs of 76 mm, 64 mm and 89 mm, respectively.

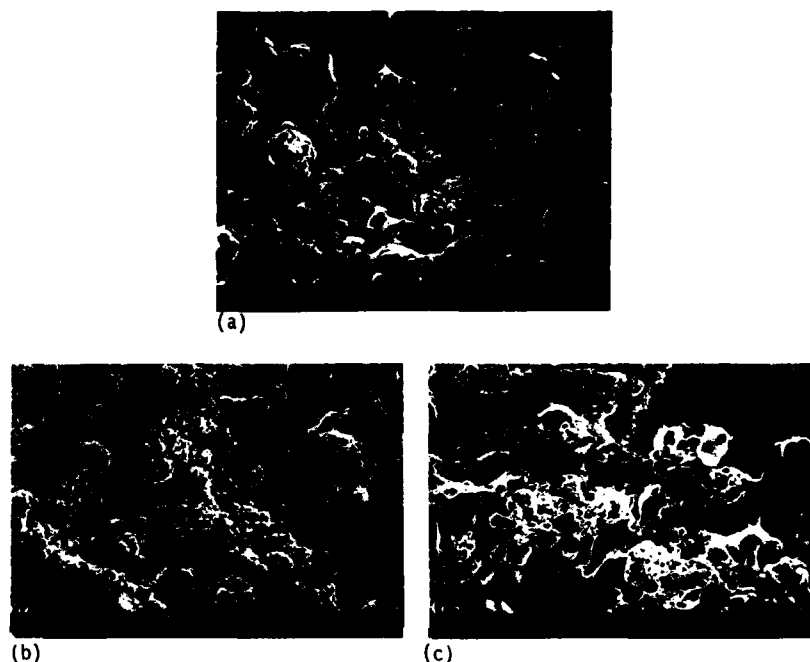


Figure 3. Surface morphologies of deposits revealed by SEM. (a) ZY01, (b) ZY03, and (c) ZY09.

X-ray diffraction measurements were conducted to qualitatively assess the phases in the coatings. The feedstock and coatings all exhibited XRD spectra which were similar and closely matched the cubic and tetragonal phases. No evidence of the monoclinic structure was detected. Although a detailed quantitative assessment has not been made, peak splitting at the (004) and (400) diffractions, as suggested in Reference 9, indicates a predominance of the tetragonal phase, or a mixture of the tetragonal and cubic phases.

Hardness measurements were taken on the coatings normal to the deposit using the Rockwell 15T method for measuring surface hardness. The averages of twelve measurements are listed in Table III.

TAGUCHI ANALYSIS

The Taguchi evaluation showed that only powder feed rate and traverse rate were significant factors affecting the deposition thickness. Their contributions to the total variation in thickness observed (rho percent, i.e., percentage of total variation due to the specific process parameter) were 83 and 13%, respectively. When other factors are pooled to represent an error term, the F factors for powder feed rate and traverse rate are 136 and 22, respectively, which indicates that there is a 99% certainty that these factors are significant. Increasing the powder feed rate increased the deposition thickness, as would be expected. The higher powder feed rate (5 lb/h) resulted in an average deposition of 488 μm (0.019 in.) compared with an average deposition of 226 μm (0.009 inch) at the lower powder

feed rate (2 lb/h). Increasing the traverse rate decreased the deposition thickness from 410 μm (0.016 in.) at 17 in./s to 304 μm (0.012 in.) at 23 in./s.

The fourfold variation in thickness of the coatings, from 154 to 587 μm , during a relatively constant processing time demonstrates the advantage of dc plasma spray coating deposition over other deposition processes: a coating can be rapidly deposited to a desired substantial thickness. To build up a zirconia coating efficiently, powder feed rate and traverse rate should be optimized. Undoubtedly, slowing the traverse rate will impact other coating qualities at some point, and increasing the powder feed rate will have an upper limit; but, assuming the microstructure remains acceptable, the key to maximizing the economics of the zirconia coating deposition is controlling powder feed rate and traverse rate.

Injection angle (33.3%), standoff distance (31.2%), traverse rate (13.8%), and secondary flow (12.9%) all had significant contributions to the variation in porosity (rho percentages). All had F factors corresponding to a 95% certainty of significance. Injecting backward at a 20 degree angle to the flow decreased the porosity compared to the perpendicular injection. The average porosity was only 9.0% during backward injection, while it was 13.9% on an average for perpendicular injection. Increasing the standoff distance from 2.5 to 3.5 in. increased the average porosity from 9.1 to 13.8%. Increasing the traverse rate also increased the average porosity, from 9.9% at 17 in./s to 13.1% at 23 in./s. Increasing the secondary flow decreased the porosity from an average of 13% at 30 scfh to 9.9% at 60 scfh. The four factors are significant and this indicates that there are strong interaction effects on porosity. For the parameter values used in these experiments, variations in amperage, primary gas flow, and powder feed rate are insignificant with respect to porosity. Thus, further study of zirconia coating porosity should be concentrated on the most influential factors -- injection angle, standoff distance, traverse rate, and secondary flow.

Porosity in a zirconia coating is desirable because it increases the coating's insulating capability. The variation in porosity displayed indicates substantial variations in plasma processing conditions. The next step is to attempt to optimize thermal insulation properties, thermal cycling, and coating integrity with porosity for the specific application. Because four of the parameters exhibit influence on porosity, the targeted coating porosity can probably be attained under a variety of plasma conditions.

The Taguchi evaluation revealed that the significant factors affecting hardness were powder feed rate and amperage. Increasing amperage decreased the hardness, while increasing the powder feed rate increased hardness. This result would need to be confirmed, however, due to questions about the validity of the hardness readings (samples ZY05 and ZY07 were too thin for the hardness measurements).

COMPUTER MODELING AND RESULTS

Modeling energy transport in a thermal plasma requires solving the equations for mass, momentum, and energy conservation for both the arc column and plume. This information is required to solve the plasma/particle interaction problem. A detailed bibliography of the work conducted in this area can be found in Reference 11.

The plasma spray torch of this study was numerically modeled using state-of-the-art computer codes for the conditions of experiment ZY01. Details, equations, results, and methodology for the plasma dynamics model are discussed in Reference 12. Typical output from this model includes temperature, enthalpy, velocity, and other properties as a function of radial and axial position in the column and plume of the arc torch.

A number of mathematical models have been developed for the treatment of particulates in dc plasma torches. A detailed bibliography of the work conducted in this area can be found in References 11-13. The plasma/particle computer program employed in this study [13] uses the temperature and velocity fields generated by the plasma plume program to calculate the dynamics of particles injected into the plasma. The injected particle's vaporization rate, average temperature, and velocity are calculated as a function of position in the plasma. Details, equations, and methodology for the particle dynamics model are discussed in Reference 13.

Table IV lists the analytical predictions for the zirconia particles. Prior plasma/particle analysis has indicated that the particle dynamics code overpredicts the amount of vaporization for alumina ceramic particles [13]. This trend is assumed to occur for the zirconia predictions of this study.

The melting and boiling points of zirconia are 2963 and 4573 K, respectively. As particle size decreases, the surface-to-volume ratio becomes larger, and thus a larger amount of heat is delivered to the particle per volume. The average temperature at the standoff distance for each specific particle shown in Table IV is a function of the heat transfer to the particle, which is a function of the unique trajectory of that particle. All the particles were predicted to exceed the melting point of zirconia for a significant portion of their trajectory. This suggests that all the particles were molten or semi-molten at impact. In the calculations, particles smaller than 30 μm are predicted to vaporize from 16 to 45% of the original particle diameter; intermediate sized particles in the range of 35 to 55 μm are predicted to vaporize from 4 to 13%, and particles larger than 60 μm are predicted to vaporize only up to 2%. Future zirconia diagnostic measurements of temperature, velocity, and size will allow correlation analysis to refine the vaporization model in the code.

The calculations indicate that the smaller the particle, the higher the velocity due to the larger acceleration from the drag forces. As particle size increases, the traversing particles pass further away from centerline. The largest particles pass through the core of the plasma, ending up in the fringes of the plasma plume.

DISCUSSION

Power density and powder feed parameters were normalized and compared to coating characteristics. Figure 4, a plot of zirconia coating thickness as a function of powder delivery (i.e., powder feed rate divided by traverse rate in lb/in.) for the various experiments, shows increasing deposition thicknesses with increasing powder delivery. This is consistent with the Taguchi analysis which indicated that powder feed rate and traverse rate were the dominant process parameters for coating thickness. Since the power density for the nine experiments is nominally 0.249 kW/scfh and the power density standard deviation is 0.046 kW/scfh, its effect on coating thickness is minimal.

Percent porosity was also examined relative to the ratio of powder delivery to power density (i.e., power divided by total flow in kW/m^3). The data in Figure 5 indicate a relatively constant percent porosity (8 to 12%) for all powders with rearward injection. This may reflect a more uniform, or more completely molten, condition at all standoff distances. Perpendicularly injected powders, however, show greater variability in porosity. Coatings formed at a 3.5 in. standoff have greater porosity than coatings formed at 2.5 in. This may be because cooling of the particles rendered them less ductile, thus allowing more void formation.

The above observations may be considered in the light of the predicted extent of heating, vaporization, and melting summarized in Table IV. The analytical model assumes that the entire particle is at one average temperature. The calculations indicate all the original particles were above

Table IV. Predicted Zirconia Particle Behavior at Standoff Distance (76 mm)

Original Diameter, μm	Velocity, m/s	Temperature, K	Final Diameter, μm	Radial ^a Location, mm
10	420	2473	5.5	-5.3
15	440	2921	10.0	-4.0
20	376	3006	14.8	-5.0
25	295	3068	19.9	-8.9
30	236	3248	25.1	-12.9
35	192	3409	30.3	-17.6
40	167	3556	35.7	-18.9
45	146	3620	41.1	-20.0
50	130	3684	46.8	-21.1
55	116	3736	52.7	-22.4
60	105	3777	58.6	-24.1
65	95	3810	64.6	-25.4
70	88	3613	70	-26.8
75	81	3275	75	-28.6

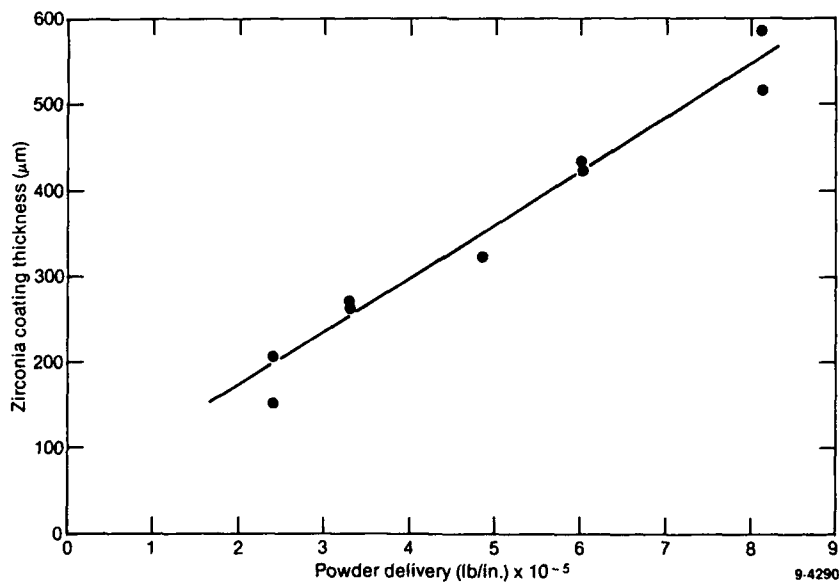
^a From centerline.

Figure 4. Zirconia coating thickness plotted as a function of powder delivery rate.

the melting point during a significant portion of their trajectory. This indicates that all the particles are molten or semi-molten at impact. Due to the varied trajectories, some of the particles cooled by the time they reached the standoff distance. In reality, internal gradients, which are not

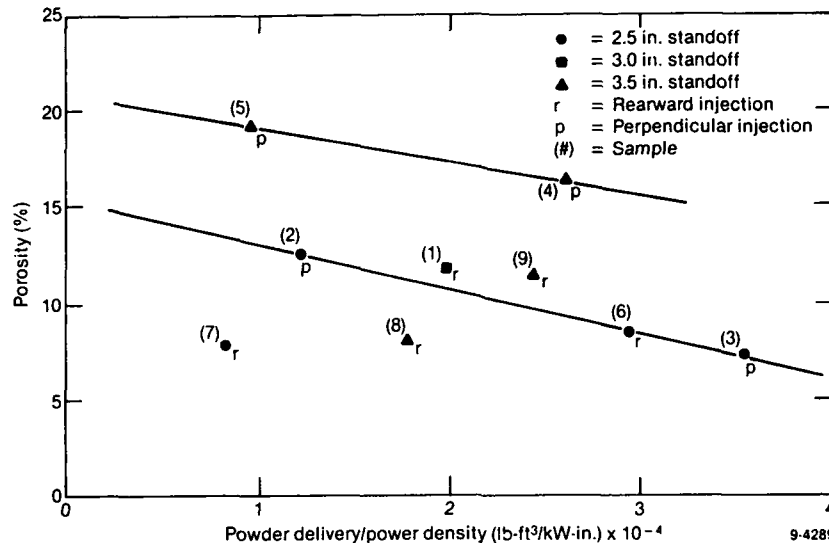


Figure 5. Porosity with respect to the amount of powder injected relative to the power density.

considered in the model, result in portions of the particles being in a more ductile state (i.e., the core of the smaller particles, the edges of the larger particles).

From trajectory analysis, particles greater than $45\text{ }\mu\text{m}$ were predicted to pass through the core of the plasma, ending up in the fringes of the plasma plume. Sieve analysis of the powder (Table I) indicates that this is approximately 60.8% of the powder, and most is probably lost as overspray. Particles in the range from 30 to $45\text{ }\mu\text{m}$ (17.2% of the powder) were completely molten; but because of their trajectories, most of these powders also ended up in the periphery of the plume as overspray. Deposition tests for alumina ceramic powder have indicated that the bulk of the coating is deposited in a pattern approximately 26 mm in diameter. Thus, particles in this core (i.e., $\pm 13\text{ mm}$ of centerline) of the plume probably account for the bulk of the zirconia particles deposited in the coating (original diameter particles in the range from 10 to $30\text{ }\mu\text{m}$). These particles comprise 22% of the powder. Based on the analysis, it is estimated that the larger particles in this size range remain totally molten, while the smaller particles solidify at the standoff distance. Since the surface to volume ratio increases with decreasing particle size, the smaller particles cool faster due to radiative and convective heat transfer.

Partially molten particles will form splats and irregularities that will ultimately result in porosity, which is an important feature of thermal barrier coatings. Porosity in these coatings is depicted in the SEM micrograph in Figure 3. As the particles are deposited on the substrate, the liquid and ductile particles form irregularities on the surface that can trap air or gas, preventing complete filling during subsequent deposition. The lowest porosity coatings would be expected for a stream of completely molten particles with high velocity. Partially molten particles result in irregular surfaces and higher porosity.

All the particles are predicted to vaporize to some extent (i.e., 45% for a $10\text{ }\mu\text{m}$ particle, 1% for a $65\text{ }\mu\text{m}$ particle). Condensation of the

predicted vaporized species into fine particles may be occurring in cooler regions in the plume. These fine particles will ultimately be deposited in the coating.

The calculations indicate that as particle size increases, the traversing particles pass farther away from centerline. Particles larger than $45\text{ }\mu\text{m}$ seem to be most responsible for the low deposition efficiency. Typical deposition efficiency for the powder ranges from 45 to 65%, which is consistent with the analytical predictions and the sieve analysis. The analysis indicates that the zirconia powder of this study should be sieved in the range of 10 to $40\text{ }\mu\text{m}$ for increased deposition efficiency.

Although greater power density intuitively suggests greater melting, at higher power the velocities are increased and residence times decreased, which results in less total heat transferred to the particles. This explains the finding of the Taguchi analysis that powder feed rate, standoff distance, traverse rate, and injection angle are more significant than power density for the coating characteristics of thickness and porosity. The greater extent in which particles remain molten results in a more dense deposit. Sample ZY03, which provided the most dense deposit in this study, was fabricated with a nominal power density, the slower traverse rate, the higher powder feed rate, and the shorter standoff distance. These process parameters appear favorable for highly molten particles at deposition. Sample ZY05, with the highest porosity of all nine samples, was fabricated with a nominal power density and the longer standoff distance (3.5 in.), which allowed a longer time for the particles to cool in the plume and resulted in resolidified, less ductile particles. Sample ZY09 had the highest power density of all nine samples but, due to the 3.5 in. standoff distance, had similar particle morphology to Sample ZY05.

Cross sections of the coatings viewed at high magnification revealed interesting contrasts (Figure 2). The more dense deposit (Sample ZY03) appears more continuous but exhibited a limited number of larger macrocracks. Other coatings appeared to have arrays of microcracks, giving the appearance that they were deposited more as a solid state or shattered by impacting particles. In addition to indicating possible differences in the deposition mechanism, these observations indicate that the finer microcracks may provide some stress relaxation to avoid the larger macrocracks.

The above discussion illustrates that the understanding and prediction of mechanisms in plasma deposition is not complete. Questions regarding the role of vaporization, degree of melting, radial distribution of particles, influence of velocity, particle loading, and residence time merit future investigations. It is hoped that in situ measurements of particle size, velocity, and temperature will provide more details to the deposition mechanisms and correlations with operating parameters.

SUMMARY AND CONCLUSIONS

An analytical and experimental study of the plasma spraying of zirconia has been presented. The experiments used a Taguchi fractional factorial approach to study the effects of varying typical process parameters. The coatings were characterized using optical microscopy, scanning electron microscopy, and x-ray diffraction.

The zirconia coating thicknesses, reflecting influences of spraying parameters, ranged from 154 to $587\text{ }\mu\text{m}$. Variances in the extent of porosity and macroscopic cracking were evident. Porosity of the coatings ranged between 7.9 and 19.3%. Hardness measurements varied from 179 to 248 Rockwell 15T. The coatings maintained a predominantly tetragonal phase or mixture of cubic and tetragonal phases. Additional understanding of particle conditions is still needed to correlate and predict porosity and deposition efficiencies.

The Taguchi analysis indicated that only traverse rate and feed rate were significant factors affecting the deposition thickness. The significant factors for hardness were feed rate and amperage. Injection angle, standoff distance, traverse rate, and secondary flow all significantly affected porosity.

The fabrication of plasma sprayed thermal barrier coatings requires that a large fraction of the powder particles be in a molten or partially molten state upon impingement on the substrate, and the particles must have sufficient velocity for the formation of the platelets. The analysis indicates that all the particles were at a molten or semi-molten state at the standoff distance. The zirconia powder should be sieved from 10 to 40 μm for increased deposition efficiency.

The objective of this and future work is to optimize zirconia coatings. It begins with generating baseline data on factors that influence coating characteristics. Other important characteristics besides thickness and porosity need to be quantitatively evaluated using a similar experimental approach to obtain a better understanding of the process so that a variety of customized coatings can be developed for specific applications.

The procedure described in this paper will provide substantial assistance in selecting and optimizing the operational parameters for future zirconia plasma spray processing experiments and applications. Future work is needed for diagnostic measurements of the plasma and particle dynamics that will be used to refine the analytical models to obtain a better understanding of the process.

ACKNOWLEDGMENTS

The technical input of T. L. Eddy and G. D. Lassahn, INEL, is gratefully acknowledged, as are the optical metallographic and SEM results provided by V. L. Smith-Wackerle and D. V. Miley, and XRD data provided by A. Erickson and J. R. Knibloe. The work described in this paper was supported by the U.S. Department of Energy under DOE Contract No. DE-AC07-76ID01570.

REFERENCES

1. E. D. Kubel, *Advanced Materials and Processes*, **132**, (6), pp. 69-80 (December 1987).
2. E. Pfender, "Fundamental Studies Associated with the Plasma Spray Process," Proceedings of the National Thermal Spray Conference, September 14-17, 1987, Orlando, Florida.
3. P. Fauchais, "State of the Art for the Understanding of the Physical Phenomena Involved in Plasma Spraying at Atmospheric Pressure," Proceedings of the National Thermal Spray Conference, September 14-17, 1987, Orlando, Florida.
4. T. E. Mantkowski, D. V. Rigney, M. J. Froning, N. Jayaraman, "Characterization of $\text{ZrO}_2\text{-Y}_2\text{O}_3$ Thermal Spray Powder Systems," in Ceramic Coatings for Heat Engines, Strasbourg, France, November 26-28, 1985.
5. C. A. Andersson, et al., "Advanced Ceramics for Industrial/Utility Gas Turbine Applications," DOE/NASA.0110-1, NASA-CR-165619, February 1982.
6. H. D. Steffens and V. Fisher, *Surface and Coatings Technology*, **32** pp. 327-338, (1987).

7. E. Lugscheider, et al., "Influence of Different Plasma Spray Processes and Various Types of Stabilized Zirconia on the Morphology of Thermal Barrier Coatings," Advances in Thermal Spraying, Montreal, Canada, September 8-12, 1986, Welding Institute of Canada pp. 261-268 (1986).
8. M. J. Froning and N. Jayaraman, "Quantitative Phase Analysis by X-Ray Diffraction of the ZrO_2 -8% Y_2O_3 System," in High Temperature Coatings, The Metallurgical Society AIME, Orlando, Florida, October 7-9, 1986, pp. 179-191.
10. G. Taguchi and S. Konishi, Taguchi Methods: Orthogonal Arrays and Linear Graphs, 1987 ASI Press.
11. R. F. Culp, SADIE, 1989.
12. D. J. Varacalle, Jr., et al., "An Analytical and Experimental Investigation of the Plume Dynamics of Nontransferred Arc Torches," American Society of Metals National Thermal Spray Conference Symposia Proceedings, Cincinnati, November 1988, pp. 45-49.
13. Y. C. Lee, "Modeling Work in Thermal Plasma Processing," Ph.D. Thesis, University of Minnesota, 1984.
14. D. J. Varacalle, Jr. et al., "Modeling Particulate Injection in Thermal Plasma Material Processing Experiments," Metallurgical Society Symposia Proceedings, The Reinhardt Schuhmann International Symposium on Innovative Technology and Reactor Design in Extraction Metallurgy, pp. 501-518.

LASER-INDUCED MATERIALS SYNTHESIS OF ULTRAFINE CERAMIC PARTICLES FROM SPECIALLY DESIGNED MOLECULAR PRECURSORS

Tongsan D. Xiao, Peter R. Strutt,* and Kenneth E. Gonsalves**

* The University of Connecticut, Institute of Materials Science and Department of Metallurgy, U-136, Storrs, CT 06268.

** Stevens Institute of Technology, Department of Chemistry and Chemical Engineering, Hoboken, NJ 07030.

ABSTRACT

The investigation involved the synthesis of Si_3N_4 surface layers on a Ti substrate by a specially designed organosilazane liquid precursor, $(\text{CH}_3\text{SiH}_2\text{NH})_x$ with $x = 3$ or 4, by pyrolysis with a 10.6 μm . continuous wave CO_2 laser. Microstructural examinations revealed that the particles of the nitride layers were spherical in shape with diameters ranging from 50 to 150 nm. Based on the experimental evidence, suggestions are made of possible mechanisms occurring during film deposition.

INTRODUCTION

The highly desirable, and in many cases unique, properties of ultrafine-particle materials are gaining rapid recognition, particularly in view of the Ultrafine Particle Project [1] and Gleiter's work [2]. There are obvious advantages, for instance, in exploiting the properties of ultrafine-particle hard materials in tribological applications. In this case, a significant increase in fracture toughness, resulting from homogeneous elastic and plastic properties, naturally favors superior wear resistance. The possibilities of structural refinement, however, become particularly intriguing when grain and particle size are reduced to the nanometer scale. Such materials, as shown by Gleiter [2] can display particularly novel mechanical, electrical, and magnetic properties. In following Gleiter's method of synthesis, Eastman and Seigel [3] have shown that nanoscale materials possess fast diffusion, low sintering temperature characteristics, and improved mechanical properties.

Gleiter's method of synthesizing nanocrystalline materials, it should be noted, involves obtaining powders by evaporation, followed by rapid condensation. In another approach, it is interesting to note that 20 nm. particles of Si_3N_4 have been synthesized by Haggerty, et al. [4,5] using laser chemical vapor deposition. Again, however, such powders have to be consolidated in order to produce bulk material. In view of this, the development of a method for integrating (i) nanoscale particle synthesis, and (ii) surface layer deposition into a single process is of considerable technological importance. The viability of achieving this, is provided by studies involving the synthesis of Si_3N_4 deposits, by the interaction of a CO_2 laser beam with a liquid precursor [6,7,8]. The particular precursors used were Hexamethylcyclotrisilazane and similar compounds. This paper presents preliminary results in a more detailed investigation involving specially designed liquid precursors. The primary features required of such a compound (in the present laser processing technique) are:

- (i) strong absorption of 10.6 μm . wavelength radiation
- (ii) high liquid to solid conversion yield
- (iii) low toxicity

(iv) high degree of purity.

EXPERIMENTAL METHOD

Precursor Synthesis and Properties

The liquid precursors were prepared by the ammonolysis of methylchlorosilane, $\text{CH}_3\text{SiHCl}_2$. Experimentally, Diethyl ether and methylchlorosilane were cannulated into a flask cooled to 0°C in an ice bath. An excess of anhydrous ammonia was bubbled into the flask with vigorous stirring until the solution was strongly basic. The reaction mixture was stirred for another two hours and then filtered under argon. The solvent was removed via trap-to-trap distillation under vacuum leaving an oily residue. The ammonolysis product consists mainly of cyclic $(\text{CH}_3\text{SiH}_2\text{NH})_x$ with $x=3$ and 4, the major component being the $x=4$ cyclic. And the molecular weight is about 290 g/mol (Fig. 1).

Fourier transform infrared spectroscopy of the precursor revealed a strong absorption peak in the $10.6\ \mu\text{m}$. wavelength region. From absorption measurements on a series of samples with varying dilution in a solvent, it was shown that Beer's law $I = I_0 \exp(-\alpha x)$ was obeyed. The term α is the absorption coefficient, and x is the liquid depth. Experimentally, the value of α at a wavenumber of $941\ \text{cm}^{-1}$ (or $10.6\ \mu\text{m}$.) was $45.196\ \text{cm}^{-1}$; this shows that 95% of the radiation is absorbed within a depth of $11\ \mu\text{m}$.

Laser Pyrolysis Processing

A general view of the processing chamber is shown schematically in Fig. 2. A port on the top of the chamber provides access for a convergent beam of a high power cw CO_2 laser. Prior to entering the main chamber, the beam passes through a small chamber maintained at a small excess pressure, and then emerges through a small aperture. This is used to minimize deposition of reaction products on the laser window. A side view-port is used to observe the plume formed above the substrate during the laser-precursor reaction. As shown in Fig. 2, and in more detail in Fig. 3, the substrate (a 1 cm. diameter and 0.025 cm. thickness Ti disc) lies inside a metal container, which is mounted on a rotation stage. Actual immersion of the Ti disc in precursor liquid is achieved by introducing a given volume of liquid into the metal container via a syringe (see Fig. 2).

Prior to laser irradiation, the processing chamber is evacuated, flushed several times with nitrogen, then backfilled with nitrogen to about 1000 torrs. The particular deposits discussed in this paper were obtained by allowing the substrate to make four revolutions at a velocity of $1.5\ \text{cm.s}^{-1}$. Before the laser irradiation tests, 0.04 ml. of precursors were introduced into the metal container, to initially immerse the substrate to a depth of 0.5 mm. Using a 700 watt beam, focussed to 3 mm. diameter on the substrate, each irradiation was carried out at $\sim 10^4\ \text{w.cm}^{-2}$ for 0.2 s.; the interaction time is calculated as beam diameter/velocity.

RESULTS AND DISCUSSIONS

In individual experiments an intense plume formed each time the substrate container passed beneath the laser beam, see Fig. 3. The high plume temperature, optically determined to be in excess of 2000°C , ensured complete pyrolysis of the

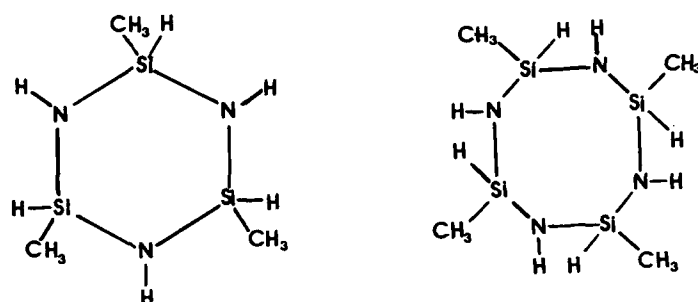


Fig. 1. Molecular structure of the organosilazane $(\text{CH}_3\text{SiH}_2\text{NH})_x$ liquid precursors.

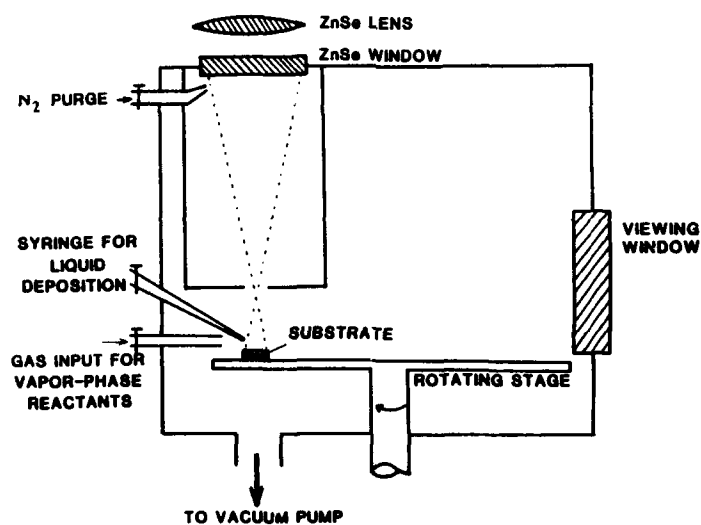


Fig. 2. Schematic diagram of the reaction chamber used in the deposition experiment.

precursors, to form Si_3N_4 molecular species. Condensation of these species from the plume results in the nucleation and growth of 50-150 nm. diameter particles. These were deposited on the:

- (i) chamber walls, where they were only weakly adherent
- (ii) laser heated Ti substrate, where they formed a consolidated, and strongly adherent deposit.

Typically, the 0.04 ml of liquid precursor is completely consumed after 4 successive rotations of the substrate beneath the beam. To examine the morphology of the Si_3N_4 deposited layers, fragments were removed from the substrate by scratching with diamond stylus. As revealed by scanning electron micrographs, see Fig. 4, it is possible to discern individual layers formed during the successive laser beam interactions. The thickness of the deposited layer has been determined by mechanical profilometry. A cross-section thickness profile obtained in this way is shown in Fig. 5, this is for deposit produced using the processing conditions given in the text. Two features are revealed in the figure: the first is the rapidity of growth which corresponds to several microns per second of laser interaction time. The second is the progressive diminution of thickness as one moves away from the center. Nevertheless, the deposited thickness is still appreciable well outside the nominal beam width.

The scanning electron micrograph (Fig. 6) of the surface of a deposit reveals the way 50-150 nm. diameter Si_3N_4 particles have sintered, under laser heating, to form a consolidated layer. Individual particles and particle clusters are shown at higher magnification in the transmission electron microscope, see Fig. 7. These were removed from a deposit by replica extraction.

From the experimental observation, the role of the laser beam in promoting Si_3N_4 particle synthesis and in facilitating substrate-particle bonding is clearly evident. It is therefore not surprising that a critical selection of process parameters was required to produce a good quality deposit, which was tenaciously bonded to the substrate. It was found, for example, that when the laser interaction is too short, the substrate temperature is too low to promote good adhesion. Conversely, when the laser interaction time is too long, strong beam coupling causes excessive heating, leading to sublimation and disintegration of the ceramic deposit. The rapidity of forming surface deposits by transient laser heating, it should be noted, is a consequence of the high sintering rates obtainable using ultrafine-particle materials. As discussed by Ashby [9], classical sintering theory predicts that the sintering rate for a compact of spherical particles is inversely proportional to the cube of the radius. Thus, an agglomeration of nanoscale spherical particles will sinter together 10^3 to 10^6 times faster than that encountered in the consolidation of 1 to 10 micron diameter ceramic particles. For example, Terwilliger and Lange [10] found that at 1 atm. pressure of nitrogen, 0.5 hour of sintering at 1500-1600°C was required to produce significant sintering of Si_3N_4 powder compacts. Finally, it is interesting to note that Eastman and Seigel [3] recently found that TiO_2 nanoscale powders could be consolidated at unusually low temperatures.

Elemental analysis of the deposited layers by auger electron spectroscopy revealed only two detectable impurities, namely carbon and oxygen. At the surface the contaminations of these were 20 and 5 atomic percent, respectively. As previously shown by Partridge and Strutt [6] in laser pyrolysis of hexamethyltricyclosilazane, the magnitude of these impurities decreased with removal of material by sputtering. A marked improvement over the previous study [6] was the absorbance vs. wave-number curve, as obtained by Fourier transform infrared spectroscopy. A comparison between the curves for a Si_3N_4 standard and a deposit is shown in Fig. 8. One

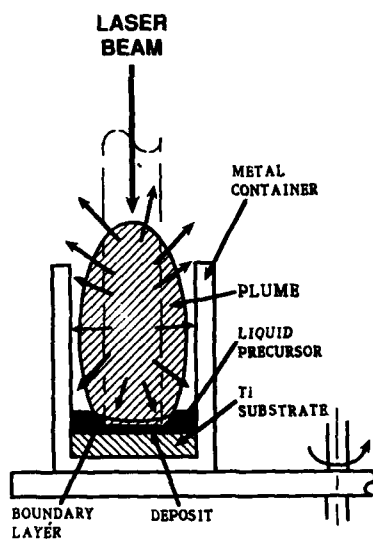


Fig. 3.
Schematic diagram of the reaction
in the metal container.



Fig. 4.
Scanning electron micrograph of a
deposit revealing three successively
formed layers.

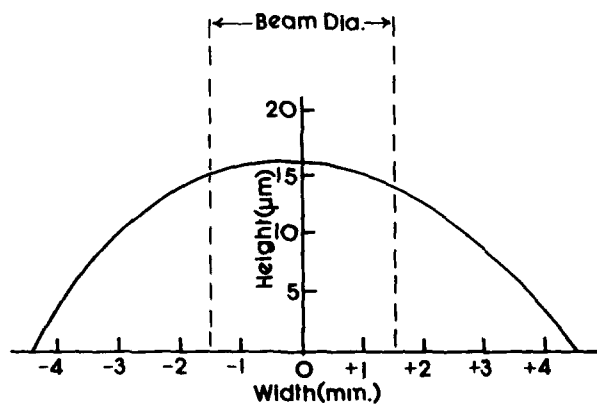


Fig. 5. Profile of a silicon nitride deposit using the process depicted
in Fig. 2.

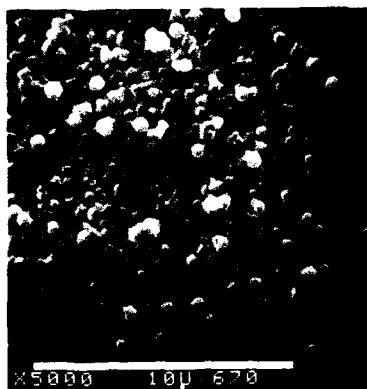


Fig. 6.
Scanning electron micrograph of
the surface of a deposited layer.



Fig. 7.
Transmission electron micrograph of
silicon nitride particles extracted
from the surface of a deposited layer.

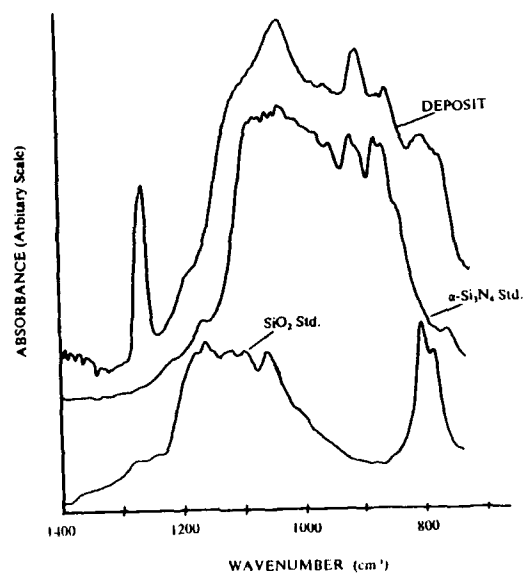


Fig. 8. Infrared absorption spectra for as-deposited Si_3N_4 , a Si_3N_4 standard and a SiO_2 standard.

feature in the curve for the deposited material is a Si-CH₃ peak at 1260 cm⁻¹ wave-number. This peak was also seen in the previous study [6], where an interesting discovery was the effectiveness of post-laser heating in nearly eliminating the peak. This technique will be investigated in a continuation of the present study.

CONCLUSION

The recent study clearly demonstrates that highly tenacious and well-sintered deposits of Si₃N₄ can be synthesized in an integrated process. This is achieved by the laser pyrolysis of a specially designed molecular precursor that strongly absorbs 10.6 μm. radiation. Specific features of the process are the high achievable growth rate (several microns per second) and particle size (typically 150 nm., but as low as 50 nm.). An interesting feature is that the process occurs at relatively high pressure (~ 1000 torrs).

ACKNOWLEDGEMENT

It is a pleasure to acknowledge the support of this work by the Office of Naval Research, under contract N0014-78-C-0580

REFERENCES

1. C. Hayashi, J. Vac. Sci. Technol. A, 5, 1375 (1987).
2. R. Birringer, V. Herr, H. Gleiter, presented at the 1986 MRS Fall Meeting, Symposium: 'Chemical Vapor Deposition of Ceramic Nanocomposites.'
3. J. Eastman & R. Seigel, Research & Development, p.56, Jan. 1989.
4. S. C. Danforth & J. S. Haggerty, J. Amer. Ceram. Soc., 66, 58 (1983).
5. W.R. Cannon, S. C. Danforth, J. H. Flint, J. S. Haggerty, & R. A. Marra, J. Amer. Ceram. Soc., 65, 324 (1982).
6. J. P. Partridge & P. R. Strutt, SPIE, 669, 150 (1986).
7. P. R. Strutt & J. P. Partridge, Mat. Res. Soc. Symp. Proc. 98, 385 (1987).
8. J. P. Partridge & P. R. Strutt, Mat. Res. Soc. Symp. Proc. 75, 273 (1987).
9. M. F. Ashby, Acta Met., 22, 275 (1974).
10. C. R. Terwilliger and F. F. Lange, J. Amer. Ceram. Soc., 57, 25 (1974).

PROCESSING AND PROPERTIES OF NANOPHASE OXIDES*

J. A. EASTMAN, Y. X. LIAO†, A. NARAYANASAMY‡ and R. W. SIEGEL

Materials Science Division, Argonne National Laboratory, Argonne, IL 60439-4838.

ABSTRACT

Nanophase oxides (Al_2O_3 , MgO , ZnO and TiO_2), with typical grain sizes in the range 2-20 nm, have been synthesized by the condensation of ultrafine particles in a convective inert gas followed by their collection and in-situ consolidation in vacuum at ambient temperature. These new materials, owing to the reduced scale of their grains along with the enhanced cleanliness of their grain boundaries, are found to have significantly improved properties relative to those of their coarser-grained, conventionally-prepared counterparts. Nanophase rutile (TiO_2) with an initial mean grain diameter of 12 nm, for example, has been found to sinter at 400 to 600°C lower temperatures than conventional rutile powders, without the need for compacting or sintering aids, while retaining a small grain size. Additionally, the importance of the extremely clean surfaces obtained with the gas condensation method has been demonstrated by comparing the sintering behavior of powders with and without air exposure prior to consolidation. The research completed on the processing and properties of nanophase ceramics is reviewed, and the potential for engineering advanced ceramics using the nanophase processing method is discussed.

INTRODUCTION

Nanophase materials (ultrafine-grained bulk materials, typically with grain sizes of 2-20 nm) produced by the gas-condensation process [1, 2] have recently been found to possess a variety of interesting and novel properties which are often superior to those of their coarser-grained counterparts. A number of review articles on this subject have recently appeared (e.g., [3-6]). Ultrafine-grained ceramics and ceramic-based composites are of particular interest because of the wide variety of potential applications which exist, where nanophase processing may impart particular advantages. For example, indications that the inherent brittleness of conventional

* Work supported by the U. S. Department of Energy, BES-DMS, under Contract W-31-109-Eng-38.

† Permanent address: Measure and Testing Center, Sichuan University, Chengdu, People's Republic of China.

‡ Permanent address: Department of Nuclear Physics, University of Madras, Madras, India.

ceramics may be overcome in ultrafine-grained TiO_2 and CaF_2 have been seen [7]. Also, it has been shown that nanophase TiO_2 powder sinters at 400-600°C lower temperatures than conventional powders, without the need for compacting or sintering aids [8], and that ultrafine grain size is maintained in the process.

While many ultrafine ceramic powders have previously been produced by the gas-condensation method (e.g., [9, 10]), it is only in the past few years that researchers have attempted to consolidate such powders in situ to produce ultrafine-grained bulk materials, as first suggested for the synthesis of nanocrystalline metals by Gleiter [11]. In the present paper, the conditions required to produce several nanophase oxides by the gas-condensation technique are described, the advantages of the gas-condensation process over other small particle-producing techniques are demonstrated, and the potential for producing materials with specially tailored properties by means of nanophase processing is discussed.

PROCESSING OF NANOPHASE CERAMICS

The nanophase ceramics produced in this study were synthesized in an ultrahigh-vacuum (UHV) system fitted with resistively-heated evaporation sources, a collection device and scraper assembly, and in situ compaction devices for consolidating the powders produced and collected in the chamber. Such an apparatus is depicted schematically in Figure 1. Ultrafine powder is produced by evaporating material in the chamber after pumping the system to a vacuum of better than 10^{-5} Pa and then backfilling with a controlled high-purity gas atmosphere [1,2,12]. The gas atmosphere is typically a few hundred Pa of an inert gas such as He. Reactive gas mixtures containing inert gases plus partial pressures of reactive gases such as oxygen can also be used if desired. Because the atoms or molecules being evaporated collide with the gas atoms in the chamber, lose their energy, and condense, small gas-borne particles are formed rather than continuous films, which would be produced by evaporating materials onto a substrate under vacuum conditions. Collection of the powders formed in close proximity to the evaporation source is carried out by establishing convective currents inside the chamber by means of a liquid nitrogen cold finger. In the apparatus presently being used, the cold finger is the powder collection device as well, and is in the form of a hollow tube which is filled with liquid nitrogen from outside the vacuum chamber. After completing the evaporation process, the powders that have been collected are removed from the tube using a Teflon annular ring, which is moved downward along the length of the cold finger. The tube is in a vertical orientation so that gravity can be used in order to transfer the powder to the in situ compaction devices located below the base of the main vacuum chamber.

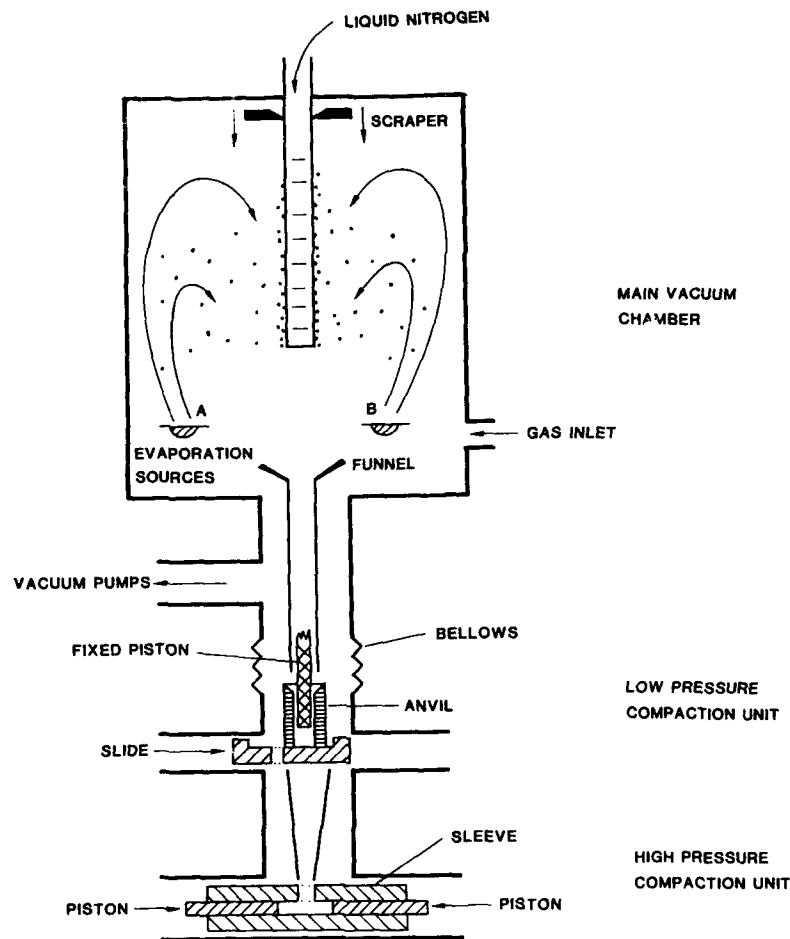


Figure 1. Schematic drawing of a gas-condensation chamber for the synthesis of nanophase materials. The material evaporated from sources A and/or B condenses in the gas and is transported via convection to the liquid-N₂ filled cold finger. The powders are subsequently scraped from the cold finger, collected via the funnel, and consolidated first in the low-pressure compaction device and then in the high-pressure compaction device, all in vacuum. From [4].

The consolidation of the powders to form a bulk ceramic is presently accomplished using a two-stage compaction unit. The upper stage consists of a simple piston and anvil arrangement which operates using very low consolidation pressures in order to form a loosely-compacted pellet. This pellet is transferred under vacuum to a second unit, in which the pellet is consolidated at ambient temperature under high pressures (typically 1.4 GPa) between two tungsten-carbide pistons. The scraping and consolidation are performed under UHV conditions after removal of the inert or reactive gases from the chamber, in order to maximize the cleanliness of the particle surfaces and the interfaces that are subsequently formed in the material. Surprisingly high densities of the as-compacted samples have been measured. Typical values are 50 to 80% of bulk density measured for TiO_2 and MgO , respectively, by weighing the samples in air and comparing with their volume; higher values of 75-90% are obtained by Archimedes method measurements [13]. (It is not certain at present whether the differences in results from these two types of measurements are due simply to a lack of precision owing to small sample size or to partial pore filling via capillarity in the application of the Archimedes method.) The resulting samples are disk-shaped and are typically 9 mm in diameter and 0.1 to 0.5 mm in thickness. While these dimensions are rather small by normal industrial standards, the need at present is only to produce samples large enough to facilitate characterization of their structure and properties. If design modifications were to be made, there are believed to be no impediments which preclude scaling the process up to produce larger commercial-sized samples.

Four nanophase oxides have been produced to date in this ongoing study: TiO_2 , Al_2O_3 , MgO and ZnO . Different procedures are required to produce the different materials. TiO_2 , the properties of which have been studied in the most detail so far [8], is produced by first evaporating Ti (99.99% purity) to form small Ti metal particles, and then subsequently introducing oxygen rapidly into the chamber. During this second process, the Ti particles collected on the cold finger, which is warmed to room temperature, are spontaneously converted to TiO_2 (predominantly the rutile phase). A rapid rate of oxygen introduction to the chamber has been found to be important; bleeding oxygen in slowly results in the formation of a mixture of rutile and other oxide phases. Following oxidation, the chamber is evacuated again; the oxide powder is then collected and consolidated under vacuum conditions. The resulting material has a log-normal grain-size distribution with a typical mean grain size of approximately 12 nm. Post-oxidation at room temperature of metal particles to form oxides has not been found to be a viable process for any materials tested yet other than Ti, however. For materials such as Al or Mg, which are also extremely reactive with oxygen, a thin protective amorphous coating is believed to form, which prevents the complete oxidation of the metal. Because of this, it has been necessary to search for different techniques to produce other oxides. In order to produce Al_2O_3 , ultrafine Al powders

are first produced and then annealed in air at 1000°C, which results in transformation of the powder to the thermodynamically stable α -phase of Al_2O_3 . Little increase in particle size occurs during the annealing process; the final average particle size obtained is about 18 nm using these conditions.

Most oxides have very high melting points and, because of this, are not good candidates for evaporation by resistive heating. MgO and ZnO are special, however, in that they have high vapor pressures at temperatures well below their melting points. This makes it possible to produce ultrafine powders of these materials by directly subliming the oxide. Ultrafine grain sized MgO has been produced by directly heating MgO in tungsten boats to 1600°C (MgO melts at 2852°C) in 200 Pa of He. The material which sublimates is oxygen deficient, but is fully converted to stoichiometric MgO by subsequent exposure to oxygen introduced into the vacuum chamber. The MgO that has been produced to date has a mean grain size of only 5 nm, but it has been determined to be not pure, single-phase MgO because of difficulties encountered in finding suitable evaporation sources that do not react. For instance, it has been found that if the MgO is sublimed from tungsten boats, the resulting material is a mixture of ultrafine-grained MgO and WO_x phases. While a composite such as this may have very interesting and desirable properties not found in other larger-scale composites, this points out a potential, troublesome limitation of vaporizing materials using Joule-heating techniques. To overcome problems such as these, alternative heating methods must be employed. An electron-beam evaporation system is currently being developed at Argonne to avoid such problems and to allow the synthesis of a wider range of nanophase materials under controlled conditions.

Production of nanophase ZnO has required considerable engineering in order to find a successful production scheme. ZnO resembles MgO in that it has a high vapor pressure at temperatures considerably below its melting point, thus making it possible to sublime ZnO by Joule heating. Ultrafine-grained ZnO powder with a mean size of 6-15 nm has been produced by subliming coarse-grained ZnO from graphite boats at 1400°C ($T_m = 1972^\circ\text{C}$). X-ray diffraction has revealed that as-produced, consolidated samples contain not only ZnO, but also significant quantities of Zn metal. This is observed even if the powder has been exposed to oxygen prior to consolidation. In some cases, only Zn is observed in x-ray θ - 2θ scans, as shown in Figure 2(a). An amorphous oxide phase must also be present in these samples, however, since chemical analysis has shown that the material contains typically 40 at.% oxygen. Annealing the material in air at 300°C for 3 hours has been found to successfully fully convert the Zn to ZnO, as shown in Figure 2(b), while maintaining a grain size under 20 nm. The degree of consolidation of the material prior to this anneal has been found to be important in determining the amount of time (and, thus, the final grain size) at a

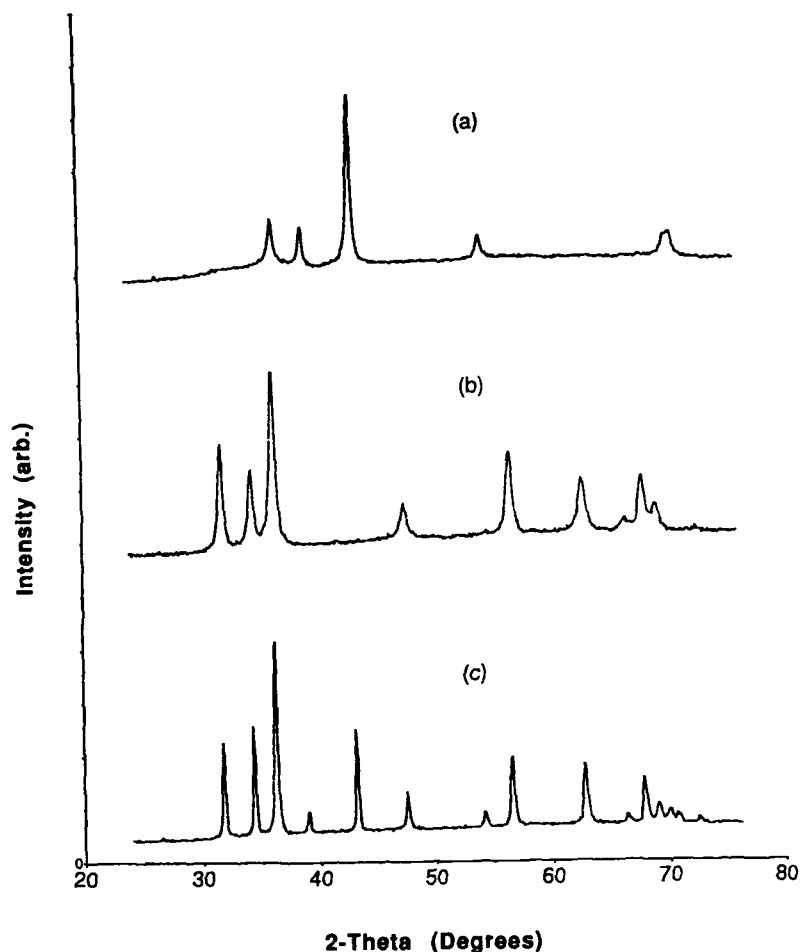


Figure 2. X-ray θ - 2θ scans from nanophase ZnO. (a) is a scan from a sample which was compacted using only the low-pressure compaction unit. Only Zn is observed; no ZnO is present in this sample. (b) shows the effect of annealing the sample in (a) for three hours at 300°C in air. Complete conversion to ZnO occurred with little accompanying grain growth. (c) shows the importance of annealing samples in an oxygen atmosphere prior to high-pressure compaction. The sample in (c) was compacted at 1.4 GPa prior to annealing and still contains both Zn and ZnO phases, even after 6 hours at 600°C. Grain growth has occurred, as seen by the sharpening of the diffraction peaks.

given temperature required for complete oxidation. Material that is only lightly compacted prior to annealing transforms more easily than highly compacted material, as shown in Figure 2. Material that has been consolidated at 1.4 GPa remains partially Zn metal even after 6 hours at 600°C (180°C above the melting point of Zn). Whether this phenomenon is due to a greater accessibility of the Zn grains to oxygen in the more lightly compacted material or to a strain-induced suppression of the phase change is not yet understood. Nanophase processing can apparently stabilize unexpected phases, as shown by the observation of new phases of erbium oxides [14] and titanium-based oxides [15] in nanophase samples.

PROPERTIES

As already mentioned, the properties of nanophase ceramics that have been measured appear to be rather different and often considerably improved in comparison with those of conventional, coarser-grained ceramics. For a more complete discussion of these properties, the reader is referred to several review articles which have recently appeared [3-5]. In the present report, only a few recent results will be emphasized. It was earlier shown [8] that 12 nm grain size nanophase TiO_2 sinters at 400-600°C lower temperatures than conventional rutile powders, and does so without the usual need for compacting or sintering aids. The rutile thus produced has hardness and fracture toughness values similar to those for coarse-grained rutile, and a reduced sintering temperature (by 200°C) for transgranular fracture [16]. While the ultrafine grain sizes and narrow grain-size distributions available in the gas-condensation method are obvious advantages to sinterability, another attribute of this synthesis method, which has recently been demonstrated, is the importance of clean powder surfaces to the sintering behavior of nanophase TiO_2 .

Figure 3 shows a comparison of the sintering behavior of ultrafine TiO_2 powder with and without exposure to air prior to initial powder consolidation, as evidenced by the effect on Vickers microhardness measurements. It can be clearly seen in this figure that not only does the vacuum-consolidated material [8] begin sintering at lower temperatures than the air-consolidated material, but also the ultimate hardness obtained is limited severely in the air-consolidated material. Presumably, this is due to the detrimental effect of surface adsorbates, primarily water vapor, resulting from the air exposure. This points out one major advantage of the gas-condensation process over chemical techniques, such as sol-gel processing, for the production of ultrafine powders. Chemical techniques, while able to produce large quantities of powders rapidly, lack the inherent control of surface chemistry available with the gas-condensation process.

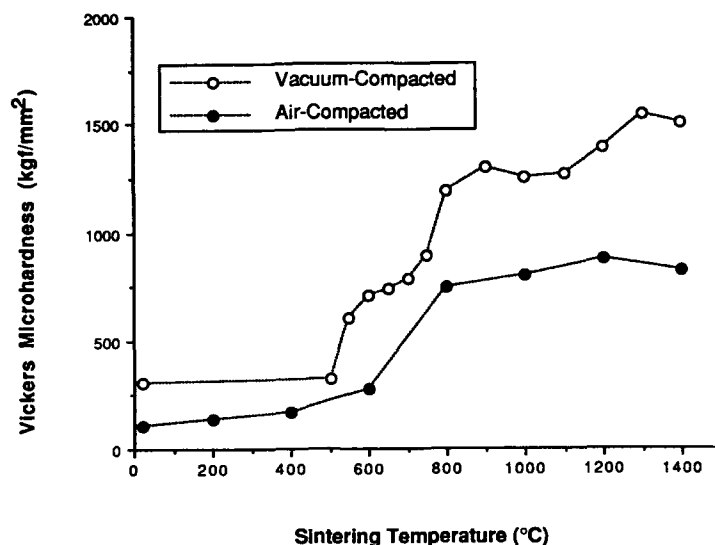


Figure 3. Vickers microhardness of 12 nm average grain-sized TiO_2 (rutile) samples measured at room temperature as a function of one-half hour sintering at successively higher temperatures in air. Results for a sample compacted in air are compared with those for a sample prepared via the normal nanophase processing route [8], which was compacted under vacuum conditions with no exposure to air. The superior sintering behavior of the in situ vacuum-consolidated sample is clearly demonstrated.

One concern with the use of nanophase ceramics in commercial applications is whether the stability of the small grain sizes is sufficient to allow use of these materials at temperatures above ambient. Characterization of mean grain size as a function of temperature has been carried out for TiO_2 , MgO (containing WO_x) and ZnO , and the results are shown in Figure 4. It is clear from this figure that these consolidated ceramics all withstand heating to at least a few hundred degrees without significant grain growth. The temperature regime in which rapid grain growth begins to take place is a function of both the melting point of the material and the diffusion behavior. However, it appears to be the general behavior of nanophase ceramics that their ultrafine grain sizes are rather deeply metastable to ca. 40-50% of their melting points. Stabilization of the grain size to even higher temperatures may be possible by suitable doping of nanophase ceramics, which is made easier by the exceptionally high atomic mobility in these materials [4, 13].

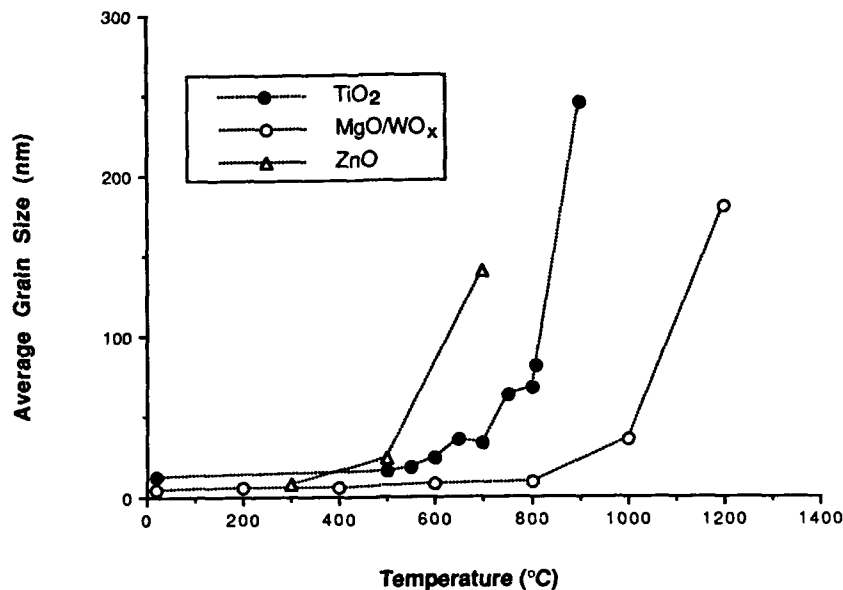


Figure 4. Variation of average grain size with sintering temperature for nanophase TiO₂, MgO/WO_x and ZnO. The samples were annealed for one-half hour in air at each temperature.

The relatively deep metastability of the ultrafine grain sizes in nanophase ceramics, coupled with their enhanced sinterability, allows for the synthesis of fully-dense ceramics with rather uniform ultrafine grain size. Figure 5 shows the 'window' between rapid sintering, as indicated by increased microhardness, and rapid grain growth for nanophase TiO₂, that demonstrates this capability of nanophase processing. Indeed, corresponding 'windows' have been measured for nanophase MgO/WO_x and ZnO. Recent density and grain size measurements [13] as a function of sintering temperature on similar TiO₂ samples to those studied previously [8] have also confirmed this possibility, and have shown that this 'window' can be opened further by sintering of the nanophase compact at elevated pressures or by appropriate doping. This is an important aspect of the processing of nanophase ceramics, since it appears that it will be generally possible to process fully-dense nanophase ceramics while retaining their ultrafine grain sizes and the unique properties associated with such grain sizes. Subsequently, the grain size can be adjusted by annealing to conform to a prescribed set of properties.

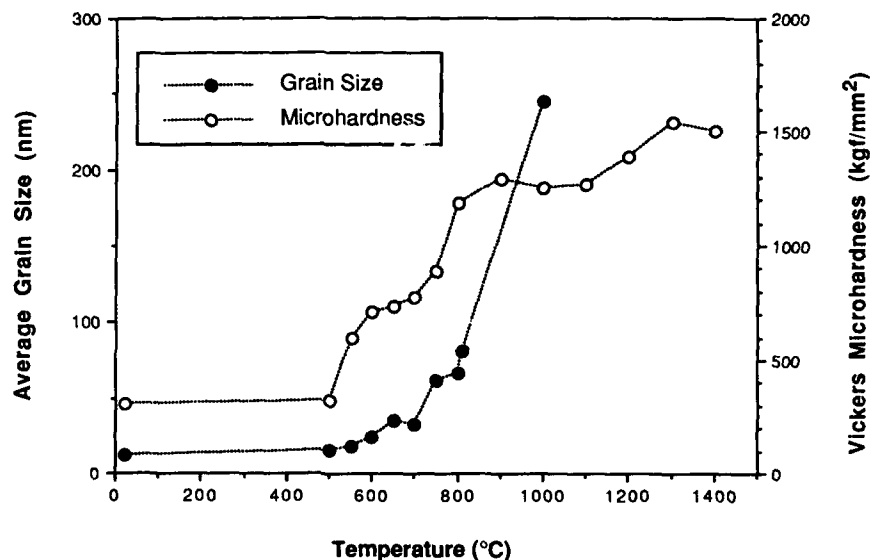


Figure 5. Nanophase TiO_2 Vickers microhardness versus temperature from Figure 3 compared with average grain size versus temperature for the same material from Figure 4. Sintering of the material is seen to occur prior to significant grain growth. From [8].

It should be pointed out that the metastability of the ultrafine grain sizes in nanophase ceramics appears to be an intrinsic result of their rather narrow grain size distributions, giving the analog to a closed-cell foam-like microstructure, and not simply caused by grain-boundary stabilization via porosity. While the latter extrinsic stabilization is observed in many cases for conventional ceramics [17-19], the ability to decrease the temperature for full densification of nanophase TiO_2 by sintering at elevated pressures while concomitantly increasing the temperature at which rapid grain growth occurs [13], clearly demonstrates that such extrinsic void stabilization does not underlie the grain-size metastability in nanophase ceramics. Furthermore, for the ultrafine grain sizes extant in nanophase ceramics, the driving forces for grain growth would likely overwhelm the drag forces due to the presence of grain-boundary porosity in any event.

The possibilities to process nanophase ceramics at considerably lower temperatures than their conventional coarse-grained counterparts are made even more interesting because of the inherent ease of their formability [7, 8] and the indications from recent strain-rate sensitivity measurements [20] of significant ductility in nanophase TiO_2 .

CONCLUSIONS

It is clear that the future of nanophase ceramics is extremely bright but still largely uncharted. Several interesting and technologically important nanophase oxides have already been produced and some of their properties are now being elucidated. A brief review has been presented here. However, much more research needs to be done on these new materials, as well as on the wide range of additional ceramic compounds that can be synthesized by the gas-condensation method. This research will need to focus on a variety of aspects regarding both processing and properties, and the relationships between these and the structure of nanophase ceramics.

In the processing area, it is clear that in addition to the very small and narrow size distributions of grains, clean particle surfaces (and hence uncontaminated grain boundaries) are important attributes of the synthesis of nanophase ceramics. Just how much further improvement of the sinterability can be achieved by reducing gas-condensed particle sizes still further must be studied. The importance of the width of the grain size distribution to the sinterability and subsequent properties of nanophase ceramics also needs to be considered further. It is possible to produce very narrow (even monosized) size distributions of atomic clusters by means of more sophisticated gas-condensation techniques than used to date for the synthesis of nanophase materials [5], but yields must be vastly increased in order to impact significantly on most materials applications. Nevertheless, it is quite apparent that with the inherent simplicity of the gas-condensation process for synthesizing nanophase materials, 'scale up' will not be a major problem as long as sufficiently new and/or improved properties are available with these materials.

The question of the properties of nanophase ceramics needs much further attention. While their mechanical properties have already received some scrutiny, largely directed toward an initial assessment of their durability, formability, and suitability for application, the electrical and optical properties of these ultrafine-grained ceramics have only begun to be investigated. These may well be the properties that find the greatest technological application in the future. The capability to easily dope nanophase ceramics with impurities at relatively low temperatures via their dense grain-boundary networks, with only few atomic jumps separating their grain interiors

from grain boundaries, for example, should allow for efficient introduction of impurity levels into the band gaps of oxides and the control over electrical and optical properties that this would yield. Many other possibilities for engineering advanced ceramics with useful properties by means of the nanophase processing method will undoubtedly occur to the reader.

REFERENCES

1. K. Kimoto, Y. Kamiya, M. Nonoyama, and R. Uyeda, *Jpn. J. Appl. Phys.* **2**, 702 (1963).
2. C. G. Granqvist and R. A. Buhrman, *J. Appl. Phys.* **47**, 2200 (1976).
3. R. Birringer and H. Gleiter, in **Encyclopedia of Materials Science and Engineering**, Suppl. Vol. 1, R. W. Cahn, ed. (Pergamon Press, Oxford, 1988) p. 339.
4. R. W. Siegel and J. A. Eastman, *Mater. Res. Soc. Symp. Proc.* **132**, 3 (1989).
5. R. P. Andres, R. S. Averbach, W. L. Brown, L. E. Brus, W. A. Goddard, III, A. Kaldor, S. G. Louie, M. Moscovits, P. S. Peercy, S. J. Riley, R. W. Siegel, F. Spaepen, and Y. Wang, *J. Mater. Res.* **4**, 704 (1989).
6. F. H. Froes and C. Suryanarayana, *J. Metals* **41** (6), 12 (1989).
7. J. Karch, R. Birringer, and H. Gleiter, *Nature* **330**, 556 (1987).
8. R. W. Siegel, S. Ramasamy, H. Hahn, Z. Li, T. Lu, and R. Gronsky, *J. Mater. Res.* **3**, 1367 (1988).
9. K. Yamauchi, S. Yatsuya, and K. Mihama, *J. Cryst. Growth* **46**, 615 (1979).
10. M. Shiojiri and C. Kaito, *J. Cryst. Growth* **52**, 173 (1981).
11. H. Gleiter, in **Deformation of Polycrystals: Mechanisms and Microstructures**, N. Hansen et al., eds. (Risø National Laboratory, Roskilde, 1981) p. 15.
12. H. Hahn, J. A. Eastman, and R. W. Siegel, *Ceramic Transactions B* **1**, 1115 (1988).
13. R. S. Averbach, H. Hahn, H. J. Höfler, J. L. Logas, and T. C. Shen, *Mater. Res. Soc. Symp. Proc.* **153**, 3 (1989).
14. Z. Li, H. Hahn, and R. W. Siegel, *Mater. Letters* **6**, 342 (1988).
15. J. A. Eastman, *Mater. Res. Soc. Symp. Proc.* **132**, 27 (1989).
16. Z. Li, S. Ramasamy, H. Hahn, and R. W. Siegel, *Mater. Letters* **6**, 195 (1988).
17. W. D. Kingery, H. K. Bowen, and D. R. Uhlmann, **Introduction to Ceramics**, Second Edition (John Wiley & Sons, New York, 1976).
18. E. A. Barringer, Ph. D. Thesis, Massachusetts Institute of Technology (1983).
19. L. H. Edelson, M. S. Thesis, Lawrence Berkeley Laboratory, University of California at Berkeley (1986).
20. M. J. Mayo, R. W. Siegel, A. Narayanasamy, and W. D. Nix, to be published.

TEMPERATURE MEASUREMENT FOR MICROWAVE PROCESSING OF ADVANCED CERAMICS

T. T. MEEK, S. S. PARK, M. A. NEHLS AND C. W. KIM

Department of Materials Science and Engineering, The University of Tennessee, Knoxville, TN 37996-2200

INTRODUCTION

The measurement of temperature in a microwave field is critical to the understanding of many phenomena which occur in materials heated in such an environment. Researchers have employed many techniques [1-4] to measure temperature in an electromagnetic field. This work examined three approaches: the use of a thermocouple, an IR meter, and a d. c. resistance technique.

Approach

The first experimental approach utilized a Pt-13 wt% Rh thermocouple inserted through a two-hole alumina tube with a shield wire wrapped around the tube. The pitch of the wire was less than a quarter wavelength of the incident electromagnetic radiation, and this shield wire was grounded to the outside cavity wall. Temperature data were taken with the thermocouple placed next to the sample being heated and with the thermocouple placed inside the sample. In all cases except the last, the object being heated was observed with an IR meter (Mikron model 91H-Q) and data were gathered simultaneously with the thermocouple data. Figures 1-9 show a comparison of temperature data taken using a conventional thermocouple with

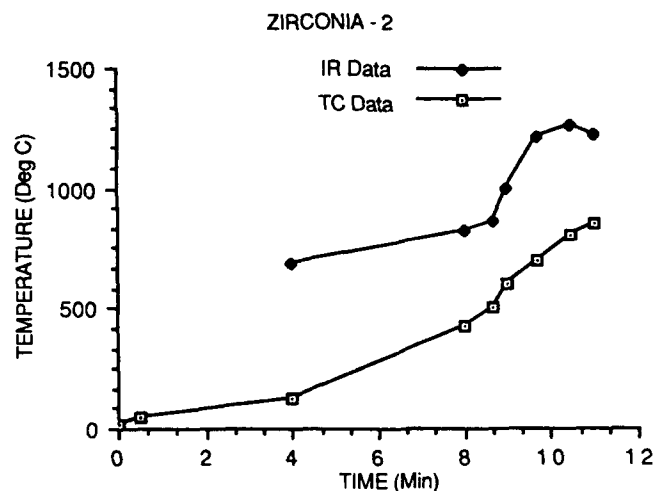


Figure 1. Thermocouple and IR meter temperature data for moderate heat up rate for zirconia heated in a 2.45 GHz microwave field. The thermocouple is placed one centimeter from sample.

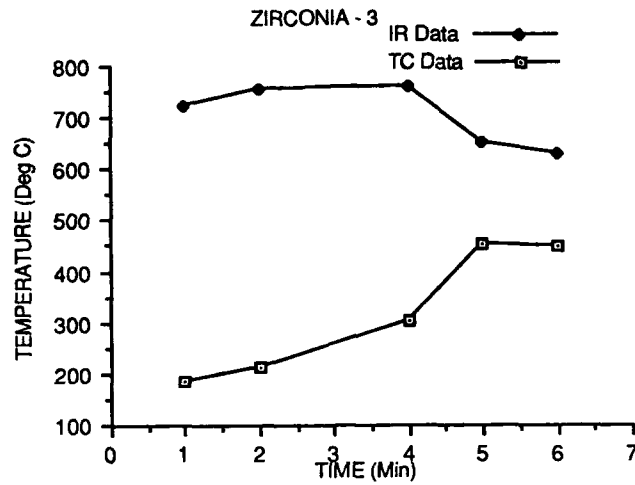


Figure 2. Same as Figure 1 except for a rapid sample heating rate.

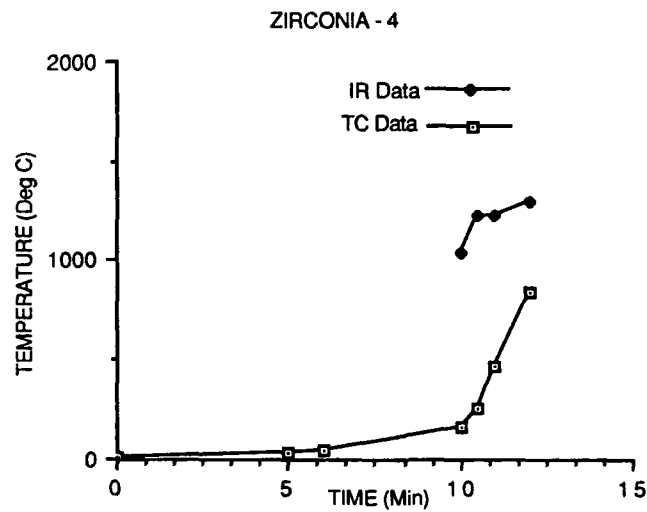


Figure 3. Here the TC is placed in the zirconia sample and initial heat up rate is slow.

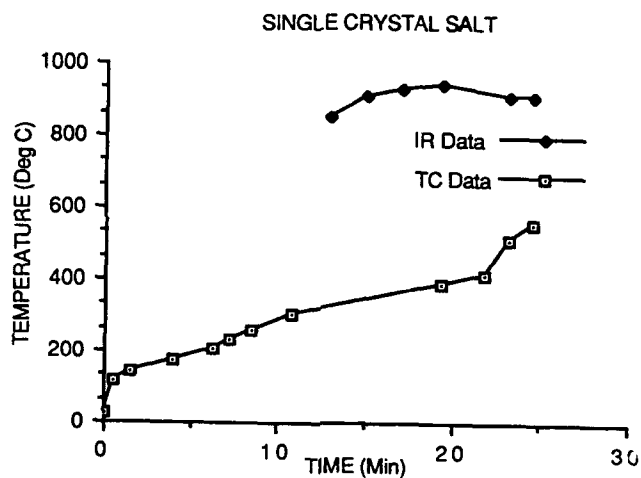


Figure 4. The melting of single crystal NaCl in a 2.45 GHz field. Thermocouple placed in sample.

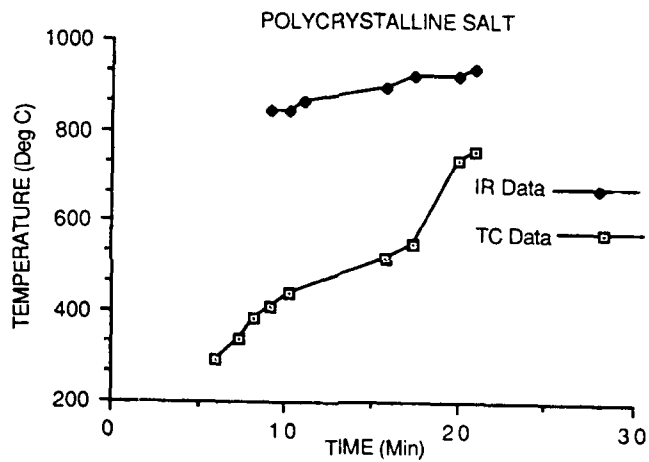


Figure 5. The melting of polycrystalline NaCl in a 2.45 GHz field. Thermocouple placed one centimeter from sample.

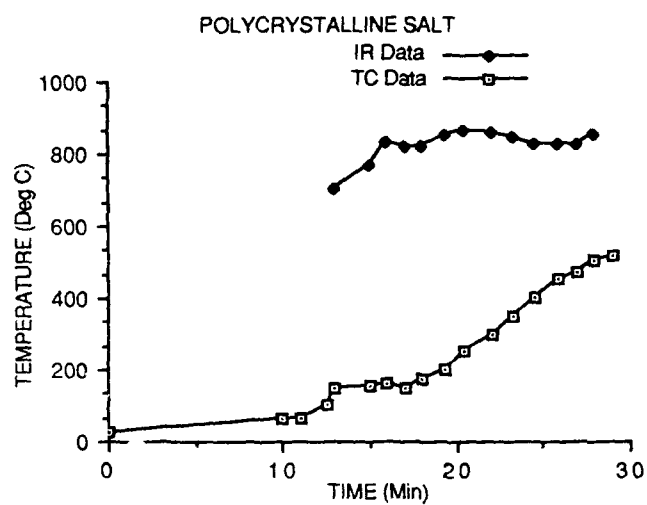


Figure 6. Polycrystalline NaCl heated using 2.45 GHz radiation. TC is placed in sample and sample is heated slowly.

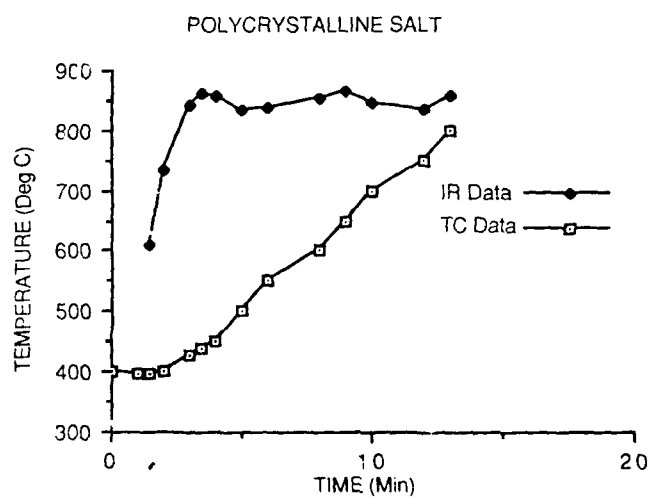


Figure 7. Polycrystal NaCl heated at 2.45 GHz. Thermocouple in sample.

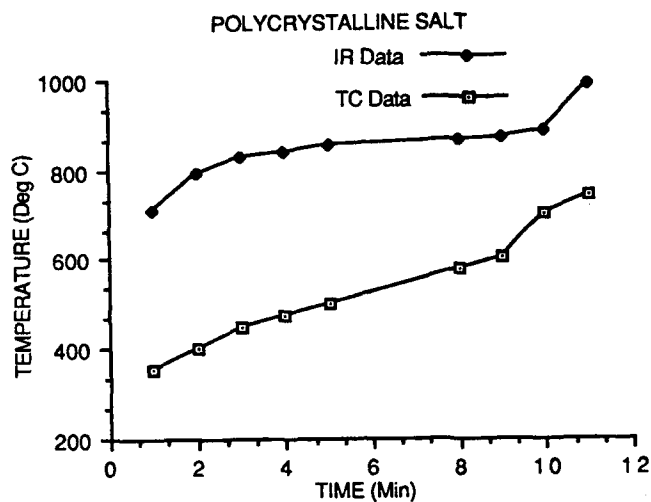


Figure 8. Polycrystalline NaCl heated using 2.45 GHz radiation. Thermocouple placed next to sample.

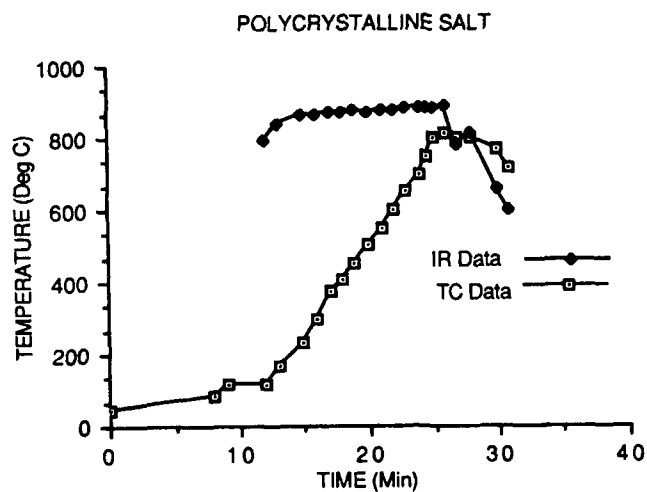


Figure 9. Polycrystalline NaCl heated using 2.45 GHz radiation. Thermocouple placed in sample.

temperature data taken using an IR meter. While there seems to be a large difference between the two sets of data, in time the two techniques may yield similar results providing the thermocouple is placed inside the sample. For the case of Figures 4-8, the thermocouple was placed in the sample. In the zirconia, the two techniques began to approach the same temperature rapidly. This is probably because the zirconia coupled well with the field. However, in the case of the salt (NaCl), less efficient initial coupling produced different results. In fact, while the sample glowed red the thermocouple still indicated a temperature several hundred degrees below red heat (around 650°C). Of more concern is not that a thermocouple may correctly indicate a local temperature in the immediate vicinity of the thermocouple, but how the TC perturbs the electromagnetic field in the sample. If one attempts to sinter 50 mm x 50 mm x 5 mm rectangular bars of zirconia-toughened alumina in a 2.45 GHz electromagnetic field, depending on the location of the bars relative to the TC, the bars will sinter around the TC. This indicates that the metal shield around the TC perturbs the electromagnetic field in such a manner that the power deposited in the sample is affected.

In any case, the data seem to indicate that neither an IR meter nor a TC yields the important temperature relative to the understanding of important physical phenomena such as cation diffusion, sintering activation energy, etc. In a recent paper by Meek et al. [5], data are reported for the diffusion of the Co cation in pyrex. A conservative estimate is that D_{Co} is an order of magnitude greater in an electro-magnetic field than in a conventional thermal field. If one really believed the temperature data (obtained using an optical pyrometer), then the diffusion coefficient for Co cation diffusion in pyrex is really as much as 5 orders of magnitude greater in a 2.45 GHz electromagnetic field than in a conventional field. The author believes the important temperature to measure is on the surface of sintering grains, in the grain boundaries between grains, or wherever there is a discontinuous change in local material dielectric properties.

A possible way to get at this temperature is to measure the d.c. resistance of a sample as a function of temperature. This was done for a zirconia-toughened alumina sample. DC resistance (as a function of temperature) data were gathered in a conventional furnace from 100°C to 971°C and compared with dc resistance data gathered at two temperatures (800 and 900°C) in a 2.45 GHz electromagnetic field. The sample used had a niobium wire implanted in each side of the 2.54 cm length by 1.0 cm diameter sample. This wire was passed through an alumina thermocouple tube and the tube shielded with a metal shield. DC resistance was measured using a standard VOM meter. Figure 10 shows a comparison of $\log R$ vs. $1/T$ data gathered by heating the sample in a conventional furnace and in a 2.45 GHz electromagnetic field. Temperature in the microwave field was measured by focusing a Mikron model 91H-Q IR meter on the sample.

The difference in the two sets of data could be due to the way the energy is distributed in the sample. In the conventional case, the sample heats uniformly with each grain at the same temperature as the volume between the grains. However, in the microwave case, perhaps the surface of each grain is heated at a much faster rate than the bulk, thus giving rise to a hotter region between grains. In the conventional case, the dc resistance is a function of the density of the uniformly heated sample. The samples were held at each temperature for thirty minutes before taking data. During the 2.45 GHz microwave run, once the desired temperature was reached, data were gathered over a thirty-minute interval with little variation noted from start to finish. Perhaps the temperature measured by this technique in the microwave environment is the intergranular temperature where the electric field intensity is much greater than in the bulk of the grains. What is important here is the rate of temperature increase, not the final temperature. Very likely, the temperature in each

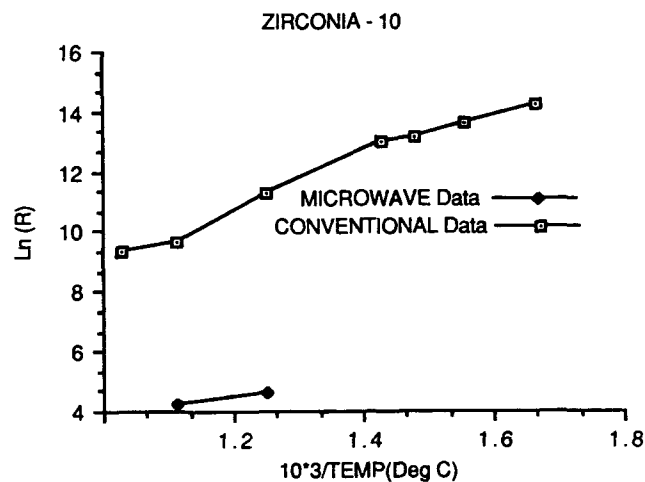


Figure 10. DC resistance of 70 wt% ZrO_2 - 30 wt% Al_2O_3 sample heated using 2.45 GHz radiation and heated convectionally.

grain will quickly increase but will always trail behind the surface temperature of each grain. As sintering progresses, the low dielectric constant region between grains vanishes, thus causing the overall bulk temperature to become more uniform.

Conclusions

Several conclusions may be drawn from this work. First, temperature is not easily measured in a microwave field. Second, neither IR meter nor thermocouple techniques give sufficiently accurate data to make observations on fundamental phenomena where the measurement of temperature is needed. Third, the determination of temperature using perhaps some noninvasive technique (such as the measurement of the reflected impedance of a coil or the dc resistance of a sample as a function of temperature) may lead to an adequate way of gathering temperature data. Last, it is important to do further experiments to determine whether indeed the intergranular regions (low dielectric constant) heat at a more rapid rate than do the bulk (high dielectric constant) grains.

Acknowledgments

The authors thank the Air Force Office of Scientific Research and DOE for funding this work.

References

1. M. Miyakawa, "1 ~ 10 GHz Microwave Applicators for Medical Applications," Electronics and Communications in Japan, Vol. 67-C, No. 5, (1984) 117.
2. M. Miyakawa, "Tissue Cooling and Its Effect on Brightness Temperatures by Contact-Type Microwave Applicators," J. of Microwave Power, Vol. 18, No. 2, (1983), 115.
3. D. Glajchen, "Temperature Measurement in Biotelemetry - A Novel Application for Microwave Dielectric Resonators," Elektron, Vol. 1, No. 8, (1984), 10.
4. L. Lawrence, R. A. Moore, J. H. Jacobi, F. A. Halgas and P. V. Brown, "A Microwave Compatible MIC Temperature Electrode for Use in Biological Dielectrics," I.E.E. Transactions on Microwave Theory and Techniques, Vol. MTT-27, No. 7, (1979), 673.
5. T. T. Meek, "Cation Diffusion in Glass Heated Using 2.45 GHz Radiation," Journal of Materials Science Letters, 7 (1988) 928-931.

**The Effect of Processing Parameters on the
Growth Rate and Microstructure of
Al₂O₃/Metal Matrix Composites**

ALAN S. NAGELBERG

Lanxide Corporation, 1 Tralee Industrial Park, Newark, DE
19714-6077

ABSTRACT

Ceramic matrix composites can be formed by the directed oxidation of a doped molten aluminum alloy into an inert reinforcement or filler. The resultant ceramic matrix consists of interconnected Al₂O₃ and partially interconnected metal. The growth kinetics of this Al₂O₃/metal ceramic matrix can be altered by numerous parameters. The effect of the growth atmosphere composition and temperature on the composite growth rate is dependent on the alloy dopant utilized. The ceramic matrix formation rate is also dependent on the alloy composition. Likewise, alloy composition has a profound effect on the mechanical properties and microstructure of the composites produced.

Introduction

Ceramic composite matrices can be formed by the directed reaction of a molten metal with an oxidant*: for example, the reaction of a molten aluminum alloy with air to form alpha aluminum oxide[1,2]. The reaction product, under appropriate conditions, grows rapidly outward from the original metal surface. The wicking of liquid metal along interconnected microscopic channels in the reaction product sustains the reaction. Typically, the resulting matrix material is a ceramic/metal composite comprised of a three dimensionally interconnected ceramic reaction product and usually at least some interconnected metal (typically about 5 to 30 percent by volume)[1-3]. Ceramic composites can be formed by placing inert reinforcing or filler materials (e.g., Al₂O₃ or SiC particles or fibers) adjacent to the parent metal surface in the path of the outward oxidative growth process, such that the reaction product forms a ceramic matrix throughout the filler mass. The process is schematically illustrated in Fig. 1 for growth into a reinforcing filler.

This new ceramic matrix composite technology[1,2] offers the ability to make low-porosity ceramic composites with a wide range of compositions and microstructures. As described elsewhere[2], this new technology contains many attractive features relative to conventional ceramic technology.

This paper presents a review of the processing parameters that affect the Al₂O₃/metal ceramic matrix growth rate and microstructure of composites grown in an oxygen containing atmosphere. These parameters include growth dopant, temperature, oxygen concentration in the growth environment, alloy

* Process technology patented by Lanxide Corporation and trademarked the DIMOX™ directed metal oxidation process.

DIMOX™ DIRECTED METAL OXIDATION PROCESS COMPOSITE FORMATION

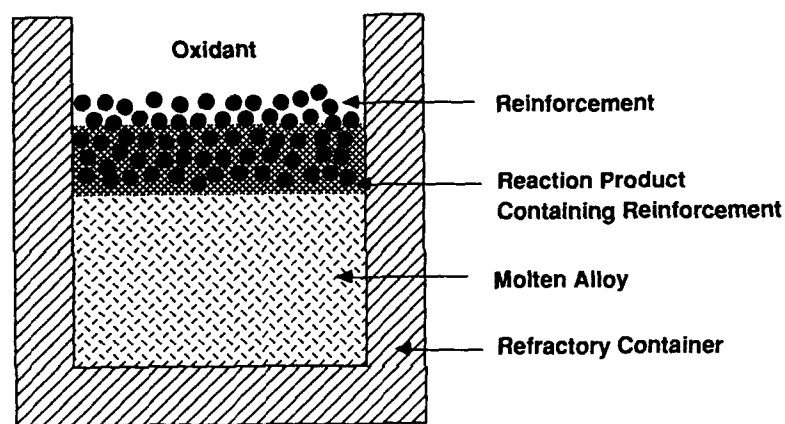


Figure 1. Schematic of the DIMOX™, directed metal oxidation process.

composition, and the presence of an inert filler. After giving a brief overview of the reported general features of the matrix microstructure, each of the processing parameters will be discussed separately. This is not to imply that they act totally independently to change the growth rate or microstructure. In the subsequent discussion, growth rate and weight gain rate will be utilized interchangeably.

Ceramic Matrix Microstructure

In previous papers, the microstructure and microstructural development of Al_2O_3 /metal composites formed by the directed oxidation of a molten metal were discussed in detail[1-4]. In this process, the addition of a growth dopant to an aluminum alloy results in the rapid formation of a ceramic composite matrix. In brief, it was found that the composite matrix consisted of both interconnected α -alumina and a metallic component, as illustrated by the SiC-reinforced composite shown in Fig. 2.

The α -alumina structure, in the absence of a filler, consisted of long continuous columnar regions containing predominantly low-angle $\text{Al}_2\text{O}_3/\text{Al}_2\text{O}_3$ grain boundaries[3]. Within the columnar regions, the alumina exhibited a preferred orientation, the c-axis being parallel to the growth direction. The $\text{Al}_2\text{O}_3/\text{Al}_2\text{O}_3$ boundaries were devoid of any grain boundary

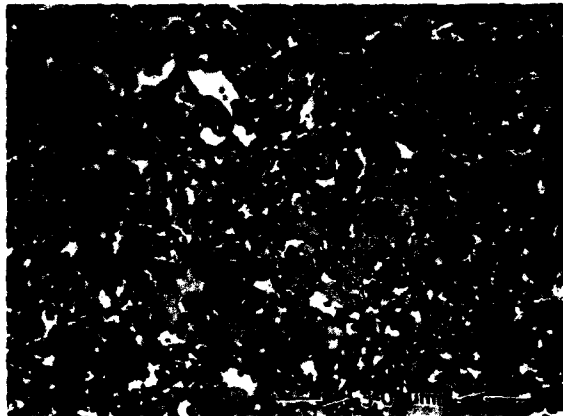


Figure 2. Microstructure of a SiC-reinforced composite. The 500 grit SiC particles are a medium gray. The dark phase in the matrix is the interconnected α -alumina and the bright phase is the partially interconnected metal constituent.

phase. The metallic component of the composite was present as both interconnected tortuous channels within and between the alumina regions and isolated small pockets. The magnesium constituent of the starting alloy was found predominantly in a layer of MgAl_2O_4 at the surface between the composite and alloy reservoir.

The microstructure of ceramic matrices grown from two different classes of alloys has been reported. The external growth surface of ceramic matrices grown from an Al-Si-Mg alloy in the absence of a filler was covered by a thin ($\sim 1-4 \mu\text{m}$) layer of MgO sometimes containing up to 5% MgAl_2O_4 [4]. The external MgO layer was typically separated from the interconnected Al_2O_3 ceramic by a thin aluminum alloy layer ($1-3 \mu\text{m}$), and only rarely was an Al_2O_3 grain found in direct contact with the external oxide layer. Within the composite itself, the metallic channels were typically $3-8 \mu\text{m}$ in width.

Conversely, when a Zn containing alloy was utilized to form the composite matrix, the external surface of the composite was covered by a thin layer of ZnO[5]. No ZnAl_2O_4 was observed. For these composites, the thin metal layer separating it from the interconnected Al_2O_3 was significantly thinner and its complete continuity was more difficult to ascertain. These composites typically contained a refined microstructure with $1-3 \mu\text{m}$ wide channels.

The incorporation of an Al_2O_3 filler into the ceramic matrix produced a refinement of the matrix, i.e., both the ceramic ligament and metal channel sizes were decreased[6]. Although the filler particles effectively broke up any macroscopically apparent columnar growth of the matrix, some preferred orientation of the Al_2O_3 was still observed by X-ray diffraction analysis. Approximately one half of the filler surface was

directly bonded to the interconnected Al_2O_3 of the matrix, without any evidence of a grain boundary phase.

Effect of Temperature and Oxygen Partial Pressure

The effect of temperature and oxygen partial pressure on the composite growth rate in the absence of a filler has been reported for composites grown from two types of alloys[5,7]. The first was an Al-Si-Mg ternary alloy containing 1-3 wt.% Mg and 1-30 wt.% Si. The second alloy was a complex Al-8.8 wt.% Si-2.8 wt.% Zn-3.1 wt.% Cu-1.1 wt.% Fe-0.2 wt.% Mg alloy.

The ceramic matrix growth rate from an Al-Si-Mg alloy was nearly linear and behaved as a thermally activated process with an activation energy of ~ 370 kJ/mol in the temperature range of 1423-1523K (Fig. 1)[7]. This activation energy has been associated with a dissolution-precipitation growth process in which electronic transport within the thin external Al_2O_3 -doped MgO layer controlled the process. The same activation energies were observed irrespective of the $P(\text{O}_2)$. Conversely, the growth rate of composites formed from an Al-Si-Zn-Cu-Fe-Mg alloy exhibited an activation energy of ~ 89 kJ/mol for temperatures between 1323K and 1473K (Fig. 3). Analogous to the Al-Si-Mg alloys, this lower activation energy was associated with a dissolution precipitation process controlled by the transport rate through the ZnO surface layer on these composites. This

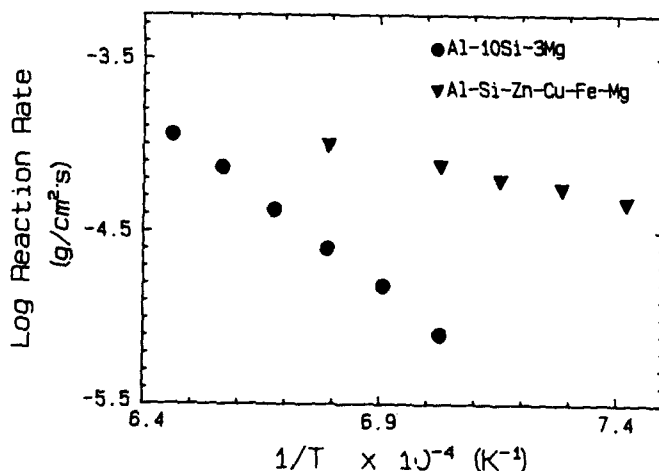


Figure 3. Comparison of the temperature effects on growth rate of ceramic matrix composites grown in 100% O_2 from an Al-10 wt% Si-3 wt% Mg alloy and an Al-8.8 wt% Si-3.2 wt% Zn-3.2 wt% Cu-0.8 wt% Fe-0.2 wt% Mg alloy.

activation energy is consistent with that for the oxidation of Zn, an environment believed to approximate the steep $P(O_2)$ gradient within the external ZnO layer. A dissolution-precipitation process is particularly consistent with the presence of large columnar regions of oriented grains containing only low-angle grain boundaries.

The oxygen partial pressure of the growth atmosphere, $P(O_2)$, affected the composite growth rate from molten Al-Si-Mg alloys, but not the rate of composites grown from the more complex Zn containing alloy. For the Al-Si-Mg alloys, the growth rate at all temperatures was proportional to $P(O_2)^{1/4}$ as illustrated in Fig. 4 for the composite growth of an Al-3 wt% Si-3 wt% Mg alloy.

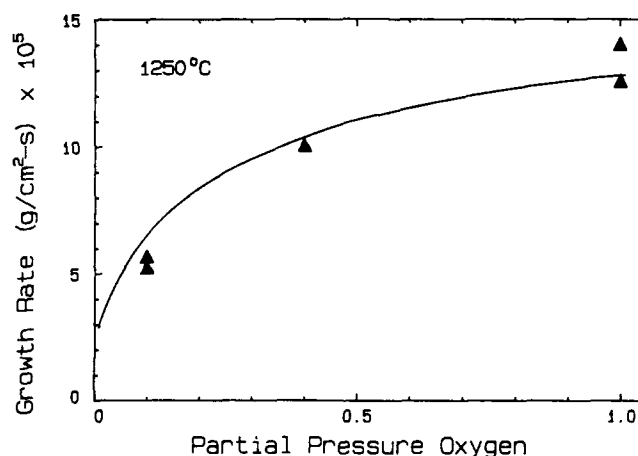


Figure 4. Effect of oxygen partial pressure on the ceramic matrix composite growth rate of an Al-3Si-3Mg alloy at 1523K.

The same effect of $P(O_2)$ was observed when either N_2 or Ar was used as the diluent. This $P(O_2)$ dependence was associated with the hole concentration within the p-type zone of the Al_2O_3 -doped MgO surface layer[7]. On the other hand, composites grown from the complex Zn containing alloy exhibited no effect of $P(O_2)$ on the growth rate[5], consistent with the diffusion behavior of an n-type surface oxide layer such as ZnO.

Effect of Alloy Composition

Alloy composition, outside of the growth dopant, can also have a pronounced effect on the composite growth rate and microstructure. For example, increasing the silicon concentration in Al-Si-Mg alloys from 3 to 10 wt.% resulted in a 50% decrease in the linear growth rate at 1523K[8]. As the silicon level was increased further, the growth rate continued to drop and changed from being nearly constant to a slowly decreasing rate. The rate of decrease of growth rate decreases with time; i.e., the growth rate vs. time curve is concave

downward. The decreasing growth rate was believed to be caused by the inability at high Si concentrations to Si from the growth front by interdiffusion at a sufficient rate to achieve a steady state Si concentration or growth rate.

Likewise, the growth alloy composition can have a large effect on the composite microstructure[8]. The addition of transition metals to the aluminum alloys refines the microstructure. The microstructural refinement expresses itself as a reduction in both the average metal channel size and Al_2O_3 interconnected network ligament thickness. As measured by the average lineal intercept, transition metal additions can result in a factor of 3 refinement of the microstructure. Transition metals from groups VIIA and IB promoted a greater microstructure refinement than metals from groups IVA and VA. The presence of transition metals, both copper and iron, in the second type of alloy, Al-Si-Zn-Cu-Fe-Mg, may explain the significant refinement of the microstructure as compared to the microstructure formed from the simpler Al-Si-Mg alloy. Associated with refinement of the microstructure is a variation in the composite mechanical properties. As predicted by Andersson et. al.[10], the decrease in metal channel size associated with refinement leads to a small decrease in composite fracture toughness and compressive strength[9]. Conversely, properties such as elastic modulus, that are more strongly dependent on the volume fraction of each constituent are not significantly affected by the variation in metal and Al_2O_3 ligament sizes while maintaining the same volume fraction.

Effect of a Filler

The introduction of a filler into the composite results in several additional effects on the composite growth rate and microstructure[11]. While acting as structure upon which the composite matrix growth process can proceed, the loose filler or green ceramic preform limits the ingress of O_2 to the growth surface and results in a more tortuous path for the metal wicking to the growth surface.

The growth rate of an Al-Si-Mg alloy into a loose bed of fused Al_2O_3 (90 grit Norton E38) was reported by Nagelberg[11]. Both oxygen partial pressure and temperature had a profound effect on growth rate. In 100% O_2 , the growth rate initially increased rapidly to a maximum value and decreased as matrix growth proceeded through the filler bed. Conversely, at low O_2 contents, with either N_2 or Ar as the diluent, the matrix growth rate increased as matrix infiltration proceeded.

The difference in behavior was associated with two effects. At high $P(\text{O}_2)$, the maximum reaction rate is well in excess of that for matrix growth alone by a factor of 2-3. If there were no wetting of the filler particles by the matrix, the effective reactive surface area of the growing matrix would be reduced in proportion to volume fraction of the filler. Conversely, when the filler is easily wetted by the growing matrix as shown in Fig. 5, the matrix/atmosphere surface area can be increased significantly, accounting for the enhanced growth rate.

The decrease in growth rate with time at higher $P(\text{O}_2)$ is caused by the buildup of Si in the metal near the growth front as Al is removed to form the interconnected Al_2O_3 network. The more tortuous diffusion path, rapid growth rate, and finer microstructure than found for matrix growth alone, result in a

decreased rate of silicon removal from the growth surface (compared to matrix growth in the absence of a filler) and thus the decreasing growth rate.

The additional effect of O_2 starvation must be considered at low $P(O_2)$. As the matrix grows and wetting of the filler proceeds into the loose bed, oxygen is locally depleted by the formation of Al_2O_3 . Since the filler is easily wetted by the matrix, thin ligaments of matrix growth extend into the filler bed, thus slowing growth deeper within the filler bed due to the depletion of oxygen. As growth proceeds further toward the surface of the filler, the rate at which the consumed oxygen can

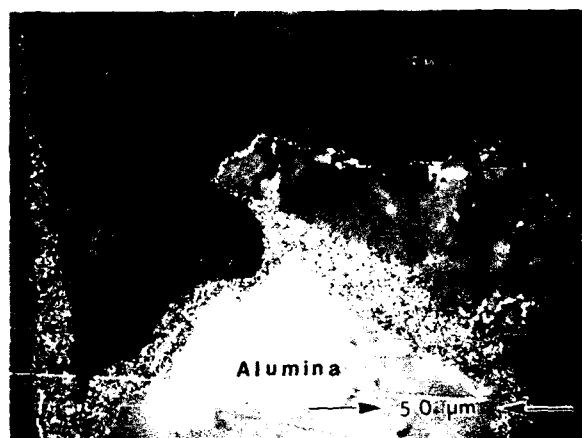


Figure 5. Micrograph showing the wetting of the Al_2O_3 filler by the ceramic matrix ahead of the dense matrix formation. Growth of Al-3 wt% Si-3 wt% Mg into 90 grit fused alumina at 1473K in 100% O_2

be replaced by interdiffusion increases and thus increases the apparent composite growth rate.

Even though the filler effectively disrupts the matrix Al_2O_3 columnar structure, a MgO-coated growth surface is retained. In addition, the presence of a thin metal layer beneath the MgO layer is also observed, implying that the same ceramic matrix growth process as reported in the absence of a filler.

Summary

The growth rates of composites formed by the directed oxidation of a molten Al alloy are affected by several processing parameters. The effect of temperature or oxygen partial pressure depends on whether a MgO or ZnO surface layer is formed at the growth surface. When the external layer consists of MgO, the activation energy for the growth process is ~ 370 kJ/mol and the growth rate varies with $P(O_2)^{1/4}$. Nagelberg, Antolin, and Urquhart[7] associated these properties with the electronic conductivity of the MgO surface layer. When an external ZnO layer forms, the activation energy is

~89 kJ/mol, and no effect of oxygen partial pressure is observed. This is consistent with the observed oxidation rate of Zn and the n-type behavior of ZnO.

The composition of the growth alloy can also have pronounced effects on the growth kinetics and resultant microstructure. Increases in the silicon concentration of Al-Si-Mg alloys lead to a reduction in the growth rate. In addition, as the silicon concentration increases, the kinetics change from a near constant growth rate to a slowly decreasing growth rate. The decreasing growth rate at high silicon contents is associated with the inability to remove the more noble Si from the composite growth front at a sufficient rate by diffusion through the composite.

The addition of transition metals to the growth alloy leads to a refined matrix microstructure. The refinement as measured by the average lineal intercept is by a factor of nearly 3. Associated with the refinement of the microstructure is a slight decrease in the composite toughness.

Finally, the presence of a filler phase leads to modification of the matrix microstructure. The large columnar zones observed in the absence of a filler are no longer apparent, but some tendency toward preferred orientation of the Al_2O_3 in the matrix is retained. The filler also affects the growth kinetics by acting as a substrate the matrix growth alloy can wet and thus increase the reactive surface area. In addition, the filler increases the tortuosity of the metal channels, thus decreasing the effective diffusivity of noble metals from the growth front.

REFERENCES

1. M. S. Newkirk, A. W. Urquhart, H. R. Zwicker, and E. Breval, *J. Mater. Res.* 1(1), 81 (1986).
2. M. S. Newkirk, H. D. Lesher, D. R. White, C. R. Kennedy, A. W. Urquhart, and T. D. Claar, *Ceramic Engineering and Science Proceedings*, 8(7-8), p. 879 (1987).
3. M. K. Aghajanian, N. H. Macmillan, C. R. Kennedy, S. J. Luszcz, R. Roy, *J. Mater. Sci.*, 24, 658, (1989).
4. S. Antolin, A. S. Nagelberg, and D. Creber, *J. Am. Cer. Soc.* (submitted for publication).
5. A. S. Nagelberg, *Solid State Ionics*, 32/33, 783 (1989).
6. E. Breval and A. S. Nagelberg, *Multicomponent Ultrafine Microstructures*, ed. L. E. Candish, B. H. Kear, and R. W. Siegel, *Mat. Res. Soc. Proc.*, Vol. 132, (1989).
7. A. S. Nagelberg, S. Antolin, and A. W. Urquhart, *J. Am. Cer. Soc.* (submitted for publication).
8. A. S. Nagelberg, presented at the 1988 Am. Cer. Soc. Annual Meeting, Cincinnati, May 1988, paper 107-C-88 (unpublished).
9. S. Antolin and M. K. Aghajanian, presented at the 1988 Am. Cer. Soc. Annual Meeting, Cincinnati, OH, May 1988, paper 109-C-88 (unpublished).
10. C. A. Andersson and M. K. Aghajanian, *Ceram. Eng. Sci. Proc.*, 9(7-8), 621 (1988).
11. A. S. Nagelberg, presented at the 1988 Am. Cer. Soc. Annual Meeting, Cincinnati, OH, May 1988, paper 108-C-88, (unpublished).

RAPID OMNIDIRECTIONAL COMPACTION OF Y₂O₃ STABILIZED TETRAGONAL ZIRCONIA

Alexander Pechenik*, Aleksander J. Pyzik** and Donald R. Beaman***

* University of California, Department of Material Science and Engineering, Los Angeles, CA 90024

** The Dow Chemical Company, Central Research, 1776 Building, Midland, MI 48674

*** The Dow Chemical Company, Michigan Applied Science and Technology Laboratory, 1897 Building, Midland, MI 48667

ABSTRACT

The Rapid Omnidirectional Compaction (ROC) technique has been applied successfully to the densification of TZP (3 mole % yttria) ceramics at 1260°C. The combination of high pressure (830 MPa) and temperature results in the plastic deformation of the ceramic particles. The extent of deformation, and consequently, the ROCing temperature, can be determined by using hot hardness of the ceramic material as an approximation of the ceramic's yield stress. The materials ROCed at 1260°C are characterized by a grain size of 0.15 μm , a flexure strength of 1300 MPa, a hardness of 1340 kg/mm², and a fracture toughness of 5.0 MPa m^{1/2}.

INTRODUCTION

Yttria-stabilized tetragonal zirconia polycrystalline ceramics (Y-TZP) have attracted significant interest due to their impressive mechanical properties [1]. Y-TZP with 3 mole % yttria exhibits an excellent combination of high bending strength (up to 1200 MPa) and high fracture toughness (6 MPa) [2]. It is known that the tetragonal-to-monoclinic, martensitic transformation aids in developing these unique properties. The transformation temperature decreases with particle size but varies with the quantity and type of stabilizer used [3,4]. Thus, precise control of the grain size is of technological value. If the grain size of Y-TZP reaches 0.5 μm , as is possible in sintering or hot pressing, the martensitic transformation occurs spontaneously on cooling, disintegrating the material. If the grain size is below 0.1 μm , the transformation is inhibited and the Y-TZP ceramic exhibits low fracture toughness. The optimal grain size depends on the Y₂O₃ concentration and whether strength or toughness is being optimized.

This paper describes the production of Y-TZP ceramic using the technique of quasi-isostatic pressing, Rapid Omnidirectional Compaction (ROC). The ROC process has already been applied to produce dense materials using Ti based alloy powders [5], WC-Co [6], B₄C-Al [7], and TiB₂-Al [8]; the process resulted in good control of the grain size and microstructures.

EXPERIMENTAL PROCEDURE

Powder Characteristics

Tetragonal zirconia powder containing 3 mole % yttria was selected for this study (TZ-3Y, Toyo Soda Co.). The powder specification [2] indicates an average particle size of 0.1 μm and specific surface area of 15 m²/g, which

corresponds to a spherical diameter of 67 nm when the theoretical density of tetragonal (6.05 g/cm^3) and monoclinic (5.76 g/cm^3) phases are used for the calculation. Transmission electron microscopy (TEM) indicated that the powder consisted of 0.1 to 0.2 μm agglomerates containing 40 - 60 nm crystallites (Figure 1). X-ray diffraction (Figure 2A) revealed the presence of about 27 volume % of the monoclinic phase, calculated according to the equation given by Garrie and Nicholson [9].

Method of Densification

Rapid Omnidirectional Compaction is a quasi-isostatic consolidation process used to densify powders. Figure 3 shows that the ROC process provides a unique set of processing conditions when compared with some pressure assisted densification methods. Typical ROC cycles are carried out at a pressure of 830 MPa, with a pressure dwell time of only five seconds. The method utilizes a conventional forging press and closed-die tooling to apply pressure to a preheated fluid die. A powder compact is subjected to pressure delivered by the molten glass or glass-ceramic mixture which is capable of plastic flow at the processing temperatures. Figure 4 outlines the basic features of the ROC process, which has been described in detail elsewhere [10].

The starting powder was cold pressed (100 MPa) into large discs (5 cm in diameter and 2 cm thick), using uniaxial compaction in a stainless steel die. No lubricants or binders were used in the pressing operation. The density of the greenware was nearly 50 % of the theoretical density. After cold pressing, the discs were placed in a glass-ceramic die, covered with powdered pyrex glass and the entire die was closed with a glass-ceramic lid. The fluid die was placed in a furnace and heated to a particular processing temperature. After one hour at the maximum temperature, the fluid die was removed from the furnace, placed into the forging press, and compacted under 830 MPa pressure for 2 seconds. The die containing samples was air cooled to ambient temperatures. The samples were removed from the die by breaking and then grinding off the surrounding glass. The discs were cut into various shapes for mechanical testing.

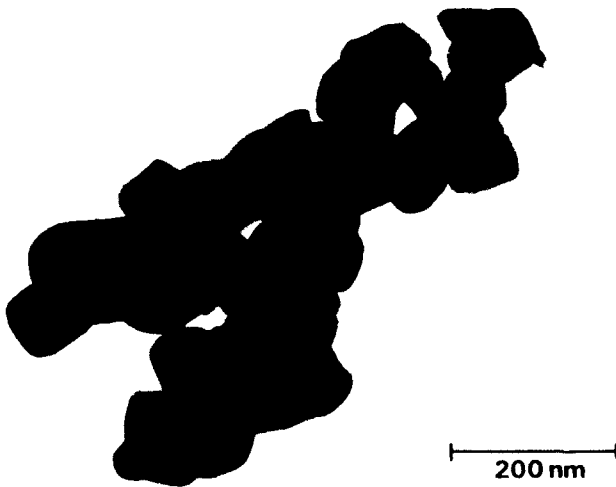


Fig.1. Transmission electron micrograph of TZ-3Y powder.

Characterization

X-ray diffraction studies were conducted with a Philips diffractometer using $\text{CuK}\alpha$ radiation and a scan rate of $0.5^\circ/\text{minute}$. X-ray diffraction patterns of the starting powder were obtained using powder samples placed in a holder with a 1 cm^2 window. Solid, 1 cm^2 samples were cut and successively polished with 15, 6, 1 and $0.5\text{ }\mu\text{m}$ diamond paste to remove any damage.

The broken pieces from 3-point bend testing were used in measuring the density with an Autopycnometer 1320 (Micromeritics Corp.); the accuracy was $\pm 0.01\text{ g/cm}^3$.

Samples for TEM examination were prepared in the following manner. An ultrasonic disc cutter was used to obtain discs 3 mm in diameter and 1 mm thick which were then prethinned to $100\text{ }\mu\text{m}$ thick using diamond plates and laps with a final $1\text{ }\mu\text{m}$ finish on each side. Dimpling from the unpolished side proceeded to a 15–20 μm thickness with a $1\text{ }\mu\text{m}$ finish. A thin section for TEM was obtained by Ar ion/atom milling from both sides using a liquid nitrogen cooled stage, 5 kV and 2–3 ma current.

Hardness and fracture toughness were measured on surfaces polished successively with 15, 6, 1 and $0.25\text{ }\mu\text{m}$ diamond paste on a LECO automatic polisher, in order to remove the surface damage introduced during grinding and rough polishing. After the final polishing step, Palmqvist cracks were produced on the polished surfaces with a specified load. The length of the cracks was used to evaluate the quality of surface preparation following the procedure outlined by Exner [11]. Properly prepared samples were indented using conventional procedures [12]. A fractometer (Terra Tec, Inc.) and short bar technique [13] were used to measure fracture toughness. The flexure strength, reported on the average of 20 measurements on $3\times 4\times 45\text{ mm}$ samples, was performed according to MIL-STD-1942 standard.

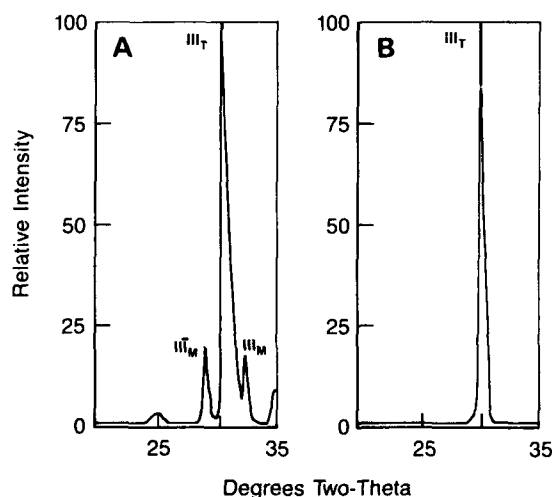


Fig.2. X-ray diffraction pattern of TZ-3Y powder before ROC (A), and after ROC (B).

RESULTS AND DISCUSSION

To develop the optimal conditions for ROCing of Y-TZP, we have made an extensive use of the model developed by Helle and others [14] for densification of metallic powders. At low temperatures, ceramic materials exhibit brittle behavior, fracturing under stress rather than yield. The process of compaction of ceramic powders at ambient temperatures occurs via the fragmentation route [15]. At temperatures of nearly half of the corresponding melting temperature, many ceramic materials undergo a brittle-to-ductile transition, and yield rather than fracture. Thus, above the brittle-to-ductile transition, ceramic materials behave under stress similarly to metals, and the equations developed to describe the densification of metal powders [15] can be applied to ceramics. Since the values of the high-temperature yield stress are not easily available for ceramic materials, we have used the high-temperature hardness to approximate the yield stress. For dull indenters (Knoop and Vickers) hardness is three times the yield stress.

After the rearrangement stage is completed, densification takes place through plastic yielding at the points of contact between individual grains. This leads to a continuous increase in the number of contact neighbors and average contact area. The density achieved at this stage, D_1 , is a function of the applied pressure, P , and the density of the compact before pressure is applied, D_0 , according to the following equation:

$$D_1 = [(1 - D_0)P/0.43 H + D_0^3]^{1/3} \quad (1)$$

Equation 1 is only valid for $D_1 < 0.9$ because at higher values a different densification mechanism occurs. When the pressure is sufficiently high to

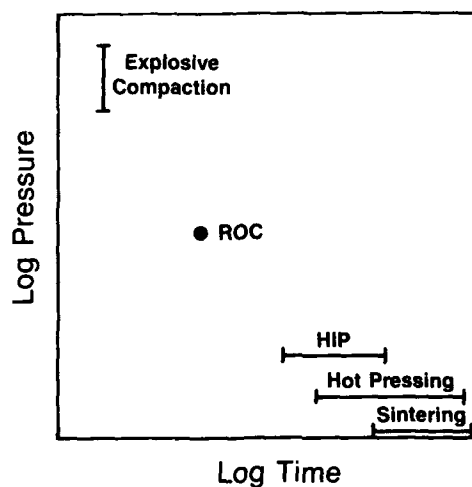


Fig.3. Qualitative comparison of various pressure densification techniques.

cause yielding of the spherical shell surrounding each pore, the density of the compact is described by

$$D_2 = 1 - \exp(-4.5 P/H) \quad (2)$$

Since no data are available for Y-TZP, we used the high temperature hardness of $2 \text{ ZrO}_2 \cdot \text{Y}_2\text{O}_3$ ceramic [16]. A minimum temperature of 1200°C to provide near theoretical density was calculated from $H = 84 \text{ kg/mm}^2$ [16] and $P = 830 \text{ MPa}$. At 830 MPa $\text{ZrO}_2 + 3 \text{ mole } \%$ yttria powder should densify plastically in less than 5 seconds. The experimental results correlate well with the calculations providing materials with 98 % of theoretical density at 1230°C and 99.7 % at 1260°C . For comparison, HIP and pressureless sintering require temperatures of 1400°C to 1600°C to achieve such densities. The lower temperatures and times associated with the ROC processing should produce materials with smaller grain sizes.

The experimental results demonstrate that while ZrO_2 grain growth does occur during the ROC process the final grain size is small (Figure 5). The 40 - 60 nm ZrO_2 grain produced ZrO_2 grain sizes of 0.13 and 0.15 μm for materials ROCed at 1230°C and 1260°C , respectively (Table I).

Only tetragonal ZrO_2 was detected by X-ray diffraction of the ROCed materials (Figure 2B). Two processes contribute to the elimination of the monoclinic phase: (i) homogenization of Y, through diffusion, can bring all grain compositions into the tetragonal phase field of the $\text{ZrO}_2 - \text{Y}_2\text{O}_3$ system, and (ii) the pressure of 830 MPa used during compaction may convert all the monoclinic grains into the tetragonal form while the reverse transformation is suppressed by the matrix of surrounding grains.

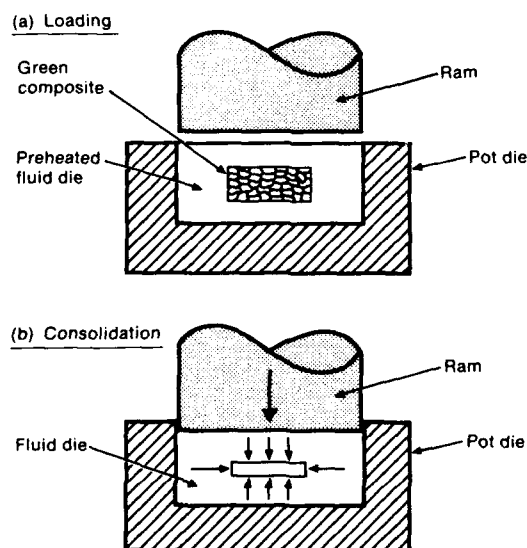


Fig.4. Schematic illustration of the ROC process.

Table I. Changes in grain size, porosity and density of the ROCed materials as a function of the ROC temperature.

ROC temp. (°C)	Average grain size (μm)	Vol.% Voids 1000X Mag. (by stereology)	Vol.% Voids 10,000X Mag. (by stereology)	Total porosity (%)	Density g/cm ³ (by pycnometer)	Density -% of theoretical
1230	0.13	0.07	1.4	1.5	5.92	98.0
1260	0.15	0.01	0.6	0.6	6.03	99.7

Analytical transmission electron microscopy revealed that the weight % of yttria in the grains observed in Figure 5 varied from 0.7 to 5.5 mole % yttria. This clearly suggests that high pressure, and not diffusion, is responsible for the transformation of the monoclinic phase into the tetragonal phase during ROC.

Scanning electron microscopy (SEM) of polished surfaces showed two types of pores. The first, 0.1 to 0.2 μm in size, resulted from incomplete local deformation between ZrO₂ grains. The second, 1 to 2 μm in size, formed between zirconia agglomerates. This porosity range of 0.1 to 2 μm limits the maximum flaw size. ROCing at 1260°C eliminates the larger pores, reduces the porosity associated with the smaller pores to 0.6 volume %, and establishes the maximum flaw size at 0.2 μm (Table I and Figure 6). There was good agreement in the porosities measured by SEM stereology and the pycnometer method.



Fig.5. Microstructure of Y-TZP ceramic ROCed at 1230°C.

Table II. Mechanical properties of the ROCed Y-TZP.

ROC temp. (°C)	Vickers hardness (kg/mm ²)	Flexure strength (MPa)	Fracture toughness (MPa m ^{1/2})
1230	1184	1340 ± 200	5.3
1260	1340	1300 ± 200	5.0

Table II presents the results of the Vickers hardness, fracture toughness and flexure strength (in three-point bending) measurements. Generally, the properties of ROCed materials are significantly different from those of conventionally sintered and HIPed materials, eg, the hardness and bending strength of ROCed ceramics are higher. These improvements are due to the smaller grain size and the reduced flaw population in the ROCed materials. The average grain size of ROCed materials (0.13-0.15 μm) is lower than the established optimal size required for achieving high fracture toughness in Y-TZP ceramics. It must be noted, however, that the non-uniform distribution of yttria in the starting powders puts ROC at a disadvantage compared to conventional densification methods. HIPing or pressureless sintering requires 1400°C to 1600°C, whereas during ROCing, full densification is achieved between 1260°C and 1300°C. ROCing temperatures do not allow for the homogenization of yttria content to take place, which leads to a reduction in the fracture toughness.

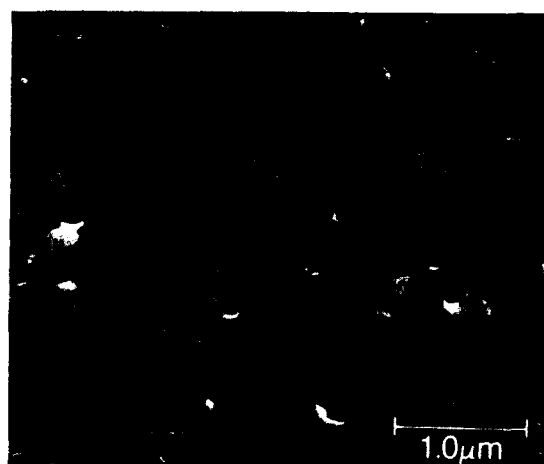


Fig.6. The microstructure of Y-TZP (ROCed at 1260°C) is characterized by the maximum void size of less than 0.2 μm .

The temperature at which particles are transformed from tetragonal to monoclinic decreases with the reduction in particle size; smaller grains require less yttria to transform. The commercially available Y-TZP powders are designed to give the best properties for conventional densification processes, which are limited to higher temperatures. Therefore, in order to further improve the properties of ROCed Y-TZP, the correlation between zirconia crystallite size and yttria content needs to be optimized for the specific conditions of the low temperature ROC consolidation process.

CONCLUSIONS

1. The Rapid Omnidirectional Compaction technique produces nearly fully dense TZP (3 mole % Y_2O_3) ceramics at 1260°C. The combination of high pressure and high temperature conditions permits ceramic to deform plastically. The degree of this deformation, and thus, the appropriate ROCing temperature, can be determined by using the hot hardness of the ceramic material to approximate the high-temperature yield stress.
2. The application of the ROC process to ceramic powders results in a reduction of the temperature and time required for densification. This, in turn, produces materials with extremely small grain size. The method shows potential for a variety of ceramic powders.
3. The ROCed Y-TZP materials obtained at 1260°C are characterized by a hardness of 1340 kg/mm², a flexure strength of 1300 MPa, and a fracture toughness of 5.0 MPa m^{1/2}. The hardness and bending strength of the ROCed Y-TZP are significantly higher than those of the conventionally densified TZPs of similar composition. The lower fracture toughness is due to the very small grain size of ROCed materials and the non-uniform distribution of yttria in the commercial starting powder. Possible further improvement of the material properties can be achieved with zirconia powders specifically designed for the low-temperature, high-pressure ROC process.

ACKNOWLEDGMENTS

The authors wish to thank the following : C. Wood for microanalysis; D. Susnitzky for TEM characterization and critical review of the manuscript; C. Mericle for conducting the compaction experiments; Drs. J. Leddy and E. Timm for critical discussions; and Drs. S. Spangenberg, A. Hart and B. Peters for their support of this research.

REFERENCES

1. J. Lankford, in Advanced Structural Ceramics, ed. by P.F. Becher and others, Materials Research Soc. Proc., 78, 61, (1986).
2. Toyo Soda Manufacturing Co., LTD, Technical Bulletin, Z-051.
3. N. Claussen, in Proc. 2nd Int. Conf. Sci. Tech. Zirconia, ed. by N. Claussen, M. Ruhle, A.H. Heuer (Am. Ceram. Soc., Columbus, Ohio), 325-51, (1984).
4. V. Lanteri, R. Chaim, A.H. Heuer, J. Am. Ceram. Soc., 69, 10, C 258-61, (1986).
5. C.A. Kelto, Rapid Omnidirectional Compaction, in Metals Handbook, 7, (Am. Soc. For Metals, Metals Park, Ohio, 1984), p.542.

6. E.E. Timm, Conf. Proc. Advances in Hard Materials Production 88, England, MPR Publ. Serv. (In press).
7. A.J. Pyzik, A. Pechenik, Ceram. Eng. Sci. Proc., **2**, 7-8, 965-74, (1988).
8. A.J. Pyzik, presented at the 2nd Int. Conf. on Ceram. Powder Processing Science, Berchtesgaden, FRG, 1988, (In press).
9. R.C. Garrie, P.S. Nicholson, J. Am. Ceram. Soc., **55**, **6**, 303-5, (1972).
10. C.A. Kelto, E.E. Timm, A.J. Pyzik, in Annu. Rev. Mater. Sci., **19**, 527-550, (1989).
11. H.E. Exner, Trans. Metall. Soc. AIME, **245**, 677, (1969).
12. K. Niihara, R. Morena, D.P.H. Hasselman, J. Mat. Sci. Letters, **1**, 13-16, (1982).
13. L.M. Barker, Int. J. of Fracture, **15**, 6, 515, (1979).
14. A.S. Helle, K.E. Esterling, M.F. Ashby, Acta Metall., **33**, 2163-74, (1985).
15. H.J. Adair, R.R. Wills, V.D. Linse, in Mat. Sci. Research, ed. by R.F. Davis, H. Palmour III, R.L. Porter, **17**, 639-55, (1984).
16. V.P. Buntushkin, I.V. Romanovich, N.I. Timofeeva, Neorg. Mater., **7**, 9, 1071-1138.

PHOTOLITHOGRAPHY: A NEW TOOL FOR CERAMIC SCIENCE

JÜRGEN RÖDEL* AND ANDREAS M. GLAESER**

*National Institute of Standards and Technology, Gaithersburg, MD 20899

**Department of Materials Science and Mineral Engineering, University of California, and
Materials and Chemical Sciences Division, Lawrence Berkeley Laboratory, Berkeley, CA
94720

ABSTRACT

A recently developed technique combining photolithography, ion beam milling, and hot pressing allows the production of submicron-scale controlled-geometry, controlled-crystallography pore structures in controlled misorientation bicrystals, single crystal-polycrystal ensembles, and polycrystal-polycrystal ensembles. Such microdesigned interfacial structures provide a new tool for studying fundamental aspects of microstructural evolution. Current applications of the technique, opportunities for future research, and future extensions and refinements of the technique are described.

INTRODUCTION

The microstructural changes that occur during sintering and high-temperature use of ceramics are generally complex. In real systems, the path of microstructural evolution reflects the outcome of a competition between many concurrent processes. For sintering, particle size, particle size distribution, and particle packing play a major role in determining the pore size, pore size distribution, and pore spacing in the green compact. These characteristics determine the thermodynamic driving forces for both coarsening and densification processes. The coupling between these topologically dictated driving forces and the transport coefficients for grain boundary, lattice, and surface transport, or interfacial reaction rate constants, or both, will ultimately determine the relative fluxes associated with competing mass source-sink pairs, and thus will determine the dominant transport mechanism.

To make theoretical modelling of microstructural evolution tractable, it is often necessary to simplify the system. For example, a single process is assumed to dominate, the properties of the system are assumed to be isotropic, and in many instances, the geometry is simplified. The systems that are dealt with in practice are much more complex. As indicated, multiple processes interact. Moreover, the materials are rarely isotropic, and the geometry of the microstructural features of interest is rarely as simple as it is assumed to be.

When significant disparities exist between theoretical predictions and experimental observations, the origin of the disparity can be difficult to pinpoint. Is there a fundamental error in the modelling, or is the disparity the result of geometrical differences and competing processes that are not accounted for? Studies on real materials can be inadequate to test theoretical models critically because the degree of control over the relevant microstructural geometry is inadequate. Thus, an experimental method that provides control over the pore, flaw, or second phase geometry has the potential to further our understanding of microstructural evolution during sintering and high-temperature use.

Our recent work has focussed on developing a new family of model experiments that utilize photolithography to produce geometries that more closely resemble those that have been theoretically modelled. Our goals are: 1) to design model experiments that permit the systematic study of particular processes under well-defined conditions, 2) to utilize these experiments to verify theory, or to identify important deficiencies, 3) to provide information that can be useful to the materials processing community, and 4) to help bridge the gap between theory and practice.

The following paper provides a brief overview of the sample preparation procedure, and then summarizes the results of new model experiments examining high-temperature crack healing, pore-boundary interactions during sintering, and pore coarsening and pore elimination. Potential extensions and refinements of the method are cited, and some future directions are suggested.

SAMPLE PREPARATION

Lithography has furnished a new tool for studying a number of processes that occur during fabrication or during use at high temperature. The combination of photolithographic methods, ion beam etching, and hot pressing provides the ability to define and introduce surface features with a controlled geometry and location, and to subsequently transform these surface features into internal features. A brief overview of the procedure follows. A more detailed description of the experimental methods has been published elsewhere [1,2].

The basic processing steps are illustrated schematically in Figure 1. A single-crystal wafer or a polycrystalline specimen is coated with a uniformly thick photoresist layer. For the studies that will be described, sapphire single-crystal wafers were used; however, the technique has much broader applicability. Using a typical range of processing conditions, the thickness of the photoresist can be varied from 1.3 to 2.6 μm . The photoresist is then selectively exposed using *uv* radiation. The shape of the exposed features reflects the mask pattern. The geometry of features on the mask is defined using pattern generation software. For positive photoresists, exposure increases the solubility of the photoresist and allows its selective removal, thus exposing the substrate. Ion beam etching is used to etch the exposed ceramic surface, and thereby transfer the pattern to the ceramic substrate.

For sapphire and alumina, an etched and an unetched sample are bonded by hot pressing (1370°C, 60 min, 15 MPa, $2.6 \cdot 10^3$ Pa), thereby transferring the surface pattern to an internal interface. A wide variety of ensembles can be produced to address a broad range of experimental interests. Specimens prepared by bonding an etched single crystal to a polished single crystal of identical orientation provide a means of simulating defects in single crystals, intragranular flaws. Controlled misorientation bicrystals can be used to study intergranular defects. Single crystal-polycrystal ensembles and polycrystal-polycrystal ensembles provide an opportunity to examine the effects of a wider range of misorientation, and to simulate and study defects in typical polycrystalline materials.

Examples of the types of surface structures that can be generated are provided in Figure 2. Features with minimum dimensions of order one to two microns can be produced using conventional lithographic procedures, and can be repeated up to 10^6 times on a single substrate. The feature depth is typically a few tenths of a micron, yielding minimum feature volumes that are $<1 \mu\text{m}^3$. Under optimum conditions, the location of the features can be controlled to within $\pm 0.1 \mu\text{m}$. The specific experimental objectives influence the design of the surface structures. Those illustrated in Figure 2 have been utilized in studies of pore-boundary separation [3], pore coarsening and pore elimination [4], Rayleigh instabilities [5], and faceting [1,6].

Once surface features have been transferred to an internal interface, several methods can be used to study their evolution. When optically transparent materials such as sapphire are used, optical microscopy provides a convenient nondestructive mode of observation for all but the finest scale features. Using this method, a single sample can be given repeated anneals, and the time evolution of specific defects can be studied. When greater resolution is required, or when opaque material is used, fracture surfaces can be examined using optical or scanning electron microscopy. Finally, for the finest features, or when high spatial resolution is required, foils containing interfacial structures can be prepared and examined using transmission or scanning transmission electron microscopy.

APPLICATION TO HIGH-TEMPERATURE CRACK HEALING

The following section provides an overview of recent work on high-temperature crack healing in sapphire. A more detailed account of this work is available in references 1 and 7. Work pertaining to the late stages of crack healing is described in greater detail in references 1 and 5.

Background:

Crack healing in oxides has been reviewed most recently by Gupta [8]. Most studies of crack healing have revealed that there are several geometrically distinct stages to the process. The initial stage is characterized by crack tip regression and blunting, sometimes accompanied by faceting [9]. Discontinuous crack pinching can also initiate at cleavage steps or other irregularities along the crack front, or on the crack face [10]. Crack regression leads to the formation of

Sample Preparation Procedure

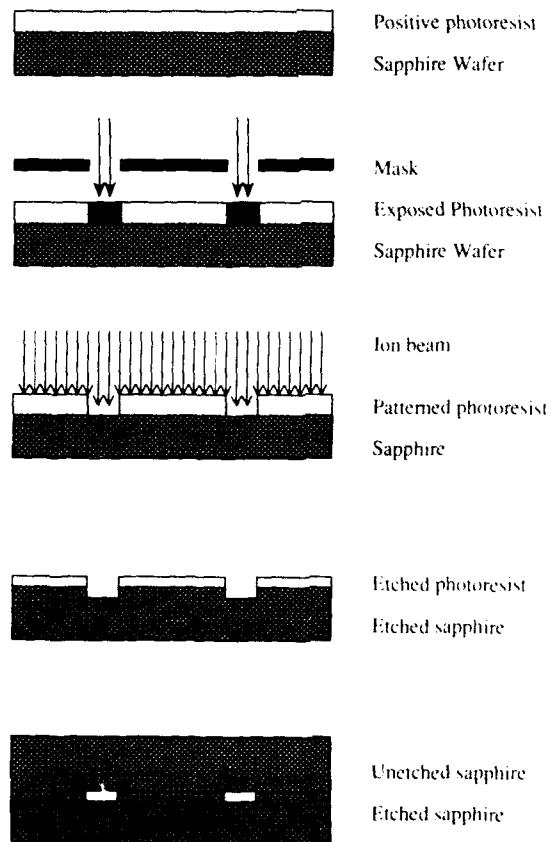


Figure 1. Schematic illustration of sample preparation procedure: a) coated substrate, b) selective exposure through a mask, c) ion beam etching of substrate and patterned photoresist, d) etched photoresist and substrate and e) bonding.

a cylindrical ring around the crack periphery. This cylindrical rim is unstable to longitudinal perturbations. The second stage of crack healing is marked by the formation of "cylindrical" pore channels. Collapsed or healed portions of the crack perimeter propagate towards the crack interior, producing cylindrical ligaments whose axes are often perpendicular to the original crack edge. These cylindrical ligaments or channels are in turn subject to Rayleigh instabilities [11], leading to the formation of discrete spherical pores. Subsequent to the formation of isolated pores, pore elimination and pore coarsening can occur.

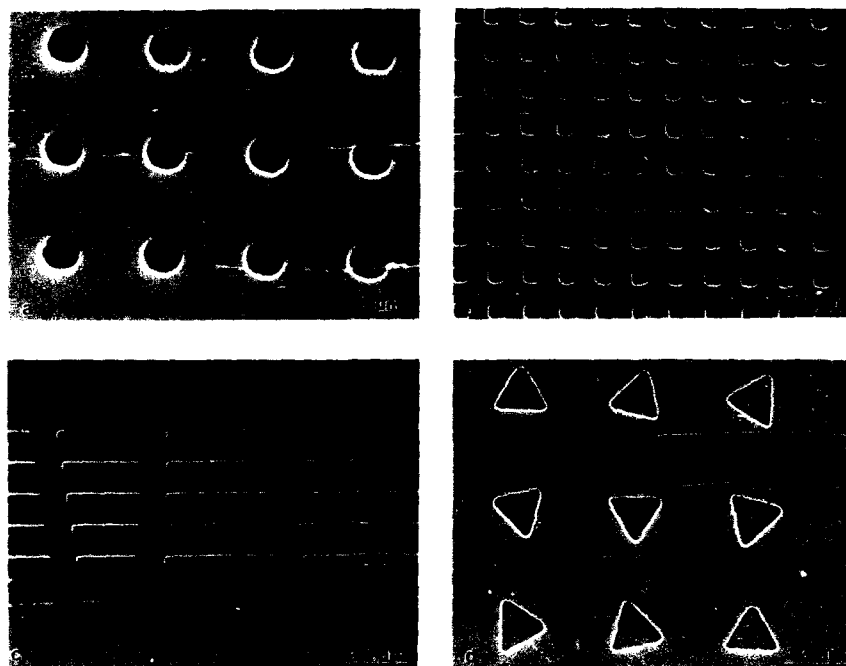


Figure 2. SEM micrographs of accessible surface structures: a) monomodal arrays used for pore-boundary separation studies, b) bimodal arrays for pore coarsening studies, c) channel-like features for studying late stage crack healing and Rayleigh instabilities, and d) nonequilibrium shapes for studying facet development and surface energy anisotropy.

Several important variables affecting crack healing and strength recovery have been identified. The crack opening displacement can affect both the morphological characteristics [10], and the rate of healing [12]. The crack face crystallography can modify the healing behavior: faceting may aid or impede "cylinderization". Maruyama and Komatsu have demonstrated the sensitivity of the morphological evolution of cracks to grain boundary misorientation [13]. Crack face microstructure can also be important: Singh and Routbort have suggested that hillock formation accompanying grain boundary grooving can induce bridging of crack faces, and thereby contribute to strength recovery [14]. Finally, both crack healing studies [15] and measurements of surface diffusivities [16] in alumina have revealed a sensitivity of the healing and transport rates to impurities. Identification and quantification of the effects of particular impurities on crack healing could shed light on their effects on transport during sintering as well.

Although there are general behavioral trends, and some of the important variables have been identified, there are also pronounced system-to-system and even sample-to-sample variabilities in behavior that are not well understood. The difficulty in identifying the origin of these differences stems in part from a difficulty in controlling and isolating the effects of specific variables on the healing behavior. In view of the demonstrated importance of crack geometry, crack face crystallography, crack face microstructure, and sample chemistry/impurities on crack healing behavior, clarification and quantification of these effects seemed warranted. Our efforts focussed on applying lithographic methods to the study of crack healing, and subsequently assessing the importance of these variables on crack healing in sapphire.

Experimental Considerations:

For simulation of cracks, the features of interest are generally sufficiently large that the spatial resolution limit of the technique is not a concern. The accessible range of crack depth is a more important issue. During ion beam milling, both the ceramic and the photoresist are etched, and consequently, the relative etching rates of the substrate and photoresist determine the maximum feature depth. The etching rate of sapphire is approximately one-third that of the photoresist. Thus, using conventional processing procedures, crack depths approaching $0.9\text{ }\mu\text{m}$ are accessible.

The minimum feature depth is limited by the quality of the polished surface; lithographically introduced defects must have a depth exceeding that of the intrinsic polishing irregularities. Using as-received polished sapphire wafers, features as shallow as 40 nm can be transferred to an internal interface. With the use of atomically smooth substrates [17], this limit could be reduced further. Thus, it is possible to produce a wide range of cracklike defects with crack opening displacements similar to those in real materials.

Figure 3 illustrates a typical cracklike flaw introduced using lithography. The morphological evolution of geometrically similar cracks lying parallel to the basal (0001) and prismatic (11 $\bar{2}$ 0) planes was characterized to assess the effects of a difference in crack tip and crack face crystallography on the healing behavior. Up to 200 identical cracklike flaws were generated in each experiment. Most anneals were conducted at 1800°C ($0.86\text{ }T_m$) in a vacuum of $\approx 1.3 \cdot 10^{-3}\text{ Pa}$. In the work that will be illustrated, optical microscopy was used to study the morphological evolution of specific cracks within a particular interface.

Results and Discussion:

Figure 3 illustrates a typical cracklike flaw viewed in a cross section taken perpendicular to the crack plane. The flaw dimensions are $100\text{ }\mu\text{m}$ by $200\text{ }\mu\text{m}$ by 180 nm . The flaw was etched into a basal plane, and after bonding, the sample was annealed for 10 min at 1800°C . The pronounced difference in curvature along the crack perimeter induces mass redistribution, which leads to recession of the crack perimeter, and the formation of an annular ring. Some facetting along the crack perimeter is evident, despite the high anneal temperature.

Figure 4 presents optical micrographs taken using transmitted light, illustrating the morphological evolution of a pair of cracks oriented parallel to the basal plane, originally $200\text{ }\mu\text{m}$ by $100\text{ }\mu\text{m}$, and with a depth of 180 nm . The directions e and g are [11 $\bar{2}$ 0] and [1 $\bar{1}$ 00], respectively. Figure 4a illustrates the as-prepared crack geometry. The same two cracks are shown in Figure 4b after 60 min at 1800°C . The annular ring, evident in the cross section in Figure 3, is unstable to growth of sufficiently long wavelength perturbations. These perturbations cause a variation in the local crack opening displacement. A decrease in crack opening displacement increases the crack regression rate, and thus, points at which the annulus is thinner will recede more rapidly. This, coupled with longitudinal mass redistribution, causes what appears as local pinch-off of the annular ring. Once closure occurs, healing via intrusion is rapid; Figure 4c shows the interface after 90 min at 1800°C , and a considerable fraction of the original crack has been healed. Figure 4d shows the crack after 135 min total annealing time. At this stage, the crack contains several cylindrical segments. These are subject to Rayleigh instabilities. This later stage of healing has also been investigated using lithographically introduced features like those shown in Figure 2c [5]. The sequence presented is qualitatively consistent with the general observations summarized by Gupta [8].

A comparison between the healing behavior of the cracks in Figure 4, and those of other basal plane cracks of identical geometry and crystallography shows that the differences in healing behavior are related to the relative extents of crack regression before perturbation initiates. The results presented in Figure 4 illustrate a case in which there was a relatively greater propensity for pinch-off along the crack perimeter. Rim perturbation was dominant, resulting in more rapid healing. The relatively finer scale of pinch-off results in a finer-scale healed structure, and accelerates break-up into spherical pores. In other cases, crack regression was dominant. This leads to a reduced healing rate, and a much coarser healed structure.

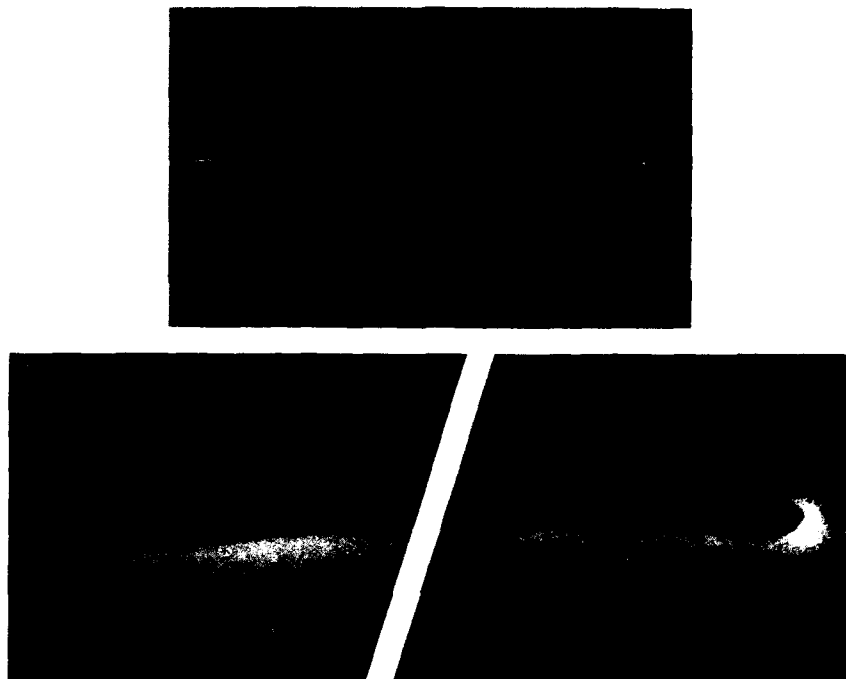


Figure 3. SEM micrograph of a cracklike flaw lying parallel to the basal plane, viewed in a cross section taken perpendicular to the crack plane after 10 min at 1800°C. $e = [11\bar{2}0]$ and $f = [0001]$

Dramatic differences in morphological evolution can occur when the crystallography of the crack edges and faces is altered. One type of healing behavior for cracks oriented parallel to the prismatic plane is illustrated in Figure 5.¹ Figures 5a and 5b show two initially 120-nm deep cracks oriented parallel to the $(11\bar{2}0)$, after 5 and 210 minutes at 1800°C. Crack healing occurs via the growth of "pillars" or columns that ultimately connect the crack faces. During continued annealing at elevated temperature, the columns expand, and thereby heal considerable portions of the crack. This mode of healing has the potential to produce a significant increase in the healing rate relative to that due to crack regression alone, and provides a mechanism for healing cracks at positions away from the crack perimeter. Hickman and Evans have observed similar behavior in calcite [10].

The potential effects of grain face microstructure on crack healing became evident when the stability of flaws at single crystal-polycrystal interfaces was studied. If the flaw intersects multiple grains, grain boundary grooves will form. When the dominant transport mechanism for grooving is either surface diffusion [18,19] or volume diffusion [20], a shoulder or hillock develops adjacent to the groove, that extends above the original surface. These hillocks, if they become sufficiently large, can bridge the crack. This hillock-induced healing was observed, and bridging appeared imminent at other sites. The degree to which this mechanism can contribute

¹ Not all prismatic plane flaws healed in this manner. Alternatively, pore channels formed parallel to the original crack front. The healing mechanism is distinct from that for basal plane cracks, and does not involve instabilities along the crack perimeter, but instead closure parallel to and away from the crack perimeter.

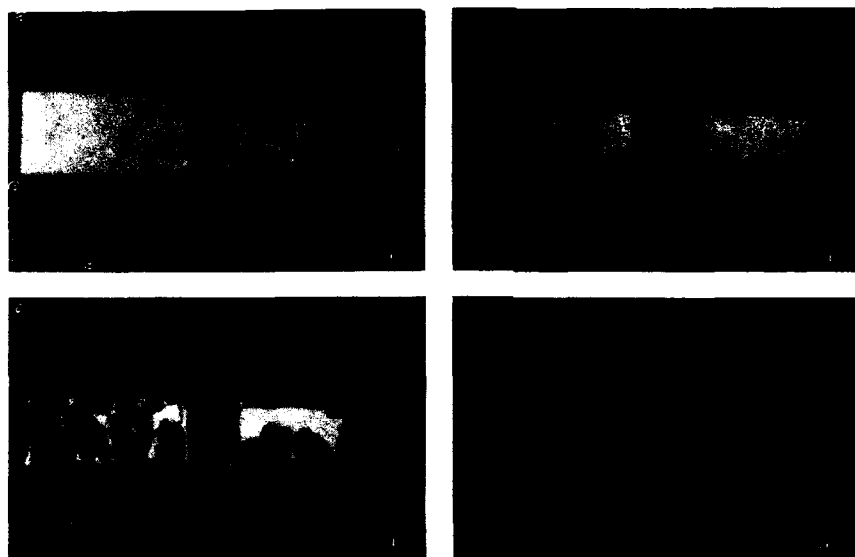


Figure 4 . Optical micrographs of a pair of $100\text{ }\mu\text{m}$ by $200\text{ }\mu\text{m}$ by 180 nm deep flaws at 1800°C after a) 0 min, b) 60 min, c) 90 min, and d) 135 min. The directions e and g are $[11\bar{2}0]$ and $[1\bar{1}00]$, respectively. Edge perturbation dominates and leads to a finer scale healed structure.

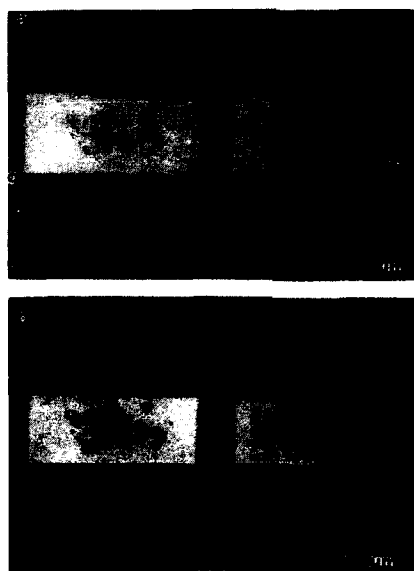


Figure 5 . Two cracks, initially 120 nm deep, oriented parallel to the $(11\bar{2}0)$, after a) 5 and b) 210 minutes at 1800°C .

to healing will be sensitive to the crack opening displacement variation with distance from the crack perimeter. The grain size will influence the spacing of the bridging sites, thus introducing a potential microstructural sensitivity to healing behavior.

All processing steps except for hot pressing are conducted in Class 100 clean rooms. Nonetheless, even with these precautions, occasional isolated contamination of the interface by airborne contaminants occurs. Figure 6 illustrates behavioral differences that we believe reflect the effects of inadvertent contamination of one crack (out of a total of 1080). The cracks shown are oriented parallel to the basal plane, and have an original depth of 180 nm. Figure 6a shows the as-prepared structure. After only 5 min at 1800°C, one of the cracks is essentially completely healed. After a total anneal time of 200 min, Figure 6c, the channels have broken up into isolated pores. The other crack has barely begun to heal. The healing rates of these two cracks are estimated to differ by two to three orders of magnitude.

Systematic studies utilizing doped or ion-implanted crystals may provide information on effects of crack face contaminants on transport during healing. Such studies could also provide useful insights on the role that these impurities play in affecting microstructural development during sintering [21]. It is conceivable that measurements of this type may also show the effects of anisotropic segregation [22] on processes whose kinetics are surface diffusion controlled.

Related Research Opportunities:

Our initial research objective has been to study several aspects of high-temperature crack healing. However, the basic sample preparation procedures that were used lend themselves to several other applications.

Since it is possible to produce cracklike defects of controlled size and location, and to transfer them to internal interfaces, the technique appears to be an ideal means of fabricating standards for nondestructive testing methods, and should provide an interesting alternative to methods relying on the burn-out of latex spheres. Since lithography can be used to produce a sharp precrack at the interface as well as a controlled geometry pore array, it should be possible to study fracture in microdesigned porous materials. There are also a growing number of cases where simple components are bonded or joined to make a complex structure. The elimination of controlled-geometry flaws at bonded interfaces as a function of time, temperature, geometry, and applied pressure is amenable to investigation. A simple extension of the procedures described should allow the study of flaw elimination at ceramic-metal interfaces.

APPLICATION TO PORE-BOUNDARY INTERACTIONS

The following section summarizes our work on the application of photolithography to studies of pore-boundary interactions and pore-boundary separation in MgO-doped and undoped high-purity alumina. A more detailed account of this work is available in references 1 and 3.

Background:

Significant advances in our understanding of sintering have resulted from modelling sintering as a competition between densification and coarsening processes [23,24], and investigating the competitive processes individually. Hot pressing provides a means of studying "pure" densification processes, and has proven helpful in identifying densification mechanisms [25].

An improved understanding of "pure" coarsening processes is also needed. Investigations of (grain) coarsening in a pore-free material are the most straightforward [26,27]. The characteristics of grain growth in porous compacts, specifically the nature of pore-boundary interactions during sintering, also have an important effect on microstructural evolution [28-33]; premature pore-boundary separation precludes complete densification during sintering.

Experimental analogues to hot pressing, capable of critically testing models of pore-boundary interactions, were lacking. As a result, experimental studies of pore drag have been limited to one of two approaches. The first is indirect, and relies on measurements of transport coefficients [5,34]. The second approach to studying pore drag yields only qualitative information [35].

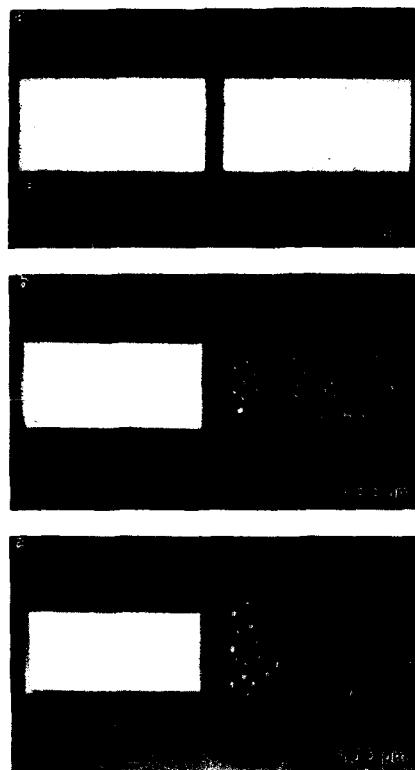


Figure 6. Effect of inadvertent contamination on healing rates of two otherwise identical cracks etched into the basal plane of sapphire. Crack evolution after a) 0 min, b) 5 min, and c) 200 min at 1800°C.

It is desirable to have an experimental procedure amenable to controlled study of pore drag, which would allow determination of the critical condition for pore-grain boundary separation [36]. Ideally, this experiment would circumvent the problems associated with sintering studies, that is, it would provide a well-defined geometry, and it would eliminate competitive densification processes. The application of lithography to pore-boundary separation has led to the development of an experimental procedure that satisfies these restrictions, and provides a new tool for studying sintering, "controlled pore drag" experiments. Such controlled pore drag experiments, together with hot pressing experiments, allow study of the two idealized or limiting paths of microstructural evolution during sintering.

Experimental Considerations:

Controlled pore drag experiments rely on the production of controlled-geometry pore structures [2] at the interface between a large grain (single-crystal sapphire) and a dense polycrystalline matrix. During subsequent heat treatments, the large "abnormal" grain consumes the adjoining polycrystalline material at a rate determined by the drag force exerted by the interfacial pore arrays. Pore-boundary separation occurs when the grain velocity exceeds the peak pore velocity. The important experimental variables are the polycrystal grain size and

chemistry, and the pore size and spacing. Since the microstructure and chemistry of the polycrystal can be controlled, and pore size and spacing can be controlled precisely and varied easily via lithography, a wide range of conditions can be examined.

Controlled surface structures like those illustrated in Figure 2a, were generated on the basal plane of sapphire. The pore width was held constant at $3\text{ }\mu\text{m}$, center-to-center pore spacings were varied ($4, 6, 8,$ and $10\text{ }\mu\text{m}$), and the pore depth was $0.24\text{ }\mu\text{m}$. Pore arrays 20 pores wide and 1800 to 4000 pores long with interarray spacings of $200\text{ }\mu\text{m}$ were produced. Etched sapphire wafers were subsequently hot pressed against highly polished, dense MgO-doped or undoped polycrystals which were fabricated using a two-stage hot pressing and hot isostatic pressing procedure, thus transferring the controlled pore structures from external to internal interfaces, as illustrated in Figure 7. Wide pore-free ligaments surrounding the pore arrays were used to almost completely suppress densification during hot pressing and annealing.

The microstructures of both undoped and 250 atomic ppm MgO-doped materials were uniform. Changes in grain size during annealing were determined using a linear intercept method. The migration rates of the sapphire-alumina interfaces were obtained by measuring boundary positions after various tempering times relative to the initial interface position as marked by lithographically introduced reference markers.

Results and Discussion:

The essential parameters in models of pore-boundary interactions are the grain boundary mobility, M_b , the pore mobility, M_p , and the areal density of pores. The mobilities can be assessed by measuring grain boundary and pore velocities under known driving forces; the areal density of pores is controlled using the procedures described previously.



Figure 7. Tailored interface with varying pore density. Pore spacing: a) $4\text{ }\mu\text{m}$, b) $6\text{ }\mu\text{m}$, c) $8\text{ }\mu\text{m}$, and d) $10\text{ }\mu\text{m}$.

The grain boundary velocity, V_g , is determined by monitoring the growth of unetched (pore-free) basal plane sapphire wafers into both doped and undoped dense alumina polycrystals. The critical condition for pore-boundary separation is determined by monitoring the growth of etched (basal plane) sapphire wafers with controlled geometry pore arrays into the same doped and undoped dense alumina polycrystals. Following an initial period during which the pore shape changes from that of a cracklike flaw to that of a more equiaxed intergranular pore, migration of the pore-laden interface commences. During migration, the pores either remain attached to the migrating interface, or under some conditions, the pores separate, and thereby become isolated in the growing single-crystal sapphire wafer. Examples of pore-boundary separation in MgO-doped alumina at two different pore spacings are provided in Figure 8. The sample was annealed for a total of 15 h at 1600°C; separation occurred after ≈ 10 h of annealing.

Measurements of the migration kinetics include measurements of the pore velocity just prior to pore-boundary separation, and therefore velocities approaching the so-called peak pore velocity. When measurement errors are taken into account, the peak pore velocity, V_p , for undoped alumina is in the range of 0.08 to 0.22 $\mu\text{m/h}$, whereas the range for MgO-doped alumina is between 4.5 to 7.0 $\mu\text{m/h}$. Using a relationship derived by Hsueh et al. [28], the peak pore velocity can be related to the surface diffusivity. Our measured pore velocities yield estimates for the surface diffusivity of $0.62\text{--}1.70 \times 10^{-7} \text{ cm}^2/\text{s}$ for the undoped alumina, and $3.47\text{--}5.40 \times 10^{-7} \text{ cm}^2/\text{s}$ for the MgO-doped alumina, suggesting that the addition of 250 ppm MgO increases the surface diffusivity by a factor of 2 to 8 at 1600°C.

Substitution of the peak pore velocities into an expression describing pore-boundary separation in the case of constant center-to-center pore spacing [33], yields critical grain size-pore spacing coordinates at which separation initiates, and which thus divide a map of grain size and pore spacing into regions of pore separation and pore attachment. In the absence of any measurement error, a single line would divide the plot into attachment and separation regions. In practice, a transition region, reflecting the uncertainty due to measurement error partitions the plot. Despite this complication, a particularly good correlation has been observed between predicted and experimental critical coordinates for undoped alumina [3]. Further experimental work is necessary to better define the transition condition for MgO-doped alumina. However, given the uncertainty in values of parameters such as the interfacial energies and dihedral angles, which enter into the analysis, the results are encouraging.

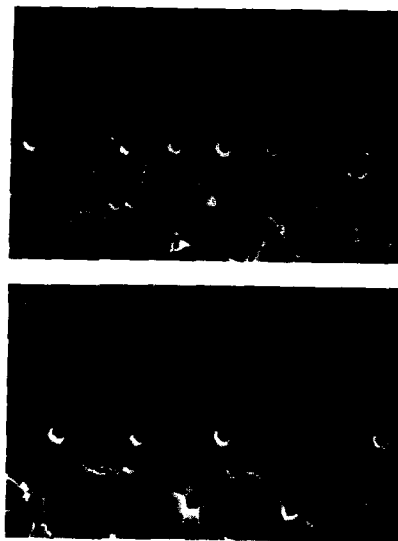


Figure 8. Illustration of pore-boundary separation in MgO-doped alumina in samples with two different pore spacings.

Related Research Opportunities:

The results indicate that quantitative measurements of pore-boundary separation conditions are now possible. Since experiments can be conducted using both doped and undoped polycrystals, a direct comparison between theory and experiment is possible, and the effects of dopant additions can be assessed. It should be possible to clarify and quantify the effects of other dopants in alumina on pore-boundary separation conditions. More generally, since the technique can be applied to other systems, it may provide a general method for screening and assessing the effects of sintering additives on pore-boundary separation. When used in conjunction with other model experiments that provide information on impurity effects on lattice and grain boundary transport, a better understanding of impurity additions on microstructure evolution may evolve.

APPLICATION TO PORE COARSENING AND PORE ELIMINATION

During the final stage of sintering, vacancies are redistributed from pores to either larger pores (coarsening) or to the grain boundary (densification). In both cases, diffusion occurs through the lattice and along the grain boundary. When diffusion is the rate controlling process, a quantitative description of coarsening and densification requires that the lattice and grain boundary diffusivities be known. Alternatively, interfacial reactions may be rate limiting. Lithography provides a means of studying pore coarsening and pore elimination under highly controlled conditions [4].

Research Opportunities:

Figures 2a and 2b establish the ability to produce monodispersed and bimodal surface features that, after bonding, yield monodispersed and bimodal pore arrays. As has been shown for other cases, these features can be transferred to an internal interface. The surface crystallography and the grain boundary misorientation can be controlled. Moreover, the impurity content of the crystals can also be varied. This combination of features provides numerous research opportunities [4].

For the sake of brevity, only diffusion-controlled processes will be considered. First, the ability to vary the "volume" fraction, size, size distribution, and spatial distribution of interfacial pores, and to systematically vary each of these parameters allows unprecedented control over the topological characteristics that influence the coarsening and densification rates. Second, through a systematic increase in boundary misorientation, from zero degree misorientation upward, it should be possible to separate the contributions of lattice and grain boundary transport to coarsening and densification. When the design of the interfacial structure permits pore elimination, effects of an applied pressure on pore elimination rates can be assessed. Finally, since the experimental technique can be applied equally well to doped and undoped material, comparisons between the behavior of doped and undoped materials under otherwise identical experimental conditions offer the possibility of clearly identifying the effects of dopants on grain boundary and lattice transport coefficients.

EXTENSIONS AND REFINEMENTS

There appear to be two logical avenues for extending the range of processes that can be investigated. The first entails increasing pattern complexity. The surface patterns generated to date have consisted of discrete entities, isolated pores, channels, cracks, etc.. The generation of controlled geometry two-dimensional continuous patterns affords new experimental opportunities. Pore networks in unfired or partially densified ceramics can be mimicked. Removal of a phase such as a liquid or a polymer can be examined; Cima and co-workers have applied the method to studies of binder removal [37]. Alternatively, the infiltration characteristics of porous networks by a vapor or a liquid metal can be investigated. Finally, the coarsening or densification behavior of such pore networks can be studied.

The second avenue for extension and refinement entails a decrease in the scale of the structures that are studied. There is a continuous effort to reduce the scale of features in the microelectronics industry, which drives the development of submicron lithographies. State-of-the-art microfabrication laboratories include facilities for lithographies that are capable of producing 0.4 μm width features. When even finer features are of interest, electron beam lithography can be applied. The National Nanofabrication Facility at Cornell University has facilities that provide 25 nm resolution [38]. Consequently, simulation and study of nanoscale microdesigned interfacial structures should be possible.

ACKNOWLEDGEMENTS

Research supported by the Director, the Office of Energy Research, Office of Basic Energy Sciences, Materials Sciences Division of the U.S. Department of Energy under Contract No. DE-AC03-76SF00098. We would also like to acknowledge the assistance of Katalin Voros, Phillip Guillory, and Bob Hamilton, and the other personnel of the Microfabrication Laboratory at the University of California at Berkeley for helping to make this research possible.

REFERENCES

1. J. Rödel, Ph.D. thesis, University of California, Berkeley, 1988.
2. J. Rödel and A. M. Glaeser, *J. Am. Ceram. Soc.*, **70**, [8], C172 (1987).
3. J. Rödel and A. M. Glaeser, Lawrence Berkeley Laboratory (LBL) Report 25225, 1988.
4. J. Rödel and A. M. Glaeser, *Materials Letters*, **6**, [10], 351, (1988).
5. J. Rödel and A. M. Glaeser, LBL Report 25147, 1988.
6. J. Rödel and A. M. Glaeser, in *Interfacial Structures, Properties and Design*, edited by M. H. Yoo, W.A.T. Clark, and C.L. Briant (Mater. Res. Soc. Proc., **122**, Pittsburgh, PA 1988) pp. 485-90.
7. J. Rödel and A. M. Glaeser, LBL Report 27197, 1989.
8. T. K. Gupta, in *Structure and Properties of MgO and Al₂O₃ Ceramics*, edited by W. D. Kingery, (The American Ceramic Society, Columbus OH, 1984) pp. 750-66.
9. R. Raj, W. Pavinich and C. N. Ahlquist, *Acta Metall.*, **23**, [3], 399 (1975).
10. S. H. Hickman and B. Evans, *Phys. Chem. Minerals*, **15**, 91 (1987).
11. Lord Rayleigh, *Proc. London Math. Soc.*, **10**, 4 (1879).
12. G. Bandyopadhyay and C. R. Kennedy, *J. Am. Ceram. Soc.*, **60**, [1-2], 48 (1977).
13. O. Maruyama and W. Komatsu, *Ceramurgia International*, **5**, [2], 51 (1979).
14. R. N. Singh and J. L. Routbort, *J. Am. Ceram. Soc.*, **62**, [3-4], 128 (1979).
15. A. G. Evans and E. A. Charles, *Acta Metall.*, **25**, [8], 919 (1977).
16. W. M. Robertson and F. E. Ekstrom, in *Materials Science Research*, Vol. 3, edited by W. W. Kriegel and Hayne Palmour, III, (Plenum, New York, 1966) pp. 273-83.
17. R. G. Horn, D. R. Clarke and M. T. Clarkson, *J. Mater. Res.*, **3**, [3], 413 (1988).
18. W. W. Mullins, *J. Appl. Phys.*, **28**, [3], 333 (1957).
19. W. M. Robertson, *J. Appl. Phys.*, **42**, [1], 463 (1971).
20. W. W. Mullins, *Trans. A.I.M.E.*, **218**, 354 (1960).
21. J. E. Blendell and C. A. Handwerker, *J. Cryst. Growth*, **75**, [2], 138 (1986).
22. S. Baik and C. L. White, *J. Am. Ceram. Soc.*, **70**, [9], 682 (1987).
23. C. A. Handwerker, R. M. Cannon and R. L. Coble, in *Structure and Properties of MgO and Al₂O₃ Ceramics*, edited by W. D. Kingery, (The American Ceramic Society, Columbus OH, 1984) pp. 619-643.
24. M. F. Yan, *Mat. Sci. and Eng.*, **48**, [1], 53 (1981).
25. M. P. Harmer and R. J. Brook, *J. Mater. Sci.*, **15**, [12], 3017 (1980).
26. S. J. Bennison and M. P. Harmer, *J. Am. Ceram. Soc.*, **66**, [5], C90 (1983).
27. S. J. Bennison and M. P. Harmer, *J. Am. Ceram. Soc.*, **68**, [1], C22 (1985).
28. C. H. Hsueh, A. G. Evans, and R. L. Coble, *Acta Metall.*, **30**, [7], 1269 (1982).
29. M. A. Spears and A. G. Evans, *Acta Metall.*, **30**, [7], 1281 (1982).

REFERENCES (continued)

30. C. H. Hsueh and A. G. Evans, *Acta Metall.*, **31**, [1], 189 (1983).
31. R. J. Brook, *J. Am. Ceram. Soc.*, **52**, [1], 56 (1969).
32. R. J. Brook, in *Treatise on Materials Science and Technology*, Vol. 9, edited by F. F. Y. Wang, (Academic Press, New York, 1976) pp. 331-64.
33. F. M. A. Carpay, *J. Am. Ceram. Soc.*, **60**, [1-2], 82 (1977).
34. T. K. Gupta, *J. Am. Ceram. Soc.*, **61**, [5-6], 191 (1978).
35. K. A. Berry and M. P. Harmer, *J. Am. Ceram. Soc.*, **69**, [2], 143 (1986).
36. M. P. Harmer, in *Structure and Properties of MgO and Al₂O₃ Ceramics*, edited by W. D. Kingery, (The American Ceramic Society, Columbus OH, 1984) pp. 679-98.
37. M. J. Cima, presented at the 1989 MRS Spring Meeting, San Diego, CA, 1989 (unpublished).
38. G. Galvin, *MRS Bull.*, **13**, (7), 31 (1988).

PART V

**Fiber and Whisker-Reinforced
Composites**

POWDER PROCESSING AND DENSIFICATION OF CERAMIC COMPOSITES

FRED F. LANGE, DAVID C. C. LAM AND OLIVIER SUDRE

Materials Department, College of Engineering, University of California, Santa Barbara, Santa Barbara, CA 93106

ABSTRACT

Two issues, packing powder/reinforcement systems and constrained densification, are reviewed. It is shown that pressure filtration has the greatest potential for packing powders containing reinforcements and packing powders within reinforcement preforms. High particle packing is achieved with repulsive interparticle potentials, and for a very small particle to reinforcement diameter ratio. It is now clear that individual reinforcements do not constrain the densification of powders. Shrinkage constraint is caused by a network of either non-touching or touching reinforcements. Network shrinkage (and thus composite shrinkage) caused by powder densification leads to the development of a denser interconnected matrix material surrounding lower density regions. Densification of the lower density regions requires the creep deformation of the denser continuum. As detailed elsewhere in this proceedings, grain growth causes this denser continuum to become more resistant to creep, and coarsening within the lower density regions causes desintering and the dissipation of sintering 'stresses'. These phenomena do not occur during the densification of glass powders and explains the different densification behavior of crystalline powder matrices relative to glass powder matrices.

INTRODUCTION

Reinforcements are incorporated into ceramics in an attempt to increase the fracture toughness of the ceramic matrix, impart R-Curve behavior (toughness increases as the crack grows), and to produce a material which can gracefully fail at high strains. To realize these properties, the reinforcements must act as bridges behind an extending crack. The extending crack must somehow by-pass the reinforcement, and the bridging reinforcement must somehow dissipate work as it acts as a bridge. Analytical fracture models are relatively well developed, but processing methods to make useful composites are lacking.

Non-powder processing methods for making ceramic matrix composites, based on forming ceramic matrixes via infiltration into reinforcement preforms, has been reviewed by Jamet et al.¹ and Naslain². They include cyclic chemical vapor infiltration/deposition, cyclic sol-gel infiltration/heat treatment, and cyclic organometallic infiltration/pyrolysis. Molten metals are also infiltrated into partially sintered powder compacts.³ In addition, several different ceramic matrixes can be 'grown' within fiber preforms via an environmental reaction method (e.g., the oxidation of certain aluminium alloys⁴) under development by the Lanxide Corporation. These methods can be synergistically used with powder methods.

Powder processing of composites involves three critical issues: 1) incorporating and consolidating powder-reinforcement systems, 2) making the powder matrix strong, and 3) controlling the matrix/reinforcement interface toughness and frictional characteristics. This review will focus on the first two of these issues.

PACKING PARTICLES AND REINFORCEMENTS

Powder Packing

Particle morphology, interparticle forces and particle size distribution are the major factors controlling the density to which mass can be consolidated in the form of powders.

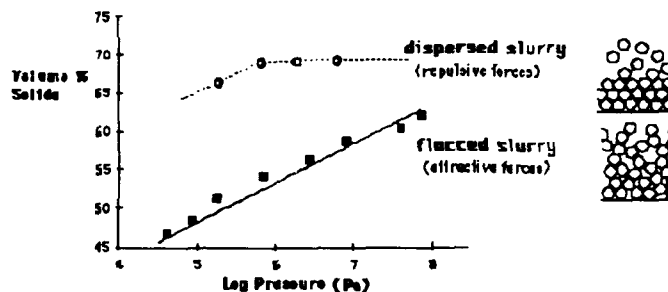


Figure 1. Packing density of Al_2O_3 powder compacts produced by pressure filtration. Graph and schematic show that repulsive interparticle forces allow particles to pack as individuals to produce high packing density which is relatively insensitive to applied pressure.

Interparticle forces have the greatest effect on particle packing. The effect of interparticle forces is best illustrated when powder is packed from the slurry state, e.g., by pressure filtration, where the interparticle forces are controlled by surface-chemical methods (charge site density through pH control, polyelectrolytes, etc.). Figure 1 illustrates the particle packing density of aqueous dispersed (pH = 2) and flocced (pH = 8) slurries of Al_2O_3 powder as a function of filtration pressure. As shown in the schematic, the repulsive interparticle forces within the dispersed slurry allow the particles to flow and pack as individuals, find their lowest free energy position as they are added to the consolidation layer, and produce a very high, pressure insensitive, packing density. The packing density produced from flocced slurries is much lower and pressure sensitive. For this case, the attractive interparticle forces produce a connective network within the slurry before they are packed. This network itself must be consolidated to form the consolidated layer by particle rearrangement. Particle rearrangement also continues within the consolidation layer. Dry powders behave much like the flocced slurry, i.e., the packing density is very pressure sensitive and they pack to a lower density relative to dispersed slurries. Thus, roundish, dispersed particles which are packed, e.g., by pressure filtration, are required to achieve high packing densities.

Packing of Mixed Powder/Whisker (Chopped Fiber) Systems

As shown in Fig. 2 mixed powder/whisker (or chopped fiber) systems can be consolidated by pressure filtration.

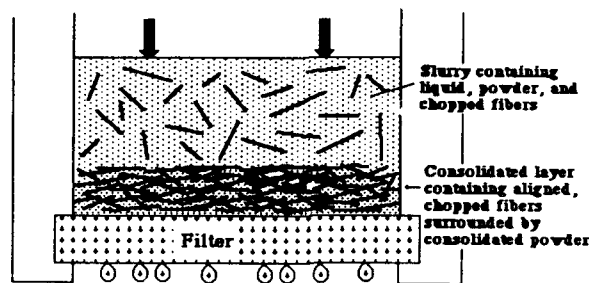


Figure 2. Pressure filtration of mixed whisker (or chopped fiber)-powder system.

The question of how whiskers influence the packing of powders and vice versa has been addressed with recent experiments⁵ where several different manufactured SiC whiskers and chopped carbon fibers (whisker and fiber aspect ratios between 10 and 20). The reinforcements were mixed with either alumina or silicon powder to form 5 different composite systems where the particle-to-whisker diameter ratio (R) was different for each system (between 0.02 and 4). Both powders packed to a relative density of 0.60 without reinforcements. Within each composite system, different mixtures were prepared with different volume fractions of reinforcements. After consolidation, one measures the bulk density of the composite and then calculates the packing density of both the powder and the reinforcement. Figure 3 illustrates the relative packing density of matrix powder (either alumina or silicon) as a function of the particle-to-fiber diameter ratio consolidated by pressure filtration at 58 MPa. Each curve represents results for a given volume fraction of reinforcement (based on solid volume). As shown, reinforcements can significantly reduce the powder packing density. Not shown in Fig. 3 is that the powder reduced the packing density of the reinforcement network. The greater R , the lower the packing density of both the powder and the reinforcement.

The reasons for the decrease in packing density of both the powder matrix and whisker network with increasing particle/whisker diameter ratio might be visualized in Fig. 4. With regard to powder packing, the whisker network defines irregular polyhedra into which powder must be packed. For a given whisker aspect ratio and packing density, the volume of the average polyhedron is proportional to the fiber diameter. When the particle volume is much smaller ($R \rightarrow 0$), the particles might be expected to pack to the same density as if the reinforcement was not present. When the volume of any given polyhedron is smaller than the particle volume ($R > 1$), the particle must be excluded. Between these two limits, the particle packing density should exhibit fractal behavior (the measured volume of a polyhedron should decrease with the increasing size of the particle used to measure volume), i.e., their packing density should decrease.

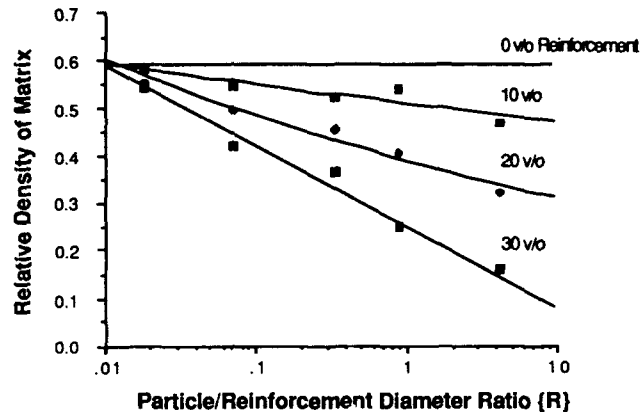


Figure 3. The packing density of the powder matrix in mixed, dispersed powder/reinforcement systems significantly decreases with increasing particle-to-reinforcement diameter ratio.

With regard to the packing density of the whisker network, it might be recognized that only four whiskers can be brought together to touch at a nodal point. Whisker packing density is proportional to the density of nodal points. The void volume at each nodal point is proportional to the whisker diameter. Particles larger than the nodal point volume will cause the whiskers to separate and thus decrease their packing efficiency. With this concept, it can be seen that the highest packing density for both the powder and the whisker network is achieved when $R \rightarrow 0$. The data in Fig. 3 suggests that R should be < 0.02 .

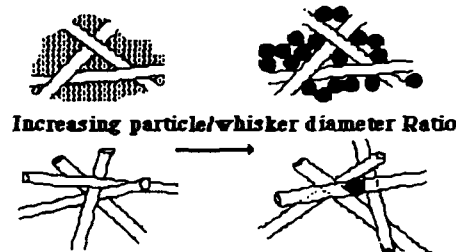


Figure 4. Particle packing within a whisker network should be greatest when the particles are much smaller ($R \rightarrow 0$) than the size of voids defined by the network. Particles that expand the nodal points of four touching whiskers will lower the packing density of the whisker network.

Packing Powders Within Reinforcement Preforms

Three-dimensional preforms can be produced by either felting or weaving continuous fibers or matting chopped fibers. The problem of packing powders within preforms was solved by Jamet et al.⁶ by pressure filtration. Our adaptation is shown in Fig. 5a. In this process the consolidated layer builds up within the preform which is fixed to the filter. The preform is not subjected to differential stresses if filled with a liquid or slurry prior to filtration; it is only subjected to the hydrostatic pressure exerted by the slurry. Our studies⁷ show that powders can be packed within the preform provided that three conditions are satisfied. First, the

particles must be small enough to flow through the preform channels and smaller yet ($R < 0.05$) to achieve high packing densities. Second, the particles in the slurry must repel one another (flocced slurries clog the channels). And, third, repulsive surface forces must exist between the preform material and the particles. These last two requirements can more than double the colloidal requirements for processing.

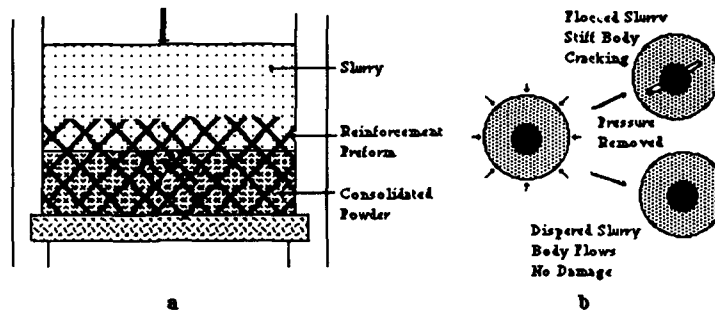


Figure 5. Powder can be packed within reinforcement preforms by pressure filtration (a). When the pressure is removed, the reinforcement material can recover either more or less strain than the powder compact. Differential strain can induce damage (b) in the powder compact unless stresses are dissipated by body flow.

High pressures are desirable because of the parabolic rate kinetics of pressure filtration and the low permeability of highly packed, sub-micron powders. During filtration, both the reinforcement material and surrounding powder are compressed. Both relieve their stored strain when the pressure is removed. Since both have different strain recoveries, stresses can arise due to differential strain recovery. Bodies formed from flocced slurries are stiff after consolidation; stresses produced by differential strain recovery can damage these bodies as shown in Fig. 5b. Bodies formed from dispersed slurries, on the other hand, still flow after consolidation and appear to dissipate stresses arising from differential strain recovery.⁷ Studies have also shown that the strain recovery is time dependent.⁸ Thus, the rheology of the consolidated body must be understood and controlled to avoid damage induced by the reinforcement during processing.

STRENGTHENING THE POWDER MATRIX

After packing powders into the desired shape, powder compacts are conventionally strengthened by a heat treatment that allows mass transport to first form necks between touching particles via sintering and then eliminate the void phase. That is, conventional strengthening produces densification and thus, shrinkage.

It is now widely recognized that the densification behavior of a crystalline powder can be dramatically influenced by an inert, second phase. The phenomena associated with this effect limits the pressureless processing of many composite systems and causes the composite processor to resort to deformation processing, viz. hot-pressing and HIPing. Deformation processing certainly must be avoided if composites are to be engineered with reinforcements architecturally situated along principal stress trajectories.

De Jonghe and coworkers⁹ were the first to systematically characterize constrained densification. They demonstrate that a very small volume fraction (0.03) of an inert (non-densifying) inclusion phase would significantly limit the densification behavior of a composite powder compact. Their isothermal data for ZnO powder compacts containing SiC inclusions show that the densification rate at any time decreases with increasing volume fraction of the SiC phase. Bordia and Raj¹⁰ have reported similar data for TiO₂ powder compacts containing Al₂O₃ inclusions. Brook et al.¹¹, reporting similar data for Al₂O₃ powder containing dense Al₂O₃ inclusions, indicate that the inclusion phase also produces a less-than-theoretical end-point density. None of these observations are predicted by a model developed by Onoda and Messing¹² which suggested that inclusions would not affect densification until they were about to form a connective network at larger volume fractions.

Models to explain the densification behavior of mixed powder-reinforcement systems are based on the fact that the densifying powder shrinks and must place the inert particles in a state of compression. Hsueh, Evans, and McMeeking¹³ argue that if the inert particles are placed in compression, the powder itself must be in a state of mean hydrostatic tension. Raj and Bordia¹⁴ had previously reached identical conclusions by modeling the composite system with a spherical inert inclusion surrounded by a concentric spherical shell of powder. Both groups suggested that the mean hydrostatic tensile stress within the powder would be relaxed by creep within the densifying powder. Both explain the lower densification rate of the composite by superimposing the hydrostatic tensile stress on the compressive sintering 'stress' commonly used to represent the driving potential for powder densification. Although these models are mathematically appealing, Scherer¹⁵ has pointed out that the parameters needed to fit data are unreasonable with respect to the mechanics of the problem and also indicated that the mean hydrostatic stress that might develop within the powder is much smaller than required by the models. In addition, neither model predicts the densification behavior at higher inclusion fractions (either closely spaced or touching), nor do they predict an end point density less than theoretical.

In recent experiments, Lange¹⁶ slip cast alumina powder rings around dense alumina discs. These specimens are a two dimensional analog of that modeled by Raj and Bordia with an equivalent inclusion volume fraction of 0.35. After slow drying, they were heated with controlled heating rates to 1550 °C. Most specimens developed hair-line, radial cracks that would span the ring. These cracks developed either during drying (differential shrinkage < 1 %) or, if not present after drying, during heating to 800 °C (densification shrinkage = 0.3 %). This catastrophic cracking phenomena, which appeared to initiate from agglomerates, occurred when the ring was weakest, i.e., when the critical stress intensity factor of the consolidated powder was small. Upon heating to 1550 °C, the hair-line cracks underwent a large crack opening displacement consistent with the shrinkage produced during densification. Constrained ring specimens that did not develop hair-line cracks (about 20 %, i.e. those that survived the 800 °C treatment) could be heated without macrocracking at any heating rate to achieve the same relative density at 1550 °C as unconstrained rings subjected to an identical heating schedule. This observation strongly suggested that a single inclusion would not alter the densification behavior of a surrounding compact provided catastrophic fracture was avoided prior to and during the formation of sintering necks between particles. This conclusion suggests that the mean hydrostatic stress, thought to decrease the driving potential for

densification in previous models, plays little role in constrained densification of single inclusions.

Experiments ¹⁷ with alumina powders containing high-volume fractions of silicon carbide whiskers showed that the powder within the whisker network did shrink and densify onto the whisker network, but the whisker network itself did not shrink. That is, the relatively rigid whisker network constrains composite shrinkage, but does not prevent the powder within the network from shrinking. Namely, as voids within portions of the densifying powder disappear, their volume is conserved by the opening displacement of other voids (e.g., incipient crack-like voids) created within the powder during packing and/or initial heating when the powder is weak. From outside the composite, the powder appears to be completely constrained from densifying; but from within, damage in the powder grows as portions of the powder undergo complete densification.

In the above experimental example the densifying powder was completely constrained and the reason for the constraint of shrinkage is easily visualized, viz., by the high density SiC whisker network. The question of how shrinkage is constrained within a composite compact where inert inclusions do not form a touching network was addressed by Lange. ¹⁸ As shown in Fig. 6a, the inert inclusions can be placed on lattice sites. In order to fit together with neighbors, each unit cell must retain its shape as the powder shrinks during densification.

The amount of powder between pairs of inclusions relative to the distance between their lattice sites will govern the amount of powder densification for a given amount of composite shrinkage.

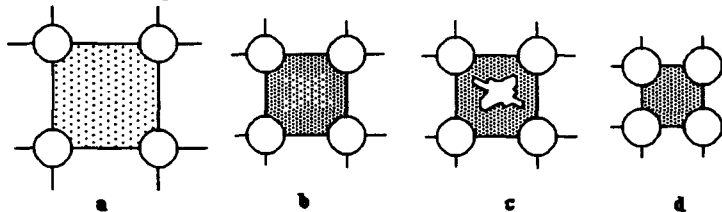


Figure 6. Schematic illustrating a) inclusions on sites of simple cubic lattice, b) uniform composite shrinkage causes powder to densify more between more closely spaced inclusions (cell edges) and prevents the same densification between inclusions of larger spacing (between diagonal sites), c) coarsening of lower density regions causes desintering and larger pore formation (pore volume conserved) and d) deformation of the denser matrix would be required to eliminate lower density region in (b) or larger void in (d).

Since the relative amount of powder (i.e., ratio of distance between inclusions to distance between lattice sites) between cell edge sites is less than the diagonal sites, a uniform cell (or composite) shrinkage will produce a different matrix density between edge and diagonal sites. Powder between site pairs forming cell edges will densify more relative to powder between diagonal pairs as shown in Fig. 6b. That is, the condition that the unit cell must retain its shape requires that the cell diagonals (or powder within the center of the cell) be constrained from shrinking to the same density as the powder between site pairs defining cell edges. If connected voids within the lower density regions can grow, then larger voids will develop to dissipate any shrinkage potential as shown in Fig. 6c. If, on the other hand, the densification potential of the lower density, constrained material can compress and deform the material along connecting cell edges (or pull the inclusions into the cell), then the matrix within the cell will fully densify without distorting the cell's shape

as shown in Fig. 6d. These concepts can be applied to a random distribution of inclusions, viz., for the same amount of composite shrinkage, the powder between more closely spaced inclusions will densify more than the powder between inclusions with larger than average spacings.

As detailed elsewhere in this proceedings¹⁹, microstructure observations have shown that during composite densification, a network of denser material is observed surrounding lower density regions. Although this observation is consistent with the constraining network model discussed above, it was difficult to unambiguously conclude that the denser network was associated with more closely spaced inclusions. Two phenomena were observed as the composite was further heat treated to increase composite density. First, grain growth occurred within the dense network material due to grain boundary motion. Second, voids within the lower density regions grew larger by a desintering process (i.e., the separation of previously sintered grains) associated with grain coarsening. These larger voids were thermodynamically more stable with regard to densification than the low density microstructure from which they developed.

These microstructure observations have lead to a model of composite densification consistent with the constraining effect of the inclusion network: As the composite shrinks, a network of denser material develops (expected to be associated with more closely spaced inclusions). The sintering 'stress' exerted by the lower density regions is small relative to the stress needed to deform the denser network. During this shrinkage process, the denser network becomes more resistant to deformation through grain growth, and the lower density regions dissipate their shrinkage potential via desintering. This model does not apply to glass powders which do not develop grain boundaries (viz., desintering can not occur between glass particles) and do not increase their creep resistance due to grain growth. Thus, this model not only explains the effect of a network of inert inclusion on the densification of a crystalline powder, but also explains why the densification of glass powders is less affected by this network.

AVOIDING DIFFERENTIAL DENSIFICATION: INNOVATIVE APPROACHES

Several studies^{5,20} have now shown that mixed powder/reinforcement systems can be pressureless-sintered to much higher densities than previously expected provided the powder can be packed to a high density. Although further gains are expected, pressureless sintering will be limited to either lower volume fractions of reinforcement or less than theoretical matrix densities. It is certainly obvious that powders packed within relatively stiff preforms will densify onto the preforms to produce extensive matrix damage. The need to avoid constrained densification leaves room for innovation. Many innovative routes can be imagined.

One innovative route is to densify the ceramic before adding the reinforcement. This route, which first appeared either very silly or too simple, has lead to two new processing methods. In the first⁷, powder is packed within a preform (see Fig 5a) made from either an organic material or carbon. During the initial stages of heating, the preform is pyrolyzed leaving a powder compact with channels remnant of the preform. Heating to higher temperatures densifies the powder; channels shrink, but do not disappear. Metal can then be intruded into these connective channels to form a metal reinforced ceramic composite. The reinforcement architecture, 'fiber' diameter, and volume fraction is dictated by the

preform. Other advantages, e.g., different ceramic/metal combinations, etc. are obvious.

In the second ²¹, the ceramic is first made by a powder method as thin sheets via tape casting. After the ceramic is densified, it is made into a laminar composite by sandwiching fiber prepreps between ceramic sheets and hot pressing. Epoxy/carbon prepreps have been used to demonstrate this processing method. Properties are impressive.

ACKNOWLEDGEMENTS

This work was supported by a DARPA/ONR contract, No. N00014-86-K-0753, and is part of a larger multi-investigator, multi-institutional research program concerned with high temperature structural materials led by A. G. Evans and R. Mehrabian.

REFERENCES

1. J.-F. Jamet, L. Anquez, M. Parlier, M.-H. Ritti, P. Peres, and L. Gâteau, "Composite Céramique: Relations Entre Microstructure et Rupture," *L'Aéronautique et l'Astronautique*, No. 123/124, 128-42 (1987).
2. R. Naslain, "Fibrous Ceramic-Ceramic Composite Materials Processing and Properties," *J. de Phys. Colloque C1, sup. au no. 2, vol. 47*, C1-703-715 (1986).
3. A. J. Pyzik, A. A. Aksay and M. Sarikaya, "Microdesigning of Ceramic-Metal Composites," in *Ceramics Microstructures '86, Role of Interfaces*, pp 45-54, Ed. by J. A. Pask and A. G. Evans, Plenum Press, N.Y. (1987).
4. M. S. Newkirk, A. W. Urquhart, H. R. Zwicker, and E. Breval, "Formation of Lanxide Ceramic Materials," *J. Mater. Res.* 1 [1] 81-9 (1986).
5. D. Lam and F. F. Lange, to be published.
6. J. Jamet, D. Damange and J. Loubeau, "Nouveaux Matériaux Composites Alumine-Alumine à Rupture Fortement Dissipative et Leur Préparation," French Patent No. 2,526,785, Nov. 18, 1983.
7. F. F. Lange, B. V. Velamakanni, and A. G. Evans "A New Method for Processing Metal Reinforced Ceramic Composites," (to be published).
8. F. F. Lange and K. T. Miller, "Pressure Filtration: Kinetics and Mechanics," *Bul. Am. Ceram. Soc.* 66 [10], 1498-1504 (1987).
9. L. C. De Jonghe, M. N. Rahaman and C. H. Hsueh, "Transient Stresses in Bimodal Compacts During Sintering," *Acta Metall.* 34 [7] 1467-71 (1986).
10. R. K. Bordia and R. Raj, "Sintering of $\text{TiO}_2\text{-Al}_2\text{O}_3$ Composites-A Model Experimental Investigation," *J. Am. Ceram. Soc.* 71 [4] 302-10 (1988).
11. R. J. Brook, W. H. Tuan, and L. A. Xue, "Critical Issues and Future Directions in Sintering Science," *Ceram. Trans.*, V 1, Ceramic Powder Science, Ed. by G. L. Messing, E. R. Fuller, and H. Hausner, 811-21, Am. Ceram. Soc. (1988).
12. G. Y. Onoda and G. L. Messing, "Packing and Sintering Relations for Binary Powders," in *Processing of Crystalline Ceramics, Materials Science Research Vol 11*, ed by H. Palmour III, R. F. Davis and T. M. Hare, pp 99-112, Plenum Press, 1978.
13. C.-H. Hsueh, A. G. Evans, and R. M. McMeeking, "Influence of Multiple Heterogeneities on Sintering Rates," *J. Am Ceram. Soc.* 69 [4] C64-6 (1986).
14. R. Raj and R. K. Bordia, "Sintering Behavior of Bi-modal Powder Compacts," *Acta Met.* 32 [7] 1003-20 (1984).
15. G. W. Scherer, "Sintering with Rigid Inclusions," *J. Am. Ceram. Soc.*, 70 [10] 719-25 (1987).

16. F. F. Lange, "Densification of Powder Rings Constrained by Dense Cylindrical Cores," *Acta Met.* 37 [2] 697-704 (1989).
17. J. R. Porter and F. F. Lange, unpublished work.
18. F. F. Lange, "Constrained Network Model for Predicting Densification Behavior of Composite Powder," *J. Mater. Res.* 2 [1] 59-65, 1987.
19. O. Sudre, D. C. C. Lam, and F. F. Lange, "Densification Behavior of ZrO_2 Reinforced Al_2O_3 Composites," *This Proceedings*.
20. M. D. Sacks, H.-W. Lee, and O. E. Rojas, "Suspension Processing of Al_2O_3/SiC Whisker Composites," *J. Am. Ceram. Soc.* 71 [5], 370-9 (1988).
21. F. F. Lange, D. B. Marshall, and C. Folsom, "Fiber Reinforced Laminated Ceramic Composite," Patent under application.

ZERO-SHRINKAGE WHISKER FRACTION IN CERAMIC MATRIX-CERAMIC WHISKER COMPOSITES

ELIZABETH A. HOLM* AND M.J. CIMA**

Ceramics Processing Research Laboratory, Dept. of Materials Science and Engineering,
Massachusetts Institute of Technology, 77 Massachusetts Avenue, Building 12-002,
Cambridge, MA 02139

ABSTRACT

A Monte Carlo computer simulation that percolates soft-core, pseudographic whiskers in a discrete matrix has been developed, and two- and three-dimensional whisker percolation thresholds were determined for various whisker aspect ratios. The percolation thresholds were found to agree with the predictions of the excluded volume theory of percolation; moreover, the thresholds were found to coincide with the zero-shrinkage whisker fraction in ceramic matrix-ceramic particle composites.

INTRODUCTION

Ceramic matrix-ceramic whisker composites are known to possess attractive values of fracture toughness and hardness which are useful in a variety of structural applications. These properties have prompted projections that such composites will comprise 30% of the weight of commercial jet engines by the year 2010 [1]. Development of such components, however, hinges on the availability of reliable and economical manufacturing methods for fabricating high-density, low-porosity composites.

Addition of whiskers or any other nondensifying dispersed phase to ceramic powders causes a severe retardation in the composite densification kinetics. This behavior is apparent at low volume fractions of dispersed phase and becomes severe as the amount of dispersed phase increases. To date, only pressure-assisted sintering techniques such as hot pressing and hot isostatic pressing are useful in producing high density composites. The large expense and low throughput of pressure-assisted sintering constitute major limitations for the commercial development of all types of dense ceramic matrix composites. The situation can be somewhat alleviated by the use of matrix additives which promote transient liquid phases during firing: the presence of a liquid phase allows the matrix to densify under the constraint of the nondensifying dispersed phase. Unfortunately, these types of additives are usually deleterious to the high-temperature properties of the material and can bond the dispersed phase to the matrix, degrading the toughness of the material. Therefore, the purpose of this paper is to determine the conditions under which a ceramic matrix-ceramic whisker composite may sinter to full density without pressure assistance or a liquid phase.

The Constrained Sintering Problem

The sintering of powder compacts during firing has long been known to include several processes such as coarsening, densification, and grain growth [2]. The thermodynamic driving forces for these processes are the exchange of solid-vapor interfacial area with solid-solid interface and the elimination of grain boundary area. That mechanism which contributes to densification can be viewed as creating a hydrostatic compressive stress or sintering pressure which favors the elimination of porosity [e.g., 3]. Complications

*presently at University of Michigan, Dept. Mat. Sci. Eng., 2022 H.H. Dow Building, Ann Arbor, MI 48109

**Massachusetts Institute of Technology, Dept. Mat. Sci. Eng., Building 12-011, Cambridge, MA 02139

arise when the free shrinkage of the powder compact is restrained by contact with a non-shrinking, mechanically rigid phase. For instance, the shrinkage of the matrix around rigid, dispersed particles causes a hydrostatic tensile stress in the matrix. If the matrix cannot shear to relieve this stress, the tensile stress may overcome the compressive sintering pressure, and densification will slow or stop [3-7]. Many researchers have tried to quantify the effect of the dispersed phase on the densification rate by proposing constitutive models to account for the matrix's ability to relax the constraining stress [3, 8, 9].

None of the constitutive models for composite sintering consider the effect of physical contact between the dispersed particles. In a real composite, however, some of the nonsintering particles can be expected to be in contact. If these particles cannot slide past one another, shrinkage between a pair of particles must stop when the particles touch. At a sufficiently high concentration of dispersed phase the number of particle contacts becomes statistically significant and may form a network preventing densification of the entire composite.

Lange has proposed a model to explain constrained sintering in terms of such networks [10]. In this model, composite sintering is viewed not in terms of strain fields around individual nonsintering particles, but rather as interactive strain fields between pairs of these particles. In a pure powder matrix, the shrinkage strain, ϵ_m , is isotropic, so that

$$\epsilon_m = 1 - (\rho_0 / \rho_m)^{1/3} \quad (1)$$

where ρ_0 is the initial bulk density and ρ_m is the density after a certain amount of shrinkage. Thus, the linear shrinkage between any two points on an imaginary point network, Δl , is

$$\Delta l = l_n \epsilon_m \quad (2)$$

where l_n is the initial separation between the points.

If identical, spherical particles of radius r are placed on each network site, the initial separation distance between particles is

$$l_n = x + 2r \quad (3)$$

where x is the length of powder matrix separating the two particles. If the matrix strain, $\Delta x/x$, equals the unconstrained strain, ϵ_m , the interparticle shrinkage strain is given by

$$\epsilon_n = \frac{\Delta x}{l_n} = \frac{\epsilon_m x}{l_n} = \frac{\epsilon_m x}{x + 2r} \quad (4)$$

From Equation (4) it is clear that the microscopic strain between two particles, ϵ_n , increases as the interparticle separation, x , increases.

The composite as a whole will undergo some macroscopic shrinkage strain that is the average of all the microscopic interparticle strains. The microscopic shrinkage strain between widely spaced particles is greater than the macroscopic shrinkage strain; therefore, the bulk of the composite constrains sintering between widely spaced particles. Conversely, the bulk of the composite enhances sintering between closely spaced particles, which have a smaller-than-average interparticle strain.

In the limiting case when two particles touch ($x = 0$), the shrinkage strain is zero. So, when the particles form a continuous, nondeformable network, matrix densification should cease regardless of the matrix properties. The first continuous network of randomly dispersed particles is defined as the percolation threshold of particles [11].

Any shape or combination of shapes may percolate on a lattice or in a continuum [12]. For instance, percolation of whisker-like particles has been considered in many physical systems. Examples include composite conductors and superconductors [13-16] and

fluid flow in rocks containing long, thin cracks [17].

Although percolation thresholds may be measured experimentally, the random nature of whisker location and orientation makes percolation an excellent candidate for modeling by a Monte Carlo computer algorithm. Note, however, that Monte Carlo simulations provide no theoretical basis for results but simply mimic physical situations.

Simulations

Pike and Seager were the first to perform Monte Carlo simulations for the study of whisker percolation phenomena [15]. Their algorithm grew line segments in a continuum matrix until spanning was detected. Balberg and Binenbaum [16] used this approach to investigate systems with whisker length distributions and anisotropic whisker orientations. Robinson [17] used a slightly different approach where lines of specified lengths were randomly oriented on a unit square in real space.

In contrast to these continuum simulations, Boissonade et al. [18] simulated three-dimensional whisker percolation in a discrete matrix. An array of zeros (unoccupied sites) represented the matrix, and whiskers were randomly placed lines of integers (occupied sites) within the array. Their whiskers were randomly assigned one of three orthogonal orientations. Holm and Cima [19] extended this approach by permitting lines of nonzero integers in directions other than orthogonal directions of the matrix. In this algorithm, the origin of the whisker is selected at random. Then, a site "n" sites from the origin is chosen at random as the whisker endpoint. Each site along the straight line from the origin to the endpoint is assigned a nonzero integer. These lines of discrete sites are referred to as "bit-mapped" or "pseudographic" whiskers. Whiskers are placed in the matrix one at a time, and spanning is detected by the Hoshen-Kopelman cluster numbering algorithm [20, 21].

An important question is whether or not whiskers placed on the lattice should be permitted to interpenetrate. Actually, both situations contain nonphysical elements. Real whiskers occupy a volume, and thus two whiskers cannot occupy the same space. Alternatively, "hard-core" whiskers, placed randomly but constrained so that they never interpenetrate, have a vanishingly small chance of actually touching. However, we know that at some volume fraction, dispersed particles act as if they do touch, as evidenced by such properties as the electrical conductivity of composites composed of metallic particles in insulating media.

Balberg and Binenbaum [22] have investigated systems of conductive whiskers and have determined that the conductive whiskers behave as if they have very little hard-core nature. He concludes that electric field effects create a soft-core "shell" around hard particles. Similar field effects would be expected to apply to whiskers in a sintering matrix, where overlapping stress fields near whiskers might be expected to cause whiskers to appear to touch.

Additionally, as whisker aspect ratio increases, both hard-core and soft-core whiskers approach the limiting case of line segment percolation; therefore, at high whisker aspect ratios, the distinction between hard-core and soft-core whisker percolation is insignificant. Therefore, particularly for high aspect ratio whiskers, it is reasonable to model whiskers in a composite as soft-core particles.

Simulation Results

Two-dimensional whisker percolation thresholds have been reported previously [19]. Figure 1 shows the area fraction of whiskers at percolation as a function of whisker aspect ratio. It is clear that the critical volume fraction of whiskers decreases sharply as aspect ratio increases. In fact, the whisker content required for percolation is surprisingly low when $A_r > 10$ which suggests that whisker percolation effects may be very important early

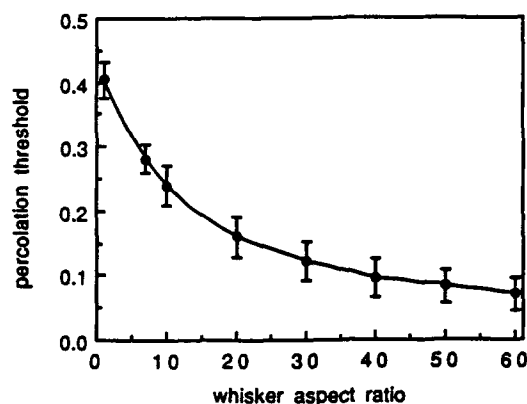


Figure 1. The effect of whisker aspect ratio on the percolation threshold for two-dimensional, randomly-oriented, soft-core whiskers. The data have been corrected for the effect of matrix size on the percolation threshold.

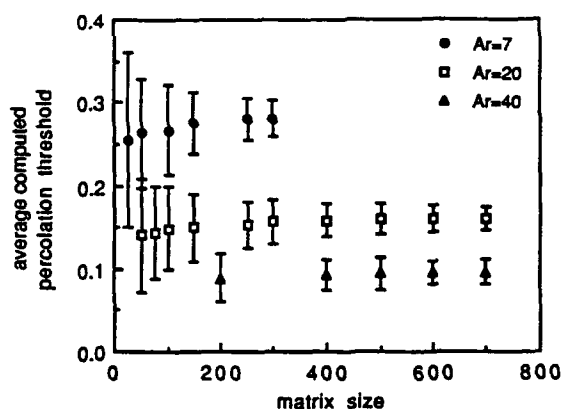


Figure 2. The average computed percolation threshold versus the percolating matrix size for various whisker aspect ratios. Even at small matrix sizes, the average computed threshold does not deviate from the true percolation threshold by more than the error of the computations themselves.

in the sintering process. These results suggest that within a distribution of whisker sizes it is the whiskers with larger aspect ratio that are most detrimental to the sintering process.

Because of the random nature of percolation, a statistical variance of the detected percolation threshold is expected. Thus, the data shown in Figure 1 are averaged over many individual simulations. Another possible source of error is the effect of matrix size. Shown in Figure 2 is the average computed percolation threshold and standard deviation as a function of matrix size. Note that for $A_r = 7$ to 40, although the percolation threshold systematically increases with matrix size, all measured thresholds are within the statistical error of the true (infinite matrix) percolation threshold. Holm [23] has further investigated the matrix size effect in accordance with percolation theory and finds that it is comprised

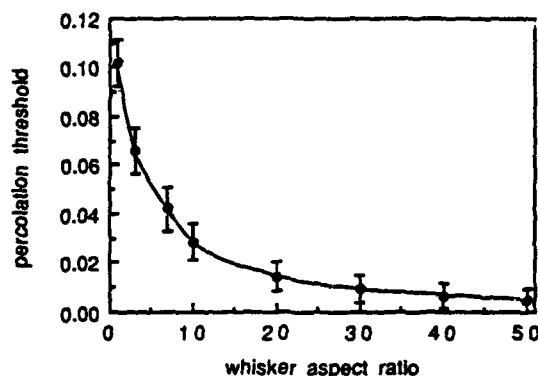


Figure 3. The effect of whisker aspect ratio on the percolation threshold for three-dimensional, randomly-oriented, soft-core whiskers.

of two independent effects: a finite cluster size effect and an effect of whisker truncation at the edge of the matrix.

Three dimensional percolation thresholds are shown in Figure 3. The behavior of the three-dimensional percolation threshold is qualitatively similar to that of the two-dimensional case. The P_c falls rapidly with increasing aspect ratio. An important difference between the two results is the *much lower volume fraction* of whiskers required for percolation in three dimensions. This result is in agreement with the rule that P_c decreases as dimensionality increases [11]. It is also notable that the P_c drops to <2% when the aspect ratio exceeds 10. This is a surprisingly low value and clearly suggests that whisker-whisker interactions play a very significant role in sintering of ceramic matrix-ceramic whisker composites.

Excluded Volume Theory

The excluded volume of a geometric object is defined as "the volume around an object into which the center of another similar object is not allowed to enter if overlapping of the two objects is to be avoided" [24]. Examples of excluded volumes are shown in Figure 4. Note that for anisotropic particles such as whiskers, the excluded volume depends on the relative orientation of the impinging whisker.

Balberg [24] speculated that the total excluded volume is the characteristic system invariant for percolation. The excluded volume (or area, in two dimensions) for a single object, V , is of the form $V(L, \theta)$ where L_i are size parameters and θ is the angle between the object under consideration and an impinging object. The average excluded volume per particle is given by the integral

$$\{V\} = \int_0^\pi VP(\theta) d\theta \quad (5)$$

where $P(\theta)$ is the probability of a given interparticle angle θ . The total excluded volume at percolation is related to the critical number of particles, N_c , by

$$\{V_{ex}\} = N_c\{V\} \quad (6)$$

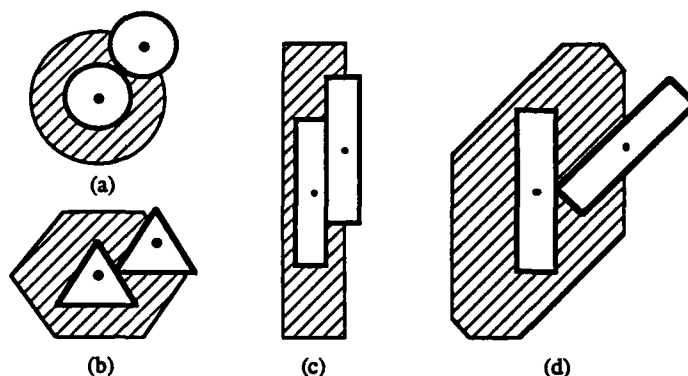


Figure 4. The excluded volumes of some common figures. Crosshatched areas are excluded volumes for (a) circles, (b) parallel triangles, (c) parallel rectangles, and (d) non-parallel rectangles.

Balberg concluded by Monte Carlo simulation that for soft-core objects, $\{V_m\}$ is not constant but is limited to a range of values that seems to vary smoothly with aspect ratio. In soft-core systems, particle overlapping implies that N_c is not directly proportional to P_c ; instead, $P_c = (N_c V_{wh} - V_{over}) / V_{tot}$ where V_{wh} is the volume of a particle, V_{tot} is the total volume of the matrix, and V_{over} is the volume of overlapping particles. Thus,

$$P_c = \frac{1}{V_{tot}} \left[\frac{\{V_{ex}\} V_{wh}}{\{V\}} - V_{over} \right] \quad (7)$$

Using expressions for the average excluded volume of two- and three-dimensional whiskers derived by Balberg [24], for high aspect ratio whiskers, one may derive the relationship

$$P_c = \frac{\{V_{ex}\}}{V_{tot}} [C_1 + C_2 A_r]^{-1} \quad (8)$$

where C_1 and C_2 are constants [23]. Thus, at high whisker aspect ratios, the percolation threshold should be inversely proportional to the whisker aspect ratio. Figure 5 shows this predicted relationship between the computed percolation thresholds and the whisker aspect ratio for both two- and three-dimensional whiskers.

Comparison with Other Simulations

It is instructive to compare the results of various three-dimensional whisker percolation simulations. Figure 6 shows percolation thresholds for the following systems: hard-core lines of spheres in a continuum matrix [25], hard-core lines of cubes oriented in the x, y, or z direction in a discrete matrix [18], soft-core capped cylinders in a continuum matrix [26], and soft-core lines of cubes in a discrete matrix.

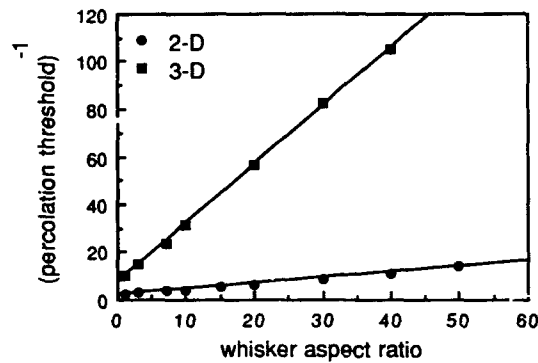


Figure 5. The inverse relationship between aspect ratio and percolation threshold for two- and three-dimensional, randomly-oriented, soft-core whiskers.

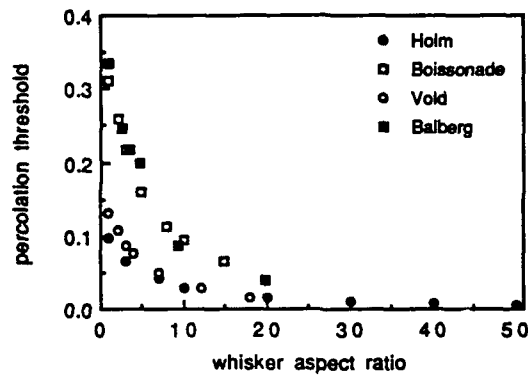


Figure 6. Computed percolation thresholds for three-dimensional whisker percolations in the literature. Vold = hard-core lines of spheres in a continuum matrix [25]. Boissonade = hard-core lines of cubes oriented in the x, y, or z direction in a discrete matrix [18]. Balberg = soft-core capped cylinders in a continuum matrix [26]. Holm = soft-core lines of cubes in a discrete matrix.

At low whisker aspect ratios, three-dimensional whisker percolation thresholds are strongly dependent upon the limiting thresholds for a whisker aspect ratio of one. (For instance, the percolation threshold of soft-core, capped cylinders in a continuum must approach the percolation threshold of soft-core spheres.) Physically, this implies that one must examine each model to determine the initial condition most applicable to the experimental system. However, at high whisker aspect ratios, all four models approach the limiting case of line segments in a continuum; thus for $A_r > 20$, the whisker attributes (hard- or soft-core, discrete or continuous) become insignificant in determining the percolation threshold.

Percolation and the Sintering of Composites

The largest fraction of experimental data to compare with the simulation results is for ceramic matrix-ceramic whisker composites that approximate two-dimensional whisker percolation. Strong planar whisker orientation is commonly observed for forming methods that involve some type of uniaxial stress. Ishii prepared such a composite by colloidally pressing a dispersion of matrix particles and whiskers [27]. He observed strong whisker orientation both microstructurally and through the anisotropic shrinkage behavior of the compacts. Whiskers were observed to preferentially align perpendicular to the direction of the applied load. Shrinkage during firing varied greatly in the axial and radial directions of the compacts, with the largest shrinkage always being perpendicular to the orientation of the whiskers.

The whisker aspect ratio used in the study was approximately 7 [27] which, according to the simulation results, should have a percolation threshold of 27% for a two-dimensional system. Figure 7 shows a plot of sintered density versus sintered volume fraction of whiskers for a colloidally pressed alumina matrix-silicon carbide whisker composite. There is a sharp decline in final density at a whisker loading of 30 vol%, which is very close to the predicted percolation threshold.

Tiegs and Becher [28] have also prepared uniaxially pressed SiC whisker- Al_2O_3 matrix composites. They followed dry pressing by cold isostatic pressing but still observed highly anisotropic shrinkage. Again shrinkage was greatest in the axial direction. Ceramographic examination of the compacts confirmed the two-dimensional nature of the whisker orientation. Additional observations are reported by Meek et al. [29] who also prepared uniaxially pressed SiC whisker-alumina composites.

The sintering data for the latter two studies is shown in Figure 8. Tiegs and Becher used whiskers with aspect ratios of approximately 40 and 25, while Meek used whiskers with aspect ratio assumed to be about 40, a typical value for ARCO SiC whiskers which were used in all three studies [27, 28]. The two density curves for whiskers of aspect ratio 40 [28, 29] show a sharp decline in sintered density at about 10 vol% whiskers, very close to the two-dimensional percolation threshold of 9.6 vol%. That curve for $A_r \sim 25$ shows the decline at about 15 vol%, which is again close to the percolation threshold of 13 vol%.

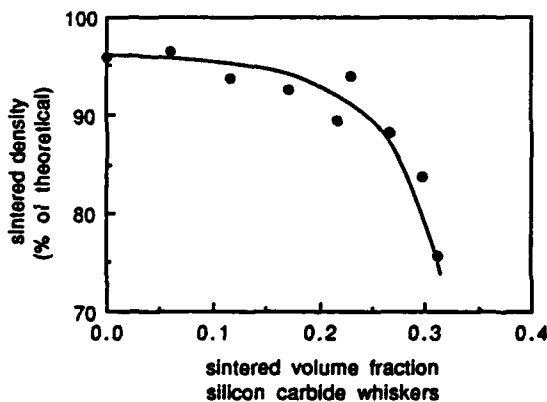


Figure 7. The effect of whisker loading on the final density of a colloid-pressed alumina matrix-silicon carbide whisker composite exhibiting two-dimensional orientation of whiskers. The whisker aspect ratio is about 7 [27].

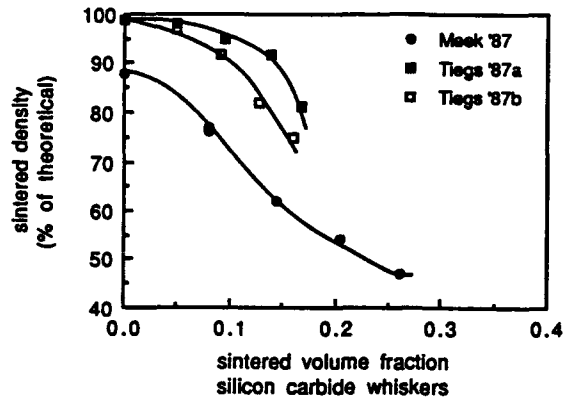


Figure 8. Composite densities for pressureless-sintered ceramic matrix-ceramic whisker composites. The composites are characterized as follows: Meek '87 = Al_2O_3 matrix with SiC whiskers ($A_v \sim 40$) [29]. Tiegs '87a = Al_2O_3 matrix with SiC whiskers ($A_v \sim 25$) [28]. Tiegs '87b = Al_2O_3 matrix with SiC whiskers ($A_v \sim 40$) [28].

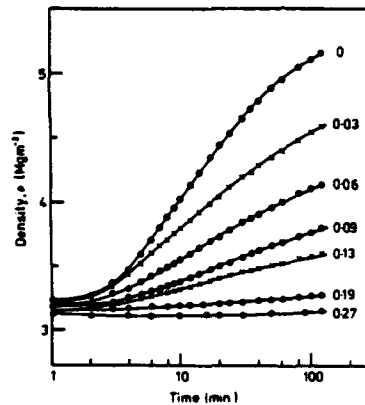


Figure 9. Density as a function of time for an isotropic ZnO matrix-SiC particle composite containing different volume fractions of equiaxed SiC particles [3].

Data for truly three-dimensional whisker percolation during sintering is much more difficult to obtain because of the great tendency for whisker alignment during forming. This difficulty is removed in the case of equiaxed particles. DeJonghe et al. [3] have prepared composites of SiC particles in a ZnO matrix and studied their densification kinetics. Their results are shown in Figure 9 and were used to show the dramatic influence of second-phase inclusions on the sintering kinetics. It is clear from the data that densification ceases between 13 and 16 vol%. For hard-core spherical particles in a random lattice, the percolation threshold is about 16 vol% [11]. This comparison must be made with some caution, however, because of the sensitivity of the P_c to assumptions about the particle interactions.

SUMMARY

The zero-shrinkage whisker fraction of a ceramic matrix-ceramic whisker composite has been modeled as the percolation threshold of whiskers. A Monte Carlo computer simulation that percolates soft-core, pseudographic whiskers in a discrete matrix has been developed, and two- and three-dimensional whisker percolation thresholds were determined for various whisker aspect ratios. The percolation thresholds were found to depend on whisker aspect ratio with the functionality predicted by excluded volume theory.

The computer percolation thresholds depend strongly upon assumptions about the system attributes for low aspect ratio whiskers. However, for high whisker aspect ratios, any whisker percolation model may be used to determine the percolation threshold.

For differently processed Al_2O_3 matrix-SiC whisker composites with whiskers oriented in two-dimensional planes, experimental sintering data show a sharp decrease in sintered density at the computed percolation threshold of whiskers. In addition, three-dimensional ZnO matrix-SiC particle composites containing equiaxed SiC particles stop sintering at the percolation threshold of hard-core spheres.

ACKNOWLEDGMENTS

This research was sponsored by the MIT-Industry Ceramics Processing Research Consortium. EAH would like to acknowledge the support of the National Science Foundation during her stay at MIT.

REFERENCES

1. AM&P, "Forecast '89: Slow Growth for Ceramics," *Adv. Mater. Proc.*, **135** (1), 29-44 (1989).
2. W.D. Kingery, H.K. Bowen, and D.R. Uhlmann, *Introduction to Ceramics*, 2nd ed. (John Wiley and Sons Publishers, New York, 1976), pp. 469-490.
3. L.C. DeJonghe, M.N. Rahaman, and C.H. Hsueh, "Transient Stresses in Bimodal Compacts During Sintering," *Acta metall.*, **34** (7), 1467-1471 (1986).
4. F.F. Lange, "Processing-Related Fracture Origins," Parts I, II, and III, *J. Am. Ceram. Soc.*, **66**, (6), 396-408 (1983).
5. M.W. Weiser, "The Effect of Inclusion Size on Sintering," proposal for PhD qualifying examination, University of California at Berkeley, 1986.
6. C.P. Ostertag, "Technique for Measuring Stresses Which Occur During Sintering of a Fiber-Reinforced Ceramic Composite," *J. Am. Ceram. Soc.*, **70** (12), C355-C357 (1987).
7. M.N. Rahaman and L.C. DeJonghe, "Effect of Rigid Inclusions on the Sintering of Glass Powder Compacts," *J. Am. Ceram. Soc.*, **70** (12), C348-C351 (1987).
8. R.K. Bordia and R. Raj, "Analysis of Sintering of a Composite with a Glass or Ceramic Matrix," *J. Am. Ceram. Soc.*, **69** (3), C55-C57 (1986).
9. C.H. Hsueh, A.G. Evans, R.M. Cannon, and R.J. Brook, "Viscoelastic Stresses and Sintering Damage in Heterogeneous Powder Compacts," *Acta metall.*, **34** (5), 927-936 (1986).

10. F.F. Lange, "Constrained Network Model for Predicting Densification Behavior of Composite Powders," *J. Mater. Res.*, **2** (1), 59-65 (1987).
11. R. Zallen, The Physics of Amorphous Solids (John Wiley and Sons Publishers, New York, 1983), pp. 135-204.
12. I. Balberg, "'Universal' Percolation Threshold Limits in the Continuum," *Phys. Rev. B*, **31** (6), 4053-4055 (1985).
13. F. Carmona, F. Barreau, P. Delhaes and R. Canet, "An Experimental Model for Studying the Effect of Anisotropy on Percolative Conduction," *J. Physique - Lettres*, **41** (11), L531-L534 (1980).
14. F. Carmona, P. Delhaes, F. Barreau, D. Ordiera, R. Canet, and L. Lafeychine, "Phénomène de Percolation dans des Matériaux Composites Modèles," *Rev. de Chim. Min.*, **18**, 498-508 (1981).
15. G.E. Pike and C.H. Seager, "Percolation and Conductivity: A Computer Study I," *Phys. Rev. B*, **10** (4), 1421-1434 (1974).
16. I. Balberg and N. Binenbaum, "Computer Study of the Percolation Threshold in a Two-Dimensional Anisotropic System of Conducting Sticks," *Phys. Rev. B*, **28** (7), 3799-3812 (1983).
17. P.C. Robinson, "Connectivity of Fracture Systems--A Percolation Theory Approach," *J. Phys. A*, **16**, 605-614 (1983).
18. J. Boissonade, F. Barreau, and F. Carmona, "The Percolation of Fibres with Random Orientation: A Monte Carlo Study," *J. Phys. A*, **16**, 2777-2787 (1983).
19. E.A. Holm, M.J. Cima, "Two-Dimensional Whisker Percolation in Ceramic Matrix-Ceramic Whisker Composites," *J. Am. Ceram. Soc.*, **72** (2), 303-305 (1989).
20. D. Stauffer, Introduction to Percolation Theory (Taylor and Francis Publishers, Philadelphia, PA, 1985), pp. 1-121.
21. J. Hoshen and R. Kopelman, "Percolation and Cluster Distribution. I. Cluster Multiple Labeling Technique and Critical Concentration Algorithm," *Phys. Rev. B*, **14** (8), 3438-3445 (1976).
22. I. Balberg and N. Binenbaum, "Scher and Zallen Criterion: Applicability to Composite Systems," *Phys. Rev. B*, **35** (16), 8749-8752 (1987).
23. E.A. Holm, "A Percolation Model for the Zero-Shrinkage Whisker Fraction in Ceramic Matrix-Ceramic Whisker Composites," Masters Thesis, Dept. Mat. Sci. Eng., Massachusetts Institute of Technology, 1989.
24. I. Balberg, C.H. Anderson, S. Alexander, and N. Wagner, "Excluded Volume and Its Relation to the Onset of Percolation," *Phys. Rev. B*, **30**, 3933-3943 (1984).
25. M.J. Vold, "Sediment Volume and Structure in Dispersions of Anisometric Particles," *J. Phys. Chem.*, **63**, 1608-1612 (1959).
26. I. Balberg, N. Binenbaum, and N. Wagner, "Percolation Thresholds in the Three-

Dimensional Sticks System," *Phys. Rev. Lett.*, 52 (17), 1465-1468 (1984).

27. T. Ishii, "Al₂O₃-SiC Whisker Composites," *Ceramics Processing Research Laboratory Report #R14*, MIT, pp. 127-134 (1988), and personal communications.
28. T.N. Tiegs and P.F. Becher, "Sintered Al₂O₃-SiC-Whisker Composites," *Cer. Bull.*, 66, (2), 339-342 (1987).
29. T.T. Meek, R.D. Blake, and J.J. Petrovic, "Microwave Sintering of Al₂O₃-SiC Whisker Composites," *Ceram. Eng. Sci. Proc.*, 8 (7-8), 861-871 (1987).

PACKING AND STRUCTURE IN SYSTEMS CONTAINING ROD-LIKE PARTICLES

LARRY A. CHICK*, CHRISTOPHER VINEY**, AND ILHAN A. AKSAY**

*Battelle, Pacific Northwest Laboratories (K2-44), Richland, WA 99352

**Department of Materials Science and Engineering (FB-10), and the Advanced Materials Technology Program, University of Washington, Seattle, WA 98195

ABSTRACT

A non-discrete Monte Carlo algorithm is used to model the packing of static rods. The results establish that inter-rod contact results solely from rod motion, not from space-filling effects. As the concentration of static rods is increased, clusters of aligned rods form and grow. The effects of rod motion are inferred through thermodynamic analysis. At sufficiently high rod concentrations, rod motion is expected to cause structural coarsening wherein the rods rearrange into larger but fewer clusters. These results should be considered when modeling the structure and mechanical behavior of whisker- and chopped-fiber-reinforced composites.

INTRODUCTION

This paper discusses theory and numerical experiments that address two important engineering questions relevant to the packing of rod-shaped particles in whisker- or chopped-fiber-reinforced ceramic composites:

- 1) How are the rods arranged spatially within the composite?
- 2) What is the maximum concentration of rods which can be incorporated into the system?

The model systems described herein are highly idealized and the answers provided are by no means complete. Nevertheless, it is hoped that this paper will at least provide some firmly-based partial answers and allow other investigators to see the remaining questions from a fresh viewpoint.

NUMERICAL ROD-PACKING EXPERIMENTS

We began our investigations by constructing an algorithm to place rods, one at a time, into a two-dimensional matrix. Using this program, we can study the effects of axial ratio and rod concentration on the structural arrangements. We chose to begin with two dimensions mainly because it is simpler to observe the arrangement of rods in a monolayer than in the bulk of a three-dimensional system. Trends observed in two dimensions are expected to reflect trends in three dimensions. We worked with monodisperse systems, i.e., all of the rods in a given experiment have the same length and diameter.

Many numerical studies of rod packing have used a discrete lattice in which the rods are represented as contiguous series of occupied square (two-dimensional) or cubic (three-dimensional) cells [1-5]. Although such lattice models greatly simplify the mathematics, the approach suffers from limited positional and orientational choices for the rods; it also distorts their shape. We have used a non-discrete model so that the position and orientation of the rods are continuously variable and the rods do maintain their true shape. This model also uses the "hard-core" assumption wherein the rods cannot interpenetrate. This leads to far more realistic representations of the structural arrangements than do "soft-core" models which allow rods to cross through one another.

The algorithm for placing the rods is shown in Figure 1. A random number generator chooses the angular orientation of the j^{th} rod. Next, candidate X and Y positional coordinates are chosen randomly. The candidate position is checked to see if it results in interpenetration with existing rods. If interpenetration is detected, a new candidate position is chosen while the original orientation is maintained. The process is continued until an appropriate vacancy for placing the rod is found. The j^{th} rod is then placed in the matrix and the process continues with the choice of an orientation for the $(j+1)^{\text{th}}$ rod. The rods are static; once a rod is placed, it is not allowed to move. If rods are placed such that they overlap the boundary of the square lattice, they "wrap around" and penetrate its opposite edge. The program keeps track of the number of tries it takes to place a rod successfully. The significance of this feature is discussed elsewhere [6,7].

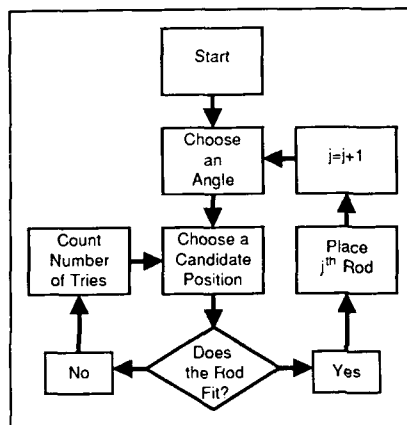


Figure 1. Monte Carlo algorithm for placing rods.

RESULTS AND DISCUSSION OF NUMERICAL ROD PACKING EXPERIMENTS

Figure 2 shows a series of rod configurations with increasing concentration, which were built up during one run of the algorithm described above. Although some rods appear to touch in the figure, these instances are entirely the result of plotter limitations. Since double precision numbers are used to describe the boundaries of each rod, the chance of any of the rods touching without interpenetrating is vanishingly small.

We digress here to discuss some implications of this observation. If our system were set up to simulate rod movement such as random vibration, streaming, stirring, or matrix contraction (due to filtration consolidation, settling or sintering), we would observe many cases where rods touch. Since any real physical experiment involves some degree of rod movement, *all* physical systems exhibit rod connectivity which increases with concentration. Such particle connectivity is commonly modelled by numerical percolation studies, using Monte Carlo algorithms based on discrete square or cubic lattices, as mentioned above. In these discrete models, there is a finite probability of adjacent rods touching without interpenetrating, even when no rod motion is allowed. Therefore, the degree of connectivity in a discrete lattice is, to some extent, an artifact of the choice to use a discrete lattice. By way of example, consider the pair of rods in a discrete, square lattice depicted in Figure 3a. If a rod placement algorithm similar to that described above is used, there is a finite probability of successfully placing a third rod that touches both of the existing rods. Such placement

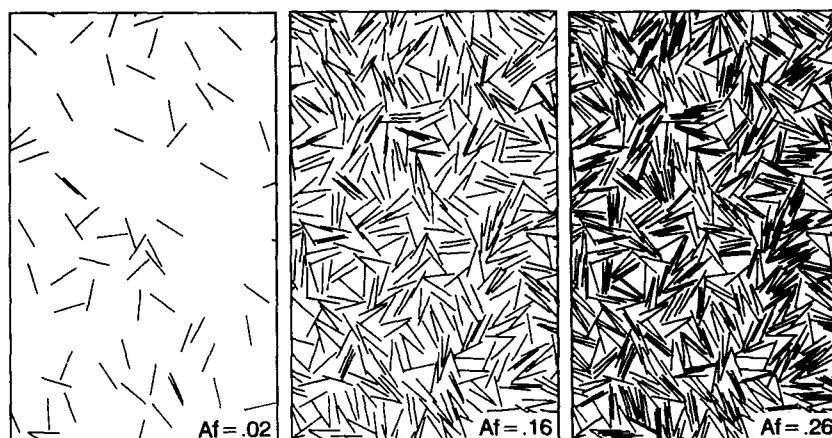


Figure 2. Three stages during the filling of the non-discrete lattice using the algorithm shown in Figure 1. Axial ratio is 25. Area fraction (Af) covered by rods ranges from 0.02 to 0.26.

would result in connectivity or percolation across the group. However, if the existing rods had been placed in a *non-discrete* lattice, as shown in Figure 3b, the probability of similarly placing a third rod in contact would be vanishingly small. The issue that emerges is that *space-filling constraints alone do not result in percolation in realistic hard-core models*. Percolation in a real system is the result of particle motion. Percolation in a discrete lattice model is an artifact of the model.

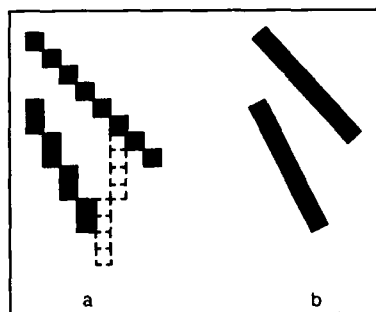


Figure 3. Rods with an axial ratio of 8 represented in a) a discrete lattice, and b) a non-discrete lattice. In the discrete lattice, there is a finite probability that a third rod can be placed so that it touches both existing rods (example shown in broken lines). The chance of this happening in the non-discrete lattice is vanishingly low.

While we have not yet incorporated rod motion into our computer model, we can illustrate the point made above with a simple physical experiment. Wooden sticks were scattered at random onto a level substrate and gently vibrated until all lay flat on the surface. The rods that were originally stacked on top of others tended to "push" their way onto the surface, causing lateral displacement of rods that were already laying flat. Figure 4a is a picture of these wooden sticks (axial ratio of 25) after vibration. Many instances of rods touching can be seen and there are several instances of rods laying close together and parallel. The resulting configuration is close to, if not at, the percolation threshold. Figure 4b was generated by the non-discrete Monte Carlo algorithm for rods with the same axial ratio and

at the same concentration (area fraction of 0.263). Although some of the lines appear to touch, we stress again that these instances are due to plotter limitations; none of the computer-generated rods are mathematically connected. The configuration of the wooden sticks can be viewed as a slightly "annealed" version of the computer-generated structure, with limited movement of the sticks resulting in extensive connectivity. A static, discrete-lattice percolation model might yet predict the degree of connectivity in these sticks. However, agreement would be merely fortuitous.

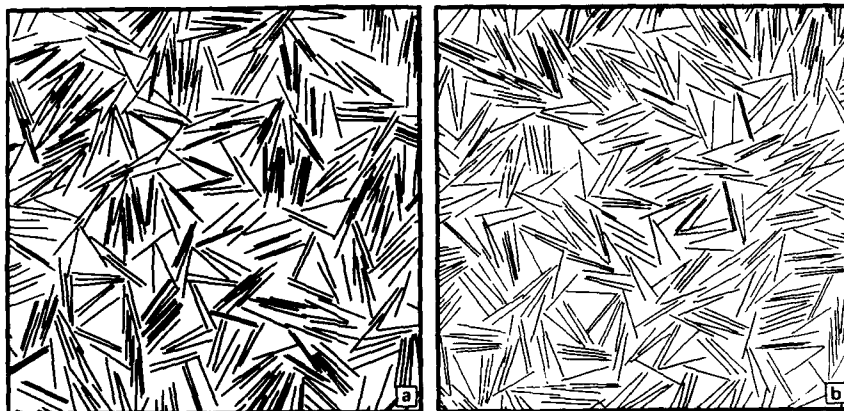


Figure 4. a) Photo of wooden sticks with an axial ratio of 25 at an area fraction of 0.26. Sticks were vibrated until they lay flat on a substrate. Extensive rod connectivity is evident. b) Plot of non-discrete Monte Carlo-generated rod configuration for rods of the same axial ratio and concentration as the sticks. None of the rods actually touch, although plotter limitations result in instances of apparent connectivity.

In addition to the problem of artificially introducing connectivity, models of rods based on discrete lattices lead to another noteworthy difficulty. Rods represented by series of occupied cells can cross through one another without their occupied cells overlapping (i.e., without interpenetrating), as shown in Figure 5. If not specifically prevented within the software, this problem will lead to the construction of physically untenable structures, even when the investigator believes that he or she has implemented the "hard-core" restriction by disallowing overlapping of occupied cells.

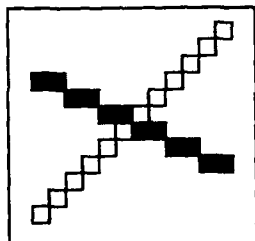


Figure 5. Example of how rods in a discrete lattice can cross without any of their occupied cells overlapping.

Returning to Figure 2 and our discussion of the non-discrete model results, we note that *clusters* of similarly aligned rods are evident. As rods are added to the lattice, both the number of clusters and the average number of rods per cluster increase. We have attempted to characterize the growth of these clusters by setting up rules to determine cluster membership. We say that rod A is clustered to rod B if the following three conditions are met:

- 1) the angle between them is less than 15° ;
- 2) the distance between their midpoints is less than one half of a rod length; and
- 3) the distance from the midpoint of either rod to the long axis of the other, measured along a direction at 90° to the long axis of the first rod, is less than one fifth of a rod length.

(These conditions are stated exactly for infinitely thin rods; the rules are actually somewhat more complicated for rods with finite axial ratios.) To propagate the clustering relationship, we say: if A is clustered to B and B is clustered to C, then A is also clustered to C as long as the angle between A and C is less than 15° . The rules are somewhat arbitrary at this point, but result in automatic choice of clusters which at least appear reasonable to the eye. The main point here is that the rules can be applied to obtain an objective *relative* measure of the degree of clustering in various rod configurations. Figure 6 shows the results of cluster membership measurements on the non-discrete Monte Carlo configurations. It is evident that, as the rod concentration increases, the cluster size of the average rod increases smoothly and ever more steeply. Furthermore, at a given rod concentration, cluster size is larger for the longer axial ratios. What causes the formation and growth of clusters in the absence of rod motion? The few small clusters appearing at low concentration are due to chance placement. The clusters that appear at high concentrations arise due to space-filling constraints. Simply put: the majority of the available vacant positions for new rods are next to, and aligned with respect to, existing rods; therefore, the most probable way to squeeze in more rods is by adding to the clusters.

Thus we have a tool to observe rod structures under very idealized conditions, with no rod motion. As stated above, these conditions will never be observed in a physical experiment. However, the results clearly demonstrate the structural effects of space-filling constraints and thereby provide a starting or limiting condition for observing the effects of rod motion. We have already seen in Figure 4 that limited rod motion can cause

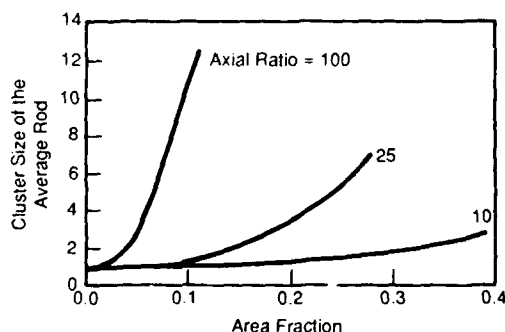


Figure 6. Data illustrating the growth of rod clusters as the rod concentration is increased in the static, non-discrete, Monte Carlo-generated configurations.

extensive rod contact. The effects of motion induced by processing operations have been studied both theoretically and empirically, using physical experiments. For example, the alignment of chopped fibers as a result of shear during extrusion or injection molding has been discussed by several investigators [8-10]. Also, the preferential orientation of fibers perpendicular to the axis of compaction has been noted in composites that were consolidated by colloidal filtration, settling or uniaxial pressing [11,12]. Other investigators [13] and our studies show that short fibers can be made to form into tightly aligned rows by the influence of sonic or ultrasonic vibration (see Figure 7). These examples all address the results of specialized, highly directed motion. Though they are extremely important technologically, they are not easily described by a single, general theory. Each case must be handled by using a model of rod motion tailored to the specific processing operation. For example, a good way to model uniaxial consolidation might be to begin with a configuration formed by non-discrete Monte Carlo space-filling and then mathematically compact the system along the axis. It would be necessary to select rules to decide when a rod becomes fixed (e.g., rod translates until it touches another rod in one spot, then rotates until it touches in a second spot, whereupon it is fixed). The results of such models might be useful, but their accuracy in modeling physical behavior will always depend upon the investigator's skill in selecting amongst all possible assumptions regarding the positions at which rods become fixed. On the other hand, certain aspects of the structural effects of *completely random rod motion* are understandable in terms of thermodynamics. The thermodynamic approach, which we have adapted from theory that was developed for molecular rods, involves only two, clearly defined assumptions: that the motion of the rods is random (thermal agitation) and that there are no attractive or repulsive forces affecting the rods. For macroscopic rods (sticks) or microscopic rods (chopped fibers or whiskers), the assumption of completely random motion within a composite certainly represents a considerable simplification of reality. Nevertheless, the results of the model have been found to explain some physical phenomena which are observed in systems containing rods.

THERMODYNAMIC ANALYSIS OF RODS

Additional details of our thermodynamic approach are described elsewhere [6,7]. In this paper, we will confine discussion to the main concepts involved in the calculations, and move on to present the results.

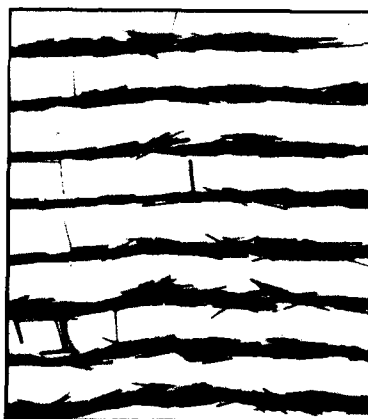


Figure 7. Optical micrograph of chopped graphite fibers ($10\text{ }\mu\text{m}$ diameter; $300\text{ }\mu\text{m}$ long) which were aligned into rows by the application of sonic vibration.

Under certain conditions, it is reasonable to expect that the behavior of large rods will be exactly like that of rigid, rod-like molecules. These conditions, as mentioned above, include the assumption that the rods move randomly, as do thermally excited molecules. Brownian motion of microscopic rods suspended in low-viscosity fluids is analogous to molecular agitation. The other assumption, that there are no attractive nor repulsive forces affecting the rods, is less restrictive than it may at first seem. Attractive forces between the fibers or whiskers and between the rods and the matrix particles in a ceramic composite are normally avoided during processing by implementation of slight electrostatic and/or steric repulsion. This is just good processing practice. It turns out that the effects of slight repulsive forces on the thermodynamic results are minor [14,15]. Therefore, the assumption that no forces affect the rods will not itself lead to unreasonable predictions. On the other hand, the effect of gravity (or centrifugal force), resulting in uniaxial compaction of large-particle systems, is analogous to directed attraction between the rods and, as such, is not implemented at present in our thermodynamic approach. To clarify these assumptions, it is useful to point out that a *stable* suspension of microscopic whiskers undergoing Brownian motion should be thermodynamically analogous to an *athermal* (no forces) system of rigid molecular rods. Under these athermal conditions, the behavior of the rods is determined solely by their *shape* (and concentration), and so their size should not affect the results. Randomly excited fir logs confined to a large vessel floating in space should behave like an athermal solution of molecular rods with the same axial ratio.

Our thermodynamic approach is directed by the well-accepted, athermal, three-dimensional model of Flory and Ronca [16]. We adapted their approach to a two-dimensional system and, whereas they used a discrete lattice model, we used our non-discrete model [6,7]. In thermodynamic terms, the athermal assumption means that the free energy of the system of rods is determined solely by *entropy*. Due to their asymmetric shape, the rods have a total entropy that is composed of two terms, one for *translational* (positional) entropy and one for *orientational* entropy. This treatment results in the phase diagram shown in Figure 8. To interpret the phase diagram, consider a system of rods with an axial ratio of 25. At low concentrations, the rods are randomly oriented. Minimum free energy is established by maximization of

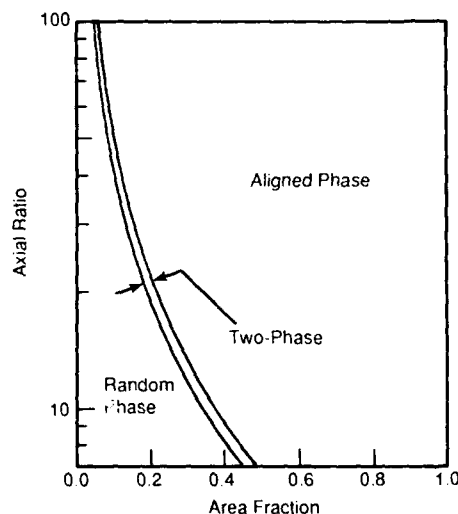


Figure 8. Phase diagram for rods based on the non-discrete Monte Carlo studies [6,7].

both positional and orientational entropy. As rods are added to the system, we reach a critical concentration, the lower phase boundary (0.16), at which an aligned phase appears. At a somewhat higher concentration, the upper phase boundary (0.18), the random phase disappears and all the rods belong to the aligned phase. It is the trade-off between positional and orientational entropy which results in the formation of the aligned phase at high rod concentrations. At high concentrations, the positional freedom of the rods is restricted. If the rods align, sacrificing orientational freedom, more than enough positional entropy is gained back to make up for the lost orientational entropy. It is simply easier to fit more rods into the system when they are aligned. As with any phase transformation governed by thermodynamics, the appearance of the aligned phase above the critical concentration will be spontaneous given that the rods experience sufficient agitation. Figure 9 is a plot showing rods in an aligned phase. Notice that the rods are not perfectly aligned, but are characterized by an average angle of disorientation from the preferred domain axis. Thus, the rods retain a small degree of orientational freedom, even in the aligned phase. As the concentration of rods is increased within the aligned phase field (above 0.18 for an axial ratio of 25), the average angle of disorientation from the preferred domain axis decreases.

This thermodynamic analysis predicts how much of each phase will be present for a given concentration of rods at equilibrium. However, it does not give us a complete picture of the structure. For example, for a system containing only aligned phase, the analysis does not predict the expected average size of the domains. This is because the analysis does not take into account the extra entropy which could be gained by having narrow regions of disorder at the domain boundaries, i.e., what one could call "grain-boundary entropy". When both the aligned and the random phase are present at equilibrium (within the narrow, two-phase region on the phase diagram), the analysis again tells us nothing about domain sizes for either phase. In spite of these limitations, however, the predictions based on the phase diagram are illuminating, as we shall see in the next section.

IMPLICATIONS OF THE PHASE DIAGRAM FOR COMPOSITE ENGINEERING

The phase diagram predicts that, given sufficient random agitation, rods above the critical concentration at the lower phase boundary will rearrange, forming an aligned phase. Such spontaneous phase transitions are well documented in liquid crystalline systems [17-19]. In such systems of molecular rods, thermal agitation of the molecules is sufficient to bring about their rearrangement. Spontaneous formation of aligned clusters has

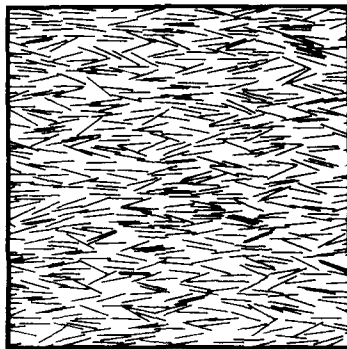


Figure 9. Example of an aligned phase generated by the non-discrete Monte Carlo algorithm [6,7]. Axial ratio is 25, area fraction is 0.19.

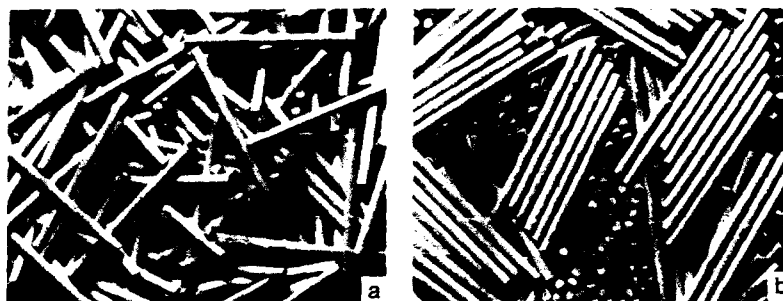


Figure 10. a) Wooden sticks with an axial ratio of 25 were dumped randomly into a beaker. b) During mechanical vibration of the beaker, the rods formed into tightly aligned clusters.

also been observed in suspensions of microscopic rods such as tobacco mosaic virus [20] and colloidal gold particles [21]. In these systems, Brownian motion is sufficient to cause rod rearrangement. Can we expect to observe spontaneous clustering during the processing of slurries for composite systems? Here, the rods are often too large and the intervening matrix particles provide too much kinetic hindrance for Brownian motion to be effective. The motion induced by common processing operations such as high-shear mixing, milling and sonication cannot be characterized as truly random. Yet, our experiments with vibration of macroscopic rods demonstrate spontaneous clustering. Figure 10a is a picture of wooden sticks dumped randomly into a beaker. The view is through the bottom of the beaker. Mechanical vibration (60 Hz) was applied to the bottom of the beaker for several minutes. During this process, the distinct, tightly-aligned clusters seen in Figure 10b were formed and the bulk density of the compact increased. Although the kinetic hindrance of matrix particles was not present, and although the role of gravitational compression was undoubtedly important, this experiment demonstrates that very large rods can spontaneously rearrange and cluster due to the type of motion commonly imposed during composite processing operations.

We have already seen that, as the rod concentration is increased, space-filling constraints result in the formation of clusters, even in the absence of rod motion (Figure 6). We believe that, for rod configurations at fixed concentration above the lower phase boundary, the introduction of motion will cause the "space-filling-nucleated" clusters to grow. That is, motion will cause structural coarsening wherein the rods rearrange into larger but fewer clusters. The Monte Carlo-generated rod configurations, used for the measurements of cluster size in Figure 6, contained randomly oriented rods. The phase diagram predicts that, above the critical concentration at the lower phase boundary, these randomly oriented configurations will be unstable with respect to the aligned phase. Careful comparison of Figure 6 with the phase diagram, Figure 8, shows that, above a cluster-membership number of about two, the random configurations described in Figure 6 should be unstable. Therefore, we believe that the lines in Figure 6 represent *minimum cluster size* for the given concentration; the clusters are expected to grow if the rods are set in motion. Figure 11 illustrates the starting and endpoint structures for a phase transition which begins with an unstable random configuration and ends with a stable aligned phase containing the same concentration of rods. Free energy curves are shown for each of these configurations. As discussed above, we would expect that the inclusion of a grain-boundary entropy term would actually predict that the minimum free

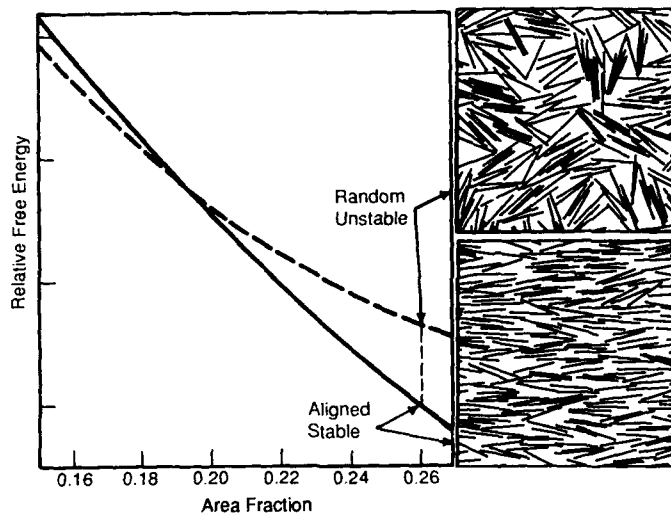


Figure 11. Monte Carlo-generated representations of an unstable random phase (above) and the stable aligned phase predicted for the rod area fraction of 0.26. Free energy curves for the two phases are shown as a function of rod concentration. The random phase has lower free energy at area fractions to the left of the point where the two curves intersect.

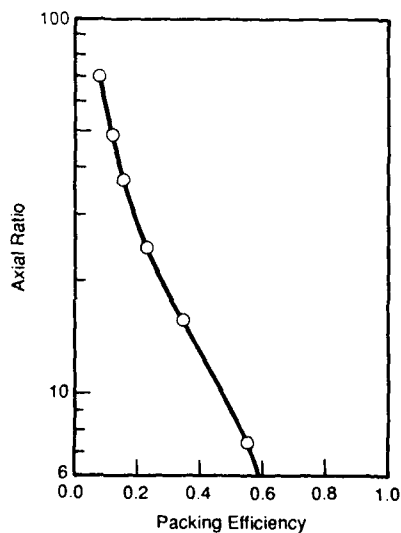


Figure 12. Proposed "maximum packing fraction" data from Milewski's three-dimensional experiments with wooden sticks and glass rods [22].

energy would be reached before the structure had coalesced into a single, large domain.

To summarize our answer to the first question at the beginning of this paper: the thermodynamic analysis, combined with the space-filling observations, set limits on the structures possible at any given rod concentration. The degree of domain coarsening experienced in a real composite will obviously depend upon such factors as the effective viscosity imposed by the matrix (particles, solvents, surfactants) and the type, magnitude and duration of motion imposed during processing.

The possible effects of rod clustering at high concentration have not been taken into account by mechanical modelers. Mechanical models for chopped fiber- or whisker-reinforced composites generally assume a scenario in which the rods are independently as well as randomly oriented. Rods within clusters should not always be considered as independent mechanical entities. For example, a crack could easily propagate along the preferred domain axis of a cluster. Further propagation would be hindered by advance of the crack into a cluster with a different orientation. Therefore, for a given stress, the unanticipated presence of extended clusters may allow some cracks to propagate further than expected. Also, during the consolidation or sintering of a system containing clusters, the parallel rods within a cluster could be easily forced together in directions perpendicular to the domain axis.

Perhaps, by now, the answer to the second question at the beginning of this paper is obvious to the reader: the concentration of rods which can be introduced into a composite is limited by kinetics. There are no absolute "maximum packing fractions", as set forth by Milewski [22]. These limits are artifacts of the degree of rod motion introduced in the physical experiments. Figure 12 shows Milewski's data, which were obtained by briefly tumbling wooden or glass rods, dumping them into cylindrical containers and measuring the bulk density attained by the random compacts. We feel that his trend may be close to the lower phase boundary for three-dimensional systems, although we cannot verify this because we have not yet extended our Monte Carlo analysis into three dimensions.

CONCLUSIONS

Though we have used assumptions which are highly idealized, and though we have left many questions unanswered, we feel that we have established the following points which are relevant to composite engineering:

- 1) Accurate, non-discrete models of rod packing demonstrate that rod contact and percolation in physical systems are due solely to rod motion. Although rod shape and concentration are undoubtedly important variables, the specific type, magnitude, and duration of motion induced in physical experiments must be regarded as influencing the degree of contact between the rods.
- 2) Whiskers or chopped fibers will inevitably form clusters due to space-filling constraints, even when no inter-rod attractive forces are present, and even in the absence of motion.
- 3) Above the critical concentration, predicted by the phase diagram, the application of common processing operations such as high-shear mixing, milling, or sonication will cause the clusters to grow.

- 4) So-called "maximum packing fractions", established by physical experiments, represent kinetic barriers which will be overcome to an extent dependent upon the kinetic hindrance of the matrix and the type, magnitude, and duration of rod motion imposed during processing.

ACKNOWLEDGMENTS

This work was sponsored by the Air Force Office of Scientific Research (AFOSR) and the Defense Advanced Research Projects Agency (DARPA), and was monitored by AFOSR under Grant no. AFOSR-87-0114. Work performed by Larry Chick was sponsored by the Advanced Education and Training Program from Battelle Pacific Northwest Laboratories in Richland, WA. We also acknowledge gratefully the IBM Corporation for its support of this research as part of a block grant on the microdesigning of ceramics and polymer/ceramic composites. Finally, we wish to thank John Milewski for the loan of his carefully prepared wooden sticks.

REFERENCES

1. E.A. Di Marzio, *J. Chem. Phys.* **35**, 658 (1961).
2. F.L. McCrackin, *J. Chem. Phys.* **69**(12), 5419 (1978).
3. D.Y. Yoon and A. Baumgartner, *Macromolecules*, **17**(12), 2864 (1984).
4. J. Boissonade, F. Barreau, and F. Carmona, *J. Phys.A*, **16**, 2777 (1983).
5. E.A. Holm and M.J. Cima, *J. Am. Ceram. Soc.*, **72**(2), 303 (1989).
6. L.A. Chick, C. Viney, and I.A. Aksay, in *Rigid Rod Polymers*, edited by W.W. Adams, R.K. Eby and D.E. McLemore (Mater. Res. Soc., Pittsburgh, PA) in press.
7. L.A. Chick, C. Viney, and I.A. Aksay, in *Fourth International Conference on Ultrastructure Processing of Ceramics, Glasses, and Composites*, edited by D.R. Uhlmann, M.C. Weinberg, and S.H. Risbud (Wiley Interscience, New York) in press.
8. H. Menendez and J.L. White, *Pol. Eng. and Sci.*, **24**(13), 1051 (1984).
9. M. Vincent and J.F. Agassant, *Rheol. Acta*, **24**, 603 (1985).
10. H.T. Kau, *Pol. Comp.*, **8**(2), 83 (1987).
11. T.T. Meek, R.D. Blake, and J.J. Petrovic, *Ceram. Eng. Sci. Proc.*, **8**(7-8), 861 (1987).
12. T.N. Tiegs and P.F. Becher, *Ceram. Bull.*, **66**(2), 339 (1987).
13. J.L. Dion, J.J. Garceau, and J.C. Morissette, *Pulp Pap. Can.*, **88**(3), 87 (1987).
14. P.J. Flory, *Proc. Roy. Soc. London A*, **234**, 73 (1956).
15. M. Warner and P.J. Flory, *J. Chem. Phys.* **73**(12), 6327 (1980).
16. P.J. Flory and G. Ronca, *Mol. Cryst. Liq. Cryst.* **54**, 289 (1979).
17. P.J. Flory, *Adv. in Polymer Sci.* **59**, 1 (1984).
18. S.P. Papkov, *Adv. in Polymer Sci.* **59**, 75 (1984).
19. C. Viney, D.Y. Yoon, B. Reck and H. Ringsdorf, *Macromolecules* (1989) in press.
20. J.D. Bernal and I. Fankuchen, *J. Gen. Physiol.* **25**, 111 (1942).
21. S. Hachisu, *J. Colloid and Interface Sci.*, **55**, 499 (1976).
22. J.W. Milewski, PhD Dissertation, Rutgers Univ. (1973).

DISPERSION AND CONSOLIDATION OF THE COLLOIDAL SUSPENSION
IN THE Al_2O_3 POWDER - Si_3N_4 WHISKER SYSTEM

YOSHIHIRO HIRATA, SHINICHI MATSUSHITA, SUSUMU NAKAGAMA, ICHIRO HARAGUCHI,
NORIAKI HAMADA, YOSHIMI ISHIHARA AND SABURO HORI*

Kagoshima University, Department of Applied Chemistry

1-21-40 Korimoto, Kagoshima 890 JAPAN

*Kureha Chemical Industry Co. LTD., Advanced Material Systems Laboratory,

3-25-1 Hyakunincho, Shinjuku-ku, Tokyo 169 JAPAN

ABSTRACT

Whisker-reinforced ceramics have high potential for structural materials application due to their high fracture toughness and high mechanical strength. In this paper, rheological property and consolidation of the colloidal suspension in the alumina powder-silicon nitride whisker system were studied to control the microstructure and density of the green and hot-pressed composite. Al_2O_3 particles of average diameter $0.15 \mu\text{m}$ and Si_3N_4 whisker of average size $0.4 \mu\text{m} \times 3.7 \mu\text{m}$ were electrostatically dispersed in water in pH range 1-11 and consolidated by filtration. A well-dispersed state of the composite suspension was achieved at low pH. Decreasing the viscosity while increasing the solid content of the suspension at the same time is the key step in making green compact with higher density and a narrower pore size distribution. These compacts were densified to relative density 98.4-99.4% by hot-pressing at 1500°C at a pressure of 39 MPa in N_2 atmosphere.

1. INTRODUCTION

Advanced ceramics generally have high mechanical strength, high hardness, low density, and high resistance to corrosion as compared with metal materials. However, it is necessary to improve their fracture toughness for structural materials application. Recently, ceramic composite materials, especially whisker-reinforced ceramics, attracted attention due to their high mechanical property [1]. As is well known, those physicochemical properties of advanced ceramics or ceramic composite materials are influenced by the microstructure of sintered samples. When processing is done with submicron-size powders, colloidal processing is

superior to conventional dry processing for the production of ceramics or ceramic composite materials with uniform microstructure [2-4]. The stability of colloidal suspension is reflected in the property of green compact which in turn controls the property of the sintered body. In this paper, effects of rheological property of the suspension in the Al_2O_3 powder- Si_3N_4 whisker system on the microstructure and density of the consolidated compact were investigated.

2. EXPERIMENTAL PROCEDURES

Colloidal processing was used to mix $\alpha\text{-Al}_2\text{O}_3$ particles^{a)} of a specific surface area $10 \text{ m}^2/\text{g}$ (equivalent spherical diameter $0.15 \mu\text{m}$) with $\beta\text{-Si}_3\text{N}_4$ whiskers^{b)} of average size $0.4 \mu\text{m} \times 3.7 \mu\text{m}$ (aspect ratio ~ 10). Figure 1 shows the transmission electron micrographs of Al_2O_3 particles and Si_3N_4 whiskers. The as-received Al_2O_3 powders consisted of irregular-shaped particles with a particle size distribution $0.04\text{--}0.60 \mu\text{m}$. The Si_3N_4 whiskers were straight ones with length of $1.7\text{--}20 \mu\text{m}$ and diameter of $0.1\text{--}1.3 \mu\text{m}$. The mixtures of Al_2O_3 powders (60-100 vol%) and Si_3N_4 whiskers (0-40 vol%) were dispersed in water of pH 3, 6 and 10 at solid content 5-30 vol%. HCl and NH_4OH were used for pH adjustment. After the suspension was stirred at room temperature for 24 hrs, ultrasonic vibration (20kHz) was applied

a) Asahi Chemical Industry Co. Ltd., impurity: Na 50 ppm, Fe 10 ppm, Si 10 ppm.

b) Ube Industries, LTD., chemical composition: N 40%, O 1%, Y 0.28%, Ca 10 ppm, Al 10 ppm, Fe 700 ppm, specific surface area: $2.5 \text{ m}^2/\text{g}$.

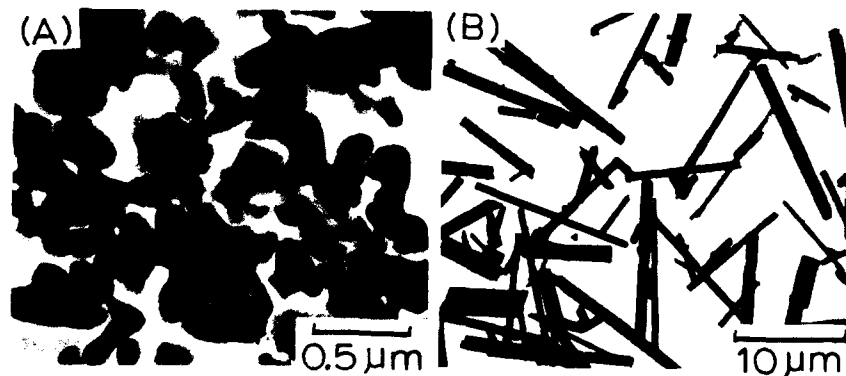


Fig. 1 Transmission electron micrographs of $\alpha\text{-Al}_2\text{O}_3$ powders (A) and $\beta\text{-Si}_3\text{N}_4$ whiskers (B).

for 5 min to facilitate the dispersion of the powder and whisker agglomerates. Air bubbles in the suspension were eliminated in a bell jar, which was connected to a vacuum pump. Viscosity of the colloidal suspension was measured by a cone and plate viscometer at 18°–25°C. Colloidal filtration through gypsum molds was used to consolidate the colloidal solid. Green compacts were dried at 110°C overnight. Density, microstructure, and pore size distribution of the green compacts were measured by the Archimedes method using kerosene, scanning electron microscopy, and an Hg porosimeter, respectively. The green compacts were hot-pressed at 1500°C for 1 hr at a pressure of 39 MPa in N₂ atmosphere.

3. RESULTS AND DISCUSSION

A. Rheological Property of Composite Suspension

Figure 2 shows the zeta potential of colloidal suspension of as-received α -Al₂O₃ powders and β -Si₃N₄ whiskers as a function of pH. The isoelectric points for Al₂O₃ powders and Si₃N₄ whiskers were pH 6.5 and 3.0, respectively. The pH dependence of zeta potential for Si₃N₄

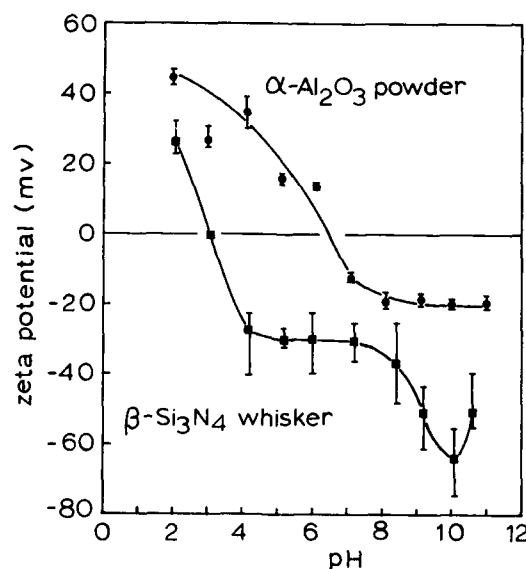


Fig. 2 Zeta potential of colloidal α -Al₂O₃ particles and β -Si₃N₄ whiskers as a function of pH.

whiskers resembles that for SiO_2 powders, and suggests that the surface of Si_3N_4 whiskers was coated by SiO_2 film [5-7]. The data in Fig. 2 predicts that well-dispersed states will be achieved at low pH (<6) for Al_2O_3 powders and at high pH (>4) for Si_3N_4 whiskers owing to the strong repulsion force among highly charged particles or whiskers.

Figure 3 illustrates the rheological property of the suspension for Si_3N_4 whiskers and the Al_2O_3 powders (95 vol%) - Si_3N_4 whiskers (5 vol%) system. The shear rate - shear stress relation of the suspension changed from Newtonian to Pseudoplastic or Bingham behavior with decreasing pH for the whisker suspension and with increasing pH for the composite suspension. Figure 4 summarizes the viscosity and yield stress of the composite suspension showing Bingham behavior as a function of solid content. In contrast with the Si_3N_4 whisker suspension, the composite suspension in the Al_2O_3 powder (95 vol%) - Si_3N_4 whisker (5 vol%) system was similar to the Al_2O_3 suspension regarding the rheological behavior. Therefore, the addition of Si_3N_4 whiskers to Al_2O_3 suspension caused little change in the rheological property at pH 3. This result indicates small interaction between Al_2O_3 particles and Si_3N_4 whiskers. One interpretation of the above experimental result is that the Si_3N_4 whiskers have low zeta potential at around pH 3. This interaction may also be small in the pH range where Al_2O_3 particles and Si_3N_4 whiskers have opposite electrical charge. The ratio of specific surface area of cylindrical Si_3N_4 whiskers of length 3.7 μm and diameter 0.4 μm and spherical Si_3N_4 particles of diameter 0.15 μm (being equal to the average diameter of Al_2O_3 particles) is 0.26 : 1. That is, coagulation effect of negatively charged whiskers against positively charged Al_2O_3 particles would be as small as about 1/4 of negatively charged Si_3N_4 particles because the coagulation effect would be proportional to the surface area of the whiskers. On the other hand, the composite suspension showed high viscosity at high pH (Fig. 3 and 4). This result suggests that the Al_2O_3 surface negatively charged in AlO_2^- at high pH has lower dispersion effect as compared with positively charged surface $\text{Al}(\text{OH})_2^+$ or AlOH^{2+} [8,9]. In addition, the relatively low zeta potential of Al_2O_3 particle at pH>7 would be one of the reasons for high viscosity of the composite suspension at high pH.

B. Density and Microstructure of the Consolidated Compact

Figure 5 summarizes the relation between viscosity of the suspension and green density of the compact consolidated by filtration through gypsum

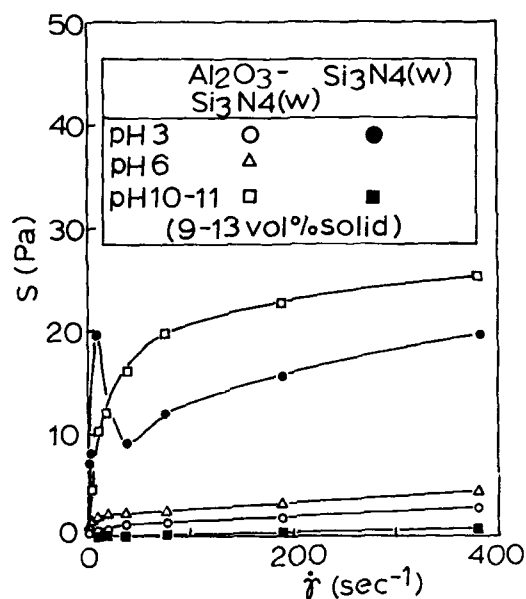


Fig. 3 The shear rate - shear stress relation for the suspension of Si_3N_4 whiskers and the Al_2O_3 powders (95 vol%) - Si_3N_4 whiskers (5 vol%) system.

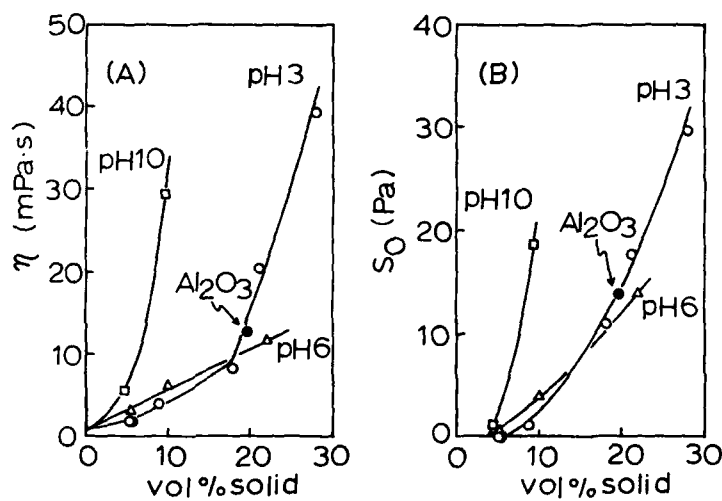


Fig. 4 Viscosity (A) and yield stress (B) of the colloidal suspension for the Al_2O_3 powders (95 vol%) - Si_3N_4 whiskers (5 vol%) system showing Bringham behavior.

molds. Figure 5 indicates that the suspension of lower viscosity and at the same time higher solid content gives a higher green density. The viscosity reflects the degree of dispersion and flexibility of Al_2O_3 particles and Si_3N_4 whiskers in the aqueous suspension. In the lower viscosity suspension, the well-dispersed colloidal particles and whiskers have a tendency to form an ordered structure during the phase transformation from colloidal liquid to colloidal solid [3,10]. Increasing the solid content in the suspension promotes the formation of nuclei of colloidal solid. An increased number of nuclei grow into a polycrystalline-like microstructure rather than glassy-like (or liquid-like) structure during the consolidation. As a result, the green density becomes higher at higher solid content of the suspension because the density of crystalline is higher than that of glass. Another potential effect of increasing the solid content in the suspension is to prevent the long range segregation between Al_2O_3 particles and Si_3N_4 whiskers due to the differential mass during consolidation [11-13]. Prevention of this segregation phenomena causes the increase of green density and uniformity of the microstructure of the compact because smaller particles fill the voids formed among larger particles or whiskers. This fact can be well recognized in the higher green density of bimodal particle size system [3,11].

Figure 6 shows the pore size distributions of green compacts from the suspension of about 10 vol% solid content. As shown in Fig. 6, the lower viscosity suspension (pH 3) formed the green compact with a narrower pore size distribution of smaller average size [14]. This result suggests that the pore size distribution of the green compact from well-dispersed suspension approaches the monosize state. In the sintering of powder

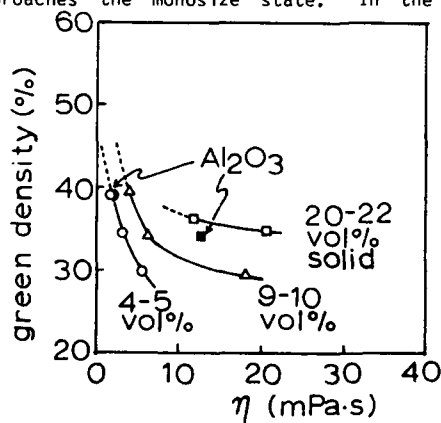


Fig. 5 Green density of the compact as a function of the viscosity of the suspension for the Al_2O_3 powders (95 vol%) - Si_3N_4 whiskers (5 vol%) system.

compact, since smaller pores are eliminated faster than larger pores, it is important to decrease the pore size along with the total pore volume [15-18]. Figure 7 illustrates the microstructures of green compacts formed from the suspensions at pH 3. From the SEM pictures, it was found that most of whiskers were consolidated with orientation where the direction in length of whisker arrayed is perpendicular to the direction of filtration [19]. That is, the ordered structure for whiskers means the oriented arrays [8].

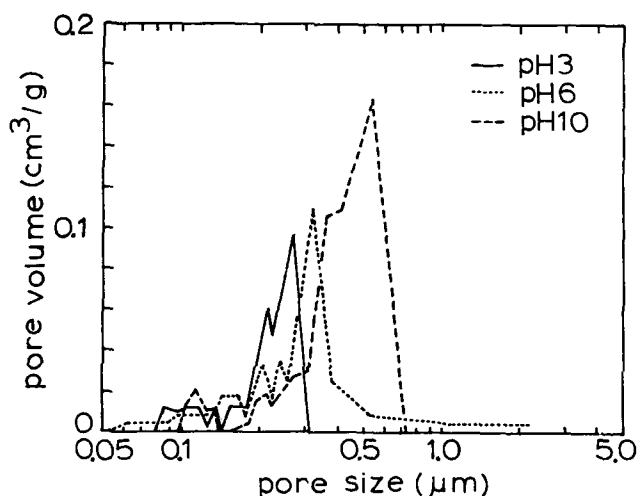


Fig. 6 Pore size distributions of the green compacts (95 vol% Al_2O_3 powders - 5 vol% Si_3N_4 whiskers) consolidated from the suspension of about 10 vol% solid content.

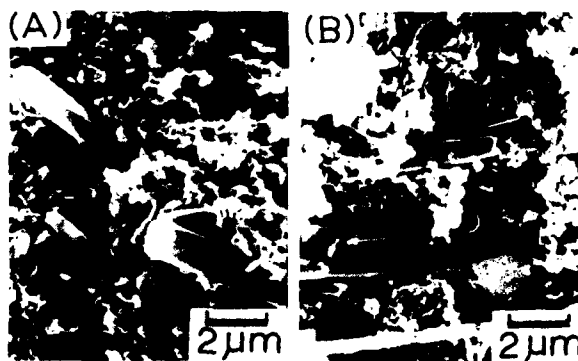


Fig. 7 Microstructures of green compacts (95 vol% Al_2O_3 powders - 5 vol% Si_3N_4 whiskers) formed from the suspension of solid content 9 vol% (A) and 28 vol% (B).

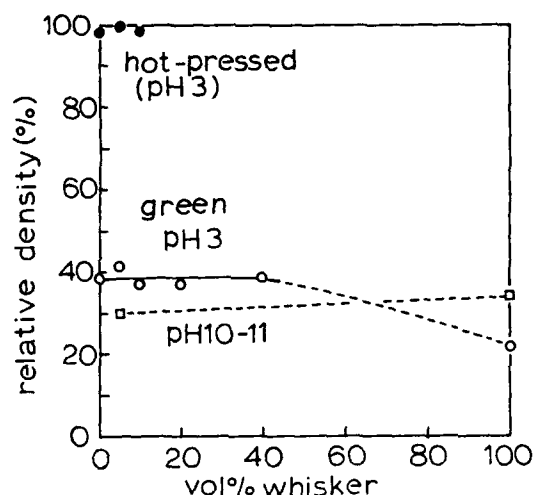


Fig. 8 Whisker content dependence of green and hot-pressed density for the Al_2O_3 powders - Si_3N_4 whiskers system. Samples were hot pressed at 1500°C for 1 hr at a pressure 39 MPa in N_2 atmosphere.

Figure 8 shows the whisker content dependence of green and hot-pressed density of compacts formed from the suspension of 20-30 vol% solid at pH 3. Although the apparent viscosity of suspension became higher with increasing whisker content, the green and hot-pressed density were not so sensitive to the whisker content, as shown in Fig. 8. These results can be explained by the result in Fig. 5. The green density changes sensitively with viscosity at low solid content. The viscous suspension containing a higher content of whisker does not appear to significantly affect the green density. However, the green density will decrease in the whisker content range 50-100 vol% because the matrix of the composite changed from Al_2O_3 powders to Si_3N_4 whiskers, which gives lower packing density due to lower repulsion force at pH 3 [13]. The green density of the monolithic whisker compact was increased by increasing pH of the suspension. This increase in green density of the monolithic whisker compact was accompanied by an increase in the orientation. This observation on the orientation of whisker compacts agreed with the array of whisker shown in Fig. 7.

4. CONCLUSIONS

Lower viscosity composite suspension of $\alpha\text{-Al}_2\text{O}_3$ particles (60-100 vol%) and $\beta\text{-Si}_3\text{N}_4$ whiskers (0-40 vol%) with isoelectric points at pH 6.5 and 3.0, respectively, was electrostatically prepared at low pH (~ 3). Decreasing the viscosity while at the same time increasing the solid content of the suspension is the key step in making green compact with higher density. The consolidated compact of higher density has a structure with narrower pore size distribution and smaller average pore size. In the compacts, whiskers showed a tendency to be arrayed with orientation. The green compacts consolidated from the suspension at pH 3 could be densified to relative density 98.4-99.4% by hot-pressing at 1500°C for 1 hr at a pressure of 39 MPa in N_2 atmosphere.

ACKNOWLEDGEMENT

The authors thank M. Tajika of Asahi Chemical Industry Co. LTD., for the supply of Al_2O_3 powders used in this study.

REFERENCES

1. Am.Ceram.Soc.Bull. Ceramic Composites Issue, 65 (2), 288-381 (1986), 66 (2), 303-375 (1987) and 68 (2), 366-442 (1989).
2. F.F.Lange, J.Am.Ceram.Soc. 72 (1), 3-15 (1989).
3. I.A.Aksay, in Ceramics : Today and Tomorrow, edited by S.Naka, N.Soga and S.Kume (Ceram.Soc.Japan, 1986), pp.71-85.
4. M.D.Sacks, H.W.Lee and O.E.Rojas, J.Am.Ceram.Soc. 71 (5), 370-379 (1988).
5. M.N.Rahaman, Y.Boiteux and L.C.De Jonghe, Am.Ceram.Soc.Bull. 65 (8), 1171-1176 (1986).
6. P.K.Whitman and D.L.Feke, J.Am.Ceram.Soc. 71 (12), 1086-1093 (1988).
7. L.Bergstrom and R.J.Pugh, J.Am.Ceram.Soc. 72 (1), 103-109 (1989).
8. J.Reed, Introduction to the Principles of Ceramic Processing (John Wiley & Sons, Inc., 1988) pp.132-151 and pp.185-199.
9. T.Tsunoda, Bull.Ceram.Soc.Japan. 22 (5), 393-399 (1987).
10. I.A.Aksay and R.Kikuchi, in Science of Ceramic Chemical Processing, edited by L.L.Hench and D.R.Ulrich (John Wiley & Sons, Inc., 1986) pp.513-521.

11. C.Han, I.A.Aksay and O.J.Whittmore, in Advances in Materials Characterization II, edited by R.L.Snyder, R.A.Condrate, Sr. and P.F.Johnson (Plenum Publ. Co., 1985) pp.339-347.
12. Y.Hirata and I.A.Aksay, in Proceedings of the International Workshop for Advanced Materials Technology, Ceramics IV (Japan Fine Ceramic Center, 1988) in press.
13. J.V.Milewski, Adv.Ceram.Mater. 1 (1), 36-41 (1986).
14. A.Roosen and H.K.Bowen, J.Am.Ceram.Soc. 71 (11), 970-977 (1988).
15. C.Herring, J.Appl.Phys. 21 (4), 301-303 (1950).
16. M.D.Sacks and J.A.Pask, J.Am.Ceram.Soc. 65 (2), 70-77 (1982).
17. Y.Hirata and I.A.Aksay, in Ceramic Microstructures '86, Role of Interfaces, edited by J.A.Pask and A.G.Evans (Plenum Press, 1987) pp.611-622.
18. T-S. Yee and M.D.Sacks, J.Am.Ceram.Soc. 71 (12), C484-C487 (1988).
19. S.Saitoh, M.Minamizawa, T.Yonezawa, T.Matsuda and C.Sakai, presented at 27th Meeting of The Basic Science Division, Abstract 2007, Ceram.Soc.Japan, 1989.

DENSIFICATION OF PARTICULATE CERAMIC COMPOSITES: THE ROLE
OF HETEROGENEITIES

LUTGARD C. DE JONGHE* AND MOHAMED N. RAHAMAN**

*Center for Advanced Materials, Materials and Chemical Sciences Division,
Lawrence Berkeley Laboratory, One Cyclotron Road, Berkeley, CA 94720

**Department of Ceramic Engineering, The University of Missouri-Rolla,
Rolla, Missouri 65401

ABSTRACT

Inert particulate inclusions in ceramic powder compacts can obstruct densification behavior significantly. The factors that are the causes of this decrease in the sinterability are reviewed. It is concluded that the origin of the sintering difficulty resides in defects that processes such as die compaction introduce during the initial forming of the composite powder compact. Alternative processing methods are suggested that should minimize the negative effects of the dispersed inclusion phase on densification.

INTRODUCTION

Particulate ceramic composites can offer important performance advantages in that they may have a higher fracture toughness and creep resistance at elevated temperatures than single phase ceramics. The potential for improved performance is, however, offset by the increased difficulties that the processing of such composites present. In particular, it has been commonly observed that free sintering of particulate composites is significantly hampered, even at modest volume fractions of the dispersed inclusions [1-3]. One way to report the retardation effects is to regard densification as driven by an externally applied, effective mechanical stress, (referred to as the sintering stress, Σ), that reproduces the combined action of surface and grain boundary tensions [4]. The relative reluctance with which the composites densify can then be expressed in terms of a hydrostatic backstress that opposes the intrinsic sintering stress that would densify an inclusion-free matrix of identical microstructure as that of the composite. The decrease of the densification rate, however, might well reside in a modification of the kinetic factors rather than of the sintering stress; and further experimentation is required to reveal the actual cause of the effective backstress. The origin of such an effective backstress has been attributed to various factors including significant viscoelastic backstresses originating in densification incompatibilities between the matrix and the dispersed phase [5,6], the formation of an undeformable network of the dispersed inclusions [7], the effects of dispersed phase clustering [8,9], and

more recently, the adverse effects of micro-crack or crack-like defects promoted by the presence of the dispersed inclusions either in the initial cold compaction or during sintering of the composite [10].

Various authors have concluded that large viscoelastic backstresses cannot realistically develop in densifying particulate composites [4,11,12]. Only those incompatibility stresses corresponding to the instantaneous viscous limit should be expected rather than those arising from a cumulative viscoelastic process. The constrained network model developed by Lange [7] offers an attractive alternative explanation for the retarding effects of the dispersed phase on the densification rate, especially at high volume fractions.

While particulate composites can usually be densified without much difficulty by pressure-assisted sintering, it would be clearly advantageous to achieve adequate densification by free sintering. The processes that oppose free densification when a useful volume fraction of the inclusion phase is present must therefore be understood so that they can be minimized or avoided altogether.

In this paper we review our understanding of the factors that can contribute to the modification of the sintering behavior of ceramic powder compact, by dispersed particulate inclusions.

EXPERIMENTAL

Apart from the usual dilatometric measurements that can be used to elucidate densification mechanisms and the factors that affect them, one can determine the low-load constant-stress creep rate of the composites as they are densifying. This technique has been described earlier [13,14], and adds an additional probe for clarifying sintering processes. In a typical experiment samples, prepared by mechanical mixing and cold die compacting, are measured by standard dilatometric methods, but controlled stresses up to a few hundred kilopascal are applied. This low applied stress superimposes a nearly constant-volume creep onto the densification, and the creep rate can be determined straightforwardly. The densification and simultaneous creep rates of single phase and particulate composite samples can then be compared.

DISCUSSION

The linear densification strain rate, $\dot{\epsilon}_d$, and the creep strain rate, $\dot{\epsilon}_c$, of a densifying powder compact can be written parametrically as

$$\dot{\epsilon}_d = \Sigma/\eta_d \quad (1)$$

and

$$\dot{\epsilon}_c = \sigma_a/\eta_c \quad (2)$$

where Σ is the sintering stress and σ_a is the applied uniaxial stress. Equations (1) and (2) also define the meaning of the densification and the creep viscosities, η_d and η_c .

Under the assumption that the densification rate of the inclusion-free, identical matrix, $\dot{\epsilon}_m$, is known, the instantaneous matrix densification rate, $\dot{\epsilon}_{com}$ of a particulate composite containing a volume fraction, f , of the dispersed phase can be shown to be [4]

$$\dot{\epsilon}_{com} = \dot{\epsilon}_m (1 + 4[\eta_c/\eta_d][f/(1-f)])^{-1} \quad (3)$$

This equation is based on the critical assumption that the densifying compact is quantitatively represented by the behavior of an inert spherical particle surrounded by a densifying, uniform mantle of matrix material. It further is based on a continuum model in which, necessarily, particle size or transport mechanism considerations must be absent. This is equivalent to the assumption that all the inclusions are of uniform size and are spatially ordered in a uniform matrix. This situation is clearly not realized in normal mixing processes where, at best, complete spacial randomness (CSR) can be achieved. Normally, the particles will be non-uniformly distributed and will not be monosized. The compact can then be regarded as consisting of an irregular space-filling assemblage of Voronoi cells each with one inclusion inside. The cell size and the inclusion size distribution represent a corresponding distribution in local volume fraction of the dispersed inclusions. Compatibility stresses must then arise during densification, opposing the driving force for sintering and leading to somewhat lower densification rates than those predicted by Eqn. (3). It is difficult to assess the magnitude of such compatibility backstresses quantitatively; at high volume fractions they could be expected to be significant, when the system approaches the constrained network sintering model proposed by Lange [7]. The effects of non-uniform distribution of the inclusion may be estimated by considering two equal volume elements of the composite containing different fractions, f_1 and f_2 , of inclusions such that the average remains f . These volume elements would need to densify compatibly requiring that their overall volumetric strain rate be equal. This is achieved by the generation of self-stresses that increase the densification rate of the slow volume element and decreases the densification rate of the fast one. The new densification rate $\dot{\epsilon}_{nm}$ of the matrix of these two volume elements can then be calculated and compared with the densification rate, $\dot{\epsilon}_{mo}$, of the volume elements if they had equal inclusion contents. After some algebra, this leads to

$$\dot{\epsilon}_{nm}/\dot{\epsilon}_{mo} = 2 F_1 F_2 / [(F_1 + F_2)F] \quad (4)$$

where, following Eqn 3, with $\eta_c/\eta_d = 2$,

$$F_1 = [1 + 8f_1/(1-f_1)] \quad (5)$$

with similar expressions for F_2 and F corresponding to f_2 and f .

Figure 1 shows a plot of the densification rate ratios using Eqn. (4), for various values of f , as a function of f_1/f . It is evident from this representation that the retarding effects due to heterogeneous distributions of inclusions is most serious at high inclusion contents and for large variations in the local inclusion contents. At low volume fractions of inclusions, say below 10-15 vol%, this calculation indicates that the

opposition to densification from this type of backstress is relatively minor.

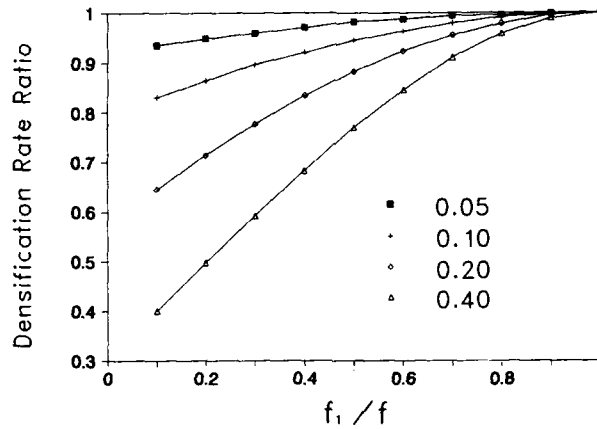


Figure 1. Densification ratio, $\dot{\epsilon}_{nm}/\dot{\epsilon}_{mo}$, as a function of f_1/f calculated from Equation (4).

Estimates of how varied the spacial density distribution of the inclusions or their network formation can be in the case of CSR can be deduced from the available expressions for the probability distribution of finding a neighbor to a particle at a distance equal to its diameter. This probability is given by [15]

$$P(d) = 1 - \exp(-\lambda \pi d^3) \quad (6)$$

where λ is the inclusion number density per unit volume or intensity of the composite, and d is the center to center distance between the dispersed inclusions.

Equation (6) can be rewritten in terms of inclusion radius, r , and volume fraction, f , when it is assumed that the dispersed inclusions are spherical and monosized:

$$P(d) = 1 - \exp(-(3/4) \cdot f \cdot (d/r)^3) \quad (7)$$

In the case of CSR the probability distribution function $P(d)$ is unaffected by inclusion size; however, in the case of clustering this may not be the case and inclusion size as well as volume fraction may affect $P(d)$. For 10 vol% of inclusion, for example, the probability of having a touching neighbor is less than 10%. This consideration again underscores that rigid network formation arguments cannot account for the strong retardation of densification at inclusion volume fractions of below about 0.1, unless there is pronounced clustering. In practice, a detailed study of the distribution of the inclusion density as a function of the

sampling area or volume can be used to characterize the homogeneity of the distribution. For CSR this sampling (quadrat count in two dimensions) would follow a Poisson distribution; for non-CSR distribution, the variance-to-mean ratio would be used as a measure of heterogeneity (or index of dispersion).

The data considered here are those in which clustering was not detected. It should be noted, however, that in another study, [8] clustering was shown to increase with decreasing inclusion size leading to increasing obstruction of densification at constant volume fraction. A significant inclusion size effect was also reported [9].

When clustering or unusual spacial density variation of the inclusions are largely absent, an evaluation of the experimental ratio $\epsilon_{com}/\epsilon_m$ in Eqn. (3), would indicate to what extent the experiments agree with the analysis that led to Eqn. (3). Data from earlier experiments by De Jonghe and coworkers [1] are shown in Table 1. The viscosity ratios, η_c/η_d , commensurate with Eqn. 3 range from near 20 at 3 vol% inclusions to about 80 at 20 vol% inclusions. This is a factor of 10 to 40 larger than the theoretically possible value of 2 deduced by Scherer [11] and also significantly more than what might be attributable to the spacial variations in inclusion density discussed above, except at the high volume fractions.

Table 1: Experimental data for the matrix densification rate of the composite after a sintering time of twenty minutes, relative to the unreinforced matrix, $(\epsilon_{com}/\epsilon_m)_{20}$, and the ratio of the creep viscosity to the densification viscosity, η_c/η_d , calculated from Equation (3) for different inclusion volume fraction, f .

f	$(\epsilon_{com}/\epsilon_m)_{20}$	η_c/η_d
0.03	0.69	19
0.06	0.51	19
0.09	0.36	24
0.13	0.26	26
0.19	0.07	81

Further insight into the origin of the strong decreases in the densification rates of ceramic matrix particulate composites may be found in a study of their creep/sintering behavior. The creep/sintering studies are done by loading dilatometry in which the creep and densification strain rates are simultaneously determined. In porous materials, the viscosity of creep and of densification are intimately related, unless stress-driven rearrangement is rapid, and it becomes possible to determine whether the obstruction to densification in a particulate composite is due to altered viscosities, e.g. by preventing inclusion-network shear, or if it involves modification of the sintering stress itself.

Some recent data [16] were obtained on creep/sintering of a particulate composite of ZnO with 10 vol% silicon carbide. The data are shown in Fig. (2). A remarkable feature of the creep data is that the time dependence of the creep rate appear to be unaffected, although the time dependence of the densification rate is significantly different. The creep rate can be written in terms of the material's structural parameters as [4]

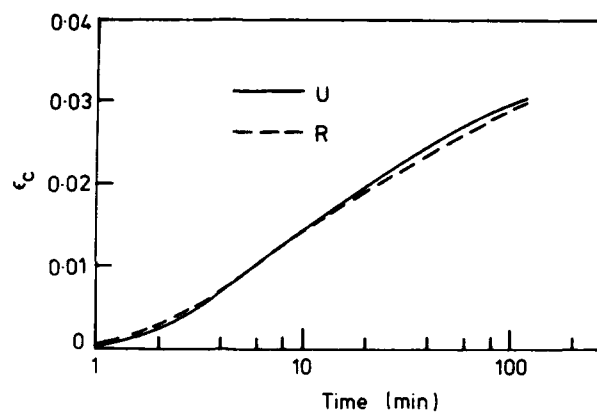


Figure 2(a). Creep strain as a function of time for unreinforced ZnO (referred to as sample U) and ZnO reinforced 10 v% SiC (sample R) sintered at 725°C under a uniaxial stress of 250 kPa.

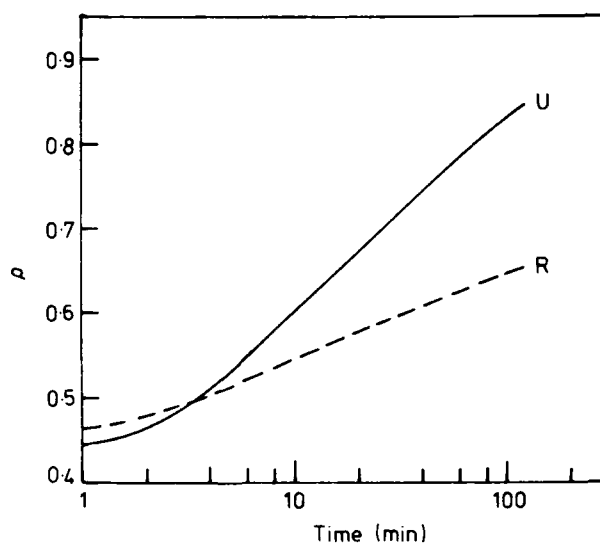


Figure 2(b). Density as function of time for samples U and R described in Fig. 2(a).

$$\dot{\epsilon}_c = \sigma_a / \eta_c = \sigma_a (K \Phi^{(n-1/2)} / X^n) \quad (8)$$

where K is a constant, X is the interpore distance, Φ is the stress intensification factor [17], and n is a transport mechanism dependent parameter. For ZnO, with volume diffusion as the dominant transport mechanism, n is equal to 2. X is determined by the coarsening processes and is therefore a function of time. Φ is determined by the overall porosity and has been found to be well represented by $\Phi = \exp(aP)$, with $a \approx 5$ for ZnO. The time-sensitivity of the viscosity must then be regarded as resulting from a fortuitous compensation between ϕ and X . The densification of the matrix would also be expressible by an equation very similar to Eqn 8, when the creep and densification are effected by the same transport mechanisms:

$$\dot{\epsilon}_m = \Sigma(1/\eta_m) = K\Phi^{(n-1/2)} / X^n \quad (9)$$

where Σ is the sintering stress. The ratio of the instantaneous densification rate to the constant stress creep rate can then give a measure of how the sintering stress is modified by the presence of the inclusions. The results indicated that the sintering stress of the composite was decreased by a factor of approximately 2, from the very onset of densification throughout the measurement range Fig. (3). At the same time, the above considerations indicate that the origin of the effective backstress cannot be sought in the viscous mismatch stresses generated by the particles since, according to Eqn. (3), it can only account for a decrease of about 20 % in Σ at 10 vol% inclusions; also, the spacial variation of the inclusion distribution at this inclusion content is also unlikely to account directly for the decrease. Another cause therefore produces the observed strong decreases in the densification rates of composites at modest inclusion content. This cause must also be present from the beginning of densification.

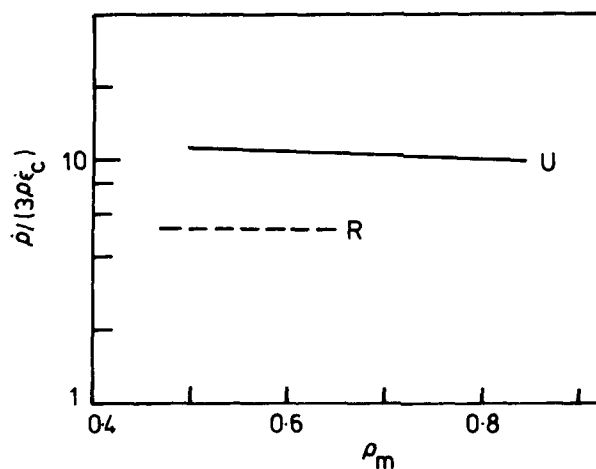


Figure 3. Ratio of the densification rate to the creep rate as a function of the matrix relative density for samples U and R described in Fig. 2(a).

The sintering stress can be lowered by several factors. A strong factor is the initial compact density; recent results indicate that the sintering stress decreases with decreasing density [18]. A lesser decrease of the sintering stress can be brought about by prolonged coarsening at low temperatures; however, since the effects are present from the very onset of densification it is difficult to maintain a coarsening-based argument. It is therefore concluded that the origin of the apparent backstress resides in difference in the microstructure that the presence of the inclusions has brought about during the cold compaction of the composite. Several effects can be considered: die compaction is likely to lead to larger variations in the spatial distribution of the matrix green density when an inclusion phase is present than without. In addition, during cold compaction the mismatch between the undeformable inclusions and the compacting matrix must also be accommodated, and this accommodation can be accomplished by local matrix density gradients as well as by matrix shear. Inhomogeneous compaction will then introduce residual stresses in the green compact that upon unloading may lead to matrix microcracking. This, in turn, can constitute a non-recoverable damage that makes the sintering process less successful, e.g., by developing a large-pore tail in the pore size distribution. Such damage has not yet been detected directly in partly sintered particulate composites, although it has been postulated by Lange [19] and shown to be present in model experiments [10] in which a large, undeformable core was included in a sintering cylindrical specimens.

The road to increasing the sinterability of particulate composites lies therefore in the improvement of the distribution of the inclusion phase and in selecting forming processes, such as slip casting and wet pressing, in which residual stresses are kept at a minimum. The present experiments indicate that such processing methods will lead to particulate composites that can be free-sintered at useful inclusion contents.

CONCLUSIONS

The arguments advanced for the explanation of the retarding effect of inclusions on densification of ceramic matrix particulate composites have been reviewed. It is concluded that the origin of the retardating effects must be sought in the pre-sintering microstructure, and methods have been indicated that could minimize the sintering difficulties.

ACKNOWLEDGEMENT

This work was supported by the Division of Materials Sciences, Office of Basic Energy Sciences, United States Department of Energy, under Contract No. DE-AC03-76SF00098.

REFERENCES

1. L. C. De Jonghe, M. N. Rahaman, and C. H. Hsueh, *Acta metall.* 34, (7), 1467-1471 (1986).
2. R. K. Bordia and R. Raj, *J. Am. Ceram. Soc.* 71 (4), 302-310 (1988).
3. W. H. Tuan, E. Gilbert, and R. J. Brook, *J. Mat. Sci.* 24, 1062-1068 (1989).

4. L. C. De Jonghe and M. N. Rahaman, *Acta metall.* 36 (1), 223-229 (1988).
5. R. Raj and R. K. Bordia, *Acta metall.*, 32 (7), 1003-1019 (1984).
6. C. H. Hsueh, A. G. Evans, R. M. Cannon, and R. J. Brook, *Acta metall.* 34 (5), 927-936 (1986).
7. F. F. Lange, *J. Mater. Res.* 2 (1), 59-65 (1987).
8. M. W. Weiser, Ph.D. Thesis, University of California at Berkeley (1987).
9. M. W. Weiser and L. C. De Jonghe, *J. Am. Ceram. Soc.* 71 (3) C-125--C-127 (1988).
10. F. F. Lange, *Acta metall.* 37 (2), 697-704 (1989).
11. G. W. Scherer, *J. Am. Ceram. Soc.* 70 (10) 719-725 (1987).
12. R. K. Bordia and G. W. Scherer, *Acta metall.* 36 2411-2416 (1988).
13. L. C. De Jonghe and M. N. Rahaman, *Rev. Sci. Instrum.*
14. M. N. Rahaman, L. C. De Jonghe, and R. J. Brook, *J. Am. Ceram. Soc.* 69 (1), 53-57 (1986).
15. J. Diggle, Statistical Analysis of Spatial Point Patterns, New York: Academic Press (1983).
16. M. N. Rahaman and L. C. De Jonghe, unpublished results, 1989.
17. J. M. Vieira and R. J. Brook, *J. Am. Ceram. Soc.* 67 (4), 245-249 (1984).
18. M.-Y. Chu and L. C. De Jonghe, unpublished results, 1989.
19. F. F. Lange, in Ceramic Transactions: Ceramic Powder Science IIB, Gary L. Messing, Edwin R. Fuller, Jr., and Hans Hausner, eds. American Ceramic Society, Ohio, 1988.

DENSIFICATION BEHAVIOR OF Al_2O_3 POWDERS CONTAINING ZrO_2 INCLUSIONS

O. SUDRE, D.C.C. LAM and F.F. LANGE

Materials Department, College of Engineering, University of California
Santa Barbara, CA 93106.

ABSTRACT

Densification experiments using ZrO_2 single-crystal particles in an Al_2O_3 powder matrix were performed to examine the microstructural changes produced by constrained densification. Observations showed the formation of large, low-density regions within a denser material network. Enlargement of pores by desintering of necks between grains was observed during grain coarsening within these low-density regions. This pore opening behavior was also investigated in a model experiment.

INTRODUCTION

Retardation of densification of a powder matrix by inclusions has been observed for a number of systems, i.e. SiC-ZnO [1], $\text{Al}_2\text{O}_3\text{-TiO}_2$ [2]. Numerous models have been proposed to model this densification behavior [3-6]. These models ascribe to the concept that powder shrinkage generates compressive stresses in the inclusions and tensile stresses in the powder matrix during densification. The tensile stresses generated within the matrix are thought to oppose the compressive 'sintering stresses' and thus retard densification. However, experiments [7] have shown that the creep rate is comparable to the densification rate, which implies that the tensile stresses are relaxed quickly. In addition, a model specimen consisting of an alumina powder ring slip-cast around a dense alumina plug was performed [8] to simulate the geometry used in the theoretical models. The results showed that the densification of the powder ring is not retarded by the central inclusion.

Evidently, existing models based on retardation stresses are inadequate in explaining the phenomenon of constrained densification. In an alternative approach, Lange [9] suggested that the densification constraint arises from the interaction between inclusions. Lange proposed that the inclusions constitute the nodes of a network. The distance between nodes varies and the amount of powder between inclusions determines the shrinkage between nodal pairs. It was concluded from this geometrical argument that the matrix can fully densify only if extensive network deformation occurs. If matrix creep is insufficient, then local variations of inclusion spacings would generate local tensile constraint giving rise to matrix disruptions such as crack-like voids.

In the present study, the microstructural evolution of an Al_2O_3 powder matrix containing ZrO_2 inclusions was investigated. The observations suggested that variation in density did arise and that neck between grains in low-density regions broke contact as grains coarsened after initial sintering. This mechanism of desintering of necks was also investigated using a model geometry.

EXPERIMENTAL PROCEDURE

ZrO₂ single crystals, 30-50 μm in size (Ceres Corporation), were mixed into a dispersed colloidal Al₂O₃ (Sumitomo AKP-50) slurry [10]. The volume fraction of crystals was 9 vol.% based on the theoretical composite density. The slurry was then flocced to prevent inclusion segregation. The composite slurry was pressure filtrated at 5 MPa to form cylindrical specimens. Large cracks were observed after both die removal and drying. The densification behavior was examined by dilatometry at constant heating rate (5°C/min) up to 1550°C. The microstructures of polished specimens sintered at different temperatures were examined using a SEM (JEOL 840). Additionally, the evolution of a specific region on a sintered specimen was followed after successive heat treatment periods at 1600 °C.

Another specimen of polycrystalline cubic ZrO₂ containing 8 mole% Y₂O₃ (Tosoh Corporation, TZ-8Y) was used as a model to study the effect of constraint on the microstructural development of polycrystalline bridges between the faces of a crack. Dispersed slurry of cubic ZrO₂ was slip cast into a plaster tube. As shown in Fig. 1, the dried specimen had a dense shell around a lower density core. A discontinuous crack developed in the middle of the specimen after drying. Powder bridges between the crack surfaces developed into polycrystalline ligaments upon sintering. Evolution of these bridges was followed by SEM during subsequent heat treatments.

OBSERVATIONS

The densification behavior of the Al₂O₃-ZrO₂ inclusion composite and that of the pure matrix are shown in Fig. 2. Microstructural observations showed that the slight decrease in matrix density in the composite was due to formation of inclusion-related cracks with large opening displacements (Fig. 3) and to density variations within the matrix (Fig. 4). Low-density regions were frequently observed along the length of high aspect ratio inclusions, whereas dense regions were often associated with the tip of the inclusions. In areas where inclusions were in close proximity, a higher matrix density was noticed; but this observation may be biased by the two-dimensional character of the cut and polished specimens.

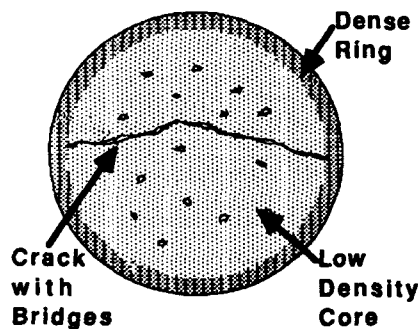


Figure 1: Model specimen to follow polycrystalline bridges across crack

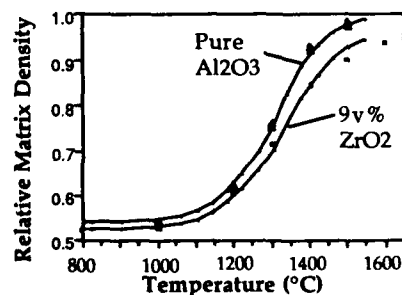


Figure 2: Densification of the composite and a pure matrix



Figure 3: Large macro-cracks associated with inclusions



Figure 4: Low density regions and surrounding denser material

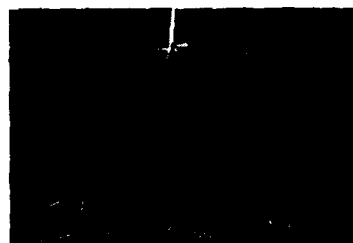


Figure 5: Differential grain growth in denser regions relative to lower density regions



Figure 6: Region followed in Figure 7

As shown in Fig. 5, differences in average grain size between the low-density and high-density areas became apparent after further heat treatments at 1600°C. The evolution of microstructure for a cut-and-polished specimen in a low-density region near an inclusion cluster (Fig. 6) is shown in Fig. 7. At first, some densification occurred leading to some pore closure. Upon further heat treatment, some initially sintered grains separated. This process resulted in the coalescence of the pores located on both sides of the neck. Three of these events are shown, but the reader can readily identify others. Grain growth has concurrently occurred during this evolution.

Evolution of the bridge in the model experiment is shown in Fig. 8. The grain size increased with annealing time. The bridging material eventually developed into large grain pairs. Further heat treatments caused grain pairs to separate by de-sintering which led to the coalescence of the adjacent cracks.

DISCUSSION

Large cracks in the composite matrix are believed to have developed during sintering from hairline defects in the green body. It is thought that these defects are created by the differential strain relaxation in the green compact during pressure release after pressure filtration or during drying. It has been shown that the number of defect can be reduced by using a dispersed suspension that will flow upon strain recovery and prevent the formation of these cracks [11].

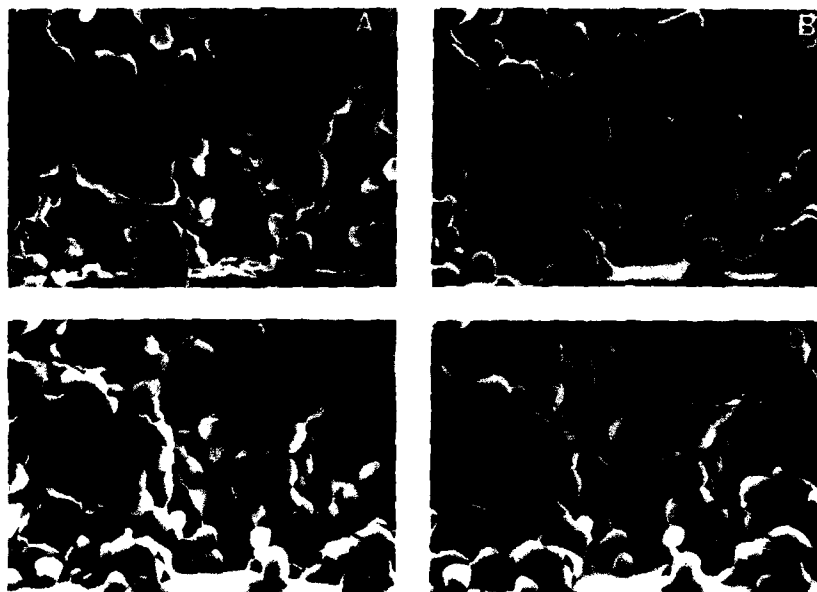


Figure 7: Evolution of the region outlined in Fig. 6 at 1600°C after (A) polishing, (B) 10 mins, (C) 2 hours, (D) 3 hours .

The microstructural observations of sintered specimens suggested that the partially dense composite was composed of a 3-D network of denser matrix which surrounded lower density regions. These density and grain size variations will create a differential in the viscoelastic properties of the matrix. These observations led the authors to propose the following retardation mechanism. During sintering, a network of denser material developed between inclusions. This denser network surrounded lower density regions. Densification of the lower density regions would require the deformation of the higher density network. Under constraint, material within the low-density regions decreased its free energy via grain growth and de-sintering. De-sintering relieved the local constraint but increased the average pore size. This mechanism created stable pores with higher coordination numbers and, thus, decreased the driving 'stress' to deform the denser regions. Consequently, densification was retarded.

The de-sintering mechanism is shown in a more dramatic fashion in the model experiment in which the polycrystalline bridge is constrained from shrinkage. The dense shell densify quickly. An equilibrium is established between the low-density core and the polycrystalline bridges, preventing any shrinkage. The grains initially coarsened into a line of monocrystals so as to decrease the free energy of the bridge. Constrained from further shrinkage, it eventually led to de-sintering of the bridge to produce one large, continuous crack.

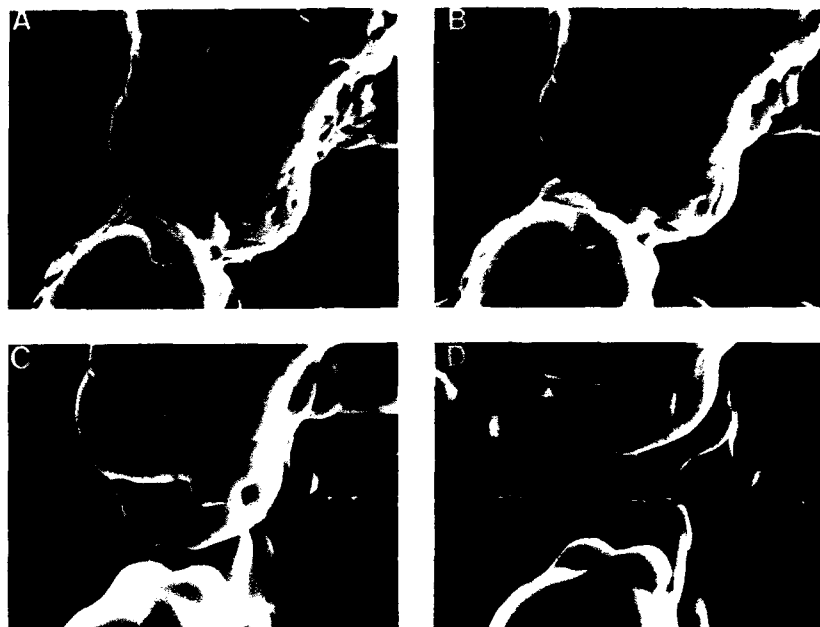


Figure 8: Evolution of a polycrystalline bridge in the model experiment with consecutive heat treatments at (A) 1450°C for 10 mins and then at 1600°C for (B) 10 mins, (C) 2 hours, (D) 3 hours.

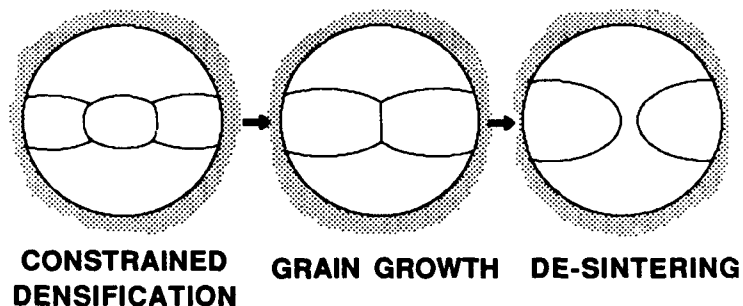


Figure 9: Schematic of de-sintering mechanism produced by coarsening.

This de-sintering process has been observed and the energetics modelled for the cases of the constrained polycrystalline fibers [12] and thin films [13]. A schematic of the microstructural evolution is shown in Fig. 9. Thermodynamic modelling has shown that the de-sintering of these grains could only occur after the grains have reached a critical aspect ratio (grain diameter to mass-center distance). Therefore, grain coarsening plays an active role in this mechanism by increasing the aspect ratio of the grains.

CONCLUSIONS

The present investigation described the microstructure of an Al_2O_3 composite powder containing ZrO_2 inclusions. Large cracks and large crack opening displacements, originating from processing flaws, were observed. More important, during densification of the powder matrix, a network of higher density material was formed, which encompassed low-density regions. Further densification of these low-density regions was constrained by the deformation of the denser material. These regions decreased their free energy by allowing de-sintering and the enlargement of pores, which subsequently led to the decrease in the driving 'stress' for further densification. The de-sintering process has also been shown using a model specimen. Previous works on constrained fibers and thin films have already described this thermodynamic instability.

ACKNOWLEDGEMENTS

The authors gratefully acknowledge stimulating and enlightening discussions with P. Mataga, A. G. Evans and K. T. Miller. E. B. Slamovich is acknowledged for supplying the specimen used in the de-sintering model experiment. This work was supported by grants from U.R.I. (contract n° N00014-86-K-0753), N.S.F. (contract n° DMR-87-13919) and the 'Société Européenne de Propulsion'.

REFERENCES

1. L.C. De Jonghe, M.N. Rahaman and C.H. Hsueh, *Acta Metall.* **34**, 1467 (1986).
2. R.K. Bordia and R. Raj, *Adv. Cer. Mat.* **3** [2], 122 (1988).
3. R. Raj and R.K. Bordia, *Acta Metall.* **32**, 1003 (1984).
4. C. H. Hsueh, A.G. Evans and R.M. McMeeking, *J. Am. Cer. Soc.* **69**, C-64 (1986).
5. P. A. Mataga and J. L. Bassani (private communication).
6. R.K. Bordia and G.W. Scherer, *Acta Metall.* **36**, 2393 (1988).
7. M.N. Rahaman and L.C. De Jonghe, *J. Am. Cer. Soc.* **67**, C-205 (1984).
8. F.F. Lange, *Acta Metall.* **37**, 697 (1989).
9. F.F. Lange, *J. Mater. Res.* **2** 59 (1987).
10. F.F. Lange, B.I. Davis and E. Wright, *J. Am. Cer. Soc.* **69**, 66 (1986).
11. B. Velamakani and F.F. Lange, submitted to *J. Am. Cer. Soc.*
12. K.T. Miller and F.F. Lange, *Acta Metall.* in press.
13. K.T. Miller, F.F. Lange, and D.B. Marshall, p.823-830 in Better Ceramics Through Chemistry III, edited by C.J. Brinker, D.E. Clark, and D.R. Ulrich, Materials Research Society (1988).

PROCESSING OF SiC-WHISKER REINFORCED Si_3N_4 M. J. Hoffmann^{*}, A. Nagel^{**} and G. Petzow^{*}

^{*}Max-Planck-Institute for Metal Research, Institute for Material Science,
Powdermetallurgical Laboratory, Heisenbergstr. 5, D-7000 Stuttgart 80,
West-Germany

^{**}Feldmühle AG, P.O. Box 1149, D-7310 Plochingen, West-Germany

Cold isostatic pressed (CIP) and slip cast Si_3N_4 composite materials containing up to 20 vol.% SiC-whiskers were densified by pressureless sintering and post-HIPing. The slips were characterized by viscosimetry and showed no influence of whisker loading on the rheology of the highly concentrated aqueous suspensions up to 15 vol.% whiskers. During casting the whiskers were preferentially aligned parallel to the mould surface and the CIPed samples showed a 3-dimensional random whisker distribution. The influence of the whisker length and orientation on the densification behaviour was studied in a high-temperature dilatometer. While the CIPed samples exhibit an isotropic shrinkage behaviour, the slip cast samples showed a strong shrinkage anisotropy with a maximum linear shrinkage of 21% perpendicular and only 7% parallel to the whisker plane for the samples with 20 vol.% whiskers. With increased whisker loading, the sintered densities decreased from 0.99 to 0.88 fractional density. The poor sinterability of the composites was attributed to the sintering stresses around the non-sintering SiC-whiskers and the formation of a whisker network which inhibits further shrinkage in the final stage of sintering. Thermodynamic calculations show the optimum fabrication conditions for SiC-whisker reinforced Si_3N_4 -composites.

INTRODUCTION

The application of many structural ceramics is limited by the brittle nature of the materials. In the past 5 years significant attention has been given to the development of whisker reinforced ceramics, which offers the possibility of high bending strength, high fracture toughness and high creep resistance, so that ceramic composites can be used in a wide range of applications [1].

The successful development of a whisker reinforced ceramic composite depends critically on the processing. Most important is the degree of homogeneity, which controls the final density and the flaw size of the sintered specimen. Whiskers with an aspect ratio of less than 30 flow and behave like powder, while whiskers with an aspect ratio of 50 to 100 bundle and clump [2]. Therefore, the commercially available SiC-whiskers, which have diameters $< 1 \mu\text{m}$ and an aspect ratio > 100 must be broken in order to avoid inhomogeneities and excessive voids in the composite.

Densification of whisker-matrix composite ceramics has mainly been achieved by hot-pressing [3,4]. Therefore, only simply shaped components, like cutting tools, could be easily manufactured. Without external pressure, the densification rate was found to be significantly reduced in whisker reinforced composites. During densification, tensile

hoop stresses will be generated around the non-sintering whiskers; those can even exceed the sintering potential and thus defect formation due to differential shrinkage is possible [5].

The purpose of the present paper is to explore different possibilities for the manufacturing of such composites. Cold isostatic pressing and slip casting are shaping methods of particular interest for composite ceramics. Uniform distribution of the whiskers, high green densities and the possibility to obtain preferred whisker orientations are attractive advantages of the slip casting process. The $\text{Si}_3\text{N}_4/\text{SiC}$ composites were slip cast and cold isostatic pressed (CIP) and subsequently densified by pressureless sintering and post-HIPing without any encapsulation. The densification behaviour will be analysed in terms of the influence of sintering temperature, whisker orientation and whisker loading. Thermodynamic calculations are used to explain the optimum temperature-nitrogen pressure region for post-HIPing.

EXPERIMENTAL PROCEDURE

The Si_3N_4 matrix powder (H.C. Starck LC 12) with 15 wt.% sintering additives (Y_2O_3 , Al_2O_3) was attrition milled for 4 h in isopropanol, dried and sieved. The SiC-whiskers (Tateho SCW 1-S, Japan) were separated into two specific length fractions by sedimentation in aqueous suspensions (5 wt% of solid) at pH 9 and stabilized by a polyacrylate (Dolapix PC 33, Zschimmer & Schwarz, FRG) [6] to investigate the influence of the whisker length on the densification behaviour. The whisker length distribution was determined by SEM-micrographs.

The specimens for the CIP-experiments were prepared by adding the matrix powder and the SiC-whiskers to isopropanol, tumbling for 24 h with plastic balls and subsequently drying in a rotation evaporator. The sieved whisker/powder mixtures were cold isostatic pressed at 630 MPa. The green compacts were densified by pressureless sintering under 0.15 MPa N_2 -pressure in a graphite-heated dilatometer at 1850 °C for 30 min and at 2000 °C with a N_2 -pressure of 0.5 MPa. Finally, hot isostatic pressing without encapsulation was performed at 100 MPa pressure at 2000 °C and with a soaking time of 10 min. To avoid whisker degradation, a N_2/Ar (100:1) gas mixture was used.

For the preparation of the $\text{Si}_3\text{N}_4/\text{SiC}$ slips, the sintering additives Y_2O_3 and Al_2O_3 were mixed before attrition milling and prereacted at 1400 °C for 4 h to form $\text{Y}_3\text{Al}_5\text{O}_{12}$. Complete reaction was confirmed by X-ray analysis. Aqueous slips with a solid content of 45 vol.% were prepared at pH 9 by deagglomeration of the powder in a ball mill for 1 h with addition of the deflocculant Dolapix PC 33. Subsequently, the sedimented SiC-whiskers were added and the slips were homogenized by tumbling for 24 h. The flow behaviour of the different slips containing 0, 5, 10, 15 and 20 vol.% SiC-whiskers was characterized by rotation viscosimetry (Haake Rotovisco RV 12, Karlsruhe, FRG). The highly concentrated slips were cast in moulds of plaster of Paris and the consolidated casts were subsequently dried in a controlled atmosphere for 3 d at 40 °C with 90% relative humidity. Dynamic dilatometry was applied to samples with defined whisker orientations during sintering in a graphite heated furnace at 1850 °C for 30 min.

The microstructure of the $\text{Si}_3\text{N}_4/\text{SiC}$ composites was characterized by optical and scanning electron microscopy (SEM) of fracture as well as polished surfaces.

RESULTS AND DISCUSSION

Slip Rheology and Shaping Methods

Figure 1 shows the flow behaviour of the aqueous slips with different whisker loadings. All slips had a solid content of 45 vol.% and exhibit a nearly Newtonian flow behaviour with a small extrapolated Bingham yield stress of 1 - 2 Pa. The viscosity, which was determined from the slope of the flow curves, was 25 - 30 mPas for the slips up to 10 vol.% SiC-whiskers and 50 mPas for the slip with 20 vol.% whiskers. No thixotropic viscosity increase could be detected for any of these slips. In contrast to successful deflocculation of the $\text{Si}_3\text{N}_4/\text{SiC}$ -slips with the addition of $\text{Y}_3\text{Al}_5\text{O}_{12}$ as sintering additive, the slip deflocculation was strongly diminished with Y_2O_3 -additions at $\text{pH} \leq 8.5$ due to the water-solubility of the Y_2O_3 [7].

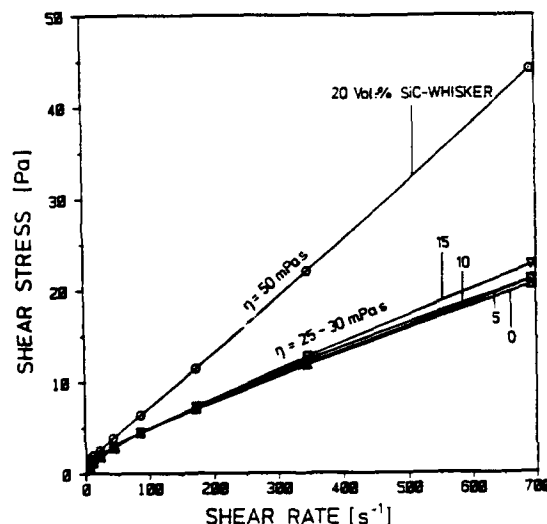


Fig. 1. Flow curves of the $\text{Si}_3\text{N}_4/\text{SiC}$ -slips with a solid content of 45 vol.% at various whisker loadings

The aqueous slips were consolidated by solid casting into moulds of plaster of Paris. During casting, the viscous flow of the water through the consolidating layer caused an alignment of the whiskers parallel to the mould surface. The whisker distribution in the slip cast and cold isostatic pressed (CIP) samples is drawn in Fig. 2. While the slip cast specimens showed an alignment of the whiskers parallel to the mould surface, the CIPed samples had a 3-dimensional random distribution of the SiC-whiskers. The green densities achieved with both shaping methods are listed in Table 1. These are calculated from the final densities of the sintered samples and from the sintering shrinkage. The values decreased from 0.64 to 0.58 (CIP) and from 0.66 to 0.62 (slip casting) with increasing whisker loading from 0 to 20 vol.%. The formation of a rigid network of impinging whiskers is believed to be the main reason for the decrease of the green densities with higher whisker loadings. This rigid network prevents a closer whisker-particle

packing. In the case of the slip cast samples, the formation of the 2-dimensional whisker network resulted in an anisotropic pore distribution with a closer particle packing perpendicular to the mould surface [7].

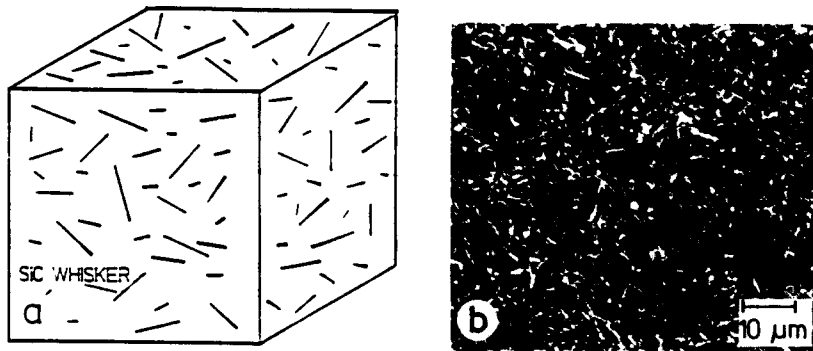


Fig. 2a. CIPed sample a) Schematic microstructure with a 3-dimensional random whisker distribution b) Optical micrograph of a composite with 20 vol.% SiC-whiskers sintered at 1850 °C and post-HIPed at 2000 °C and 100 MPa pressure.

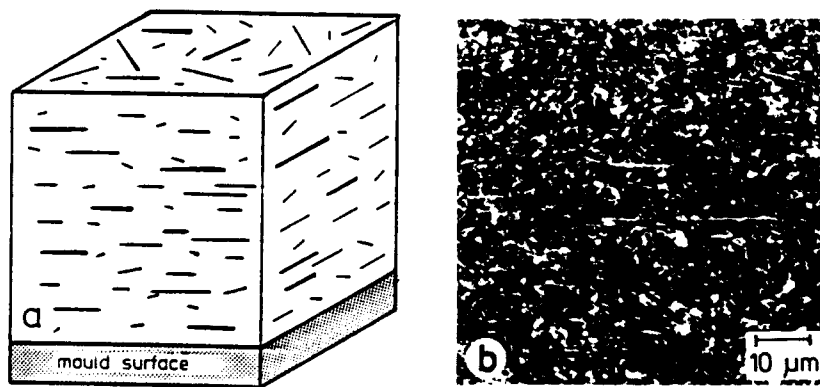


Fig. 2b. Slip cast sample a) Schematic of the microstructure with the 2-dimensional alignment of the whiskers parallel to the mould surface b) Optical micrograph of the whisker alignment in a slip cast sample with 20 vol.% whiskers after sintering at 1850 °C

Sintering

Figure 3 shows the densification behaviour of the CIP-samples with a whisker loading from 0 to 20 vol.% during linear heating with 45 K/min and subsequent isothermal sintering at 1850 °C for 30 min.

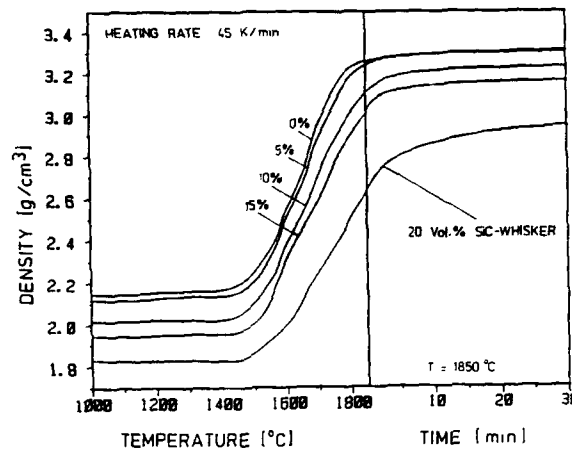


Fig. 3. Densification of the CIPed Si_3N_4 composites containing 0-20 vol.% SiC-whiskers during heating with 45 K/min and subsequent isothermal sintering for 30 min.

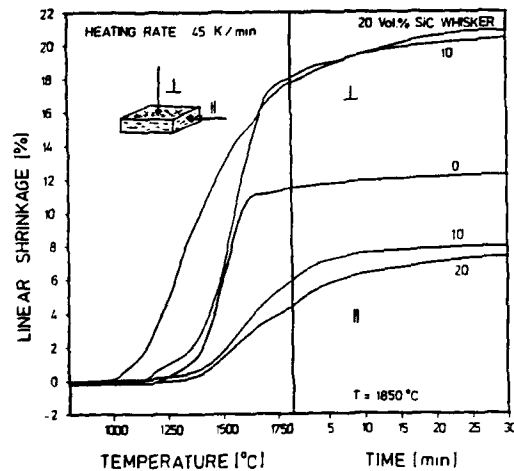


Fig. 4. Linear shrinkage of slip cast $\text{Si}_3\text{N}_4/\text{SiC}$ composites with 0, 10 and 20 vol.% whiskers perpendicular (\perp) and parallel (\parallel) to the whisker planes during linear heating with 45 K/min and subsequent isothermal sintering at 1850 °C.

While the shrinkage of all specimens started at a temperature of 1450°C, the sample without whiskers showed almost complete densification at the beginning of the soaking time and the composites revealed further shrinkage during isothermal sintering.

Slip cast samples had a strong anisotropic shrinkage behaviour in contrast to the CIPed specimens. The linear shrinkage parallel and perpendicular to the whisker orientation plane during linear heating with 45 K/min and subsequent soaking is shown in Fig 4. The sample without whiskers had a linear isotropic shrinkage of 12 %, while the shrinkage of the composites depends on the orientation of the SiC-whiskers. The specimen containing 20 vol.% SiC-whiskers had a linear shrinkage of 21% perpendicular and only 7% parallel to the whisker alignment.

The fractional green and the sintered densities of the CIPed and slip cast samples are listed in Table 1. Although the green densities of the CIPed specimen were much lower compared to the slip cast samples, the final densities were nearly the same.

Table 1. Fractional green and sintered densities (after sintering at 1850 °C for 30 min) of slip cast and CIP samples

whisker content vol. %	CIP		slip cast	
	green density	sintered density	green density	sintered density
0	0.64	0.99	0.66	0.98
5	0.63	0.99	0.65	0.98
10	0.61	0.97	0.64	0.97
15	0.60	0.94	0.61	0.94
20	0.57	0.89	0.62	0.89

Two main effects are considered to control the densification of the whisker composites: i) sintering stresses will generate around the non-sintering SiC-whiskers due to the extended volume shrinkage of the Si₃N₄ matrix [5,8] and ii) a rigid network of whiskers is formed which inhibits further shrinkage [9].

The densification process of the Si₃N₄ matrix is described as a solution-diffusion-reprecipitation mechanism. In the present investigated additive system (Y₂O₃ and Al₂O₃), the densification rate is assumed to be controlled by the grain boundary diffusion along the liquid film [10]. For the densification rate (dp/dt) the general expression [11]

$$\frac{dp}{dt} = \frac{A D_b \Omega}{kT} \frac{1}{G^m} \Sigma \quad (1)$$

can be derived. A is a geometrical constant, D_b the grain boundary diffusion coefficient, Ω denotes the molecular volume, k is the Boltzmann constant and T is the absolute temperature. The dependence of the grain size (G) is determined by the coefficient m, which is 3 in the case of a grain boundary diffusion controlled densification mechanism [12]. The sintering potential Σ is the driving force for the densification.

Viscoelastic backstresses $\sigma(t)$, which are generated around the whisker inclusion are assumed to reduce the sintering potential and therefore the densification rate of the composite according to the relation [8]:

$$\left(\frac{dp}{dt}\right)_{\text{matrix}} / \left(\frac{dp}{dt}\right)_{\text{composite}} \sim \Sigma / \left[\Sigma - \sigma(t) \frac{v}{1-v} \right] \quad (2)$$

where v is the volume fraction of the SiC-whiskers.

The viscoelastic backstresses can be described in the general form [13]

$$\sigma(t) = \int_0^t \Delta \dot{\epsilon}(u) F(G, K, \eta, t-u) du \quad (3)$$

where t denotes the time, $\Delta \dot{\epsilon}(u)$ the linear densification strain rate differential and F is the stress relaxation function, which depends on the shear (G) and bulk (K) moduli and on the viscosity η .

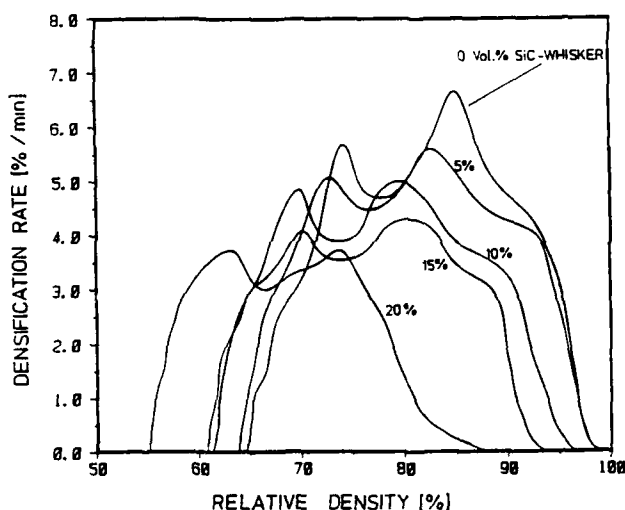


Fig.5. Densification rates of CIPed Si_3N_4 /SiC-whisker composites with different whisker loadings

Figure 5 indicates that the densification rates at the first characteristic maximum were significantly reduced from 5.6 %/min to 3.7 %/min, when the whisker content was increased from 0 to 20 vol.%. The reduced densification rate in this intermediate stage of sintering is due to the sintering stresses and the formation of the whisker network. With further increase in density the network-effect by impinging whiskers is getting more dominant so that the densification rate at the second characteristic maximum is reduced from 6.5 %/min for the material without whiskers to 3.7 %/min for the composite with 20 vol.% whiskers.

The strong shrinkage anisotropy of the slip cast samples can be mainly attributed to the formation of the whisker network. The shrinkage of the matrix within the whisker planes will be hindered by the impinging SiC-whiskers, so that the constraint volume element exhibits a high linear shrinkage of 21 % perpendicular to the whisker alignment in contrast to the shrinkage of 7 % in the direction parallel to it. A consequence of the anisotropic densification behaviour is the requirement of a uniform whisker orientation throughout the whole volume of the ceramic component. A nonuniform whisker orientation causes normal stresses, which cannot be relieved by creep and result in the formation of crack-like voids, as demonstrated in Fig. 6.

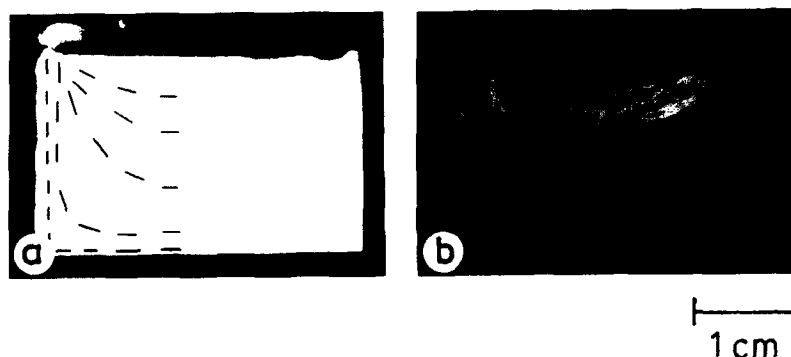


Fig. 6. Slip cast sample with 20 vol.% whiskers a) green compact with the schematic whisker distribution b) Crack formation during sintering due to the anisotropic shrinkage

Figure 7 shows the effect of the whisker network on the densification behaviour of CIPed samples. The density of the composites decreased with increasing whisker loading and an increasing whisker length and aspect ratio, respectively. In a specimen with 20 vol.% SiC-whiskers, the fractional density decreased from 0.89 to 0.845 when the mean whisker length was increased from 3.3 to 8.8 μm .

Table. 2. Fractional density of CIPed samples at different sintering conditions

Whisker content vol. %	fractional density		
	1850°C (30 min)	2000°C (30 min)	2000°C (60 min)
0	0.99	1.00	1.00
5	0.99	1.00	1.00
10	0.97	0.98	0.99
15	0.94	0.95	0.97
20	0.89	0.95	0.96

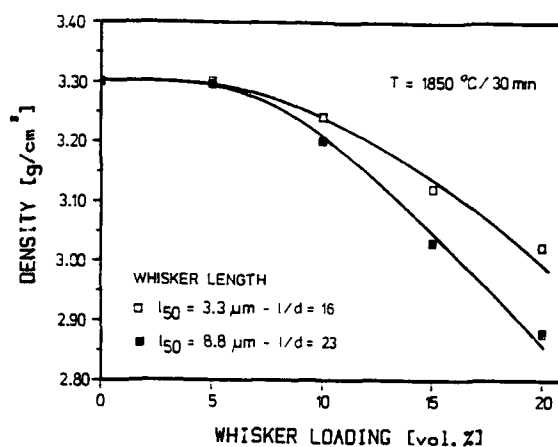


Fig. 7. Influence of the whisker loading and whisker length on the final densities of Si_3N_4 composites after pressureless sintering at 1850°C for 30 min.

Equation (3) indicates that the viscoelastic stresses could be reduced by a lower viscosity η . This can be realized by using a sintering additive system with a low viscous oxynitride melt, by increasing the amount of additives, or by sintering at higher temperatures. The lower viscosity of the liquid phase also decreases the stiffness of the whisker network and increases the final densities of the composites. Table 2 gives the fractional densities of the CIPed composites with a mean whisker length of $3.3\text{ }\mu\text{m}$ sintered at 2000°C for 30 and 60 min in comparison to the CIPed samples sintered at 1850°C for 30 min.

Post-HIPing

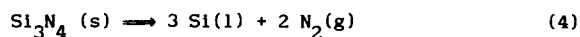
The CIPed samples, which were sintered at 1850°C were subsequently HIPed without encapsulation at 2000°C with a pressure of 100 MPa. The final densities after sintering and post-HIPing are listed in Tab. 3.

Table 3: Fractional sintered densities of the composite ceramics after pressureless sintering and subsequent HIPing.

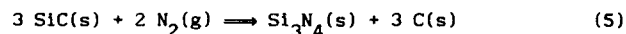
whisker content vol. %	fractional density	
	sintered	HIPed
0	0.99	1.00
5	0.99	1.00
10	0.97	1.00
15	0.94	0.97
20	0.89	0.90

The densities revealed that a further increase in density could be achieved in composites up to 15 vol.% SiC-whiskers. The residual porosity in the sample with 15 and 20 vol.% whiskers is due to open porosity.

Thermodynamic considerations [14] showed that the matrix decomposition reaction



and the whisker degradation reaction



must be taken into account to find the optimum temperature and pressure conditions for the HIPing of Si₃N₄/SiC composites. Fig. 8 indicates that stable composite materials without whisker or matrix degradation can only be obtained when the external nitrogen pressure and the sintering temperature lie between the two equilibrium curves for equations (4) and (5). The thermodynamic calculations show that a successful HIPing of Si₃N₄/SiC composites with an applied pressure of 100 MPa at 2000 °C could be performed with a gas mixture of argon to nitrogen of 100 to 1.

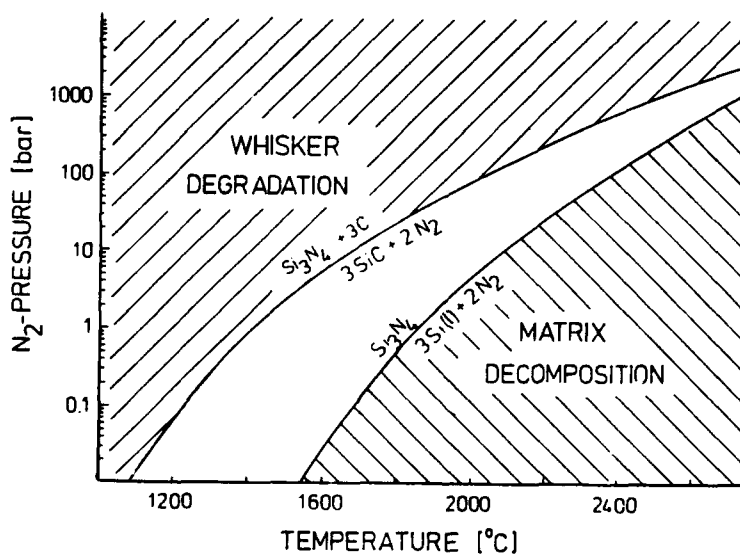


Fig. 8. N₂-partial pressures as a function of temperature for the Si₃N₄ decomposition and whisker degradation reactions according to eqs. (4) and (5). Undegraded composites will be obtained only in the limited area between both curves [14].

CONCLUSIONS

Shaping methods using slip casting and cold isostatic pressing were investigated for SiC-whisker reinforced Si_3N_4 . The highly concentrated slips exhibit a nearly Newtonian flow behaviour and were consolidated into green compacts of high densities. Pressureless sintering of the composites showed the influence of the whisker length, whisker loading and whisker orientation on the densification behaviour. The reduced densification rate of the composites was explained by hydrostatic sintering stresses and the formation of a rigid whisker network. Slip cast samples exhibit a strong anisotropic shrinkage and showed the formation of crack like voids due to a nonuniform whisker orientation. The final density after pressureless sintering was independent of the whisker orientation and the green densities. Sintering temperatures of 2000 °C, higher amounts of sintering additives and additive compositions with a lower viscosity of the liquid phase will reduce the sintering stresses and increase the final densities. Further densification without any matrix decomposition and whisker degradation could be achieved by HIPing in a N_2/Ar atmosphere in accordance with the thermodynamic calculations.

REFERENCES

1. L.J. Schioler and J.J. Stiglich, *Am.Ceram.Soc.Bull.*, **65**, 289, (1986).
2. J. V. Milewski, *Advanced Ceramic Materials*, **1**, 36, (1986).
3. N. Claussen and G. Petzow, *Journal de Physique*, 693, (1986).
4. G.C. Wei and P.F. Becher, *Am. Ceram. Soc. Bull.*, **64**, 298, (1985).
5. R. Raj and K. Bordia, *Acta Met.*, **32**, 1003, (1984).
6. M.J. Hoffmann, P. Greil and G. Petzow, in *Science of Ceramics 14*, edited by D. Taylor, (Stoke-on-Trent, 1987), p.825.
7. M.J. Hoffmann, A. Nagel, P. Greil and G. Petzow, *J. Am. Ceram. Soc.*, **72**, [5], 765, (1989).
8. L.C. DeJonghe and M.N. Rahaman, *Acta metall.*, **36**, (1988), 223.
9. F.F. Lange, *J. Mater. Res.*, **2**, (1987), 59.
10. S. Hampshire and K.H. Jack in *Progress of Nitrogen Ceramics*, edited by F.R. Riley, (Nijhoff Publishers, 1983), p.225.
11. M.N. Rahaman, L.C. De Jonghe and R.J. Brook, *J. Am. Ceram. Soc.*, **69**, 53, (1986).
12. R.L. Coble, *J. Appl. Phys.*, **30**, 234, (1959).
13. C.H. Hsueh, A.G. Evans, R.M. Cannon and R.J. Brook, *Acta Met.*, **34**, 927, (1986).
14. K.G. Nickel, M.J. Hoffmann, P. Greil and G. Petzow, *Advanced Ceramic Materials*, **3**, 557, (1988).

Acknowledgement

The Federal Ministry for Science and Technology (BMFT) is gratefully acknowledged for the financial support under contract No 03 M 2012 8.

Author Index

- Akinc, Mufit, 31
 Aksay, Ilhan A., 73, 83, 155, 171, 331

 Bagley, B. G., 95
 Barboux, P., 95
 Beaman, Donald R., 283
 Beier, W., 103
 Berglund, Kris A., 106, 119, 127
 Bolt, John D., 149
 Brunson, Ronald R., 23
 Byers, Charles H., 23

 Carr, M. J., 37
 Celikkaya, Ahmet, 31
 Chang, Chi K., 109
 Chick, Larry A., 331
 Cima, M. J., 319
 Coleman, D. J., 163

 Davis, Robert F., 213
 De Jonghe, Lutgard C., 353

 Eastman, J. A., 255
 Eatough, M. O., 37

 Frischat, G. H., 103

 Gagliardi, Charles D., 127
 Glaeser, Andreas M., 293
 Gonsalves, Kenneth E., 247
 Greulich, F. A., 37

 Hamada, Noriaki, 343
 Haraguchi, Ichiro, 343
 Harris, Michael T., 22
 Hirano, Shin-Ichi, 181

 Hirata, Yoshihiro, 3, 343
 Hoffmann, M. J., 369
 Holm, Elizabeth A., 319
 Hori, Saburo, 3, 343

 Irons, G., 235
 Ishihara, Yoshimi, 343

 Katatae, Y., 13
 Kato, Akio, 13
 Kato, Kazumi, 181
 Khan, S. A., 95
 Kim, C. W., 267
 Kim, Seong-II, 83
 Kuwabara, Makoto, 205

 Lam, David C. C., 309, 363
 Lange, Frederick F., 191, 309, 363
 Lannutti, John J., 155
 Lessard, Ronald B., 109, 119
 Liao, Y. X., 255
 Lipeles, R. A., 163
 Liu, Jun, 73, 83

 Marshall, L., 65
 Matsushita, Shinichi, 343
 McGrath, J. E., 137
 Meek, Thomas T., 267
 Miller, K. T., 191

 Nagel, A., 369
 Nagelberg, Alan S., 275
 Nakagama, Susumu, 343
 Narayanasamy, A., 255
 Nehls, M. A., 267
 Nocera, Daniel G., 109, 119

Oertling, W. Anthony, 109

Panitz, J. K. G., 37

Park, S. S., 267

Pechenik, Alexander, 283

Petzow, G., 369

Pyzik, Aleksander J., 283

Rahaman, Mohamed N., 353

Rajagopalan, Raj, 53

Rhee, Dong-Joo, 171

Rödel, Jürgen, 293

Sarikaya, Mehmet, 83

Schilling, Christopher H., 155

Schnoeller, M., 45

Shigaki, Yoshiki, 3

Shih, Wan Y., 73, 83

Shih, Wei-Heng, 73, 83

Siegel, R. W., 255

Smolik, G. R., 235

Sōmiya, Shigeyuki, 3

Spinu, M., 137

Stangle, Gregory C., 171

Strutt, Peter R., 247

Sudre, Olivier, 309, 363

Takeshita, Y., 13

Torres, F. E., 95

Valone, Steven M., 227

Varacalle, Jr., D. J., 235

Viney, Christopher, 331

Voight, J. A., 37

Wallace, Mary M., 109

Walter, J. A., 235

Wersing, W., 45

Wilson, G. C., 235

Xiao, Tongsan D., 247

Yanagida, Hiroaki, 199

Yoshimura, Masahiro, 3

Zukoski, IV, C. F., 65

Subject Index

- AlN fibers, 149
- aggregation, 73
- aligned phase, 331
- alkoxides, 127
- Al₂O₃, 255, 363
 - SiO₂, 3
 - TiO₂, 3
 - ZrO₂, 3
- Al₂O₃/Al₂O₃/metal, 275
- Al₂O₃/SiC/metal, 275
- alumina, 23, 293
 - fibers, 149
 - powder, 343
- aluminum
 - alkoxides, 23
 - nitride, 213
 - oxide, 213
 - titanate, 3
- analytical modeling, 235
- anisotropic shrinkage, 369
- axial ratio, 331
- binder removal, 171
- BL capacitor, 205
- boron nitride, 213
- bulk density, 103
- carbon contents, 103
- catalyst, 103
 - free, 137
- celi model, 53
- ceramic
 - composites, 353
 - fibers, 149
 - films, 213
 - particles, ultrafine, 247
- ceramic dispersions
 - structure of, 53
- ceramic matrix composite, 319
 - microstructure, 275
 - processing, 275
- ceramics, 95, 309
- chemical
 - durability, 103
 - processing, 181
 - sensor, 199
 - shifts, 103
- chemical vapor deposition, 3
 - plasma-assisted, 213, 227
 - remote plasma, 213
- chopped-fiber composites, 331
- close packing, 65
- cluster size, 331
- clusters of rods, 331
- coarsening, 363
- coatings, 213
- cold plasmas, 213
- colloid, 73, 83
- colloidal
 - crystals, 53
 - forces, 53
 - interactions, 53
- composite(s), 309
 - ceramic matrix, 319
 - chopped-fiber, 331
 - engineering, 331
 - whisker, 319, 331
- composite materials
 - cold isostatic pressed (CIP), 369

- slip-cast Si_3N_4 , 369
- computer simulation, 319
- condensation, 103
- constitutive relationships, 171
- constrained densification, 309, 363
- crack healing
 - high-temperature, 293
- cracking, 163
- cryptate, 119
- crystallization, 37, 73
- CVD (chemical vapor deposition), 3
 - plasma-assisted, 213
 - remote plasma, 213
- densification, 53, 293, 353, 363
 - behavior, 369
 - constrained, 309, 363
- density, 103
- Derjaguin-Landau-Verwey-Overbeek
 - potentials, 53
- desintering, 363
- diamond, 213, 227
- dielectric properties, 149
- diffusion, 163
- diffusion-limited kinetics, 163
- directed metal oxidation, 275
- disordered porous materials, 171
- dispersion, 343
- drying
 - gel, 163
 - rates, 163
- elastic content, 83
- electron cyclotron resonance, 213
- electronic packaging materials, 149
- epitaxial, 191
- epitaxy, 191
- equation of state, 53
- evaporation, 163
 - kinetics, 163
 - rate, 163
- fibers, alumina, ceramic, 149
 - short, 149
 - woven/nonwoven, 149
- films, 127
- filtration, 343
- flaw elimination, 293
- fluorescence, 109
- fluoropolymer composites, 149
- fractal aggregates, 53
- freeze drying, 37
- functionalized polydimethylsiloxane, 137
- GaAs, 213
- gas chromatography, 163
- gas condensation method, 255
- gel(s), 83, 127
 - silicon tetramethoxide, 163
- gelling time, 103
- grain boundary mobility, 293
- grain-size stability, 255
- H_2S , 31
- hafnium isopropoxide, 127
- hard spheres, 65
- hardness, 103
- heterogeneities, 353
- high-temperature crack healing, 293
- homoepitaxial, 191
- homogeneous precipitation, 13
- hot pressing, 283
- hydrolysis, 103
- infrared spectroscopy, 247
- injection molding, 171
- inorganic polymer, 155
- intelligent material, 199
- interface design, 199
- internal stress distribution, 171
- ionic compound, 37

- IR, 127, 267
- isothermal compressibilities, 53
- kinetics
 - of precipitation, 31
 - processing, 275
- Knoop microhardness, 103
- lanthanide, 119
- $\text{Li}(\text{Nb}, \text{Ta})\text{O}_3$ films, 181
- liquid/glass phase transition, 65
- liquid-like ordering, 53
- liquid precursors, 191
- materials synthesis, 247
- maximum packing fraction, 65
- mechanical model, 331
- metal alkoxide, 181
- metalloporphyrins, 109
- metallo-organic solution
 - deposition (MOSD), 163
- methoxy, 137
- MgO , 255
 - doped, 293
- microstructural evolution, 293
- microstructure, 205
- microwave, 267
 - applications, 45
 - plasmas, 213
- mixed linkages, 103
- model experiments, 293
- monodisperse, 31
- monolithic samples, 103
- Monte Carlo, 331
 - simulations, 53
- mullite, 3
- nanocrystalline materials, 247
- nanophase oxides, 255
- nanoscale, 293
- network, 103
- nonaqueous suspension, 155
- nucleation
 - on surface, 227
- ordered phase, 53
- organic modifiers, 137
- orientation, 369
- osmotic pressures, 53
- p/n contact, 199
- packing, 73
 - of rods, 331
- particle/particle interactions, 155
- $\text{Pb}(\text{Fe}, \text{W})\text{O}_3$ ferroelectrics, 205
- percolation, 171, 319, 331
- periodic colloid structures, 53
- phase transitions, 53, 73
 - liquid/glass, 65
- phosphorescence, 119
- photolithography, 293
- plasma spray, 235
- plastic deformation, 283
- polymer degradation, 171
- pore drag structures, 293
- pore-size distribution, 343
- porous granular materials,
 - partially saturated, 171
- porphyrins, 109
- positional relaxation, 53
- powder(s), 31, 37, 309
- powder preparation, 3
- precipitation
 - homogeneous, 13
 - kinetics of, 31
- precursor(s), 247
 - solutions, 103
- preferred orientation film, 181
- pressure
 - densification, 283
 - filtration, 83
- processing, 309

- processing aids
 - removal of, 171
- Raman, 127
 - spectroscopy, 109
- reaction kinetics, 103
- remote plasma CVD, 213
- rheology, 95, 343
- ROC process, 283
- rod
 - alignment, 331
 - concentration, 331
- rod-shaped particles, 331
- salt, 267
- sedimentation behavior, 155
- ^{29}Si NMR, 103
 - spectrum, 103
- silicate networks, 137
- silicon
 - carbide, 213
 - nitride whisker, 343
 - tetramethoxide gels, 163
- Si_3N_4 surface layers, 247
- $\text{SiO}_2\text{-TiO}_2\text{-ZrO}_2$ gel
 - glasses, 103
 - products, 103
- Si-O-Ti bonds, linkages, 103
- sintering, 255, 293, 319, 353
 - stresses, 369
- site percolation, 319
- sol-gel, 45, 95, 137, 163
 - film, 109
 - glass, 109, 119
 - method, 181
 - processing, 127
- sols, 127
- specific surface, 103
- spherical titania particles, 13
- SrTiO_3 -based, 205
- stress distribution, 171
- structural
 - coarsening, 331
 - transitions, 53
- superconductor, 95
- surface
 - diffusivities, 293
 - structures, 293
- synthesis, 255
 - materials, 247
- temperature, 267
- tetramethylorthosilicate (TMOS), 137, 163
 - evaporation, 163
- theoretical model, 171
- thermal
 - conductivity, 149
 - expansion, 149
 - plasmas, 213
- thermal decomposition
 - of thioacetamide, 31
- thermocouple, 267
- thermodynamic calculations, 369
- thermogravimetric analysis/mass spectrometry, 171
- thermogravimetry, 163
- thin films, 191
- TiO_2 , 255
- titania, 23
- titanium
 - dioxide, 213
 - isopropoxide, 127
 - nitride, 213
 - oxysulfate, 13
- transport
 - in porous materials, 171
- ultrafine ceramic particles, 247
- urea, 13
- viscoelasticity, 83

viscosity, 95, 103

whisker

composites, 319, 331

length, 369

network, 369

xerogels, 45

X-ray diffraction, 45

XRD, 31

yield strain, 83

zeta potential, 343

zinc oxide (ZnO), 213, 255

zirconia, 191, 267

coatings, 235

zirconium propoxide, 103, 127

ZnS powders, 31

ZrO₂, 191, 283, 363

ZrO₂-toughened Al₂O₃ (ZTA), 3

ZTA (ZrO₂-toughened Al₂O₃), 3